2

UCRL-21086, Vol. 2

Seismic Coupling of Nuclear Explosions

Volume 2

Defense Advanced Research Projects Agency
1400 Wilson Blvd.
Arlington, VA 20305

Donald B. Larson, Editor

Lawrence Livermore National Laboratory

UCRL--21086-Vol.2
DE93 005499

SEISMIC COUPLING OF NUCLEAR EXPLOSIONS

Defence Advanced Research Projects Agency
1400 Wilson Blvd.
Arlington, VA 20305

Donald B. Larson, Editor

DISCLAIMER

TABLE OF CONTENTS

SOURCE AND MATERIAL MODELING PROJECT:

EXPERIMENTAL FACILITIES AND WAVE

PROPOGATION RESULTS

D. B. Larson

CONTENTS

SUMMARY AND CONCLUSIONS
WITH
RECOMMENDATIONS

The new Giant Magnet Experimental Facility employing digital recording of explosion induced motion has been constructed and successfully tested. Particle velocity and piezoresistance gage responses can be measured simultaneously thus providing the capability for determining the multi-component stress-strain history in the test material. This capability provides the information necessary for validation of computer models used in simulation of nuclear underground testing, chemical explosion testing, dynamic structural response, earth penetration response, and etc.

Noise sources such as the explosive detonating system and AC power have been located and eliminated so that the limiting signal to noise ratio is determined by the noise level inherent in the amplifiers that are required to obtain particle velocity data at the extremely low strains of interest to this project.

Multiple turn particle velocity gages have been fabricated and shown experimentally to amplify the particle velocity signal accurately without significant amplification of noise.

With the use of multiple turn gages it has been possible to obtain particle velocity time histories to strains as low as 5×10^{-7} and yet maintain signal to noise ratios greater than 5 to 1. Therefore, the primary objective of this experimental project, "To obtain accurate particle velocity measurements at strains where rocks are believed to be linear", has been accomplished.

Fully coupled and cavity decoupled explosions of the same energy (0.622 kJ) were carried out as experiments to study wave propagation and attenuation in polymethylmethacrylate (PMMA). These experiments produced particle velocity time histories at strains from 2×10^{-3} to as low as 5.8×10^{-6}. Other experiments in PMMA, reported recently by Stout and Larson[8], provide additional particle velocity data to strains of 10^{-1}.

In the work by Stout and Larson both particle velocity time histories and piezoresistance gage response were measured and used to infer the multi-component stress-strain history in PMMA. The results of that work suggest that in the shock front nonequilibrium thermodynamics and dissipation processes are occurring in PMMA, but at stresses below dynamic yielding and behind the shock front an isotropic elastic material response is a reasonable first model for material behavior. Furthermore, the dissipation processes occurring in the shock front provide for a strong attenuation of the wave amplitude as it propagates, with the strongest attenuation occurring at the greater scaled distances. At these greater distances the wave front is more dispersive, with the decay of peak particle velocity inversely proportional to distance cubed, indicating a strong preferential loss of the high frequency components of the wave.

The experiments on Sierra White granite were successful in obtaining wave propagation data over the strain interval between 2×10^{-2} and 5×10^{-7} for use in deriving the attenuation properties of this medium. Unfortunately, despite the contrary recommendations of this author, the

limited funds remaining were spent on dome salt rather than on completing the work on Sierra White granite. Therefore, the multiple explosion experiments to obtain the maximum strain level for superposition were not carried out nor were enough cavity decoupling experiments conducted to define in any detail the cavity decoupling phenomenology.

A long standing reluctance to scale the attenutation response in granite and other geologic media because of an apparent sensitivity of attenuation, as measured by Q, to frequency may have been removed as a result of some work by Blair of CSIRO Australia. He has shown that a factor of five difference in Q's determined from resonance experiments at ~10 kHz as compared to Q's from wave propagation experiments at ~1 MHz can be accounted for by imposing simple elastic scattering on the grain clustors which characterize the particular granite that he studied. The obvious preliminary conclusion is that scaling in granite is a problem only as it is affected by grain size considerations and the resulting scattering. Thus small scale simulations of geologic media must eliminate scattering as an important process by minimizing grain size or the grain size must be scaled so that the scattering effect is identical between the medium of interest and the small-scale simulant.

ACKNOWLEDGEMENT

I would like to express my appreciation to all the people who have contributed to the construction and testing of the Giant Magnet Experimental Facility. In particular I would like to thank D. Watwood, S. Spataro, J. Finkes, J. Hearst, L. Dibley, G. Hickman, T. Erven and B. Selleck.

Thanks must also go to M. Denny for his continual support and encouragement. I would also like to extend my appreciation to the Department of Energy Containment Program and to the Defense Advanced Research Projects Agency for their financial support.

PART A

THE GIANT MAGNET EXPERIMENTAL FACILITY

Introduction

A new Giant Magnet Experimental Facility employing digital recording of explosion induced motion has been constructed at the Site 300 test area of the Lawrence Livermore National Laboratory. This magnet facility is unique in that it can accommodate material models as large as a 1.5 meter cube. These large models not only allow measurements at relatively high strains (i.e. 10^{-1} to 10^{-3}) but also at strains where geologic and other materials are believed to become linear in their response (i.e. 10^{-5} to 10^{-7}).[1-3] The facility is designed so that both particle velocity gages and piezoresistance gages can be used simultaneously in a single experiment or independently in duplicate experiments. Such measurements coupled with analysis of piezoresistance gage response provide the capability of determining the multi-component stress-strain history that is produced in the test material by explosion loading using spherical chemical explosive energy sources.[4-8] Furthermore, if these measurements are made accurately and at small enough radial spacing, they provide the basis for determining the equation of state or flow path over the interval of measurements for explosion induced wave propagation in the material under study. Thus, this capability can provide the information necessary for validation of computer models used in simulation of nuclear underground testing, chemical explosion testing, dynamic structural response, earth penetration response, and etc.

This facility because of its size is also amenable to study of the phenomenology associated with cavity decoupling as well as some forms of enhanced decoupling. In these cases the experiments can be carried out in either "mined" or explosion formed cavities, where the explosion formed cavities are produced previously in blocks of material, perhaps salt, that are subjected to high confining pressure in order to eliminate explosion induced surface fracturing or spalling of the blocks during cavity formation.

This experimental facility allows the use of at least two techniques for applying confining pressure. One technique employs a yoke and flat-jacks to apply a uniaxial pressure of up to ~2000 psi. The second technique uses a pressure vessel which contains the material model and which is loaded hydrostatically to as much as 5000 psi by introducing a pressurized fluid into the chamber of the vessel.

The facility can also be used to study: The phenomenology of cavity formation and its dependence upon material properties and confining pressure. The phenomenology associated with explosion induced fracturing in various materials as a function of confining pressure, explosion source geometry and energy. The phenomenology associated with layering, faults and other forms of material discontinuity as they are influenced by confining pressure and material properties. And a slightly more difficult problem, the phenomenology associated with explosions in highly porous media and how this phenomenology is influenced by material strength, by various levels of water saturation, and by pore pressure.

All such experimental data can be used directly for validating computer models used in chemical or nuclear explosion simulations. Furthermore, the preponderance of ground motion data suggests, that most if not all of this phenomenology can likely be directly scaled to the larger scale chemical explosions and/or nuclear explosions of interest to DARPA, DNA and DOE (see Figures A1 - A5).

The Experimental Facility

The experimental facility shown schematically in Figure A6 is composed of the giant magnet system, the explosive detonation system, the signal cables, the signal amplifier system, the digital recording system and the computer.

The poles of the Giant Magnet shown in Figures A7 and A8 are each composed of six donut shaped rings with 2.74 m outside diameter, 1.84 m inside diameter and 0.09 m thickness. These poles of final thickness 0.6 m are placed in the Helmholtz configuration to provide an optimum volume of uniform magnetic field through which the particle velocity gages move. The distance between the poles or pole gap at the Helmholtz spacing is 1.1 m and provides a reasonably uniform magnetic field of 2060 gauss at the geometric center when 800 amperes of current are applied to the coils. Figure A9 shows the change in magnetic field strength with distance from the geometric center in both the horizontal and vertical directions. The volume of uniform magnetic field ($\pm$ 1%) is a 20 cm cube.

Power for this magnet is provided by a 600 kw direct current power supply system with output current regulated. The system is 500 volts and 1200 amperes nominal. A ripple filter was installed as part of the magnet power system to reduce ripple in the magnetic field to a level below the sensitivity of the signal recording system.

The uniform magnetic field which is applied externally to the material model provides a stationary magnetic field through which the gages embedded in the material model move. The gages are thin (from 0.1 to 0.5 mm thick) and are made of a metal foil of copper encapsulated in a plastic insulator called Kapton. The motion of these thin metal foils, caused by the explosion induced shock wave propagating through the model, cut magnetic field lines and produce a voltage which is the product of the particle velocity of the gage (Up), the magnetic field strength (B), the effective length of the gage (ℓ), and the number of turns of the gage (n).

$$\varepsilon = (\hat{U}p \times \hat{B} \cdot \hat{\ell})\, n \qquad \ldots.(1)$$

In equation (1) the caps ($\hat{}$) represent vector quantities. Shown in Figures A10 and A11 are the standard gage design and a schematic of an experimental assembly, respectively. Various types of particle velocity gages were used. Close to the energy source where relatively high particle velocities were expected, a single element or single turn gage with an effective length of 9.00 mm was used. At greater distances, to increase the signal strength without increasing the noise, both the

effective length and the number of elements or turns of the gage were increased. The most "sensitive" gage had an effective length of 38.40 mm and 5 elements or turns which magnified the signal by a factor of 192 when compared to the single turn standard gage. These wider and thicker gages require more time for the shock wave to traverse and ring-up the gage but that time is only a small fraction of the rise time of the propagating wave at the distances and in the materials where these particular gages were employed. Therefore, these wider and thicker gages provide no limitation on the data that was recorded.

The signals induced in these gages are transmitted through ~30 m of AG108A/U triaxial cable to the amplifiers. This type of cable was used to operate the amplifier in common mode and isolate the signals from ground. The cables were twisted to eliminate extraneous signals. The amplifiers are Tektronix model AM502. They have a band pass DC to 1 MHz and a gain range from 100 to 100,000 with a noise level of ~15 μV referred to the input. The amplified signals are recorded on Transiac (now DSP Technology) Model 2010 wave form digitizers. These digitizers have up to 20 MHz sampling rate with 10 Bit resolution and 8K memory. A Transiac program called "Personalized Signal Processing Data Acquisition Software" is used to acquire and process the data on an IBM AT computer with 1 M Bit on-board memory and 30 M Bit hard disc memory.

The data acquisition system is designed to provide data in the range of strains between 10^{-1} and 10^{-7}. In the process of accomplishing this objective it was found that the amplifier noise of ~15 μV

limited the signal to noise ratio to ~10 to 1 at a strain of 10^{-6} and that the amplifier band width also limited the rise time that could be recorded to ~0.3 μs. However, this later restriction is not a practical limitation because high frequencies are strongly filtered during wave propagation within the medium (at least in the media that have been studied to data) which increases the rise time at the lower strains where amplification of the signal is required.

The explosions are typically 99 mg of PETN initiated by a mild detonating fuse (mdf), that is initiated by an SE-1 detonator which in turn is initiated by a capacitor bank discharge. The one meter length of mdf is used to provide ~150 μs for the electrical noise associated with the detonator to disappear before signals are produced by motion of the gages in the magnetic field.

The explosion initiation system turned out to be a source of electrical noise. This undesirable contribution to the gage signal caused a great deal of frustration before the source of it was located and eliminated. It was discovered that the undesirable parts of the signal were produced by the small piece of mdf that was inside the material model. These unwanted signals were of two kinds (see Figure A12 and A13). The first kind of noise was the result of the mdf energy coupling directly into the model material and propagating at sound speed through the model. This type of noise arrived at the gages following the arrival of the main explosion signal. This type of noise was eliminated by placing the mdf in a stainless steel tube and then decoupling the tube

from the material model by using a solid foam spacer. The second kind of noise was essentially constant in time, arriving at all gages a few microseconds before the main explosion wave arrival at the first gage. Examination of results from numerous tests indicated that the source of this noise was likely a local perturbation of the magnetic field caused by the lead jacket of the mdf moving in the magnetic field as the fuse detonated. This signal was reduced significantly when the mdf was placed in a stainless steel tube and virtually eliminated when the lead jacket was reduced from a diameter of 2.09 mm to a diameter of 1.57 mm.

Once these adjustments were made to the explosive initiating system it was possible to obtain records like the one shown in Figure A14 where the only significant systematic constraints on the quality of the data were the amplifier noise and noise or reflections associated with the finite boundaries of the model.

Summary and Conclusions

The new Giant Magnet Experimental Facility employing digital recording of explosion induced motion has been constructed and successfully tested. Particle velocity and piezoresistance gage responses can be measured simultaneously to provide the capability of determining the multi-component stress-strain history in the test material. This capability can provide the information necessary for validation of computer models used in simulation of nuclear underground testing, chemical explosion testing, dynamic structural response, earth penetration response, and etc.

Noise sources such as the explosive detonating system and AC power have been located and eliminated so that the limiting signal to noise ratio is determined by the noise level inherent in the amplifiers that are required to obtain particle velocity data at the extremely low strains of interest to this project.

Multiple turn particle velocity gages have been fabricated and shown experimentally to amplify the particle velocity signal accurately without significant amplification of noise.

With the use of multiple turn gages it has been possible to obtain particle velocity time histories to strains as low as 5×10^{-7} and yet maintain signal to noise ratios greater than 5 to 1. Therefore, the primary objective of this experimental project, "To obtain accurate particle velocity measurements at strains where rocks are believed to be linear", has been accomplished.

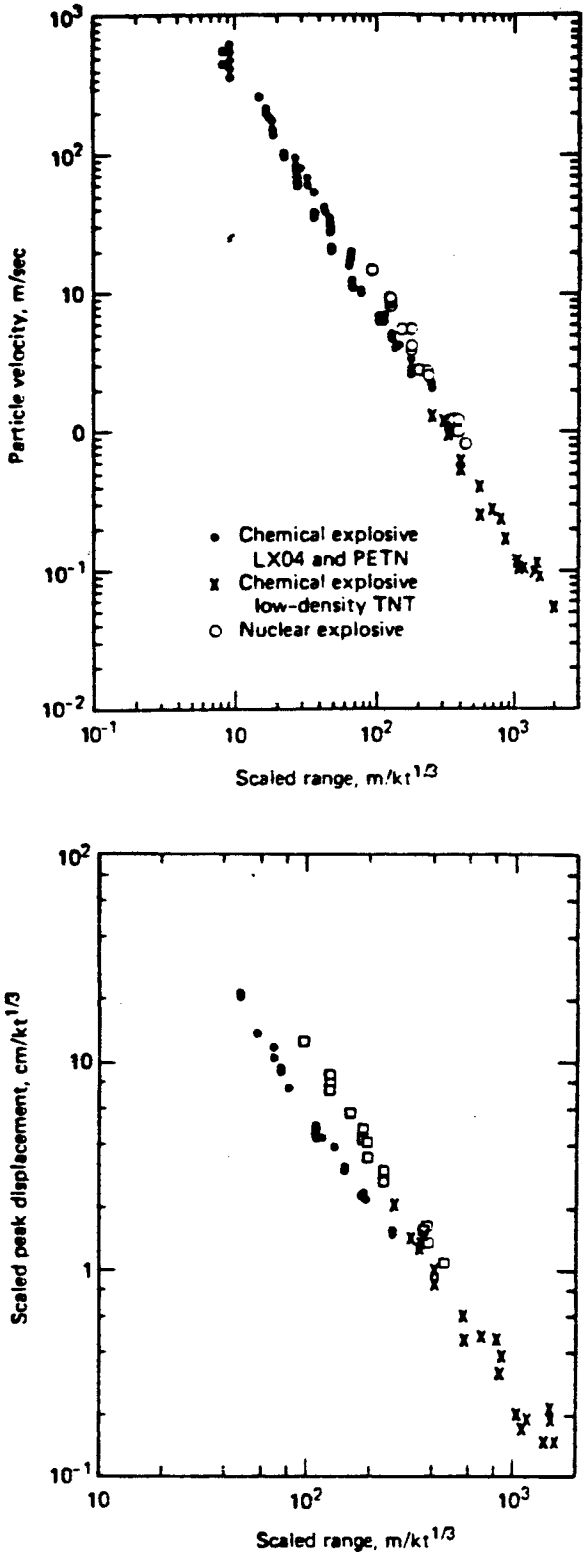

Figure A1. A comparison of peak particle velocities and peak displacements obtained from small scale experiments in pressed salt, the Cowboy series of chemical explosions in a salt dome and the Salmon nuclear explosion in a salt dome. The data are cube root scaled to one kiloton of energy. (see reference 9).

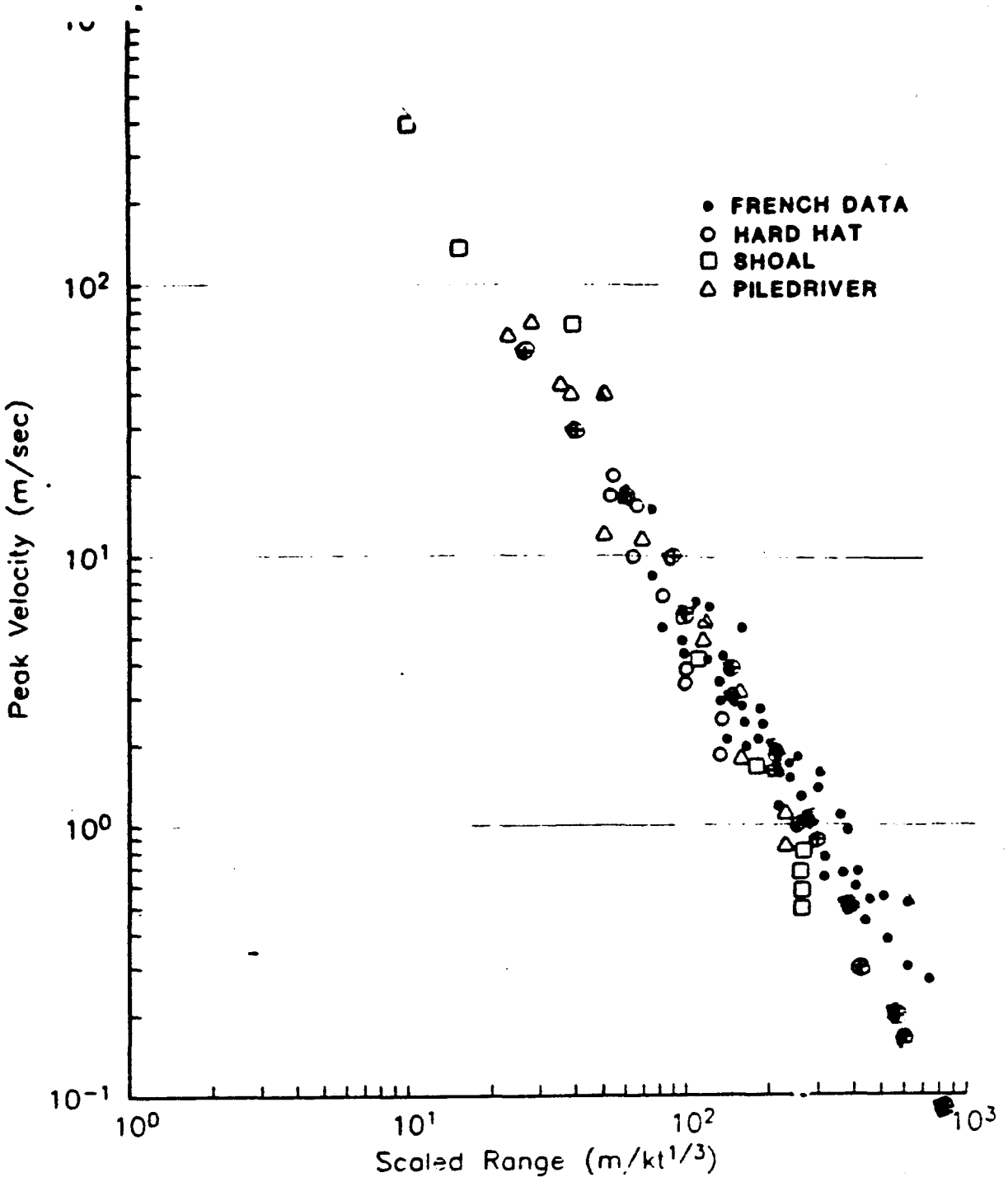

Figure A2. A comparison of peak particle velocities obtained from several nuclear explosions in granite and data obtained from small scale experiments in Sierra White granite (⊕). (see Part C of this paper).

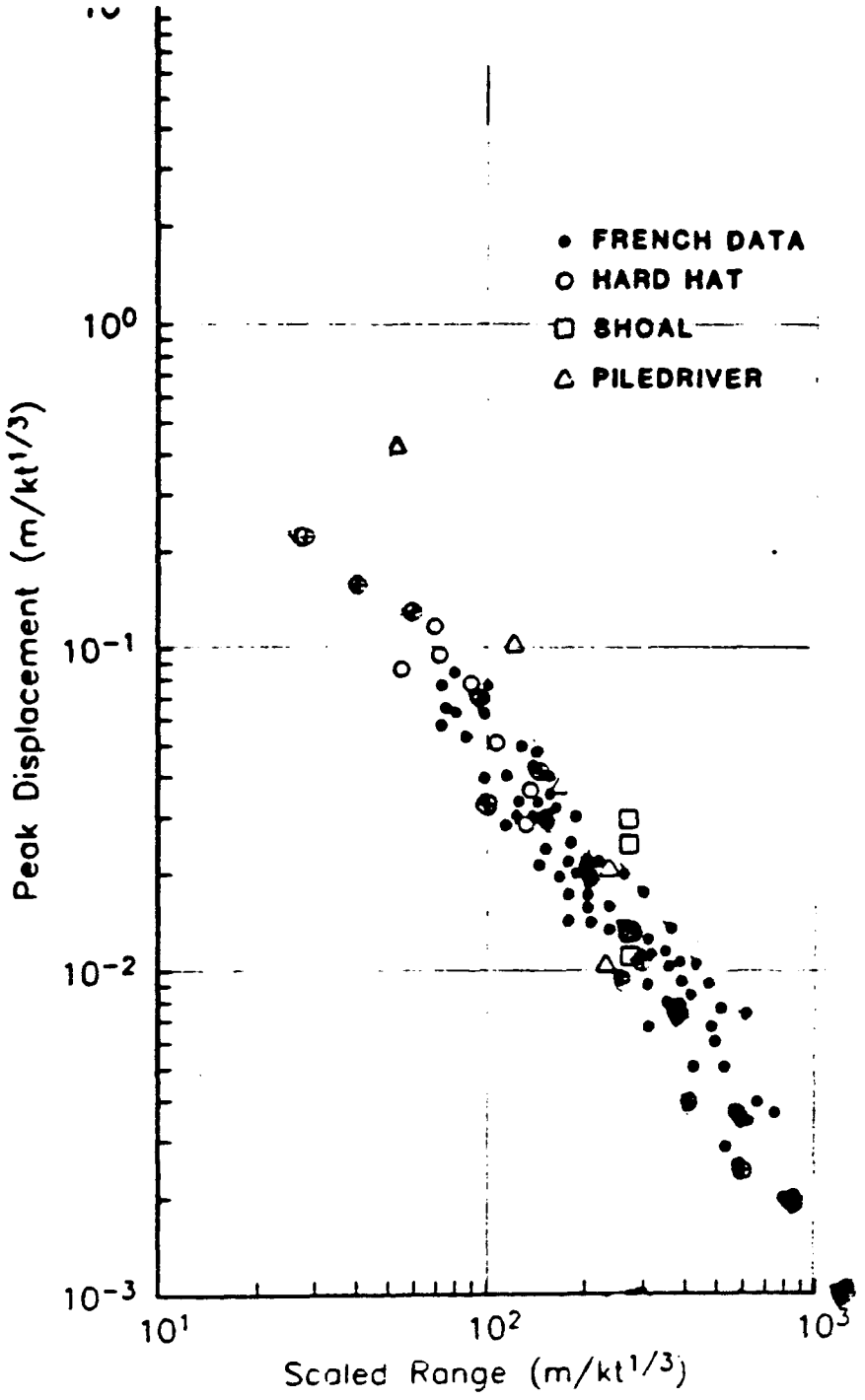

Figure A3. A comparison of scaled peak displacement versus scaled range for several nuclear experiments and several small scale experiments (⊕) in granite.

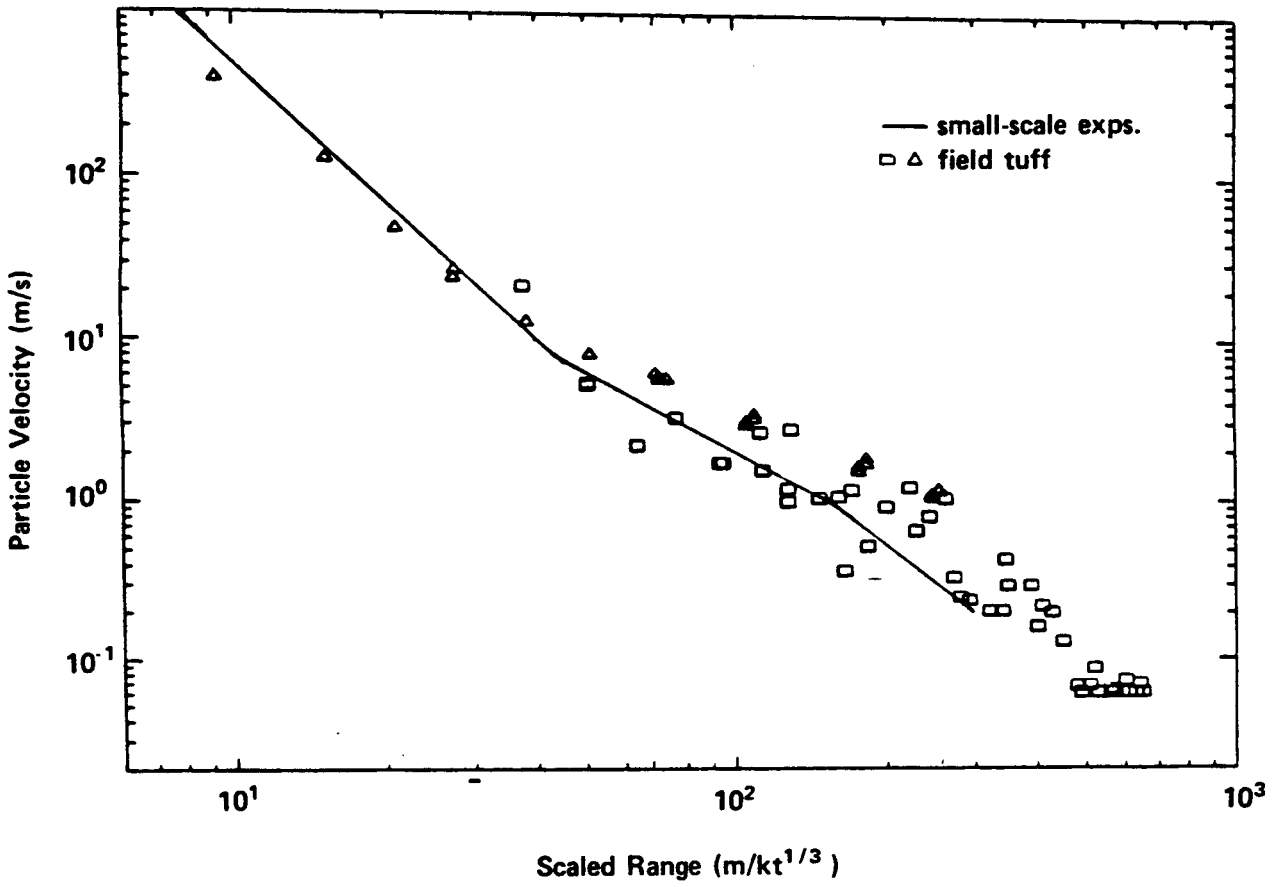

Figure A4. A comparison of small-scale experimental data with nuclear experimental data in dry tuff. (see reference 10).

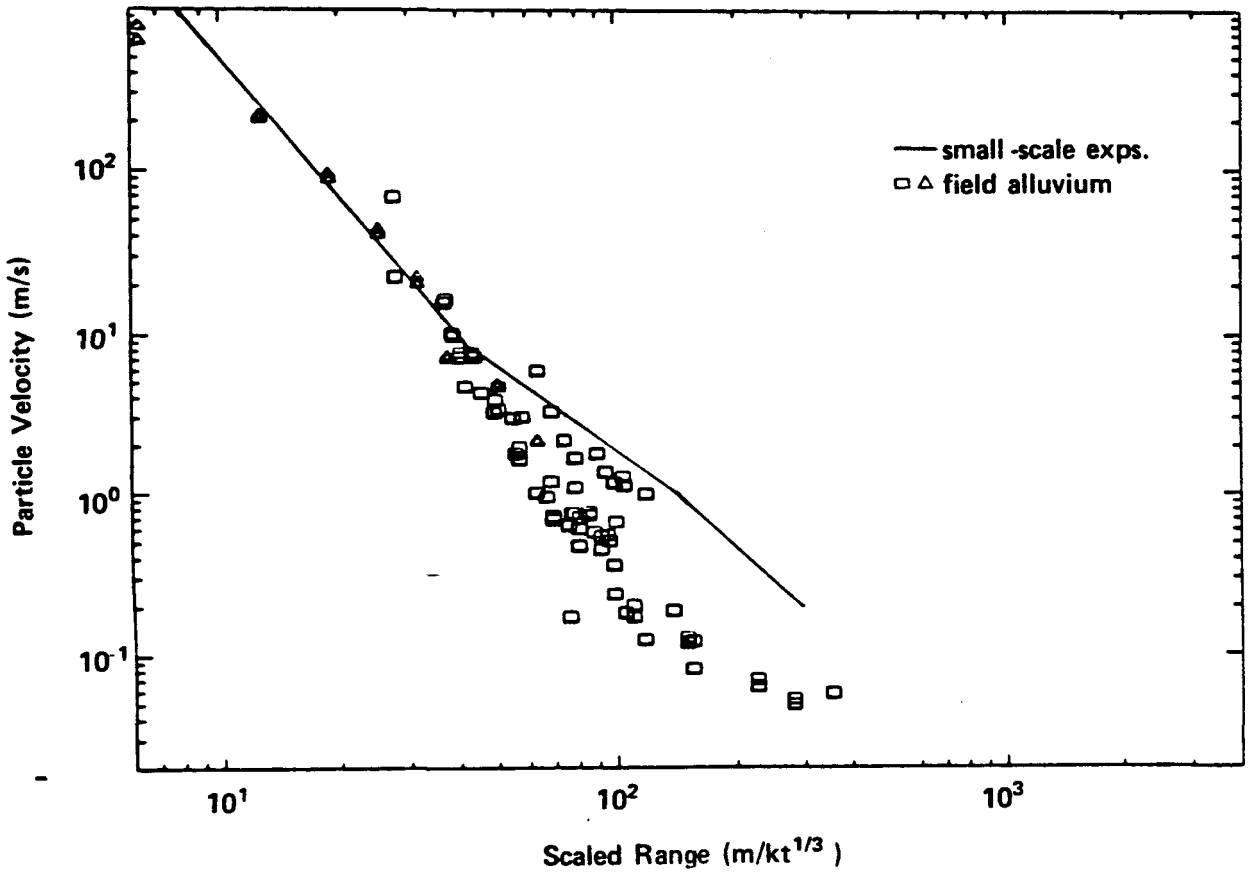

Figure A5. A comparison of small-scale experimental data with nuclear experimental data in dry alluvium.

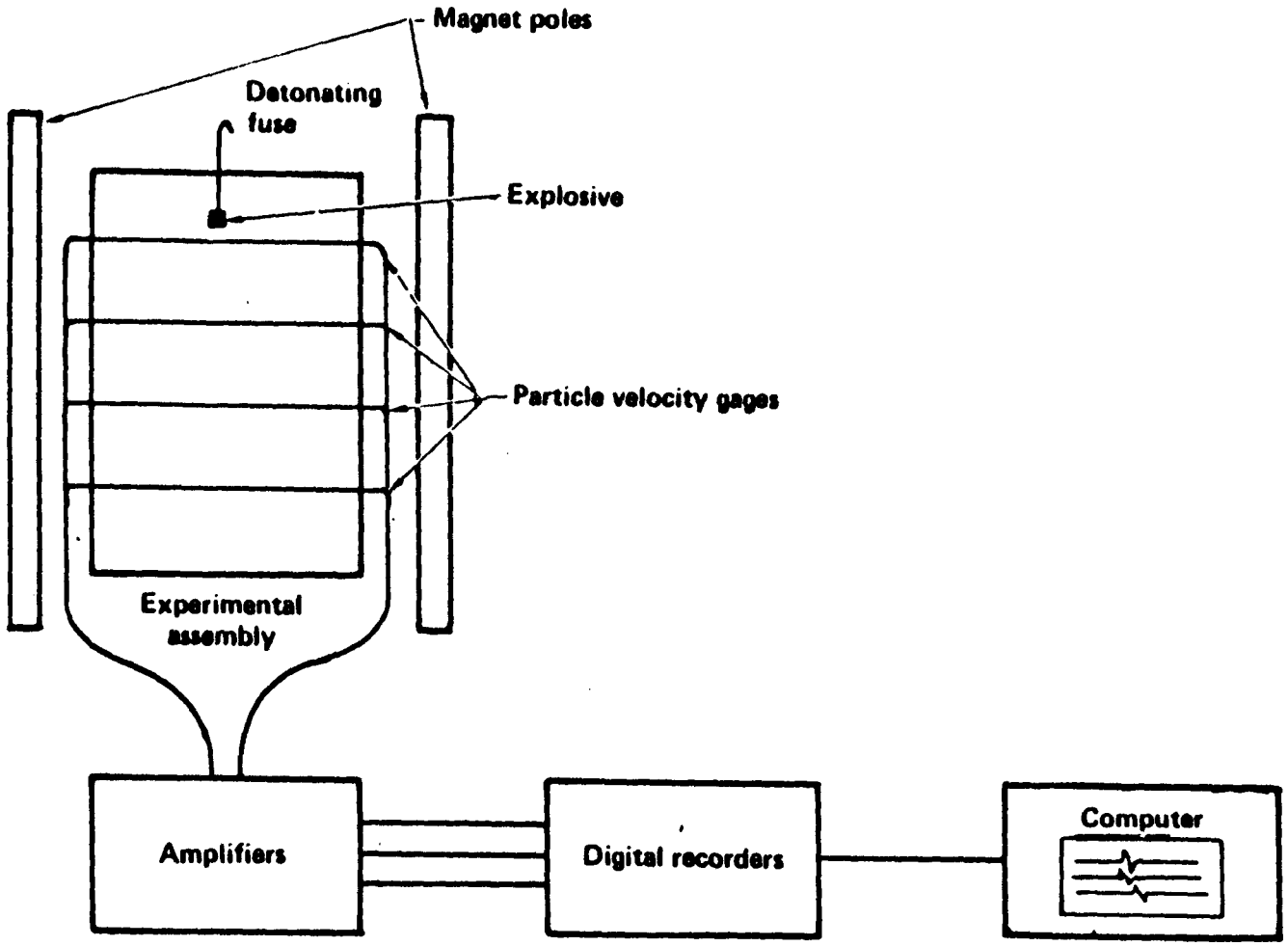

Figure A6. A schematic of the Giant Magnet Experimental Facility showing the magnet and digital recording system.

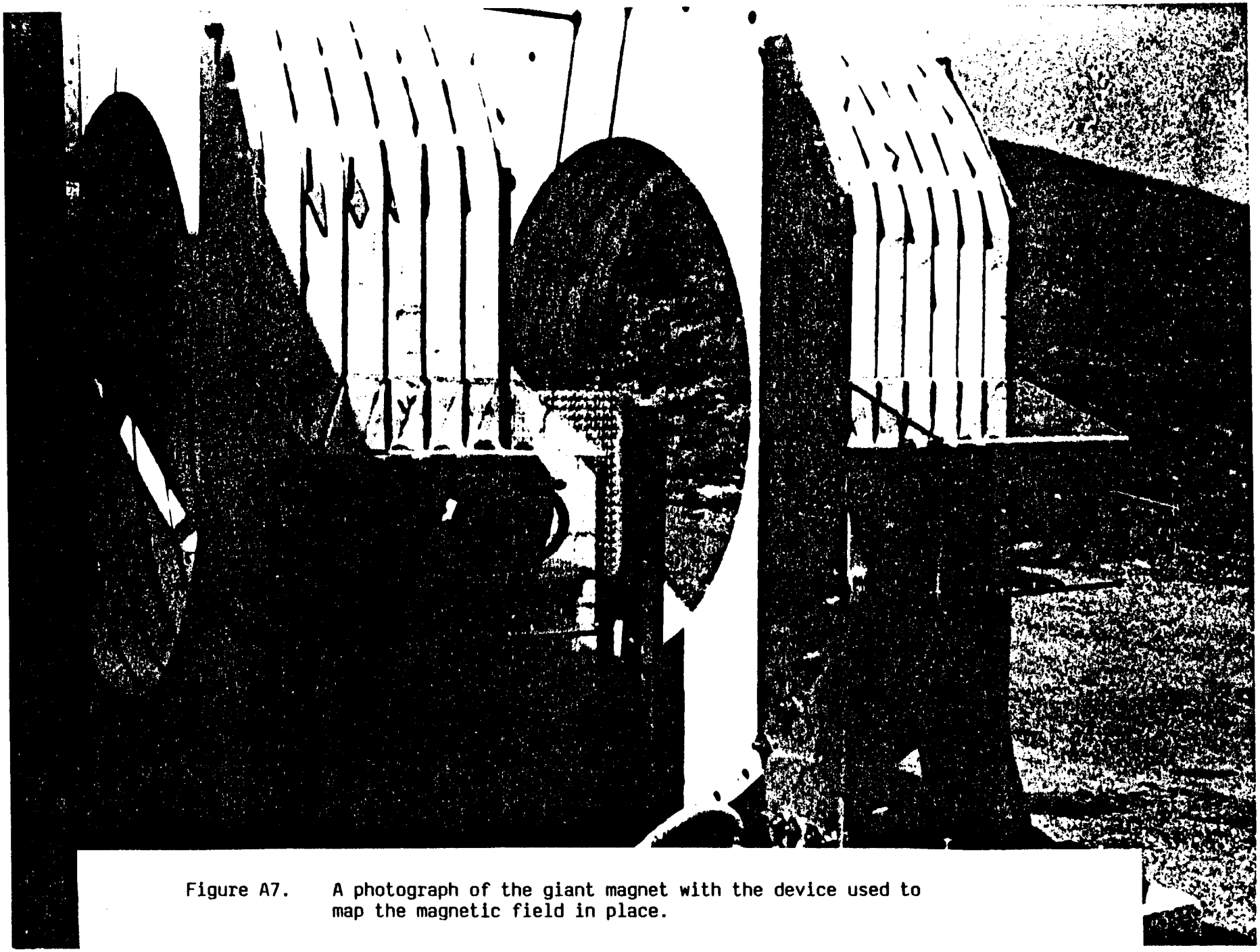

Figure A7. A photograph of the giant magnet with the device used to map the magnetic field in place.

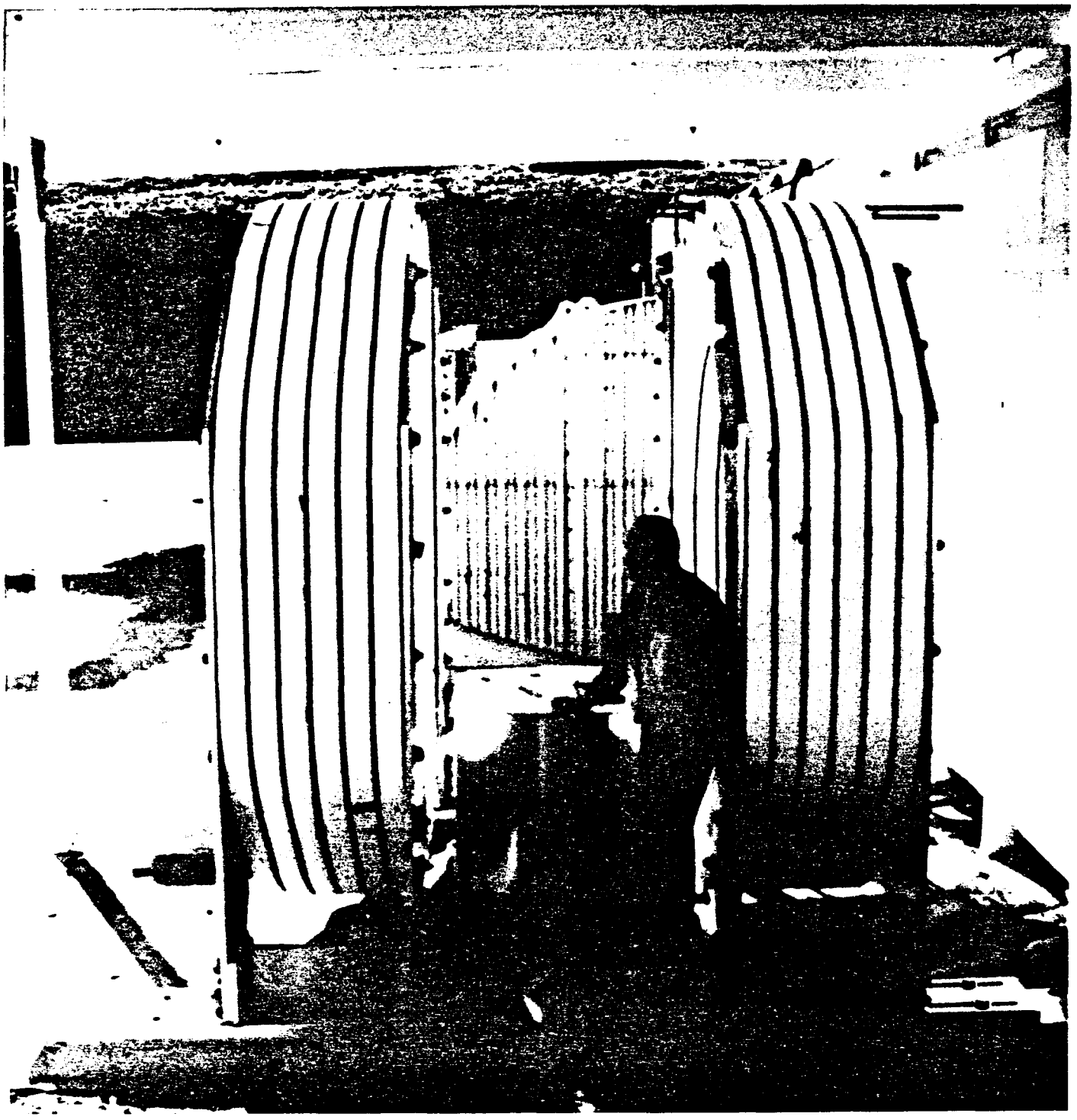

Figure A8. A photograph of the giant magnet showing the 1.1m gap and a scientist contemplating his next move.

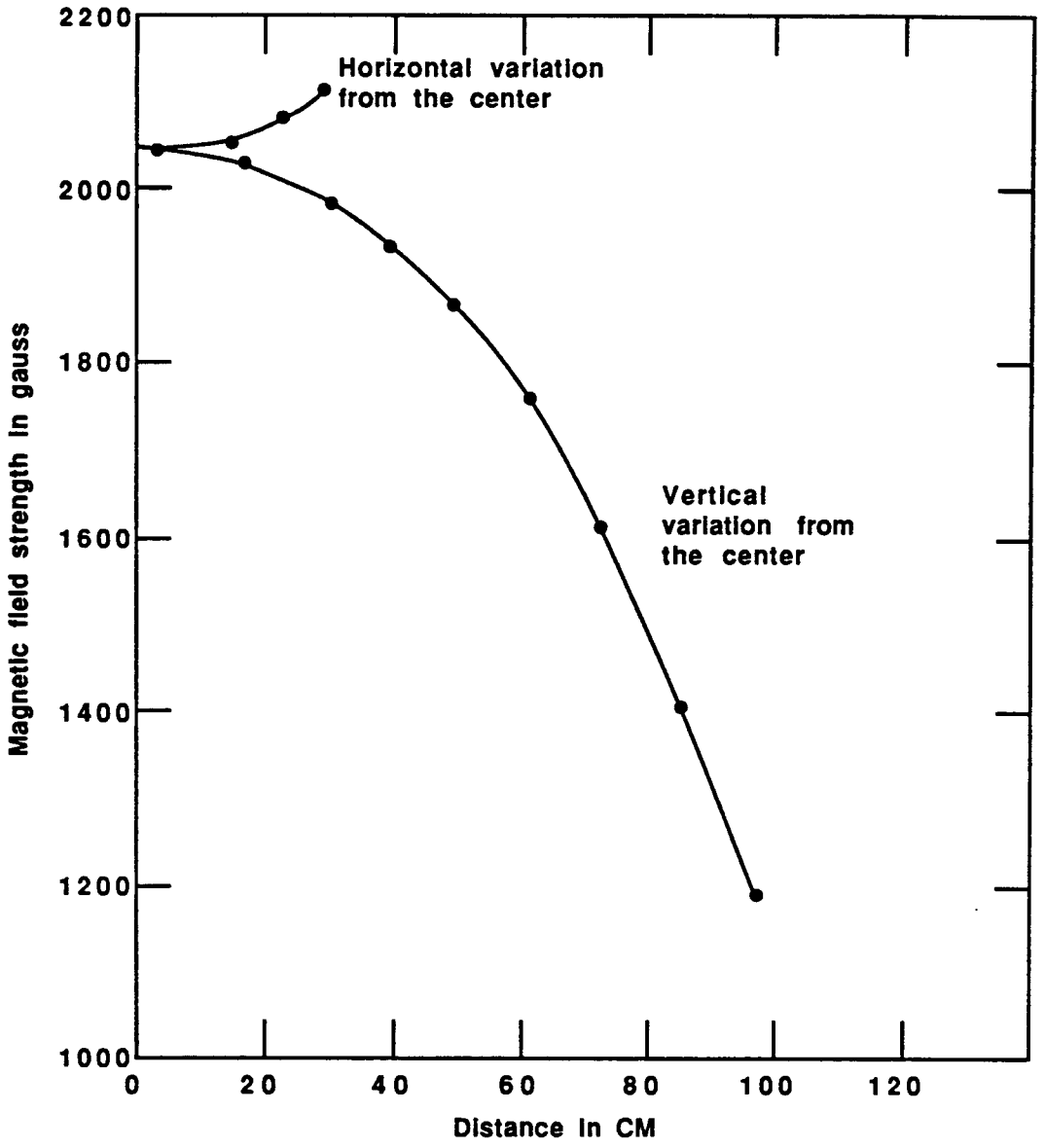

Figure A9. Variations in the magnetic field strength with distance from the geometric center. 800 amperes of current was used to produce this field.

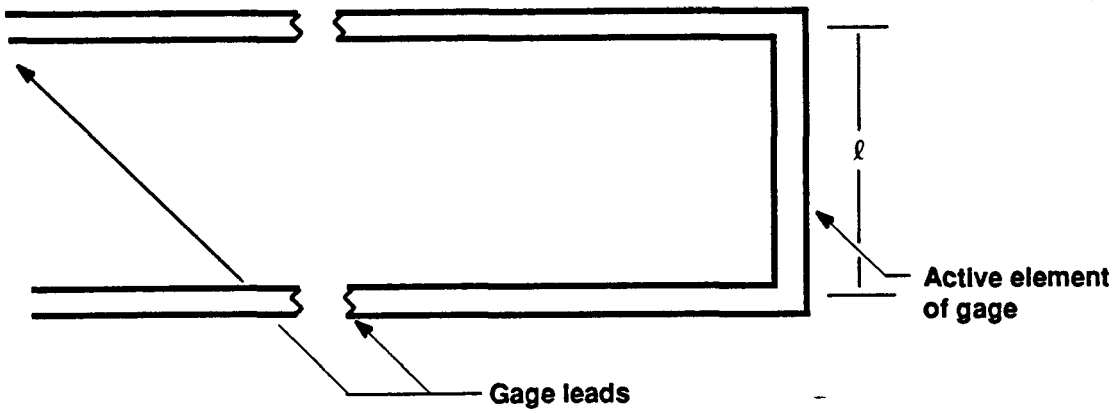

Figure A10. The basic design of a particle velocity gage showing the active element with effective length ℓ (9mm for the standard gage) which cuts magnetic field lines as it moves through the field. The gage leads are of various lengths depending upon the material model and move parallel to the magnetic field lines.

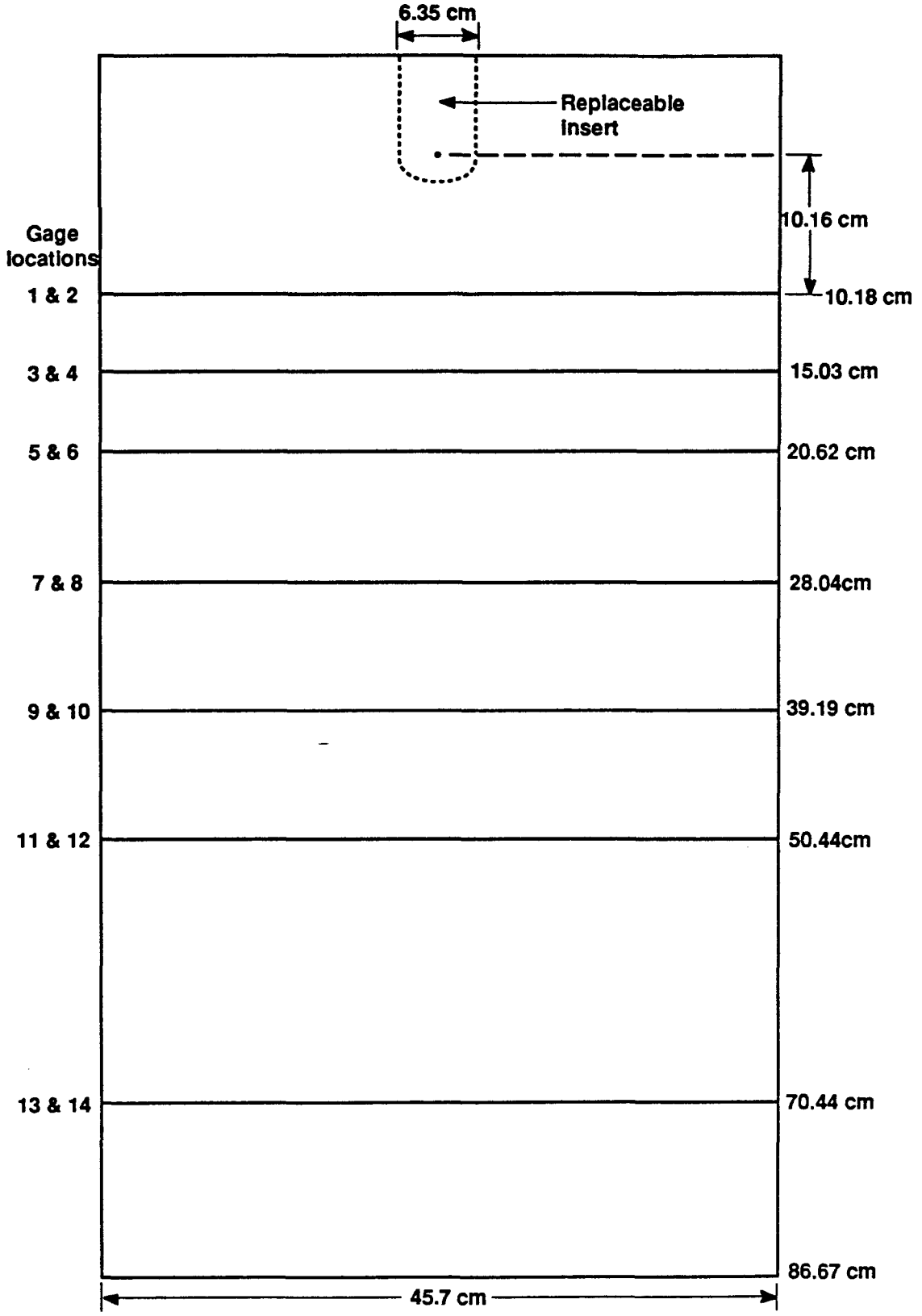

Figure A11. A schematic of the PMMA assembly showing the gage locations, the distance from the center of the explosion to the various gages and the replaceable insert that contains the explosion damage and thereby allows repeating experiments.

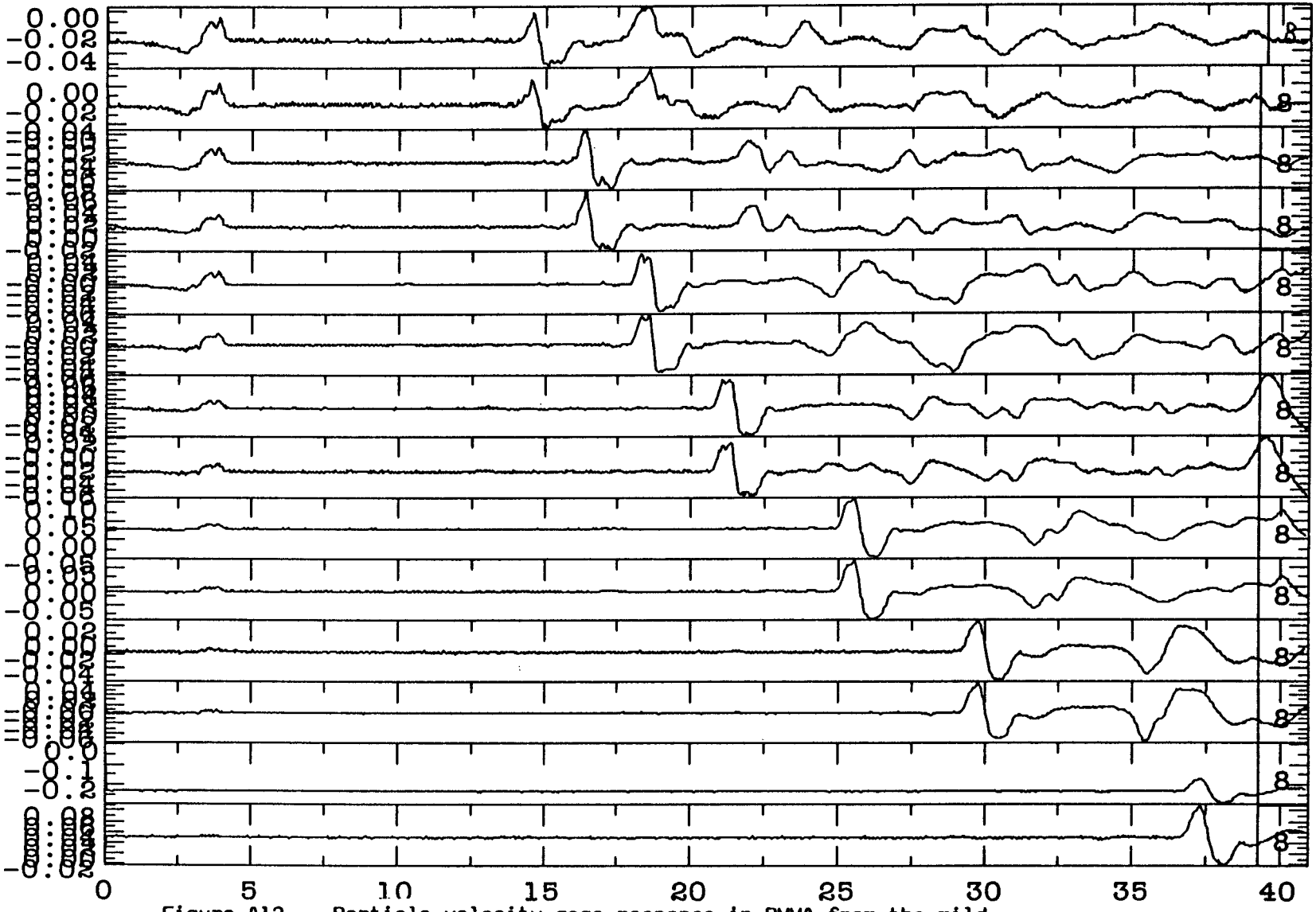

Figure A12. Particle velocity gage response in PMMA from the mild detonating fuse showing the two kinds of noise produced by the fuse. The first noise burst at 25 μs is essentially constant in time for all gages, while that beginning at 150 μs in the first gage propagates to the different gages at sound speed in PMMA

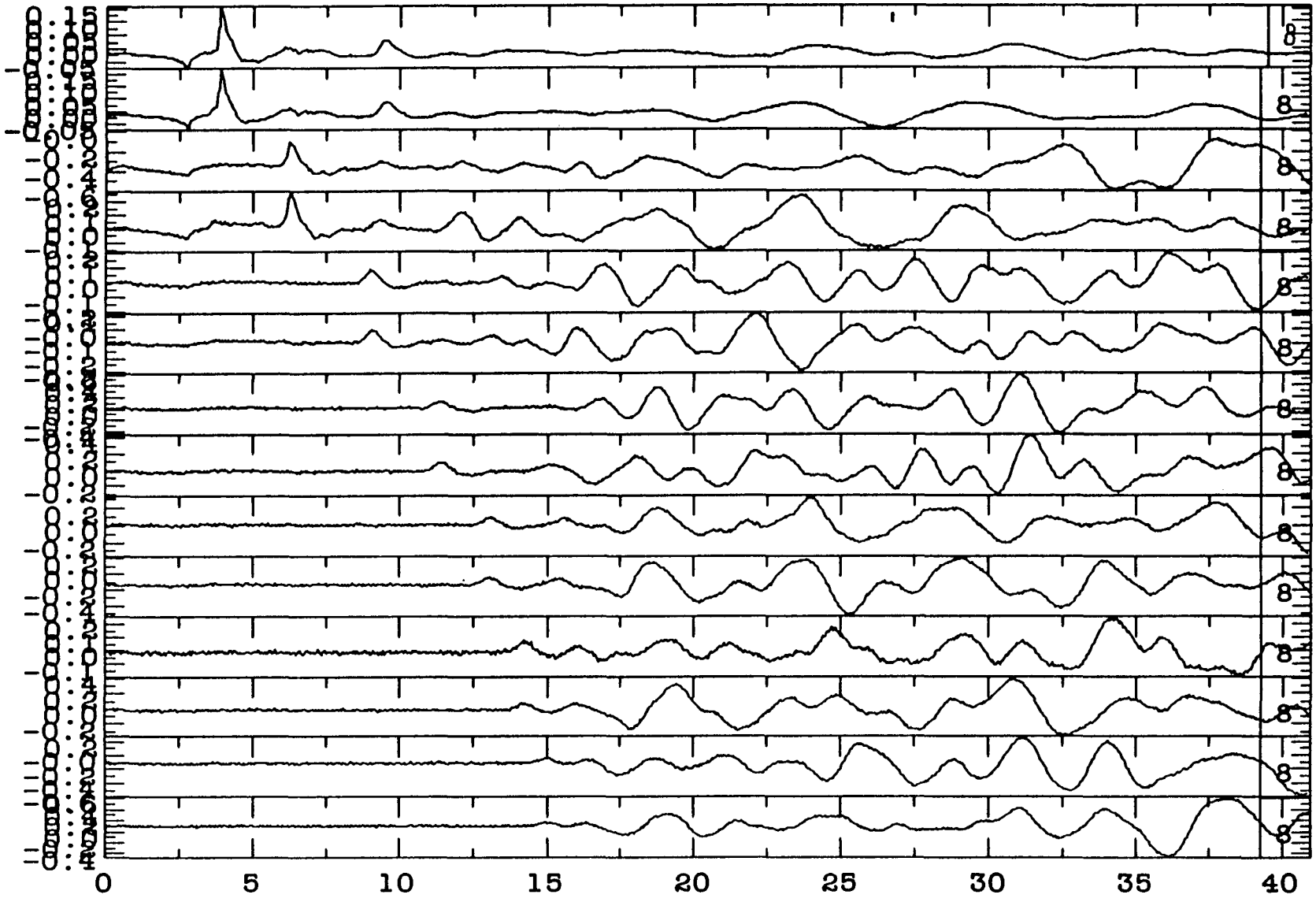

Figure A13. These records in Sierra White granite show the effect on wave propagation data of that part of the noise signal that is essentially constant in time at all gages. The effect of the other noise source is masked by the data itself.

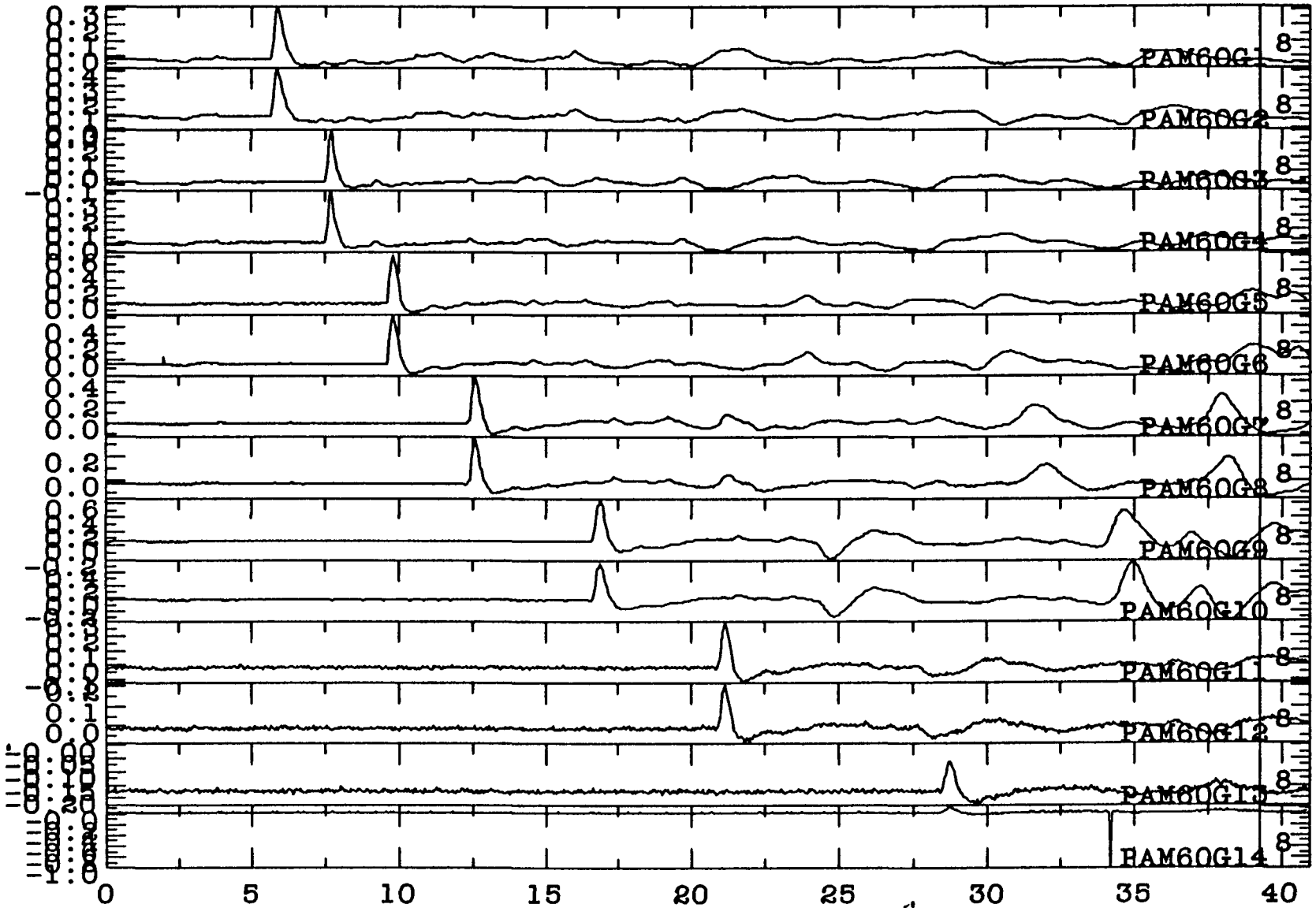

Figure A14. These records from a decoupled 0.622kJ explosion in PMMA show the effect of elimination of the mdf as a source of signal pollution.

PART B

WAVE PROPAGATION STUDIES IN PMMA

Introduction

Polymethylmethacrylate (PMMA) was selected as a test material for use in debugging the new digital data acquisition system and as it turned out in debugging the explosive initiation system as well. PMMA has advantages over geologic materials as a test medium because it has been extensively studied under dynamic loading conditions and because it is a non-conductor, non-magnetic, isotropic, and homogeneous. These material characteristics are essential to high-accuracy reproducible particle velocity and piezoresistance gage measurements.

These results in PMMA coupled with results from other studies, primarily the results reported recently by Stout and Larson[8] on "Multi-Component Stress-Strain History Measurements and Analysis," provide the data necessary to validate a material response model for PMMA when subjected to dynamic or shock wave loading in the stress interval below dynamic yielding. This interval covers the range of strains from 1.5×10^{-2} to the limit of these data which is a strain of 5.8×10^{-6}.

Experimental Procedures and Results

The PMMA used in these studies has a density of 1.185 Mg/m^3, a longitudinal sound speed of 2.66 km/s and a Poisson's ratio of 0.327. An experimental model is shown schematically in Figures B1 and B2. Figures B3 and B4 show photographs of the PMMA assembly inside the magnet with the signal cables attached to the gage leads.

Figure B1 shows a schematic of the PMMA assembly with the various gage levels specified along with their distance from the center of the explosion source. In these tests the explosive was 99 mg of PETN which produces 0.622 kJ of energy upon detonation. In Figure B2 details of the replaceable inserts used to contain the explosion are shown along with modifications of these inserts that were required in order to eliminate signal noise attributed to the mild detonating fuse. The solid insert with the 3.18 cm radius hemisphere end is inserted into a similar shaped hole in the upper PMMA block of the assembly for tamped explosions. Initially the 0.5 cm diameter sphere of PETN was lowered through a slightly oversized hole to the center of this hemisphere insert and then the hole was backfilled with mineral oil to confine the explosion. However, the mdf was found to couple energy into the PMMA and to also cause a perturbation of the magnetic field. To correct this problem a 1.27 cm diameter hole was drilled in the insert to replace the 0.5 cm hole. The explosive and the mdf, with the mdf placed inside a stainless steel tube which in turn was placed inside a solid foam insert, were then inserted into the PMMA through the 1.27 cm diameter hole. This

arrangement decoupled the mdf energy from the PMMA and confined the lead of the mdf jacket so that perturbations of the magnetic field were minimized. The other inserts of Figure B2, those with concave hemispheres, are placed in the PMMA model to produce a 6.35 cm diameter spherical cavity which is used as an energy decoupling cavity. This cavity, with a 99 mg sphere of PETN explosive at the center, can be used either evacuated or air filled to reduce the explosion induced displacements at the cavity wall. In PMMA, using an evacuated cavity 6.35 cm in diameter and a 0.622 kJ explosion, the peak particle velocity is reduced by a factor of ~6 over that recorded from a tamped explosion of the same energy (see Figure B7). Cavity decoupling allows the measurement of particle velocity time histories in PMMA to strains as low as 5.8×10^{-6} using the model shown schematically in Figure B1.

The data acquired, once the debugging of the recording system and the explosion initiation system were completed and other sources of electrical noise associated with the Site 300 bunker Bldg. 850 were eliminated, are shown in Tables BI and BII and Figures B5-B10. Experiment PAM62 and PMMAT23 are 99 mg tamped explosions, PMMAT17 is a 99mg air filled cavity decoupled explosion and PAM60 is a 99 mg evacuated cavity decoupled explosion. Peak particle velocities versus scaled distance are shown in Figure B7 for PAM62 and PAM60 as well as for another series of experiments which used higher energy explosion sources. Figures B8-B10 show peak particle velocities, peak displacements and peak accelerations for the experiments described in Tables BI and BII. The data given in Table BII is of a lessor quality

TABLE BI. Experimental data from a 0.622 kJ tamped explosion (PAM62) and a 0.622 kJ evacuated cavity decoupled explosion (PAM60) in PMMA*.

		PAM62			PAM60		
Distance (cm)	Scaled Distance ($m/kt^{1/3}$)	Peak Particle Velocity (m/s)	Peak Displacement (μm)	Peak Acceleration (Mm/s^2)	Peak Particle Velocity (M/s)	Peak Displacement (μm)	Peak Acceleration (Mm/s^2)
10.18	192.2	5.04	11.69	7.08	0.860	3.13	0.912
		5.05	11.42	8.83	0.851	2.92	1.35
15.03	283.8	3.00	6.46	3.43	0.442	1.35	0.448
		2.95	5.98	3.64	0.489	1.23	0.491
20.62	389.3	2.02	4.60	2.67	0.324	0.89	0.263
		1.83	4.47	2.44	0.292	0.92	0.263
28.04	529.4	1.14	2.97	1.31	0.187	0.577	0.165
		1.21	2.85	1.42	0.192	0.560	0.170
39.19	739.9	0.570	1.65	0.54	0.0970	0.333	0.055
		0.554	1.63	0.47	0.0946	0.339	0.065
50.44	952.3	0.219	0.604	0.19	0.0380	0.119	0.034
		0.205	0.579	0.20	0.0364	0.107	0.038
70.44	1330	0.0783	0.260	0.059	0.0155	0.052	0.013

*The wave speeds observed in these experiments were nearly constant at 2.66 km/s.

TABLE BII. Experimental data from a 0.622 kJ tamped explosion (PMMAT23) and a 0.622 kJ air filled cavity decoupled explosion (PMMAT17) in PMMA.

	PMMAT23			PMMAT17	
Distance (cm)	Scaled Distance ($m/kt^{1/3}$)	Peak Particle Velocity (m/s)	Peak Particle (m/s)	Peak Displacement (μm)	Peak Acceleration (Mm/s^2)
9.93	187.5	6.86	2.15	4.46	5.42
		6.74	2.03	4.50	4.04
14.76	278.7	3.79	1.07	2.56	1.79
		3.88	1.10	2.50	1.92
20.25	382.3	2.30	0.606	1.61	0.73
		--	0.725	1.62	0.93
27.69	522.8	1.22	0.268	0.653	0.34
		1.24	0.270	0.633	0.29
38.86	733.7	0.803	0.169	0.370	0.190
		0.603	0.127	0.345	0.110
50.23	948.3	0.347	0.0700	0.171	0.049
		0.416	0.0814	0.189	0.060
69.89	1320	0.126	0.0217	--	--
		0.120	0.0240	0.054	--

*The wave speeds observed in these experiments were nearly constant at 2.64 km/s.

than that in Table BI because some of the gages were not properly aligned with respect to the magnetic field. Nevertheless, these data taken from experiments in two different PMMA physical models show important similarities in the slopes of decay with distance of peak particle velocity, peak displacement and peak acceleration. In particular, the 3 to 1 decay in peak particle velocity at the greater scaled distances is definately not peculiar to either physical model and cannot be affected by any reflections from external surfaces (see Figure B11) Figure B11 shows the times of arrival of reflections from the upper surface, T7, and the bottom surface, T8, and the time, T9, when the shock wave reaches the external leads that may cause noise because of gage leads vibrating in the magnetic field. Other possible sources of reflections are the epoxy bonded interfaces where the gages are located. However, these interfaces are rather thin with only the gage impedance mismatch which should ring-up in nanosecond. Therefore, it is not surprising that there is no visible evidence of such reflections. Figures B12-B15 show the measured particle velocity time histories for PAM62 along with calculated, acceleration histories and displacement histories. One thing to note from the displacement data is that there is no evidence of any significant permanent displacement for any of these gages.

The series of experiments using higher energy explosions (see Figure B7) was work performed by Stout and Larson. In that work both particle velocity time histories and piezoresistance gage response were measured and used to infer the multi-component stress-strain history in PMMA. The results of that work suggest that at least in the shock front

nonequilibrium thermodynamics and dissipation processes are occurring in PMMA, but at stresses below dynamic yielding and behind the shock front an isotropic elastic material response is a reasonable first model for material behavior. Thus, for this linear elastic response regime in PMMA, the three non-zero stress components in spherical geometry are

$$\sigma_{rr} = (\lambda + 2\mu)\, \gamma_{rr} + 2\lambda\, \gamma_{\phi\phi} \qquad \text{and}$$

$$\sigma_{\phi\phi} = \sigma_{\theta\theta} = \lambda\, \gamma_{rr} + (2\lambda + 2\mu)\, \gamma_{\phi\phi} \qquad \ldots \text{B1}$$

where σ_{rr} is the radial stress and $\sigma_{\phi\phi}$ and $\sigma_{\theta\theta}$ are the hoop stresses, γ_{rr} and $\gamma_{\phi\phi} = \gamma_{\theta\theta}$ are the radial and hoop strains, and λ and μ are the Lame elasticity parameters (44.2 and 23.0 kbars respectively for PMMA). The strains γ_{rr} and $\gamma_{\phi\phi}$ can be derived directly from the measured particle velocity time histories using the relations

$$\gamma_{rr} = \frac{\partial U_p}{\partial R} \qquad \text{and}$$

$$\gamma_{\phi\phi} = \gamma_{\theta\theta} = \frac{U_p}{R} \qquad \ldots \text{B2}$$

where U_p is the particle velocity and R is the distance from the center of the energy source to the point where the particle velocity is measured.

This simple relationship between stress time history and particle velocity time history in PMMA at stresses below dynamic yielding was discovered by Stout and Larson[8] using a triple material piezoresistance gage which records the simultaneous piezoresistive response of ytterbium, manganin and constantan when subjected to a propagating shock wave. From Stout's analysis there are three simultaneous equations relating piezoresistive response, radial stress and hoop strain. These equations are:

$$\left(\frac{\Delta R\phi\phi}{R}\right)_{Yb} = (R\phi r)_{Yb}\ \sigma rr + (R\phi\phi)_{Yb}\ Y\phi\phi + (R\phi\phi)_{Yb}\ Y\phi\phi$$

$$\left(\frac{\Delta R\phi\phi}{R}\right)_{Mn} = (R\phi r)_{Mn}\ \sigma rr + (R\phi\phi)_{Mn}\ Y\phi\phi + (R\phi\phi)_{Mn}\ Y\phi\phi \quad \ldots B3$$

$$\left(\frac{\Delta R\phi\phi}{R}\right)_{Cn} = (R\phi r)_{Cn}\ \sigma rr + (R\phi\phi)_{Cn}\ Y\phi\phi + (R\phi\phi)_{Cn}\ Y\phi\phi$$

where the coefficients (Rϕr)Yb, etc can be derived directly from the work of Chen et al[9]. From Larson's experimental measurements came the shock wave induced piezoresistive response for all three of these materials and the particle velocity time history from which $Y\phi\phi = Y\theta\theta$ can be easily derived. Thus, the only remaining unknown in Equations B3 is the radial stress time history. The stress history that was found to satisfy the very different piezoresistant responses of these three materials was the stress history given by the simple isotropic elastic material response described previously.

The dissipation processes occurring in the shock front provide for a strong attenuation of the wave as it propagates, with the strongest attenuation occurring at the greater scaled distances (see Figure B7). At these greater distances the wave front is more dispersive, indicating preferential loss of the high frequency components of the wave, nevertheless, the wave front continues to move at a constant wave velocity of 2.66 km/s as determined from time of arrival measurements between gages.

Summary and Conclusions

Fully coupled and cavity decoupled explosions of the same energy (0.622 kJ) were carried out as experiments to study wave propagation and attenuation in polymethylmethacrylate (PMMA). These experiments produced particle velocity time histories from strains of 2×10^{-3} to as low as 5.8×10^{-6}. Other experiments in PMMA, reported recently by Stout and Larson[8], provide additional particle velocity data to strains of 10^{-1}.

In the work by Stout and Larson, both particle velocity time histories and piezoresistance gage response were measured and used to infer the multi-component stress-strain history in PMMA. The results of that work suggest that in the shock front nonequilibrium thermodynamics and dissipation processes are occurring in PMMA, but at stresses below dynamic yielding and behind the shock front an isotropic elastic material response is a reasonable first model for material behavior. Furthermore, the dissipation processes occurring in the shock front provide for a

strong attenuation of the wave amplitude as it propagates, with the strongest attenuation occurring at the greater scaled distances. At these greater distances the wave front is more dispersive, with the decay of peak particle velocity inversely proportional to distance cubed, indicating a strong preferential loss of the high frequency components of the wave.

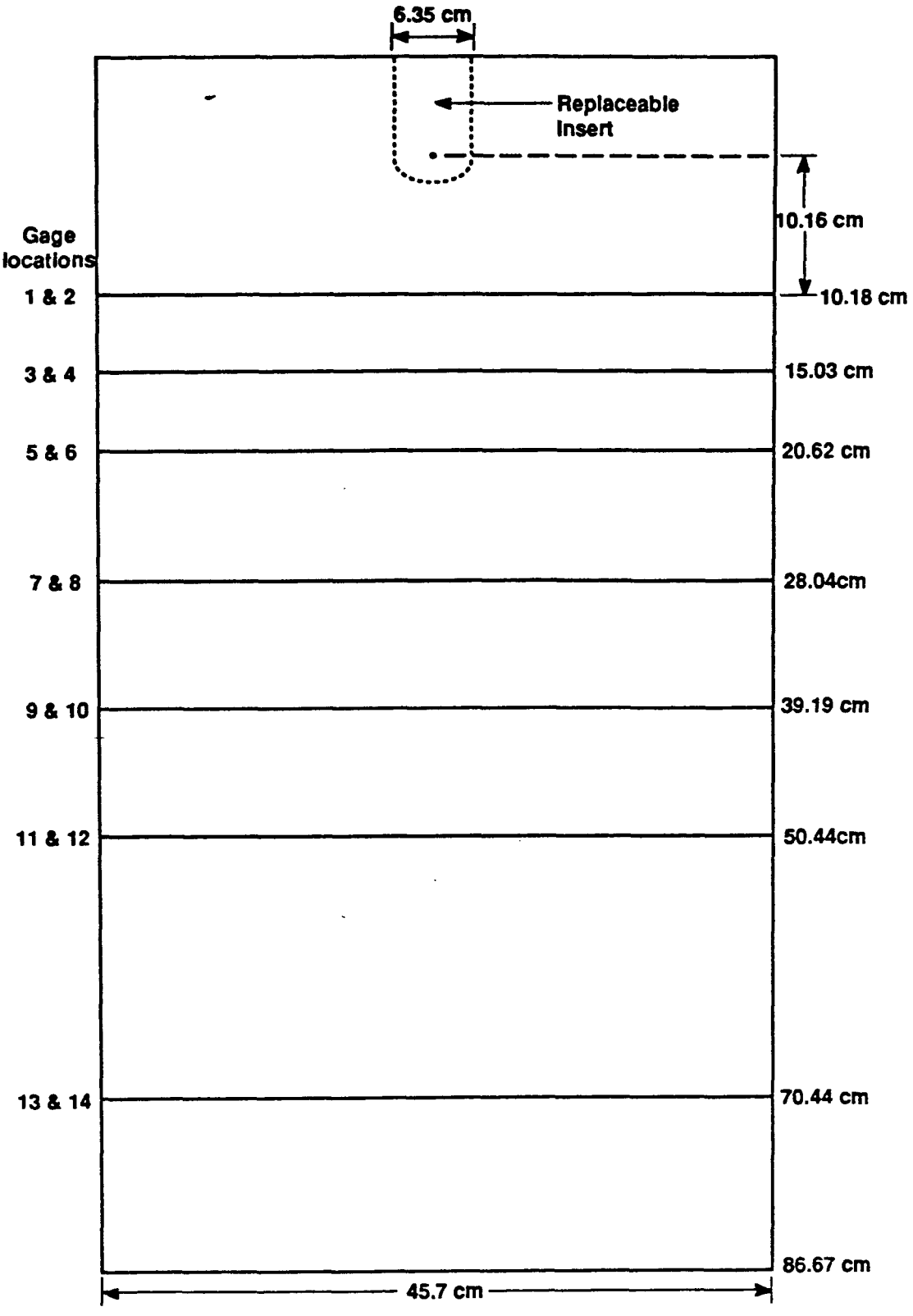

Figure B1. A schematic of the PMMA experimental assembly. The seams where the gages are located were epoxy bonded. The distances to the various gages from the center of the explosive include the bond thickness.

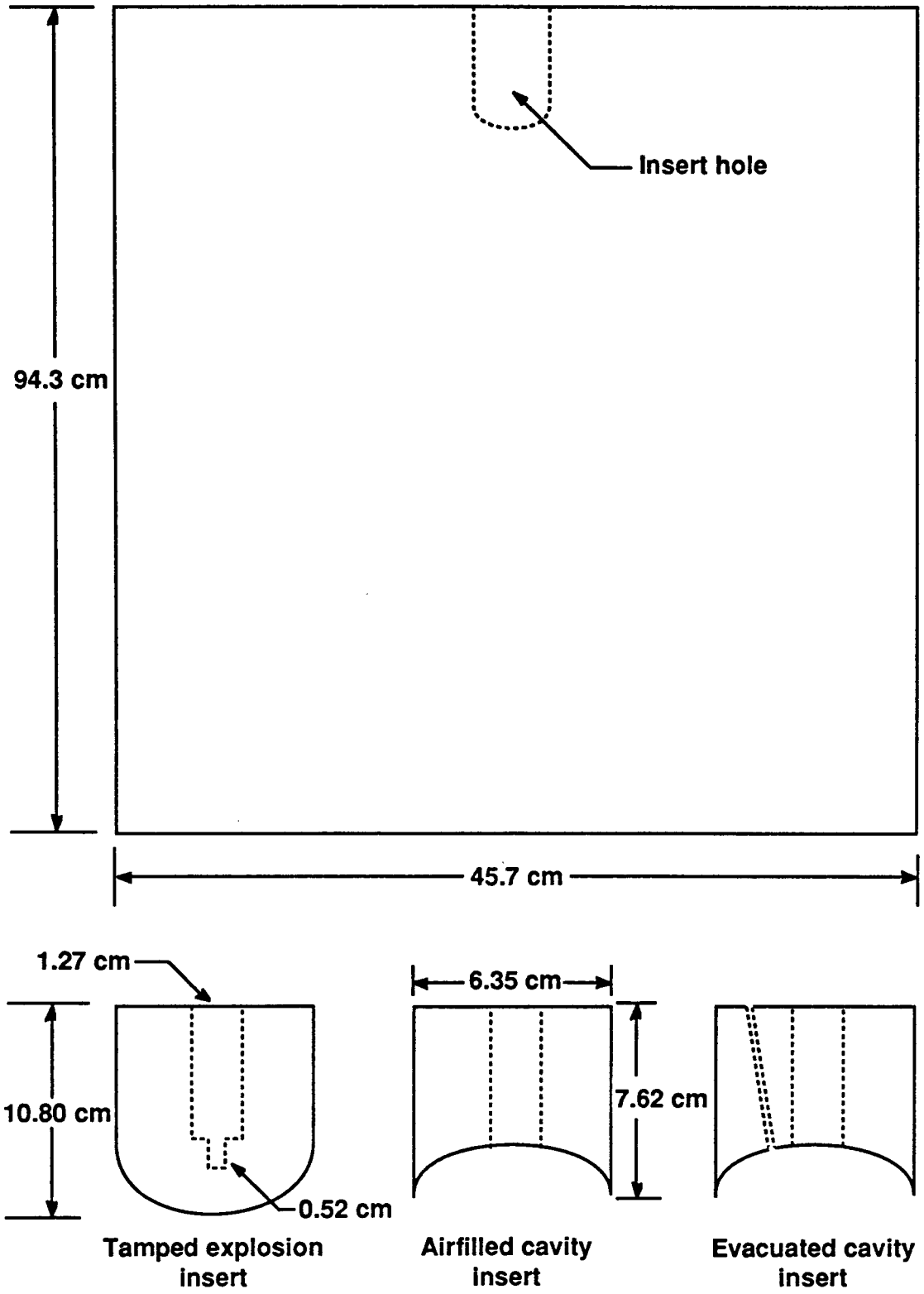

Figure B2. A schematic of the PMMA model showing the insert hole. Also shown are the various replaceable inserts used for tamped and cavity decoupled explosions. The original inserts had a 0.52 cm hole drilled for the explosive and mdf rather the 1.27 cm hole indicated on these drawings.

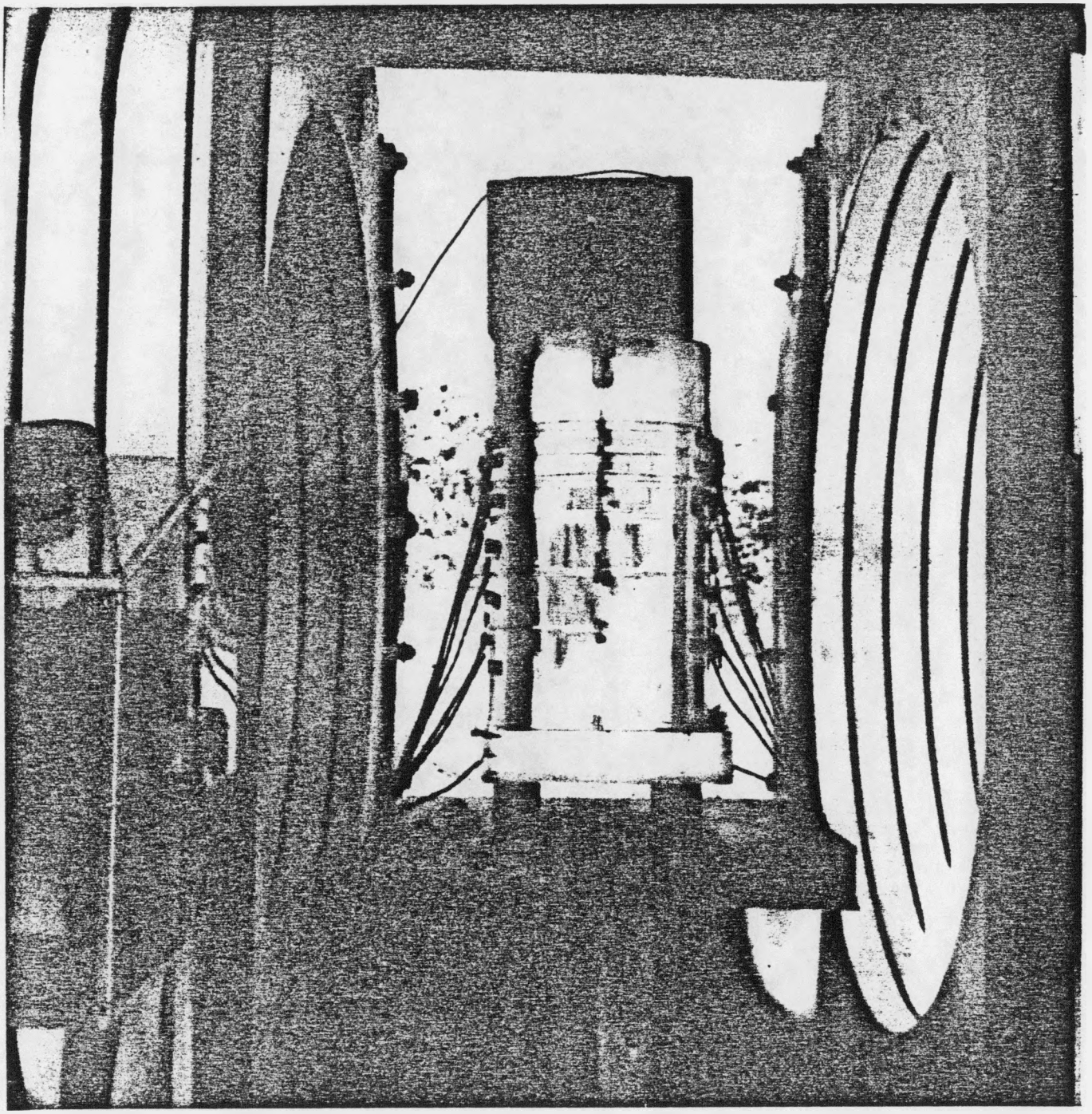

Figure B3. A photograph of the PMMA model inside the magnet with gage cables attached and the explosive in place.

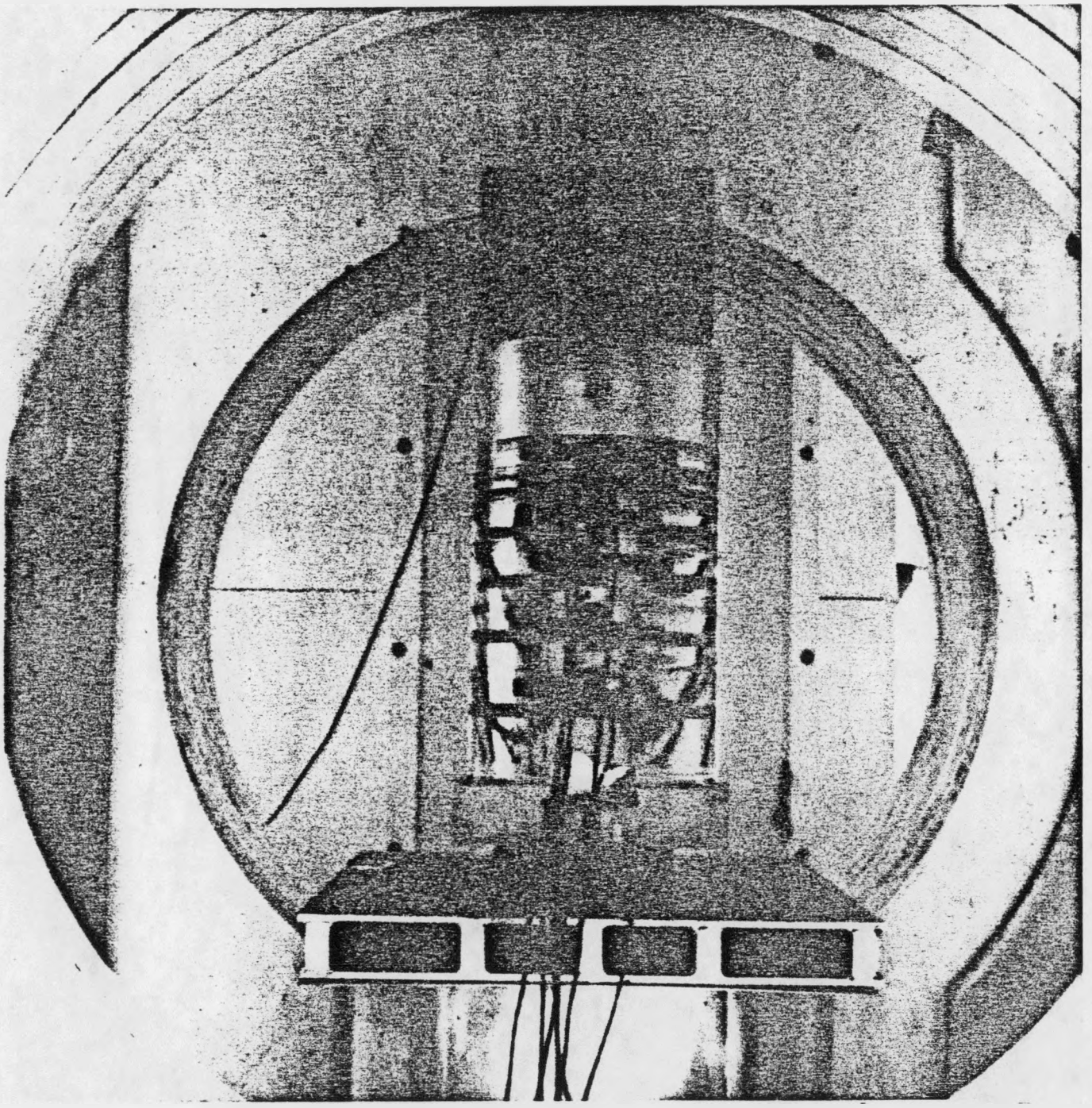

Figure B4. A view of the PMMA model through the south pole of the magnet.

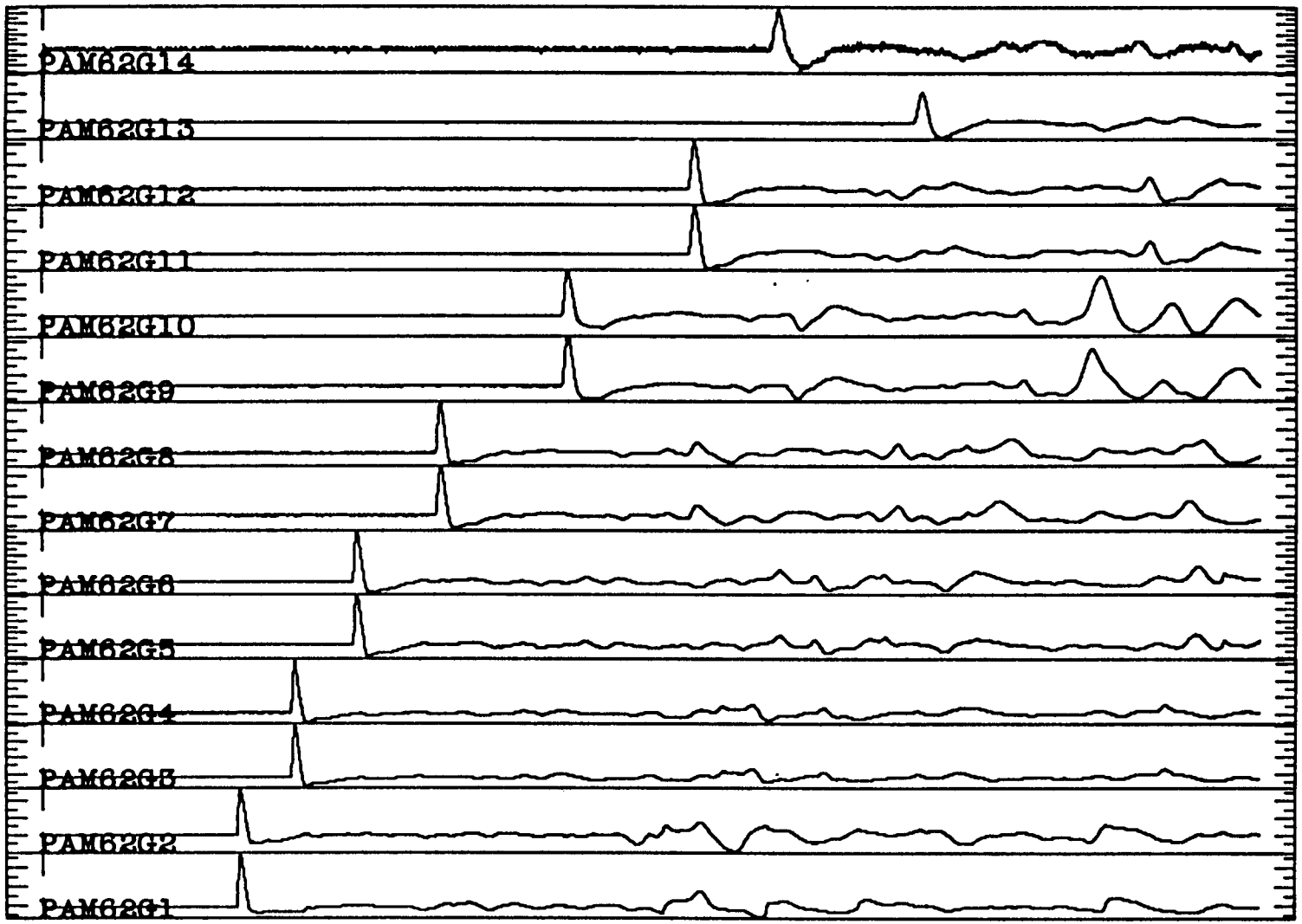

Figure B5. Signals recorded by the various gages from the 0.622 kJ tamped explosion (PAM62) in PMMA.

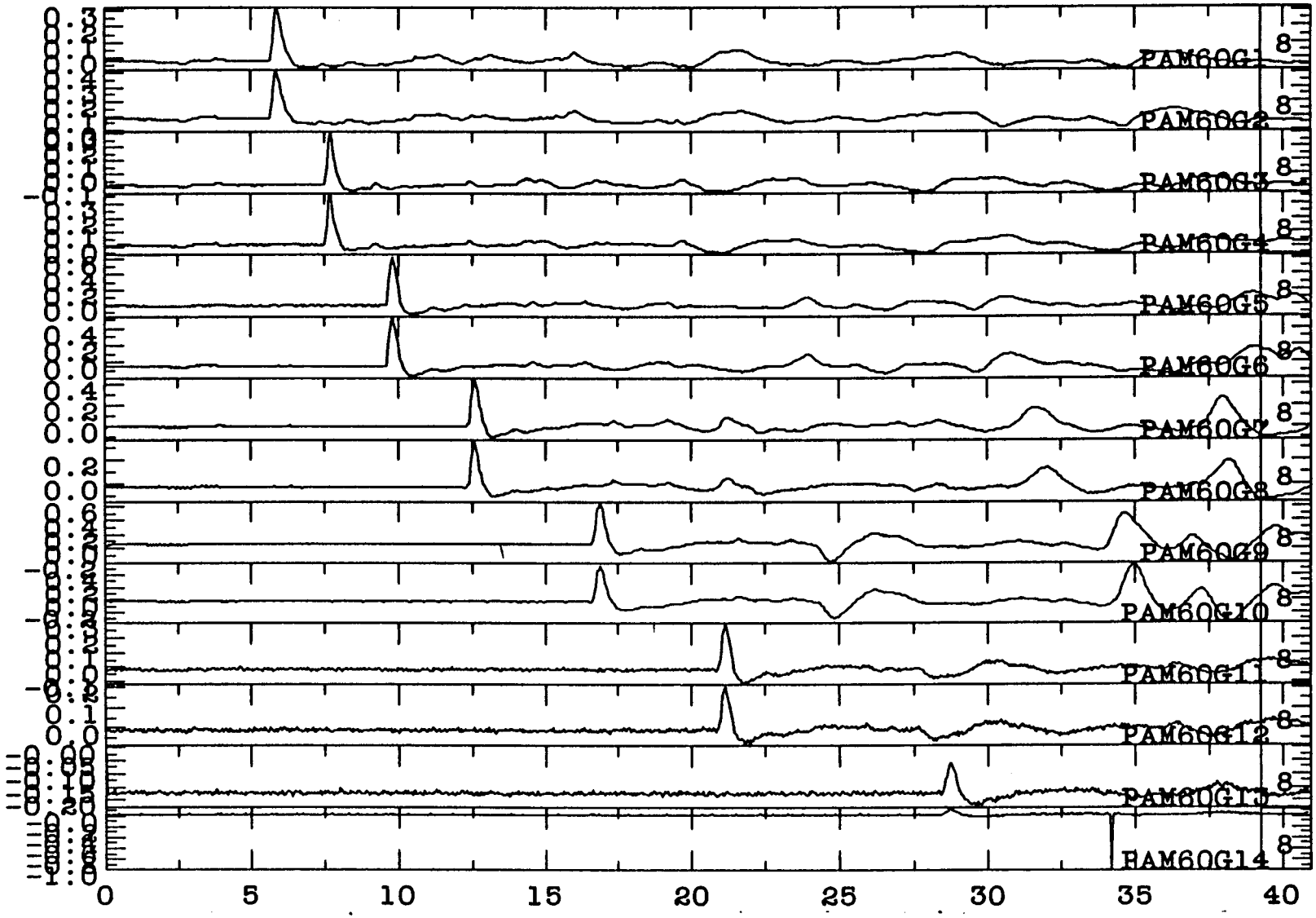

Figure B6. Signals recorded by the various gages from the 0.622 kJ evacuated cavity decoupled explosion (PAM60) in PMMA.

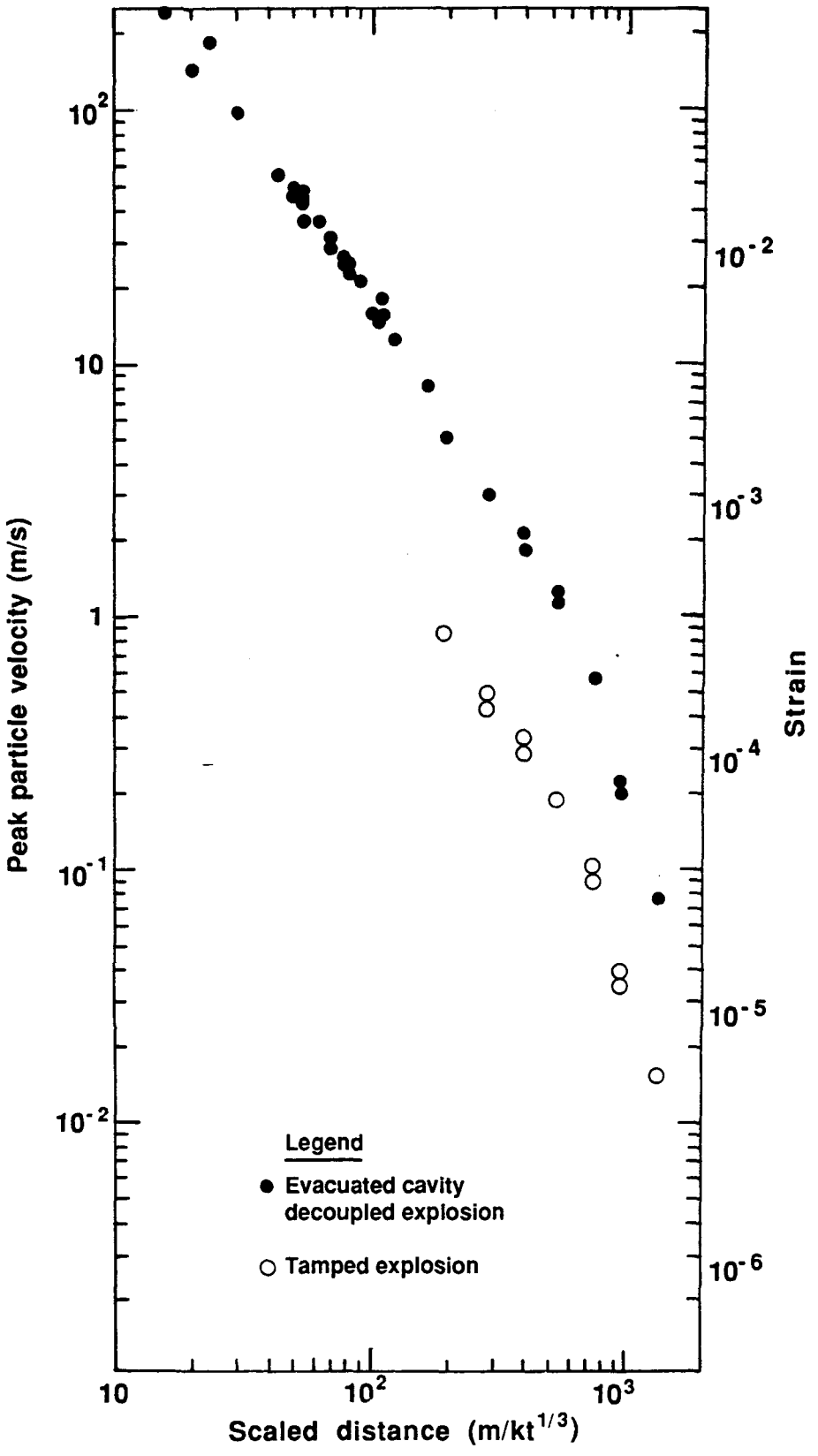

Figure B7. Peak particle velocities versus scaled distance from the explosion center for tamped (solid circles) and cavity decoupled (open circles) explosions in PMMA. The strain interval covered by these experiments is 10^{-1} to 5 x 10^{-6}.

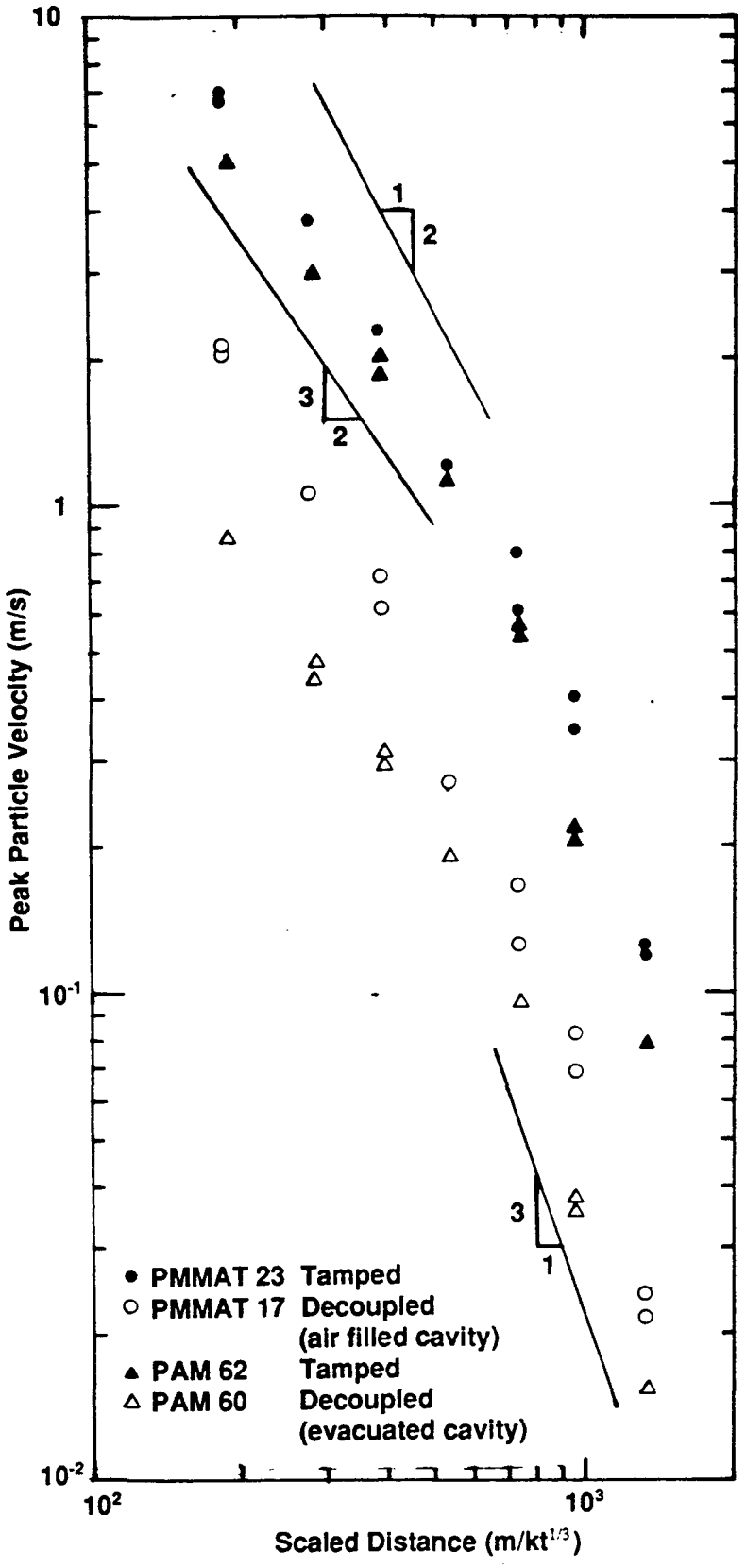

Figure B8. Peak particle velocities for two tamped and two decoupled 0.622 kJ explosions in PMMA. The lines on the graph are drawn for reference slopes of -1.5, -2 and -3.

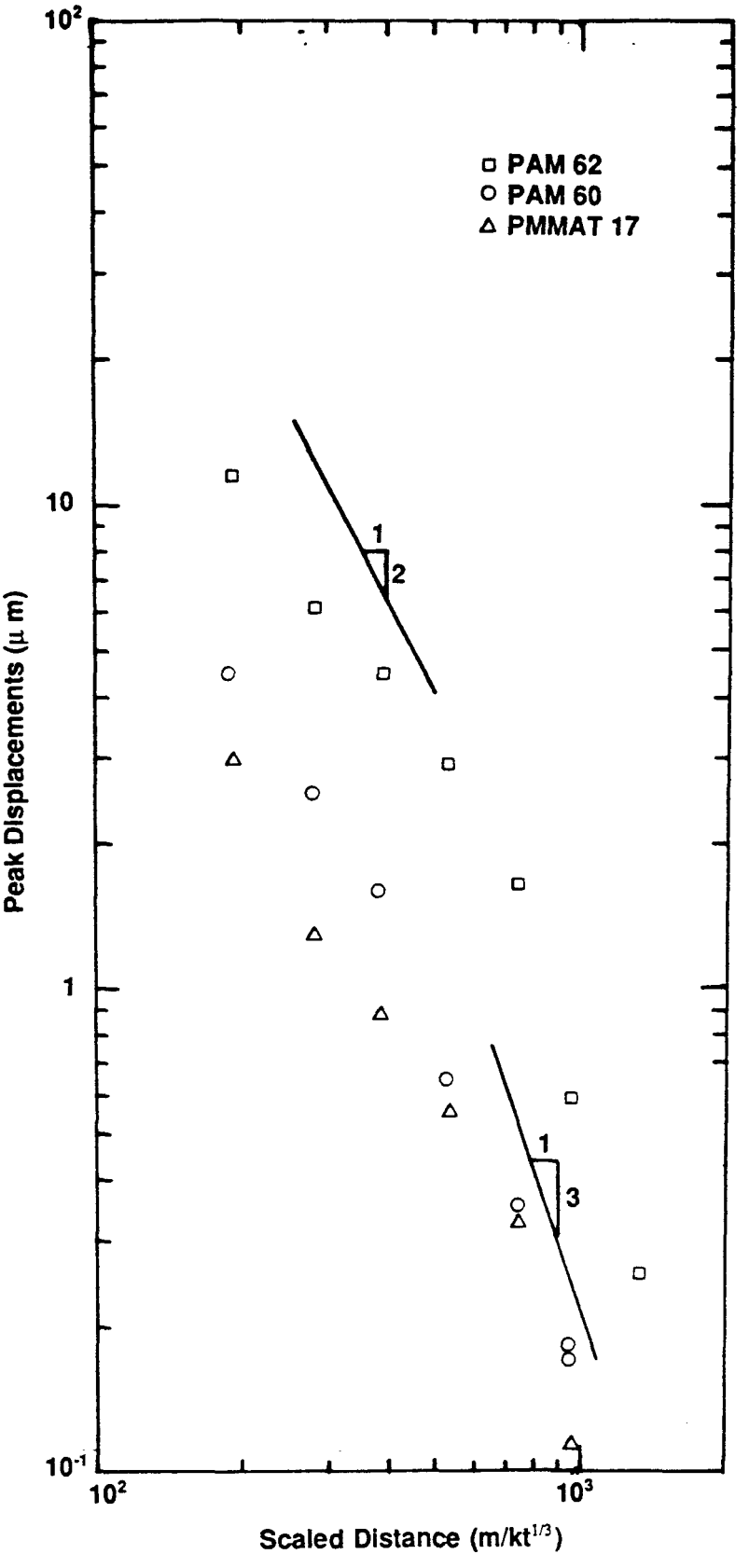

Figure B9. Peak displacements for one tamped and two decoupled 0.622 kJ explosions in PMMA. The lines on the graph are drawn for reference and have slopes of -2 and -3.

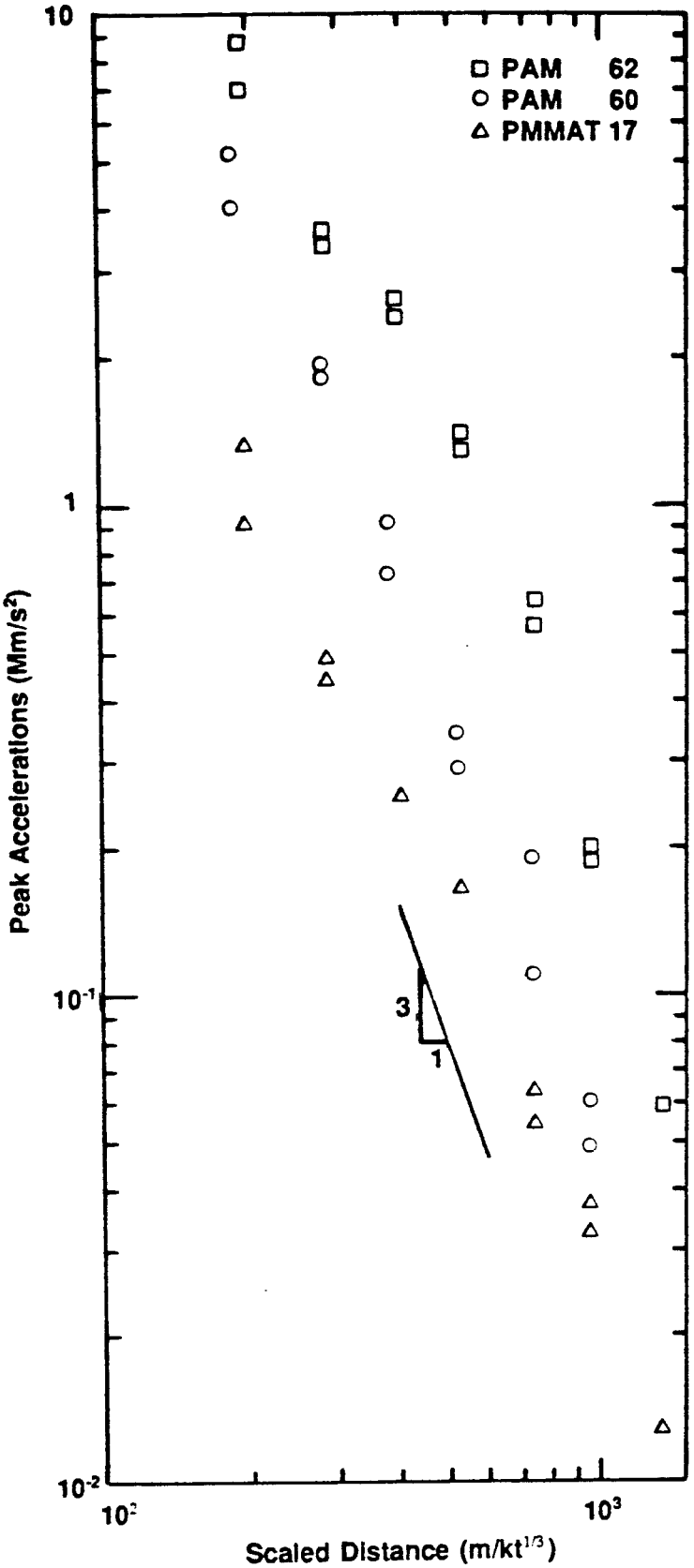

Figure B10. Peak accelerations for one tamped and two decoupled 0.622 kJ explosions in PMMA. The line on the graph is drawn for reference and has a slope of -3.

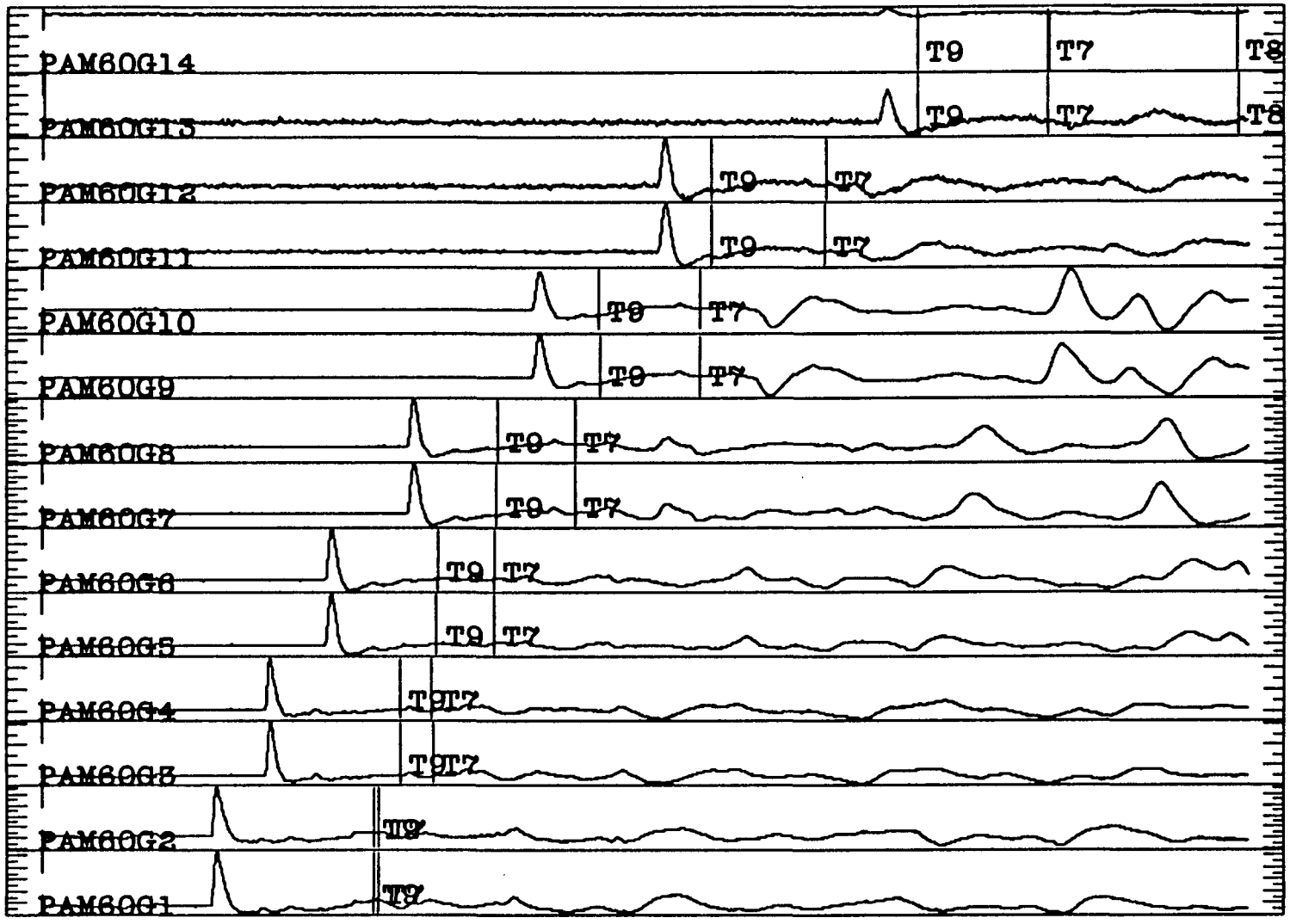

Figure B11. Signals recorded by the various particle velocity gages in experiment PAM60. The index T7 indicates the time of arrival of the reflected wave from the top surface, T8 the reflected wave from the bottom surface and T9 is the time of arrival of the shock wave at the point were the gage leads are at the surface of the PMMA model.

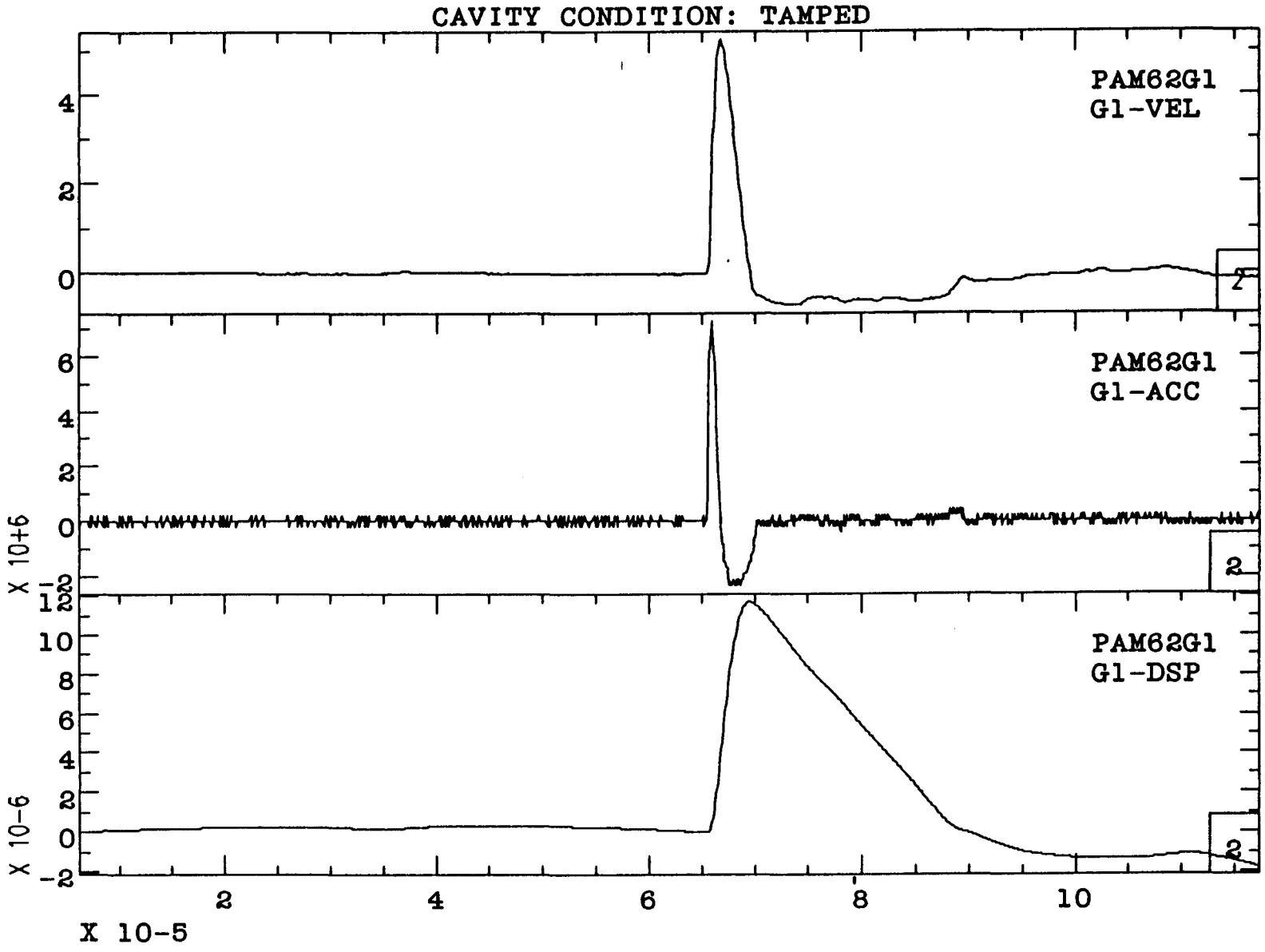

Figure B12. The particle velocity time history for the gage at 10.18 cm in PAM62 along with derived acceleration and displacement time histories.

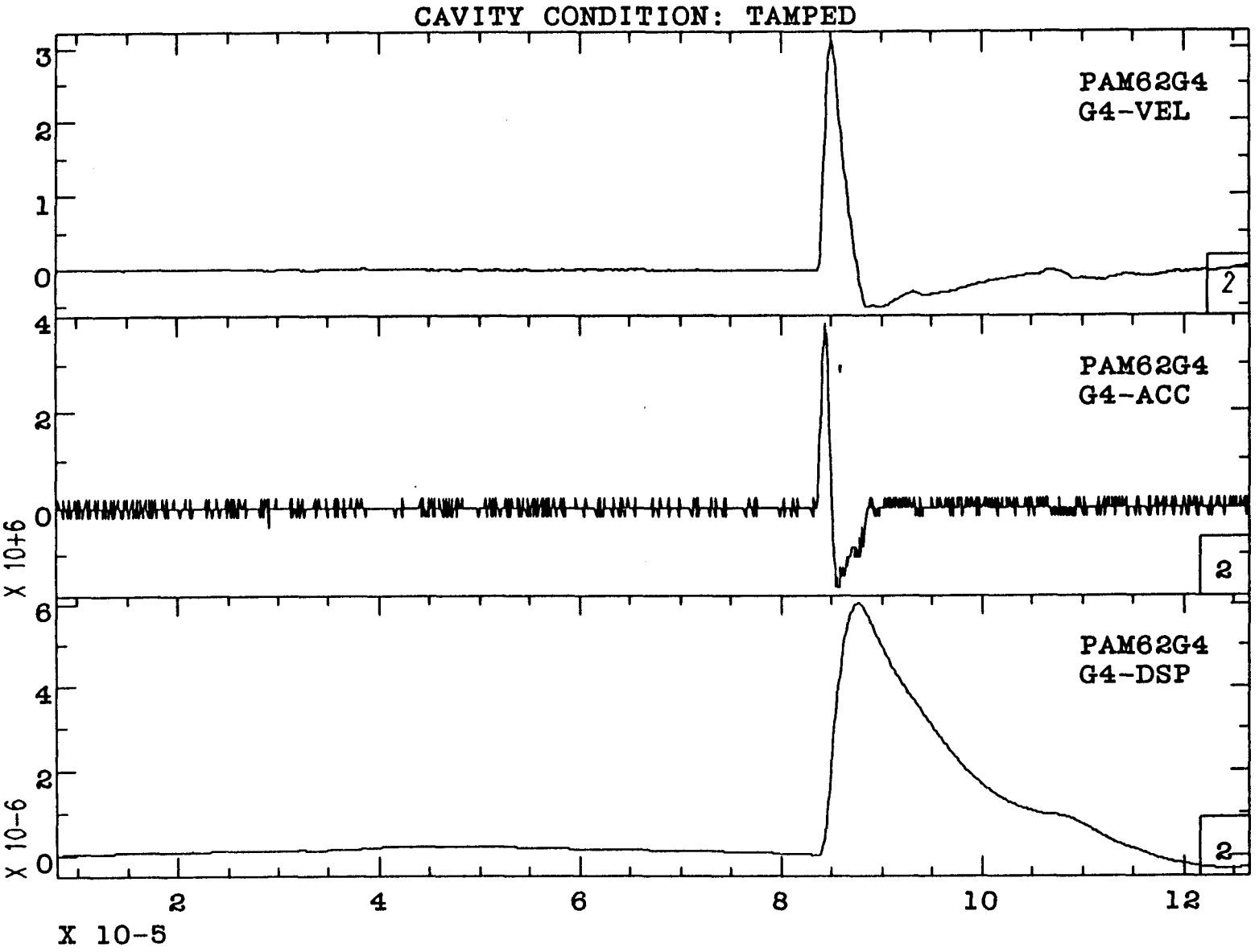

Figure B13. The particle velocity, acceleration and displacement time histories for a gage at 15.03 cm in PAM62.

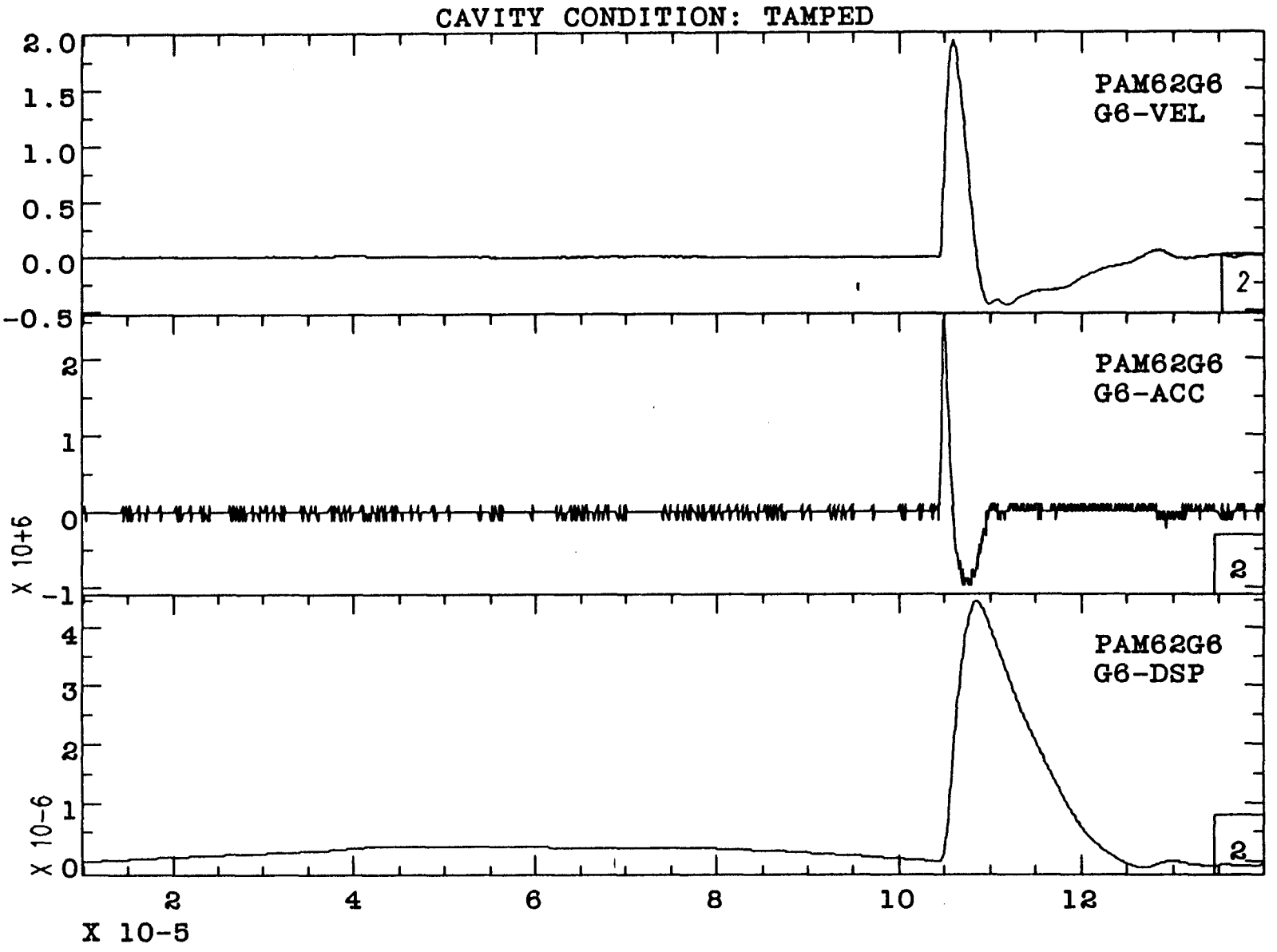

Figure B14. The particle velocity, acceleration, and displacement time histories for a gage at 20.62 cm in PAM62.

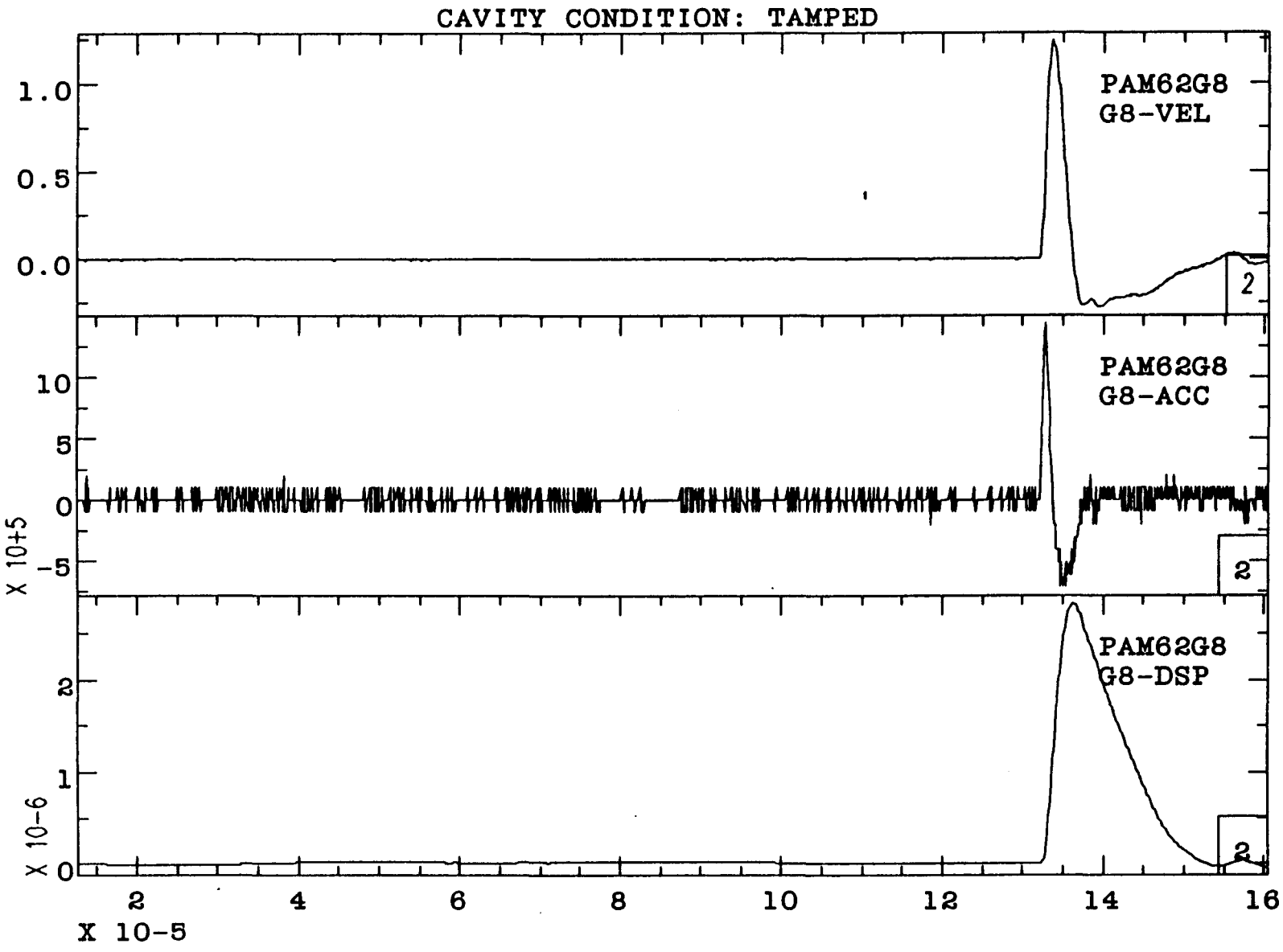

Figure B15. The particle velocity, acceleration, and displacement time histories from a gage at 28.04 cm in PAM62.

PART C

WAVE PROPAGATION STUDIES IN SIERRA WHITE GRANITE

Introduction

The objectives of these experimental studies in geologic media are to use explosion induced wave propagation data to first derive the attenuation properties of each medium as a function of strain and frequency, second determine the maximum strain level for superposition, and finally, determine the cavity decoupling factors for each medium as a function of frequency by comparing cavity decoupled and tamped explosions.

Sierra white granite was selected to be the first geologic medium tested for several reasons. First, granite is relatively easy and inexpensive to acquire in large flat pieces because of its commercial use for optics tables, for monuments, and for building purposes. Second, granite is of premium interest to seismic verification because of its past and potential future use as a test medium. Third, comparisons can be made with experimental data acquired by SRI using the same geologic medium. And finally, the Sierra White granite provides relatively clean experimental data because it has a relatively small amount of magnetic minerals which produce electrical noise by perturbing the magnetic field during particle velocity measurements.

Experimental Procedures and Results

The Sierra White granite was obtained from a quarry near Raymond, California. All of the material used in this study was cut from one master block at the quarry with orientation identified on each of the smaller cut blocks. The finished granite pieces were ground and lapped flat and parallel by the Standridge Granite Corp. of Santa Fe Springs, California. Experiments were conducted in two different Sierra White granite physical models. One was dubbed the large model and the other the small model. The finished pieces for the large experimental model were assembled inside the magnet at Site 300 east of Livermore. Figures C1-C5 show photographs and a schematic of the large Sierra white granite experimental assembly. The particle velocity gages were placed between the blocks as they were stacked. The gages were typically in pairs with the active elements adjacent to one another and the gage leads going in opposite directions (see Figures C1 and C2). Figure C3 shows the stacking process, Figure C4 is a photograph of the nearly completed assembly, and Figure C5 is a schematic of the completed assembly. The dimension of each block are shown on the schematic. The long dimension, which extends through the donut holes of the magnet poles, is the direction of the gage leads and allows increased useful recording time for the gages. Figure C6 shows the recorded results from the various gages for a tamped explosion of 0.622 kJ energy. The only major noise other than the amplifier noise polluting these data is the burst of high frequency noise at ~400 μs. This particular type of electrical noise occurs randomly and is apparently associated with the Site 300 Bldg. 850 bunker power.

Schematics of the two experimental arrangements using the small Sierra White granite model are shown in Figures C7 and C8. The first experiment using this small model was called Sierra 1 and was a 510 mg PETN explosion with 3.24 kJ of energy. Figure C7 shows the dimensions of the experimental assembly and the locations of the gages. Figure C9 shows the signals recorded by the various gages. The wave structure after the peak is anomalous and subsequent experiments indicated that the anomalous feature occurred because energy from the mdf was being coupled into the granite.

The schematic shown in Figure C8 is the small Sierra white granite model used in Sierra 1 with the top plate removed, the remainder of the model turned upside down, and with a new top plate that has an insert hole so that the model can be reused and both tamped and cavity decoupled experiments can be performed. Figure C10 shows the signals recorded for a 0.622 kJ tamped explosion (Sierra 6) in the granite model of Figure C8. A comparison of signals from Sierra 1 and Sierra 6 at approximately the same particle velocity (see Figure C11) shows that most of the anomalous signal has been removed by enclosing the mdf in a stainless steel tube and decoupling the tube from the granite using foam. The structure in the negative phase of the signal from Sierra 6 between 30 and 50 μs is probably the remnant of the mdf induced signal and therefore part of the source signal for this particular experiment.

In Tables CI-CVII and in Figure C12 various comparisons are made of the peak particle velocities recorded in the various experiments using Sierra White granite. Also included are data from decoupled explosions in the small and the large model and in Figure C12 data from an

experiment conducted by Stanford Research Institute. The significance of these data are that they stretch over five orders of magnitude of strain and provide the attenuation response of granite from strains where the behavior is believed to be non-linear (10^{-1} to 10^{-5}) to where it is believed to be linear (10^{-5} or 10^{-6} and below).

These data when coupled with calculations place severe restrictions upon the constitutive model that can be used to reproduce the complete particle velocity time histories. Nevertheless, without complete information about the stresses (i.e., without the complete stress-strain histories), a unique description of material response is impossible. Not-withstanding these restrictions, these data can be used to characterize the attenuation response of Sierra White granite using a reduced velocity potential description, which however, is often perceived as being confined to the frequency band of these small scale experiments because of uncertainties about scaling attenuation response with frequency.

TABLE CI. Results from experiment Sierra 1 using the small Sierra White granite physical model. Distances are measured from the center of the explosive source. This was a tamped explosion of 510 mg of PETN yielding 3.24 kJ of energy.

Distance (cm)	Scaled Distance ($m/kt^{1/3}$)	Peak Particle Velocity (m/s)	Time of Arrival (μm)	Average Shock Wave Velocity (km/s)	Acceleration (Mm/s^2)
2.45	26.7	57.14	31.958		218
3.80	41.4	28.5	34.527		102
		28.6	34.609	5.17	124
5.85	63.7	16.12	38.642		44.0
		16.47	38.448	5.15	43.3
8.60	93.65	8.33	44.311	4.81	23.7
13.17	143.4	3.73	54.17		11.2
		3.70	54.215	4.60	9.3
19.64	213.9	1.60	69.25		2.9
		1.55	68.89	4.35	3.9
28.74	313.0	0.902	91.71		0.79
		0.936		4.02	0.72

TABLE CII. Results from experiment Sierra 6 a tamped explosion of 0.622 kJ of energy in the small Sierra White granite physical model. The average wave speed for this experiment was 3.86 km/s.

Distances	Scaled Distances	Peak Particle Velocity	Positive Phase Width	Displacement		Acceleration
				Actual	Scaled	
(cm)	($m/kt^{1/3}$)	(m/s)	(μs)	(μm)	(cm)	(Mm/s^2)
5.461	103.1	6.63	6.24	17.7	3.34	16.3
		6.17	6.10	17.7	3.34	16.3
13.195	249.1	1.04	10.66	5.28	1.00	1.44
		1.02	10.71	5.20	0.98	1.53
22.222	419.6	0.297	15.25	2.09	0.395	0.18
		0.301	15.50	2.09	0.395	0.18
31.330	591.5	0.158	16.77	1.385	0.261	
		0.157	16.00	1.275	0.241	
37.799	713.6	0.119	16.61	1.028	0.194	
		0.122	17.52	1.113	0.210	
42.366	799.9	0.102	18.42			
		0.104				
45.116	851.8	0.937				
		0.0915				

TABLE CIII. Results from experiment Sierra L3 which was a 0.622 kJ tamped explosion in the large Sierra White granite physical model.

Distance (cm)	Scaled Distance ($m/kt^{1/3}$)	Peak Particle Velocity (m/s)	Positive Phase Width (μs)	Time of Arrival (μs)	Average Shock Wave Velocity (km/s)	Peak Displacement (μm)	Peak Acceleration (Mm/s^2)
7.810	147.5	3.11				14.2	5.44
10.810	204.1	1.77	13.08	50.66		9.91	3.34
14.420	272.2	0.963	17.64	60.56		6.48	1.25
		0.973	16.98	59.96	3.76	6.73	1.35
20.475	386.6	0.432	19.26	76.70	3.68	3.65	0.292
30.368	573.3	0.1805	19.06	104.60		1.82	0.0567
		0.195	18.98	104.20	3.57	1.80	0.0589
45.702	862.9	0.0807	23.80	145.08	3.77	0.946	0.0170
66.901	1263	0.0398	25.08	202.68		0.522	0.0059
		0.0394	23.60	204.12	3.63	0.440	0.0054
92.479	1746	0.0214	25.38	268.6	3.92	0.311	--
120.94	2283	0.0128	27.26	340.4		0.205	--
		0.0129	27.32	340.4	3.96	0.205	--
150.5	2841	0.0083	31.94	411.2	4.18	0.130	--

TABLE CIV: Data from experiment Sierra L4 using the large Sierra white granite physical model. Distances are measured from the center of the explosive source. This was a tamped explosion of 0.622 kJ of energy.

Distance (cm)	Sealed Distance ($m/kt^{1/3}$)	Peak Particle Velocity (m/s)	Positive Phase Width (μs)	Time of Arrival (μs)	Average Shock Wave Velocity (km/s)
7.810	147.5	3.03	9.93	43.62	
10.810	204.1	1.85	12.98	51.62	3.75
14.420	272.2	1.08	16.73	60.82	
		1.05	16.77	61.23	3.76
20.475	386.6	0.488	17.79	78.02	3.56
30.368	573.3	0.217	18.83	104.92	
		0.198	18.88	105.11	3.66
45.702	862.9	0.0876	22.04	146.35	3.71
66.901	1263	0.0434	24.11	202.91	
		0.0425	23.43	203.33	3.73
92.479	1746	0.0241	26.65	265.96	4.07
120.94	2283	0.0141	28.22	336.88	
		0.0140	29.42	335.83	4.04
150.50	2841	0.00846	31.44	407.27	
		0.00854	32.38	406.05	4.20
180.72	3412	0.00690	38.63	478.0	4.24

TABLE CV. Results from experiment Sierra L42 a tamped explosion yielding 0.622 kJ of energy in the large Sierra White granite physical model.

Distance (cm)	Scaled Distance ($m/kt^{1/3}$)	Peak Particle Velocity (m/s)	Positive Phase Width (μs)	Time of Arrival (μs)	Average Shock Wave Velocity (km/s)	Peak Displacement (μm)	Peak Acceleration (Mm/s^2)
7.81	147.5	2.27	8.826	50.191		9.70	3.40
10.810	204.1	1.23	16.618	56.857	4.50	6.68	1.46
14.420	272.2	0.679	21.813	67.316		4.65	0.600
		0.702	18.549	67.156	3.45	4.56	0.720
20.475	386.6	0.342	24.198	83.688	3.67	2.97	0.178
30.368	573.3	0.150	22.95	111.43		1.57	0.0436
		0.161	23.00	111.01	3.56	1.58	0.0484
45.702	862.9	0.0683	25.69	153.05	3.65	0.901	0.0166
66.901	1263	0.0342	27.66	211.02		0.492	0.0059
		0.0337	26.73	211.86	3.66	0.465	0.0064
92.479	1746	0.0191	30.39	275.94	3.99	0.303	--
120.94	2283	0.0116	32.26	348.02		0.202	--
		0.0115	33.58	346.54	3.95	0.204	--
150.5	2841	0.0071	39.64	418.11		0.150	--
		0.0075	40.32	417.66	4.13	0.155	--
180.72	3412	0.0052	38.66	497.16	3.80	0.100	--

TABLE CVI. Results from experiment Sierra 2 an explosion of 99 mg of PETN yielding 0.622 kJ of energy in an air filled cavity in the small Sierra White granite physical model. The average wave speed was 3.78 km/s.

Distance	Scaled Distance	Peak Particle Velocity	Displacement Actual	Displacement Scaled
(cm)	($m/kt^{1/3}$)	(m/s)	(μm)	(mm)
5.461	103.1	0.834	2.07	3.91
		0.855	2.30	4.34
13.195	249.1	0.1268	0.480	0.906
		0.1268	0.483	0.912
22.222	419.6	0.0498	0.227	0.429
		0.0498	0.237	0.447
31.330	591.5	0.0289	0.144	0.272
		0.0289	0.160	0.302
37.799	713.6	0.0233	0.141	0.266
		0.0233	0.125	0.236
42.366	799.9	0.0200	0.114	0.215
		0.0200	0.116	0.219
45.166	851.8	0.0157	0.102	0.192
		0.0157	0.108	0.203

TABLE CVII. Results from experiment Sierra L5 a 0.622 kJ decoupled explosion in a 5.08 cm diameter air filled cavity in the large Sierra White granite physical model.

Distance (cm)	Scaled Distance ($m/kt^{1/3}$)	Peak Particle Velocity (m/s)	Pulse Width (μs)	Time of Arrival (μs)	Average Shock Wave Velocity (km/s)	Peak Displacement (μm)	Peak Acceleration (Mm/s^2)
7.81	147.5	0.318	8.44	43.5		1.69	0.311
10.81	204.1	0.220	11.05	51.8	3.61	1.14	0.181
14.42	272.2	0.127	10.10	62.3		0.574	0.078
		0.125	9.60	61.9	3.50	0.593	0.075
20.475	386.6	0.072	10.70	78.7	3.65	0.345	0.038
30.368	573.3	0.0333	10.90	106.3		0.176	0.012
		0.0357	11.45	105.8	3.62	0.171	--
45.702	862.9	0.0152	13.70	147.4	3.71	0.0828	--
66.901	1263	0.00725	14.50	203.9		0.0414	--
		0.00753	15.00	203.4	3.77	0.0618	--
92.479	1746	0.00403	15.90	267.6	4.00	0.0332	--
120.94	2283	0.00204	16.10	338.7		0.0192	--
		0.00228	17.50	337.7	4.03	0.0216	--
150.50	2841	0.00120	19.50	409.5	4.15	--	--

The reluctance to scale attenuation response arises because of the apparent sensitivity of attenuation, as measured by Q, to frequency. Sierra White granite and a second granite (Blair CSIRO Australia - private communication), show Q's determined from resonance experiments at ~10 kHz that are approximately five times the Q's that are observed from wave propagation experiments at ~ 1 MHz. However, this difference may have been explained by the recent work of Blair. Using resonance experiments and checking the attenuation of different modes Blair found that Q was frequency independent from 1 to 50 kHz. This observation suggested that the lower Q's were from losses peculiar to the wave propagation process and probably due to scattering. Blair was able to account for this factor of five difference in attenuation as measured by Q by imposing simple elastic scattering on the grain clusters which characterized the particular granite that he studied. The obvious preliminary conclusion based upon Blair's work is that scaling is a problem only as it is affected by grain size consideration and the resulting scattering. Thus small scale simulations of a geologic medium must eliminate scattering as an important process by minimizing grain size or the grain size must be scaled so that the scattering effect is identical between the medium of interest and the small-scale simulant.

Figures C13 through C42 show the particle-velocity time histories and displacement time histories from tamped (Sierra 6) and decoupled (Sierra 2) explosions in Sierra White granite using the small model shown in Figure C8. Gage pairs are compared, so that these data show the reproducibility and the useful writing time for the gages. The information from these gages is no longer useful when the responses from these two gages start to diverge from one another. This limit on useful writing time or divergence of gage response is a result of electrical noise caused by the shock wave moving the external leads of the gages or is a result of reflected waves arriving from either the upper or lower surface of the model.

Summary and Conclusions

The experiments on Sierra White granite were successful in obtaining wave propagation data over the strain interval between 2×10^{-2} and 5×10^{-7} for use in deriving the attenuation properties of this medium. Unfortunately, over the objection of this author, the limited funds remaining were spent on dome salt rather than on completing the work on Sierra White granite. Therefore, the multiple explosion experiments to obtain the maximum strain level for superposition were not carried out nor were enough cavity decoupling experiments conducted to define in any detail the cavity decoupling phenomenology.

A reluctance to scale the attenuation response because of an apparent sensitivity of attenuation, as measured by Q, to frequency may have been removed as a result of some work by Blair of CSIRO Australia. He has shown that a factor of five differences in Q's determined from resonance experiments at ~10 kHz as compared to Q's from wave propagation experiments at ~1 MHz can be accounted for by imposing simple elastic scattering on the grain clustors which characterize the particular granite that he studied. The obvious preliminary conclusion is that scaling is a problem only as it is affected by grain size considerations and the resulting scattering. Thus small scale simulations of geologic media must eliminate scattering as an important process by minimizing grain size or the grain size must be scaled so that the scattering effect is identical between the medium of interest and the small-scale simulant.

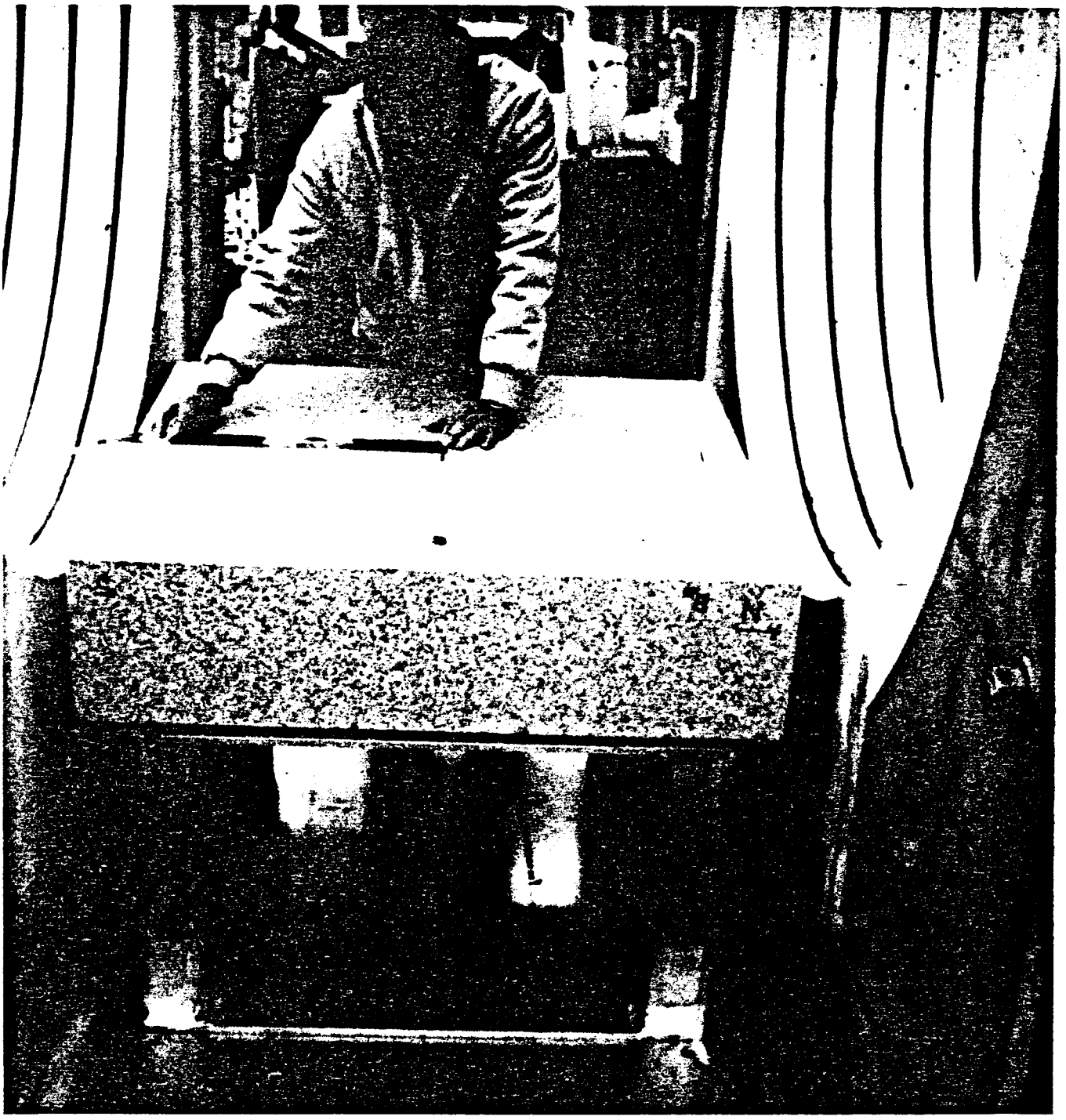

Figure C1. The first particle velocity gage (i.e. the gage most distant from the explosive source) being installed in the large Sierra White granite experimental assembly.

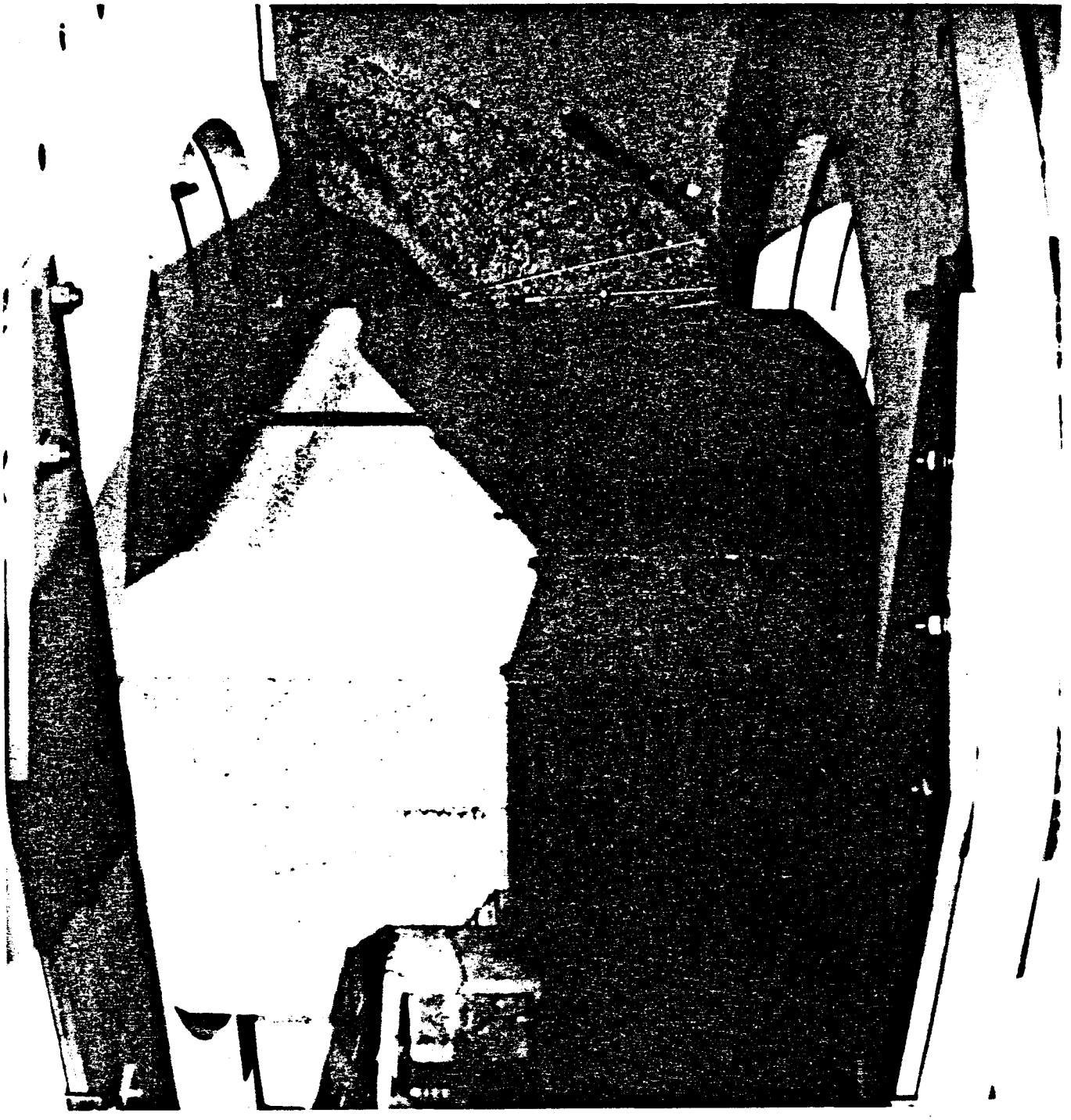

Figure C2. A particle velocity gage pair at the fourth level from the bottom of the large Sierra White granite model. The gage leads run parallel with the magnet field lines and active elements at the center cut magnetic lines as they move radially from the explosion source.

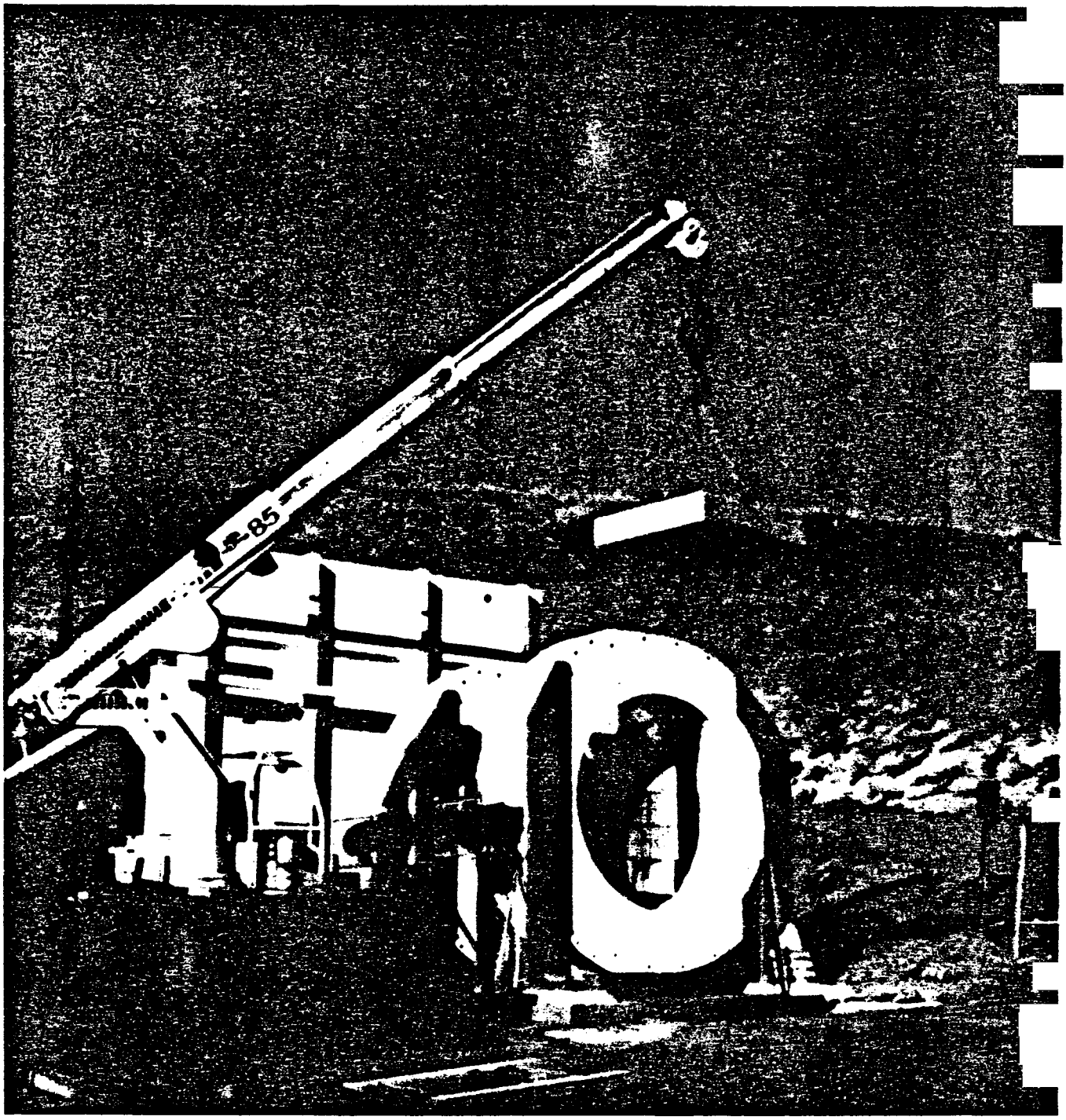

Figure C3. A block of the Sierra White granite model is being lowered into place between the magnet poles.

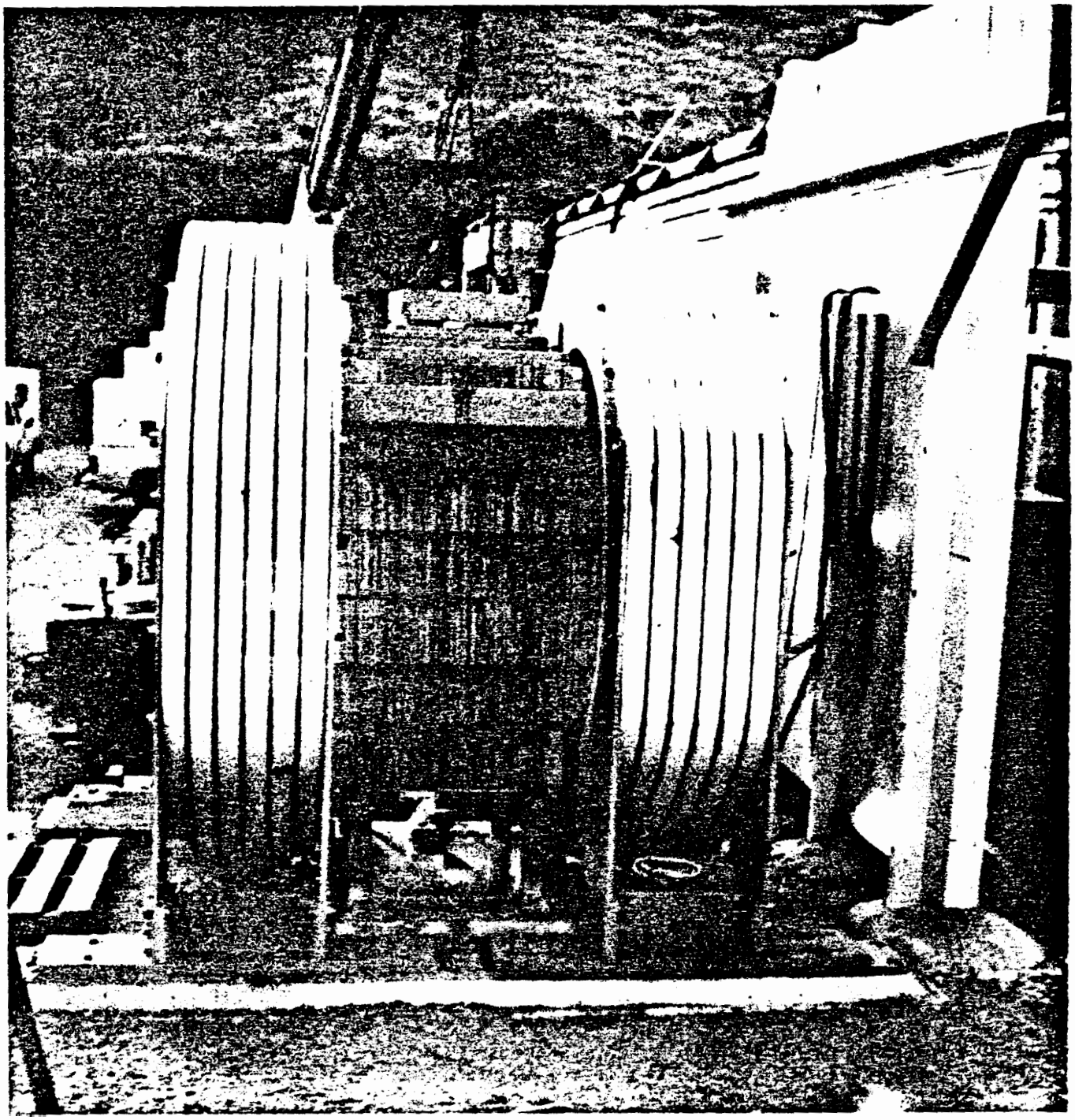

Figure C4. The nearly completed large Sierra White granite experimental assembly. The upper plate, not yet in place, hold the explosive inserts. Another plate is placed on top to increase writing time before reflected waves from the upper surface reach the gages.

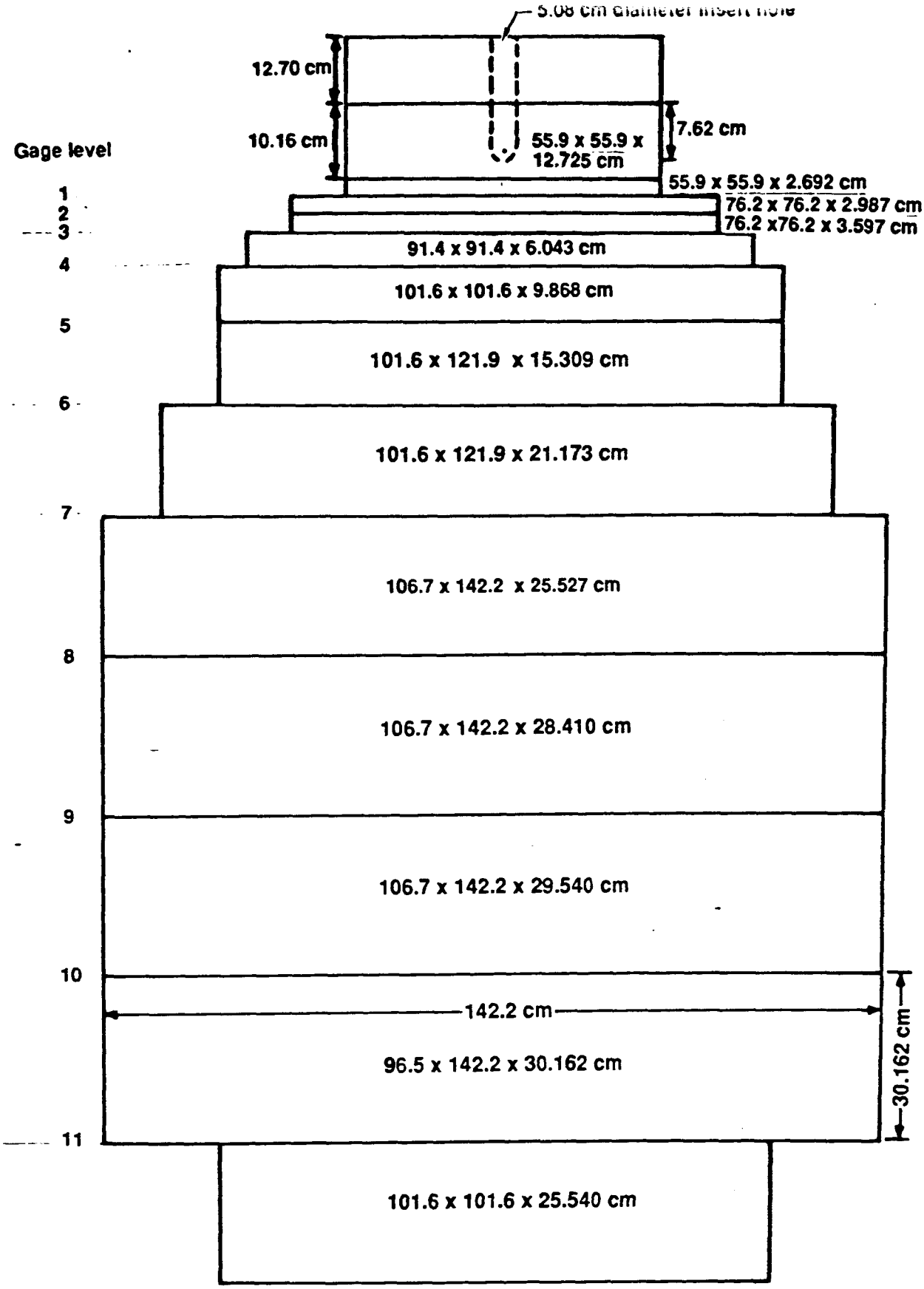

Figure C5. A schematic of the large Sierra White granite experimental assembly showing the dimensions and the various levels where gages are located. The blocks are epoxy bonded together and the thicknesses of these bonds are 0.127mm for levels 1, 2, 3 & 4, 0.254mm for levels 5, 6 & 7, and 0.508mm for levels 8, 9, 10 & 11.

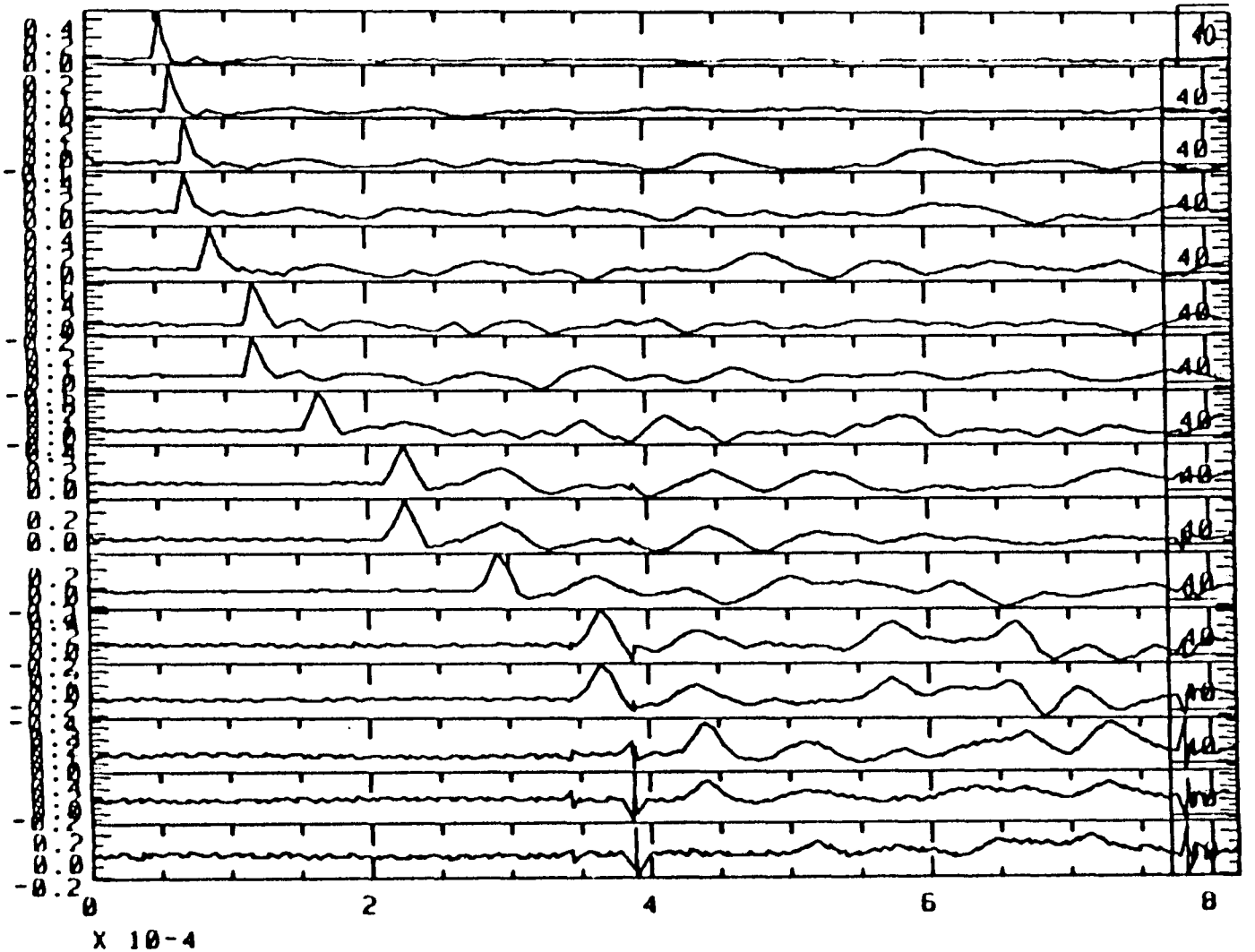

Figure C6. Gage record from the various gages in the large Sierra White granite experimental model using a 0.622 kJ tamped explosion as the energy source.

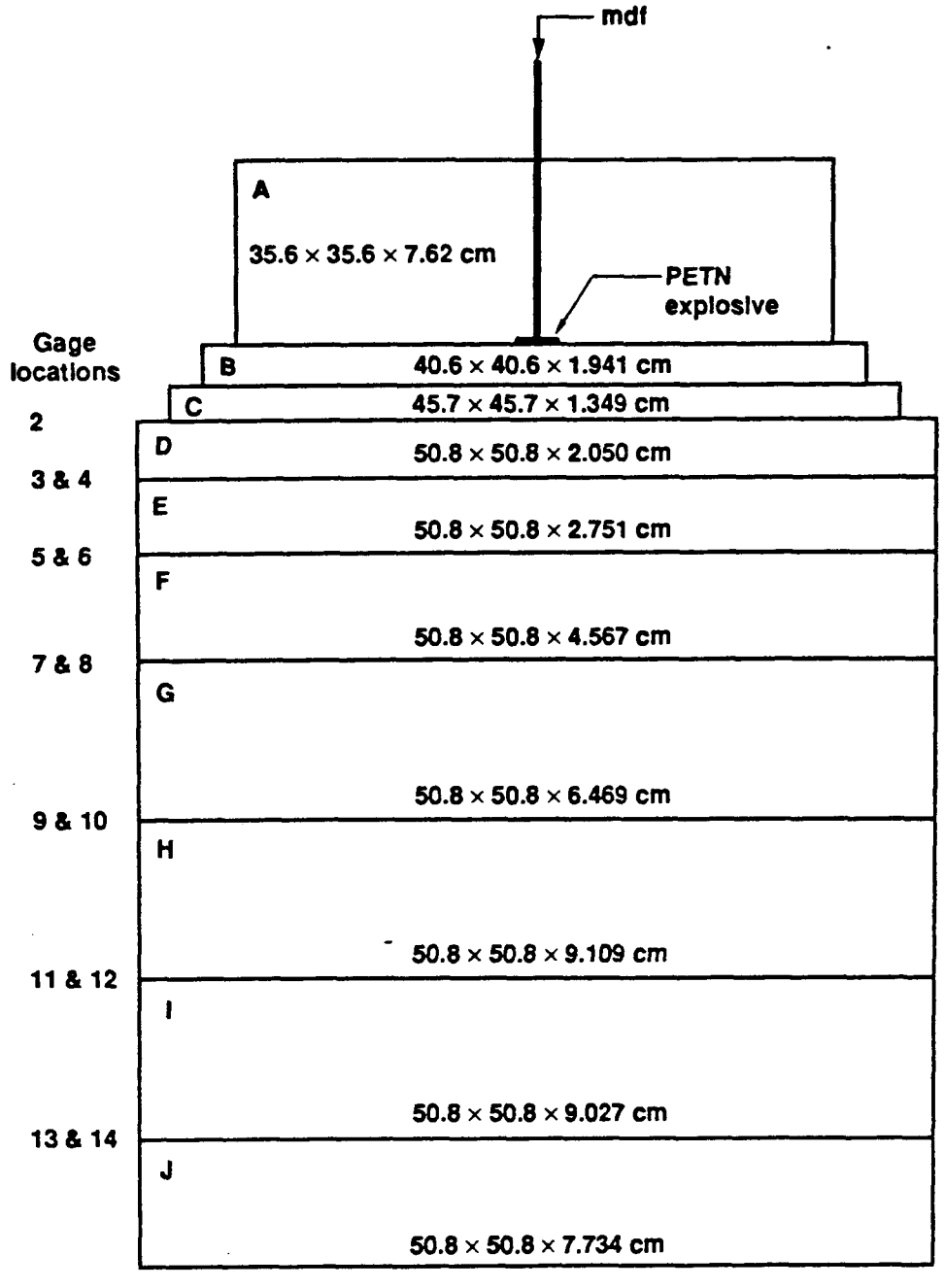

Figure C7. A schematic of the experimental assembly for the Sierra 1 experiment in Sierra White granite. The gage locations and dimensions are indicated on the figure. The PETN explosive yielded 3.24 kJ of energy. The distance from the explosive center to plate B is 5.11mm. The epoxy bond thickness between plates A and B is 0.51mm. The other epoxy bond thicknesses are 0.127mm and are included in the thicknesses given.

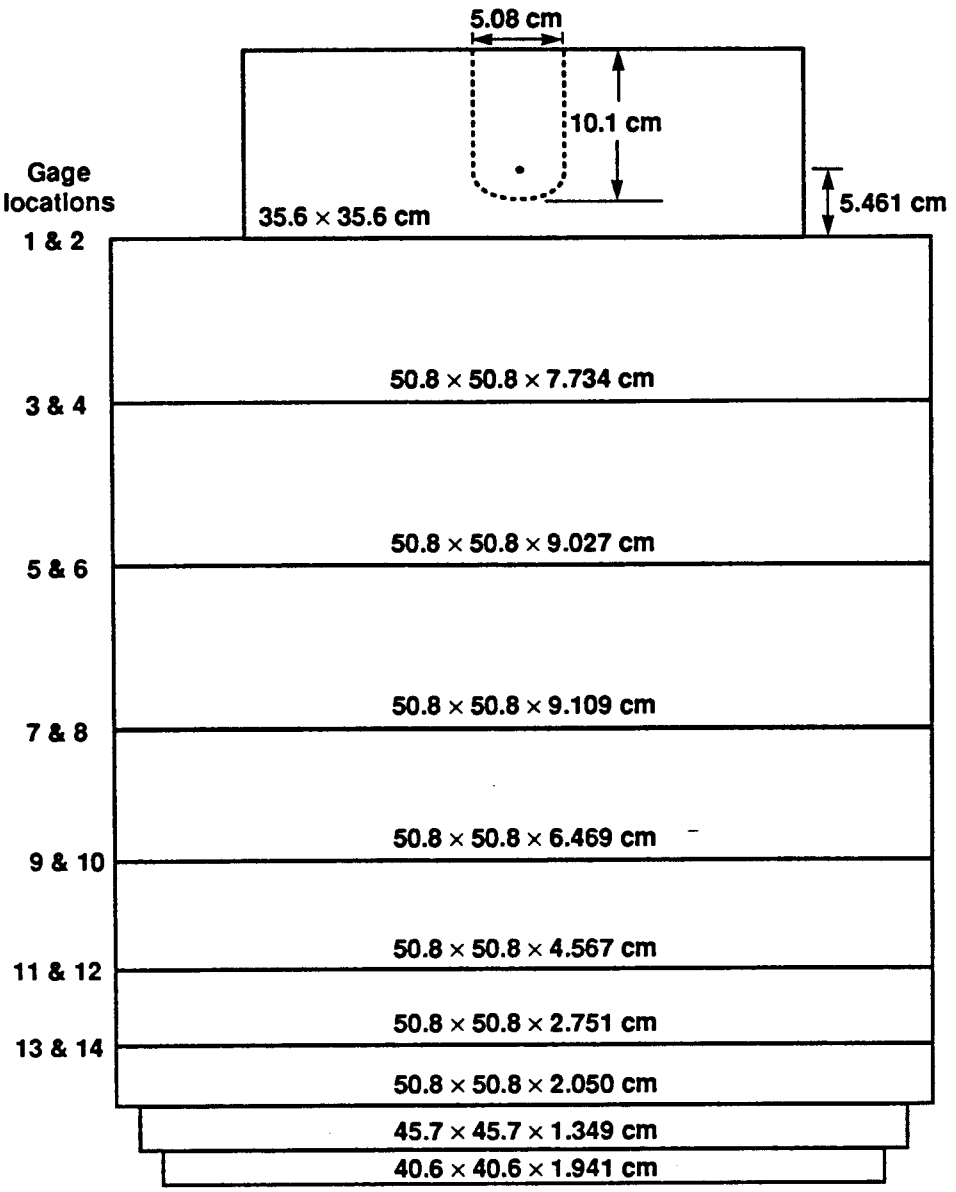

Figure C8. Schematic of the small Sierra White granite experimental model used for the Sierra 6 & Sierra 2 experiments. Gage locations and dimensions are given. Granite inserts were used in this reusable design so that both tamped and decoupled explosions were possible.

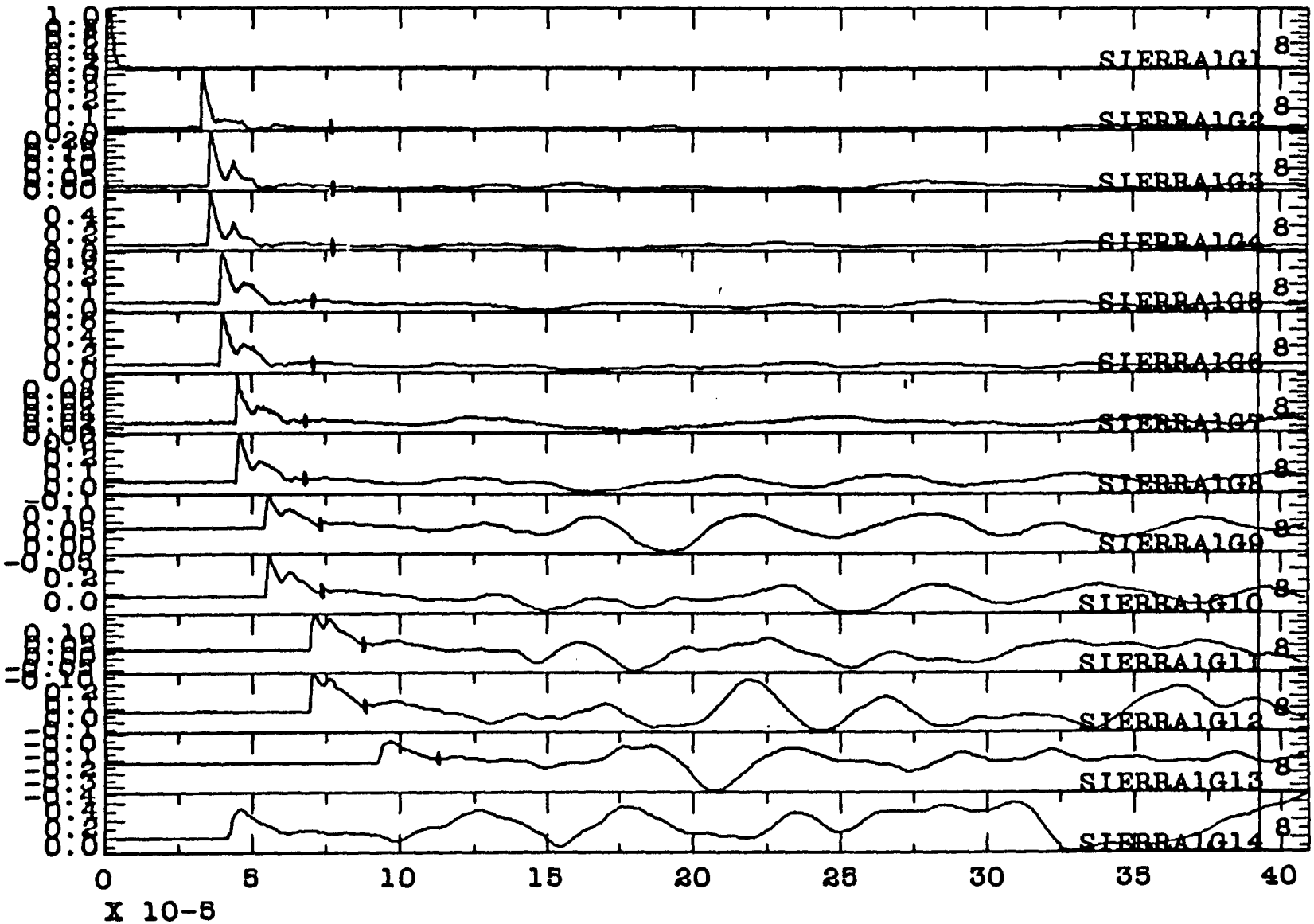

Figure C9. Experimental results from the various gages employed in the experiment Sierra 1. The anomalous shape of the pulse following the peak was shown to arise from coupling of the mdf energy into the granite block.

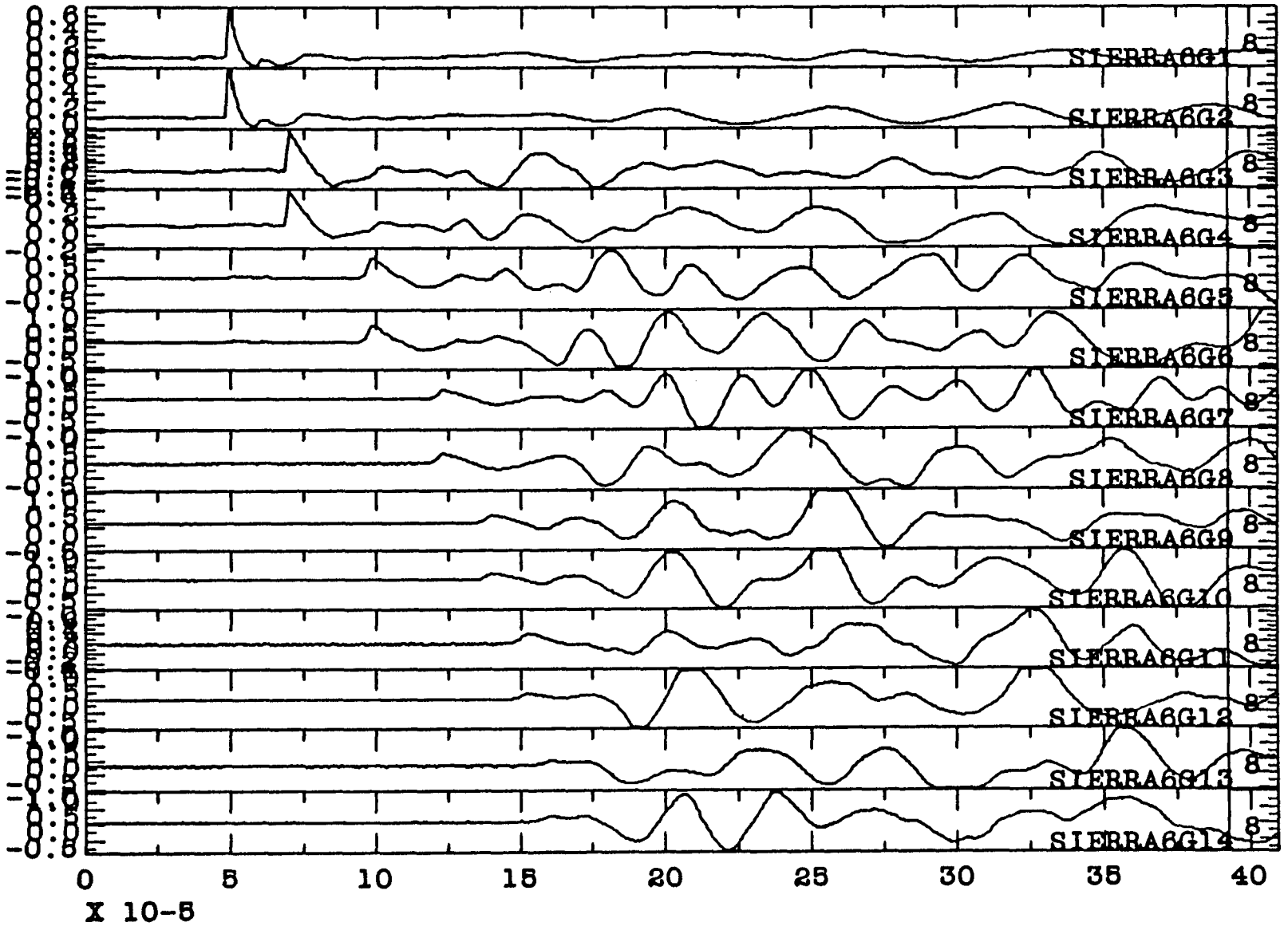

Figure C10. Results from a tamped explosion in Sierra White granite using the model shown in Figure C8. The anomalous features following the peak have been greatly reduced.

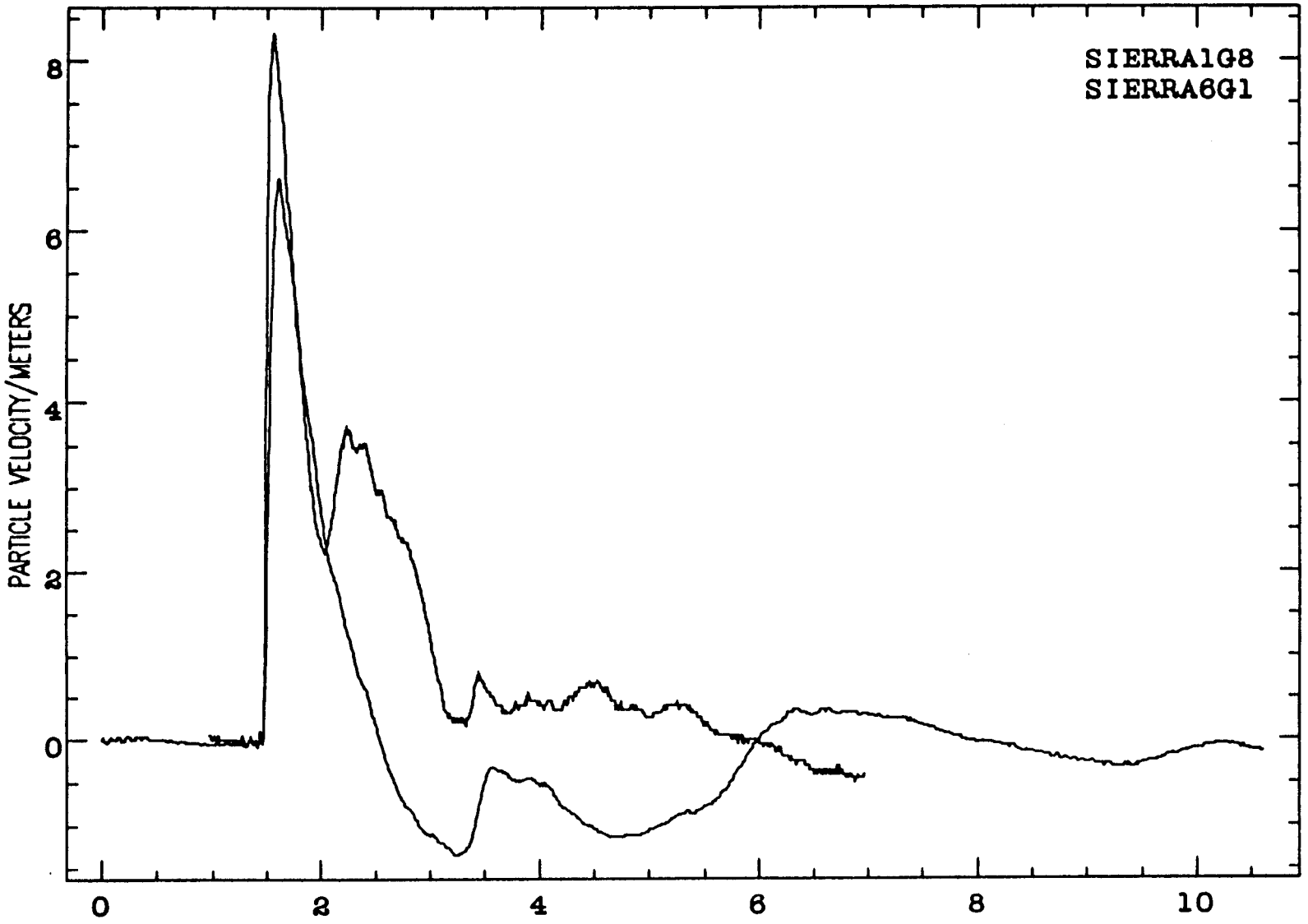

Figure C11. A comparison of particle velocity records from Sierra 1 and Sierra 6 at nearly the same peak particle velocity. Most of the anomalous structure behind the peak seen in Sierra 1 has been eliminated in Sierra 6 by placing the mdf in a stainless steel tube and by decoupling the tube from the granite with solid foam.

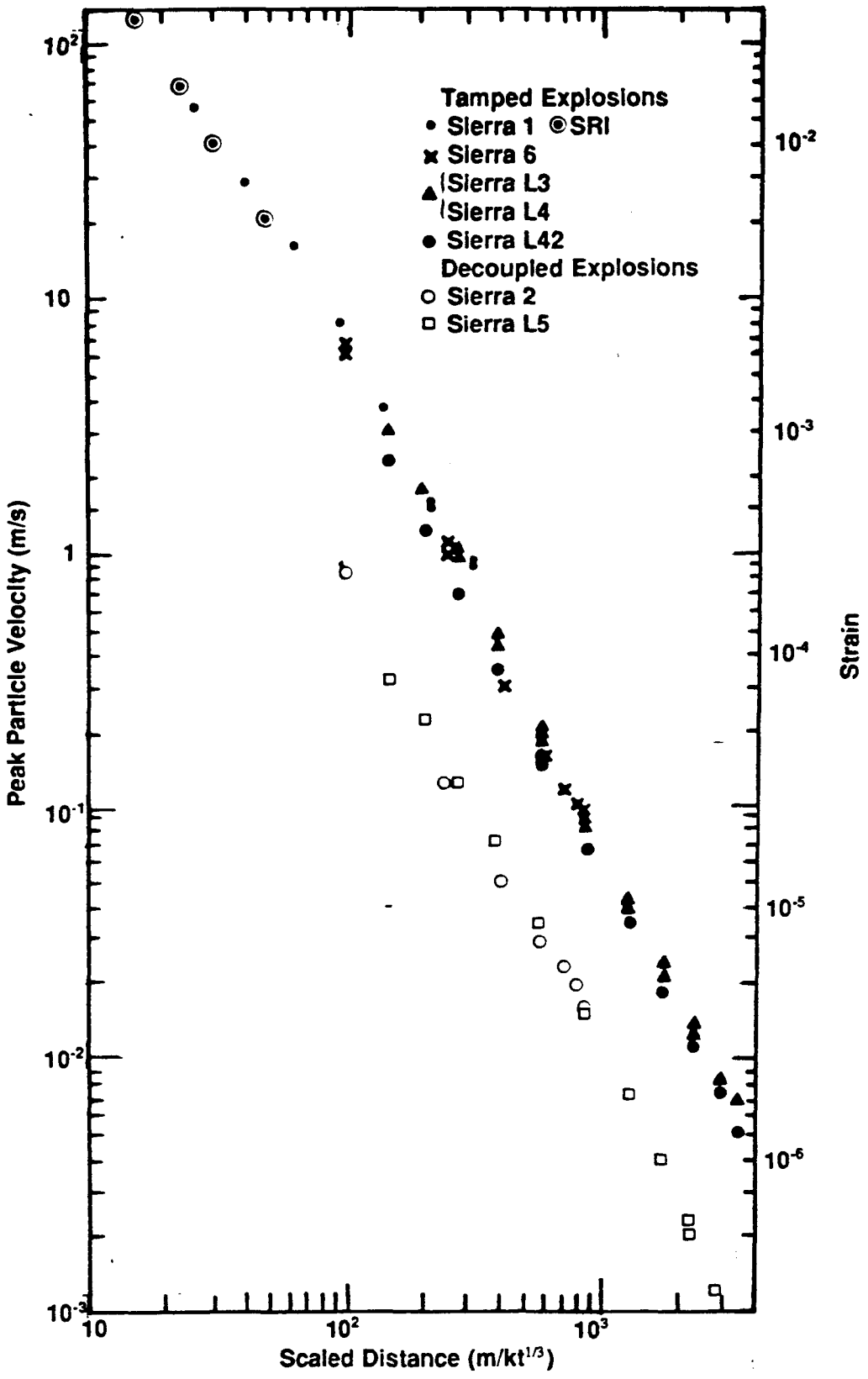

Figure C12. A comparison of peak particle velocities from various tamped explosions in Sierra White granite. Included in the comparison are data from SRI. Also shown are the results from two cavity decoupled explosions.

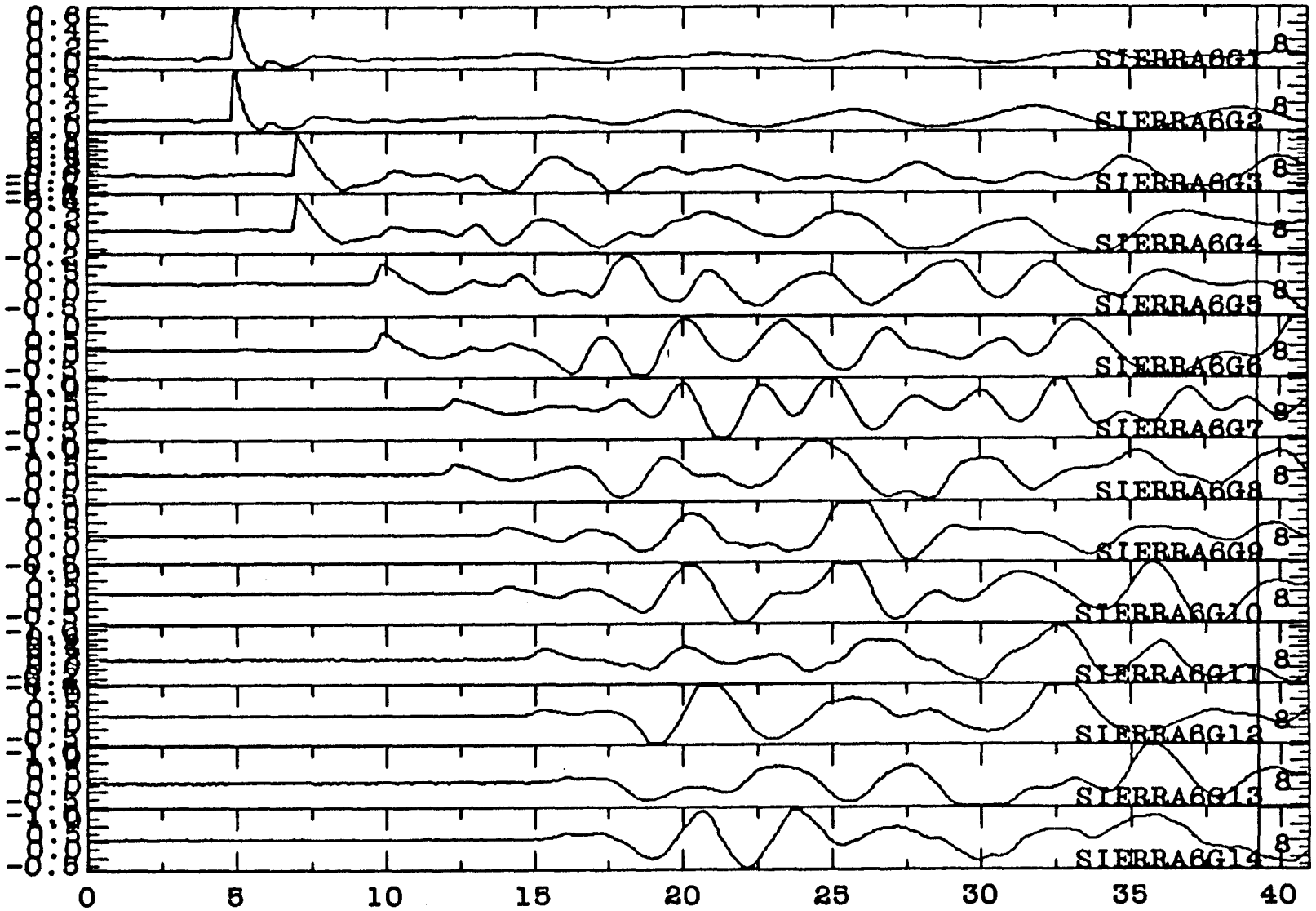

Figure C13-C42. The particle velocity records and the displacements calculated from the particle velocity records for all the gages of experiments Sierra 6 (tamped) and Sierra 2 (cavity decoupled). The data are displayed as gage pairs to indicate reproducibility and useful writing

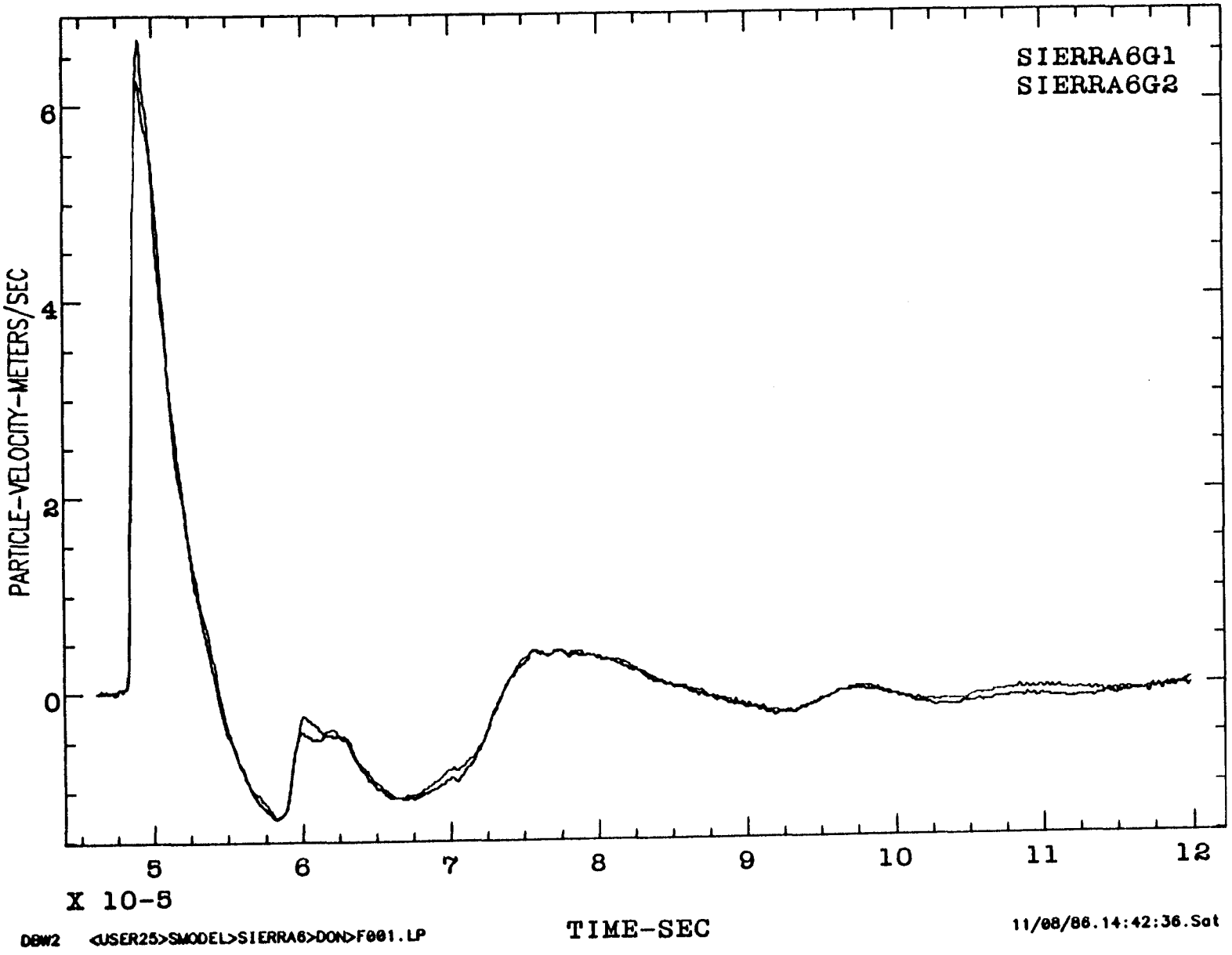
SIERRA6G1
SIERRA6G2
PARTICLE-VELOCITY-METERS/SEC
6
4
2
0
5
6
7
8
9
10
11
12
X 10-5
TIME-SEC
DBW2 <USER25>SMODEL>SIERRA6>DON>F001.LP
11/08/86.14:42:36.Sat

C 17

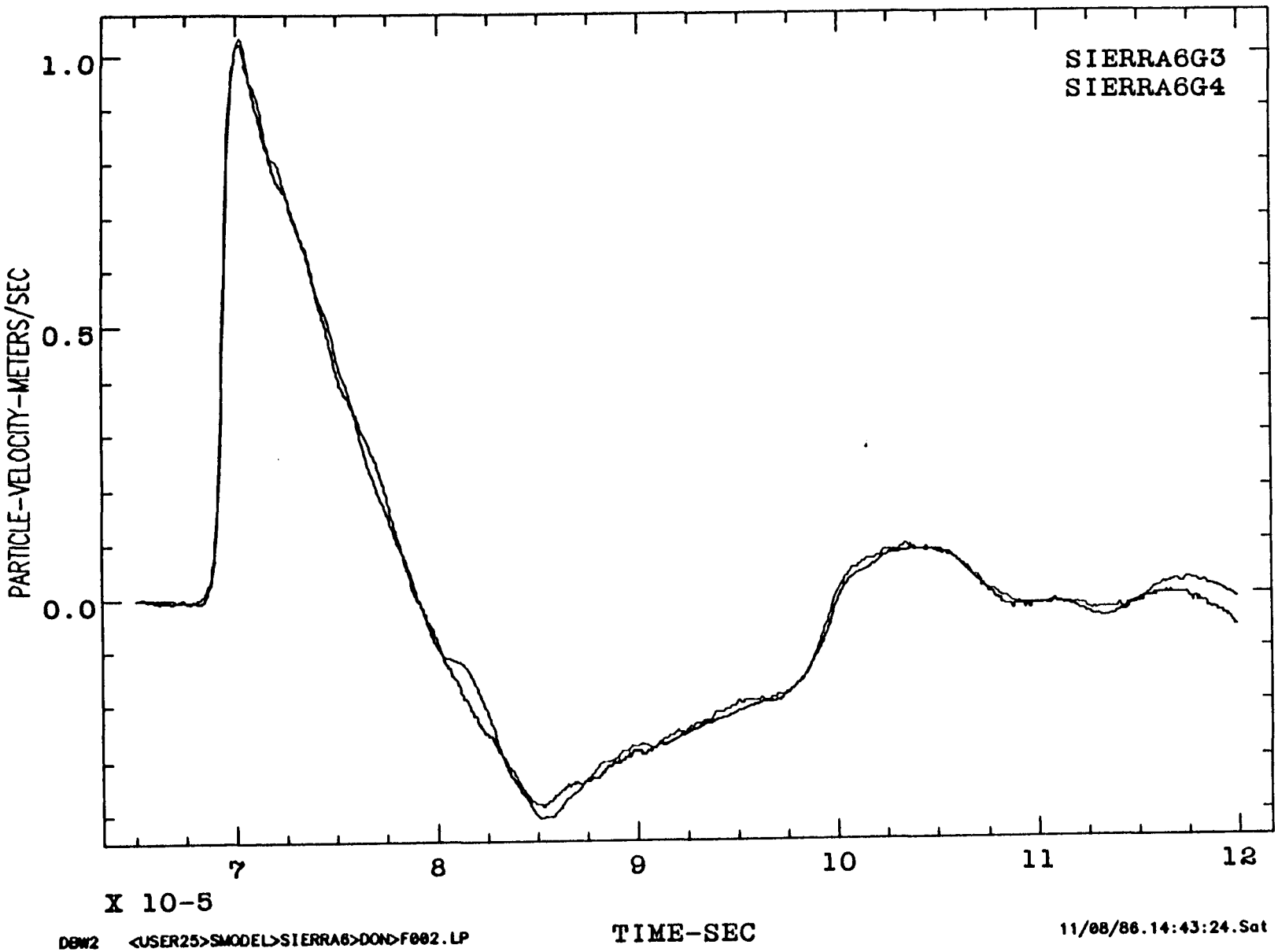
SIERRA6G3
SIERRA6G4
1.0
0.5
0.0
PARTICLE-VELOCITY-METERS/SEC
7
8
9
10
11
12
X 10-5
TIME-SEC
DBW2 <USER25>SMODEL>SIERRA6>DON>F002.LP
11/08/86.14:43:24.Sat

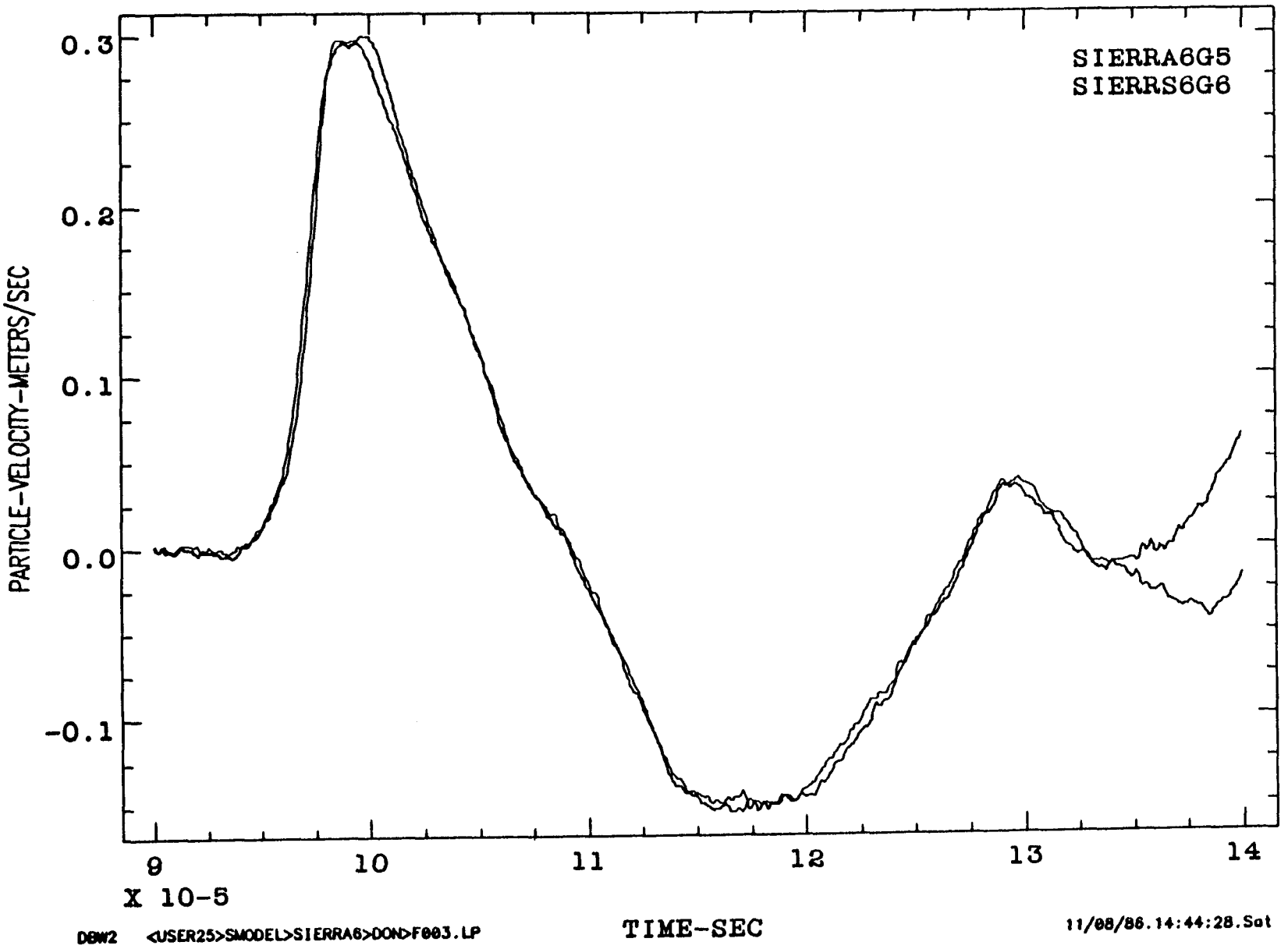
SIERRA6G5
SIERRS6G6
PARTICLE-VELOCITY-METERS/SEC
0.3
0.2
0.1
0.0
-0.1
9
10
11
12
13
14
X 10-5
TIME-SEC
DBW2 <USER25>SMODEL>SIERRA6>DOND>F003.LP
11/08/86.14:44:28.Sat

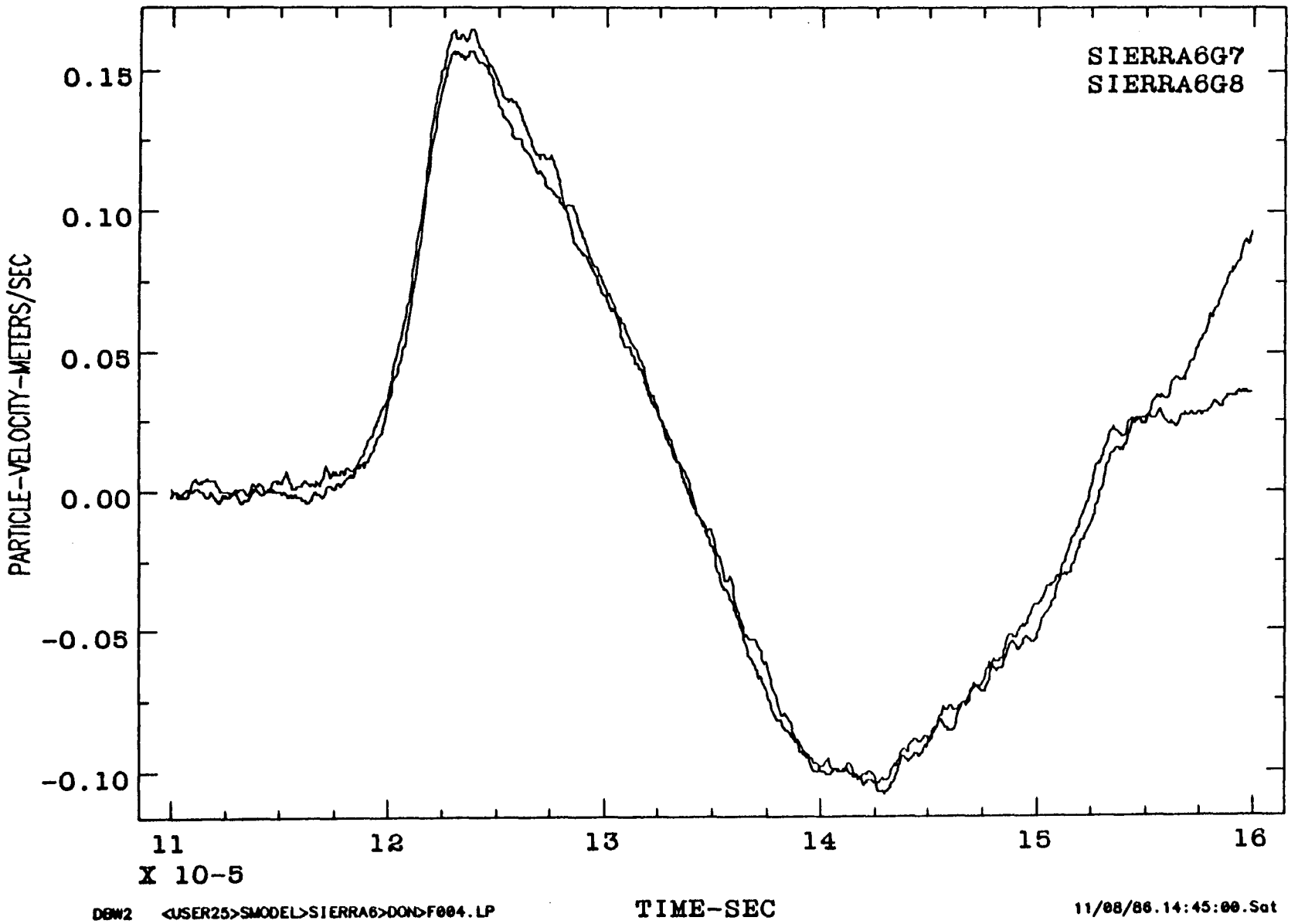
SIERRA6G7
SIERRA6G8
PARTICLE-VELOCITY-METERS/SEC
0.15
0.10
0.05
0.00
-0.05
-0.10
11
12
13
14
15
16
X 10-5
TIME-SEC
DBW2 <USER25>SMODEL>SIERRA6>DON>F004.LP
11/08/86.14:45:00.Sat

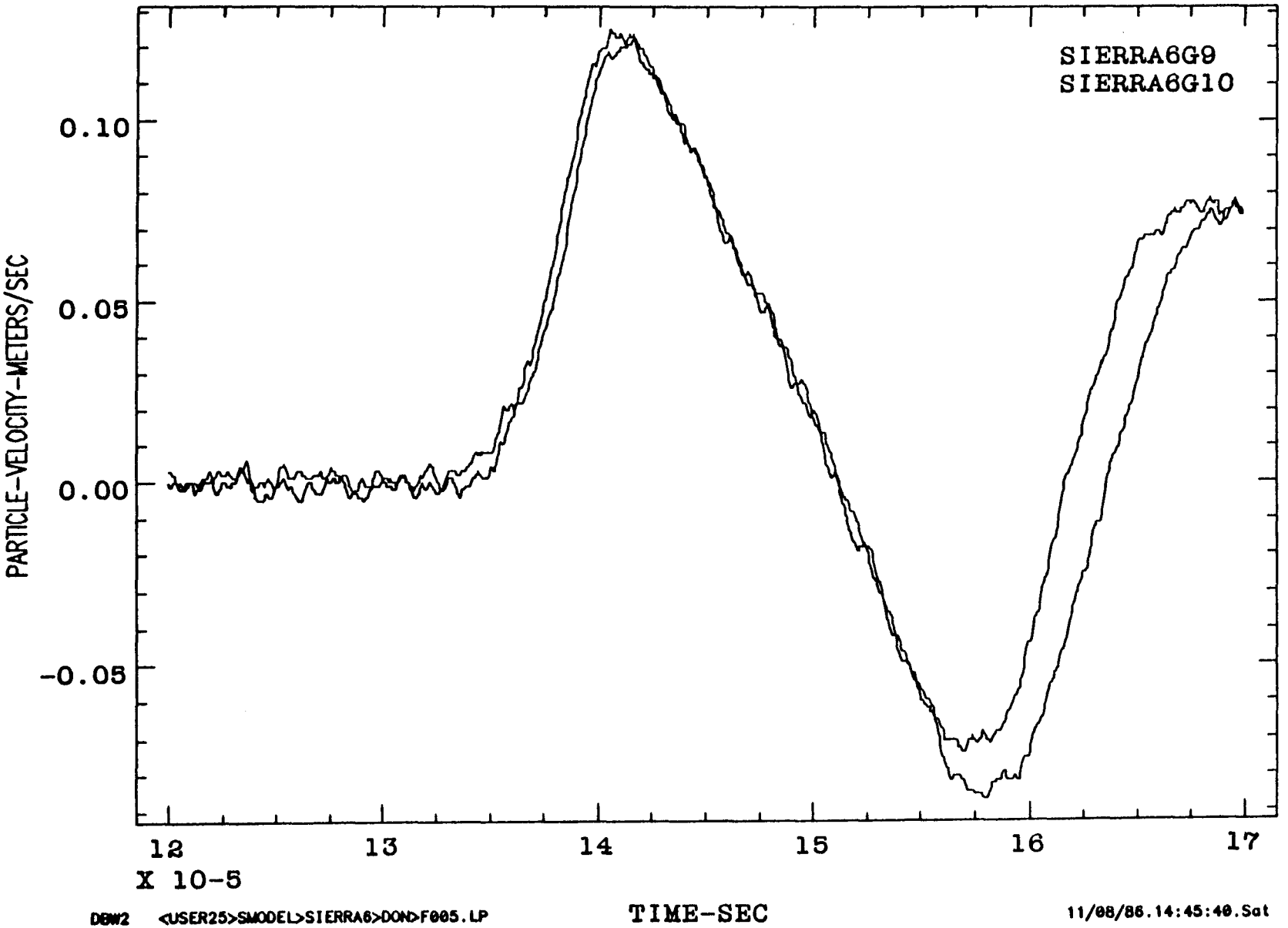
SIERRA6G9
SIERRA6G10
0.10
0.05
0.00
-0.05
PARTICLE-VELOCITY-METERS/SEC
12
13
14
15
16
17
X 10-5
TIME-SEC
DBW2 <USER25>SMODEL>SIERRA6>DON>F005.LP
11/08/86.14:45:40.Sat

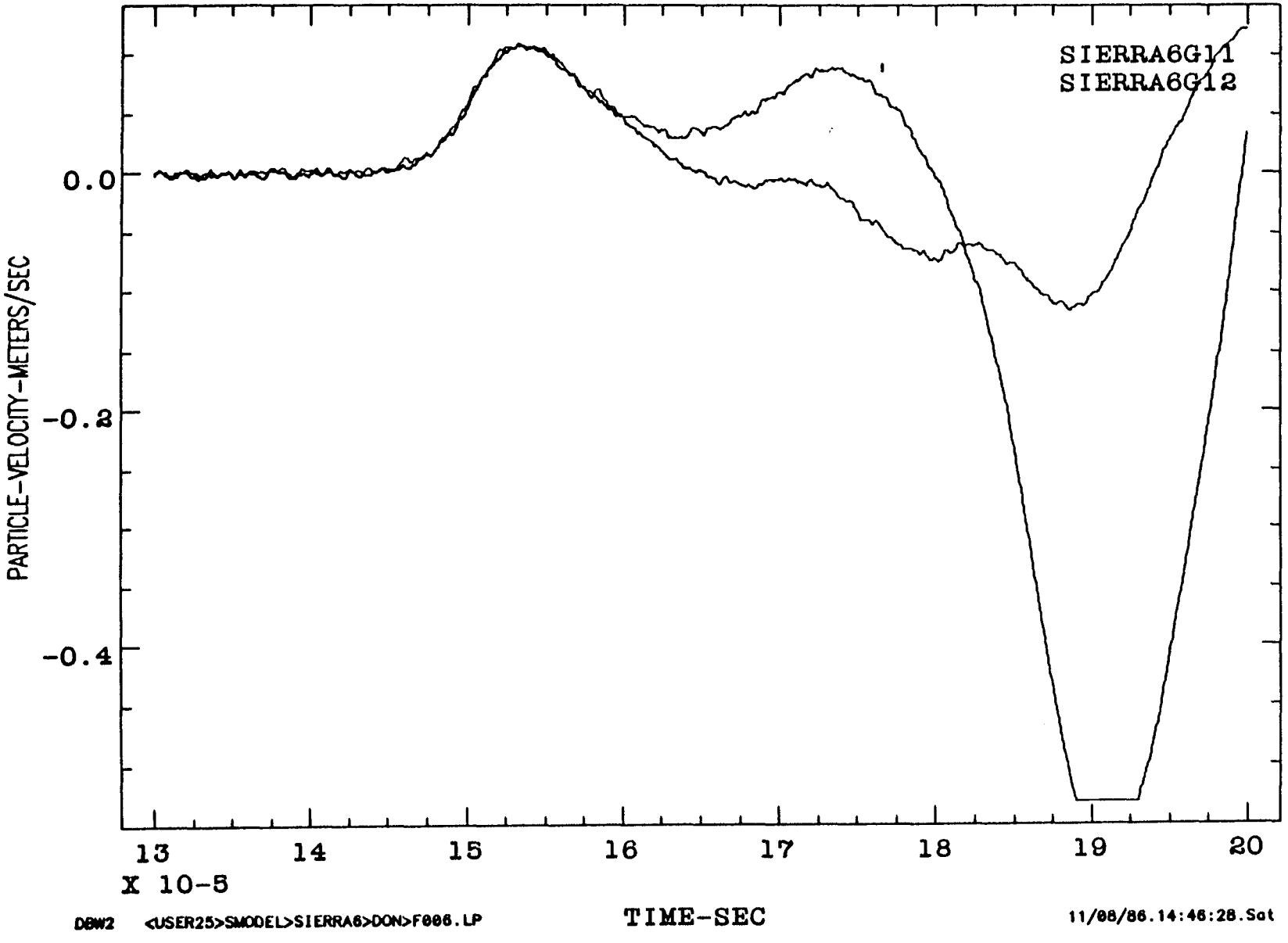
SIERRA6G11
SIERRA6G12
0.0
-0.2
-0.4
PARTICLE-VELOCITY-METERS/SEC
13
14
15
16
17
18
19
20
X 10-5
TIME-SEC
DBW2 <USER25>SMODEL>SIERRA6>DON>F006.LP
11/06/86.14:46:28.Sat

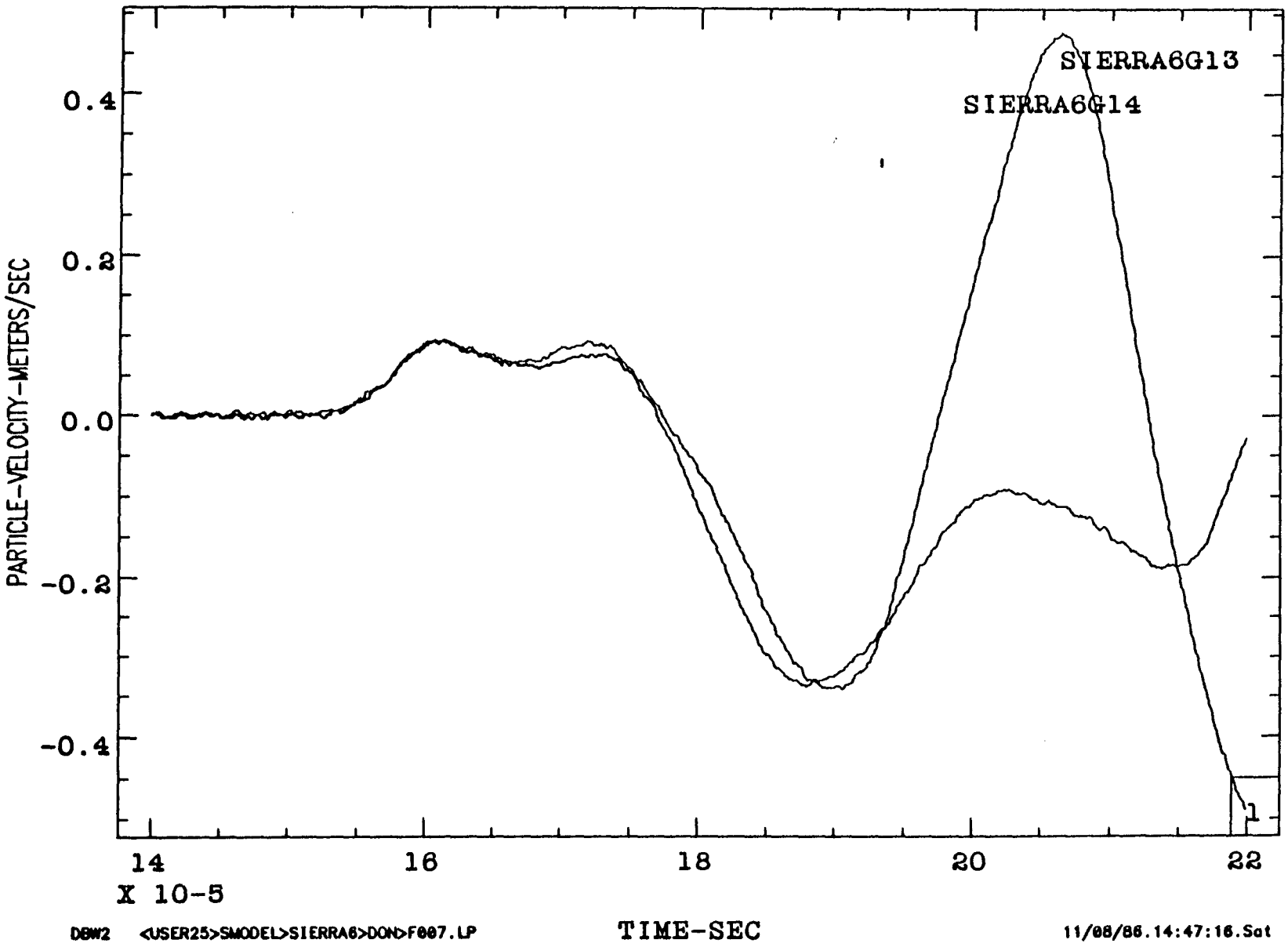
SIERRA6G13
SIERRA6G14
0.4
0.2
0.0
-0.2
-0.4
PARTICLE-VELOCITY-METERS/SEC
14
16
18
20
22
X 10-5
TIME-SEC
DBW2 <USER25>SMODEL>SIERRA6>DON>F007.LP
11/08/86.14:47:16.Sat

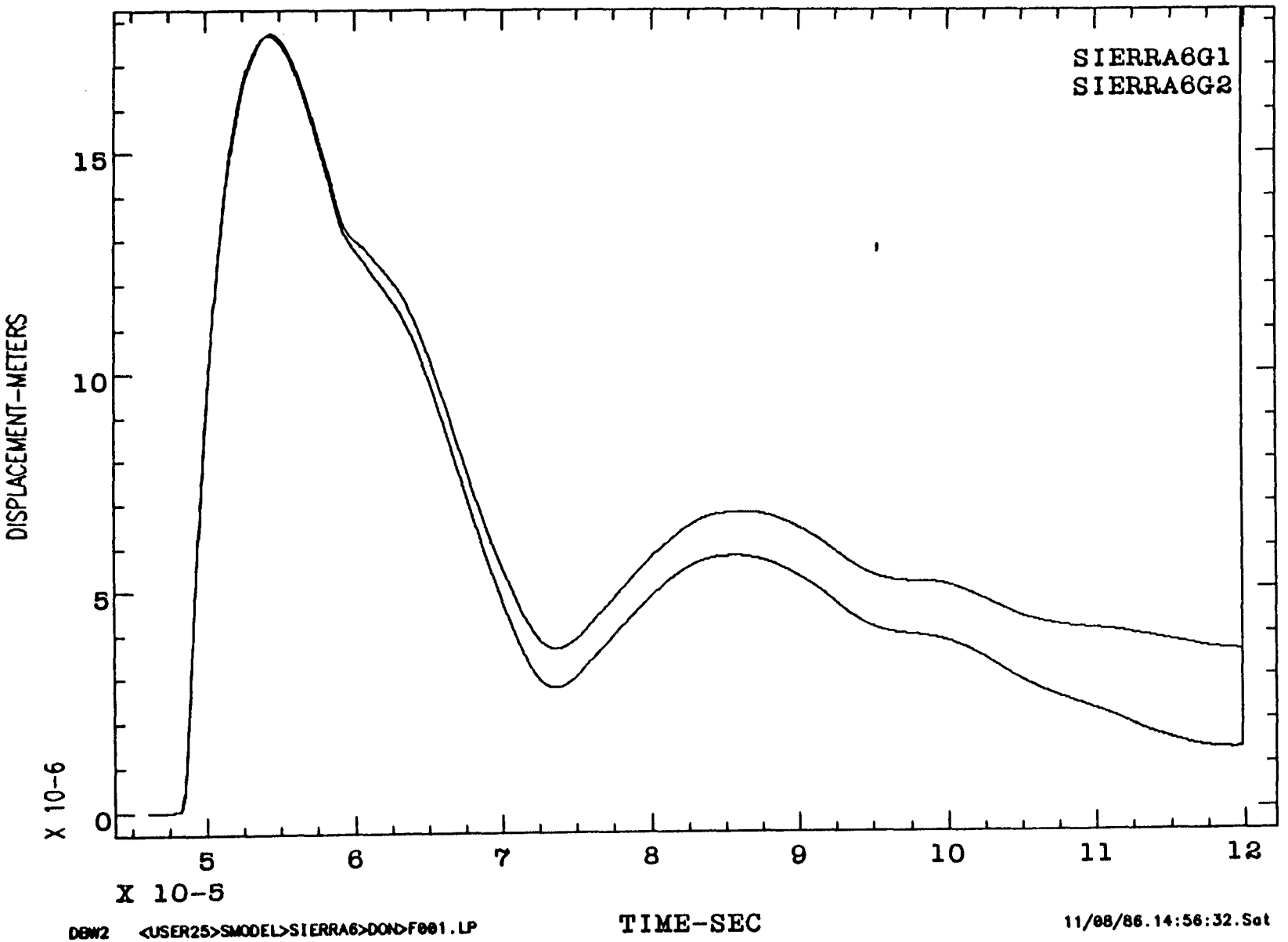
SIERRA6G1
SIERRA6G2
DISPLACEMENT-METERS
X 10-6
15
10
5
0
5
6
7
8
9
10
11
12
X 10-5
TIME-SEC
DBW2 <USER25>SMODEL>SIERRA6>DON>F001.LP
11/08/86.14:56:32.Sat

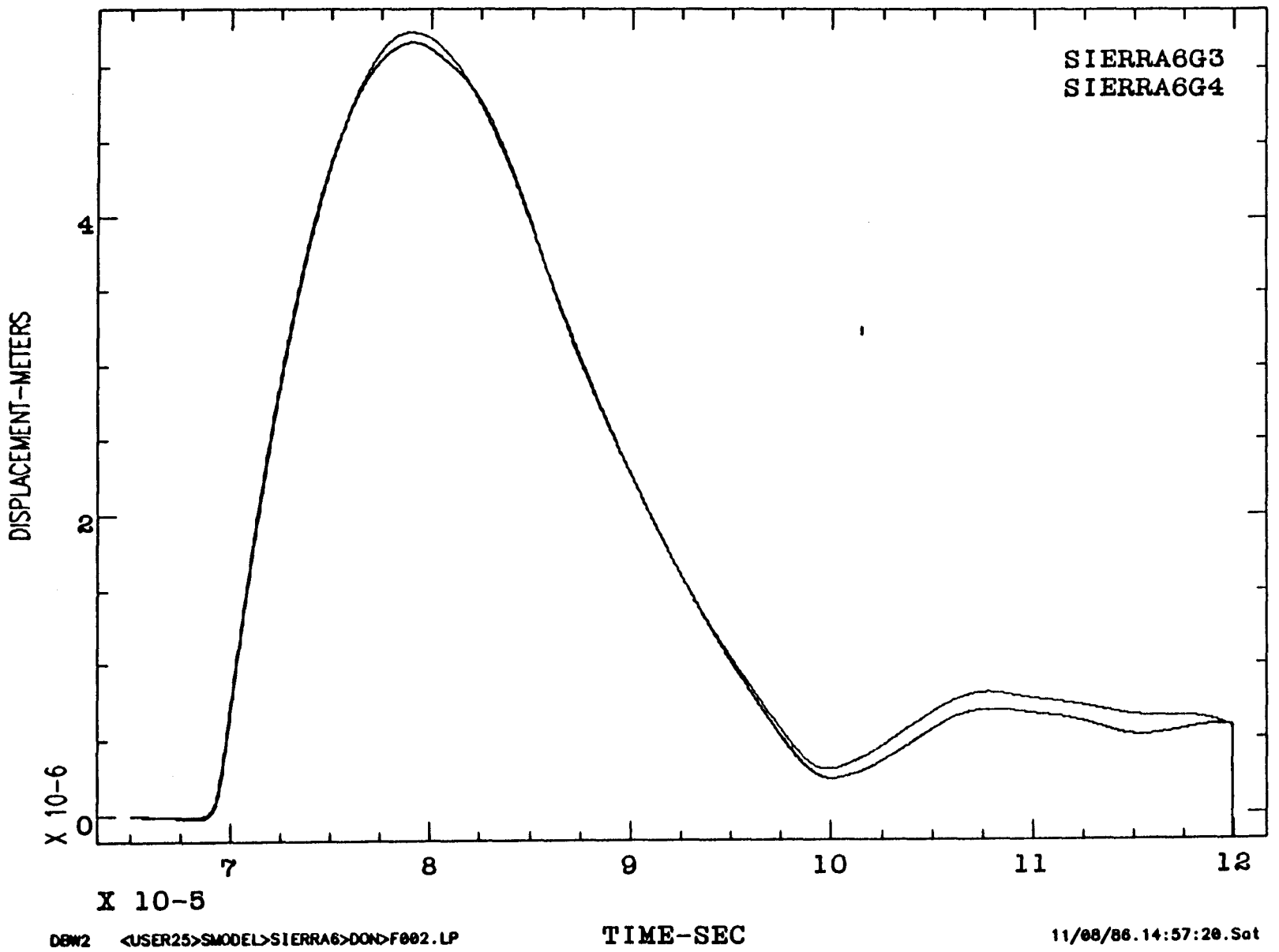
SIERRA6G3
SIERRA6G4
DISPLACEMENT-METERS
X 10-6
0
2
4
7
8
9
10
11
12
X 10-5
TIME-SEC
DBW2 <USER25>SMODEL>SIERRA6>DON>F002.LP
11/08/86.14:57:20.Sat

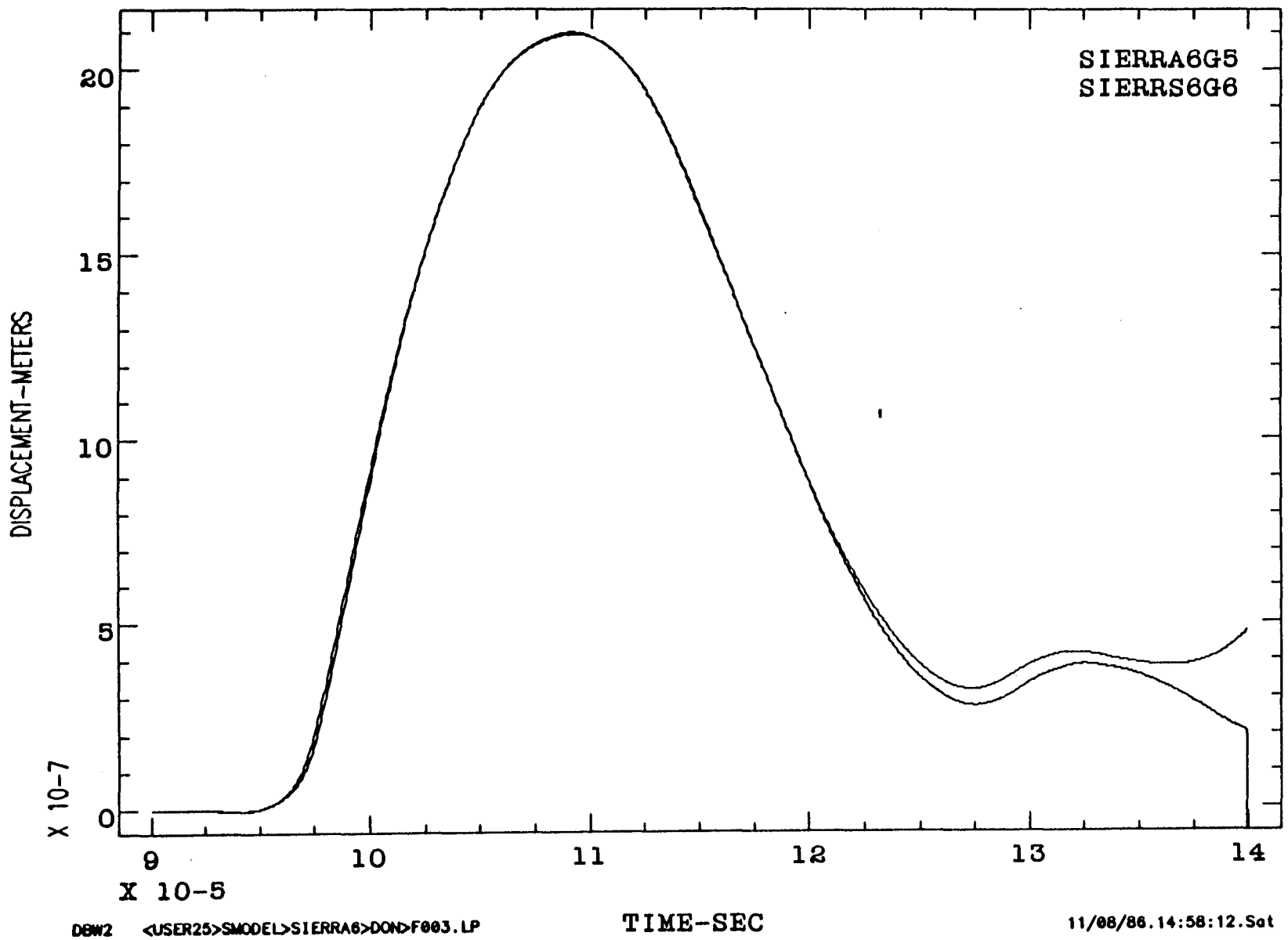
SIERRA6G5
SIERRS6G6
DISPLACEMENT-METERS
X 10-7
20
15
10
5
0
9
10
11
12
13
14
X 10-5
TIME-SEC
DBW2 <USER25>SMODEL>SIERRA6>DON>F003.LP
11/08/86.14:58:12.Sat

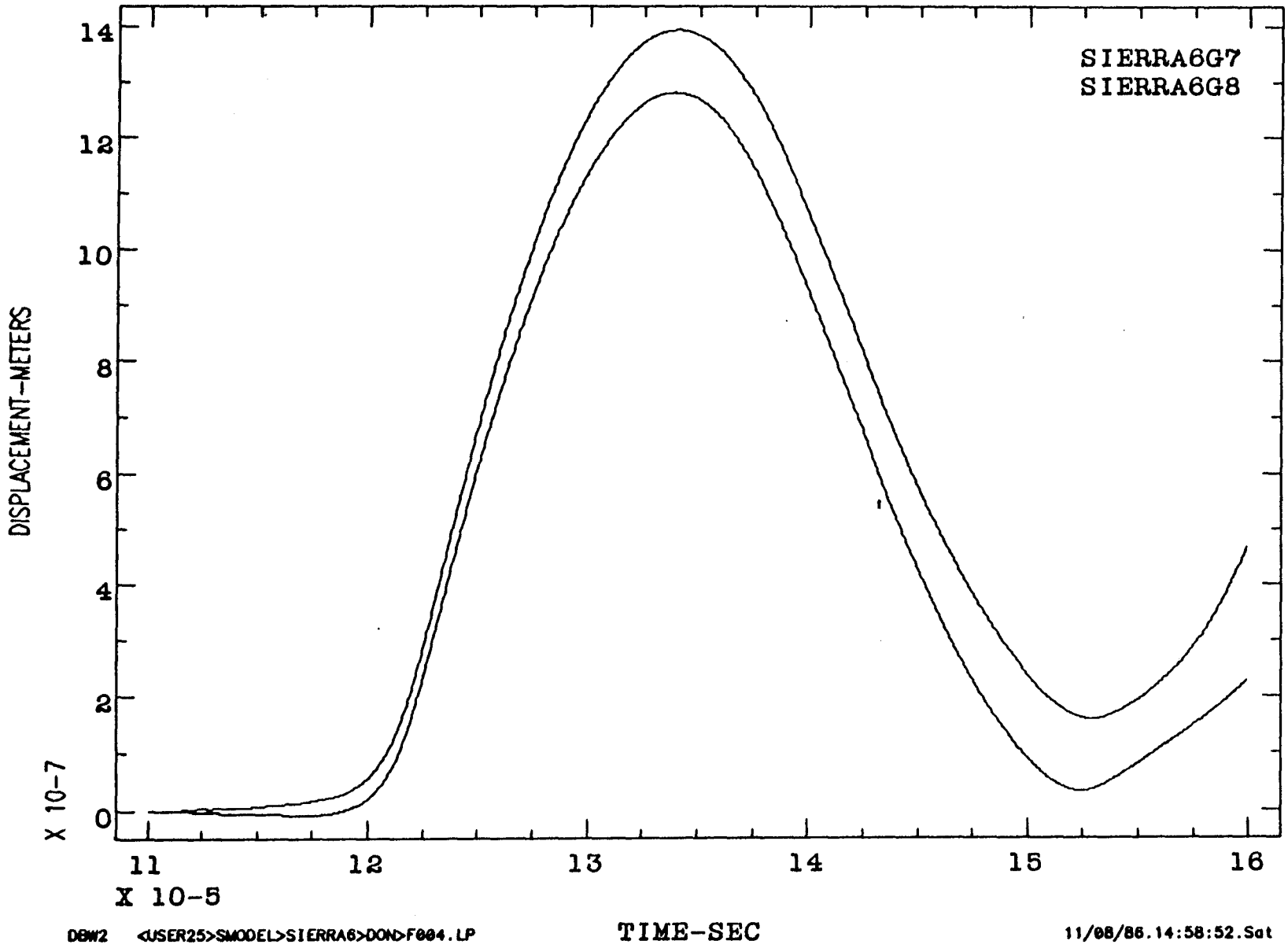
SIERRA6G7
SIERRA6G8
DISPLACEMENT-METERS
X 10-7
14
12
10
8
6
4
2
0
11
12
13
14
15
16
X 10-5
TIME-SEC
DBW2 <USER25>SMODEL>SIERRA6>DON>F004.LP
11/08/86.14:58:52.Sat

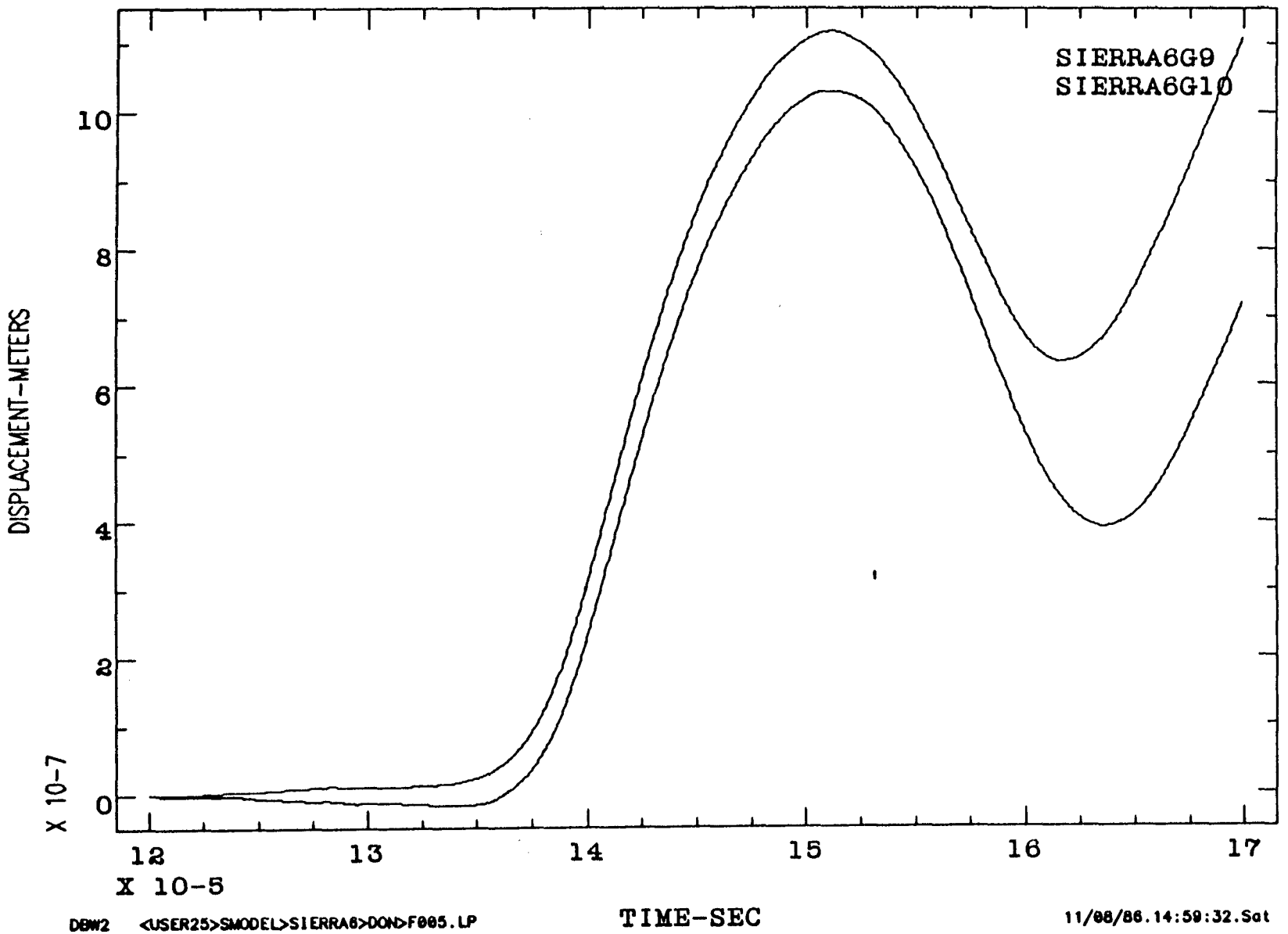
SIERRA6G9
SIERRA6G10
DISPLACEMENT-METERS
X 10-7
0
2
4
6
8
10
12
13
14
15
16
17
X 10-5
TIME-SEC
DBW2 <USER25>SMODEL>SIERRA6>DON>F005.LP
11/08/86.14:59:32.Sat

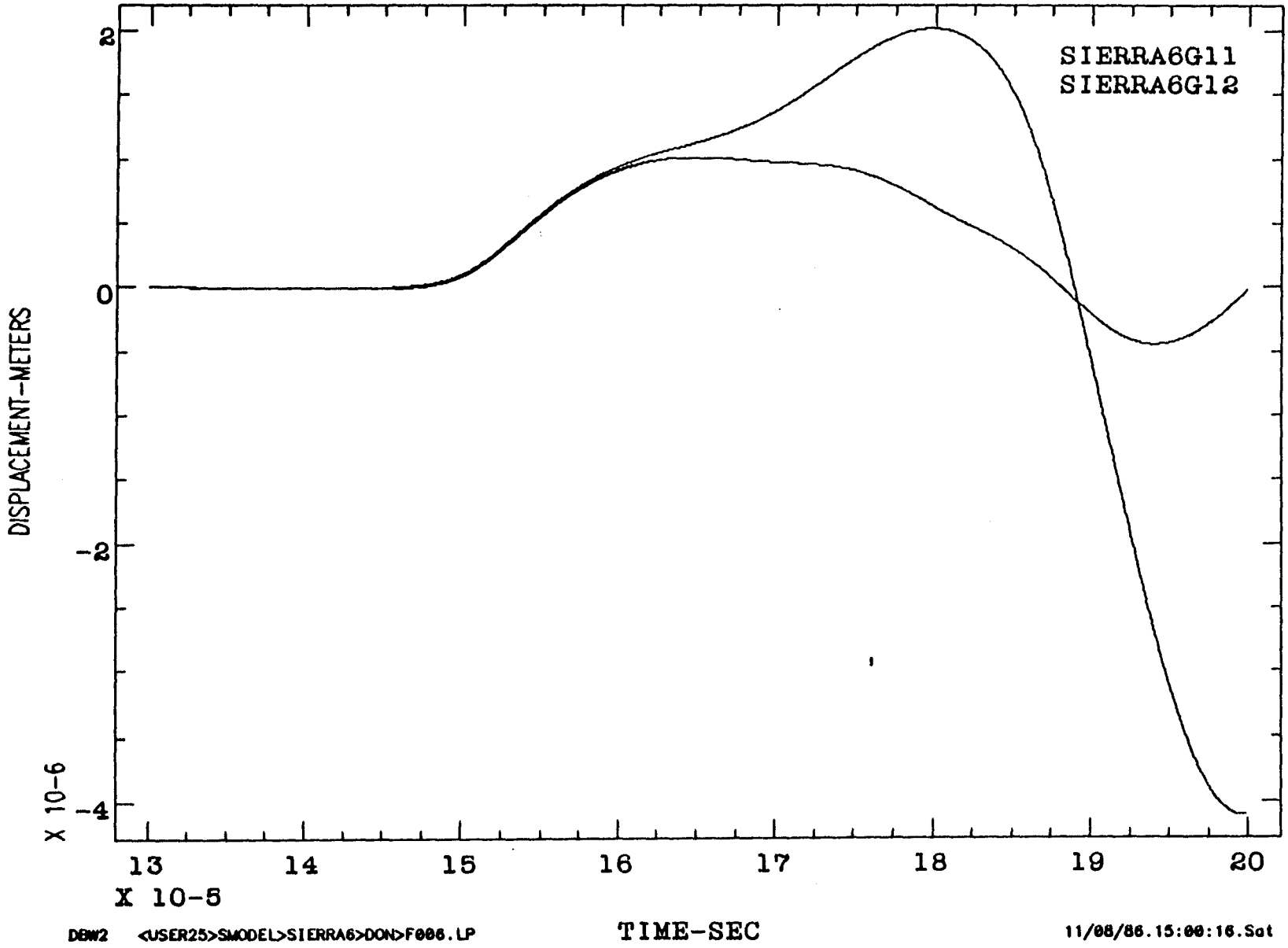
SIERRA6G11
SIERRA6G12
DISPLACEMENT-METERS
X 10-6
2
0
-2
-4
13
14
15
16
17
18
19
20
X 10-5
TIME-SEC
DBW2 <USER25>SMODEL>SIERRA6>DON>F006.LP
11/08/86.15:00:16.Sat

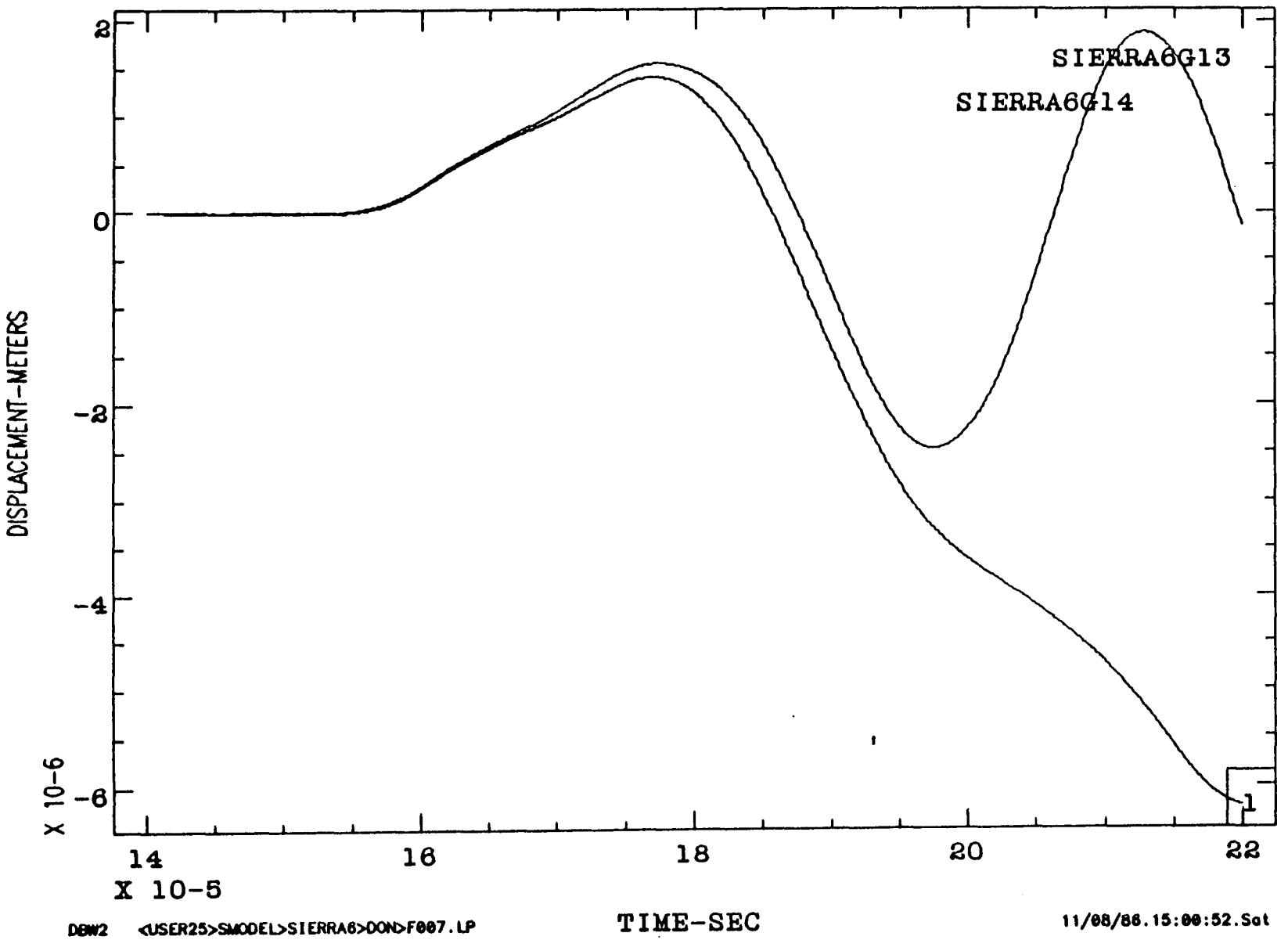
SIERRA6G13
SIERRA6G14
2
0
-2
-4
-6
X 10-6
DISPLACEMENT-METERS
14
16
18
20
22
X 10-5
TIME-SEC
DBW2 <USER25>SMODEL>SIERRA6>DON>F007.LP
11/08/86.15:00:52.Sat

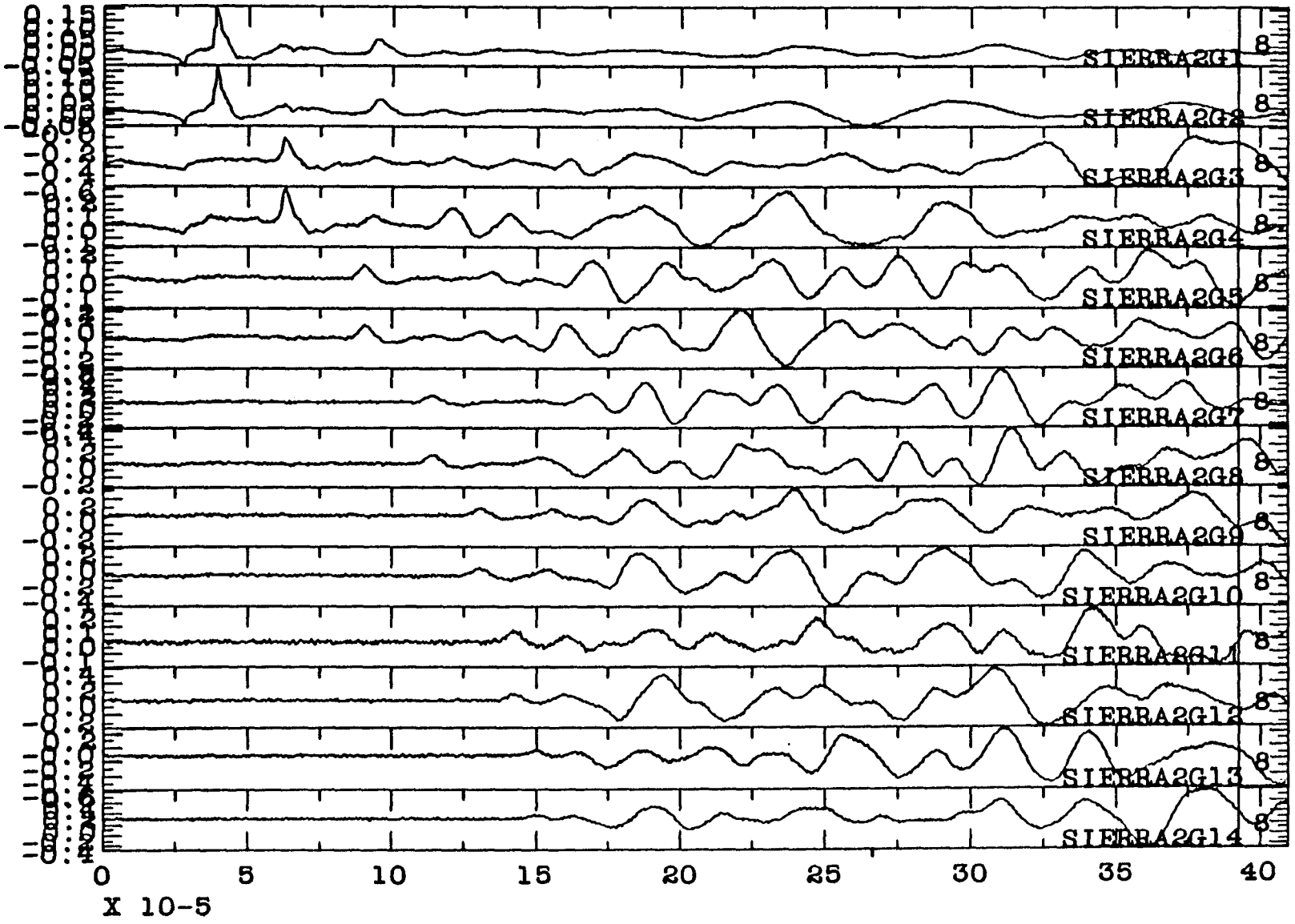
SIERRA2G1
SIERRA2G2
SIERRA2G3
SIERRA2G4
SIERRA2G5
SIERRA2G6
SIERRA2G7
SIERRA2G8
SIERRA2G9
SIERRA2G10
SIERRA2G11
SIERRA2G12
SIERRA2G13
SIERRA2G14
0
5
10
15
20
25
30
35
40
X 10-5
DBW2 <USER25>SMODEL>SIERRA2>LARSON>F001.LP
11/26/86.11:29:44.Wed

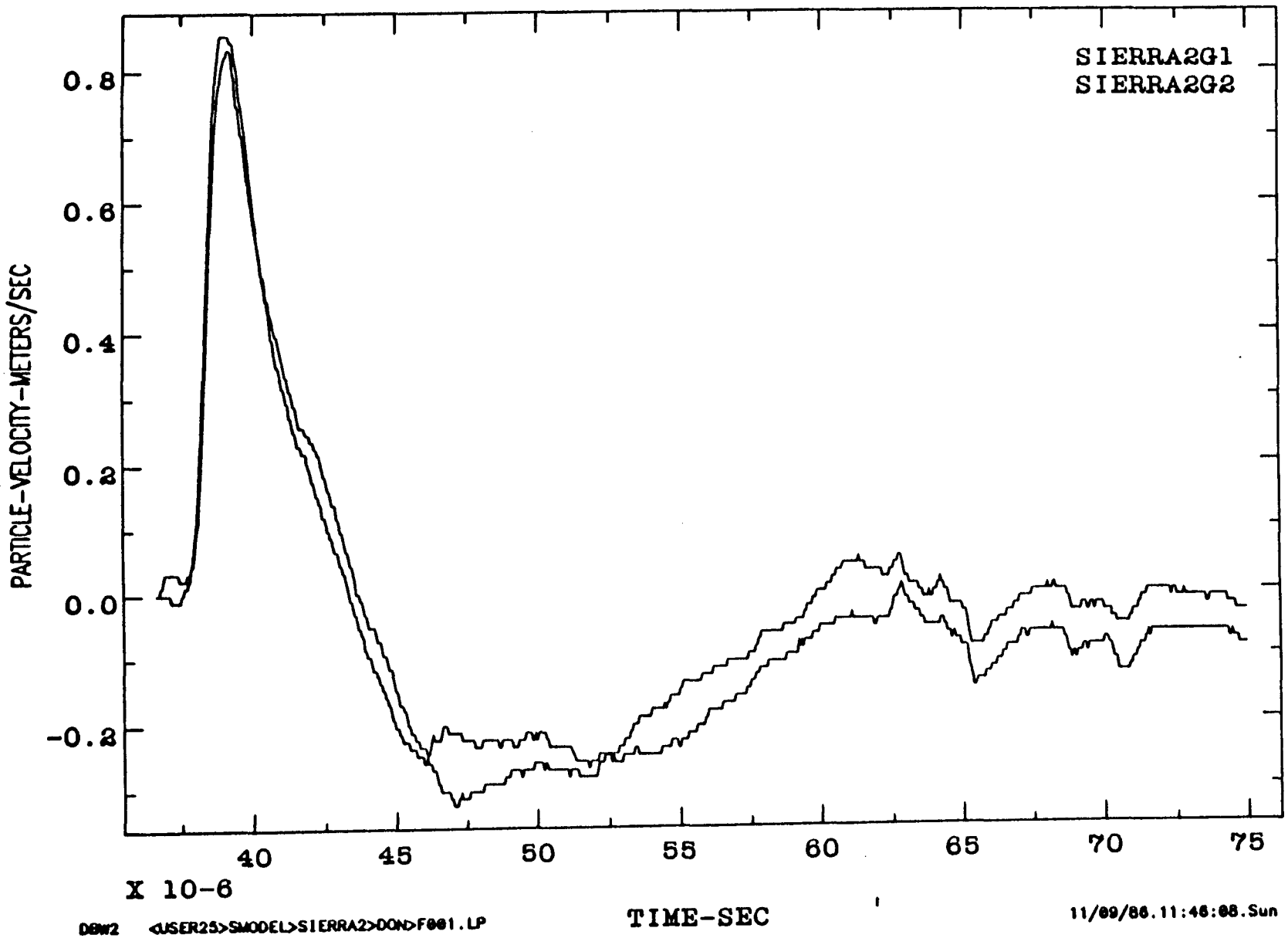
SIERRA2G1
SIERRA2G2
PARTICLE-VELOCITY-METERS/SEC
0.8
0.6
0.4
0.2
0.0
-0.2
40
45
50
55
60
65
70
75
X 10-6
TIME-SEC
DBW2 <USER25>SMODEL>SIERRA2>DON>F001.LP
11/09/88.11:46:08.Sun

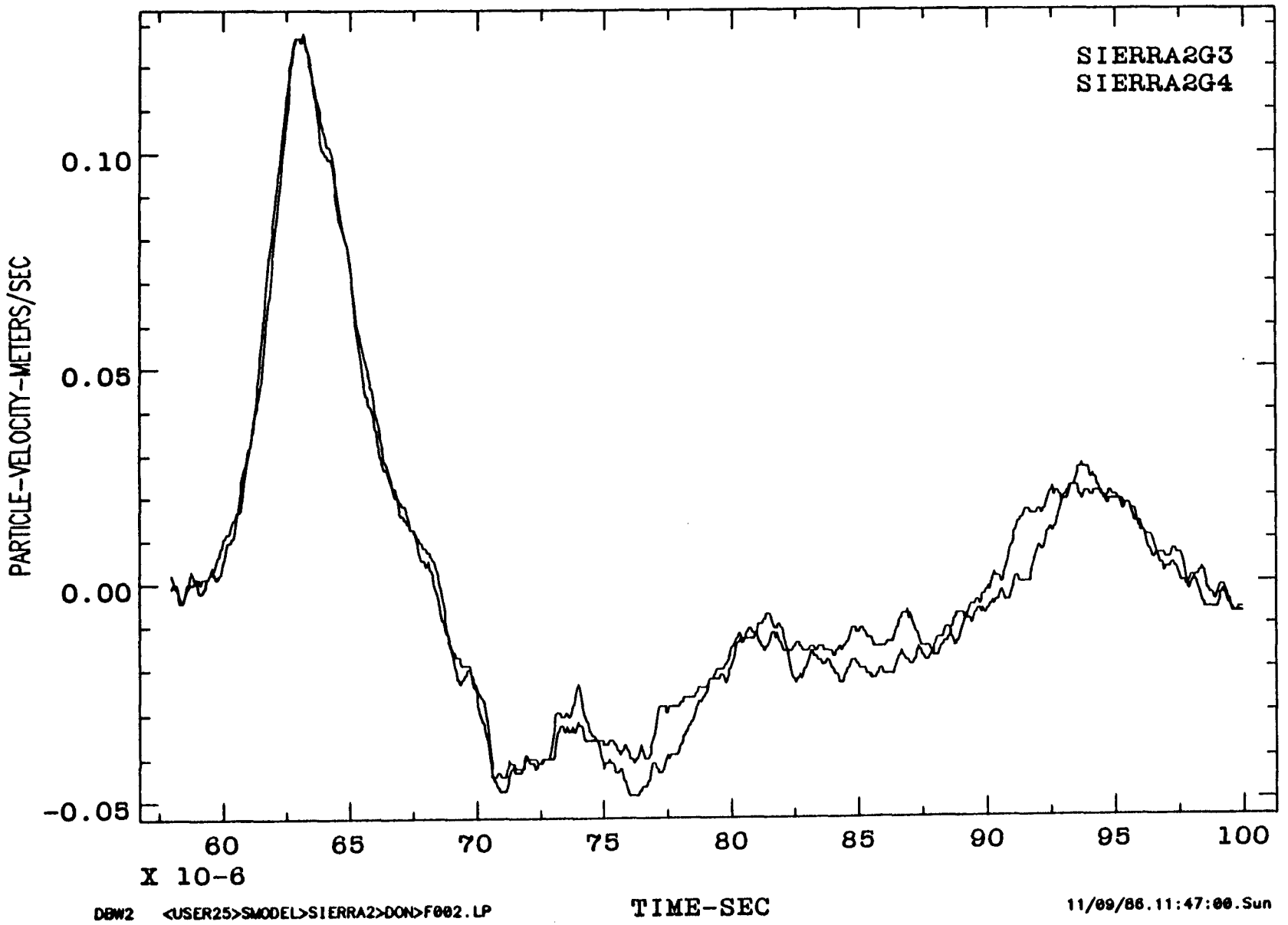
SIERRA2G3
SIERRA2G4
PARTICLE-VELOCITY-METERS/SEC
0.10
0.05
0.00
-0.05
60
65
70
75
80
85
90
95
100
X 10-6
TIME-SEC
DBW2 <USER25>SMODEL>SIERRA2>DON>F002.LP
11/09/88.11:47:00.Sun

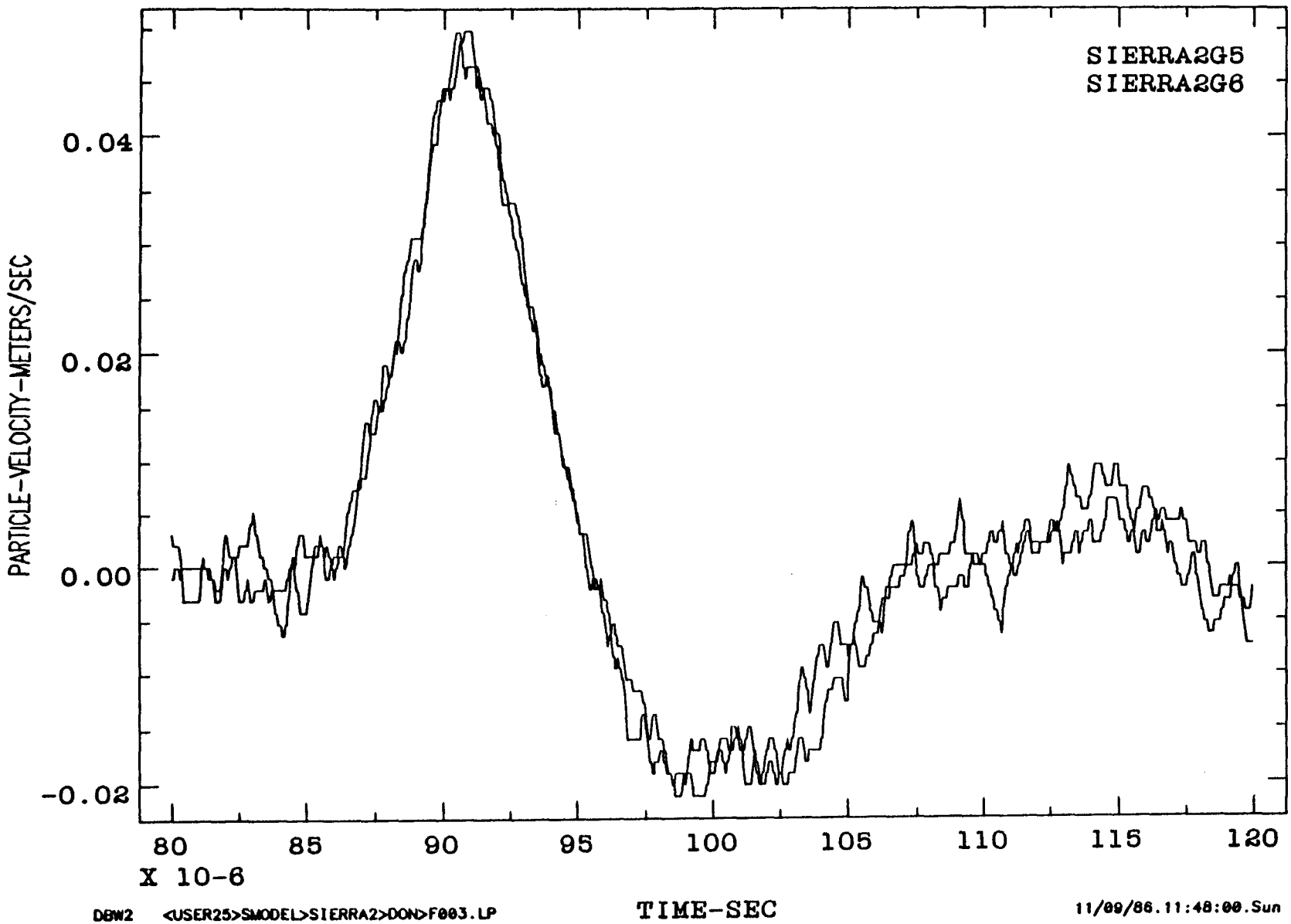
SIERRA2G5
SIERRA2G6
PARTICLE-VELOCITY-METERS/SEC
0.04
0.02
0.00
-0.02
80
85
90
95
100
105
110
115
120
X 10-6
TIME-SEC
DBW2 <USER25>SMODEL>SIERRA2>DON>F003.LP
11/09/86.11:48:00.Sun

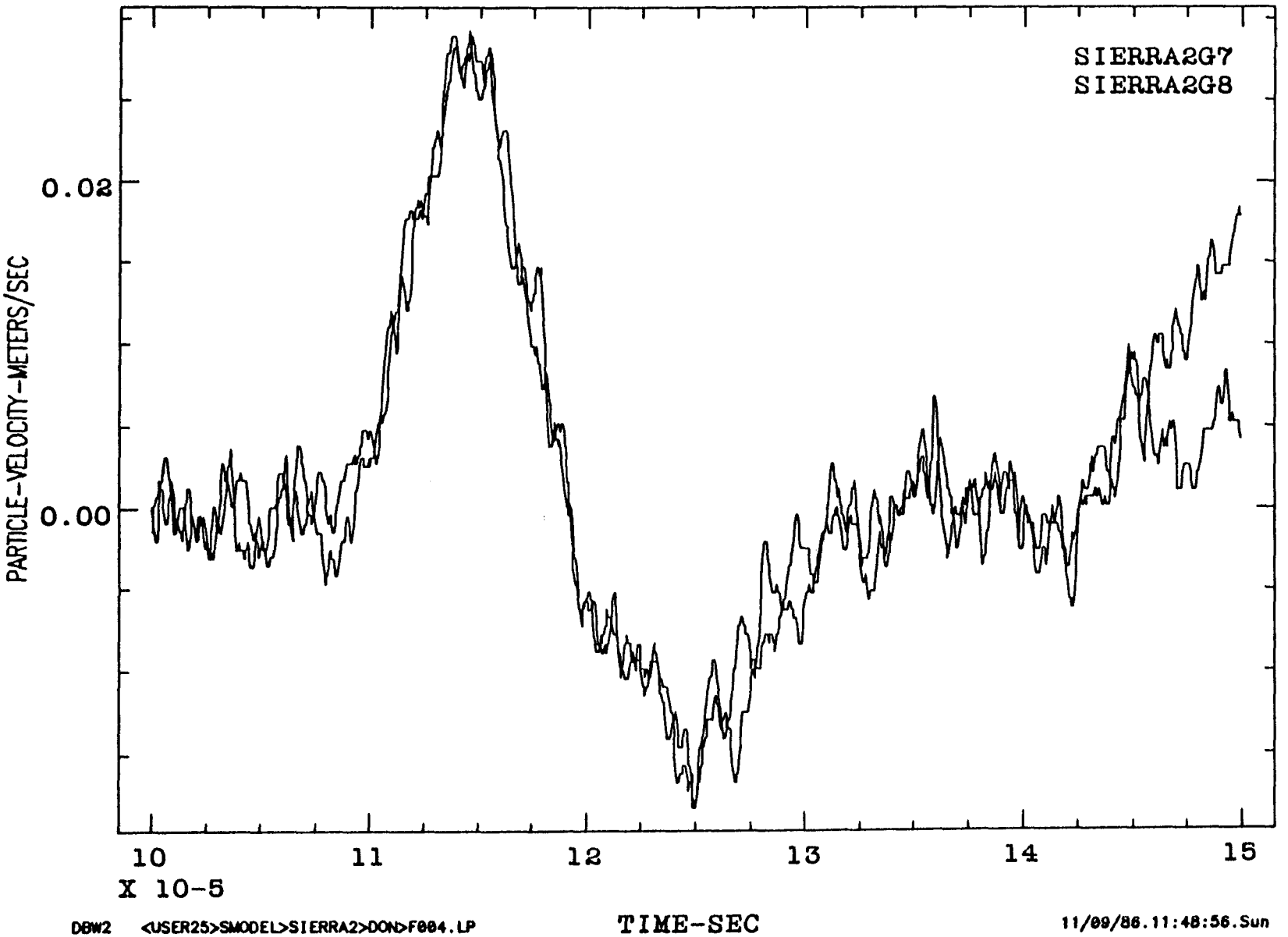
SIERRA2G7
SIERRA2G8
0.02
0.00
PARTICLE-VELOCITY-METERS/SEC
10
11
12
13
14
15
X 10-5
DBW2 <USER25>SMODEL>SIERRA2>DON>F004.LP
TIME-SEC
11/09/86.11:48:56.Sun

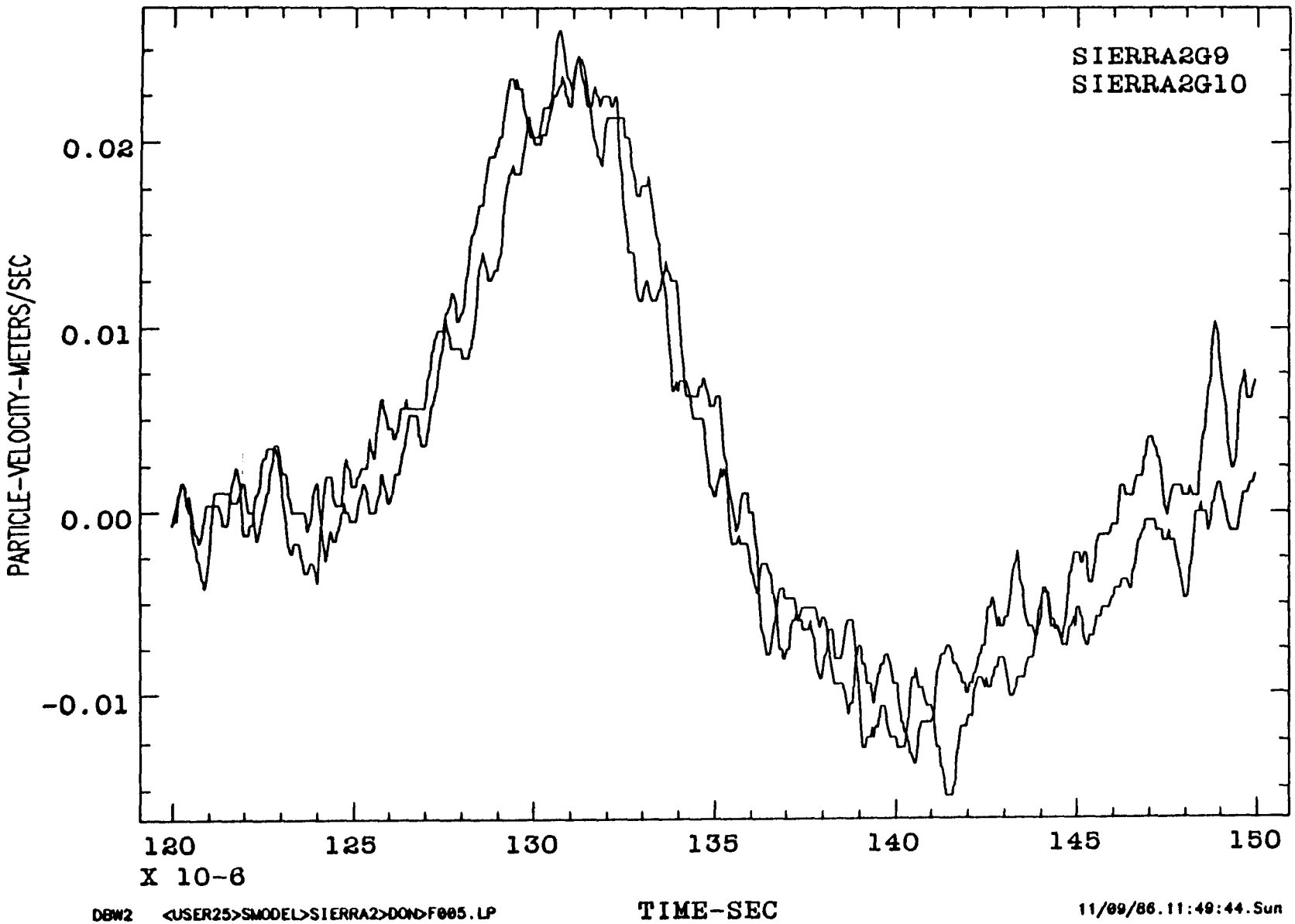
SIERRA2G9
SIERRA2G10
0.02
0.01
0.00
-0.01
PARTICLE-VELOCITY-METERS/SEC
120
125
130
135
140
145
150
X 10-6
TIME-SEC
DBW2 <USER25>SMODEL>SIERRA2>DON>F005.LP
11/09/86.11:49:44.Sun

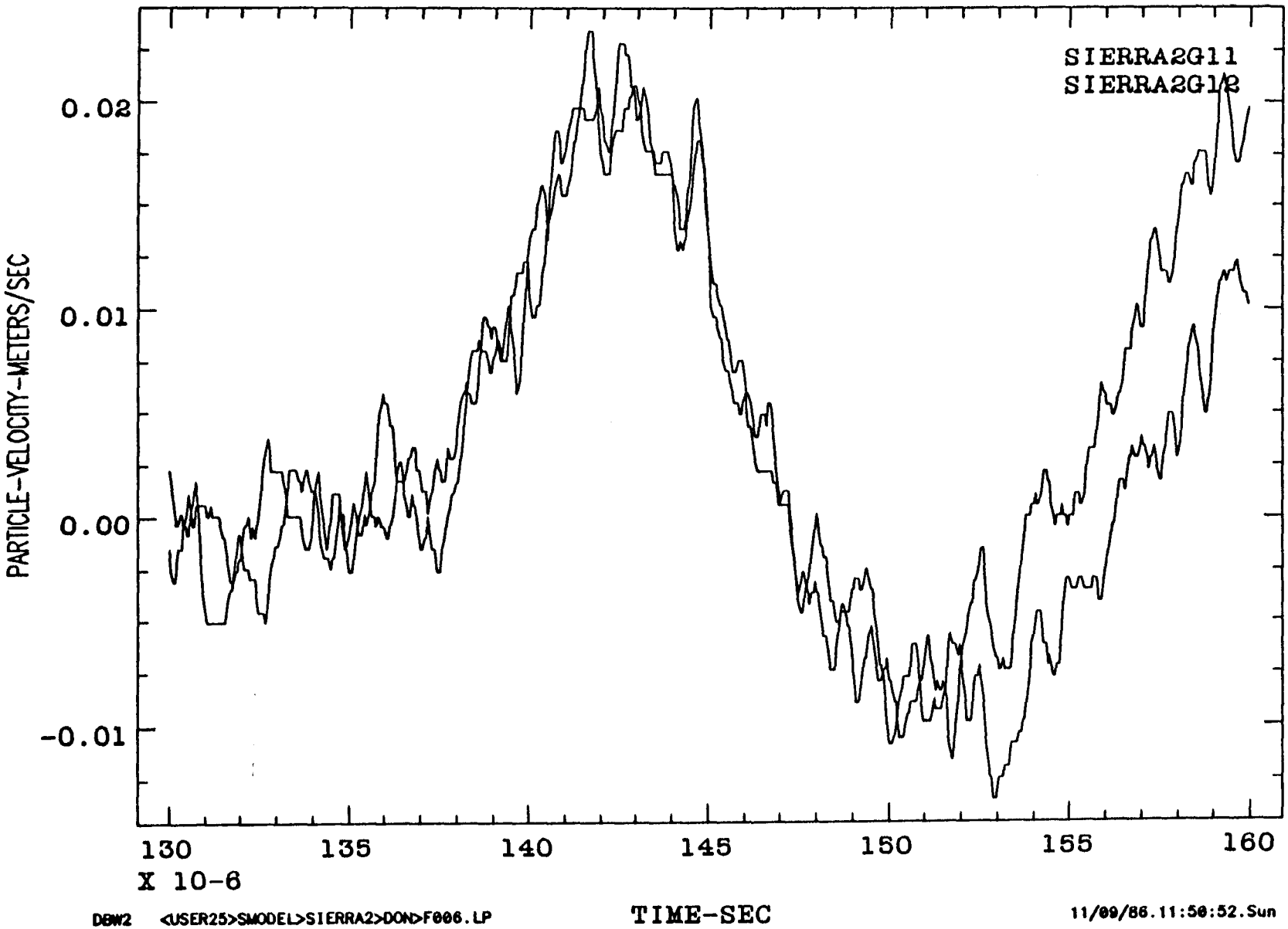
SIERRA2G11
SIERRA2G12
0.02
0.01
0.00
-0.01
PARTICLE-VELOCITY-METERS/SEC
130
135
140
145
150
155
160
X 10-6
TIME-SEC
DBW2 <USER25>SMODEL>SIERRA2>DON>F006.LP
11/09/86.11:50:52.Sun

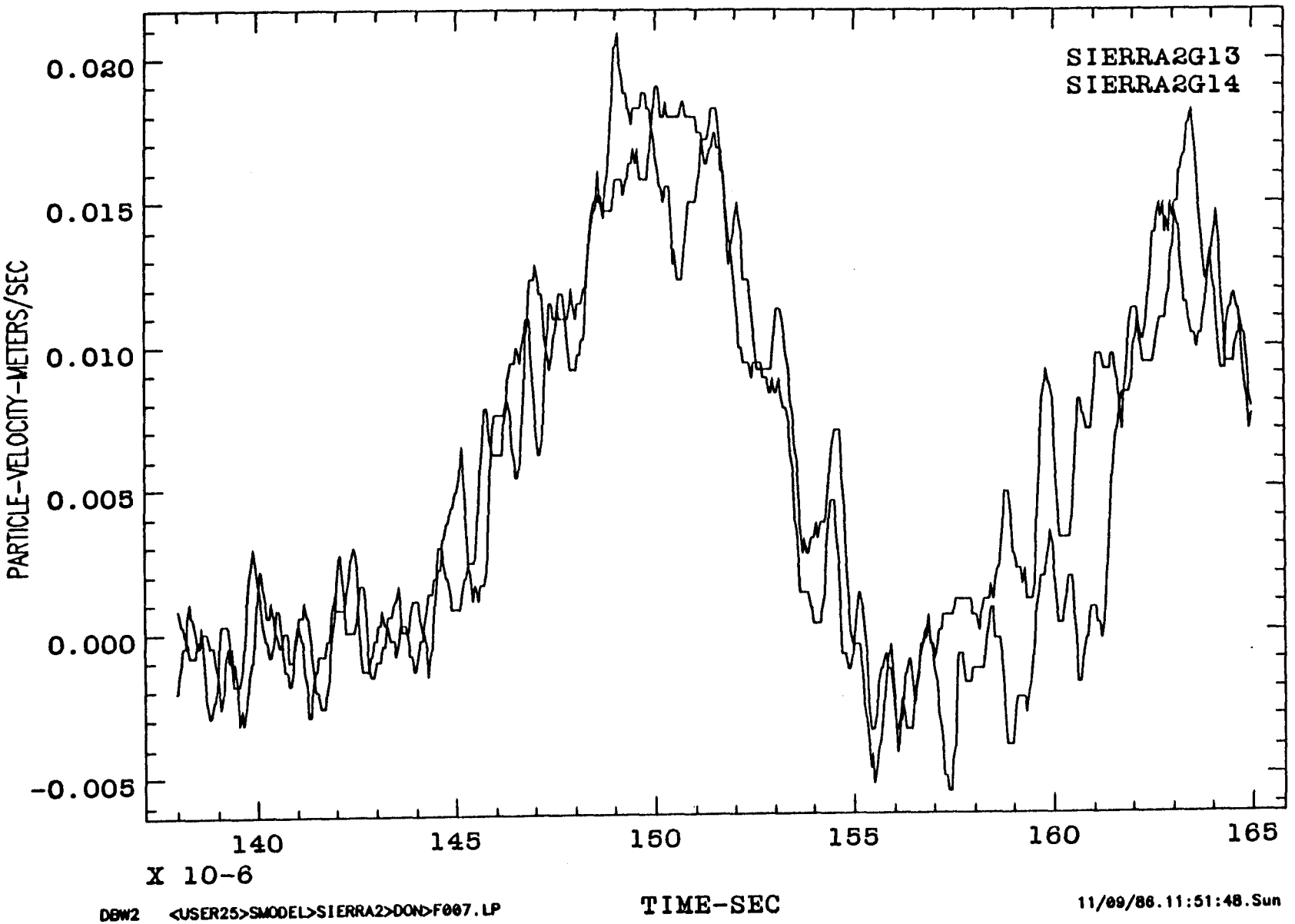
SIERRA2G13
SIERRA2G14
PARTICLE-VELOCITY-METERS/SEC
0.020
0.015
0.010
0.005
0.000
-0.005
140
145
150
155
160
165
X 10-6
TIME-SEC
DBW2 <USER25>SMODEL>SIERRA2>DON>F007.LP
11/09/86.11:51:48.Sun

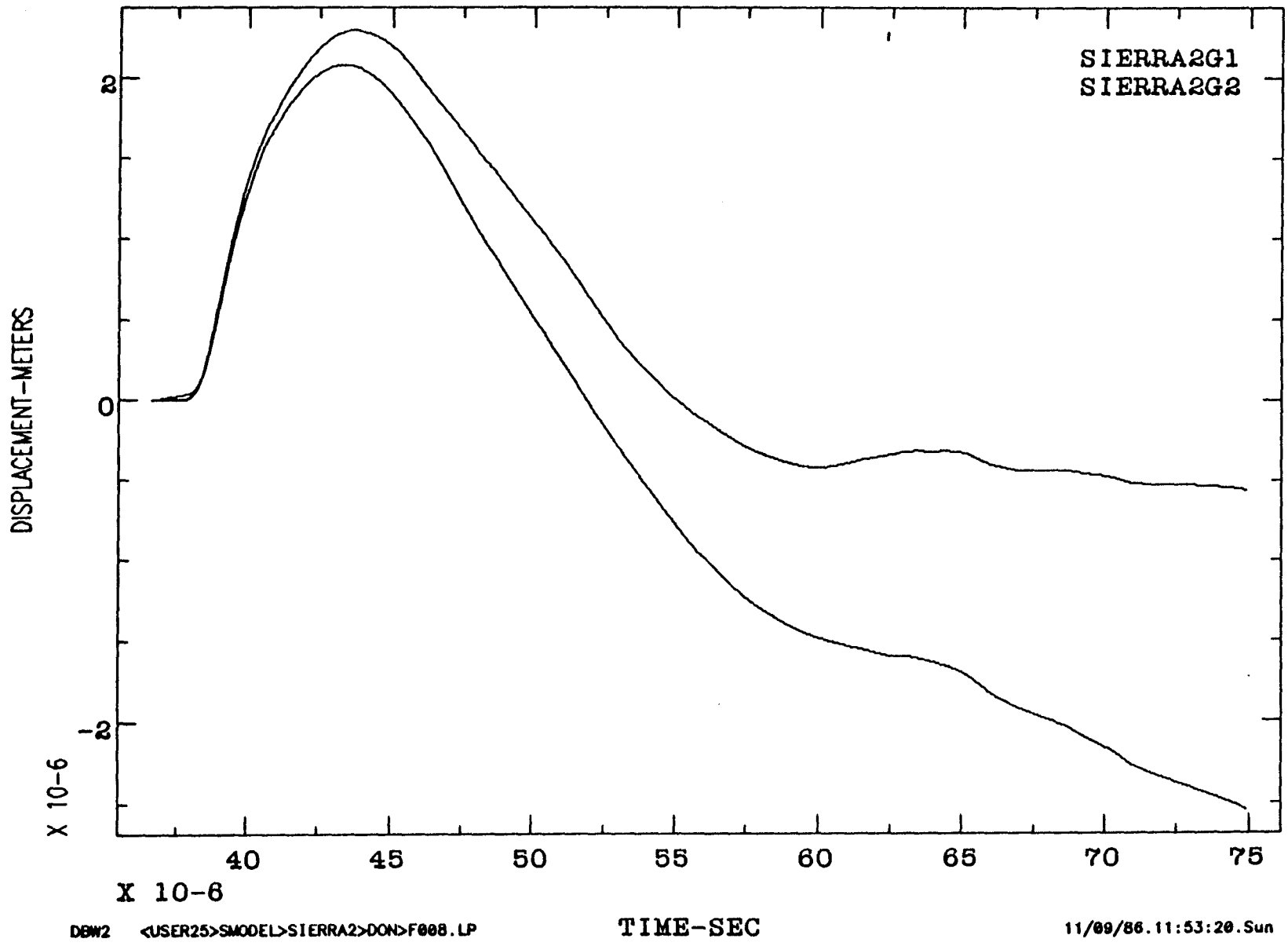
SIERRA2G1
SIERRA2G2
DISPLACEMENT-METERS
X 10-6
2
0
-2
40
45
50
55
60
65
70
75
X 10-6
TIME-SEC
DBW2 <USER25>SMODEL>SIERRA2>DON>F008.LP
11/09/86.11:53:20.Sun

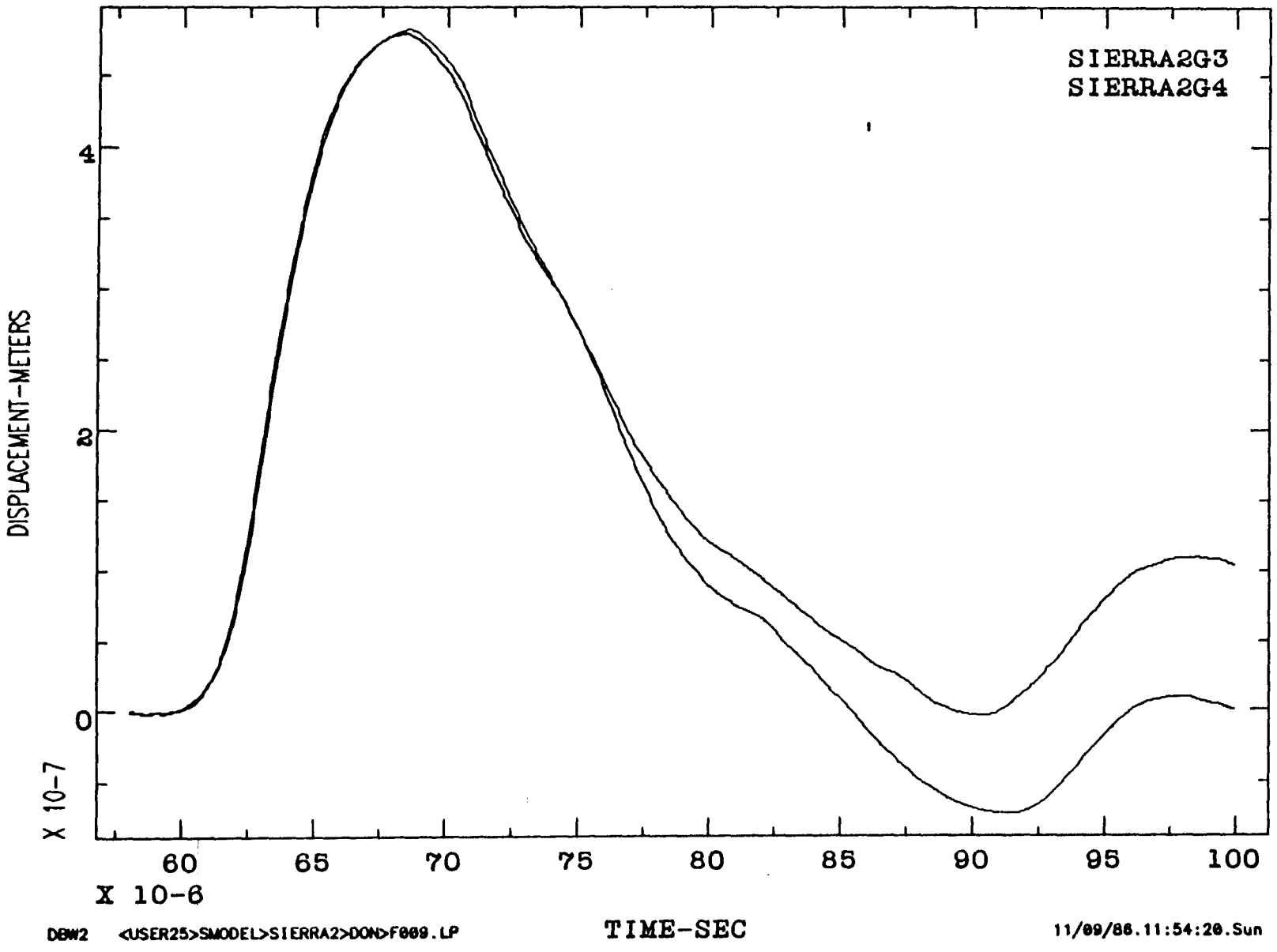
SIERRA2G3
SIERRA2G4
DISPLACEMENT-METERS
4
2
0
X 10-7
60
65
70
75
80
85
90
95
100
X 10-6
TIME-SEC
DBW2 <USER25>SMODEL>SIERRA2>DON>F009.LP
11/09/88.11:54:20.Sun

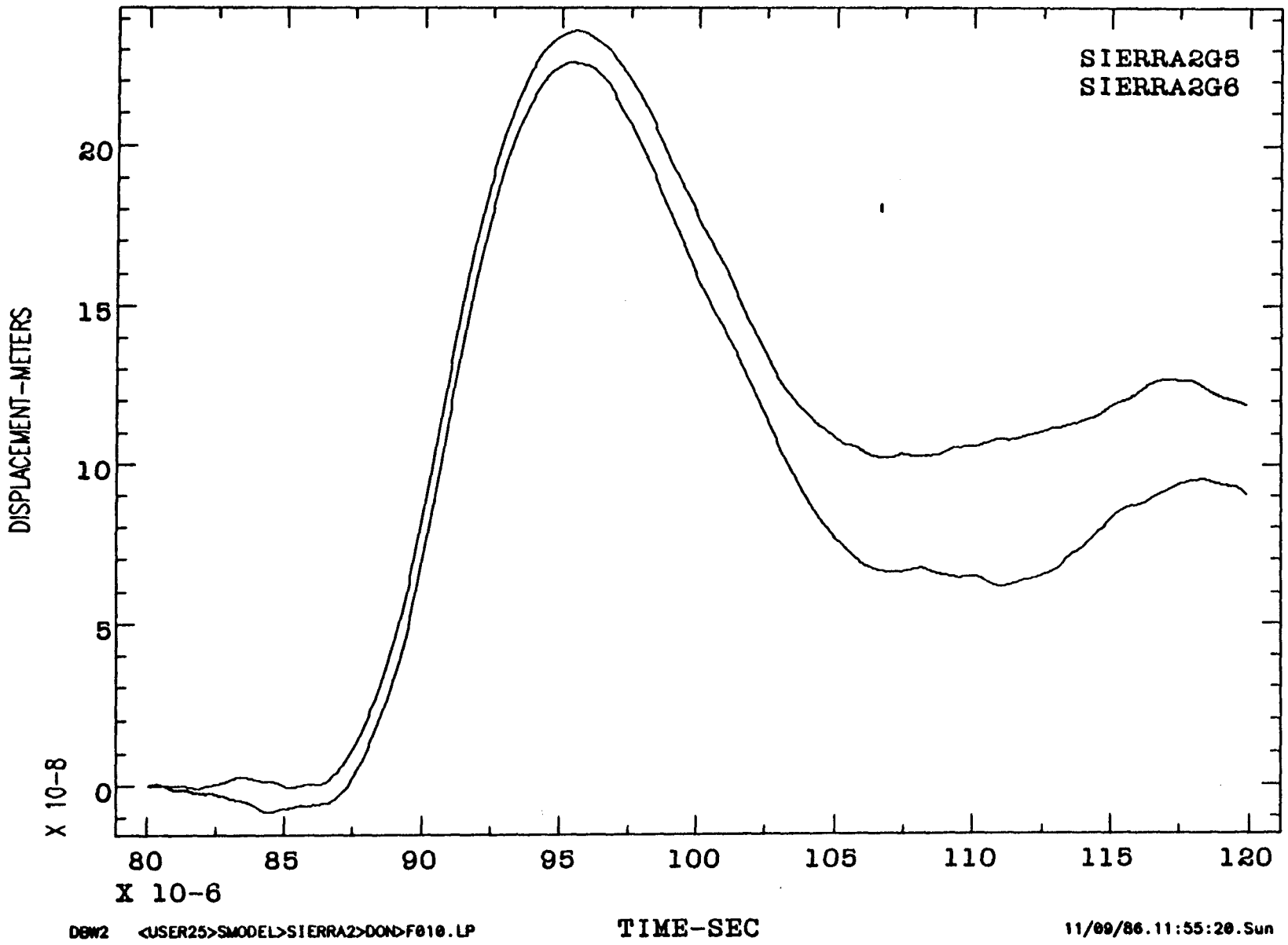
SIERRA2G5
SIERRA2G6
DISPLACEMENT-METERS
X 10-8
20
15
10
5
0
80
85
90
95
100
105
110
115
120
X 10-6
TIME-SEC
DBW2 <USER25>SMODEL>SIERRA2>DON>F010.LP
11/09/86.11:55:20.Sun

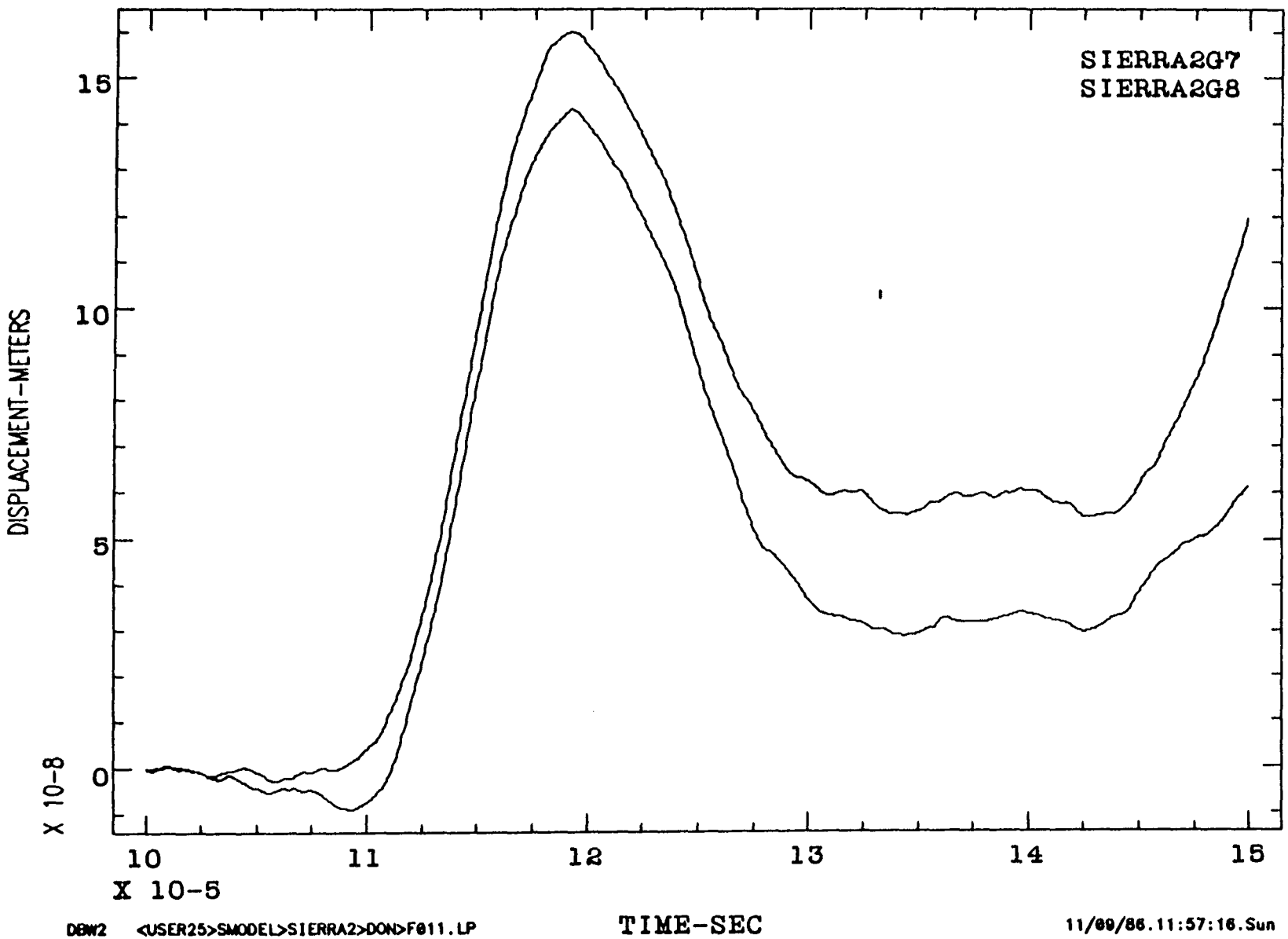
SIERRA2G7
SIERRA2G8
DISPLACEMENT-METERS
X 10-8
15
10
5
0
10
11
12
13
14
15
X 10-5
TIME-SEC
DBW2 <USER25>SMODEL>SIERRA2>DON>F011.LP
11/09/86.11:57:16.Sun

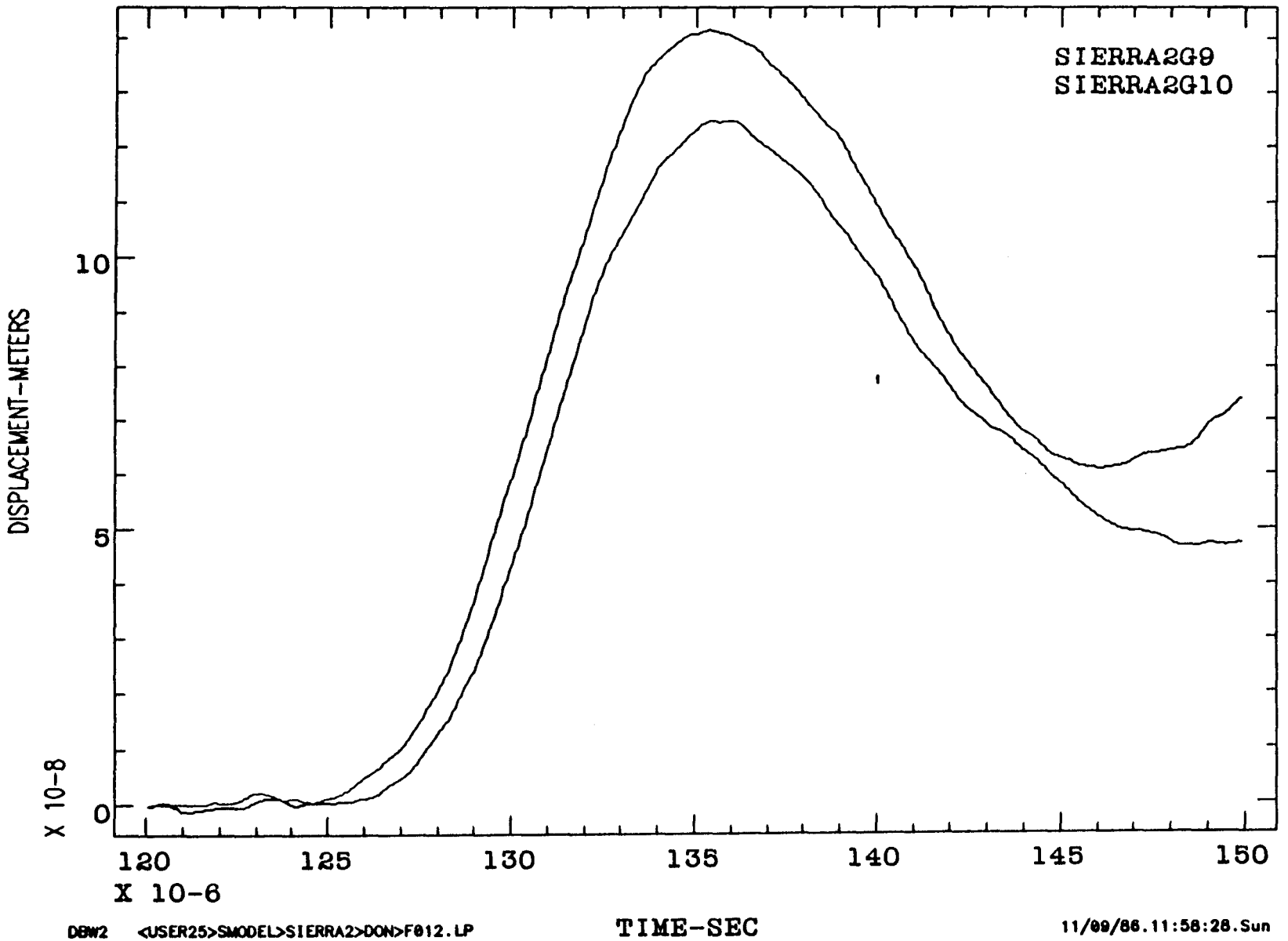
SIERRA2G9
SIERRA2G10
DISPLACEMENT-METERS
X 10-8
10
5
0
120
125
130
135
140
145
150
X 10-6
TIME-SEC
DBW2 <USER25>SMODEL>SIERRA2>DON>F012.LP
11/09/86.11:58:28.Sun

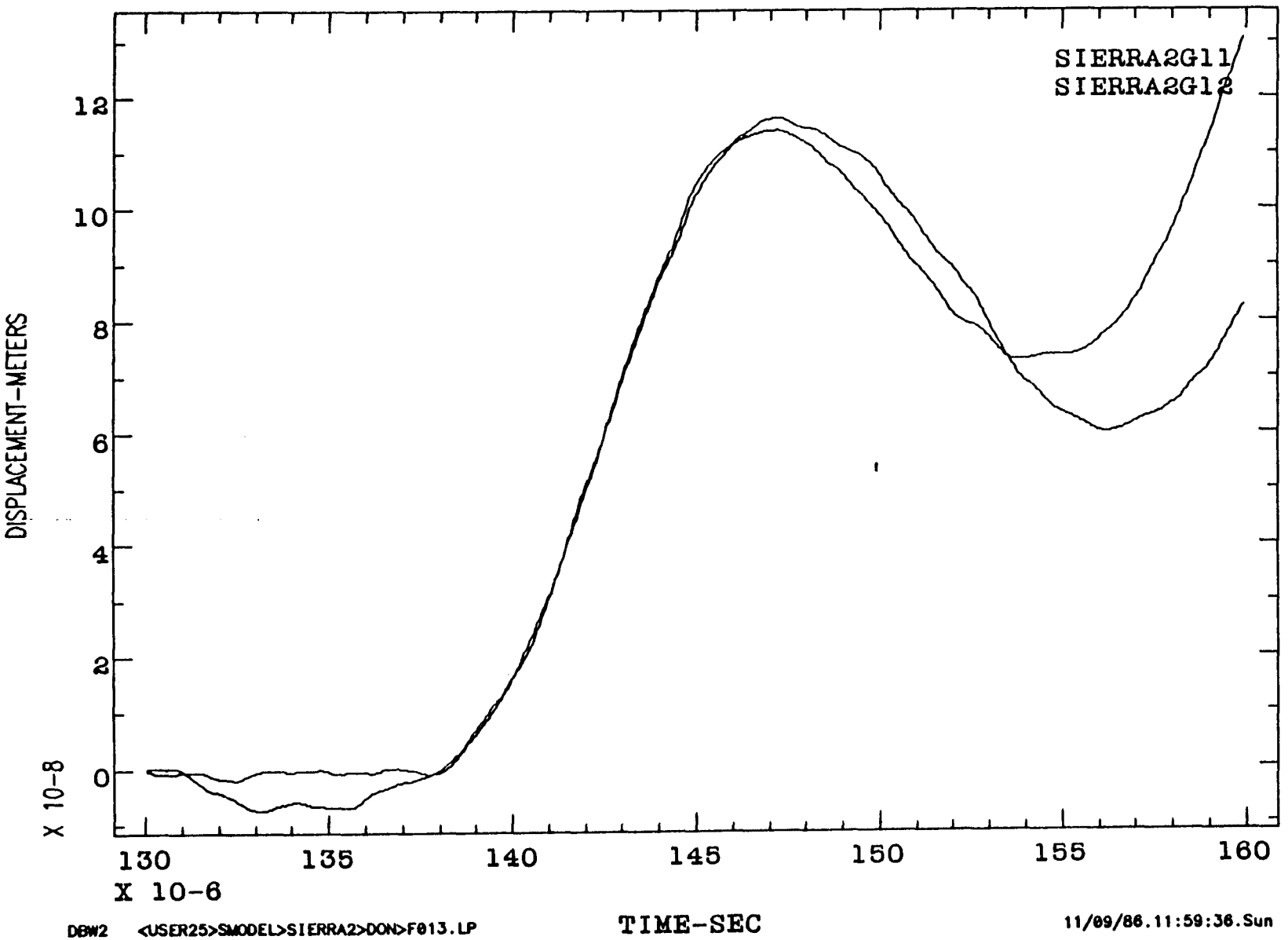
SIERRA2G11
SIERRA2G12
DISPLACEMENT-METERS
X 10-8
12
10
8
6
4
2
0
130
135
140
145
150
155
160
X 10-6
TIME-SEC
DBW2 <USER25>SMODEL>SIERRA2>DON>F013.LP
11/09/86.11:59:36.Sun

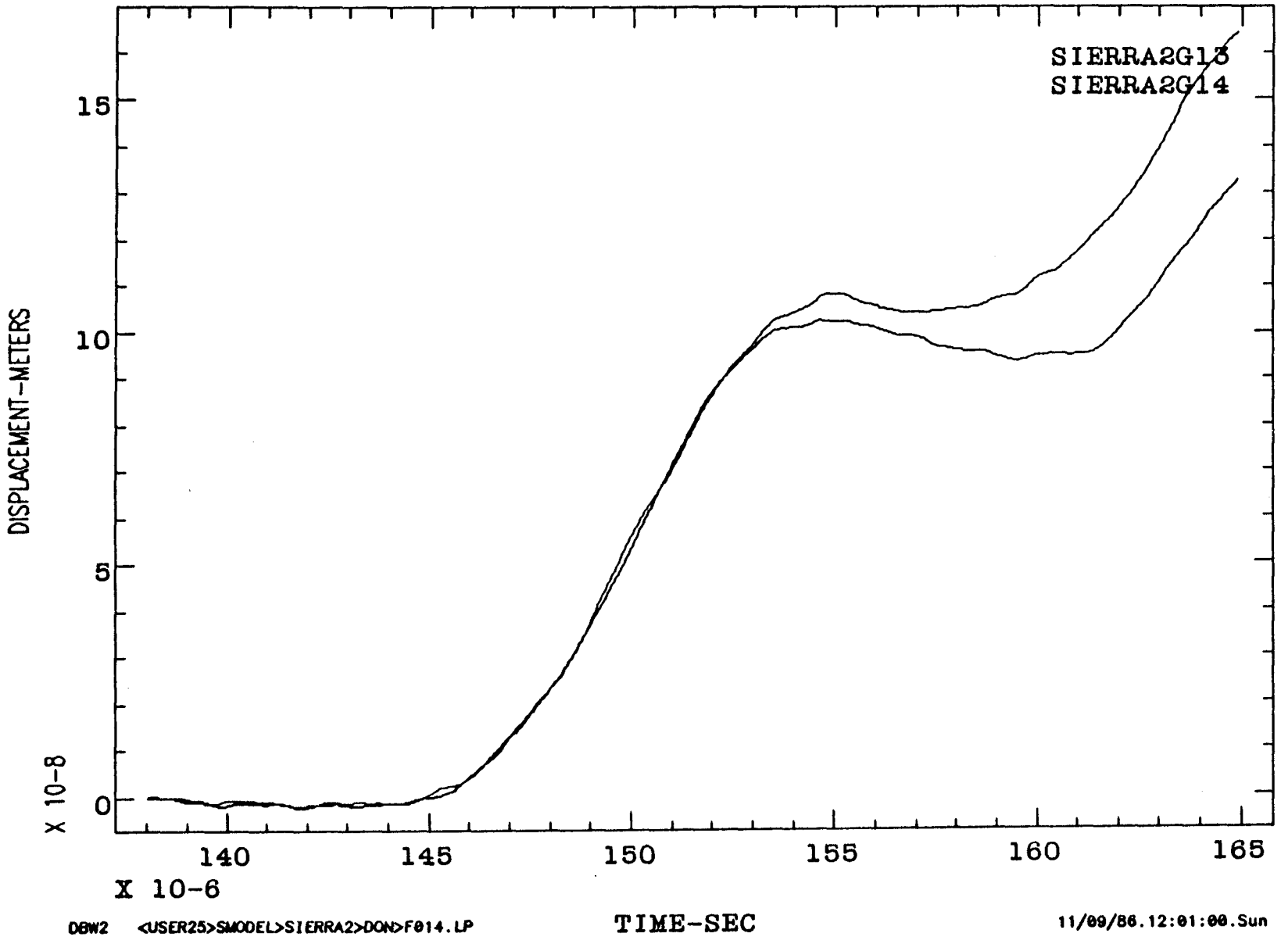
SIERRA2G13
SIERRA2G14
DISPLACEMENT-METERS
X 10-8
15
10
5
0
140
145
150
155
160
165
X 10-6
TIME-SEC
DBW2 <USER25>SMODEL>SIERRA2>DON>F014.LP
11/09/86.12:01:00.Sun

PART D

WAVE PROPAGATION STUDIES IN DOME SALT

Introduction

Dome salt was selected for study because of its prominence as a medium for evasion through cavity decoupling and because of the extensive work, both experimental and theoretical, that has occurred in this medium or other forms of salt. The work reported to date has produced many anomalies and it was hoped that this wave propagation study would provide the basis for resolving some or all of these problems.

Experimental Procedures and Results

The whole process of locating, acquiring, fabricating, assembling, and executing experiments in Dome salt was an unbelievable "nightmare" interrupted by enough "vistas" of success to keep the process going. It took many weeks to locate a company with a salt dome that was willing to attempt to cut blocks. Domtar Industries, Inc., located on an island ~ 40 km from New Iberia, LA, was willing and apparently successful as they provided six ~1 meter cubed blocks of salts from their dome. Many weeks were also required in locating someone to cut and lap the salt blocks to the proper dimensions for the experiments. Wayne Harrington of PW Calibrators, Campbell, CA, finally accepted the challenge, but again many additional weeks were lost in trying to sole source and establish a contract acceptable to both parties. Once the

contract was in force and the work began, the tempo of the nightmare blossomed. As deadlines for experimental results were drawn, the pace of work was increased from 40 to 100 hour weeks, resulting in more contract negotiations and daily commuting to Campbell to reduce overtime charges. Finally, the fabrication work was done! There was some concern about strain relief in the thinner blocks, but all seemed well as the model was assembled with all the gages in place. It wasn't until the Dome salt model was successfully transported to and placed inside the magnet, and the first experiment performed, that the nightmare <u>really</u> bared its ugly head. The data for whatever reason showed tremendous variation in wave velocity, which negated the assumed simulation of Dome salt and made any analysis of the data of limited worth in addressing the intended problems.

Figure D1 shows a schematic representation of the dome salt model with the dimension and the gage locations indicated. The bulk density was 2.11 ± 0.04 Mg/m^3 and wave velocities reported by Karl Coyner of New England Research are P-wave 4.25 Km/s and S-wave 2.35 km/s. The average wave velocities (p-wave) through each block or between gages when subjected to a tamped explosion are shown in Table DI.

Table DI. P-Wave velocities from the experiment in Dome salt.

Block	P-Wave Velocity (km/s)
B	2.25
C	3.67
D	2.93
E	2.77
F	3.67
G	3.97
H	3.09

The implication of these large differences in wave velocity is a large difference in crack density between blocks. Furthermore, even the highest wave velocity is significantly below (3.97 compared to 4.25 km/s) the acoustic p-wave velocity measured by Koyner, a value which is consistent with the velocity expected in the dome. The source of these large differences in wave velocity are attributed to cracking as a result of strain relief as the blocks of salt were cut and then machined flat and parallel. Clear evidence of this strain relief occurred when a 5 cm thick piece was cut from the main block. As the cutting proceeded the 5 cm thick piece began to warp away from the blade. Hindsight, as always, indicates what should have been done in the way of material quality control. But on the other hand, experience, although often expensive, is a great teacher. Figure D2 shows the wave profiles recorded by the various gages and Figure D3, shows the particle velocity time histories. The data from the gages beyond block C of Figure D1 are probably useful for attenuation studies in highly cracked dome salt, but their relevance to in-situ dome salt is unknown.

Summary and Conclusions

The penalty of limited funding and a time barrier working together was essentially failure in the attempt to acquire quality wave propagation data and the resulting attenuation properties of dome salt. However, much was learned about the precautions necessary to assure a proper physical model for use in future wave propagation studies in dome salt and in other geologic materials.

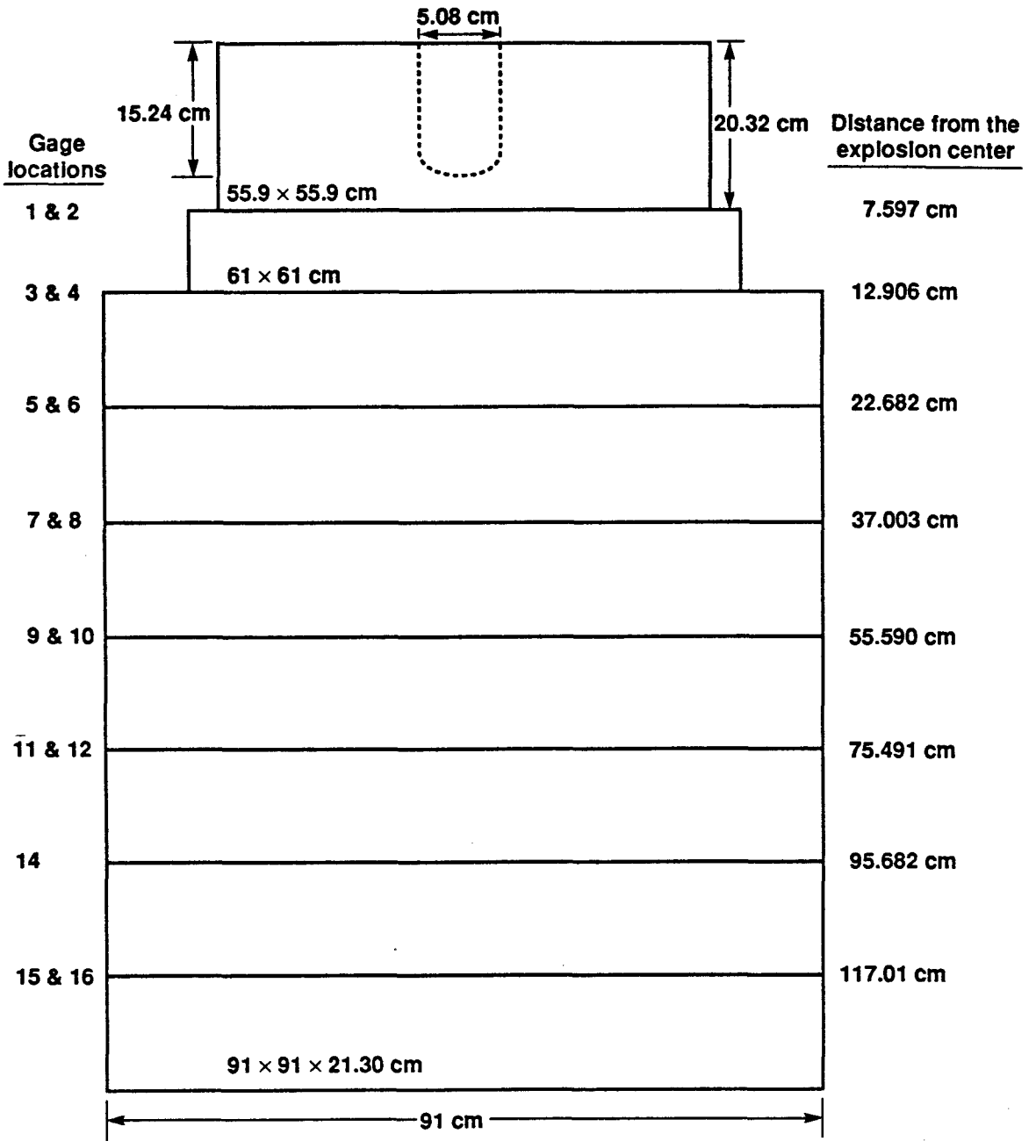

Figure D1. Schematic of the Dome Salt experimental model showing the dimensions, the gage locations and the distance from the explosion center to each gage level.

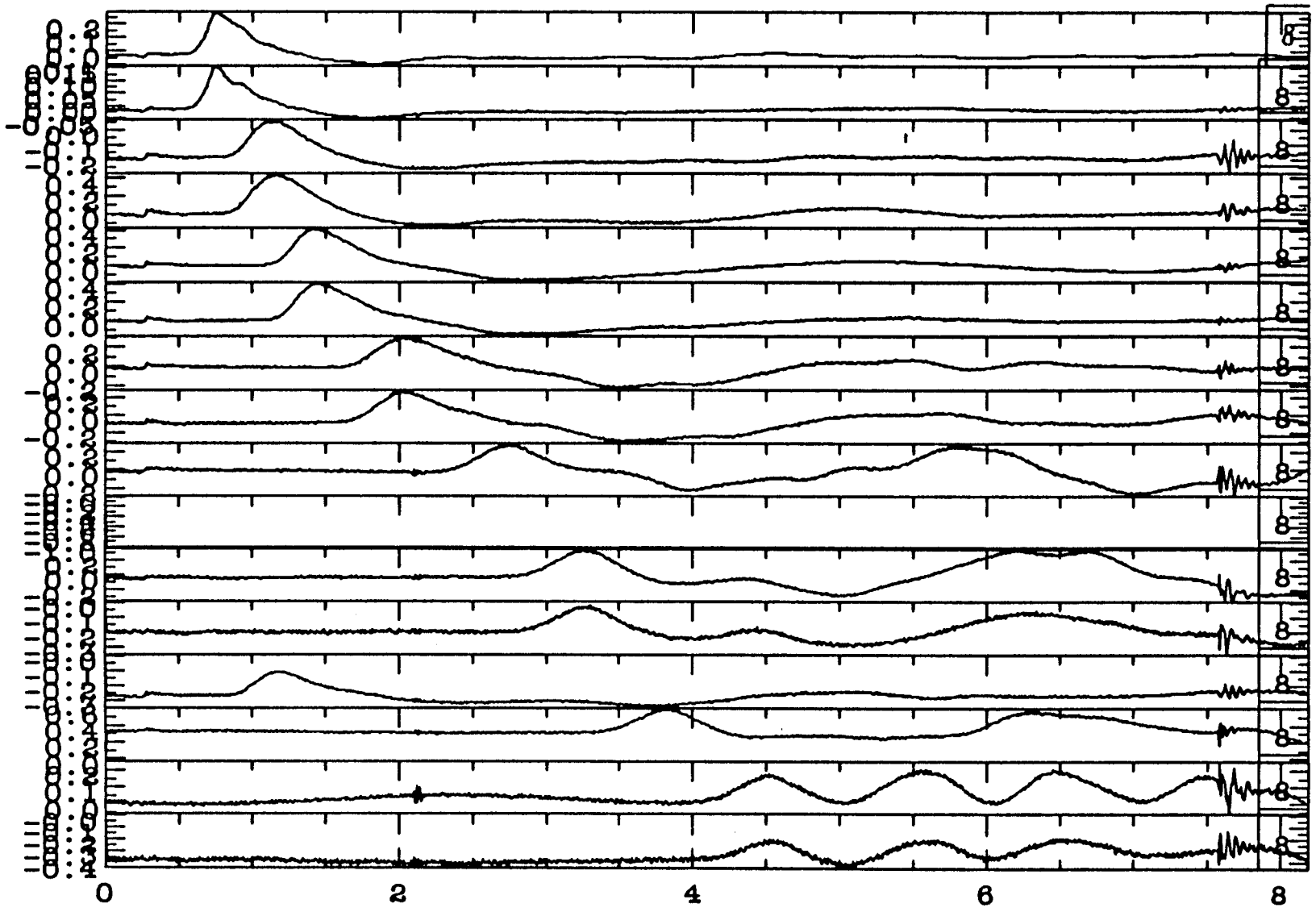

Figure D2. Experimental records from the various gages of a 0.622 kJ tamped explosion in Dome Salt. Gage 13 is at the same location as gages 3 and 4 and the gage 10 record is missing.

REFERENCES

(1) Gordon, R. B., and L. A. Davis (1968). Velocity and attenuation of seismic waves in imperfectly elastic rock. J. Geophys. Res. 73, 3917-3935.

(2) Johnston, D. H. (1978). The attenuation of seismic waves in dry saturated rocks. Ph.D. Dissertation, Massachusetts Institute of Technology, Cambridge, Massachusetts.

(3) Winkler, K. and A. Nur (1979). Pore fluids and seismic attenuation in rocks. Geophys. Res. Letters 6, 1-4.

(4) Stout, R. B., and D. B. Larson (1985). Finite deformations, onsager irreversible thermodynamics, and stress wave analysis of shock waves. Third Symp. on Containment of Underground Nuclear Explosions, Vol. 1, pp 314, C. Olsen, Ed., Lawrence Livermore National Laboratory.

(5) Larson, D. B. (1985). Stress gauge measurements in spherical diverging flows. Third Symp. on Containment of Underground Nuclear Explosions, Vol. 1, pp 214, C. Olsen, Ed., Lawrence Livermore National Laboratory.

(6) Stout, R. B. (1987). Electric resistivity due to elastic-plastic deformations," Lawrence Livermore National Laboratory UCRL-94738.

(7) Larson, D. B., and R. B. Stout (1986). Particle velocity and stress gage measurements in spherical diverging flow. Techniques and Theory of Stress Measurements for Shock Wave Applications, edited by R. B. Stout, F. R. Norwood, and M. E. Fourney, Am. Soc. of Mech. Eng. Symposium Publication AMD-Vol. 83.

(8) Stout, R. B., and D. B. Larson (1987). Multi-component stress history measurements and analysis, Lawrence Livermore National Laboratory, Report UCRL-96319, August 1987, to be published in the Fourth Containment Symposium held in Colorado Springs, CO.

(9) Chen, D. Y., Y. M. Gupta, and M. H. Miles (1984). Quasistatic experiments to determine material constants for the piezoresistance foils used in shock wave experiments. J. Appl. Phys., Vol. 55, pp 3984.

REPORT DOCUMENTATION PAGE

1a. REPORT SECURITY CLASSIFICATION UNCLASSIFIED	1b. RESTRICTIVE MARKINGS N/A since Unclassified
2a. SECURITY CLASSIFICATION AUTHORITY N/A since Unclassified	3 DISTRIBUTION / AVAILABILITY OF REPORT
2b. DECLASSIFICATION / DOWNGRADING SCHEDULE N/A since Unclassified	
4. PERFORMING ORGANIZATION REPORT NUMBER(S) SRI Project PYC-2336	5. MONITORING ORGANIZATION REPORT NUMBER(S)
6a. NAME OF PERFORMING ORGANIZATION SRI International 6b. OFFICE SYMBOL (If applicable)	7a. NAME OF MONITORING ORGANIZATION Lawrence Livermore National Laboratory and Defense Advanced Research Projects Agency
6c. ADDRESS (City, State, and ZIP Code) 333 Ravenswood Avenue Menlo Park, CA 94025-3493	7b. ADDRESS (City, State, and ZIP Code) 7000 East Avenue 1400 Wilson Blvd. Livermore, CA 94550 Arlington, VA 20305
8a. NAME OF FUNDING / SPONSORING ORGANIZATION 8b OFFICE SYMBOL (If applicable)	9. PROCUREMENT INSTRUMENT IDENTIFICATION NUMBER 9168505
8c. ADDRESS (City, State, and ZIP Code)	10. SOURCE OF FUNDING NUMBERS PROGRAM ELEMENT NO. / PROJECT NO / TASK NO. / WORK UNIT ACCESSION NO.

11 TITLE (Include Security Classification)
SPHERICAL WAVE PROPAGATION IN LOW-POROSITY BRITTLE ROCKS

12. PERSONAL AUTHOR(S)
Nagy, Geza and Florence, Alexander L.

13a. TYPE OF REPORT	13b. TIME COVERED	14. DATE OF REPORT (Year, Month, Day)	15. PAGE COUNT
Technical Report	FROM 860616 TO 870415	870400	

16. SUPPLEMENTARY NOTATION

17 COSATI CODES			18. SUBJECT TERMS (Continue on reverse if necessary and identify by block number)			
FIELD	GROUP	SUB-GROUP	Spherical Waves	Porosity	Pore Pressure	Particle Velocity
			High Amplitude	Fractured	Effective Stress	Displacement
			Granite	Pore Water	Confinement	Wave Shape

19. ABSTRACT (Continue on reverse if necessary and identify by block number)

Laboratory experiments were performed to support theoretical modeling efforts directed at predicting the response of low-porosity brittle rocks to high-amplitude waves near an explosive source. The overall objective of the research is to improve nuclear monitoring capability.

The experimental work, conducted in dry and water-saturated samples of Sierra White granite with enhanced porosity, investigated the effects of confining pressure, pore water, and pore pressure on the shape of spherical waves. The waves were generated with a small spherical explosive charge and were measured in the form of particle velocities at discrete radial locations. The work consisted of three major parts: modification of the experimental apparatus to allow independent control of confining and pore pressures, sample preparation including porosity enhancement, and particle velocity experiments. The material preparation, using a gas-fracturing process, provided the granite samples

20. DISTRIBUTION / AVAILABILITY OF ABSTRACT ☐ UNCLASSIFIED/UNLIMITED ☒ SAME AS RPT. ☐ OTIC USERS	21. ABSTRACT SECURITY CLASSIFICATION UNCLASSIFIED
22a. NAME OF RESPONSIBLE INDIVIDUAL Dr. Hap Pitkin and Dr. Robert Blandford	22b. TELEPHONE (Include Area Code) / 22c. OFFICE SYMBOL LLNL and DARPA

DD FORM 1473, 84 MAR 83 APR edition may be used until exhausted. All other editions are obsolete.

19. ABSTRACT (Continued)

with an initial porosity of about 2.5%, about 2.5 times greater than the intact material.

The results in which parametric variations had a substantial effect are as follows:

(1) In dry rock with a porosity of 2.5%, lowering the confining pressure from 2000 to 1000 psi increases peak displacements by about 25% in regions away from the source due to wider pulses.

(2) For dry and saturated rock with a porosity of 2.5%, zero pore pressure, and confining pressures of 2000 and 1000 psi, the maximum particle velocities and displacements are substantially higher in the water saturated rock in regions away from the source (water effect).

(3) In water-saturated rock at high (1600 to 2000 psi) confining and pore pressures and zero effective stress, increasing the porosity from 1 to 2.5% substantially increases peak velocities, increases pulse durations by a factor of 2 near the source to a factor of 4 far from the source, and increases peak displacements by a factor of 1.5 to 2 in the same range (porosity effect).

(4) In water-saturated rock with a porosity of 2.5% and high (1600 to 2000 psi) confining pressure, lowering the pore pressure to 1000 psi or zero produces substantially smaller displacements (effective stress effect.

SUMMARY

Following our earlier work,[1-4] in this experimental program we continued to study the behavior of low-porosity brittle rocks by conducting particle velocity measurements in Sierra White granite, which is representative of such geologic materials, having an intact porosity of 0.8-1.0%. The objective of this phase of the work was to investigate the influence of confining pressure and pore pressure (or effective stress) on particle velocities and displacements in dry and water-saturated granite with an enhanced porosity of about 2.5%.

The work consisted of three major parts: modification of the experimental apparatus to allow independent control of confining and pore pressures for water-saturated samples, sample preparation including porosity enhancement, and particle velocity experiments. The material preparation provided test samples with approximately 2.5% porosity, about 2.5 times higher than the intact value.

The particle velocity experiments conducted in the latest segment of the program are summarized in Table S-1, and those conducted in the preceeding phases in Table S-2. The principal parameters varied in the experiments listed in Tables S-1 and S-2 were porosity, pore condition, confining pressure, and pore pressure. The investigations progressed from experiments performed in intact and thermally fractured (20% porosity increase) rock to experiments in gas-fractured rock with porosity increased to approximately 2.5 times that of the intact material. The earlier investigations (Table S-2) concentrated on the effects of porosity and saturation using the same confining and pore pressures (zero effective stress), whereas the latest work (Table S-1) focused on the effects of confining pressure, and pore pressure. For the saturated experiments listed in Table S-1, the pore pressure was adjusted at different levels below the confining pressure to allow a study of the influence of nonzero effective stress.

Table S-1

PARTICLE VELOCITY EXPERIMENTS IN SIERRA WHITE GRANITE

Test No.	Fracture Type	Porosity %	Pore Condition	Confining Pressure (psi)	Pore Pressure (psi)
485	Gas	2.8	Dry	2000	-
488	Gas	2.7	Dry	1000	-
491	Gas	2.9	Saturated	2000	50
492	Gas	2.6	Saturated	1000	50
494	Gas	2.9	Saturated	2000	1000

Table S-2

EARLIER PARTICLE VELOCITY EXPERIMENTS IN SIERRA WHITE GRANITE

Test No.	Fracture Type	Porosity (%)	Pore Condition	Confining Pressure (psi)	Pore Pressure (psi)
361[a]	Intact	0.8-1.0	Dry	2000	-
308	Thermal	1.2	Dry	2000	-
309	Intact	0.8-1.0	Saturated	2000	2000
310	Thermal	1.2	Saturated	2000	2000
473	Gas	2.5	Saturated	1800	1800
474	Gas	2.4	Saturated	1600	1600
476	Gas	2.4	Dry	2000	-

[a]Test 361 is from Reference 3.

In this self-contained summary of the effects of the test parameters, the observations are based on the results of both the latest and the earlier segments of the work. For most of the parameters studied only a single experiment was performed, which should be considered in evaluating the results and conclusions.

In general, the most significant effects were observed when the porosity was increased to 2.5%. The results in which the parametric variations had a substantial effect are summarized as follows:

(1) In dry rock with a porosity of 2.5%, lowering the confining pressure from 2000 to 1000 psi increases peak displacements by about 25% in regions away from the source due to wider pulses.

(2) In rock with a porosity of 2.5%, zero pore pressure, and confining pressures of 1000 and 2000 psi, the maximum particle velocities and displacements are substantially higher in water-saturated rock than in dry rock in regions away from the source (water effect).

(3) In water-saturated rock at high (1600 to 2000 psi) confining and pore pressures and zero effective stress, increasing the porosity from 1 to 2.5% substantially increases peak velocities, increases pulse durations by a factor of 2 near the source to a factor of 4 far from the source, and increases peak displacements by a factor of 1.5 to 2 in the same range (porosity effect).

(4) In water-saturated rock with a porosity of 2.5% and high (1600 to 2000 psi) confining pressure, lowering the pore pressure to 1000 psi or zero produces substantially smaller displacements (effective stress effect).

The experimental results show that rock response depends not only on the magnitude of the change in the parameters, but also on range. The conclusions reached from the experimental results reflect both of these factors. Below we summarize the conclusions reached from the experimental results in six specific areas of interest: (1) porosity effect in dry rock at high confining pressure, (2) confining pressure effect in 2.5% porosity dry rock, (3) porosity effect in saturated rock with zero effective stress, (4) influence of effective stress in 2.5% porosity saturated rock at high confinement, (5) pore water effect in 2.5% porosity rock with near zero pore pressure, and (6) effect of

confining pressure in 2.5% porosity saturated rock with constant nonzero effective stress.

(1) Effect of porosity increase in dry rock with high confining pressure (2000 psi):

- A small porosity increase (20%) has a negligible influence on peak velocities, pulse shapes, and peak displacements (Figures S-1 and S-2).
- Increasing the porosity from 1.0% to 2.5% results in lower peak velocities (at least in one experiment, Test 485) and wider pulses far from the source (Figure S-1), but does not affect the amplitude and attenuation of peak displacements (Figure S-2).

(2) Effect of confining pressure in high (2.5%) porosity dry rock. A comparison of the results at 1000 and 2000 psi confining pressures indicates that a reduction of the confining pressure:

- Does not affect peak velocities (Figure S-3).
- Widens the pulses to produce larger peak displacements (Figure S-4).

(3) Effect of porosity in saturated rock with zero effective stress (pore pressure equal to confining pressure):

- A small (20%) increase in porosity has no effect on peak velocities, pulse shapes, and peak displacements (Figures S-5 and S-6).
- Increasing the porosity from 1.0% to 2.5% lowers peak velocities, steepens peak velocity attenuation (Figure S-5), and widens the pulses by a factor of 2 to 4 over the range of the gages.
- Increasing the porosity from 1.0% to 2.5% increases peak displacements by a factor 1.5 to 2 due to the wider pulses and lowers peak displacement attenuation (Figure S-6).

(4) Influence of effective stress in high (2.5%) porosity saturated rock. Increasing the effective stress from zero to near the confining stress (or decreasing the pore pressure to nearly zero) with a constant (2000 psi) confining pressure:

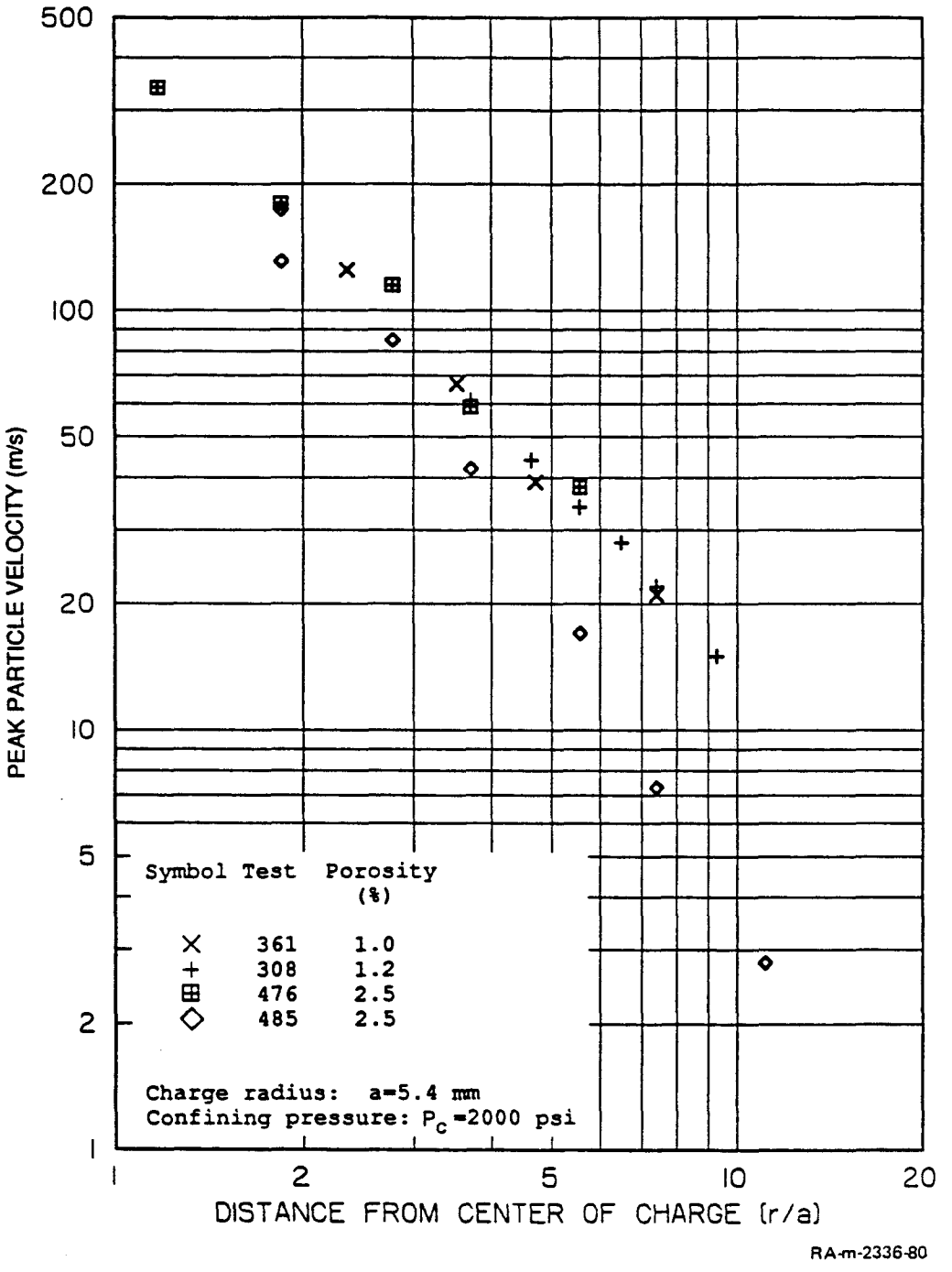

FIGURE S-1 EFFECT OF POROSITY ON PEAK VELOCITY ATTENUATION IN DRY SIERRA WHITE GRANITE WITH A CONFINING PRESSURE OF 2000 psi

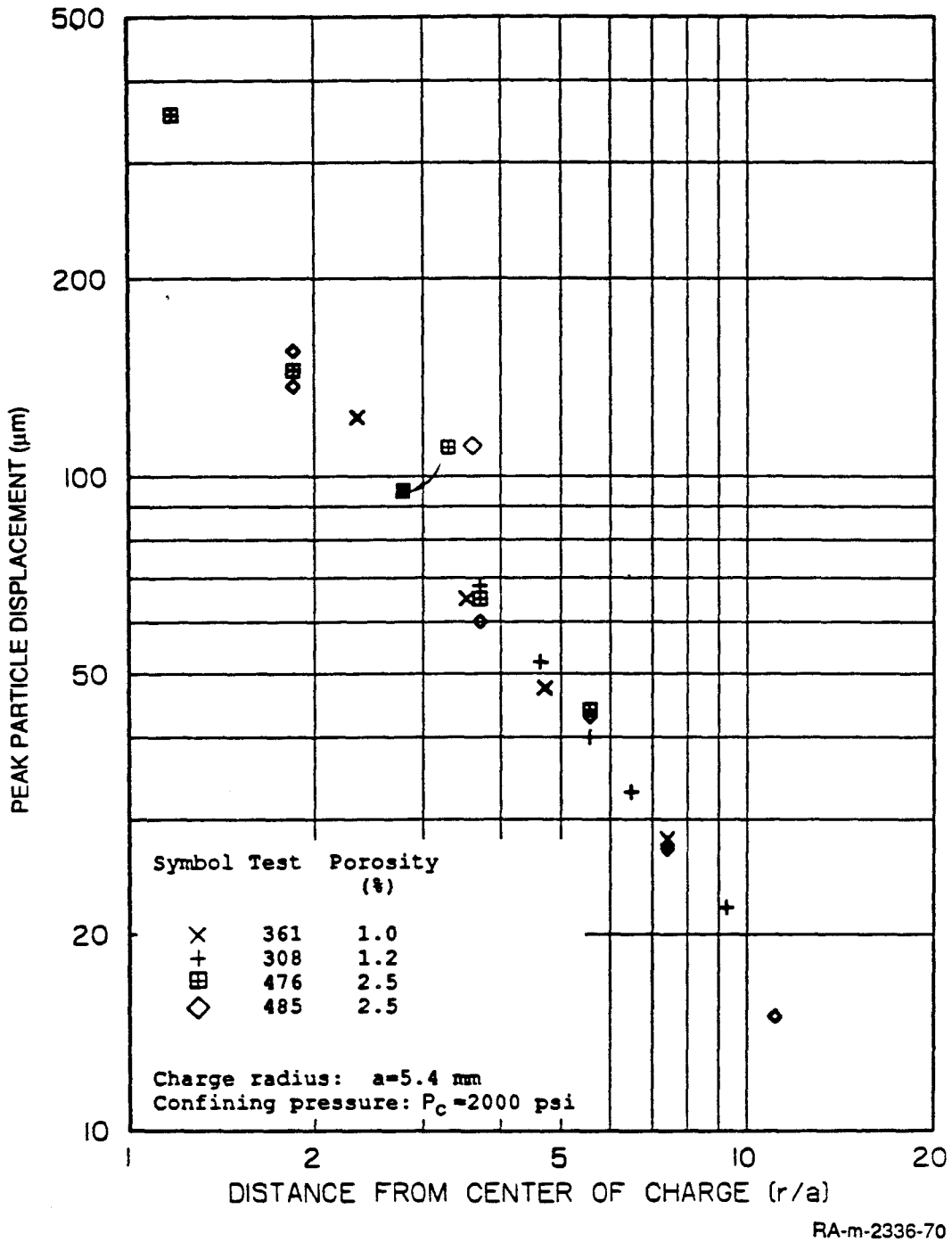

FIGURE S-2 EFFECT OF POROSITY ON PEAK DISPLACEMENT ATTENUATION IN DRY SIERRA WHITE GRANITE WITH A CONFINING PRESSURE OF 2000 psi

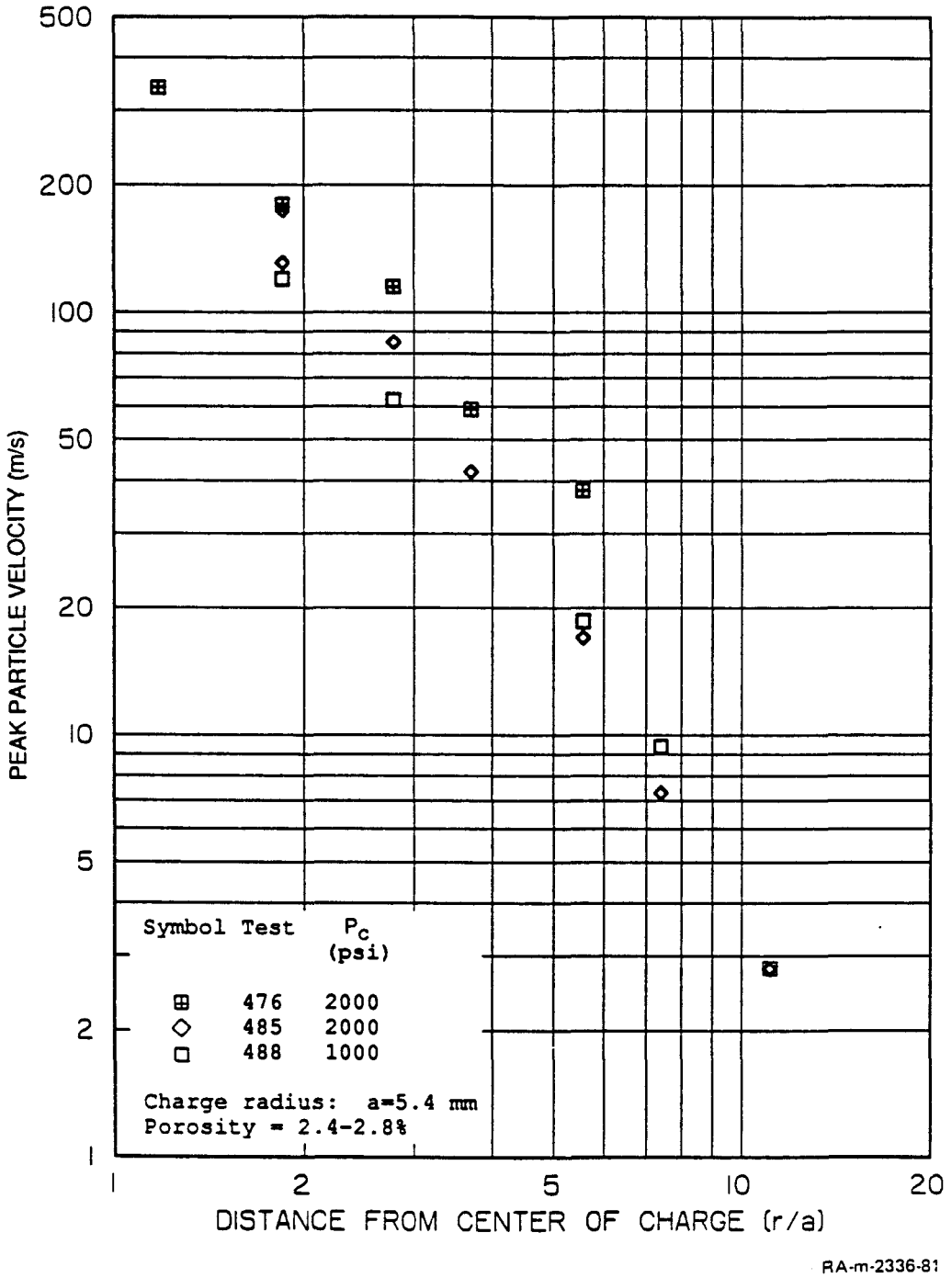

FIGURE S-3 EFFECT OF CONFINING PRESSURE P_c ON PEAK PARTICLE VELOCITY ATTENUATION IN DRY, GAS-FRACTURED SIERRA WHITE GRANITE WITH POROSITY OF 2.4 - 2.8%

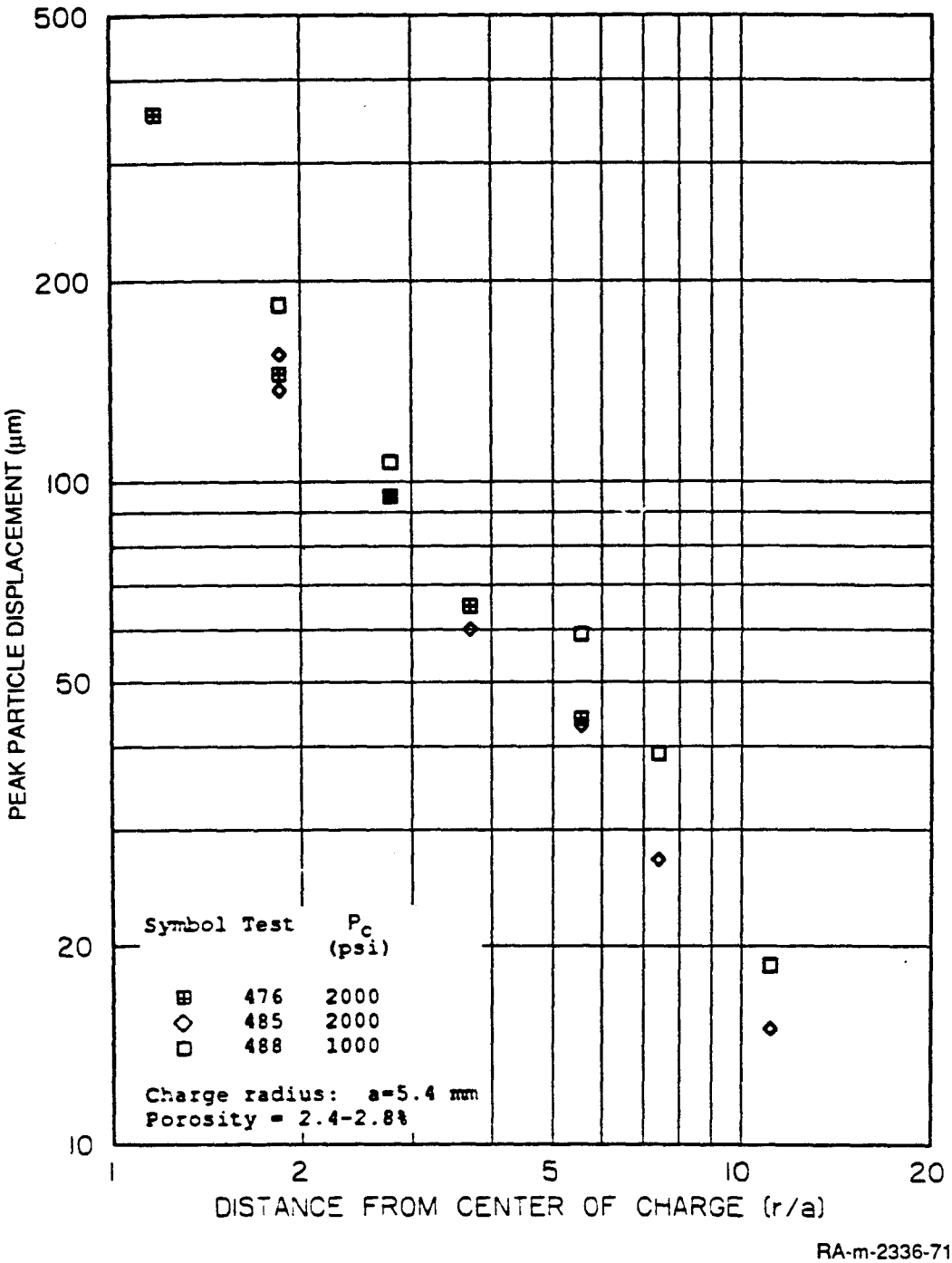

FIGURE S-4 EFFECT OF CONFINING PRESSURE P_c ON PEAK DISPLACEMENT ATTENUATION IN DRY, GAS-FRACTURED SIERRA WHITE GRANITE WITH POROSITY OF 2.4-2.8%

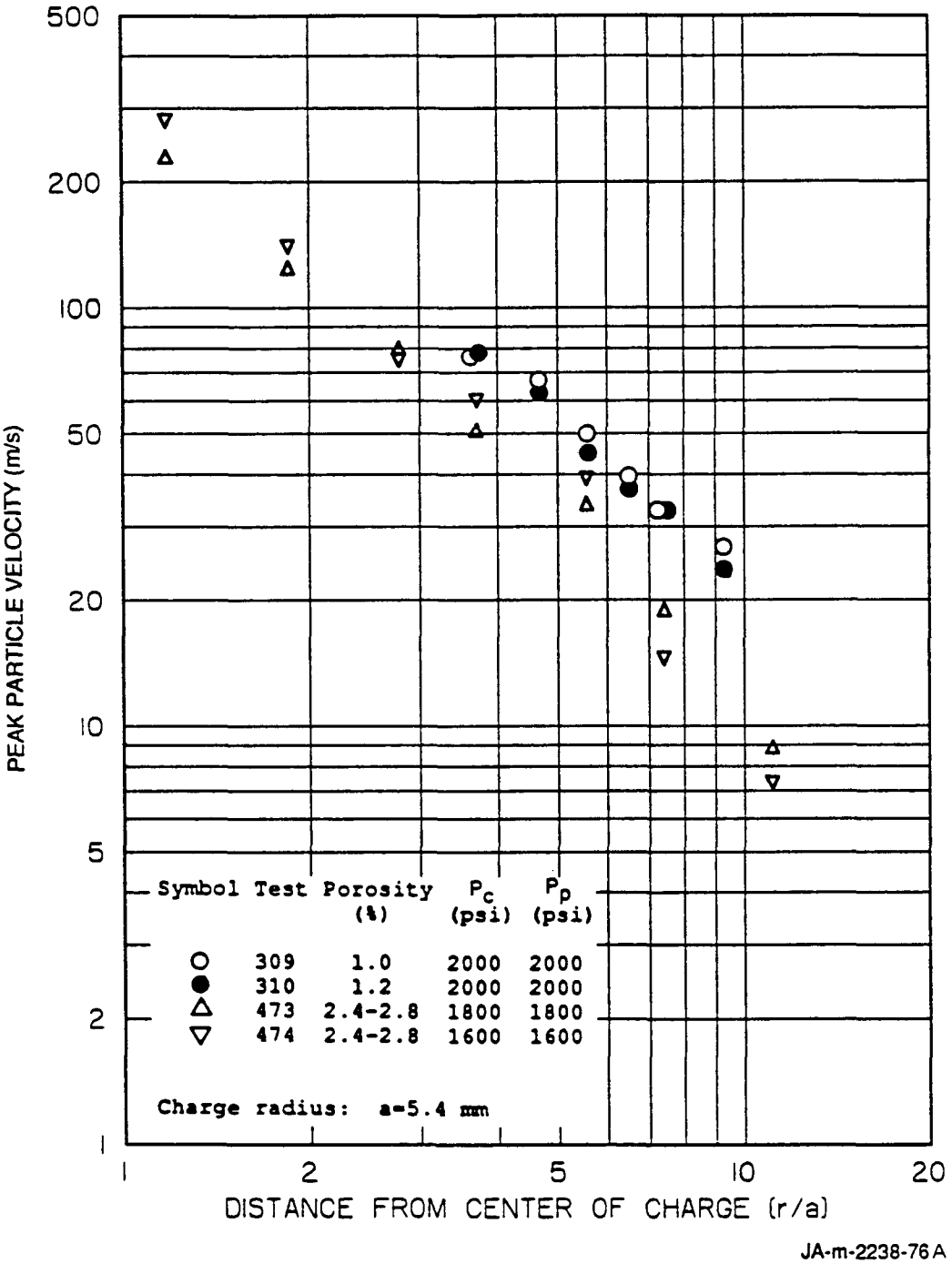

FIGURE S-5 EFFECT OF POROSITY ON PEAK VELOCITY ATTENUATION IN SATURATED SIERRA WHITE GRANITE WITH ZERO EFFECTIVE STRESS (CONFINING PRESSURE EQUAL TO PORE PRESSURE)

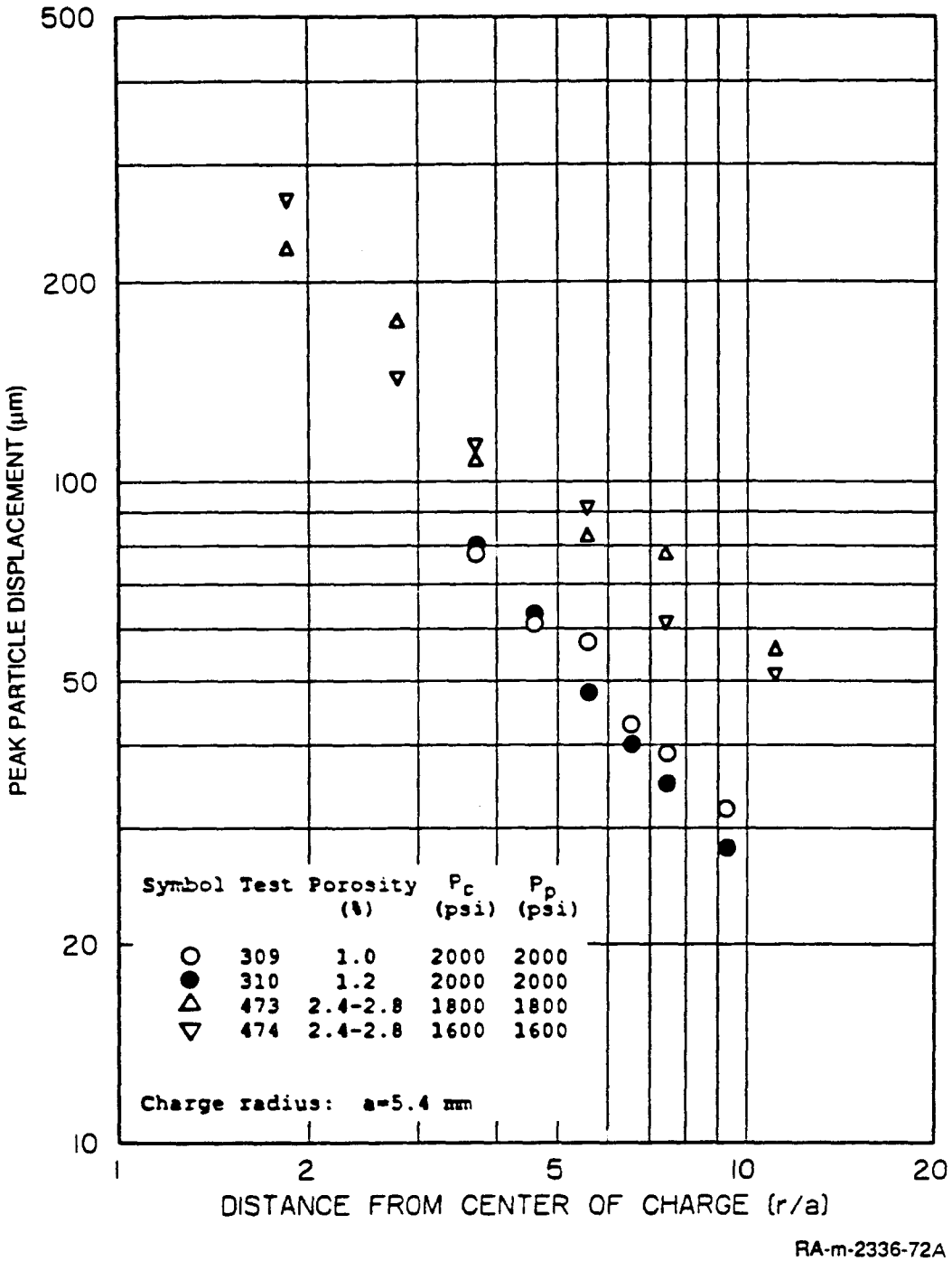

FIGURE S-6 EFFECT OF POROSITY ON PEAK DISPLACEMENT ATTENUATION IN SATURATED SIERRA WHITE GRANITE WITH ZERO EFFECTIVE STRESS (CONFINING PRESSURE EQUAL TO PORE PRESSURE

- Does not influence peak velocities except next to the source, where near zero pore pressure gives higher velocity (Figure S-7).
- Causes narrower pulses in general, but next to the source this effect is observed only for near zero pore pressure.
- Reduces peak displacements by narrowing the pulses, and increases peak displacement attenuation. However, after a significant effect of an initial effective stress increase to 1000 psi, an additional increase to 2000 psi has negligible further effect (Figure S-8).

(5) Pore water effect in high (2.5%) porosity rock with near zero pore pressure. A comparison of the response of dry rock with that of saturated rock with zero pore pressure indicates that, at the two confining pressures investigated (1000 and 2000 psi), pore water:

- Does not influence the peak velocities near the source (except for high confining pressure, which produces a high velocity next to the source), but causes higher velocities and reduced rise times farther from the source (Figure S-9).
- Increases the pulse duration and widens the pulse shape next to the source at both confining pressures, but not at greater ranges.
- Increases peak displacements at all ranges for high confinement and for regions far from the source for low confinement (Figure S-10). Next to the source this increase is due to wider pulses (low confinement) or higher velocity (high confinement), and away from the source due primarily to higher velocities.

(6) Effect of confining pressure in high (2.5%) porosity saturated rock with constant effective stress. At a given effective stress (1000 psi), an increase in confining pressure by a factor of two (from 1000 to 2000 psi) has a negligible effect on peak velocities and results in slightly lower peak displacements away from the source due to slightly narrower pulses (Figures S-11 and S-12).

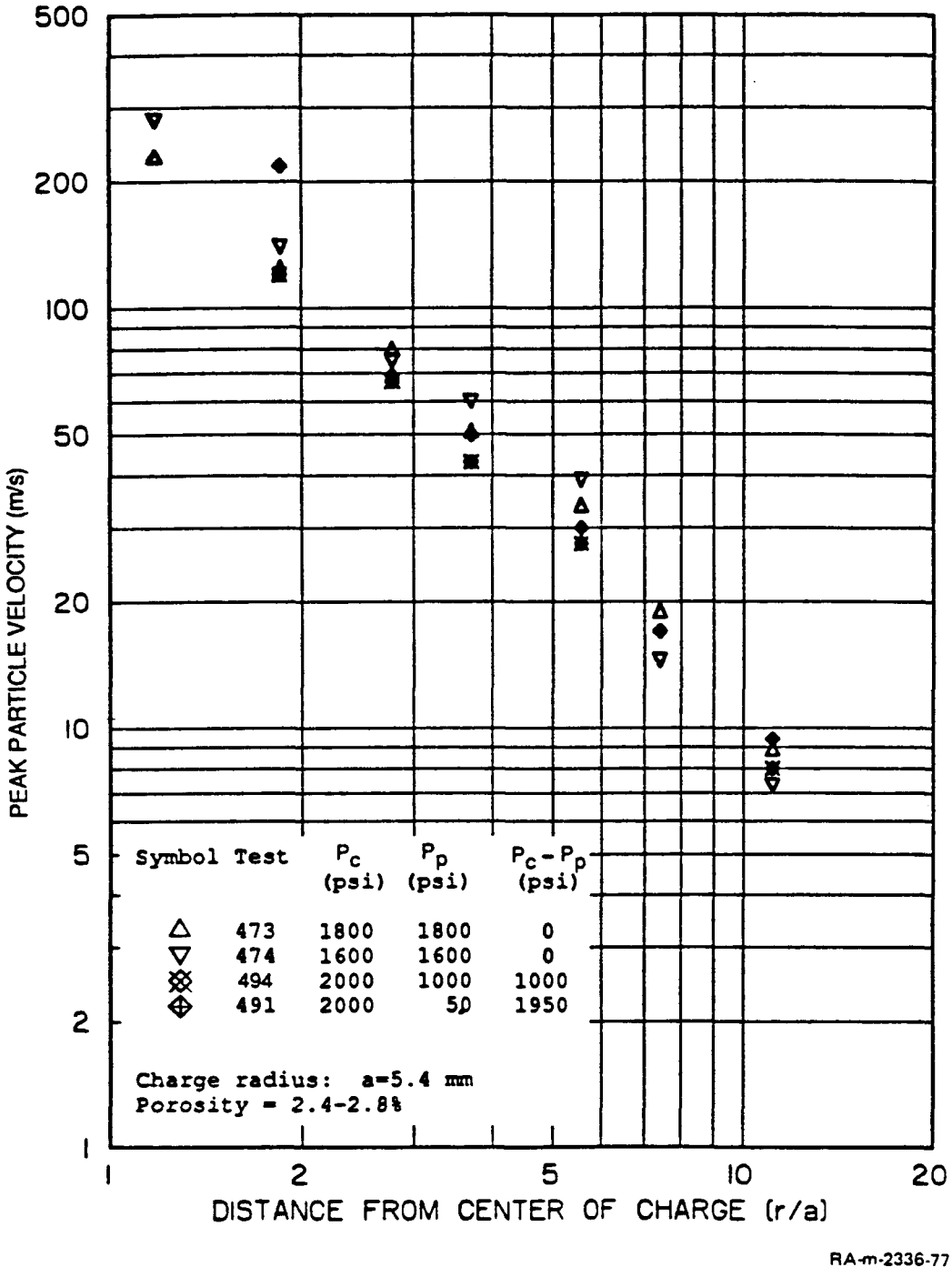

FIGURE S-7 THE INFLUENCE OF EFFECTIVE STRESS ON PEAK VELOCITY ATTENUATION IN GAS-FRACTURED, SATURATED SIERRA WHITE GRANITE WITH POROSITY OF 2.4-2.8%

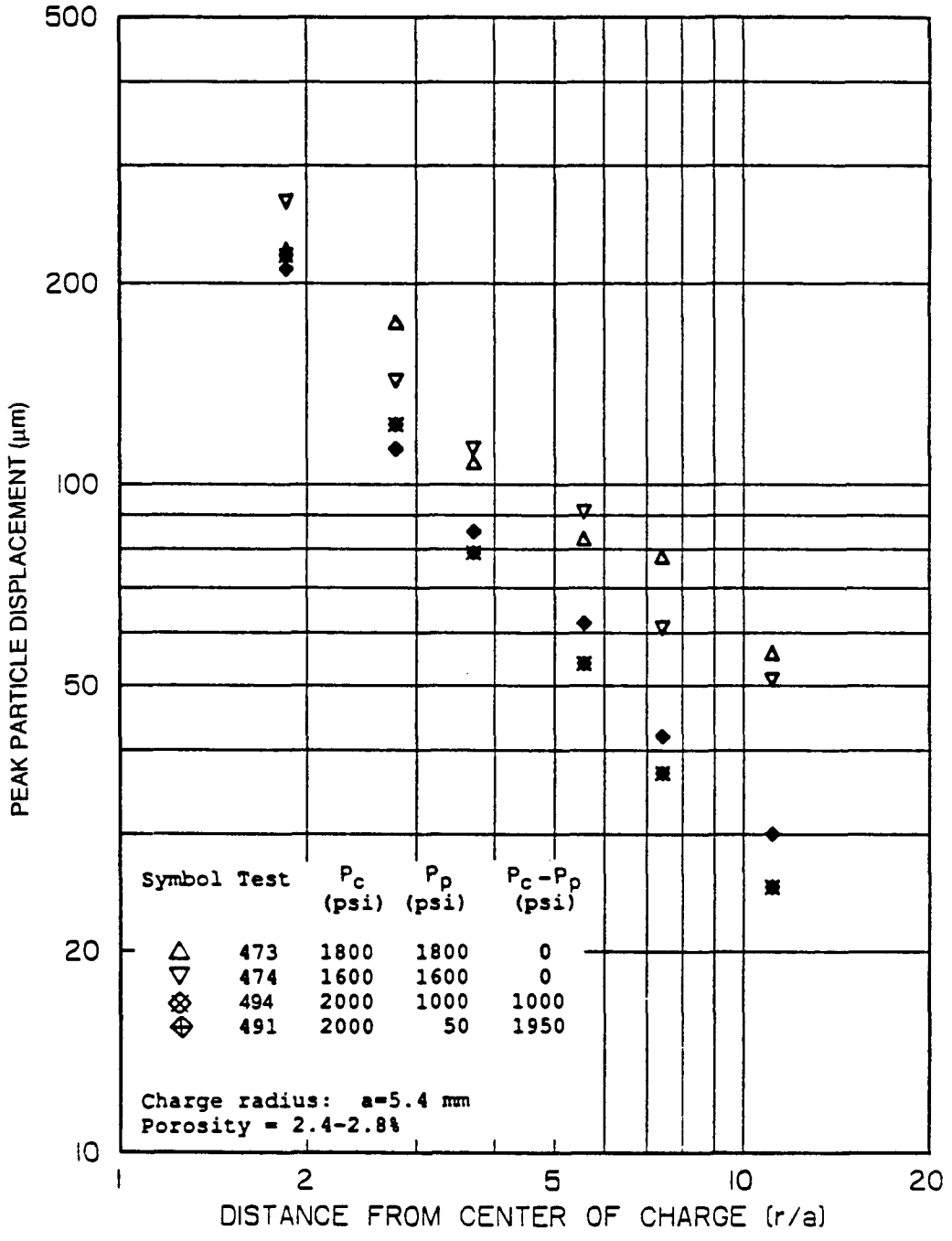

FIGURE S-8 THE INFLUENCE OF EFFECTIVE STRESS ON PEAK DISPLACEMENT ATTENUATION IN GAS-FRACTURED, SATURATED SIERRA WHITE GRANITE WITH POROSITY OF 2.4-2.8%

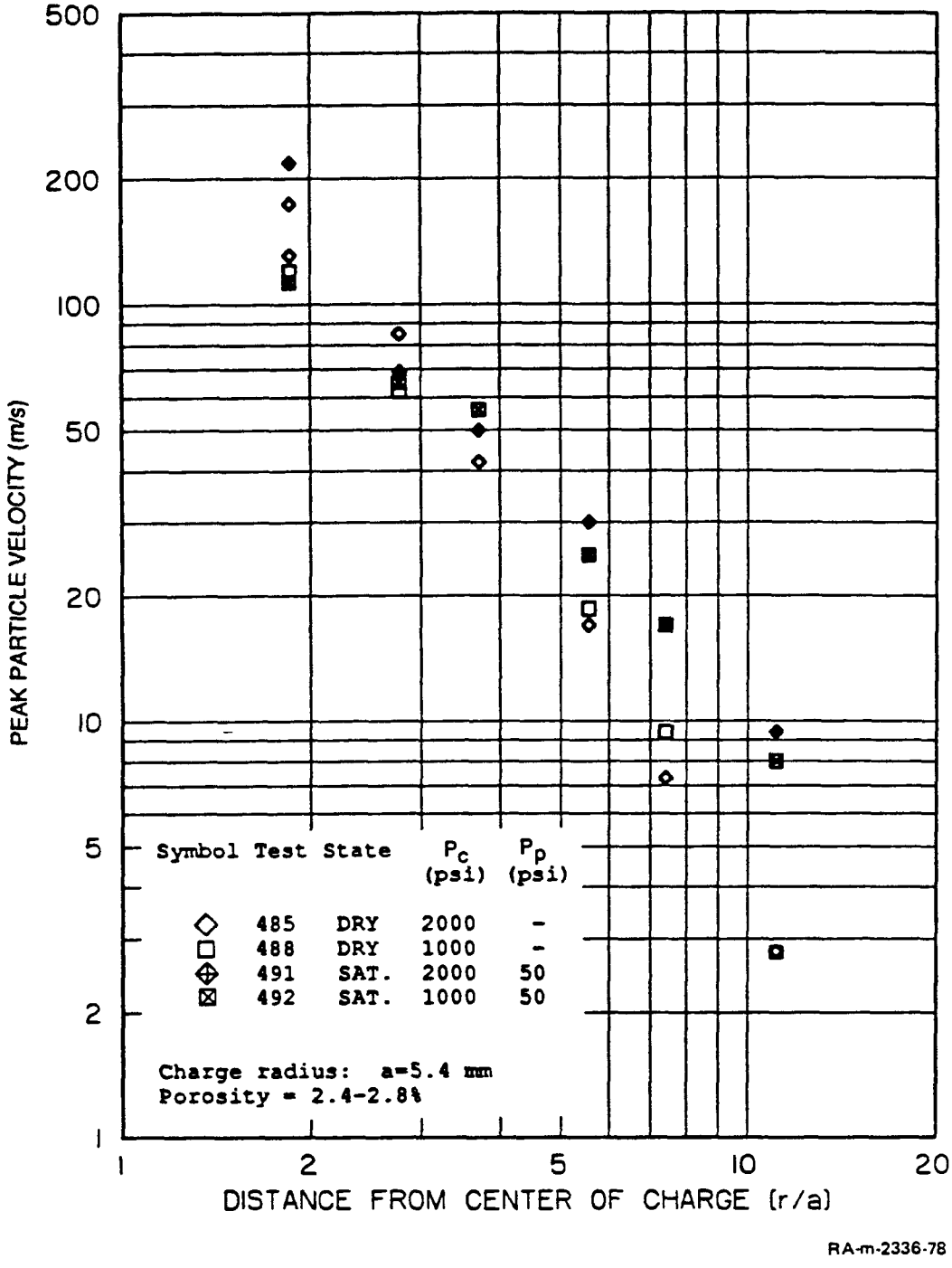

FIGURE S-9 THE INFLUENCE OF PORE WATER ON PEAK VELOCITY ATTENUATION IN GAS-FRACTURED SIERRA WHITE GRANITE WITH POROSITY OF 2.4 - 2.8%, AT TWO CONFINING PRESSURES WITH NEGLIGIBLE PORE PRESSURE

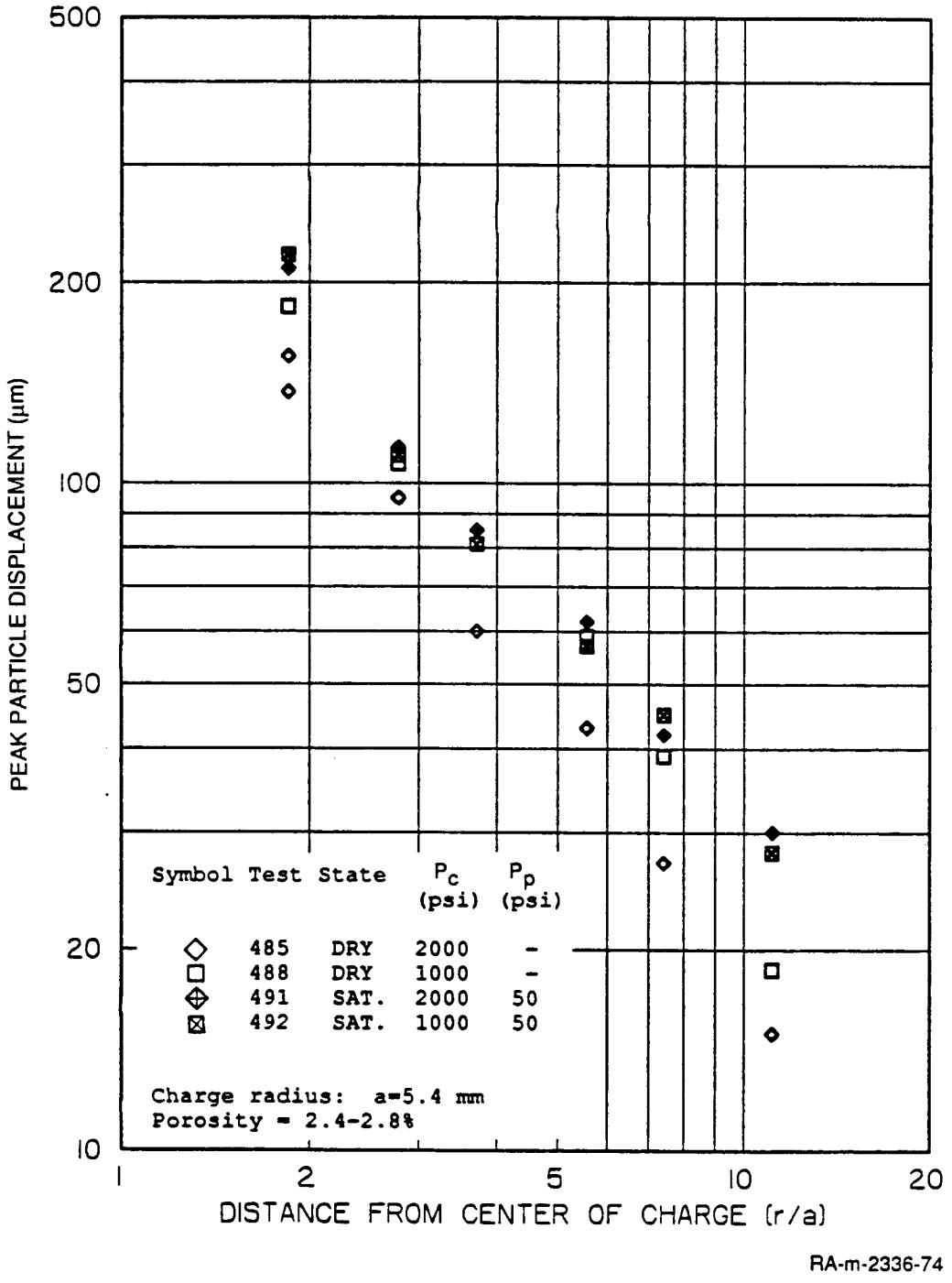

FIGURE S-10 THE INFLUENCE OF PORE WATER ON PEAK DISPLACEMENT ATTENUATION IN GAS-FRACTURED SIERRA WHITE GRANITE WITH POROSITY OF 2.4-2.8%, AT TWO CONFINING PRESSURES WITH NEGLIGIBLE PORE PRESSURE

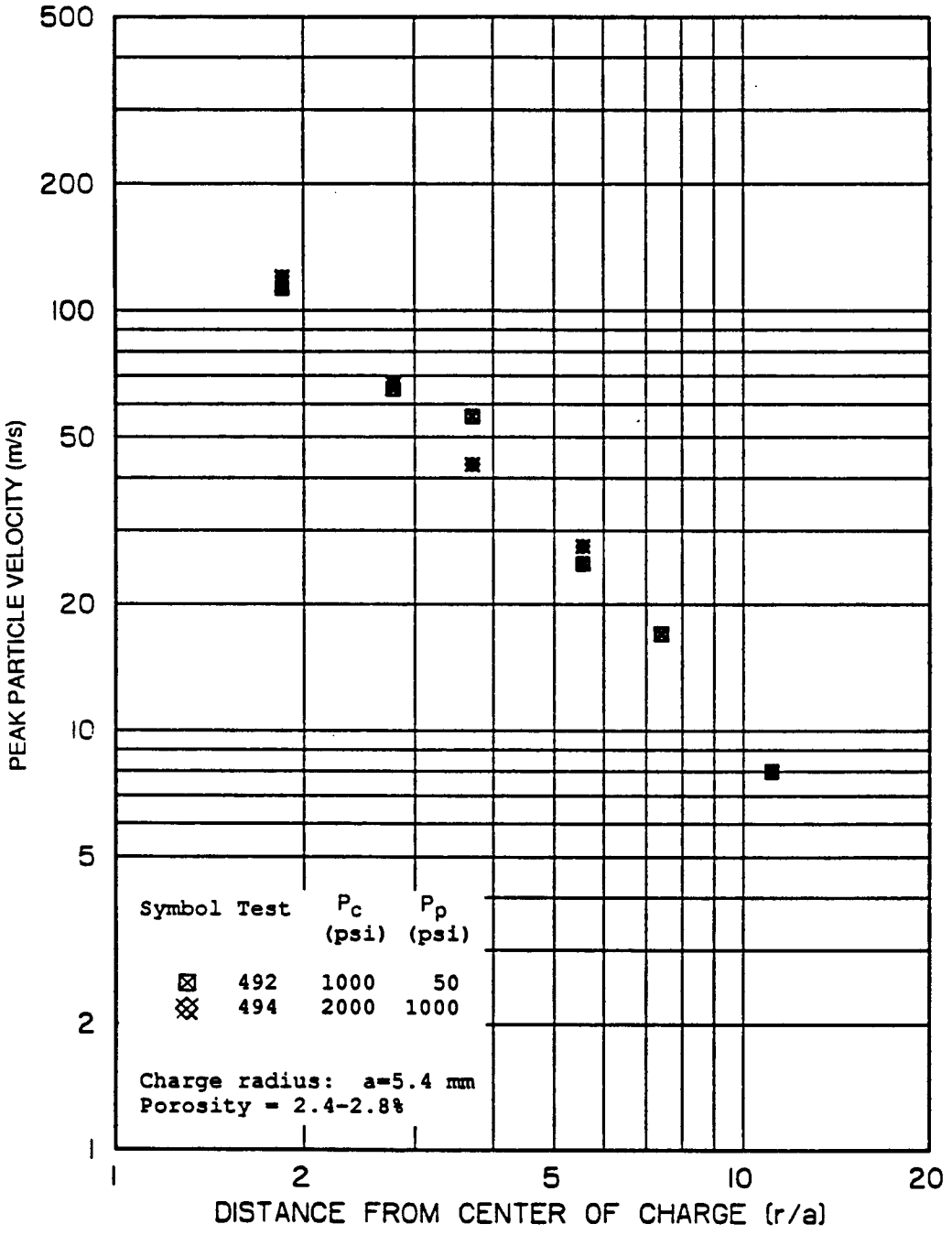

FIGURE S-11 THE EFFECT OF CONFINING PRESSURE ON PEAK VELOCITY ATTENUATION IN GAS-FRACTURED, SATURATED SIERRA WHITE GRANITE WITH POROSITY OF 2.4 - 2.8% AND AN EFFECTIVE STRESS OF 1000 psi

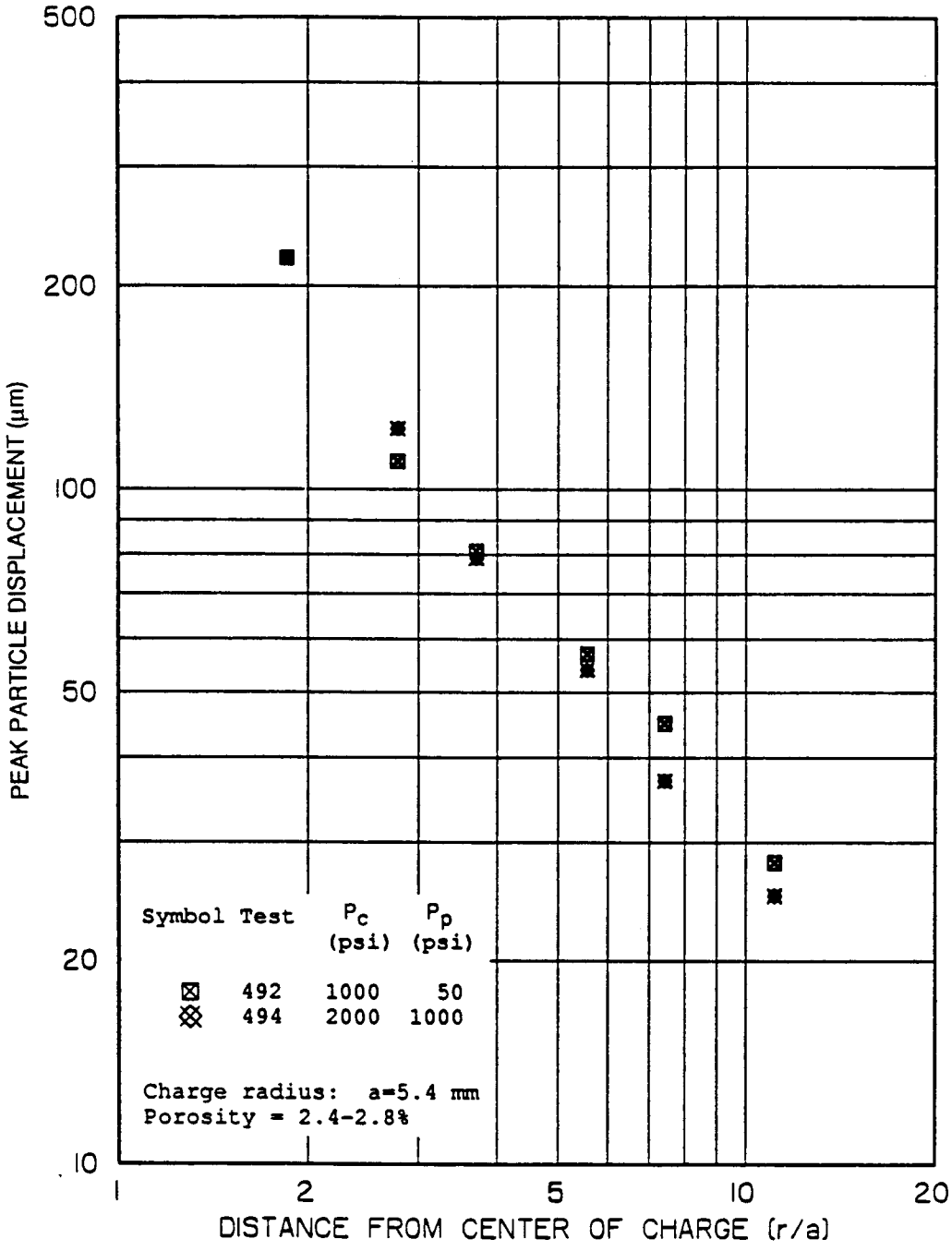

FIGURE S-12 THE EFFECT OF CONFINING PRESSURE ON PEAK DISPLACMENT ATTENUATION IN GAS-FRACTURED, SATURATED SIERRA WHITE GRANITE WITH POROSITY OF 2.4-2.8% AND AN EFFECTIVE STRESS OF 1000 psi

PREFACE

This research was conducted under Subcontract No. 9168505 for the University of California, Lawrence Livermore National Laboratory in support of material modeling efforts within DARPA's nuclear monitoring program.

The authors are indebted to the technical monitor, Dr. Robert R. Blandford, for overall guidance and suggestions. We also appreciate Dr. Norton Rimer at S-CUBED for his suggestions on the experiments and the insight provided by his theoretical work and critical commentaries, as well as Dr. Randolph Martin at New England Research who supported our work by his material characterization experiments.

The authors are also indebted to the personnel at SRI International who contributed directly to the research program. In particular, appreciation is extended to Mr. Leonard J. Dary for preparing the test specimens, Mr. Neal Berryman for performing the porosity enhancement of the test samples and assisting with all phases of the experiments, Mr. Alex M. Thibert for assisting with the pore pressure control development, Mr. William B. Heckman and Mr. Michael A. Merritt for performing the electronics, Mrs. Betty P. Bain for processing the data, and Mrs. Joyce Berry and her staff for preparing the illustrations.

Conversion factors for U.S. Customary to metric (SI) units of measurement

MULTIPLY → / ← TO GET	BY → / ← BY	TO GET → / ← DIVIDE
angstrom	1.000 000 X E -10	meters (m)
atmosphere (normal)	1.013 25 X E +2	kilo pascal (kPa)
bar	1.000 000 X E +2	kilo pascal (kPa)
barn	1.000 000 X E -28	meter^2 (m^2)
British thermal unit (thermochemical)	1.054 350 X E +3	joule (J)
calorie (thermochemical)	4.184 000	joule (J)
cal (thermochemical)/cm^2	4.184 000 X E -2	mega joule/m^2 (MJ/m^2)
curie	3.700 000 X E +1	*giga becquerel (GBq)
degree (angle)	1.745 329 X E -2	radian (rad)
degree Fahrenheit	$t_k = (t°f + 459.67)/1.8$	degree kelvin (K)
electron volt	1.602 19 X E -19	joule (J)
erg	1.000 000 X E -7	joule (J)
erg/second	1.000 000 X E -7	watt (W)
foot	3.048 000 X E -1	meter (m)
foot-pound-force	1.355 818	joule (J)
gallon (U.S. liquid)	3.785 412 X E -3	meter^3 (m^3)
inch	2.540 000 X E -2	meter (m)
jerk	1.000 000 X E +9	joule (J)
joule/kilogram (J/kg) (radiation dose absorbed)	1.000 000	Gray (Gy)
kilotons	4.183	terajoules
kip (1000 lbf)	4.448 222 X E +3	newton (N)
kip/inch^2 (ksi)	6.894 757 X E +3	kilo pascal (kPa)
ktap	1.000 000 X E +2	newton-second/m^2 ($N-s/m^2$)
micron	1.000 000 X E -6	meter (m)
mil	2.540 000 X E -5	meter (m)
mile (international)	1.609 344 X E +3	meter (m)
ounce	2.834 952 X E -2	kilogram (kg)
pound-force (lbs avoirdupois)	4.448 222	newton (N)
pound-force inch	1.129 848 X E -1	newton-meter (N·m)
pound-force/inch	1.751 268 X E +2	newton/meter (N/m)
pound-force/foot^2	4.788 026 X E -2	kilo pascal (kPa)
pound-force/inch^2 (psi)	6.894 757	kilo pascal (kPa)
pound-mass (lbm avoirdupois)	4.535 924 X E -1	kilogram (kg)
pound-mass-foot^2 (moment of inertia)	4.214 011 X E -2	kilogram-meter^2 ($kg·m^2$)
pound-mass/foot^3	1.601 846 X E +1	kilogram/meter^3 (kg/m^3)
rad (radiation dose absorbed)	1.000 000 X E -2	**Gray (Gy)
roentgen	2.579 760 X E -4	coulomb/kilogram (C/kg)
shake	1.000 000 X E -8	second (s)
slug	1.459 390 X E +1	kilogram (kg)
torr (mm Hg, 0° C)	1.333 22 X E -1	kilo pascal (kPa)

*The becquerel (Bq) is the SI unit of radioactivity; 1 Bq = 1 event/s.
**The Gray (Gy) is the SI unit of absorbed radiation.

A more complete listing of conversions may be found in "Metric Practice Guide E 380-74," American Society for Testing and Materials.

CONTENTS

ILLUSTRATIONS

ILLUSTRATIONS (Continued)

ILLUSTRATIONS (Continued)

ILLUSTRATIONS (Continued)

ILLUSTRATIONS (Continued)

ILLUSTRATION (Continued)

ILLUSTRATIONS (Continued)

ILLUSTRATION (Concluded)

TABLES

Section 1

INTRODUCTION

Nuclear monitoring requires sound theoretical models for predicting ground motions caused by nuclear explosions. The theoretical models incorporate material properties and conditions that affect both the seismic coupling near the source and the wave characteristics far from the source. Air-filled pore and crack porosity, pore water content, and pore pressure are among the most important characteristics that may influence wave shape, amplitude, and attenuation. Our laboratory work is a continuation of earlier research to determine how porosity and pore water content affect high-amplitude spherical waves in low-porosity brittle rocks. The experiments were conducted in Sierra White granite, and the waves were monitored in the form of particle velocities.

Our experiments were performed in a coordinated effort with theoretical work performed by S-CUBED, and the material properties work performed by New England Research. In the previous segment of our research, it was found that significant porosity increase and pore water content had a large effect on the pulse shapes of high-amplitude waves in granite. The specific objectives of this segment of our research were to gain further understanding of the effect of these parameters and the effects of confining pressure, pore pressure, and effective stress.

To achieve these objectives, we undertook the following three specific tasks:

(1) Modification of the existing experimental apparatus to allow independent control of overburden and pore pressure in water saturated granite test samples.

(2) Increase the natural porosity of the test samples by dynamic gas fracturing to achieve the desired initial rock conditions, and preparation of instrumented particle velocity samples with fractured/dry and fractured/saturated initial rock conditions.

(3) Particle velocity experiments with appropriate overburden and pore pressure states.

Section 2.1 summarizes the test program, and Section 2.2 reviews the techniques for the spherical wave particle velocity experiments. Section 3 presents the experimental results for this program and contains a discussion of the effects of the parameters under investigation, including the earlier experiments. Appendix A contains volumetric strains calculated from particle velocities, and Appendix B tabulates the peak velocities and displacements for all gas-fractured experiments, including those of previous phases of our program. In Appendix C we reproduce for convenience some of the records obtained in earlier phases of the program in dry and saturated samples of gas-fractured (2.5% porosity) granite (Tests 476, 473, and 474) and intact and thermally fractured (1.2% porosity) granite (Tests 308, 309, and 310). Appendix D presents basic material properties for Sierra White granite.

Section 2

EXPERIMENTAL PROGRAM AND TECHNIQUES

2.1 PROGRAM

The effects of porosity increase and pore water content in a low-porosity brittle rock have been demonstrated in previous phases of our work.[1,2] The primary objective of this phase of the program was to determine the individual and combined effects of porosity, pore water content, confining pressure, and pore pressure on spherical stress waves in this material. The work was conducted in direct support of developing and validating theoretical models used for predicting ground motions in such materials near an exploding spherical cavity.[5-7] The material used in the experiments was Sierra White granite. The test matrix for the program is shown in Table 1. A summary of particle velocity experiments conducted during earlier programs, including intact and thermally fractured states, is shown in Table 2.

The current work included three major tasks: (1) the development of a method to independently control confining and pore pressures in water-saturated samples, (2) generating the desired initial porosity conditions in the test specimen and preparing the experimental models, and (3) performing the particle velocity experiments.

Two particle velocity experiments, Tests 485 and 488, were performed with dry samples, and three experiments, Tests 491, 492, and 494, were conducted with 100% saturated samples with the confining and pore pressures listed in Table 1. The two dry experiments were designed to investigate the effect of confining stress in the absence of pore water. The three saturated experiments were designed to answer questions about the influence of pore water, confining stress, and the difference between confining and pore pressures (effective stress).

Table 1

PARTICLE VELOCITY EXPERIMENTS IN SIERRA WHITE GRANITE

Test No.	Fracture Type	Porosity %	Pore Condition	Confining Pressure (psi)	Pore Pressure (psi)
485	Gas	2.8	Dry	2000	-
488	Gas	2.7	Dry	1000	-
491	Gas	2.9	Saturated	2000	50
492	Gas	2.6	Saturated	1000	50
494	Gas	2.9	Saturated	2000	1000

Table 2

EARLIER PARTICLE VELOCITY EXPERIMENTS IN SIERRA WHITE GRANITE

Test No.	Fracture Type	Porosity (%)	Pore Condition	Confining Pressure (psi)	Pore Pressure (psi)
361[a]	Intact	0.8-1.0	Dry	2000	-
308	Thermal	1.2	Dry	2000	-
309	Intact	0.8-1.0	Saturated	2000	2000
310	Thermal	1.2	Saturated	2000	2000
473	Gas	2.5	Saturated	1800	1800
474	Gas	2.4	Saturated	1600	1600
476	Gas	2.4	Dry	2000	-

[a]Test 361 is from Reference 3.

2.2 EXPERIMENTAL TECHNIQUES

In this section, we describe the concepts and experimental techniques used in our study.

2.2.1 Spherical Wave Experiments

The essential features of the technique used to generate and monitor spherical stress waves in geologic materials are shown in Figure 1. A spherical explosive charge is installed at the center of a cylindrical rock specimen. External hydraulic confining pressure represents overburden. The wave motion is measured by particle velocity gages consisting of circular loops of conductors located in the mid-height plane of the specimen. A constant, uniform, and homogeneous magnetic field generated by a solenoid is directed perpendicular to the plane of the gages. Expansion and contraction of a circular conductor caused by a spherical wave induces a voltage equal to the product of the magnetic field strength, the current gage length, and the component of the velocity normal to the magnetic field (if the plane of the gage also contains the source center, as in Figure 1, the recorded signals represent spherically radial motion). Integration of the particle velocity records gives particle displacements. An adequate number of particle velocity loops allows the determination of the history and geography of strain components and the volumetric strain.

2.2.2 Porosity Increase

Because porosity is believed to have a major influence on wave propagation in such materials, it was desirable to induce a homogeneous porosity increase in the test material from its intact value of 0.8 to 1.0% by a factor of two or three. Thermal methods used in the past can induce only about a 20% increase in porosity. Figure 2 shows schematically the technique developed in our earlier work and used in the current program to prepare the test specimen with the desired initial pore conditions.

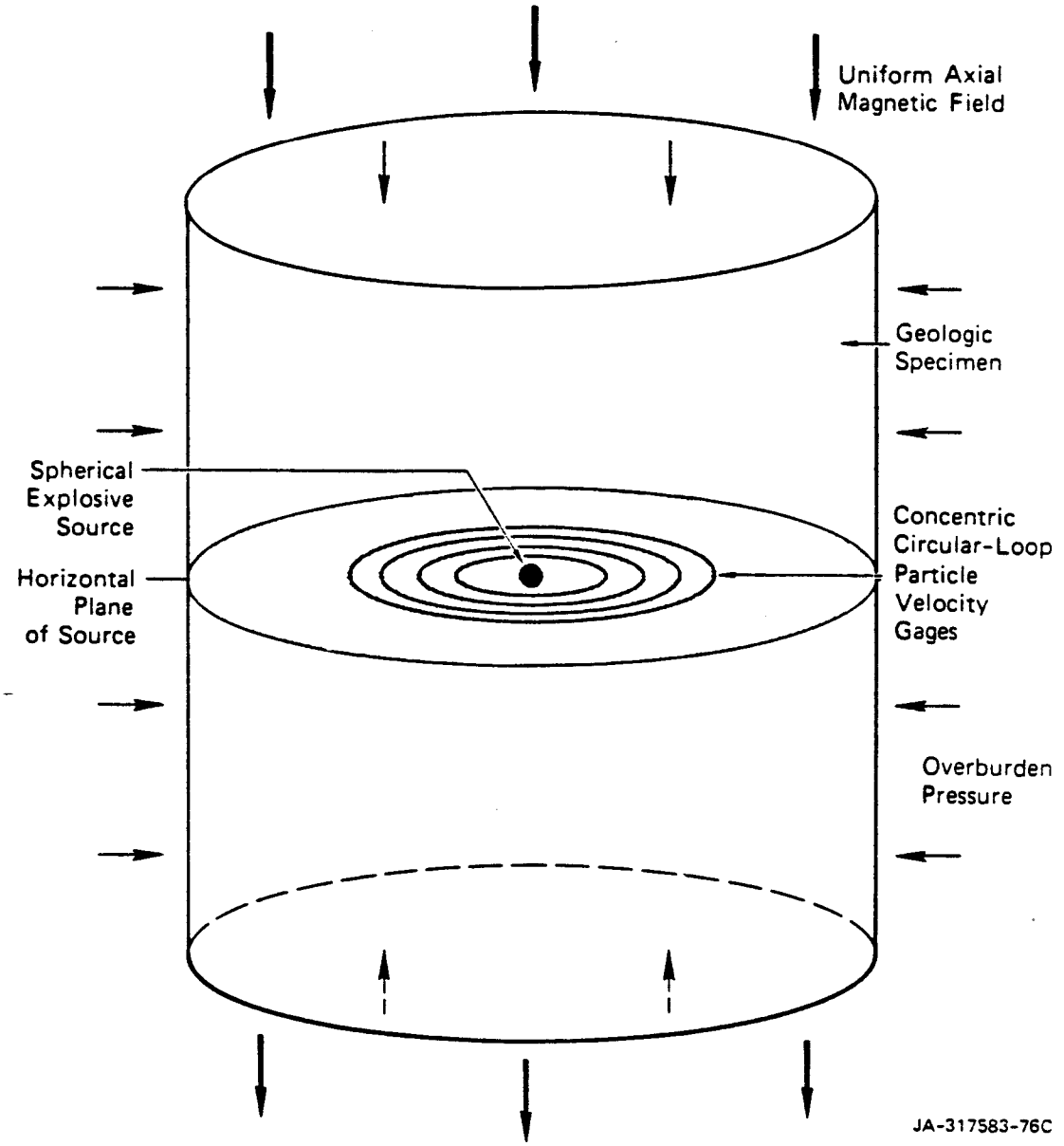

FIGURE 1 EXPERIMENTAL CONCEPT FOR PARTICLE VELOCITY MEASUREMENTS

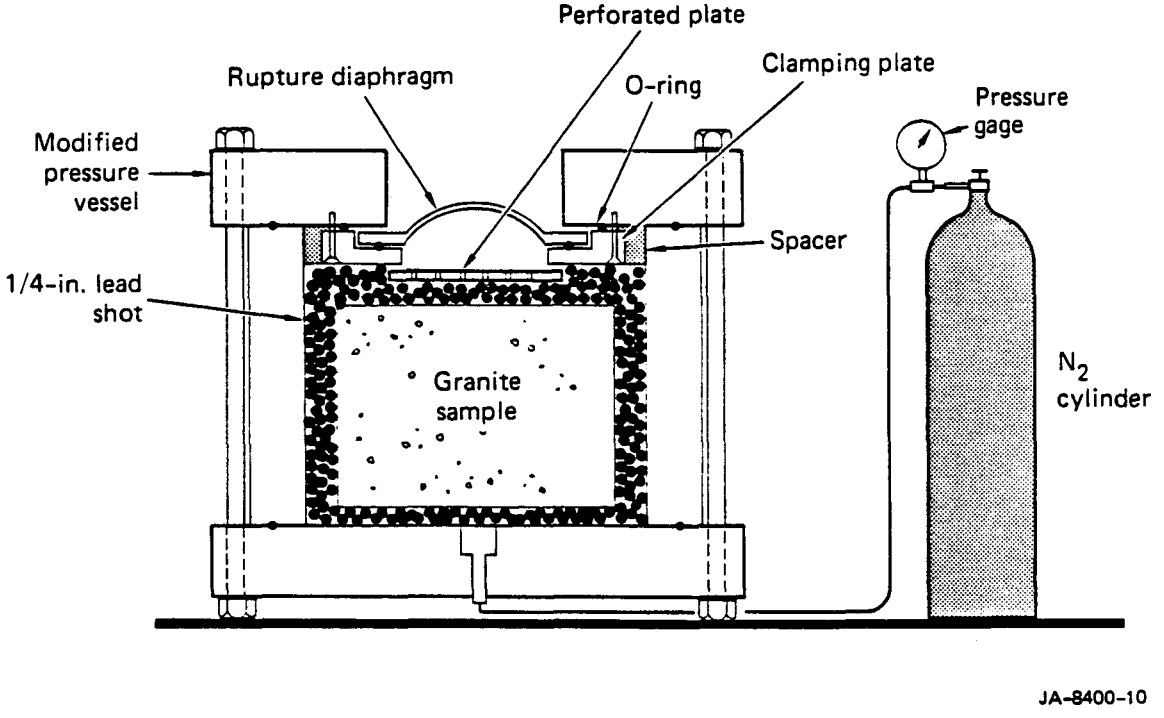

FIGURE 2 SCHEMATIC OF GAS- FRACTURING ARRANGEMENT FOR PREPARATION OF VELOCITY SAMPLES TO ACHIEVE DESIRED POROSITY

The basic concept is to permeate a rock specimen with high pressure gas, then rapidly decrease the surrounding pressure by means of a rupture diaphragm, thereby allowing the connected pore space to be temporarily pressurized. As it escapes, the gas continues to exert pressure on the pores and generates a large amount of expanded pore space and numerous cracks. The key to the success of the method using relatively low gas pressures (about 2000 psi), much below the tensile strength, is the low fracture toughness of the rock compared to its tensile strength. The slender pore shapes allow high stress concentrations and induce fractures at the crack tips. A highly porous but relatively rigid region, consisting of packed lead shot, surrounds the sample to supress the formation of wide cracks and prevent disintegration of the sample. The details of the technique, along with preliminary material properties, are discussed in a previous report.[1] A detailed study investigating the mechanical characteristics of the material was made by Martin and coworkers at N.E.R.[8] They found the properties to be homogeneous and isotropic.

2.2.3 Sample Preparation

The granite samples used for the experiments were cored out of 1-ft^3 pieces cut from the same large block of granite[9] to ensure minimum variation within test samples. (This large block, in turn, was adjacent to another block used by LLNL in their experiments investigating the low-amplitude response of this material). As a means to maximize uniformity among the specimens, the cylindrical samples were cored out of the cubes with their axes normal to the bedding plane marked on each cube. Each cylinder was sectioned at its midheight for charge and particle velocity gage installation. Each half-cylinder was slowly heated to 350°C and cooled to generate a uniform, thermally induced porosity increase of about 20%, before the application of the gas-fracturing process described in Section 2.2.2. The porosity of each fractured sample was measured directly by the weight difference between dry and 100% saturated states. The sample porosities ranged between 2.4 and 2.9%. The porosity for each experiment is listed in Table 1. One

fractured cylinder (two halves) was sent to N.E.R. for their material characterization experiments.[8]

The end faces of the samples used for the particle velocity experiments were ground flat, smooth, and parallel. The explosive source and the particle velocity gages were installed in the test samples according to the diagram shown in Figure 3. The centrally located charge in our experiments consisted of 3/8 gram of PETN contained in a thin Lucite shell, packed to a nominal density of 1 g/cm^3. The mild detonating fuse (MDF) used to explode the charge is installed in the top half of the samples through an access hole and is placed inside a steel tube, which in turn is ancored to the sample at two points, at the top of the sample and near the cavity. This arrangement minimizes the coupling of the waves generated by the detonating MDF into the test sample.

The particle velocity gages consisted of 10-mil-diameter Formvar insulated copper wire installed with waterproof epoxy in narrow (0.012-inch-wide), shallow (0.020-inch-deep) grooves cut concentrically around the charge cavity in the bottom half of the sample. The gage radii were 1.0, 1.5, 2.0, 3.0, 4.0, and 6.0 cm for all experiments. Test 485 had two additional deeper grooves installed at the first two locations, as discussed in Section 3.1.1 below. The configuration for the assembled test samples is shown in Figure 4. As in previous work, the sample halves were assembled without any bonding material, which would introduce a compliant layer at the interface. The two halves of the specimen were pressed together during the experiments as a result of the difference between confining and pore pressures (at least 1000 psi). The saturated samples also had two short, 1/4-inch-diameter steel pins anchoring them together near the edges to avoid damaging and saturating the charge by possible relative horizontal motion of the two sample halves. These pins had no effect on the monitored wave motions.

All samples were sealed with a rubber Wilson seal around the cylindrical surface. The seal was cemented to aluminum plates placed on the top and bottom surfaces. The top plate had feed-throughs for the

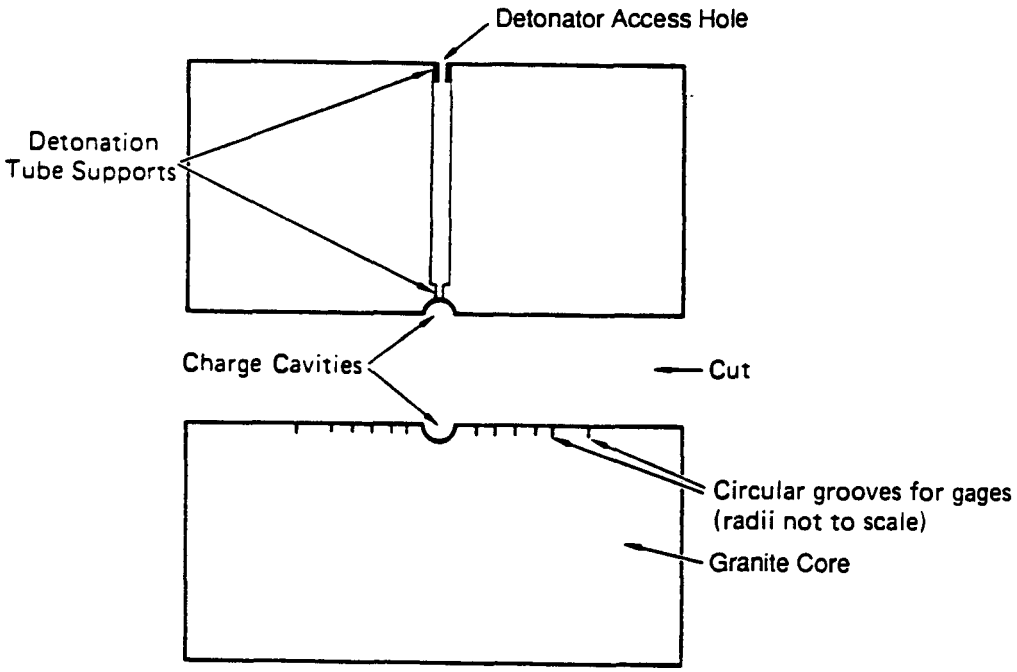

FIGURE 3 INSTALLATION OF PARTICLE VELOCITY LOOPS IN GRANITE SAMPLES

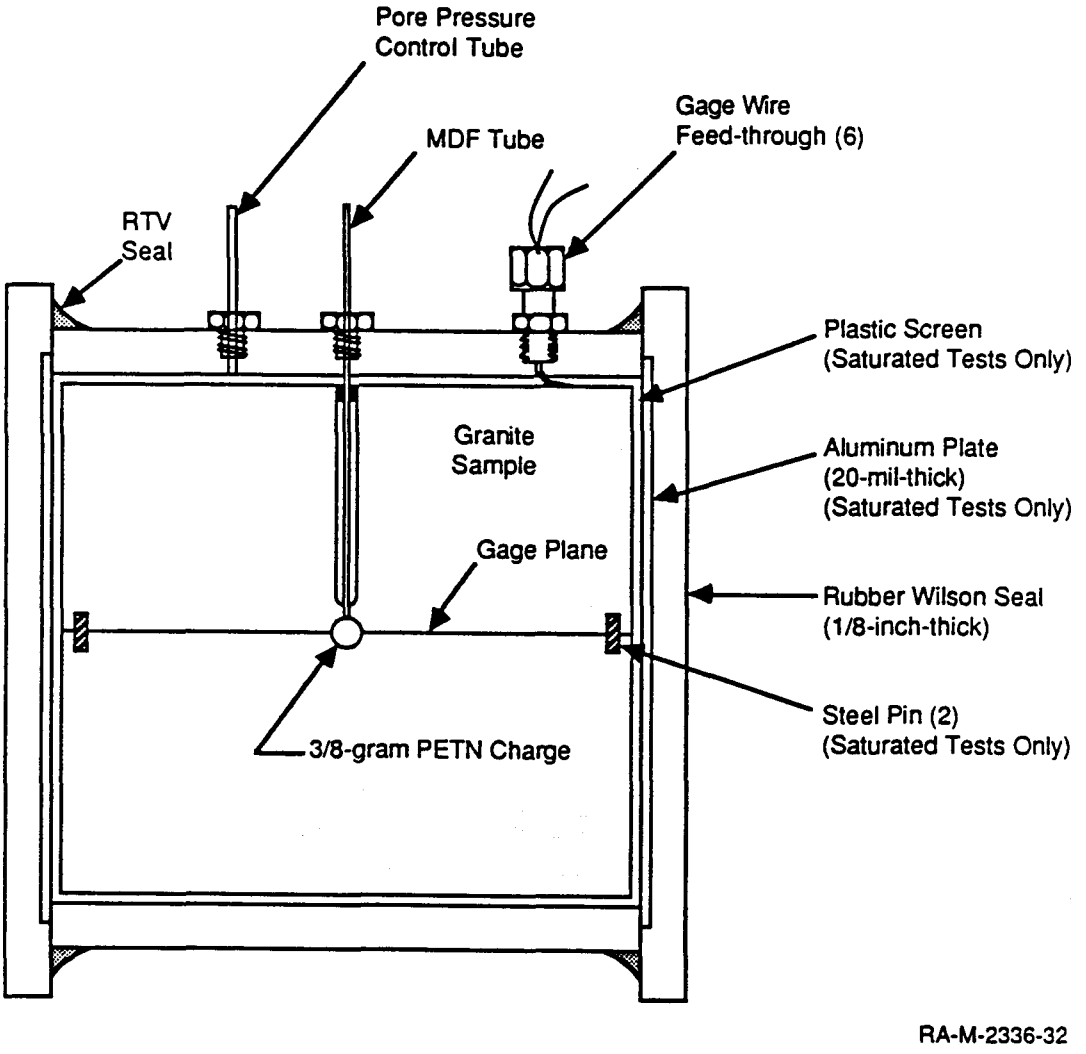

FIGURE 4 TEST SAMPLE CONFIGURATION FOR PARTICLE VELOCITY EXPERIMENTS

gage wires, the MDF tube, and for pore water control. In addition, the samples used for the saturated experiments were surrounded by a thin plastic screen and a thin aluminum sheet. This arrangement ensured free migration of the water around the sample and minimized the time required for evacuating and saturating the samples and for adjusting the pore pressure to the desired value.

The detonator access hole drilled perpendicular to the gage plane and the gage plane itself are the two major experimental artifacts that may be sources of imperfections in the measured particle velocity signals. These imperfections can result from the mechanical coupling of the detonating MDF into the rock through the detonator access hole and from the separation of the gage plane following charge detonation. The presence of two secondary peaks in the particle velocity records, starting around the zero crossing, indicate a possible effect of these imperfections.

Because of the special care taken during sample preparation to isolate the MDF from the sample, we do not believe that MDF coupling into the sample contaminates the records. A simple experiment performed with one of the dry test samples already used for a particle velocity measurement, with the particle velocity gages left intact, confirmed this assumption. The test sample was reassembled exactly as an actual particle velocity experiment, with the MDF, but without the PETN explosive. The resulting particle velocity records had a negligible amplitude, indicating that the MDF had no effect on the experiments.

However, dynamic separation, or "cracking," of the interface occurs in the experiments and is probably the cause of the secondary peaks in the records. We believe that these signals are sufficiently late in time and low in amplitude that they do not significantly affect the essential features of the results and thus the conclusions based on them.

2.2.4 Test Setup and Pore Pressure Control

Test Setup. The experimental arrangement is shown schematically in Figure 5. For both the dry and saturated experiments, through appropriate valving, the sample and the pressure vessel are first evacuated, then the space around the sample is filled with deionized, degassed water. The confining pressure is controlled by a manostat that allows the application of nitrogen pressure to the water through an impermeable diaphragm. This ensures precise pressure control and no nitrogen absorption into the water. For the dry experiments, the pore space of the sample is isolated from the water by the appropriate valve, and the confining pressure is adjusted through the manostat.

Pore Pressure Control. For the saturated experiments, the vacuum line is blocked off and the water around the sample is allowed to exit the vessel and enter the sample through the access tube. The manostat pressure then can be applied simultaneously to the outside and inside of the sample ensuring complete saturation. The pore pressure is adjusted by blocking the exit tube from the vessel and opening the vent valve. The pore pressure control arrangement was tested before the particle velocity experiments were performend using a dummy sample. For the saturated experiments a pore pressure of at least 50 psi was maintained to ensure complete saturation.

2.2.5 Instrumentation and Data Processing

The particle velocity voltage signals were fed into differential amplifiers, with a frequency response of 2 MHz, for common-mode noise rejection. Because the signals were reasonably high, the amplifiers were set to unity gain and the output was recorded on single-ended digital oscilloscopes with 100 or 200 ns/point time resolution. The current in the solenoid was recorded on one channel of a chart recorder, and the trigger signal on the other. This provided the magnetic field intensity at the time of the detonation. The rate of change of magnetic field strength due to coil heating and other effects has an unmeasurable effect on the velocity signals.

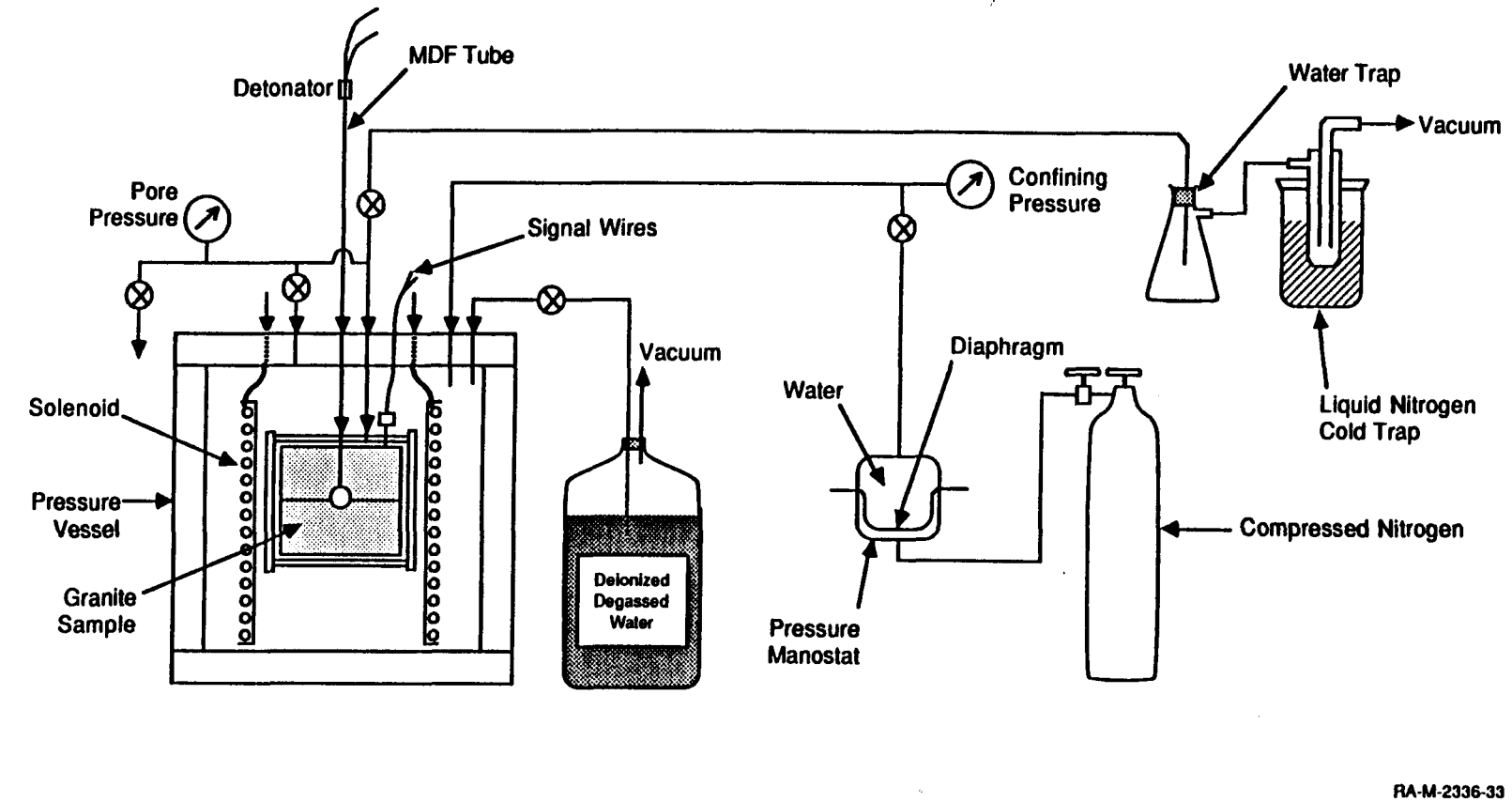

FIGURE 5 SCHEMATIC OF EXPERIMENTAL ARRANGEMENT FOR PARTICLE VELOCITY MEASUREMENTS IN DRY OR SATURATED SIERRA WHITE GRANITE WITH PORE PRESSURE CONTROL

The signal voltages were converted to velocities from the knowledge of the magnetic field strength and the gage radii. Because the particle displacements are very small, the increasing gage length during wave passage has a negligible effect on the calculated velocities.

Section 3

EXPERIMENTAL RESULTS

In this section, we present and discuss the experimental results. Sections 3.1 through 3.3 contain the results obtained in the last phase of our research with a discussion of the specific parameters under investigation. We describe the measured particle velocities in dry and saturated rock in Section 3.1, then the integrated displacements in Section 3.2, and the calculated volumetric strains in Section 3.3. In Section 3.4 we summarize our conclusions about the observed effects on rock response of the parameters investigated, based on the collection of results obtained throughout the program.

3.1 PARTICLE VELOCITIES

3.1.1 Dry Experiments

To investigate the effect of confinement in fractured/dry Sierra White granite, two experiments, Tests 485 and 488, were conducted under confining pressures of 2000 and 1000 psi, respectively. Test 485 was a repeat of Test 476 conducted in earlier work, the records of which are reproduced in Appendix C for convenience. Because the interface next to the charge separates during the experiment, the effect of gage distance from the interface on gage response was investigated by installing two additional gages in deeper grooves at the 1.0- and 1.5-cm locations in Test 485, as shown in Figure 6. This arrangement provided a direct comparison between the standard shallow gage grooves and the deep ones at the first two radii. The particle velocity records obtained in Tests 485 and 488 are shown in Figures 7 through 14.

Effect of Groove Depth. Figures 7 and 8 show the comparison between deep and shallow gages for Test 485. As shown in Figure 7, at

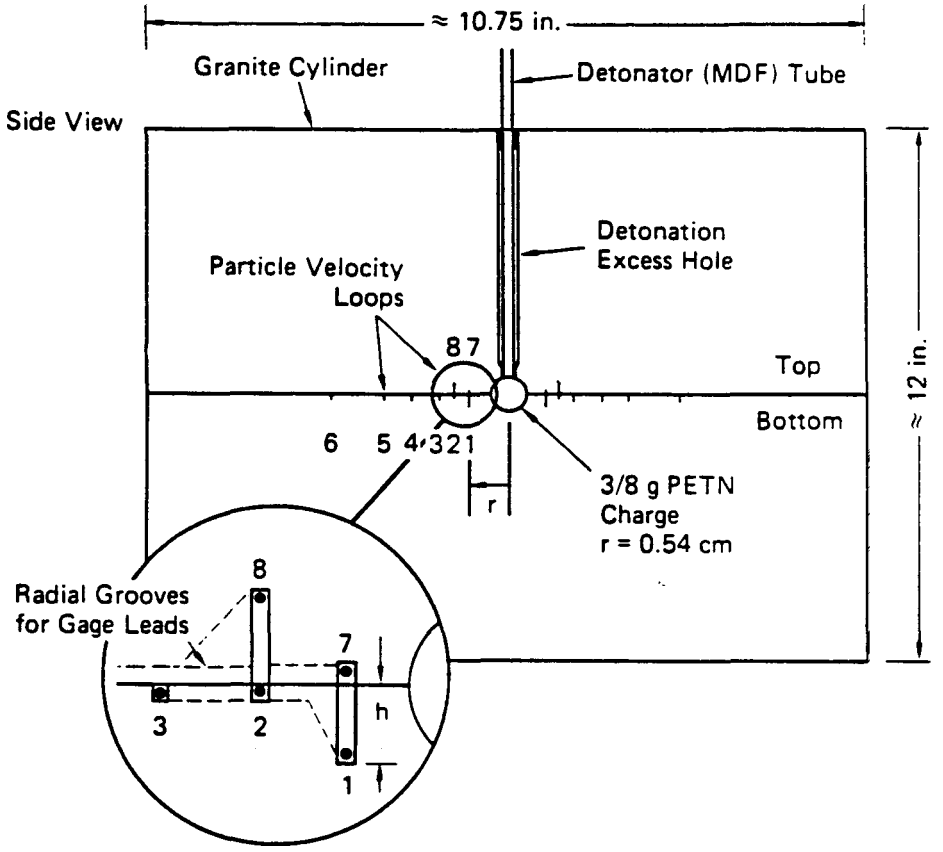

Gage No.	Sample Half	Gage Radius (cm)	Gage Depth, h (mm)
1	Bottom	1.0	1.524
2	Bottom	1.5	0.508
3	Bottom	2.0	0.508
4	Bottom	3.0	0.508
5	Bottom	4.0	0.508
6	Bottom	6.0	0.508
7	Top	1.0	0.508
8	Top	1.5	1.524

Groove width at gage location ≈ 0.3 mm (0.012 in.)
Wire diameter ≈ 0.254 mm (0.010 in.)

RA-2336-15A

FIGURE 6 GAGE ARRANGEMENT FOR PARTICLE VELOCITY EXPERIMENTS (groove detail not to scale)

Gages 7 and 8 used only for Test 485. Gage 1 was deep only for Test 485, shallow for all others.

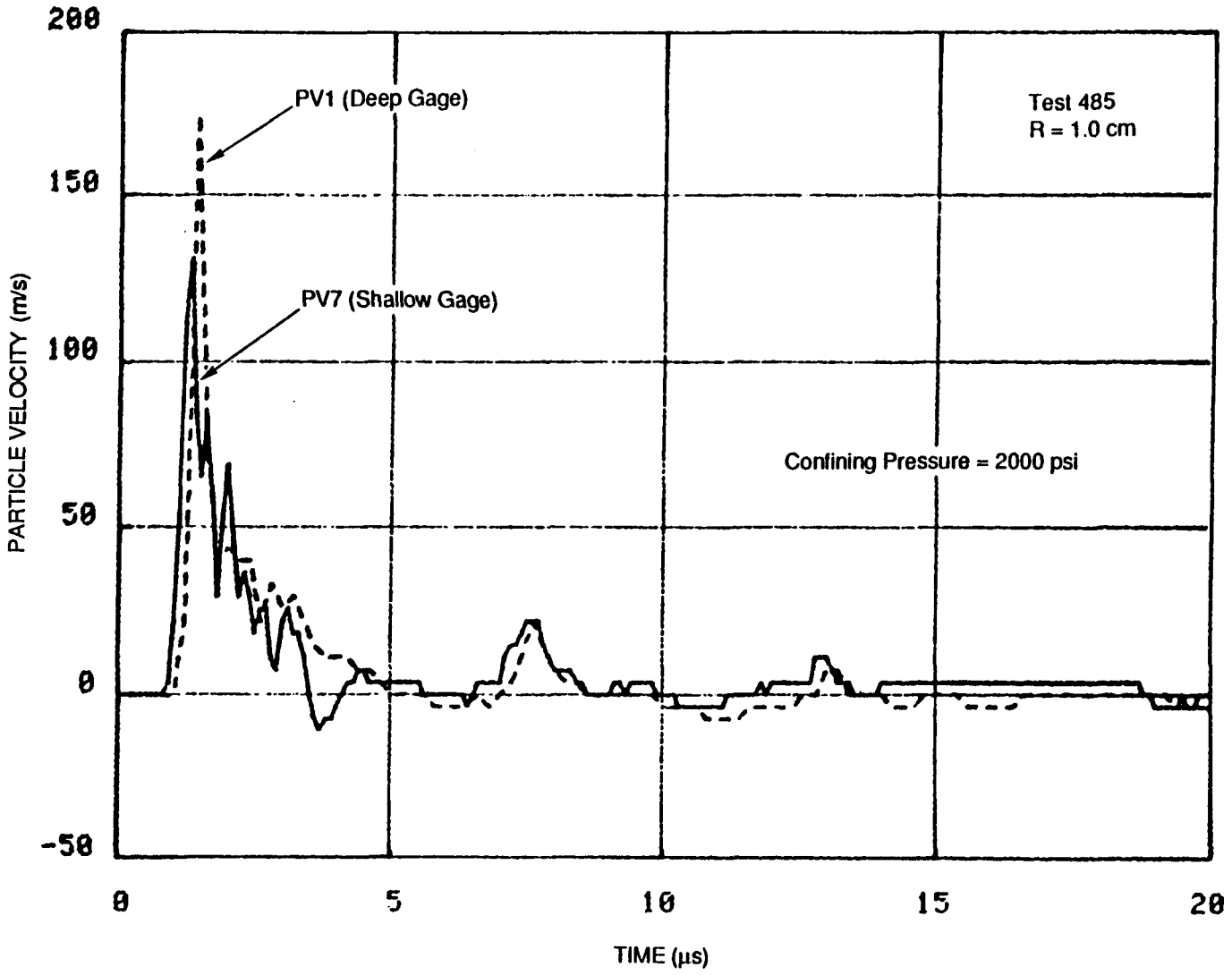

FIGURE 7 PARTICLE VELOCITIES 1.0 cm FROM CENTER OF COUPLED EXPLOSION IN FRACTURED/DRY SIERRA WHITE GRANITE, TEST 485

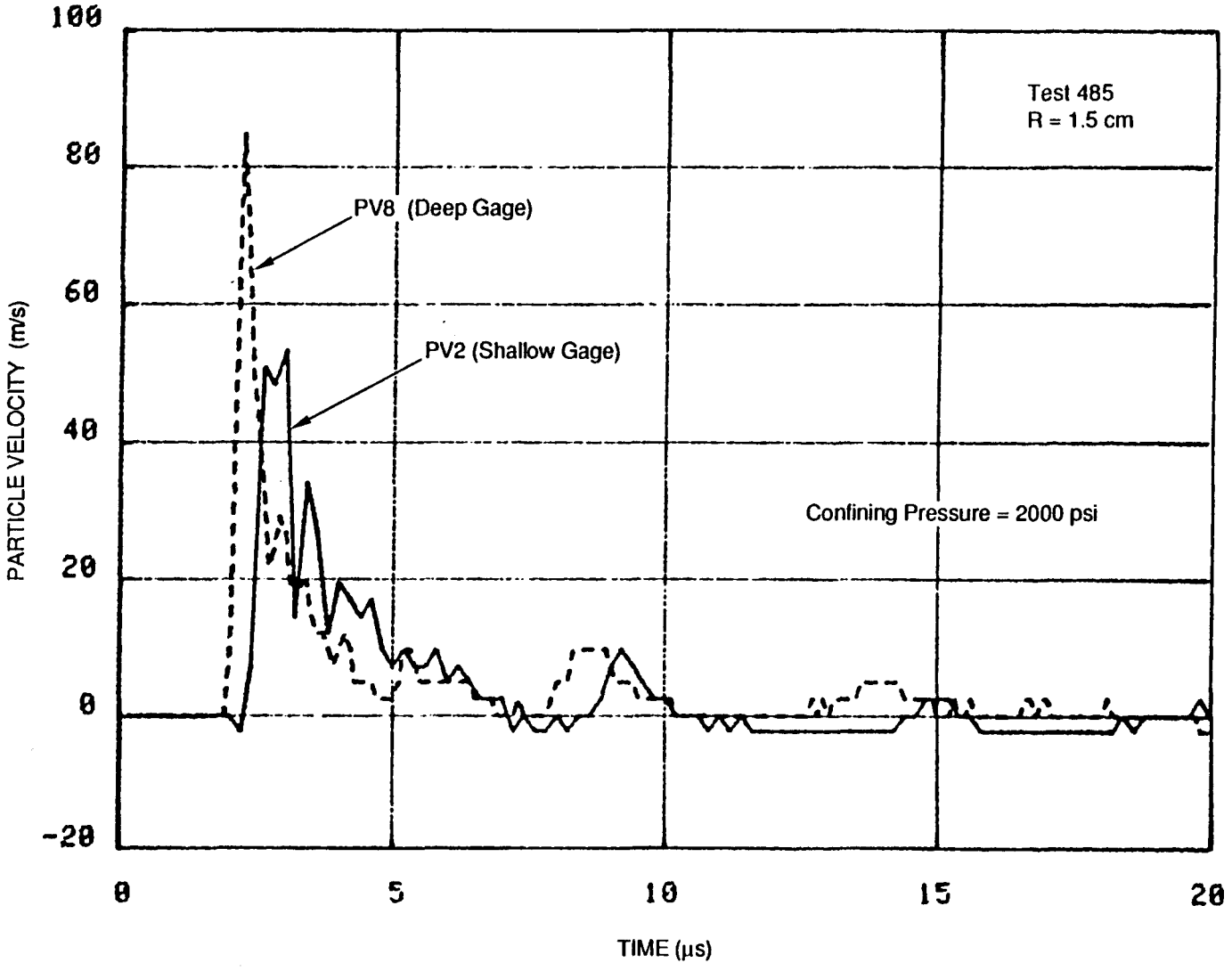

FIGURE 8 PARTICLE VELOCITIES 1.5 cm FROM CENTER OF COUPLED EXPLOSION IN FRACTURED/DRY SIERRA WHITE GRANITE, TEST 485

the 1.0-cm location the records have the same essential features of pulse width and duration, but the deep gage (PV1) has slightly higher peak and a cleaner pulse shape, indicating a possible benefit of placing the gage further from the interface at locations close to the charge. This benefit is overshadowed by the detrimental effect that the relatively compliant cylindrical annulus of the deep groove has on the response of the gage immediately behind it and possibly on the next several gages. This effect can be clearly seen in Figure 8 by comparing the response of the relatively undisturbed signal of PV8 to that of PV2, which shows a significantly lower peak, ill-defined arrival time, and irregular shape. Because of this detrimental effect of the deep grooves, all subsequent experiments had only shallow gages, as was the practice in our previous work.[1,2]

Effect of Confinement. The effect of reducing the confining pressure by a factor of two, from 2000 psi in Test 485 to 1000 psi in Test 488, is shown by the velocity records in Figures 9 through 14. Although the peak velocity at the 1.5-cm location is considerably higher for the higher confining pressure case (Test 485), no consistent conclusions can be drawn about the influence of confining pressure (at least at these magnitudes) on peak velocities. However, the comparison of the records indicates that reducing the confining pressure increases pulse widths, especially near the charge, leading to greater displacements (see Section 3.2). An exception is PV3 at the 2.0-cm location in Test 488 (Figure 11), which is inconsistent with the records at the other radii, both in peak velocity and in pulse width, except at the base giving about the expected positive pulse duration. Because the pulse duration is about right, we believe that the amplifier for this particular gage drifted to less than unity gain at the time of the test, giving the correct zero voltage at zero velocities, but smaller voltages (in absolute value) at all nonzero velocities. The reduced confinement also increases the rise-time slightly, especially at the farthest location (Figure 14).

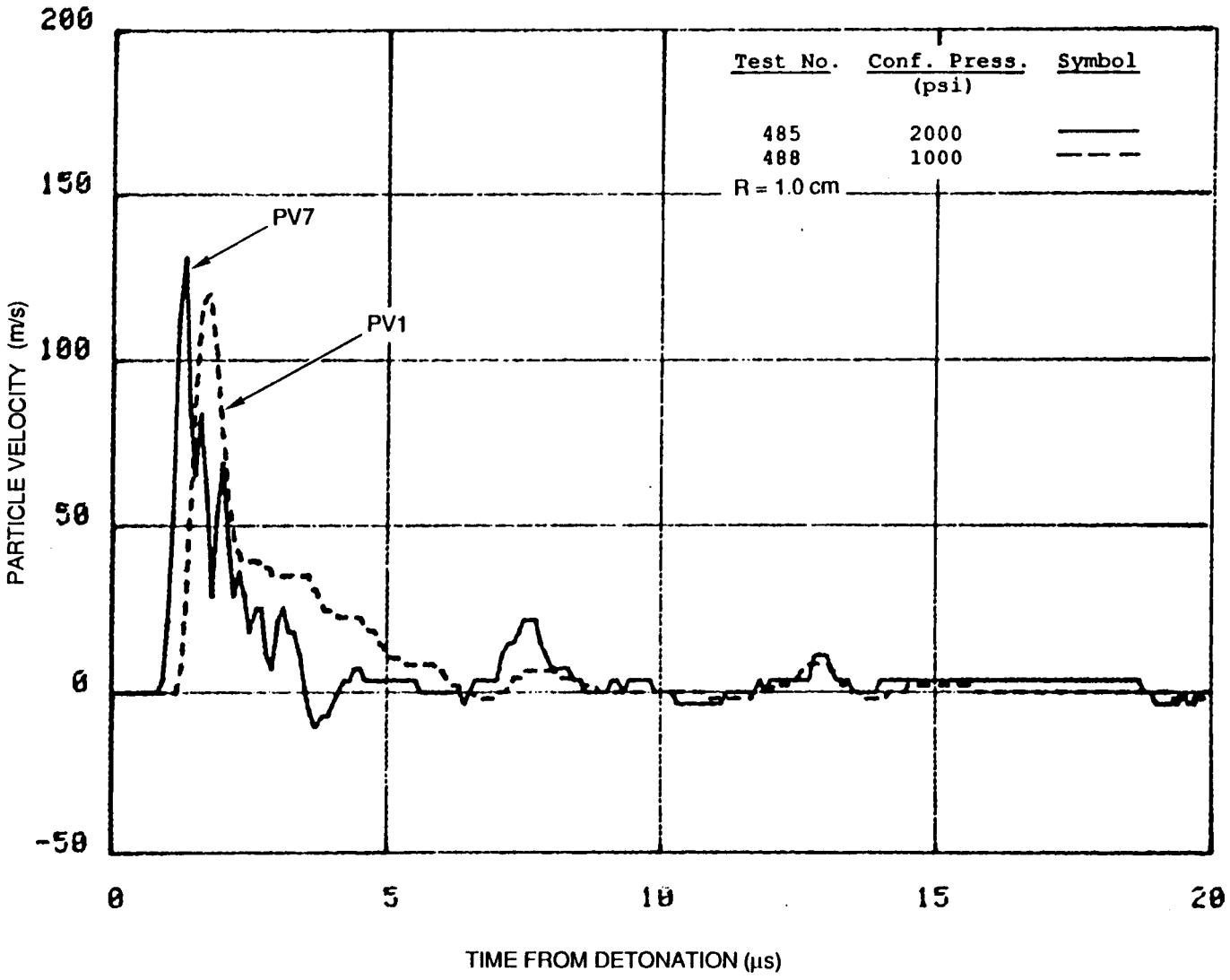

RA-m-2336-36

FIGURE 9 PARTICLE VELOCITIES 1.0 cm FROM CENTER OR COUPLED EXPLOSION IN FRACTUTED/DRY SIERRA WHITE GRANITE, TESTS 485 AND 488

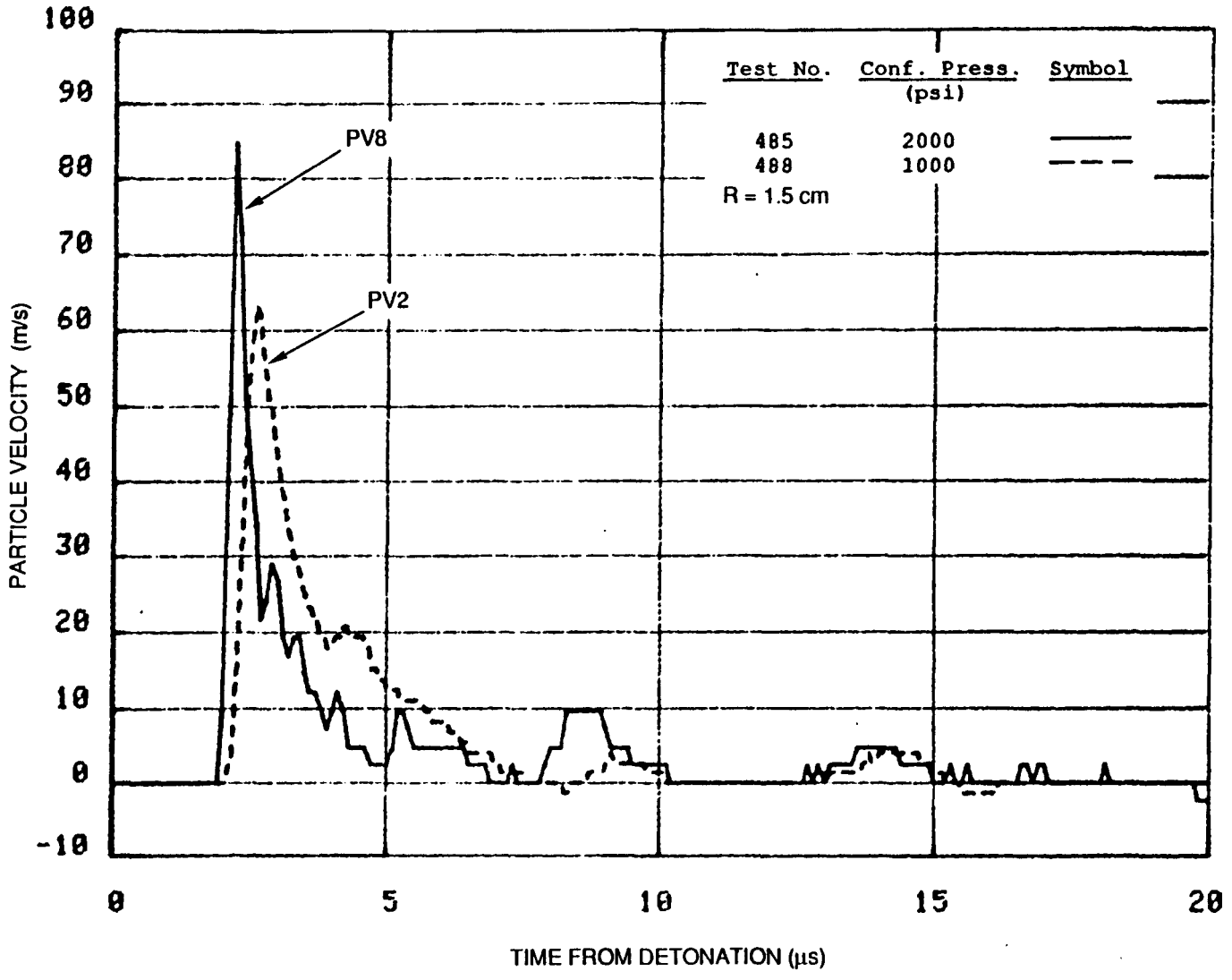

FIGURE 10 PARTICLE VELOCITIES 1.5 cm FROM CENTER OF COUPLED EXPLOSION IN FRACTURED/DRY SIERRA WHITE GRANITE, TESTS 485 AND 488

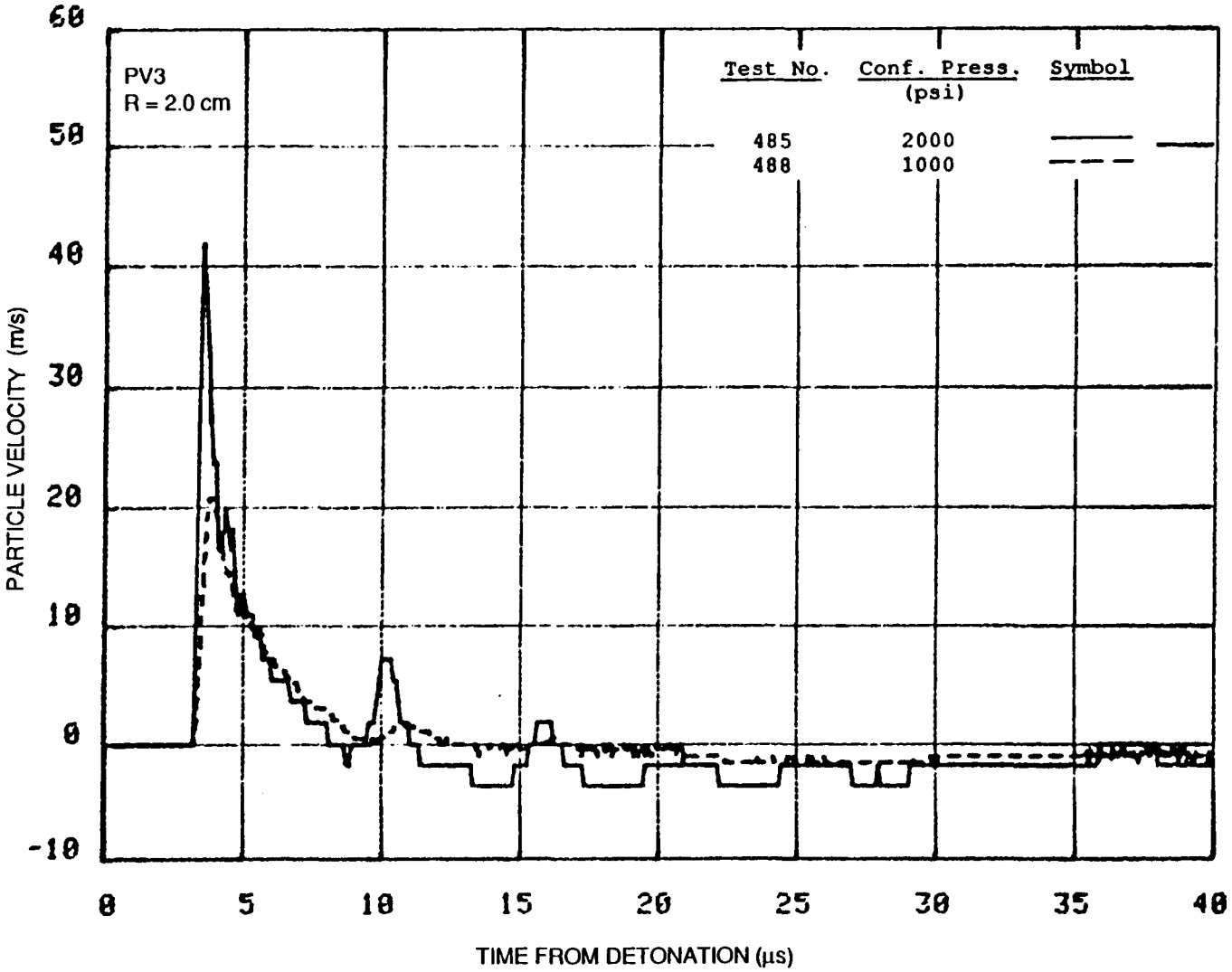

FIGURE 11 PARTICLE VELOCITIES 2.0 cm FROM CENTER OF COUPLED EXPLOSION IN FRACTURED/DRY SIERRA WHITE GRANITE, TESTS 485 AND 488

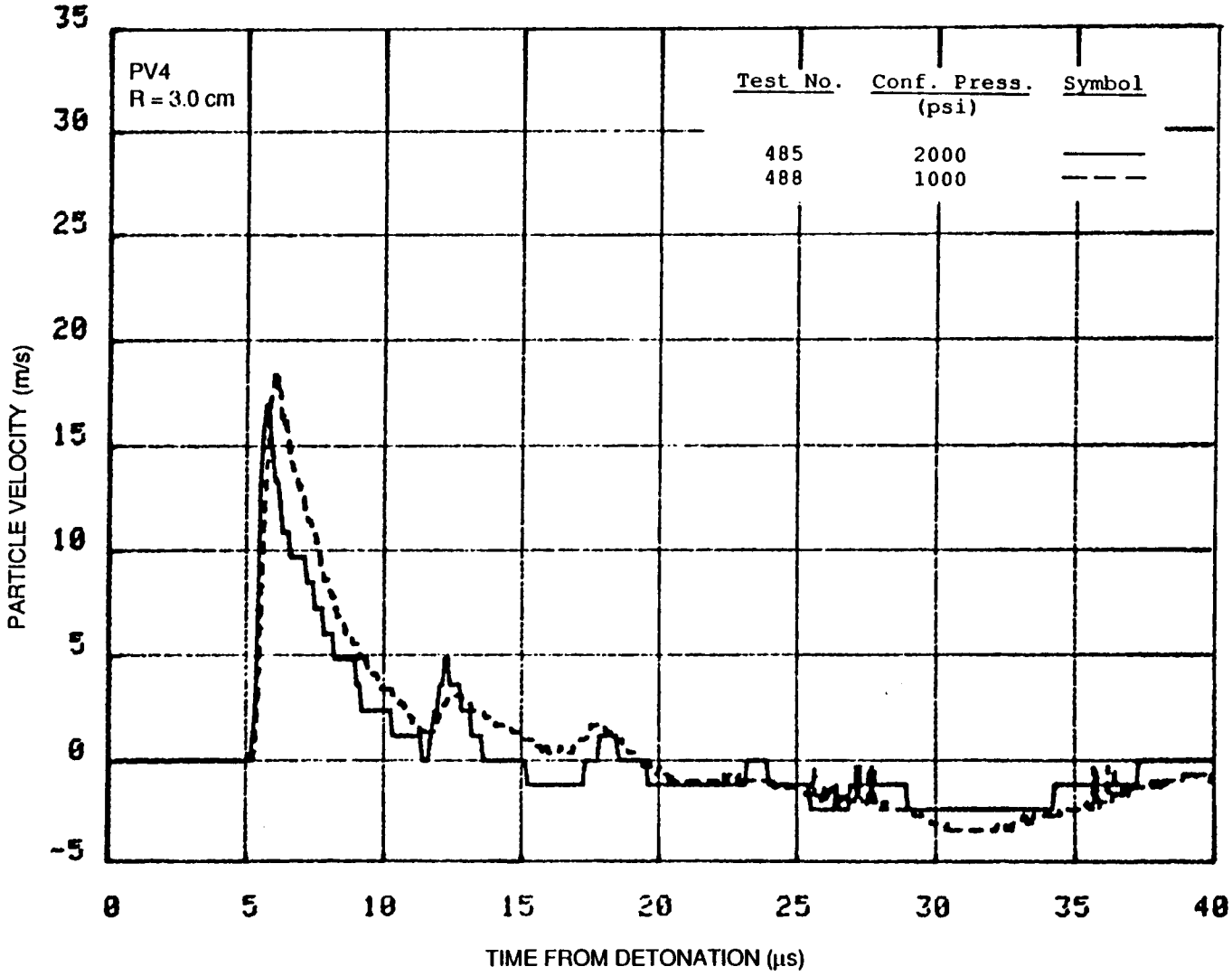

RA-m-2336-67

FIGURE 12 PARTICLE VELOCITIES 3.0 cm FROM CENTER OF COUPLED EXPLOSION IN FRACTURED/DRY SIERRA WHITE GRANITE, TESTS 485 AND 488

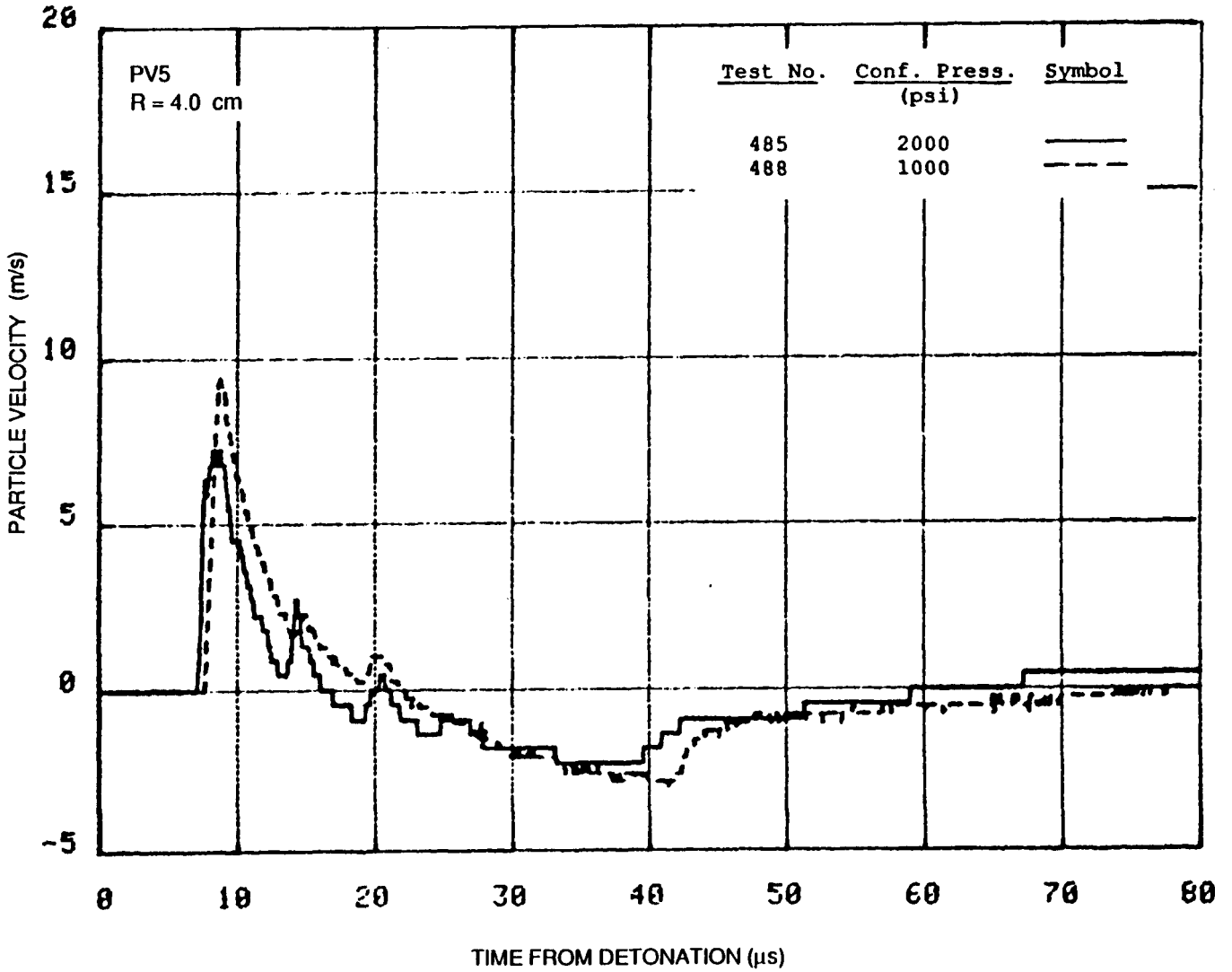

FIGURE 13 PARTICLE VELOCITIES 4.0 cm FROM CENTER OF COUPLED EXPLOSION IN FRACTURED/DRY SIERRA WHITE GRANITE, TESTS 485 AND 488

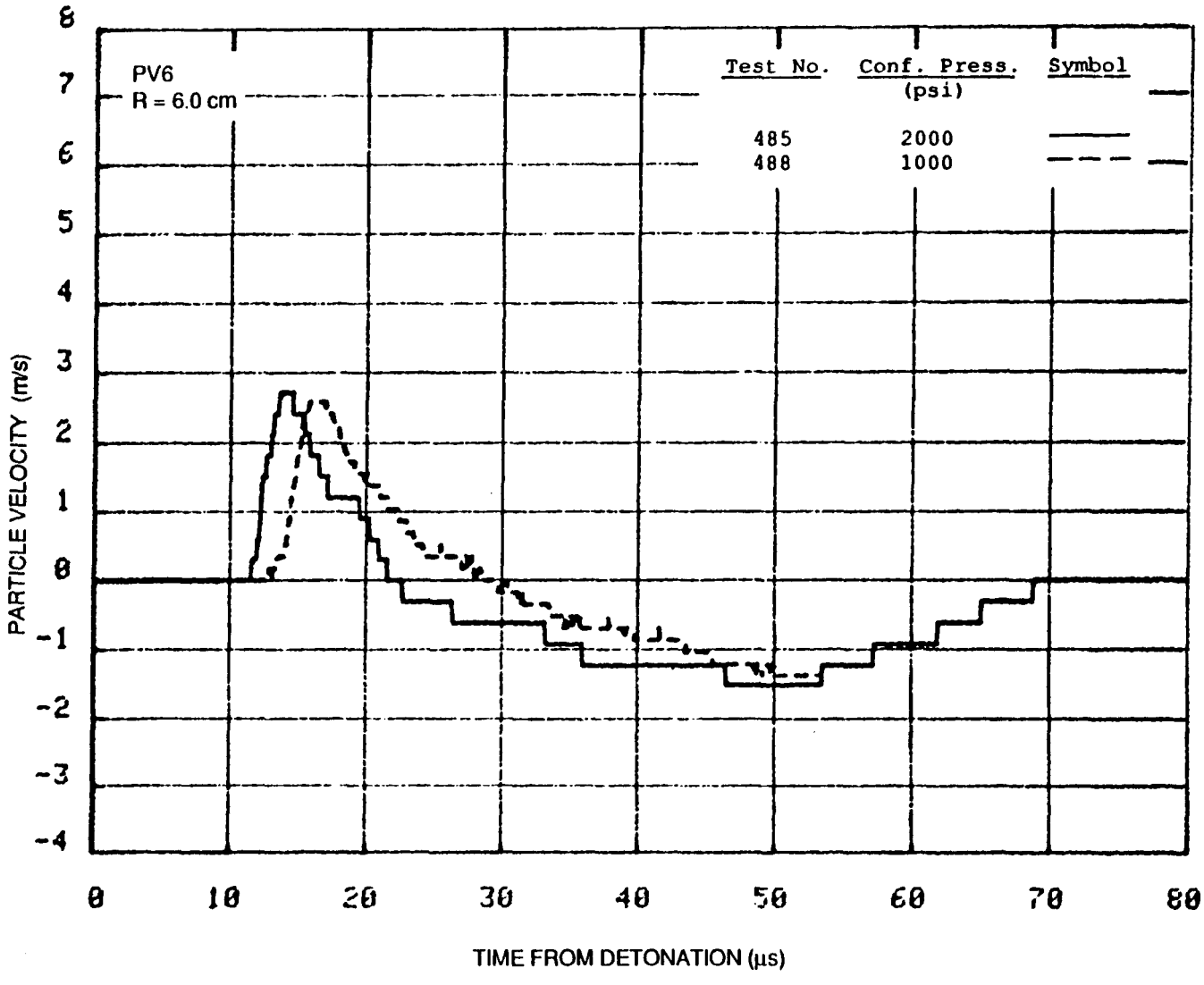

FIGURE 14 PARTICLE VELOCITIES 6.0 cm FROM CENTER OF COUPLED EXPLOSION IN FRACTURED/DRY SIERRA WHITE GRANITE, TESTS 485 AND 488.

Other features of the signals, particularly the lack of rebound near the charge (at the 1.0 and 1.5 cm radii) and a long-duration rebound farther out, were not affected qualitatively by the confining pressure. The exploded cavity diameters, including those of earlier experiments, are shown in Table 3 and indicate very small cavity expansion. The exploded cavity wall and a narrow region near the cavity was highly porous and appeared dilated.

3.1.2 Saturated Experiments

Two of the three saturated experiments, Tests 491 and 492, were performed to investigate the effect of pore water at the confining stress levels of 2000 and 1000 psi, respectively, with near zero pore pressure. These confining pressure levels were the same as those used for the dry experiments, Tests 485 and 488. The effective stress in these two experiments was thus nearly equal to the confining pressure. The third saturated experiment, Test 494, had a pore pressure of 1000 psi and a confining pressure of 2000 psi, giving it the same 1000-psi effective stress as Test 492 but twice the confining pressure, thus testing the effect of confining stress alone at a given effective stress. The particle velocity histories obtained in these three experiments are shown in Figures 15 through 20, and the attenuation of peak velocities with range, including all dry or saturated high-porosity (gas-fractured) experiments, is shown in Figure 21. The results indicate the following:

- Except for the 1.0-cm radius (Figures 15 and 21), the records are similar in both pulse amplitude and pulse shape, indicating only a small effect of either confining pressure or the effective stress. At the 1.0-cm location Test 491, having the highest effective stress, shows about twice the peak amplitude and about half the pulse width as the other cases, indicative of enhanced coupling. This difference does not exist farther from the source, which, in the absence of repeat experiments, indicates that this possibly strong effect of high effective stress near the source decays very rapidly with distance.

Table 3

EXPLODED CAVITY DIAMETERS

Test No.	Porosity (%)	Pore Condition	Confining Pressure (psi)	Pore Pressure (psi)	Cavity Diameter (mm)
361[a]	0.8-1.0	Dry	2000	-	11.7
308	1.2	Dry	2000	-	12.9
309	0.8-1.0	Saturated	2000	2000	13.0
310	1.2	Saturated	2000	2000	12.8
473	2.5	Saturated	1800	1800	11.3
474	2.4	Saturated	1600	1600	11.1
476	2.4	Dry	2000	-	11.0
485	2.8	Dry	2000	-	11.1
488	2.7	Dry	1000	-	11.0
491	2.9	Saturated	2000	50	11.5
492	2.6	Saturated	1000	50	11.5
494	2.9	Saturated	2000	1000	11.3

[a]Test 361 is from Reference 3.

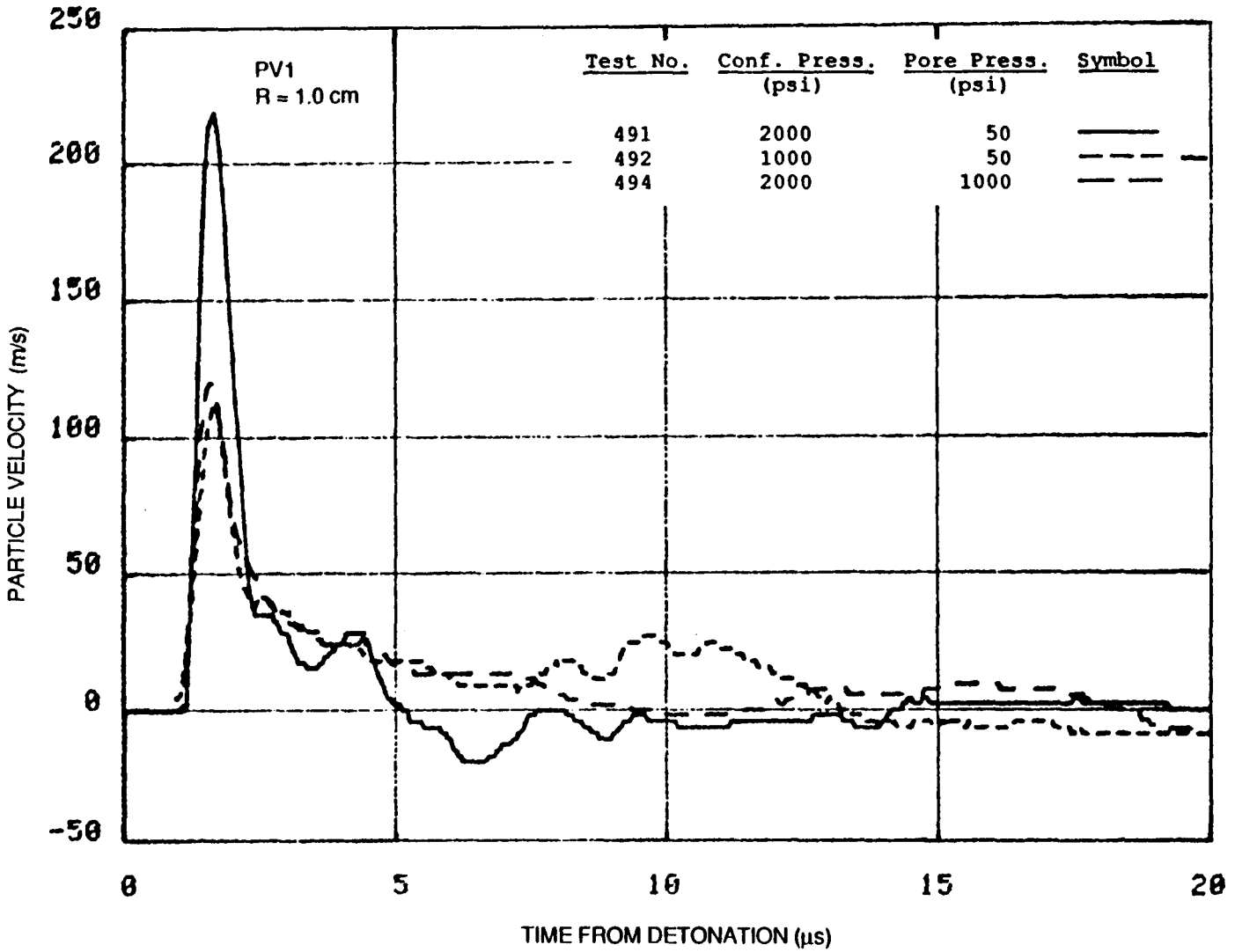

FIGURE 15 PARTICLE VELOCITIES 1.0 cm FROM CENTER OF COUPLED EXPLOSION IN FRACTURED/SATURATED SIERRA WHITE GRANITE, TESTS 491, 492, AND 494

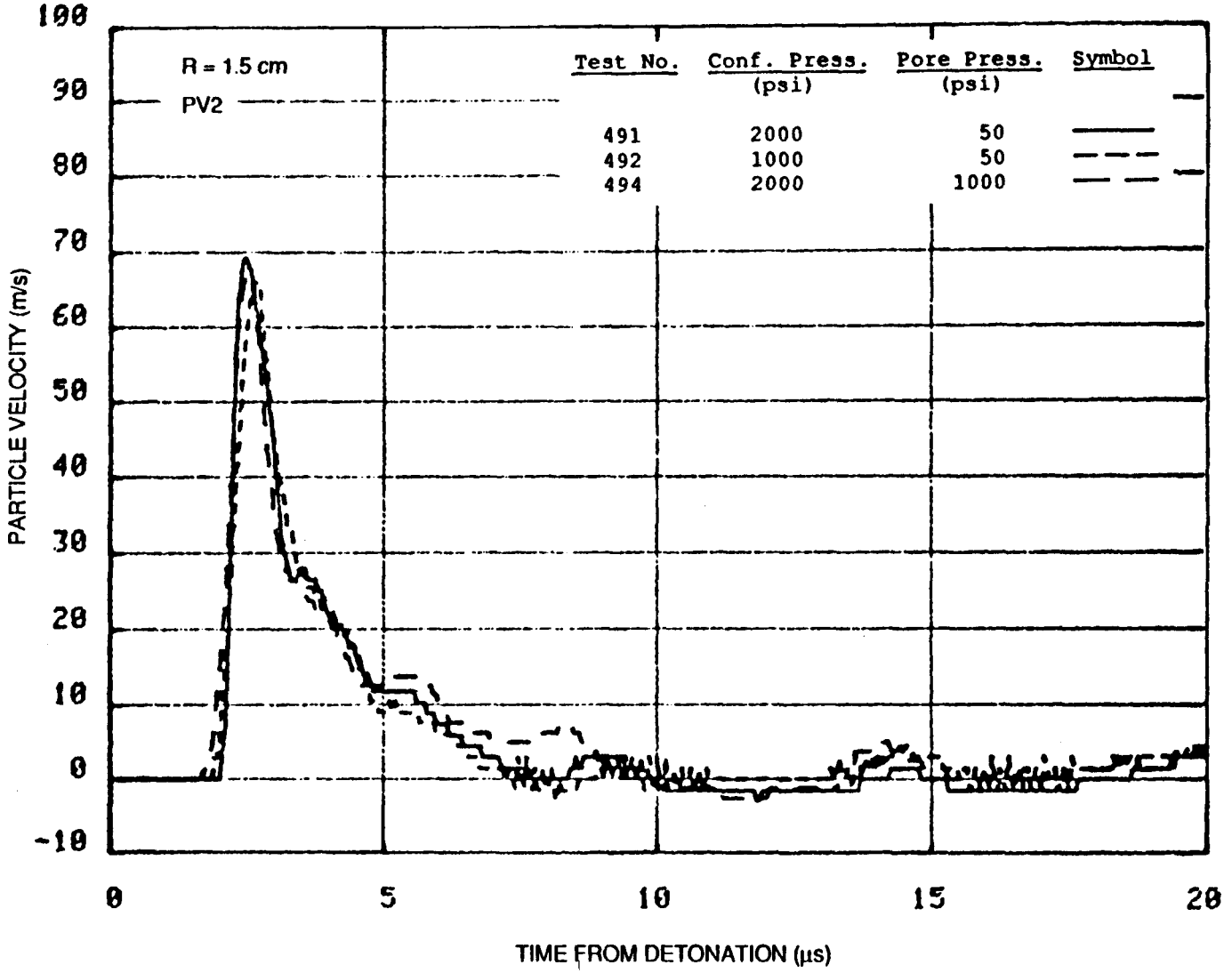

FIGURE 16 PARTICLE VELOCITIES 1.5 cm FROM CENTER OF COUPLED EXPLOSION IN FRACTURED/SATURATED SIERRA WHITE GRANITE, TESTS 491, 492, AND 494

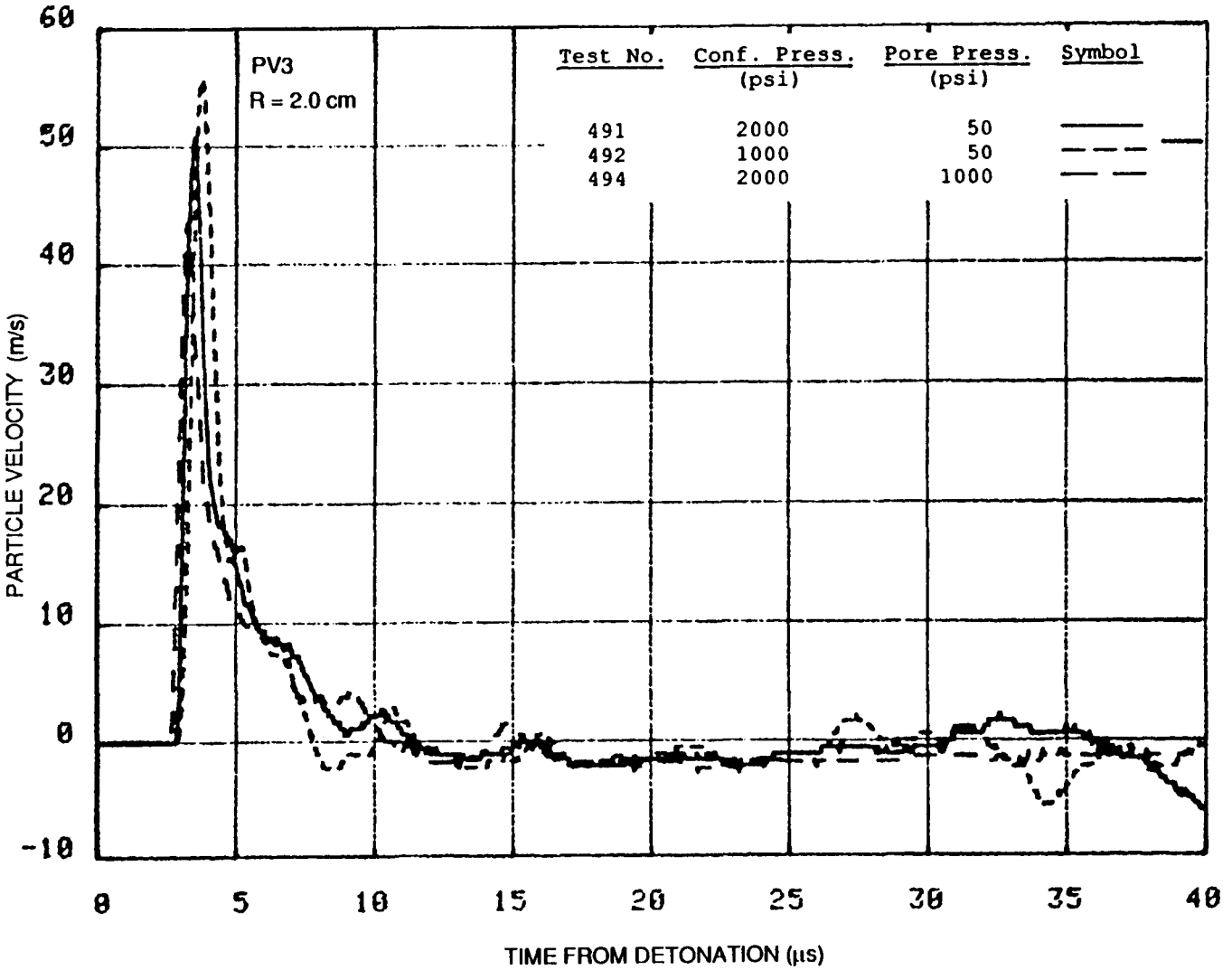

FIGURE 17 PARTICLE VELOCITIES 2.0 cm FROM CENTER OF COUPLED EXPLOSION IN FRACTURED/SATURATED SIERRA WHITE GRANITE, TESTS 491, 492, AND 494

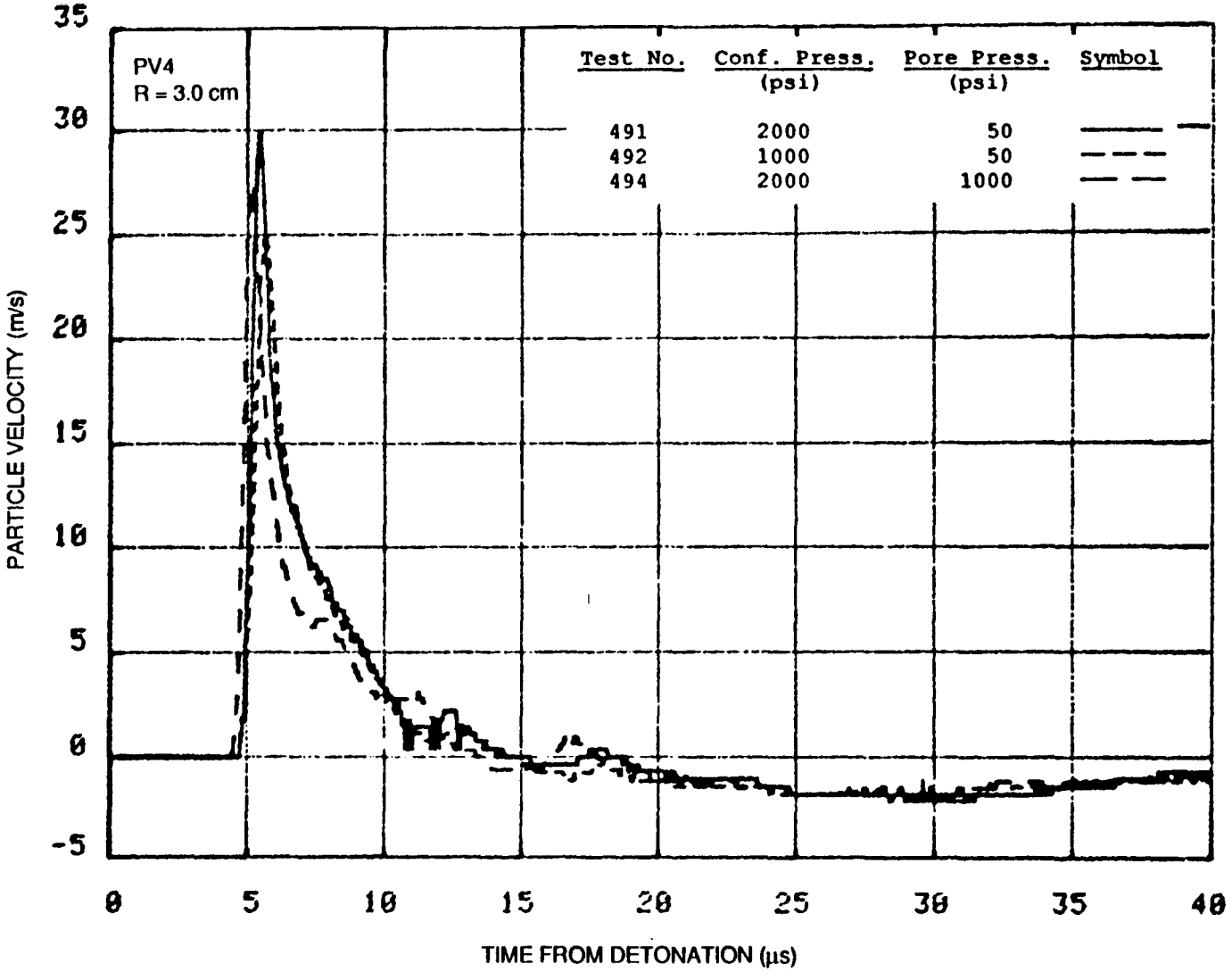

FIGURE 18 PARTICLE VELOCITIES 3.0 cm FROM CENTER OF COUPLED EXPLOSION IN FRACTURED/SATURATED SIERRA WHITE GRANITE, TESTS 491, 492, AND 494

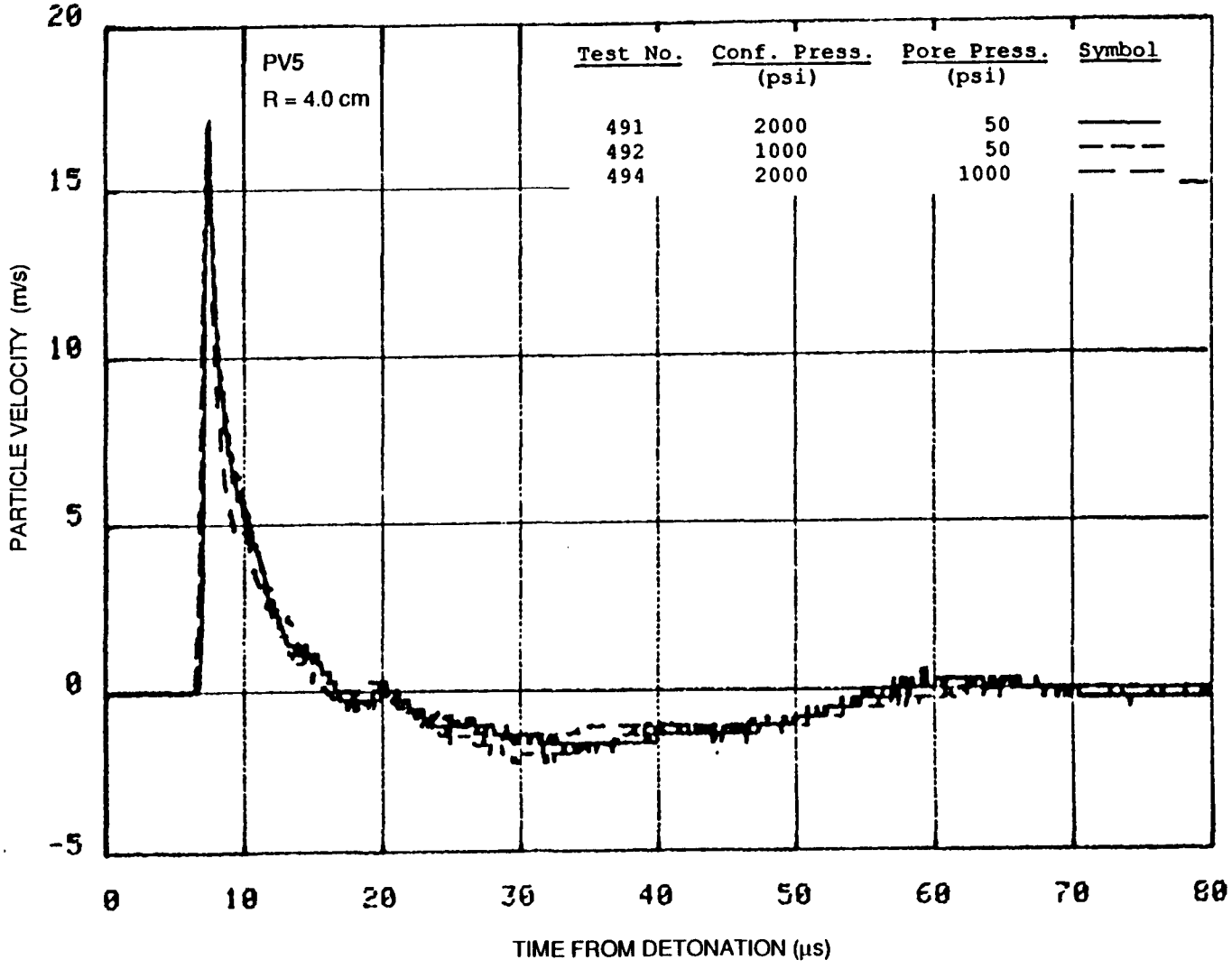

FIGURE 19 PARTICLE VELOCITIES 4.0 cm FROM CENTER OF COUPLED EXPLOSION IN FRACTURE/SATURATED SIERRA WHITE GRANITE, TESTS 491, 492, AND 494

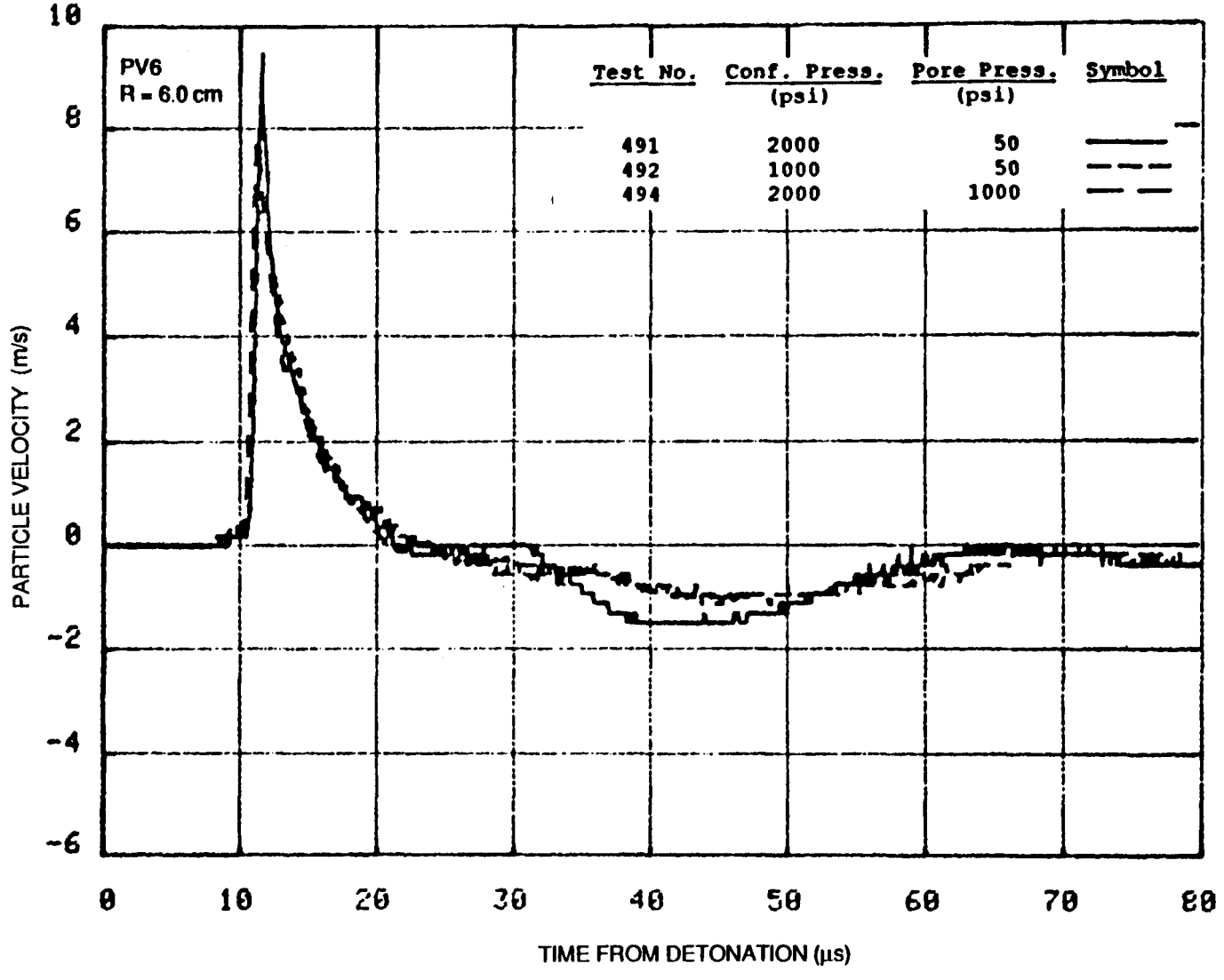

FIGURE 20 PARTICLE VELOCITIES 6.0 cm FROM CENTER OF COUPLED EXPLOSION IN FRACTURED/SATURATED SIERRA WHITE GRANITE, TESTS 491, 492, AND 494

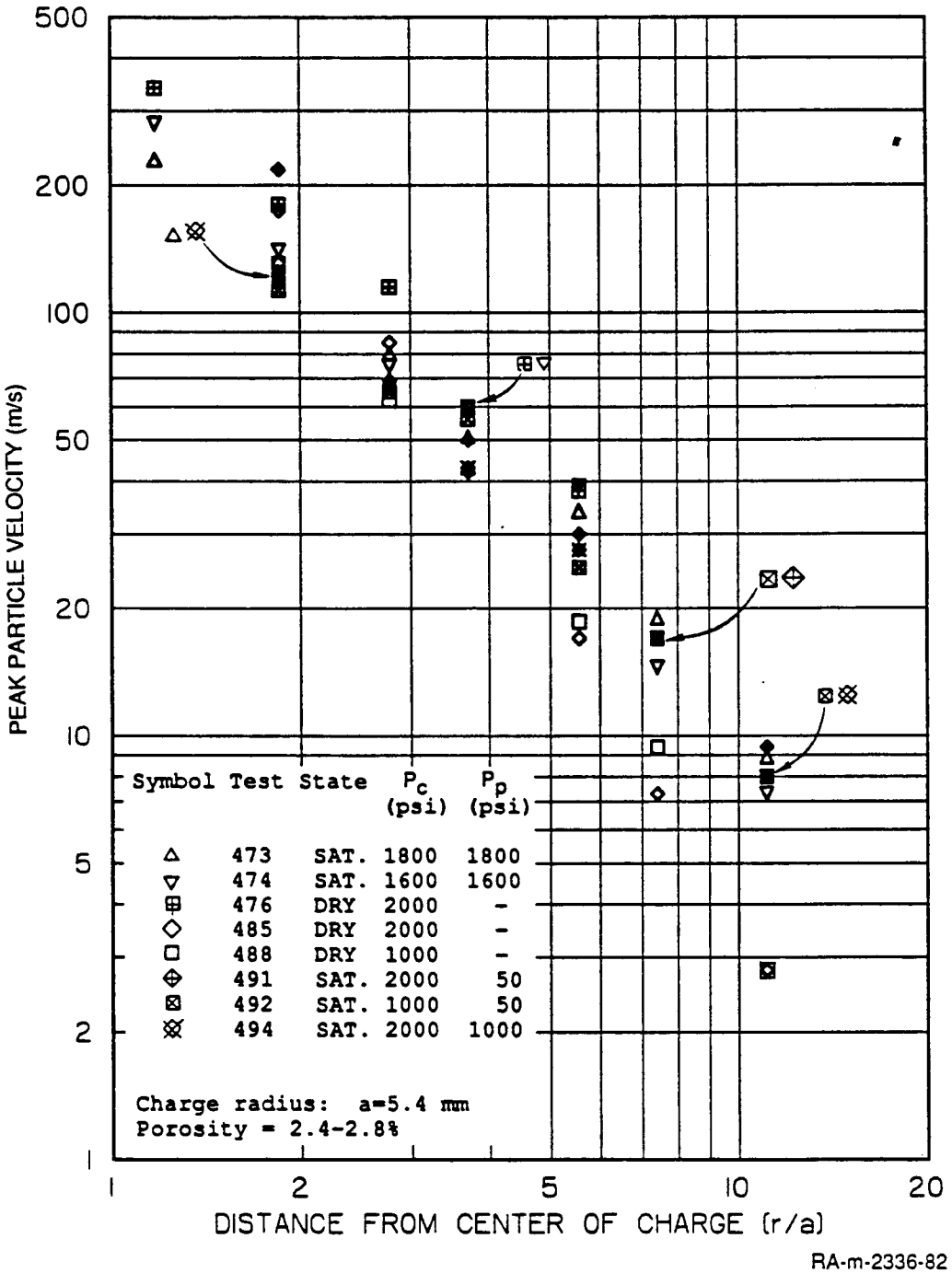

FIGURE 21 ATTENUATION OF MAXIMUM PARTICLE VELOCITY IN GAS-FRACTURED SIERRA WHITE GRANITE WITH POROSITY OF 2.4-2.8%

- Near the source the peak velocities are close to those in the dry material (Figures 9, 10, 15, 16, and 21), but become much higher with increasing range (Figures 14, 20, and 21).
- Beyond 1.0 cm, the pulse durations for all three saturated tests gradually widen with range from 5 μs near the source to about 10 μs at the greatest range (Figures 15 through 20), and they are not much different from those in the corresponding dry experiments (Tests 485 and 488, Figures 10 through 14). The rebound is negligible at the first two locations, as in the dry experiments, with the exception of the 2000-psi effective stress case (Test 491), which shows a small rebound at the 1.0-cm location (Figure 15).

A more detailed discussion of what the velocity pulses indicate about the effects of these parameters is given in Section 3.4.

3.2 PARTICLE DISPLACEMENTS

The particle displacements obtained by integrating the particle velocity records are shown in Figures 22 through 25, the attenuation of peak displacements with range including all dry or saturated high-porosity (gas-fractured) experiments, is shown in Figure 26. In Figures 22 and 24 dotted lines are used as estimates of displacements in the regions where noise in the particle velocity records lead to unreasonable displacements.

For the dry experiments at 2000 psi confining pressure, reasonable agreement is shown in Figures 22 and 23 for peak displacements between the repeat experiments, Tests 476 and 485. The agreement in the shapes is not as good becase of the generally higher peak velocities in Test 476. The effect of confining pressure on the dry material is judged primarily by a comparison of Tests 485 and 488 in Figures 22 and 23. The peak displacements for Test 488 with reduced confinement are consistently higher than those of 485 or 476 by virtue of wider pulses.

The particle displacements for the saturated tests, shown in Figures 24 and 25, are similar. Note the following observations:

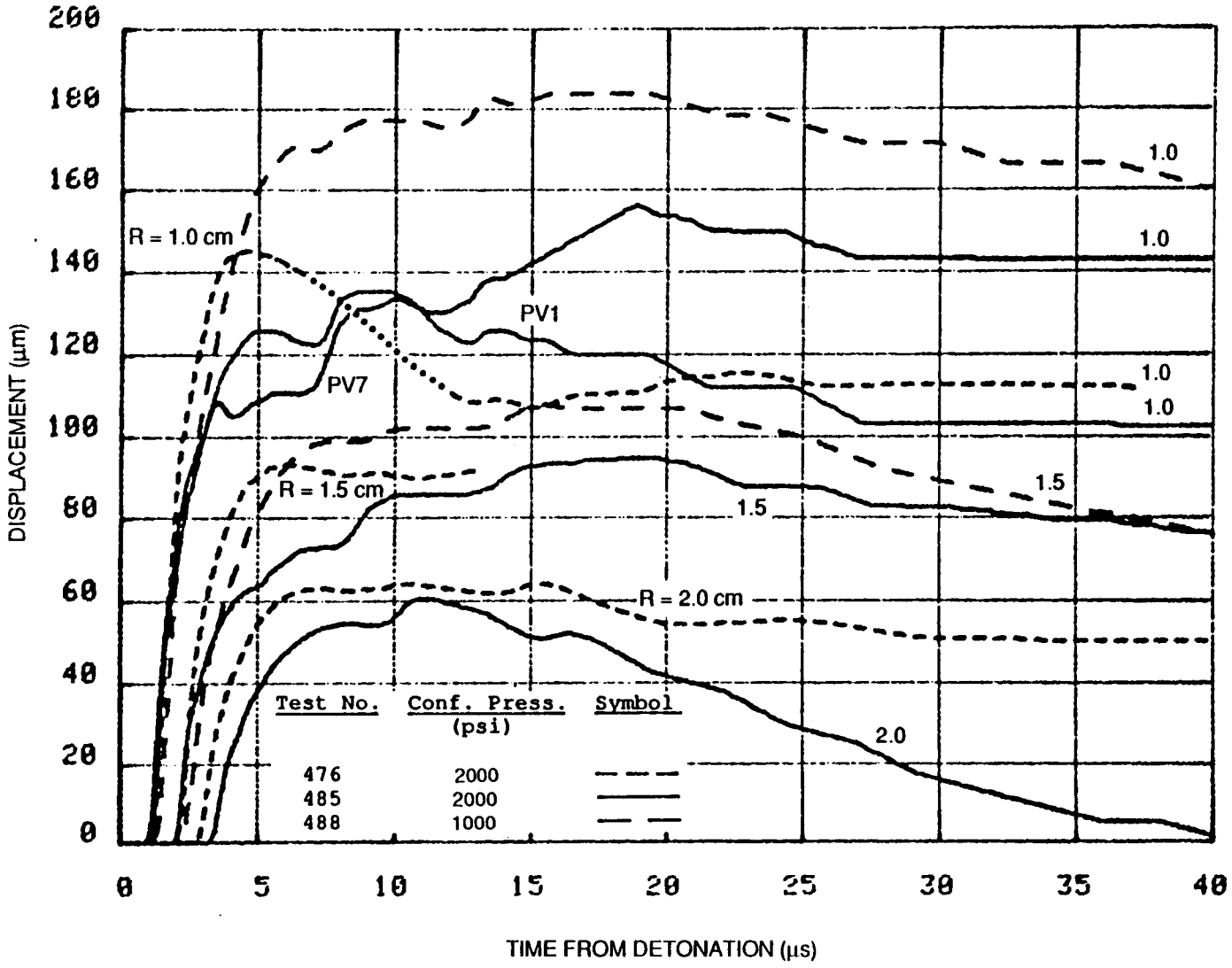

FIGURE 22 PARTICLE DISPLACEMENTS AT 1.0, 1.5, AND 2.0 cm FROM CENTER OF COUPLED EXPLOSION IN FRACTURED/DRY SIERRA WHITE GRANITE, TESTS 476, 485, AND 488

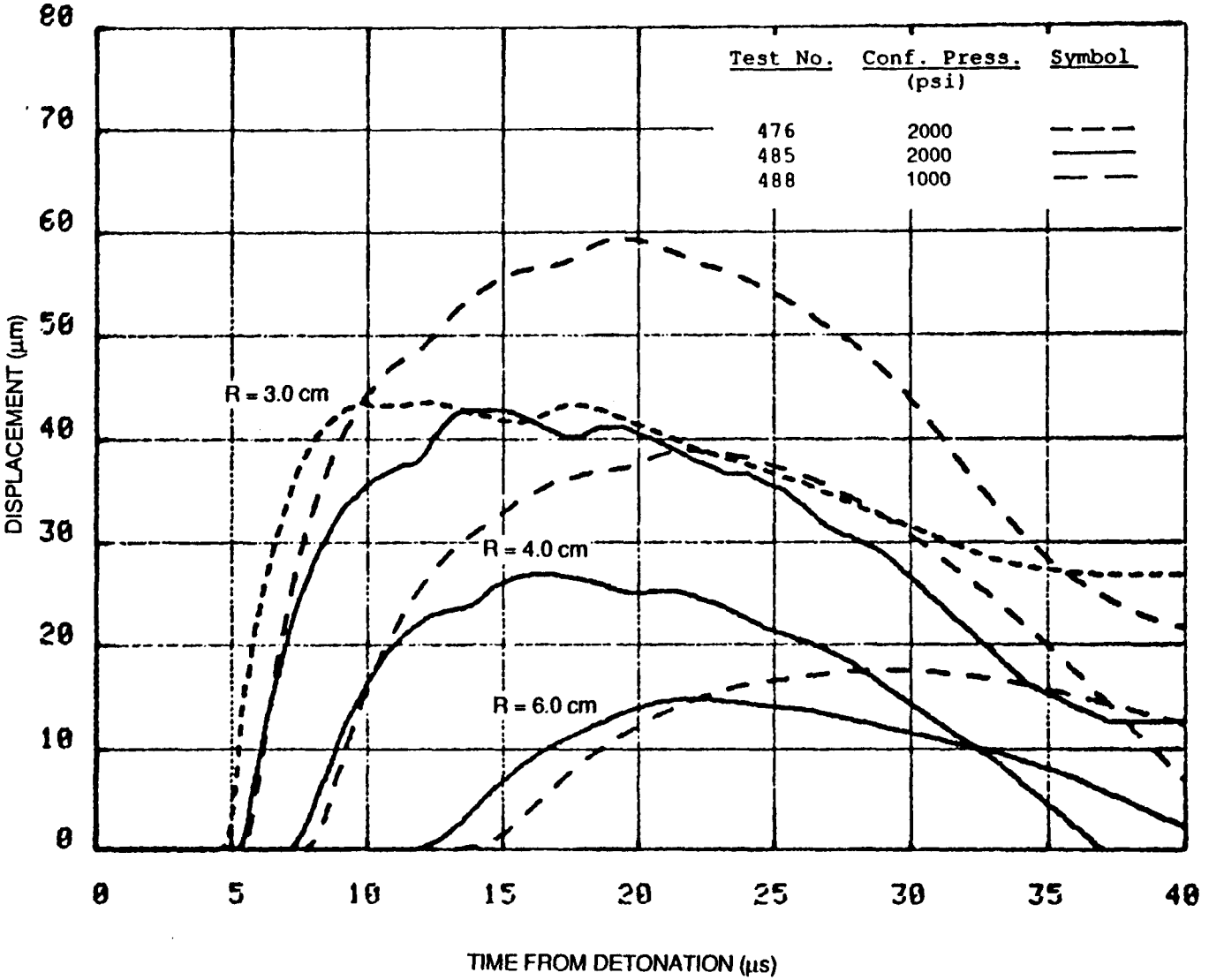

RA-m-2336-45

FIGURE 23 PARTICLE DISPLACEMENTS AT 3.0, 4.0, AND 6.0 cm FROM CENTER OF COUPLED EXPLOSION IN FRACTURED/DRY SIERRA WHITE GRANITE, TESTS 476, 485, AND 488

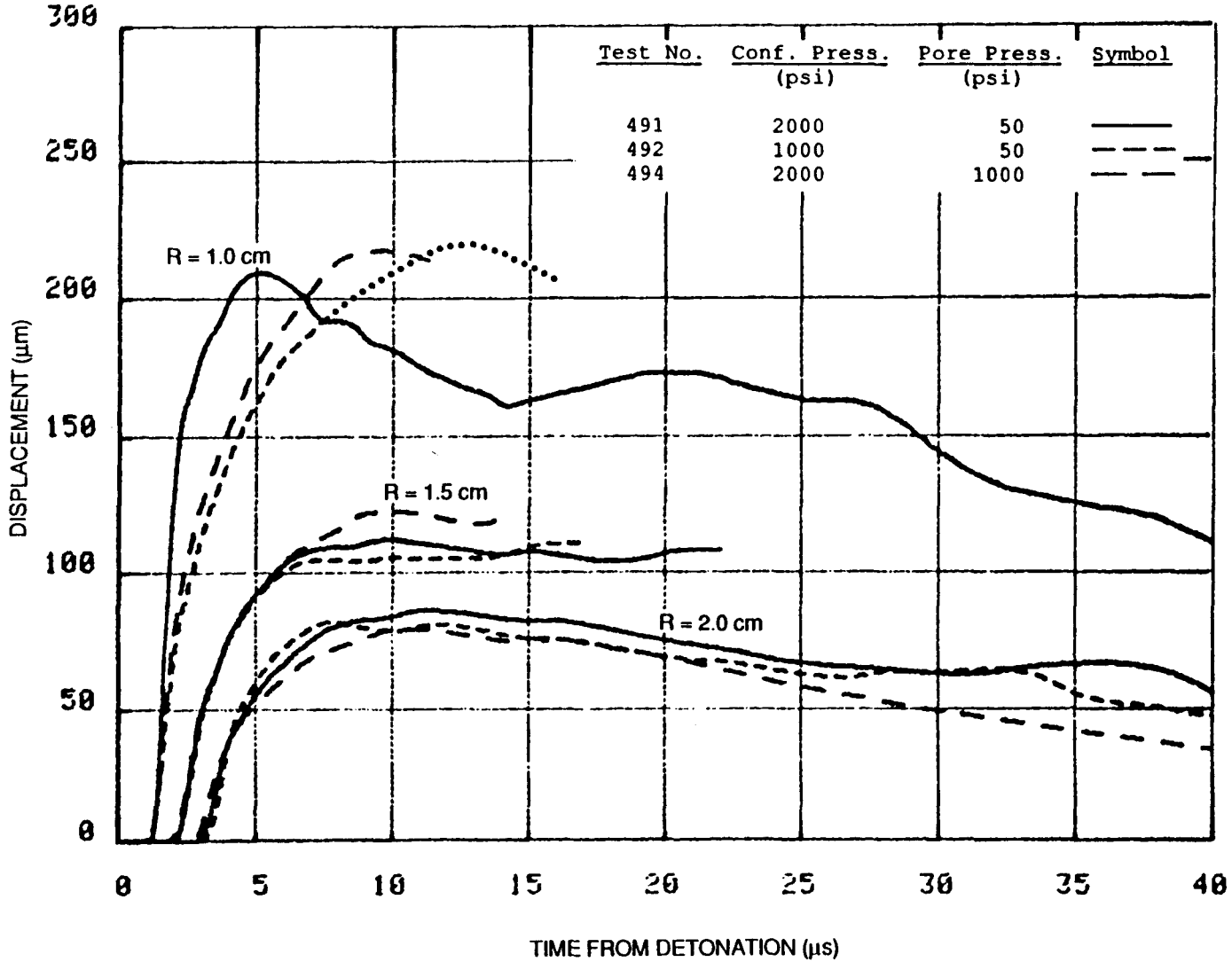

FIGURE 24 PARTICLE DISPLACEMENTS AT 1.0, 1.5, AND 2.0 cm FROM CENTER OF COUPLED EXPLOSION IN FRACTURED/SATURATED SIERRA WHITE GRANITE, TESTS 491, 492, AND 494

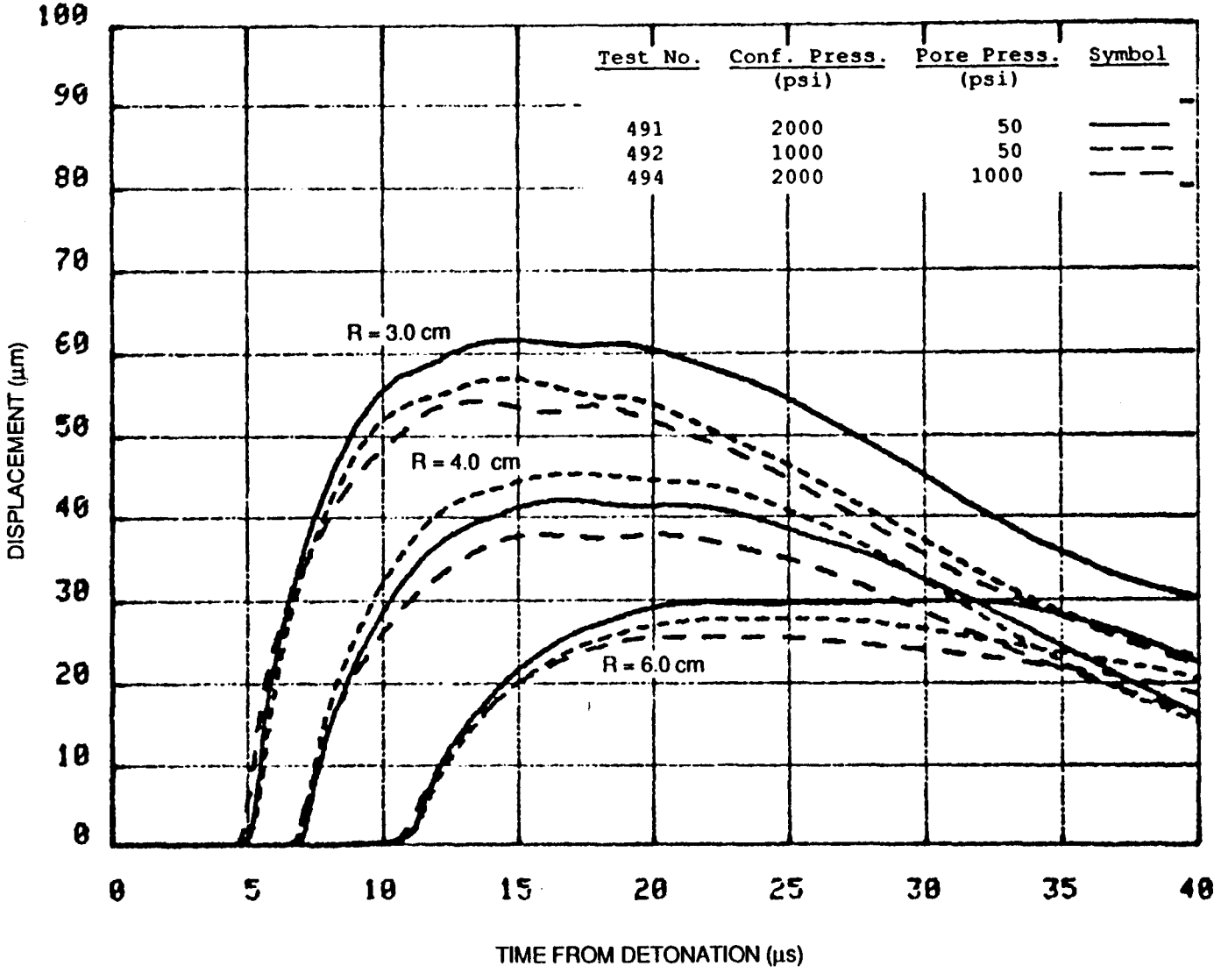

RA-m-2336-47

FIGURE 25 PARTICLE DISPLACEMENTS AT 3.0, 4.0, AND 6.0 cm FROM CENTER OF COUPLED EXPLOSION IN FRACTURED/SATURATED SIERRA WHITE GRANITE, TESTS 491, 492, AND 494

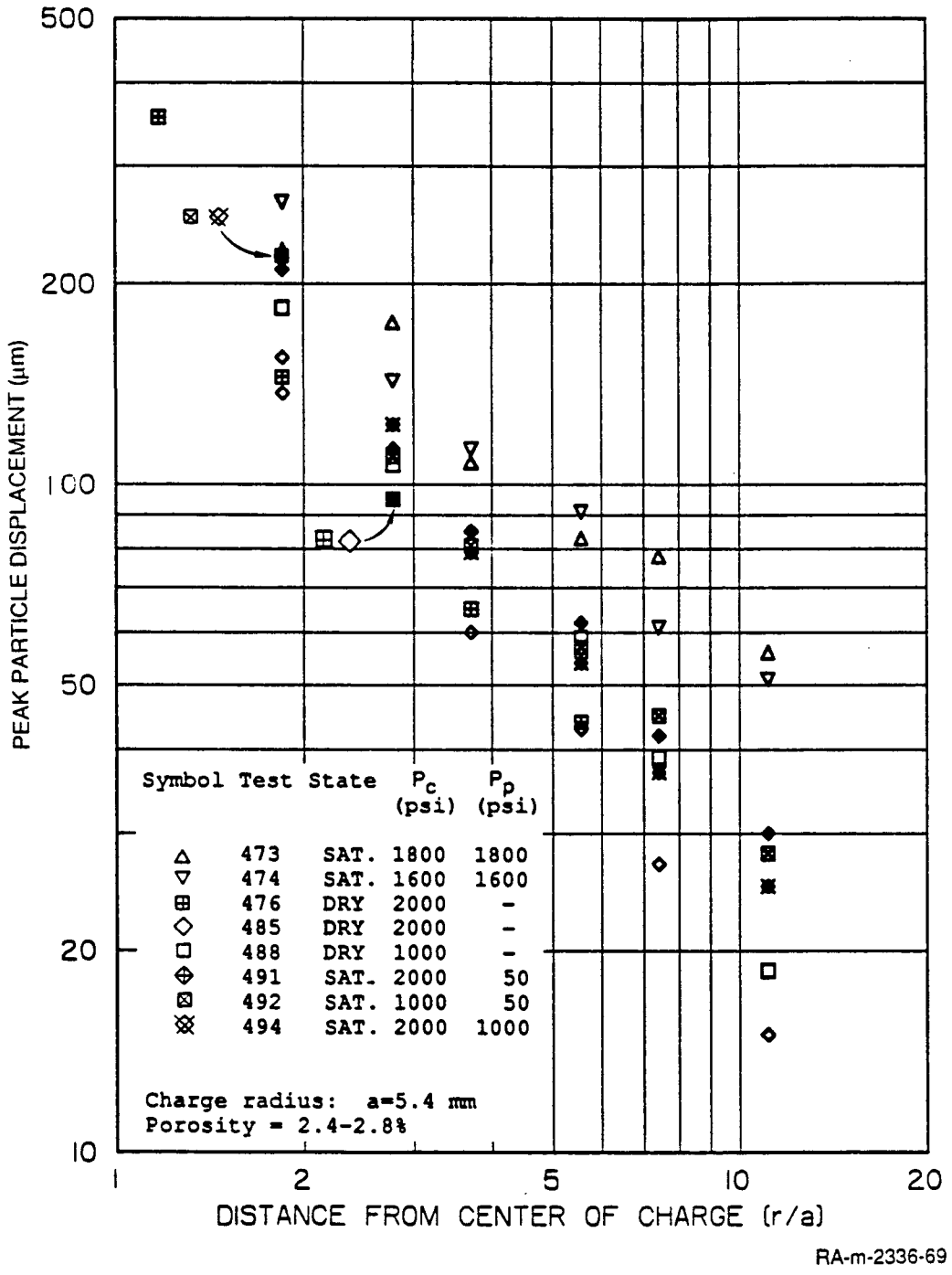

FIGURE 26 ATTENUATION OF MAXIMUM PARTICLE DISPLACEMENT IN GAS-FRACTURED SIERRA WHITE GRANITE WITH POROSITY OF 2.4-2.8%

- Test 494 (with 2000 psi confining pressure and 1000 psi pore pressure) has consistently lower peak displacements than the other tests beyond a radius of 2.0 cm, indicating a possible correlation with increasing confinement for a constant, nonzero effective stress (Figure 25).
- The peak displacements in water-saturated rock are consistently higher than in dry rock at the high confining pressure, but only higher far from the source at the lower confining pressure (Figure 26).

Further discussion of the displacements along with those of the earlier experiments is given in Section 3.4.

Figures 27 and 28 present the wave arrival time versus range for all gas-fractured dry and gas-fractured saturated experiments. Figure 27 shows that reduced confinement reduces wave speed in dry rock beyond a radius of 3.0 cm, whereas Figure 28 indicates no strong influence of the experimental parameters on wave speed in saturated rock.

3.3 VOLUMETRIC STRAINS

Plots of the volumetric strain histories calculated from the displacements for regions between the gage locations for Tests 485 through 494 are shown in Appendix A. The volume strain plots indicate initial compression followed by dilatation of similar magnitude for regions near the cavity. For the region between the first two gage locations (1.0 to 1.5 cm), the initial compressive volumetric strain is about 1% for both the dry and saturated material. An exception is the saturated experiment, Test 491, with high confining pressure (2000 psi) and near zero pore pressure, which shows an initial compressive volumetric strain of nearly 2% near the source.

3.4 DISCUSSION OF EXPERIMENTAL RESULTS

In this section, we summarize the observations on the effects of porosity, pore water, pore pressure, and confining pressure on the response of dry and saturated Sierra White granite to high-amplitude spherical stress waves, as observed from particle velocity and integrated displacement records. The experiments under consideration are

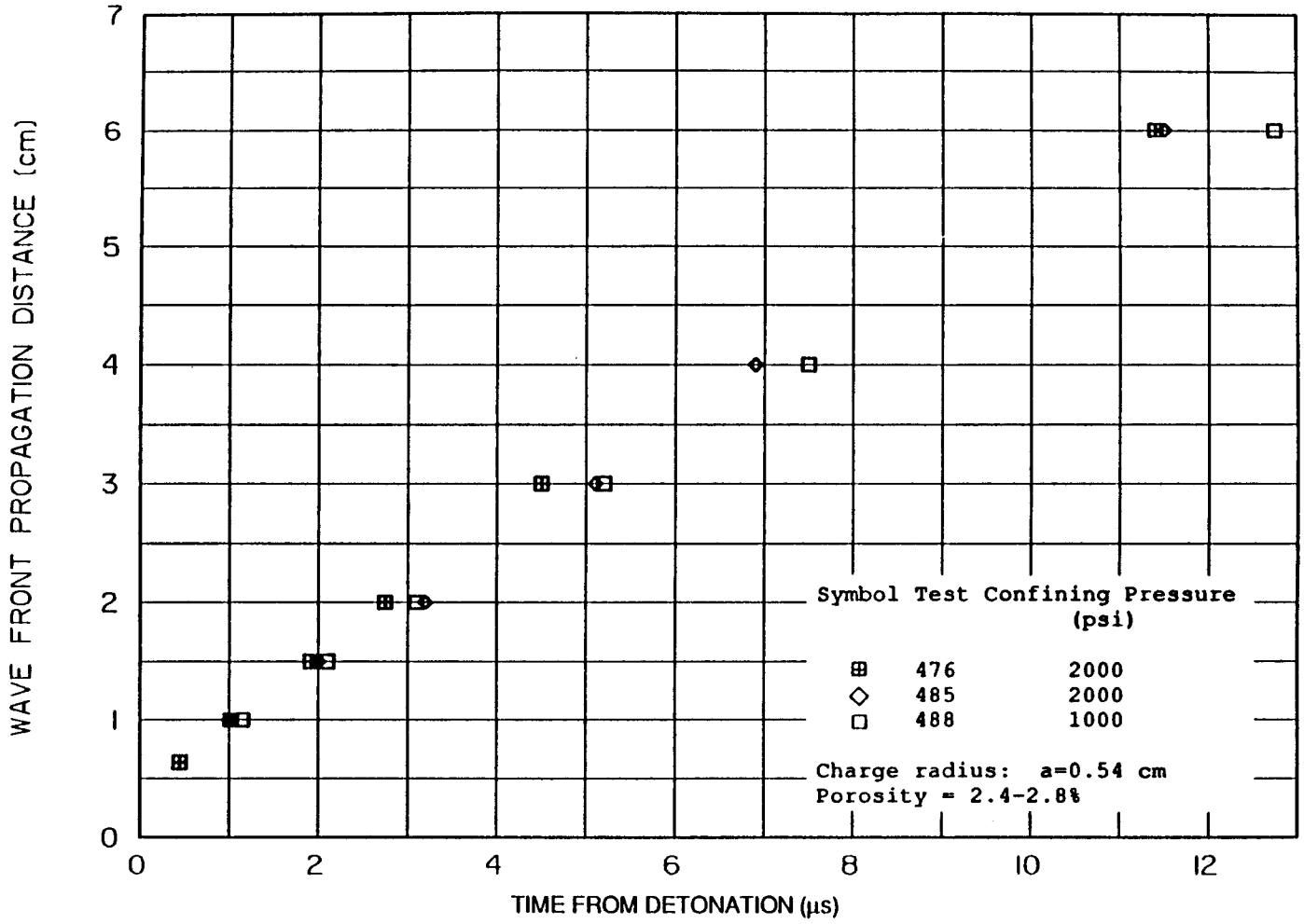

FIGURE 27 TIME OF ARRIVAL VERSUS RANGE FOR GAS-FRACTURED, DRY SIERRA WHITE GRANITE

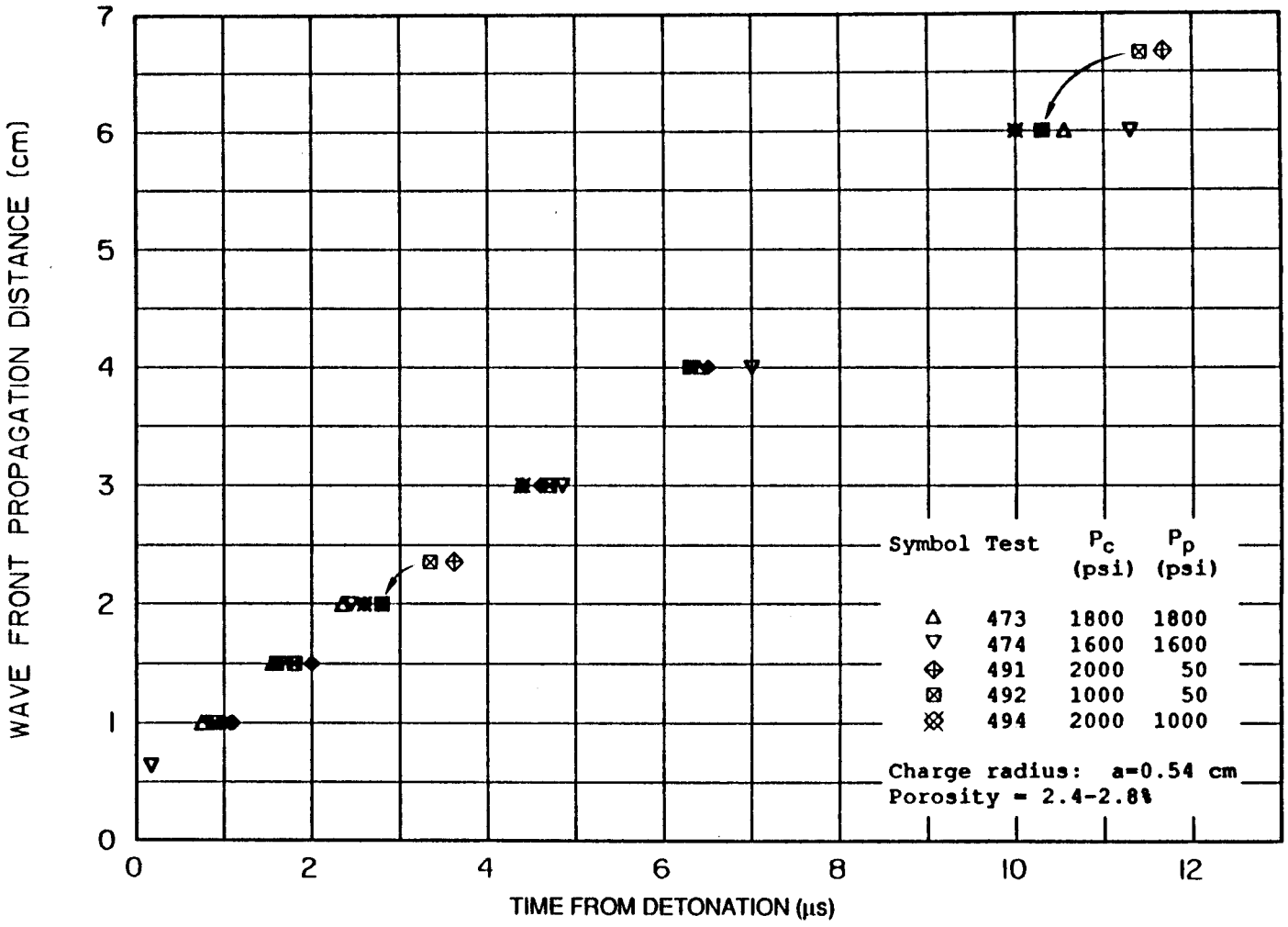

FIGURE 28 TIME OF ARRIVAL VERSUS RANGE FOR GAS-FRACTURED, SATURATED SIERRA WHITE GRANITE

those listed in Tables 1 and 2. In Figures 29 through 40 representative particle velocity and displacement plots are shown at the 3.0-cm location (approximately 6 charge radii) to highlight the effects of the various parameters. The effect of these parameters on the peak velocity and peak displacement attenuations with range are shown by the plots in Figures 41 through 52. Representative particle velocity records for the earlier high-porosity dry experiment (Test 476), high-porosity saturated experiments (Tests 473 and 474),[1] and low-porosity dry and saturated experiments (Tests 308, 309, and 310)[2] are shown in Appendix C for reference.

In general, the highest peak velocities and lowest peak velocity attenuations are obtained in intact or thermally fractured saturated granite (with no appreciable difference between them). On the other hand, the highest peak displacements and lowest peak displacement attenuations are obtained in the gas-fractured saturated rock with a porosity of about 2.5 times that of the intact material and no effective stress. In the following we describe the observed effects of the parameters studied. "High porosity" refers to the gas-fractured material with approximately 2.5% porosity, and "low porosity" refers to intact or thermally fractured material with about 1% porosity.

Effect of Porosity in Dry Rock at Constant Confinement. At a high confinement (2000 psi) a small porosity increase (20%, achieved by thermal fracturing) has a negligible influence on peak velocities and peak displacements, as shown by the peak velocity and displacement attenuation plots of Figures 41 and 47, and on pulse shapes (Figures C-9 through C-11 in Appendix C). Although the two high-porosity dry experiments, Tests 476 and 485, are considerably different in peak velocity at most locations with Test 485 being lower, they are similar in pulse width and peak displacement. This indicates that, especially near the source in a high stress regime, the peak velocity is not a good measure of the effect of porosity in dry rock. With this in mind, the results show that in dry granite at a high confining pressure, a significant porosity increase

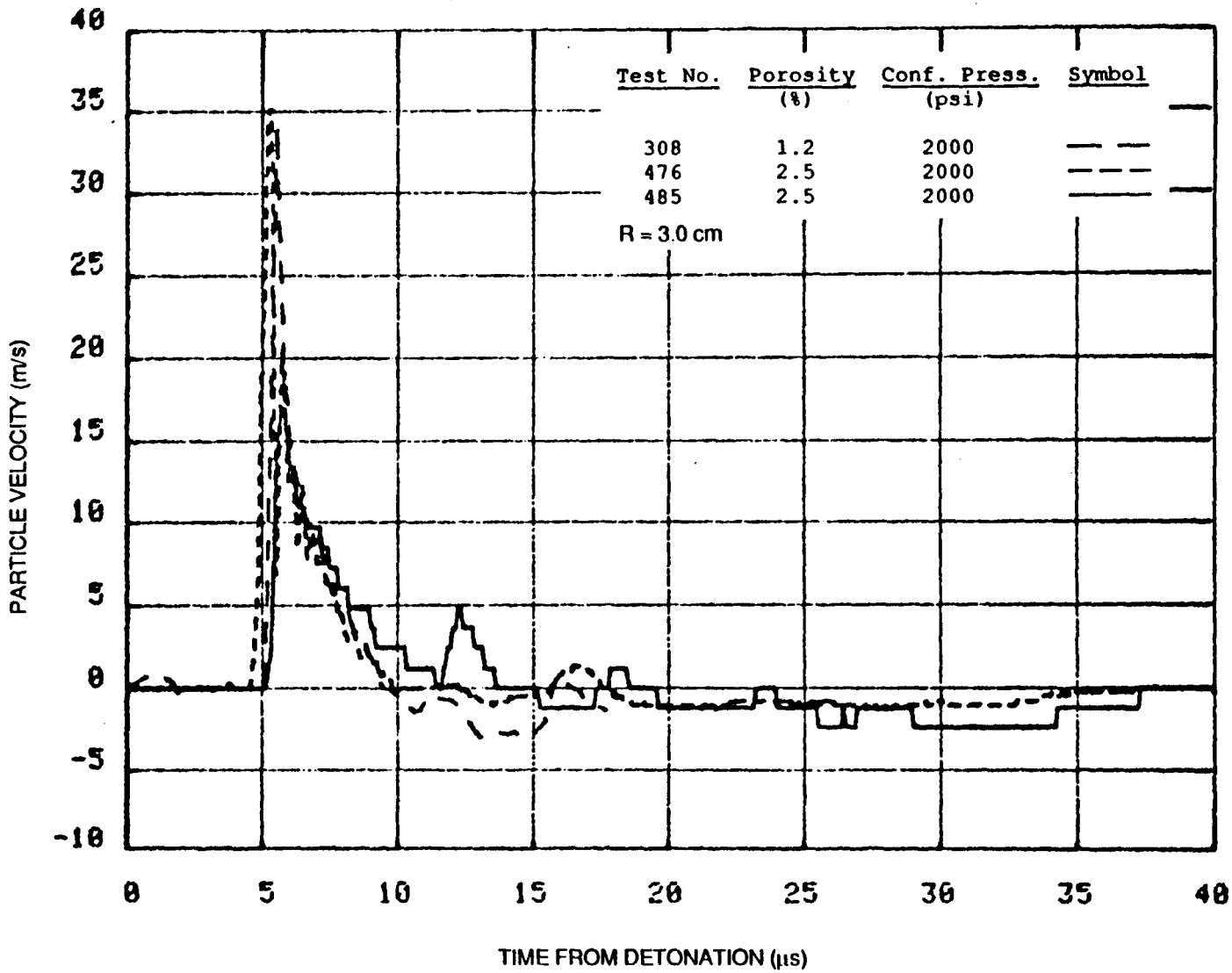

FIGURE 29 PARTICLE VELOCITY AT 3.0 cm FROM CENTER OF COUPLED EXPLOSION IN FRACTURED/DRY SIERRA WHITE GRANITE, TESTS 308, 476, AND 485

Porosity effect at constant confining pressure.

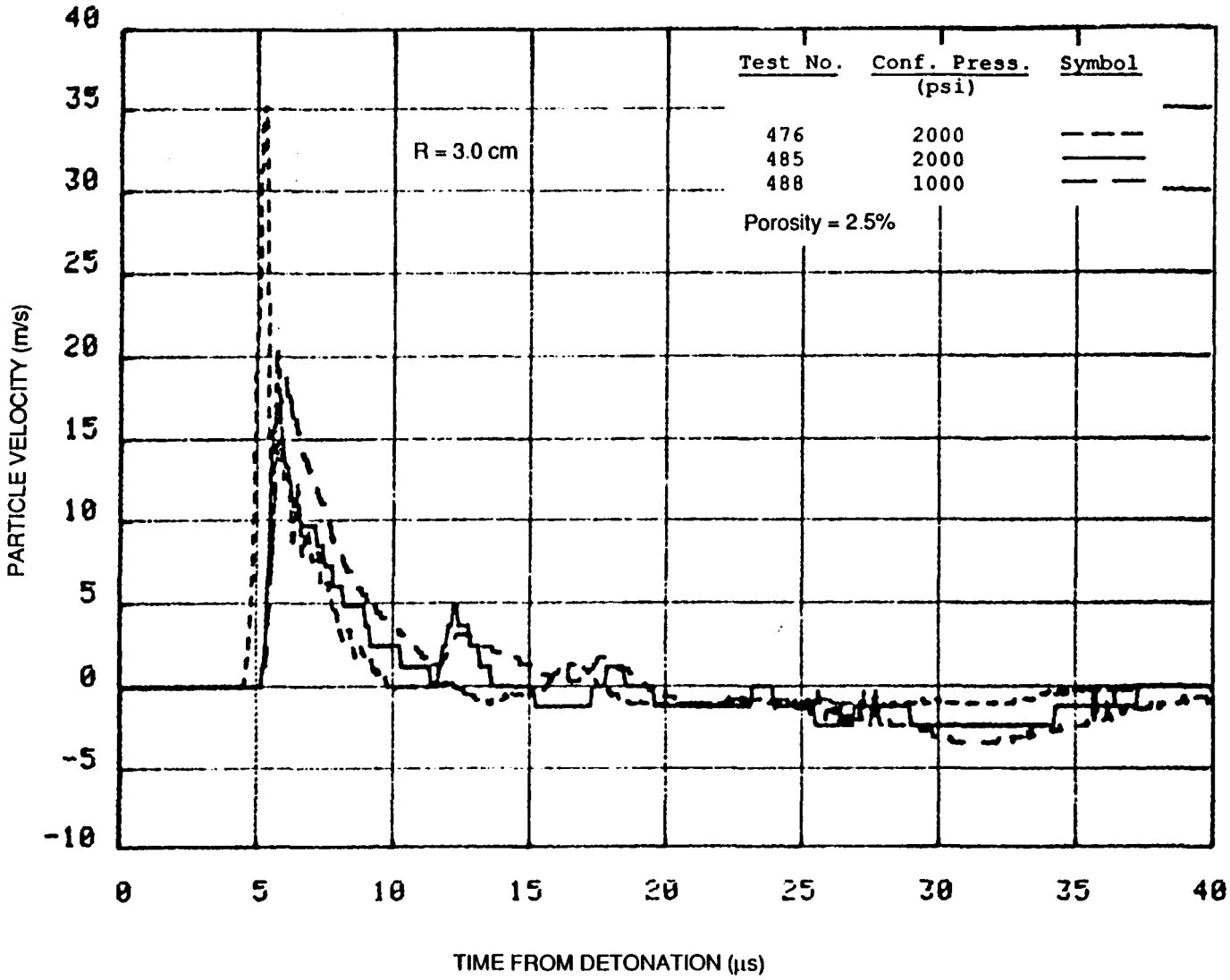

RA-m-2336-49

FIGURE 30 PARTICLE VELOCITIES AT 3.0 cm FROM CENTER OF COUPLED EXPLOSION IN FRACTURED/DRY SIERRA WHITE GRANITE, TESTS 476, 485, AND 488

Confining pressure effect at constant porosity.

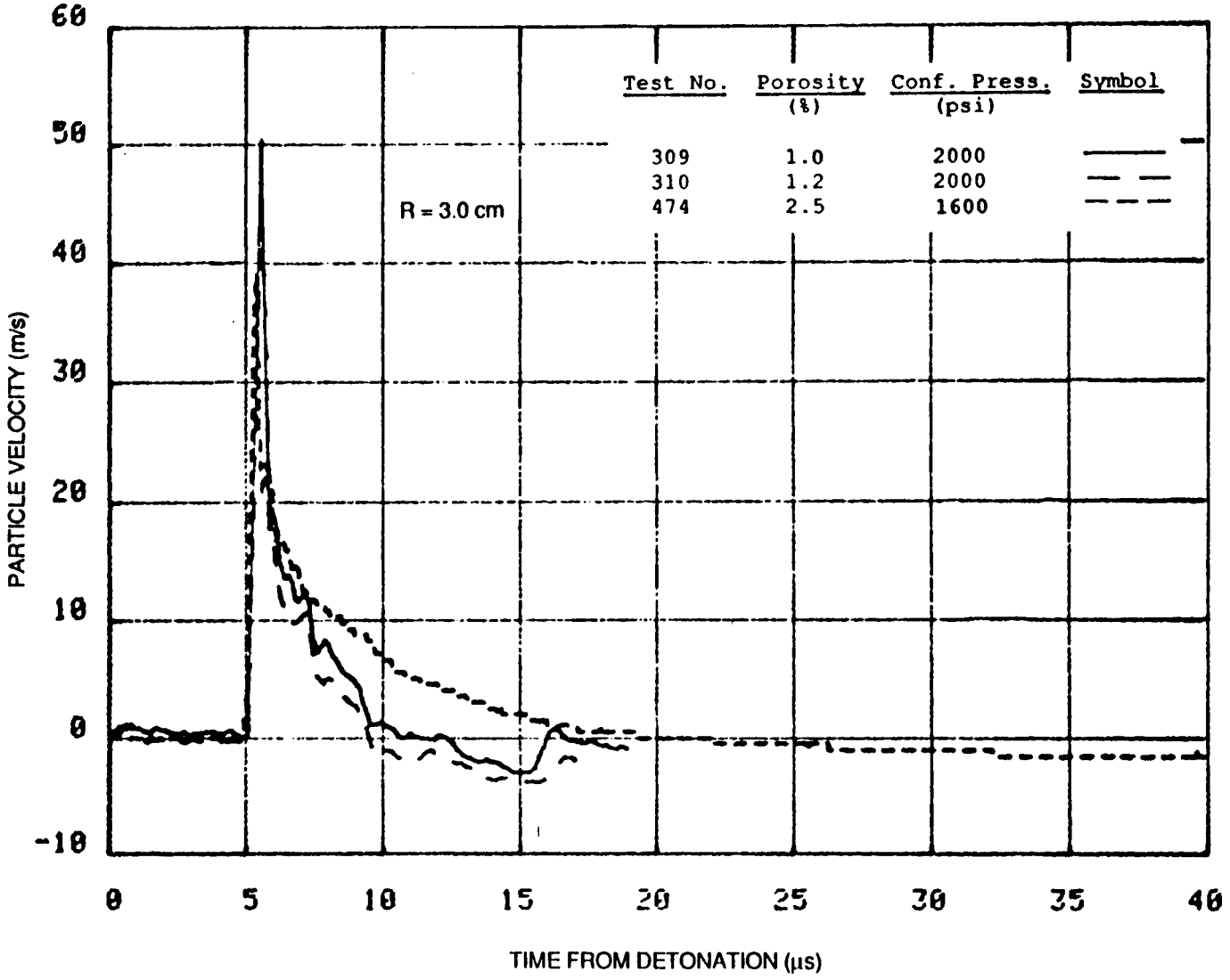

RA-m-2336-50

FIGURE 31 PARTICLE VELOCITIES AT 3.0 cm FROM CENTER OF COUPLED EXPLOSION IN FRACTURED/SATURATED SIERRA WHITE GRANITE, TESTS 309, 310, AND 474

Porosity effect at constant confining pressure and zero effective stress.

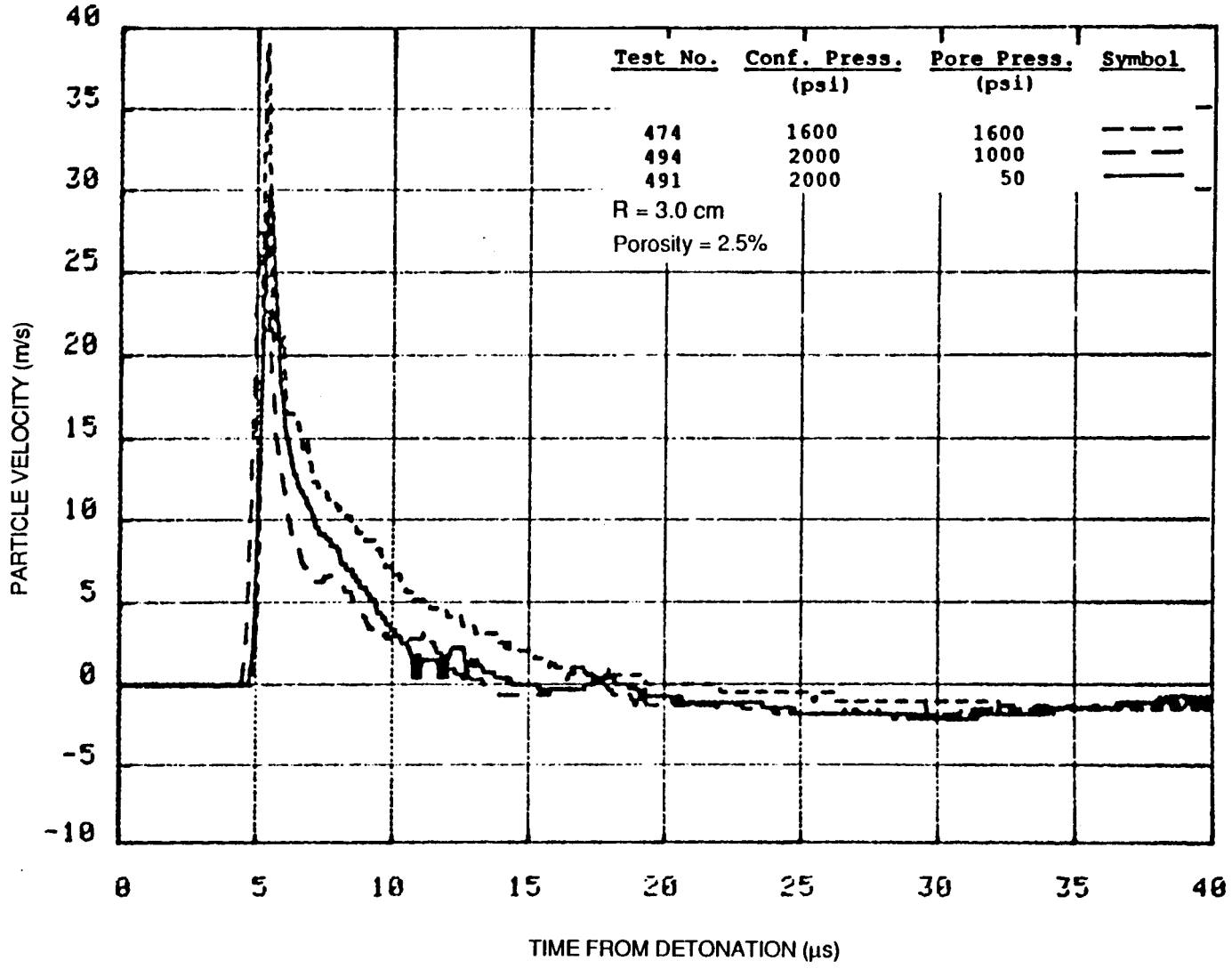

FIGURE 32 PARTICLE VELOCITIES AT 3.0 cm FROM CENTER OF COUPLED EXPLOSION IN FRACTURED/SATURATED SIERRA WHITE GRANITE, TESTS 474, 491 AND 494

Effective stress (pore pressure) effect at constant porosity and confining pressure.

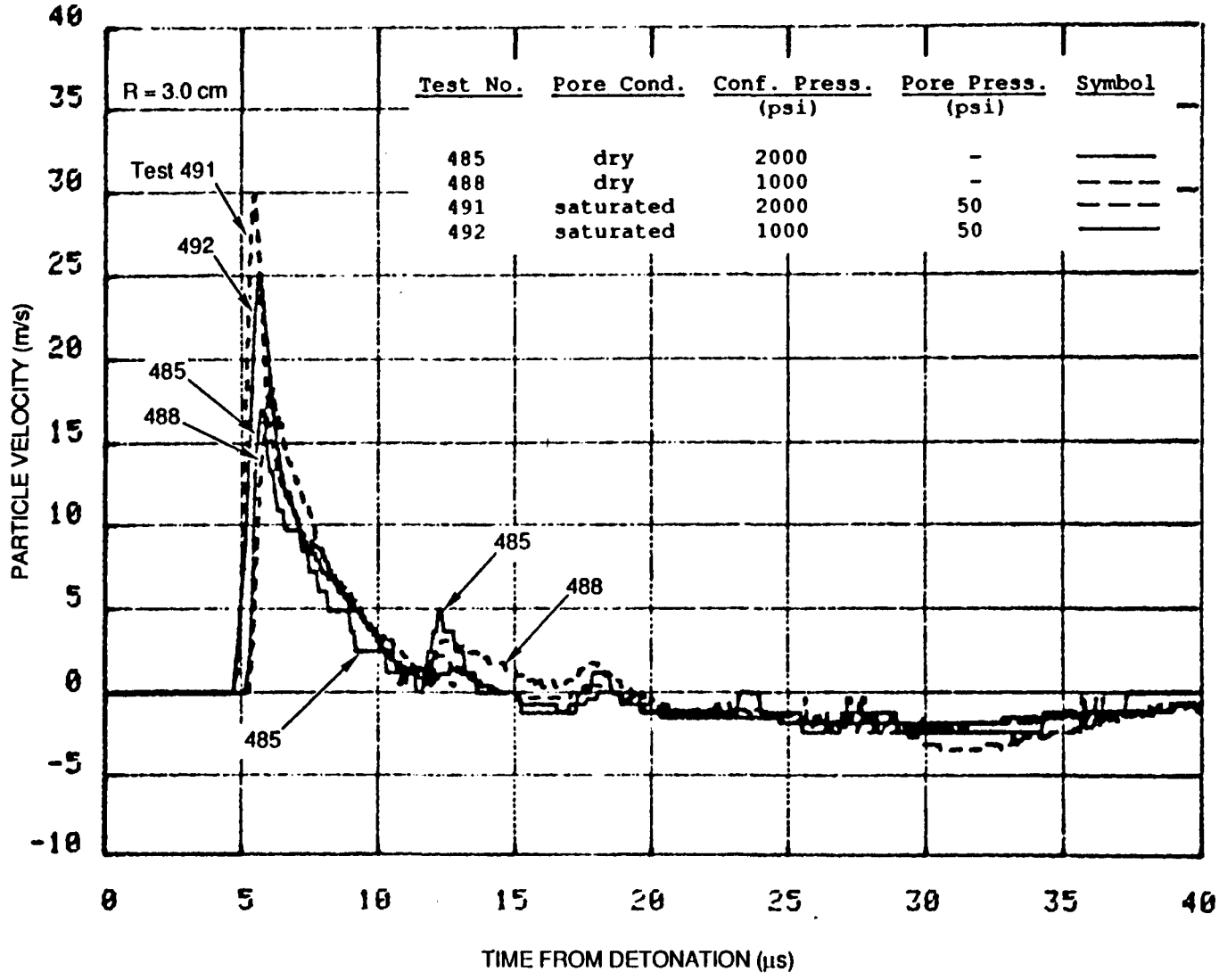

RA-m-2336-52

FIGURE 33 PARTICLE VELOCITIES AT 3.0 cm FROM CENTER OF COUPLED EXPLOSION IN FRACTURED/SATURATED SIERRA WHITE GRANITE, TESTS 485, 488, 491, AND 492

Pore water effect at zero pore pressure for two confining stresses.

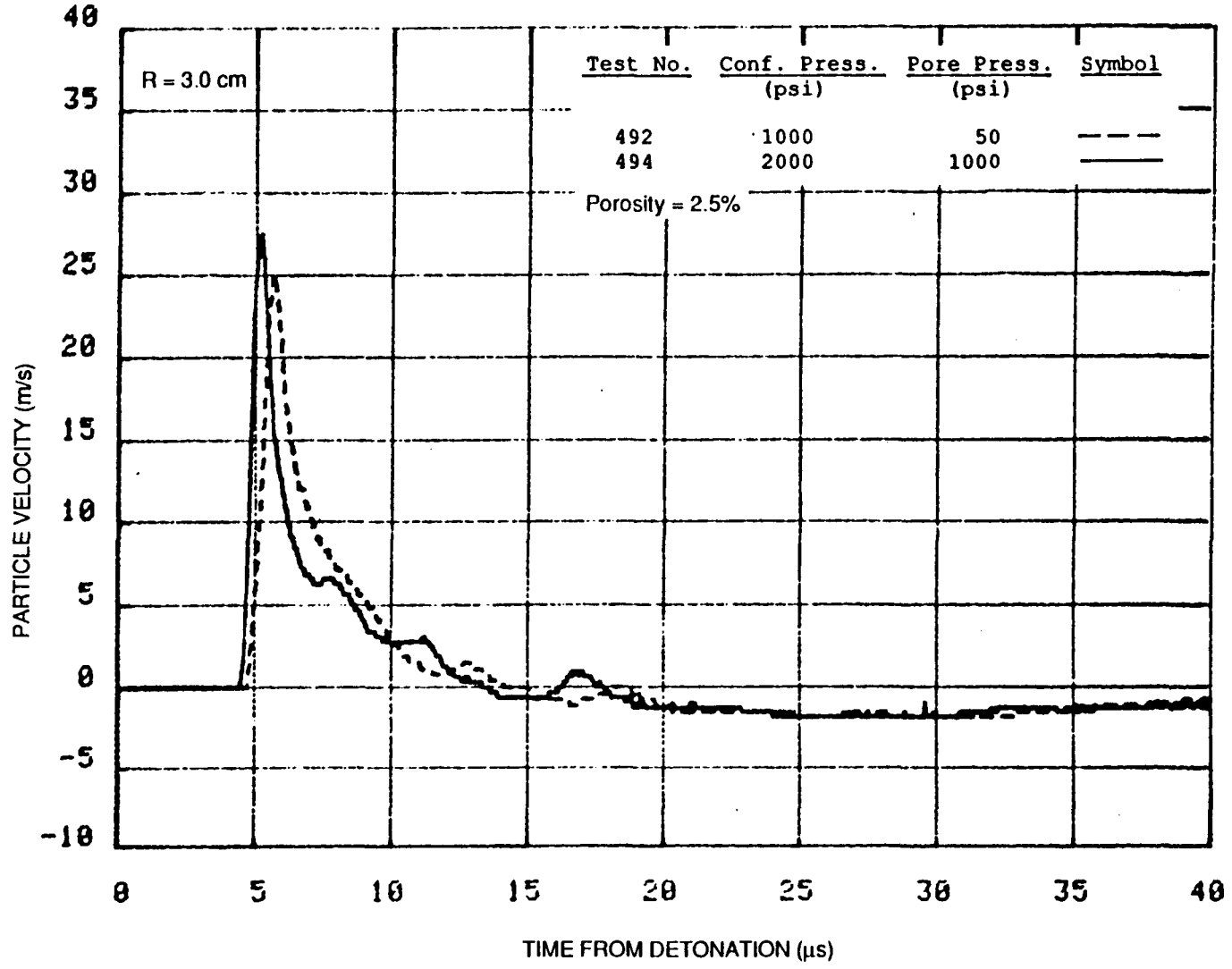

RA-m-2336-53

FIGURE 34 PARTICLE VELOCITIES AT 3.0 cm FROM CENTER OF COUPLED EXPLOSION IN FRACTURED/SATURATED SIERRA WHITE GRANITE, TESTS 492 AND 494

Confining pressure effect at constant effective stress and constant porosity.

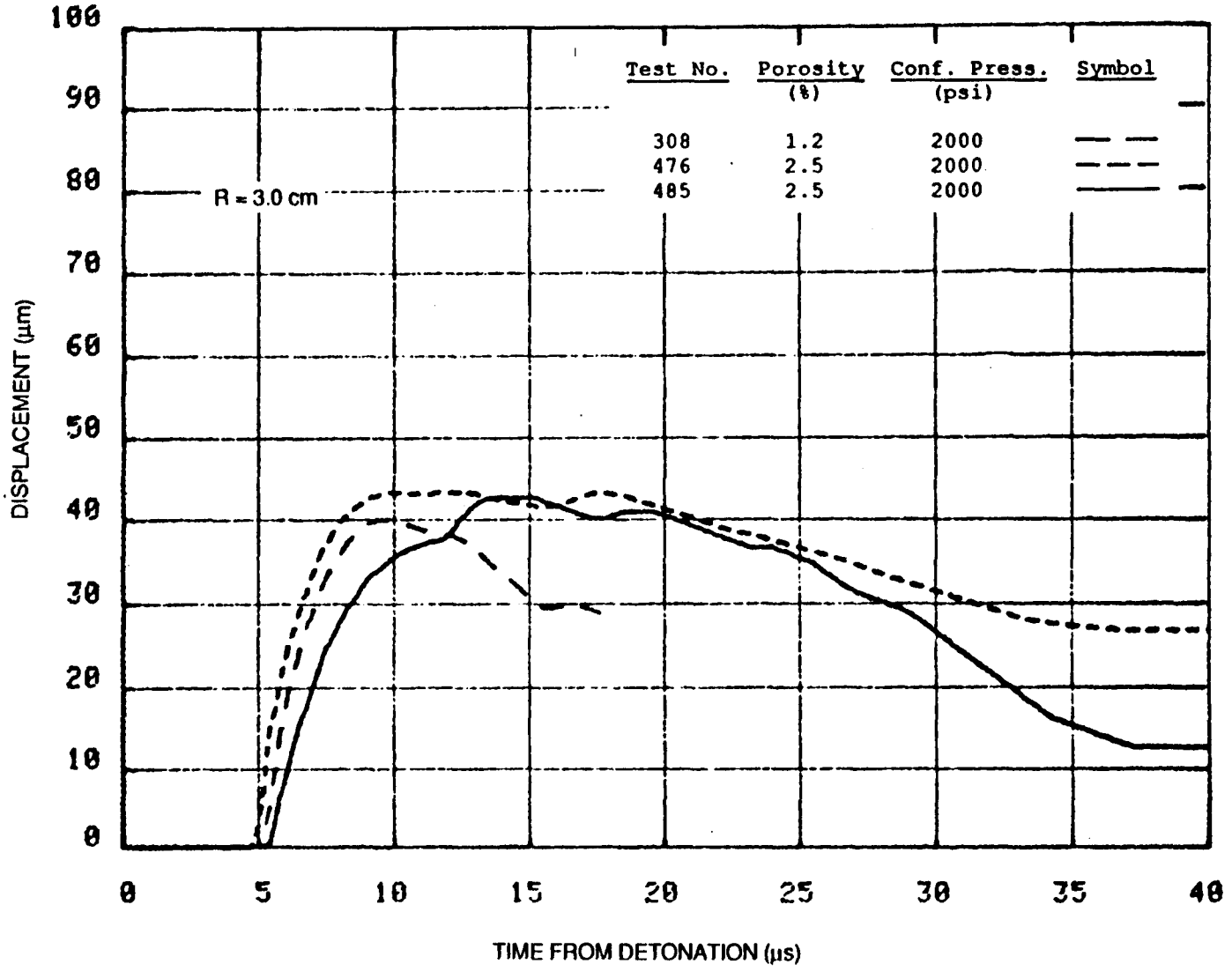

RA-m-2336-54

FIGURE 35 PARTICLE DISPLACEMENTS AT 3.0 cm FROM CENTER OF COUPLED EXPLOSION IN FRACTURED/DRY SIERRA WHITE GRANITE, TESTS 308, 476, AND 485.

Porosity effect at constant confining pressure.

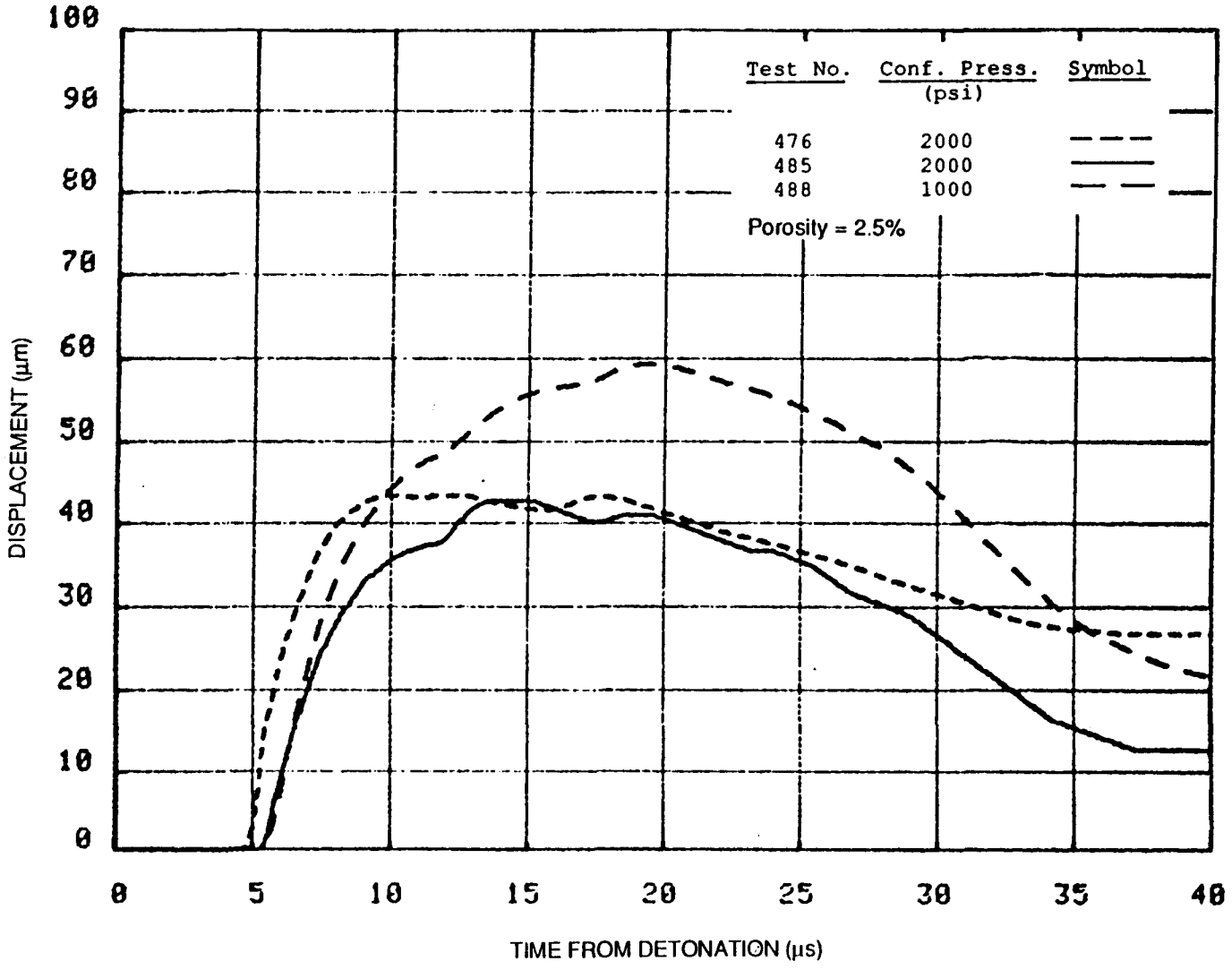

RA-m-2336-55

FIGURE 36 PARTICLE DISPLACEMENTS AT 3.0 cm FROM CENTER OF COUPLED EXPLOSION IN FRACTURED/DRY SIERRA WHITE GRANITE, TESTS 476, 485, AND 488

Confining pressure effect at constant porosity.

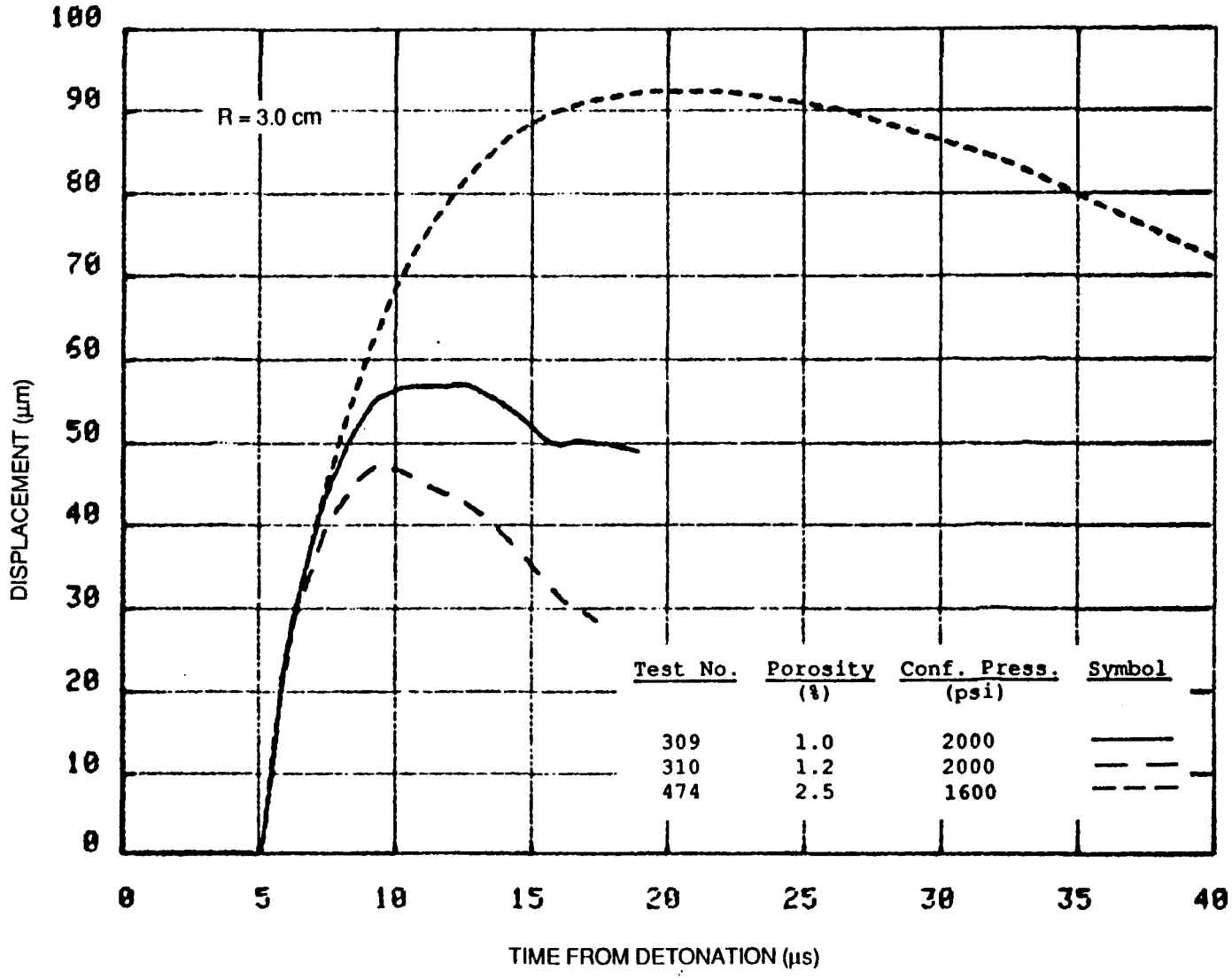

RA-m-2336-56

FIGURE 37 PARTICLE DISPLACEMENTS AT 3.0 cm FROM CENTER OF COUPLED EXPLOSION IN FRACTURED/SATURATED SIERRA WHITE GRANITE, TESTS 309, 310, AND 474

Porosity effect at constant confining pressure and zero effective stress.

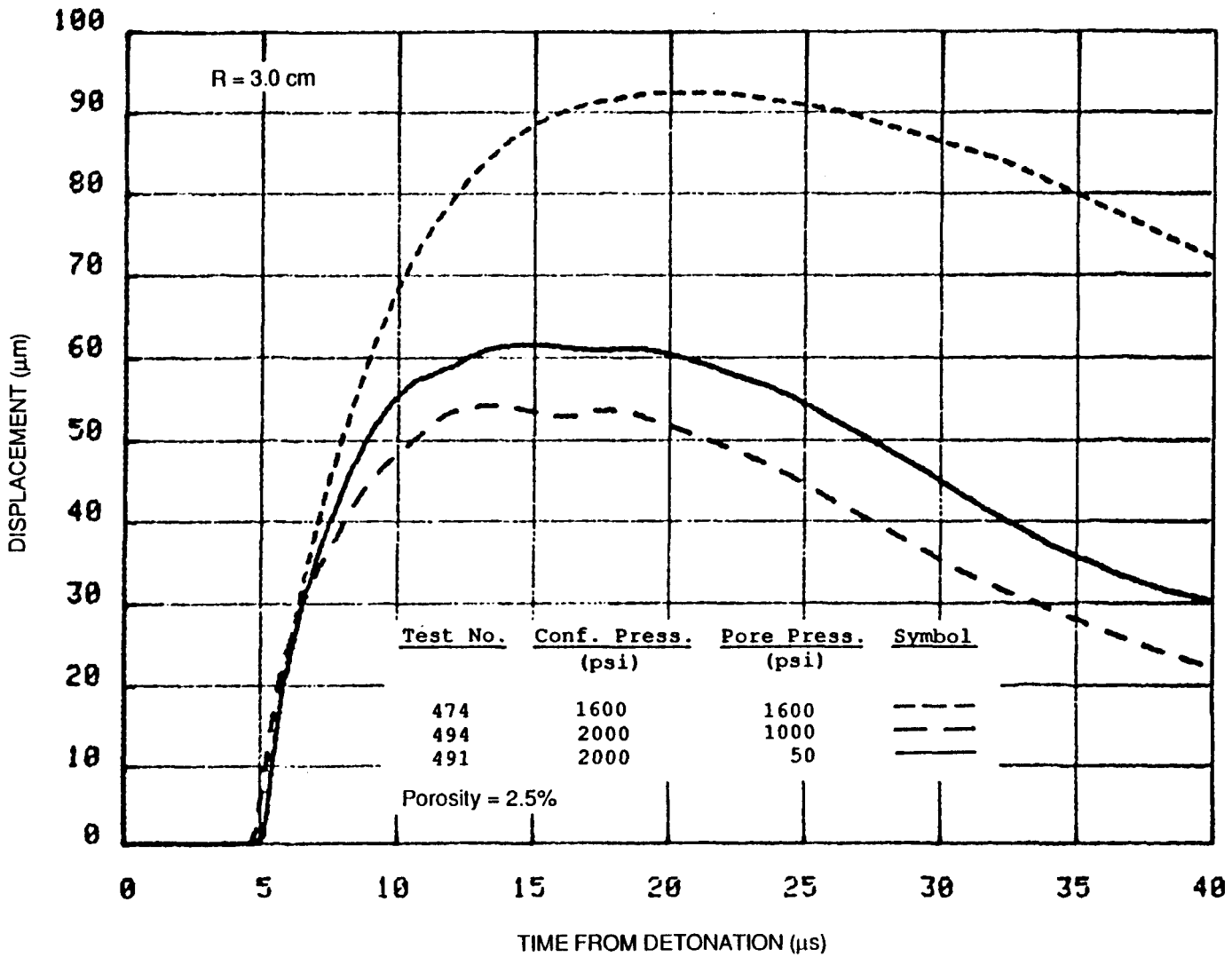

FIGURE 38 PARTICLE DISPLACEMENT AT 3.0 cm FROM CENTER EXPLOSION IN FRACTURED/SATURATED SIERRA WHITE GRANITE, TESTS 474, 491, AND 494

Effective stress (pore pressure) effect at constant porosity and confining pressure.

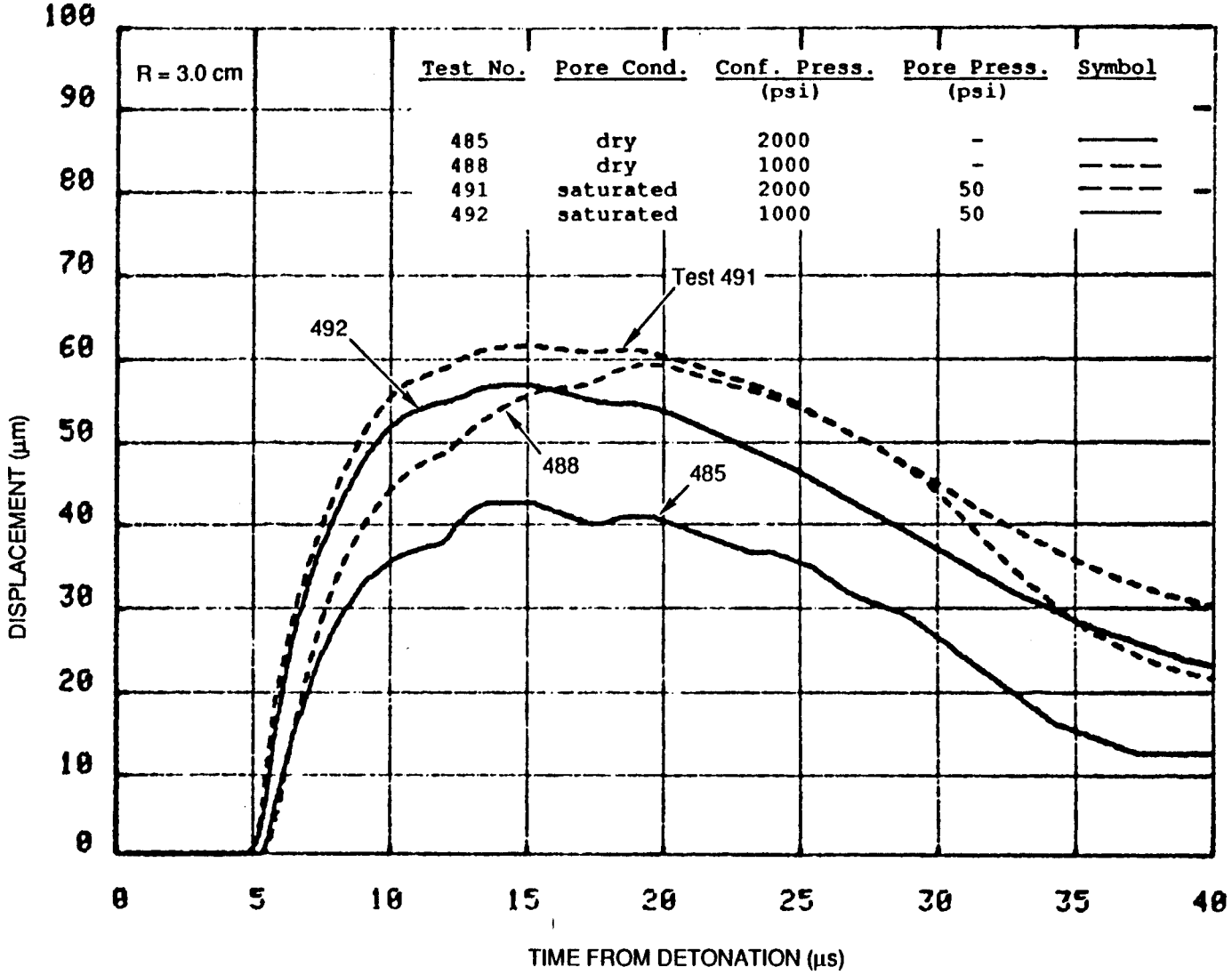

RA-m-2336-58

FIGURE 39 PARTICLE DISPLACEMENTS AT 3.0 cm FROM CENTER OF COUPLED EXPLOSION IN FRACTURED/SATURATED SIERRA WHITE GRANITE, TESTS 485, 488, 491, AND 492

Pore water effect at zero pore pressure for two confining stresses.

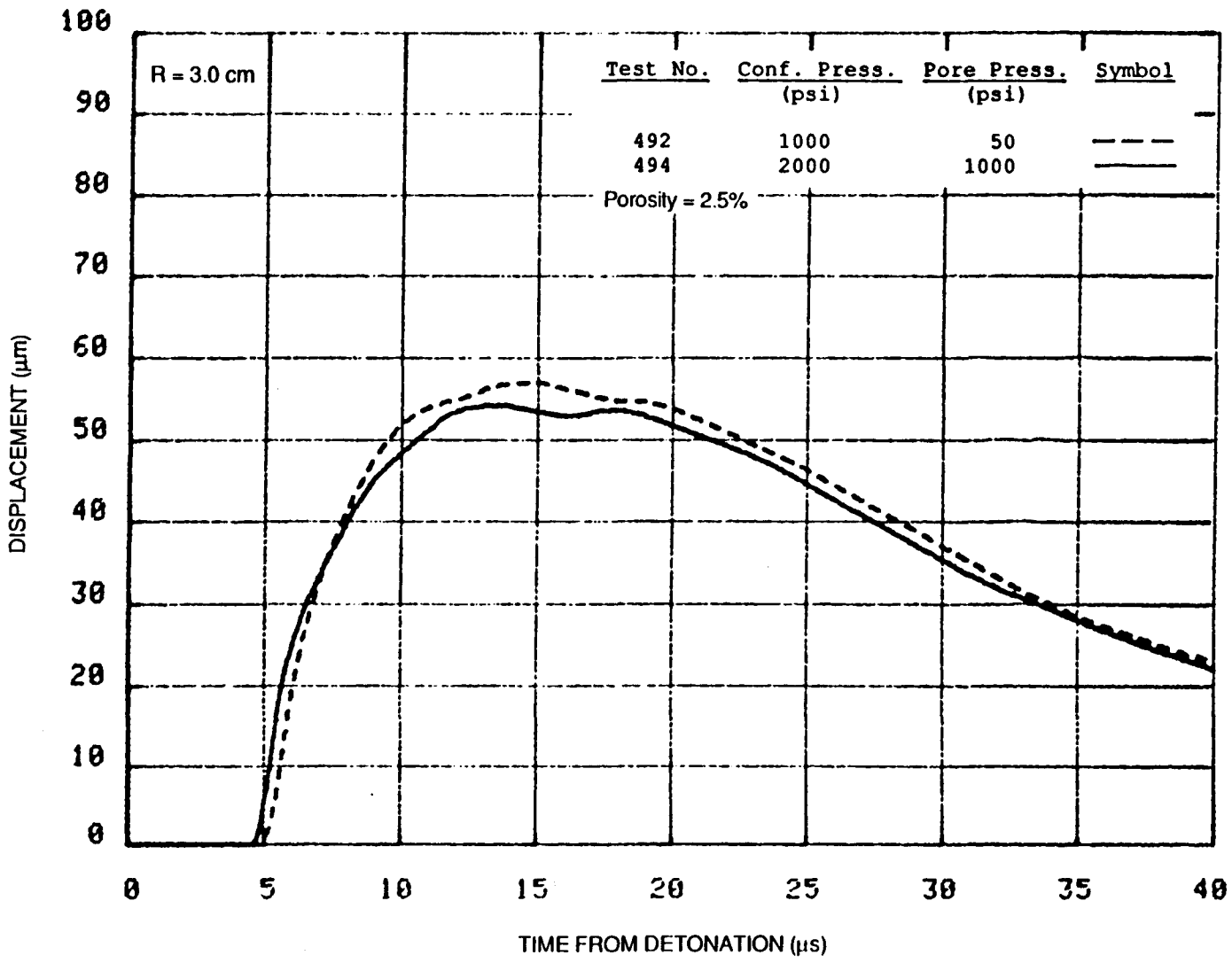

RA-m-2336-59

FIGURE 40 PARTICLE DISPLACEMENT AT 3.0 cm FROM CENTER OF COUPLED EXPLOSION IN FRACTURED/SATURATED SIERRA WHITE GRANITE, TESTS 492, AND 494

Confining pressure effect at constant effective stress and constant porosity.

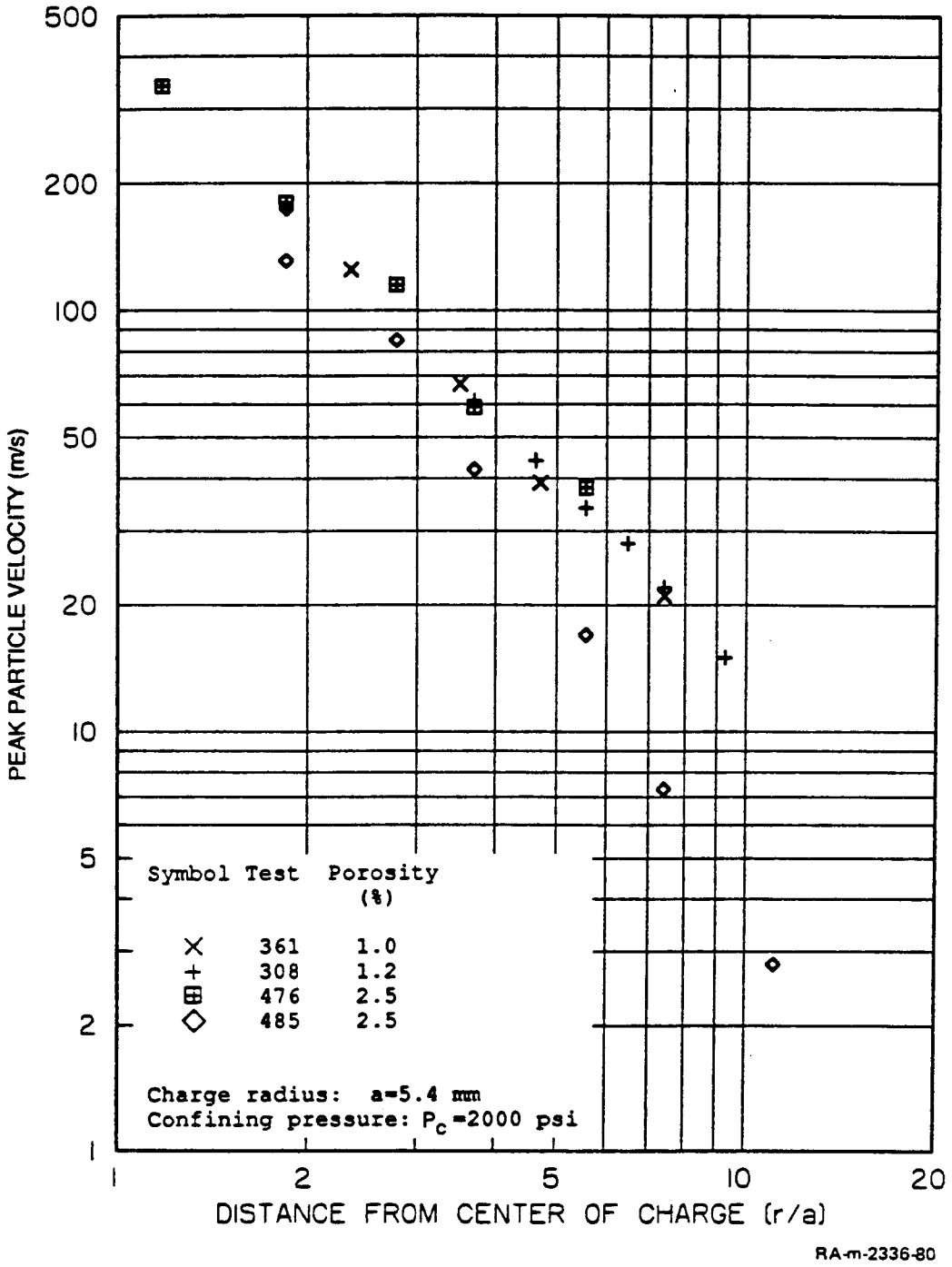

FIGURE 41 EFFECT OF POROSITY ON PEAK VELOCITY ATTENUATION IN DRY SIERRA WHITE GRANITE WITH A CONFINING PRESSURE OF 2000 psi

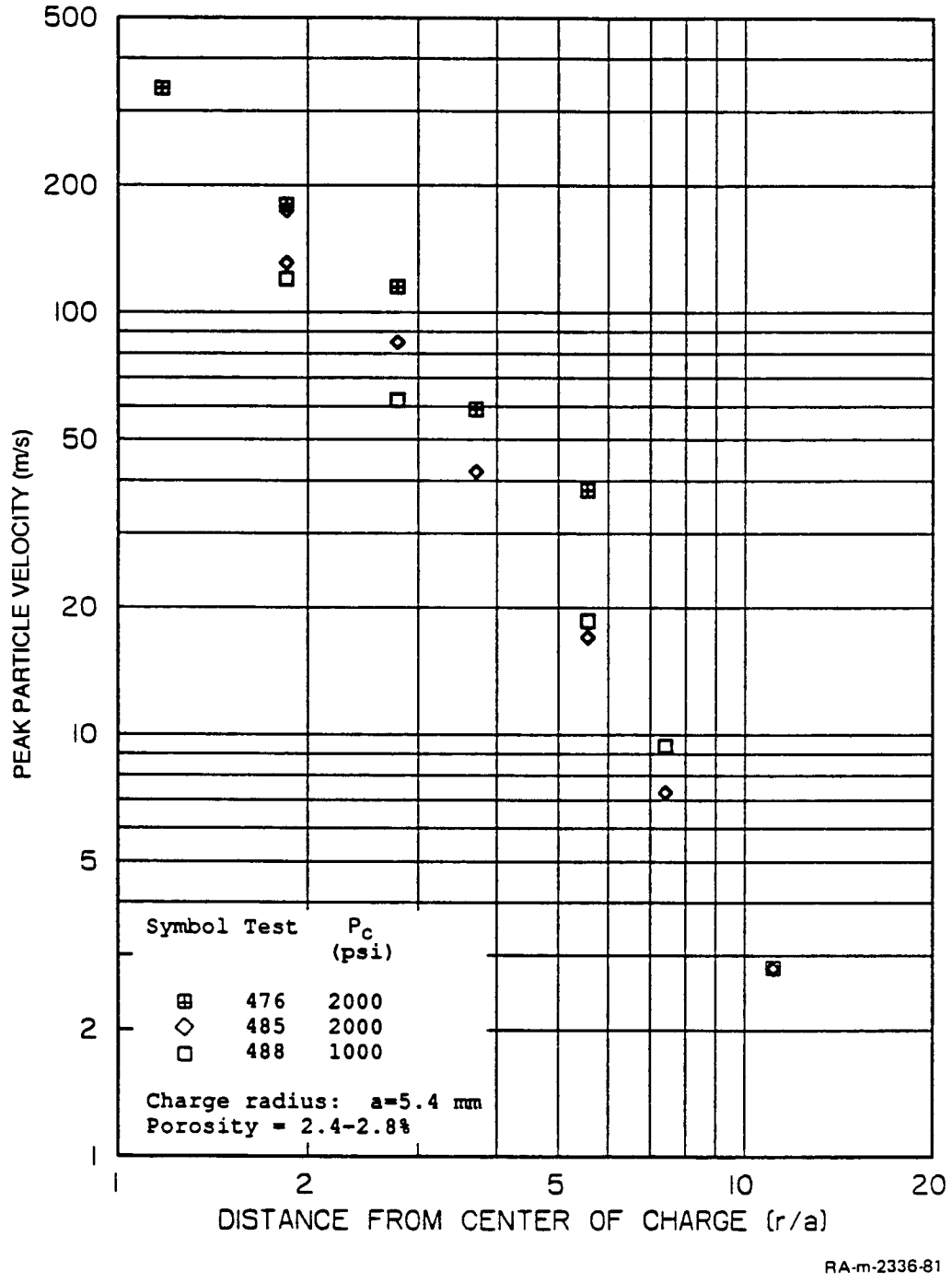

FIGURE 42 EFFECT OF CONFINING PRESSURE P_c ON PEAK PARTICLE VELOCITY ATTENUATION IN DRY, GAS-FRACTURED SIERRA WHITE GRANITE WITH POROSITY OF 2.4 - 2.8%

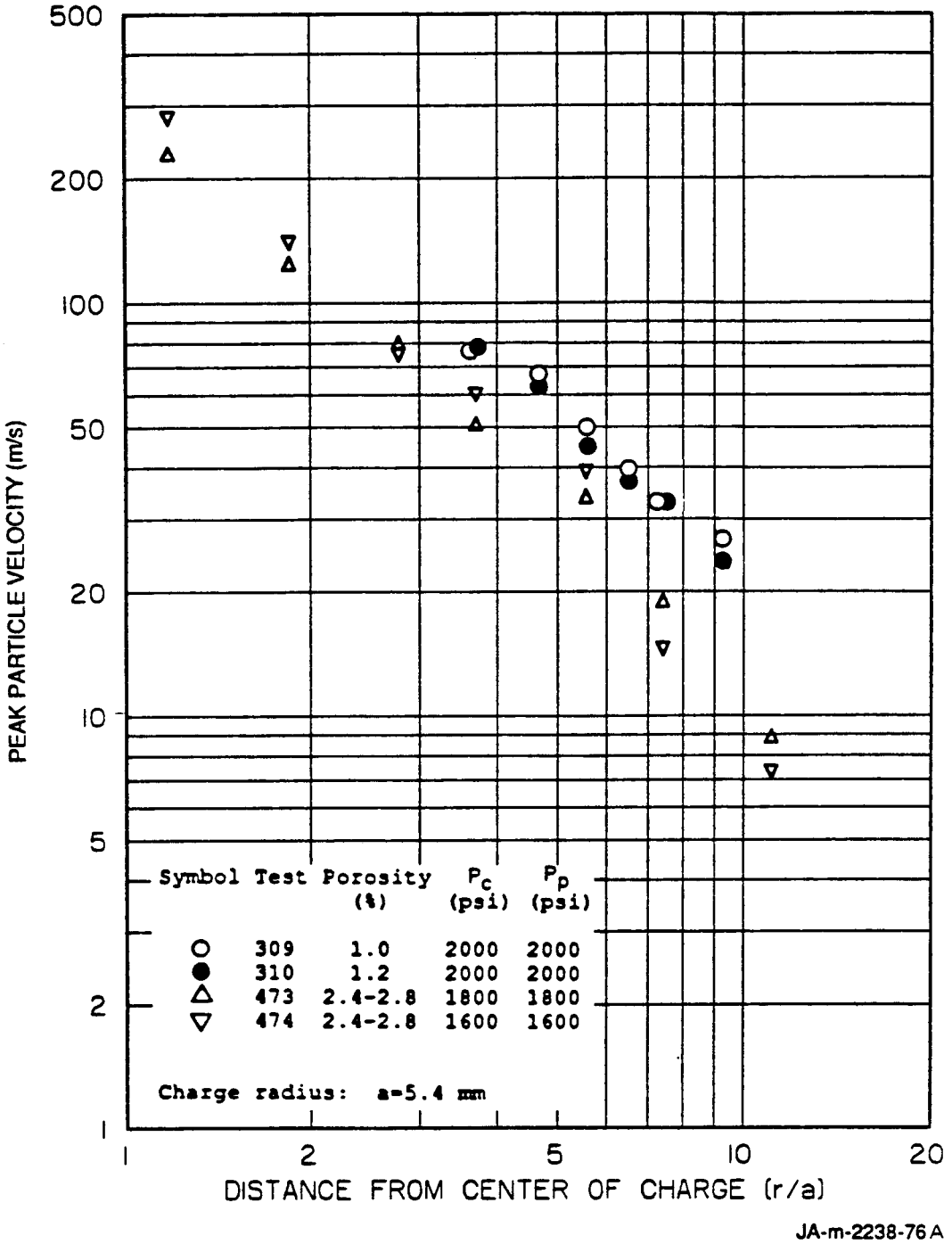

FIGURE 43 EFFECT OF POROSITY ON PEAK VELOCITY ATTENUATION IN SATURATED SIERRA WHITE GRANITE WITH ZERO EFFECTIVE STRESS (CONFINING PRESSURE EQUAL TO PORE PRESSURE)

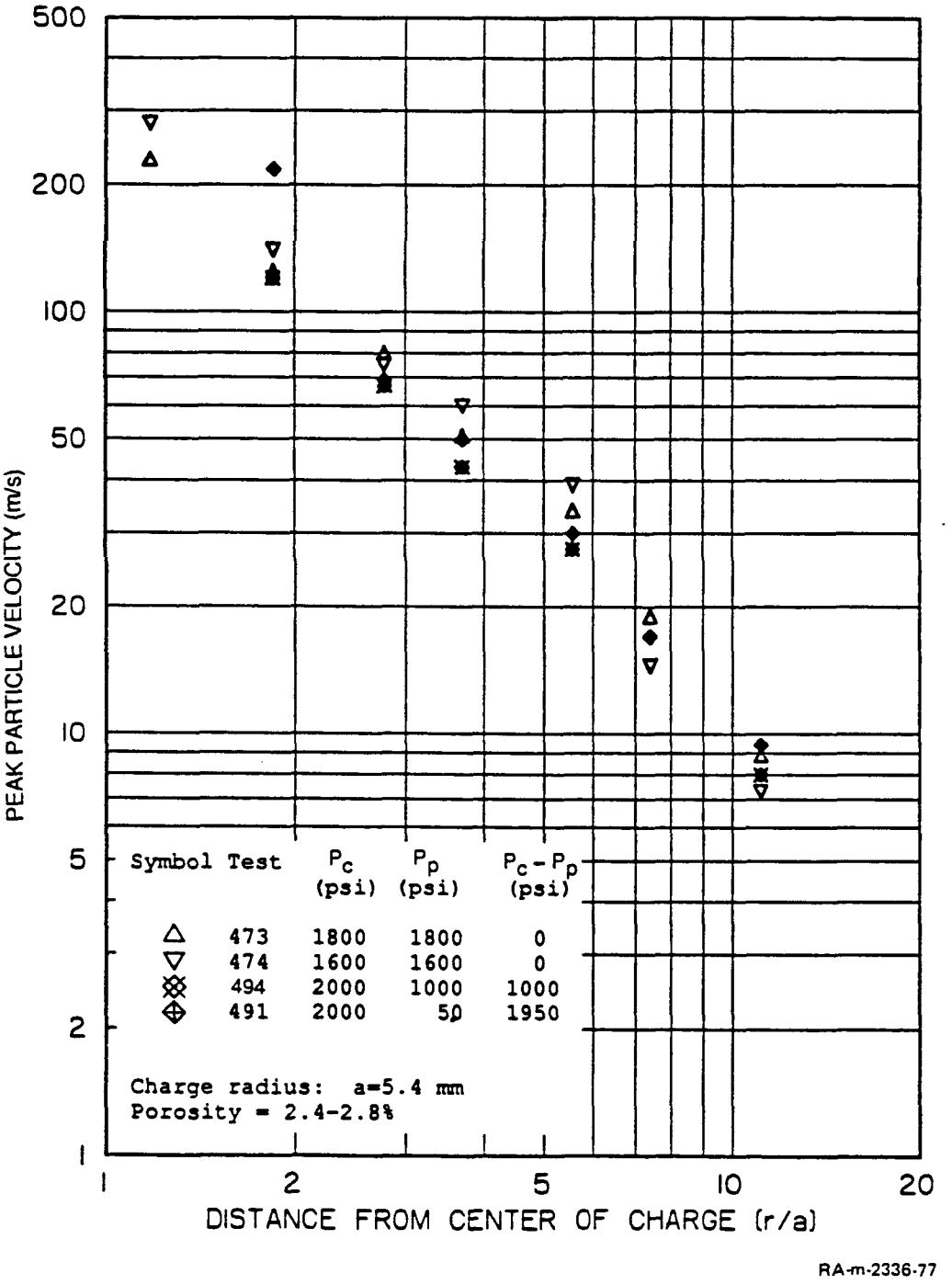

FIGURE 44 THE INFLUENCE OF EFFECTIVE STRESS ON PEAK VELOCITY ATTENUATION IN GAS-FRACTURED, SATURATED SIERRA WHITE GRANITE WITH POROSITY OF 2.4-2.8%

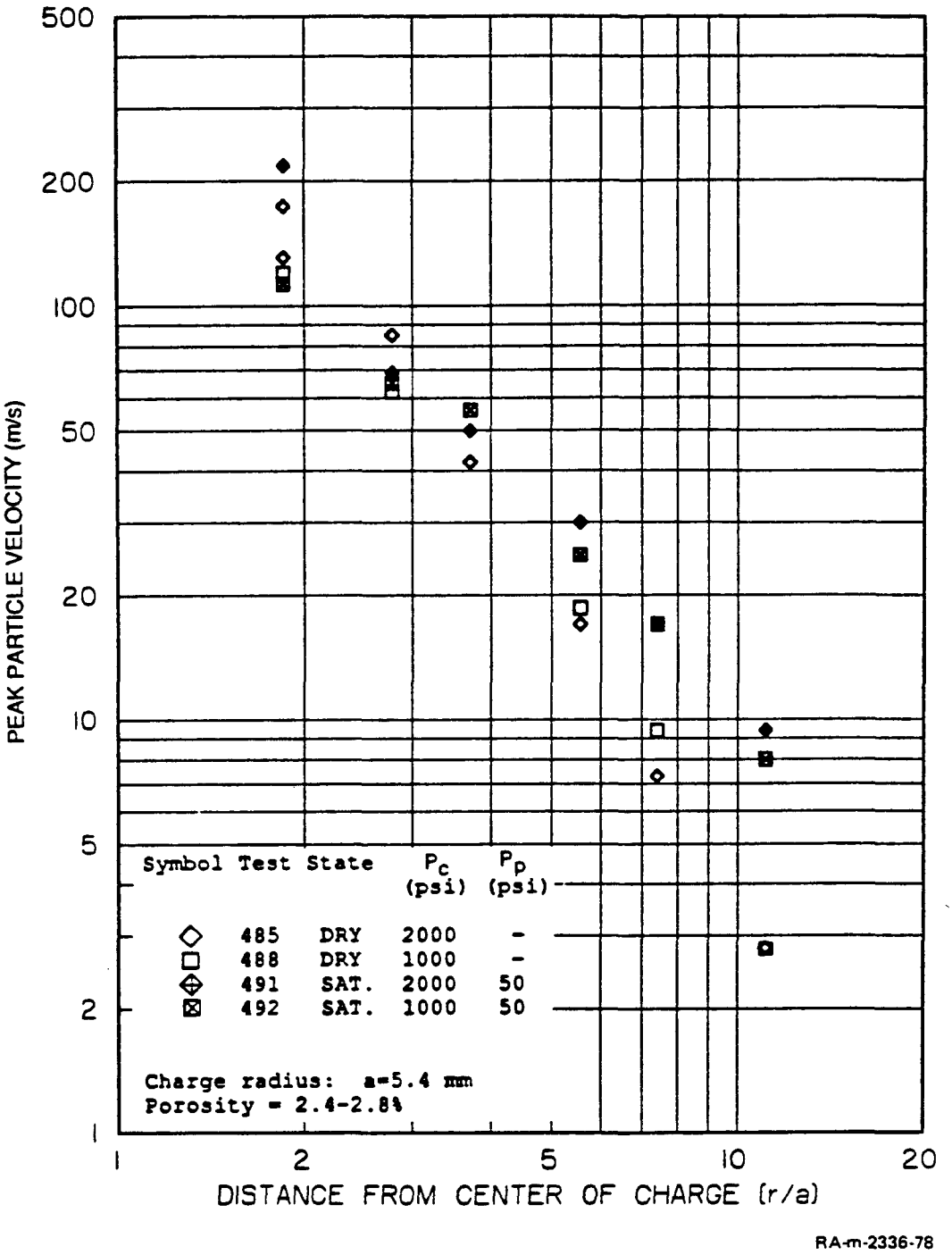

FIGURE 45 THE INFLUENCE OF PORE WATER ON PEAK VELOCITY ATTENUATION IN GAS-FRACTURED SIERRA WHITE GRANITE WITH POROSITY OF 2.4 - 2.8%, AT TWO CONFINING PRESSURES WITH NEGLIGIBLE PORE PRESSURE

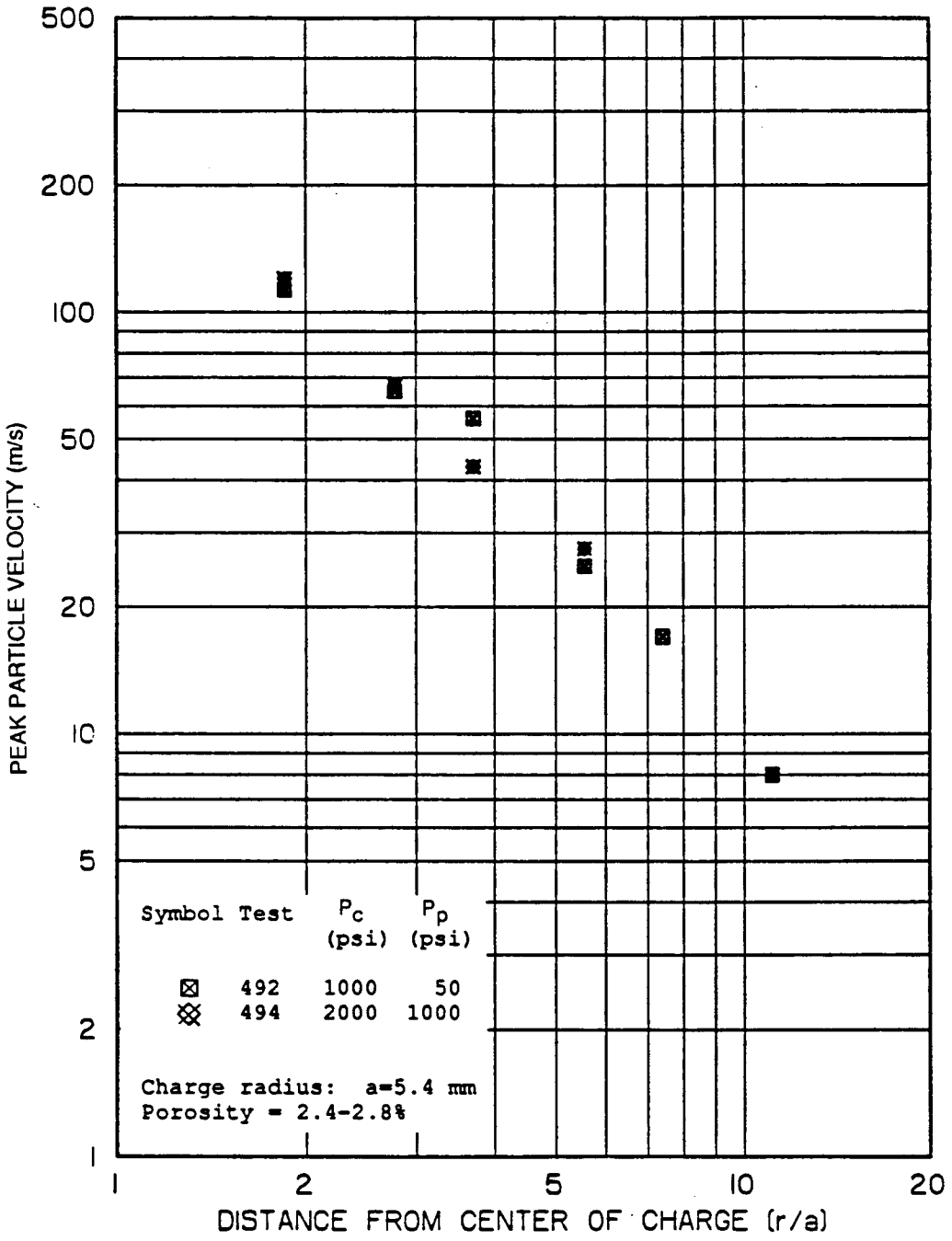

FIGURE 46 THE EFFECT OF CONFINING PRESSURE ON PEAK VELOCITY ATTENUATION IN GAS-FRACTURED, SATURATED SIERRA WHITE GRANITE WITH POROSITY OF 2.4 - 2.8% AND AN EFFECTIVE STRESS OF 1000 psi

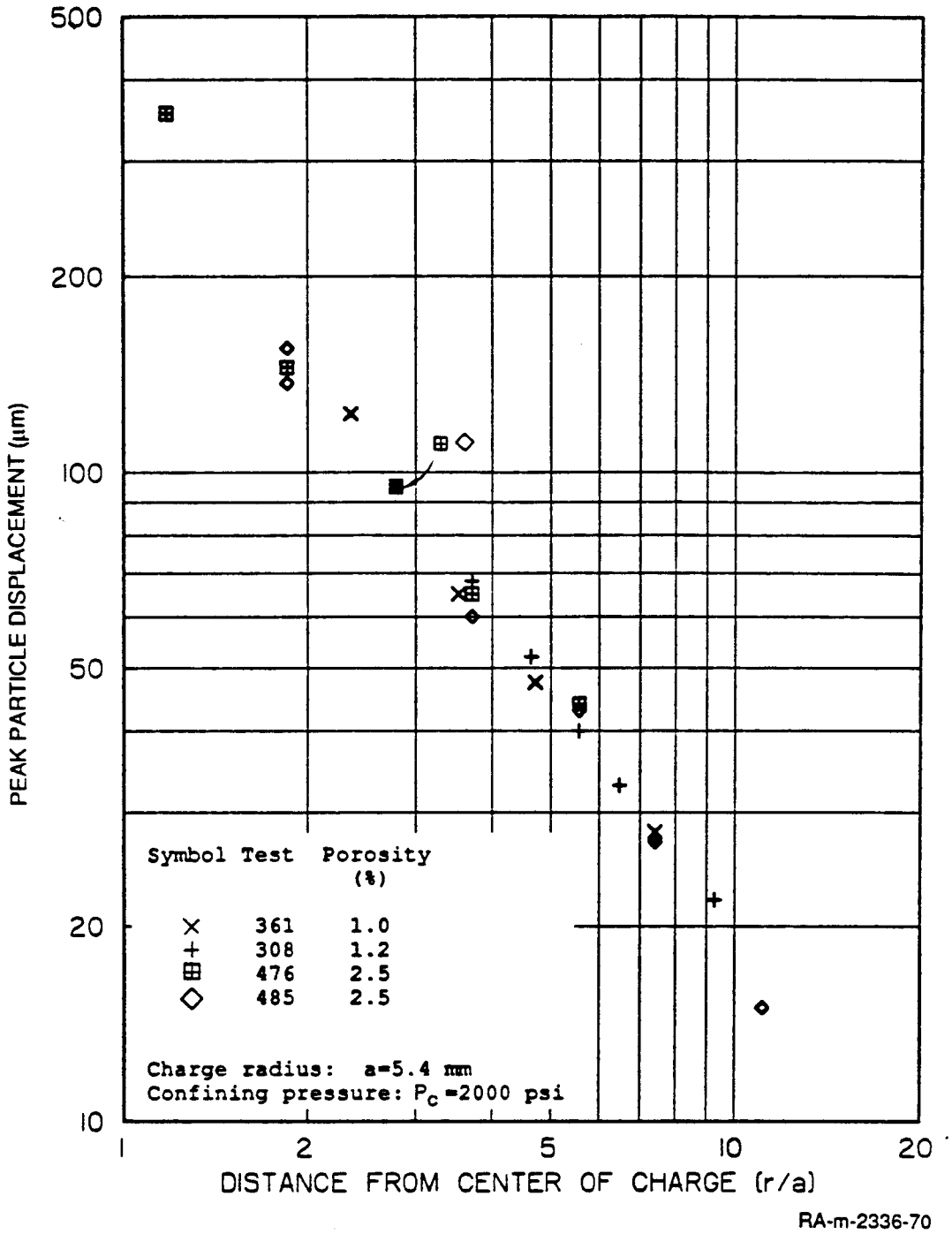

FIGURE 47 EFFECT OF POROSITY ON PEAK DISPLACEMENT ATTENUATION IN DRY SIERRA WHITE GRANITE WITH A CONFINING PRESSURE OF 2000 psi

- Has a small effect on wave shapes near the source to a radius of 3.0 cm (Figure 29), but causes a decrease in peak velocity and a widening of the pulse at greater ranges (Figures C-5 and C-11 in Appendix C).
- Does not greatly affect the amplitude and attenuation of peak displacements, as shown by the attenuation plot of Figure 47. Near the source, this result is due to the unaffected pulse shapes, but farther from the source it is due to the combined effects of lower peak velocities and wider pulses.

Effect of Confinement in High-Porosity Dry Rock. The effects of confining pressure on the response of high-porosity dry granite are indicated in the velocity records of Figures 9 through 14 and 30, the displacement records of Figures 22, 23, and 36, and the attenuation plots of Figures 42 and 48. The results show the following effect of reducing the confining pressure:

- Peak velocities are not affected (Figure 42), but pulses are widened, especially near the source (Figures 9, 10, and 14).
- Peak displacements are increased, mainly by virtue of the wider pulses (Figures 22, 23, and 48).

The scatter in the peak velocities and similarity in the peak displacements between the two experiments at high confinement (Tests 476 and 485, Figure 42) indicates that the peak velocity is not a good measure of the effect of this parameter.

Effect of Porosity in Saturated Rock with Zero Effective Stress. The effect of porosity in saturated rock with zero effective stress (pore pressure equal to confining pressure) was specifically investigated in our earlier research and is repeated here for completeness. The velocity and displacement plots of Figures 31 and 37 and the attenuation plots of Figures 43 and 49 illustrate the effect and indicate the following:

- A small (20%) increase in porosity has an almost negligible effect on peak velocities, pulse shapes, and peak displacements (Figure 43).
- Increasing the porosity from 1.0% to 2.5% lowers peak velocities, steepens peak velocity attenuation (Figure

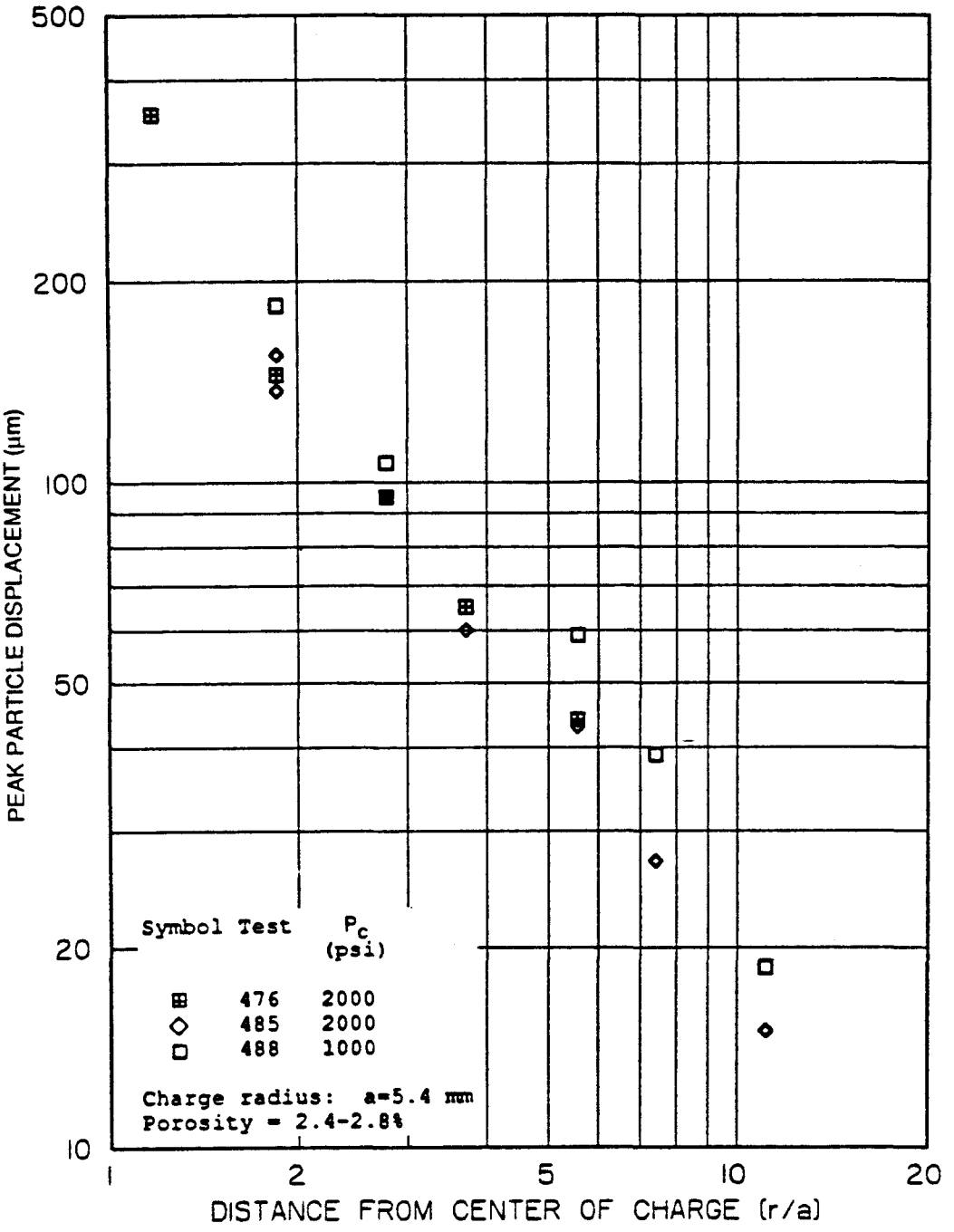

FIGURE 48 EFFECT OF CONFINING PRESSURE P_c ON PEAK DISPLACEMENT ATTENUATION IN DRY, GAS-FRACTURED SIERRA WHITE GRANITE WITH POROSITY OF 2.4-2.8%

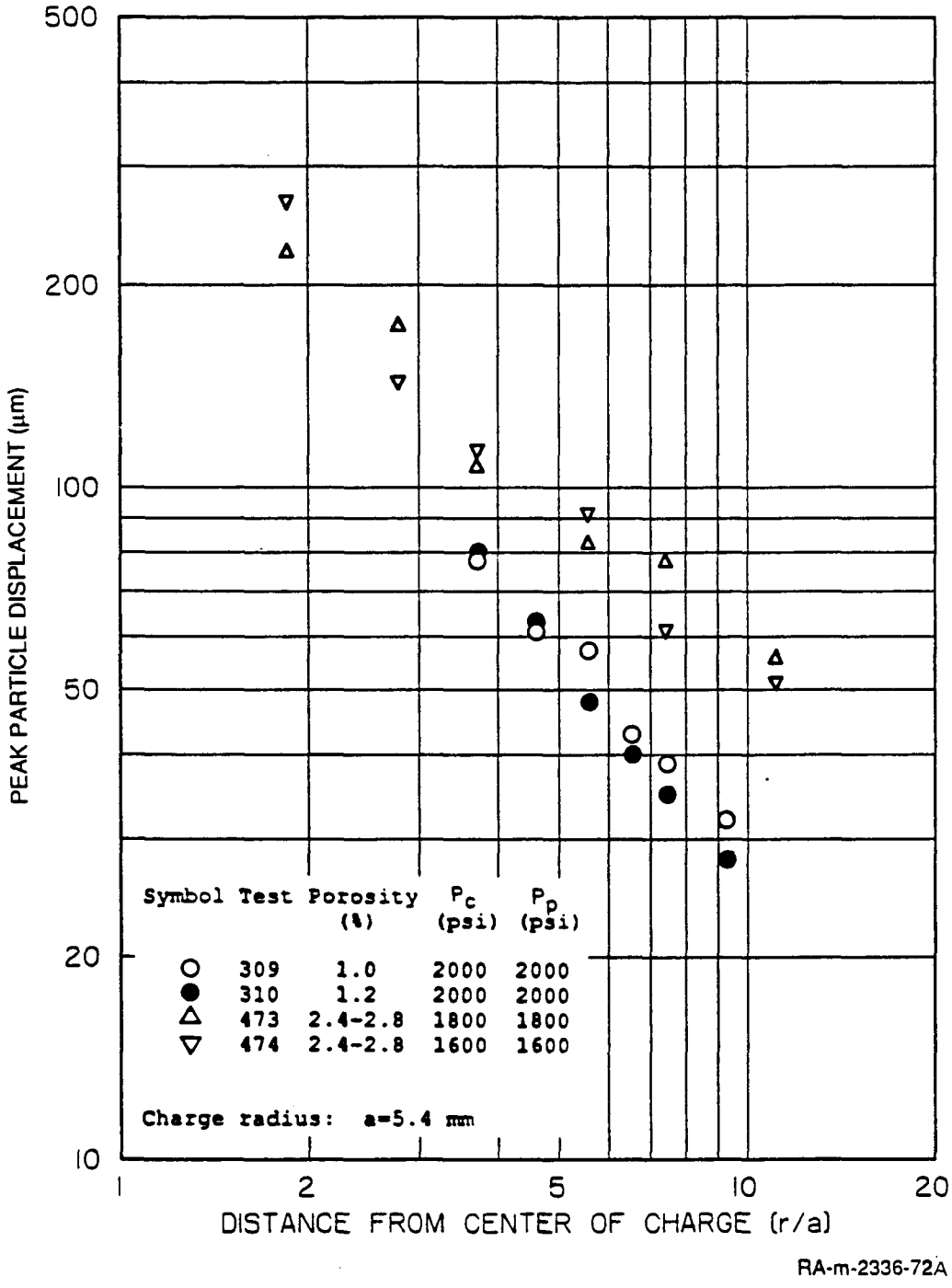

FIGURE 49 EFFECT OF POROSITY ON PEAK DISPLACEMENT ATTENUATION IN SATURATED SIERRA WHITE GRANITE WITH ZERO EFFECTIVE STRESS (CONFINING PRESSURE EQUAL TO PORE PRESSURE)

43), and widens the pulse (Figure 31). The pulse width increases from a factor of 2 near the source to a factor of 4 far from the source (Figures C-6 through C-11, Appendix C).

- Increasing the porosity from 1.0% to 2.5% significantly increases peak displacements due to the wider pulses and lowers peak displacement attenuation (Figures 37 an 49).

Influence of Effective Stress in High-Porosity Saturated Rock. The effects of increasing the effective stress from zero to nearly the confining stress (or decreasing the pore pressure to nearly zero) in high-porosity granite with the confining pressure held constant at 2000 psi are illustrated by the the velocity records of Figures 15 and 32, the displacement plot of Figure 38, and the attenuation plots of Figures 44 and 50. These comparisons show that at a given confinement (2000 psi), increasing the effective stress from zero

- Does not influence peak velocities except very near the source, where zero pore pressure produces a higher velocity (Figures 15 and 44).
- Causes narrower pulse widths in general, similar to those in the dry material (compare Figures 32 and 12). Very near the source (at the 1.0-cm location) this effect is not observed until the effective stress reaches the confining stress (zero pore pressure), (see Figure 15), which suggests that the influence of effective stress depends on the stress level (range).
- Reduces peak displacements by narrowing the pulses and increases peak displacement attenuation (Figures 38 and 50). However, the magnitude of these effects does not show a consistent dependance on the magnitude of the effective stress. In particular, these effects are caused mainly by a significant increase of the effective stress from zero, but an additional increase in the effective stress has negligible further effect (Figure 50).

Effect of Pore Water in High-Porosity Rock with Zero Pore Pressure. The influence of pore water alone in high porosity rock at two confining pressures (1000 and 2000 psi) is seen by comparing the records in dry rock with those in saturated rock with near zero pore pressure (effective stress equal to confining stress). The results, shown by the velocity plots of Figures 9 through 20 and 33, the displacement plots of

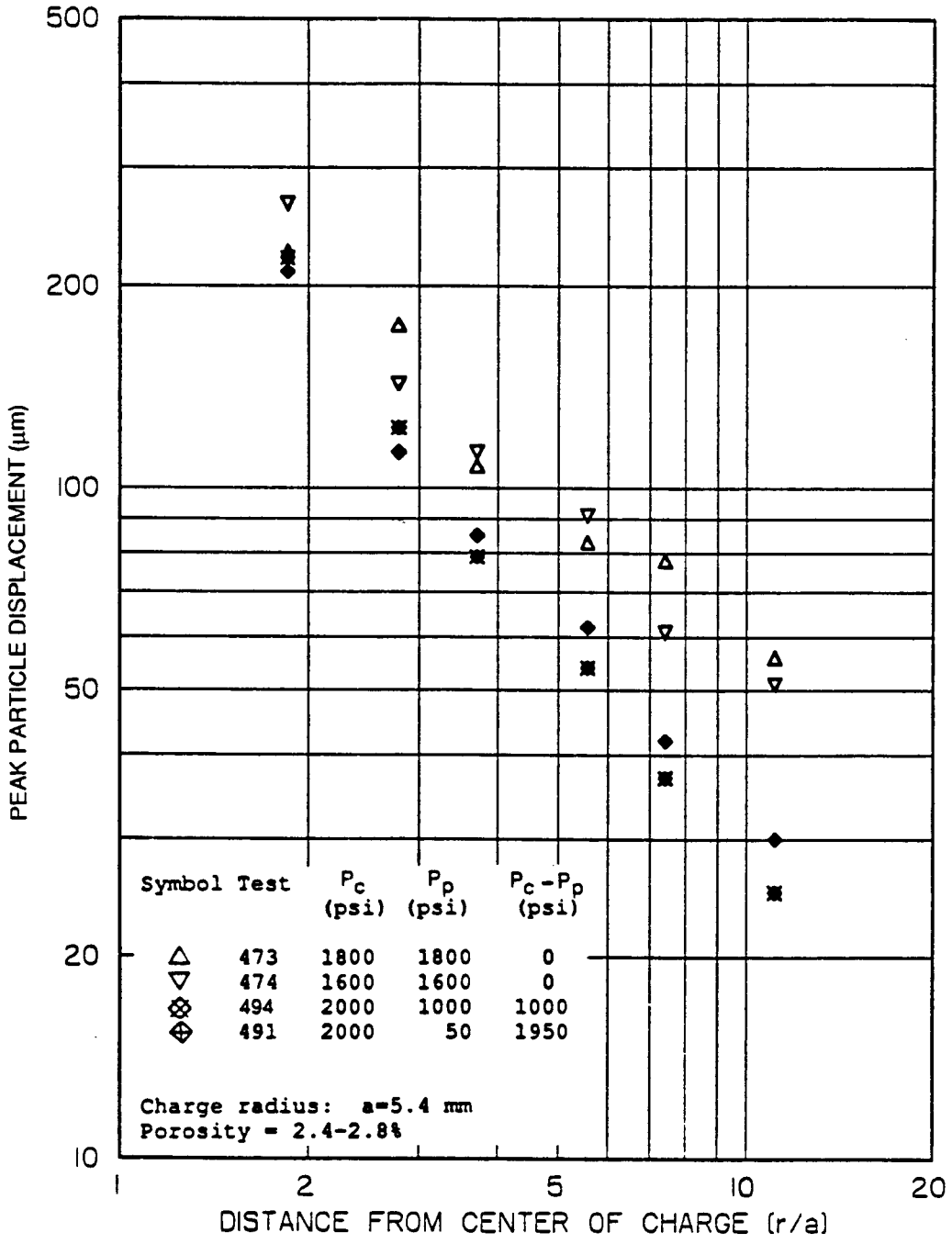

FIGURE 50 THE INFLUENCE OF EFFECTIVE STRESS ON PEAK DISPLACEMENT ATTENUATION IN GAS-FRACTURED, SATURATED SIERRA WHITE GRANITE WITH POROSITY OF 2.4-2.8%

Figures 22 through 25 and 39, and the attenuation plots of Figures 45 and 51, indicate the following:

- Pore water does not influence the peak velocities near the source, except for high confining pressure, which results in a high velocity at the nearest location (Figure 15), but causes higher velocities farther from the source and a corresponding decrease in peak velocity attenuation (Figure 45). Rise times are reduced by pore water for ranges greater than 2.0 cm (compare Figures 9 through 14 with Figures 15 through 20).
- Pore water causes a slight increase in pulse duration and pulse width next to the source at both confining stress levels, but not at greater ranges (compare Figures 9 and 10 with Figures 15 and 16, and see Figure 33).
- Pore water increases peak displacements at all ranges for high confinement and for regions far from the source for low confinement (Figure 51). Next to the source this increase is due primarily to wider pulses (Figures 9 and 15), except for Test 491 at the 1.0-cm location where the peak velocity is also higher than in the corresponding dry test (Test 485). Away from the source the higher peak displacements are due primarily to higher velocities (Figures 13, 14, 19, and 20).

Effect of Confinement in High-Porosity Saturated Rock with Constant Effective Stress. Comparison of the results for Tests 492 and 494 indicate that, at a given effective stress (1000 psi), an increase in confining pressure by a factor of two (from 1000 to 2000 psi) has a negligible effect on peak velocities (Figure 46) and causes only a slight reduction in peak displacements away from the source due to slightly narrower pulses (Figures 52, 34, and 40) although in the absence of repeat tests this effect may be within experimental scatter.

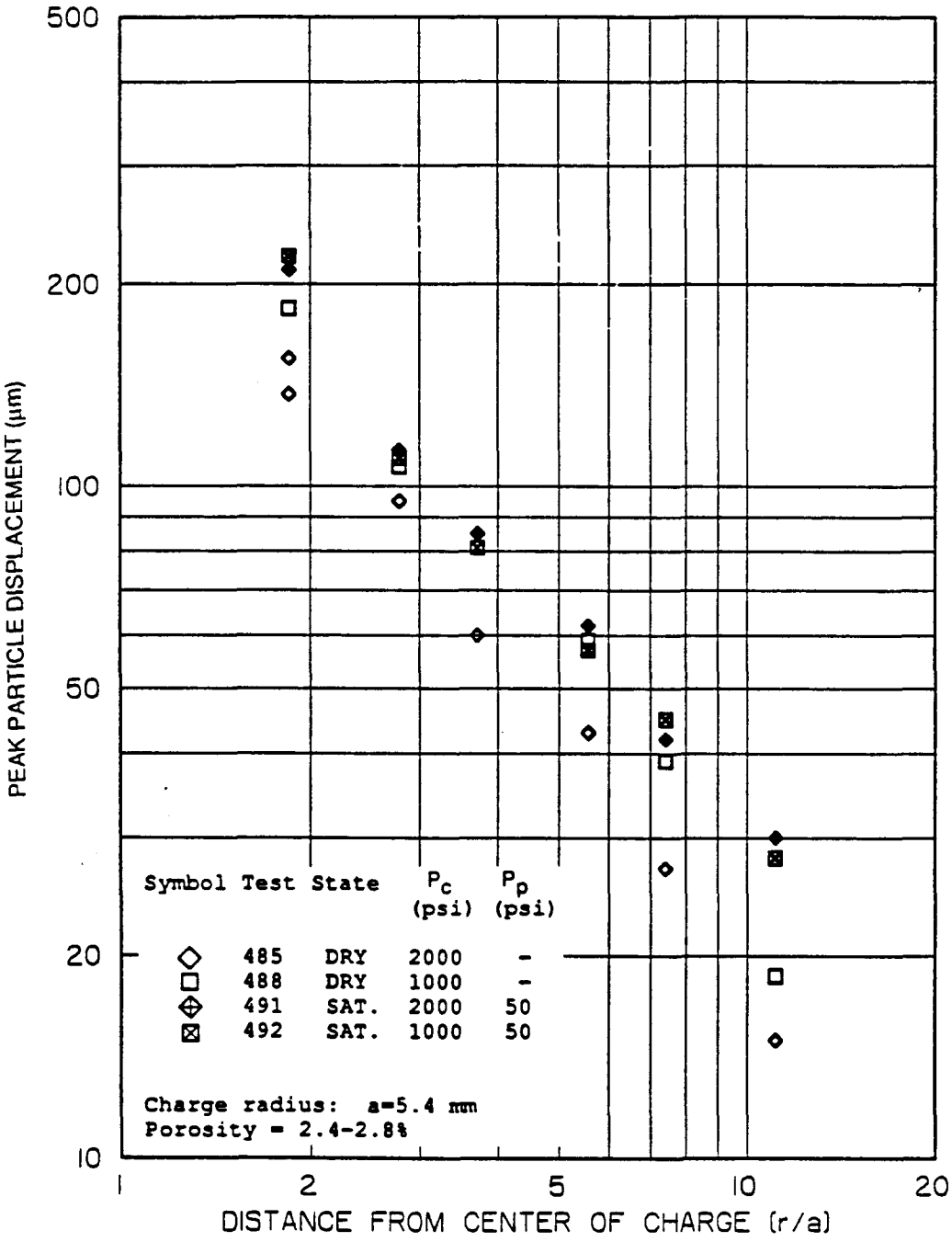

FIGURE 51 THE INFLUENCE OF PORE WATER ON PEAK DISPLACEMENT ATTENUATION IN GAS-FRACTURED SIERRA WHITE GRANITE WITH POROSITY OF 2.4-2.8%, AT TWO CONFINING PRESSURES WITH NEGLIGIBLE PORE PRESSURE

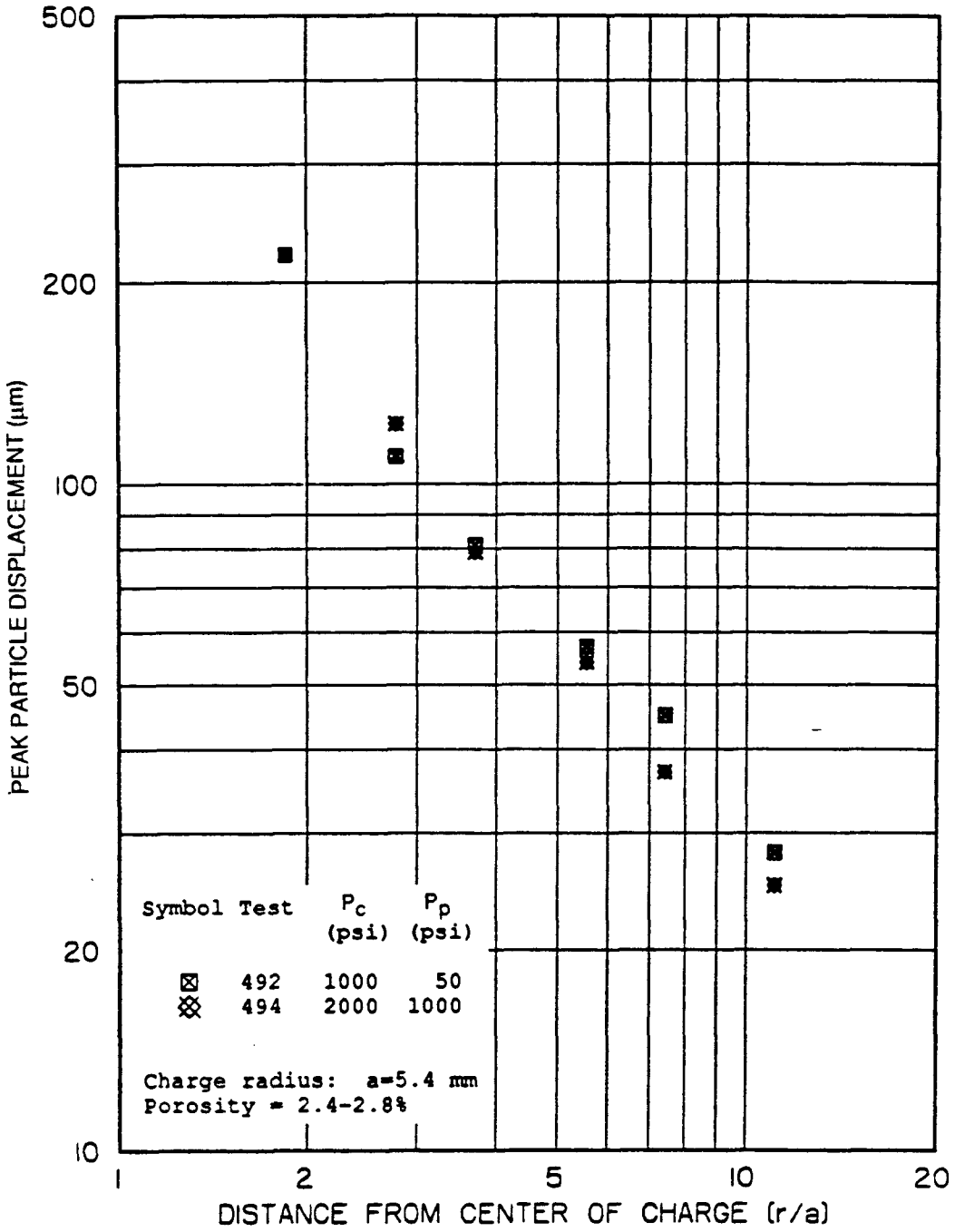

FIGURE 52 THE EFFECT OF CONFINING PRESSURE ON PEAK DISPLACMENT ATTENUATION IN GAS-FRACTURED, SATURATED SIERRA WHITE GRANITE WITH POROSITY OF 2.4-2.8% AND AN EFFECTIVE STRESS OF 1000 psi

REFERENCES

1. G. Nagy and A. L. Florence, "Spherical Wave Propagation in Low-Porosity Brittle Rocks," Draft Final Report, Contract DNA 001-85-C-0248, SRI International, Menlo Park, CA (May 1986).

2. G. Nagy and A. L. Florence, "Spherical Wave Propagation in Rocks," Draft Final Report, Contract DNA 002-83-C-0024, DARPA 4757, SRI International, Menlo Park, CA (May 1984).

3. J. C. Cizek and A. L. Florence, "Laboratory Investigation of Containment of Underground Explosions," Final Report DNA-TR-84-11, Contract DNA 002-83-C-0024, SRI International, Menlo Park, CA (December 1983).

4. G. Nagy and A. L. Florence, "Laboratory Investigation of Containment of Underground Explosions," Draft Final Report, Contract DNA 002-84-C-0010, SRI International, Menlo Park, CA (March 1985).

5. N. Rimer, J. L. Stevens, and K. H. Lie, "Effects of Pore Pressure and Fractures in Ground Motions in Granite," Draft Final Report, Contract DNA 001-85-C-0249, S-CUBED, La Jolla, CA (June 1986).

6. J. T. Cherry and N. Rimer, "Verification of the Effective Stress and Air Void Porosity Constitutive Models," Chapter IX in Proceedings of the Workshop on the Theoretical Foundations of Nonlinear Material Behavior, Edited by S. Nemat-Nasser, R. J. Asaro, and G. A. Hegemier, October 24-26, 1983 (Martin Nijhoff Publishers, Boston, 1984), 215-239.

7. J. T. Cherry and N. Rimer, "Verification of the Effective Stress and Air Void Porosity Constitutive Models," Topical Report SSS-R-82-5610 to DARPA, S-CUBED, La Jolla, CA (August 1982).

8. R. J. Martin, "Physical Properties of Sierra White Granite," Progress Report, Prepared for University of California, Lawrence Livermore National Laboratory, Livermore, CA, Contract 9092405, New England, Norwich, VT (February 1987).

9. Raymond Granite Co., Raymond, CA.

Appendix A

VOLUMETRIC STRAINS CALCULATED FROM PARTICLE VELOCITY RECORDS

Figures A-1 through A-5 show the volumetric strains obtained from the calculated particle displacements for Tests 485, 488, 491, 492, and 494. The curves represent average volumetric strains for regions between gages.

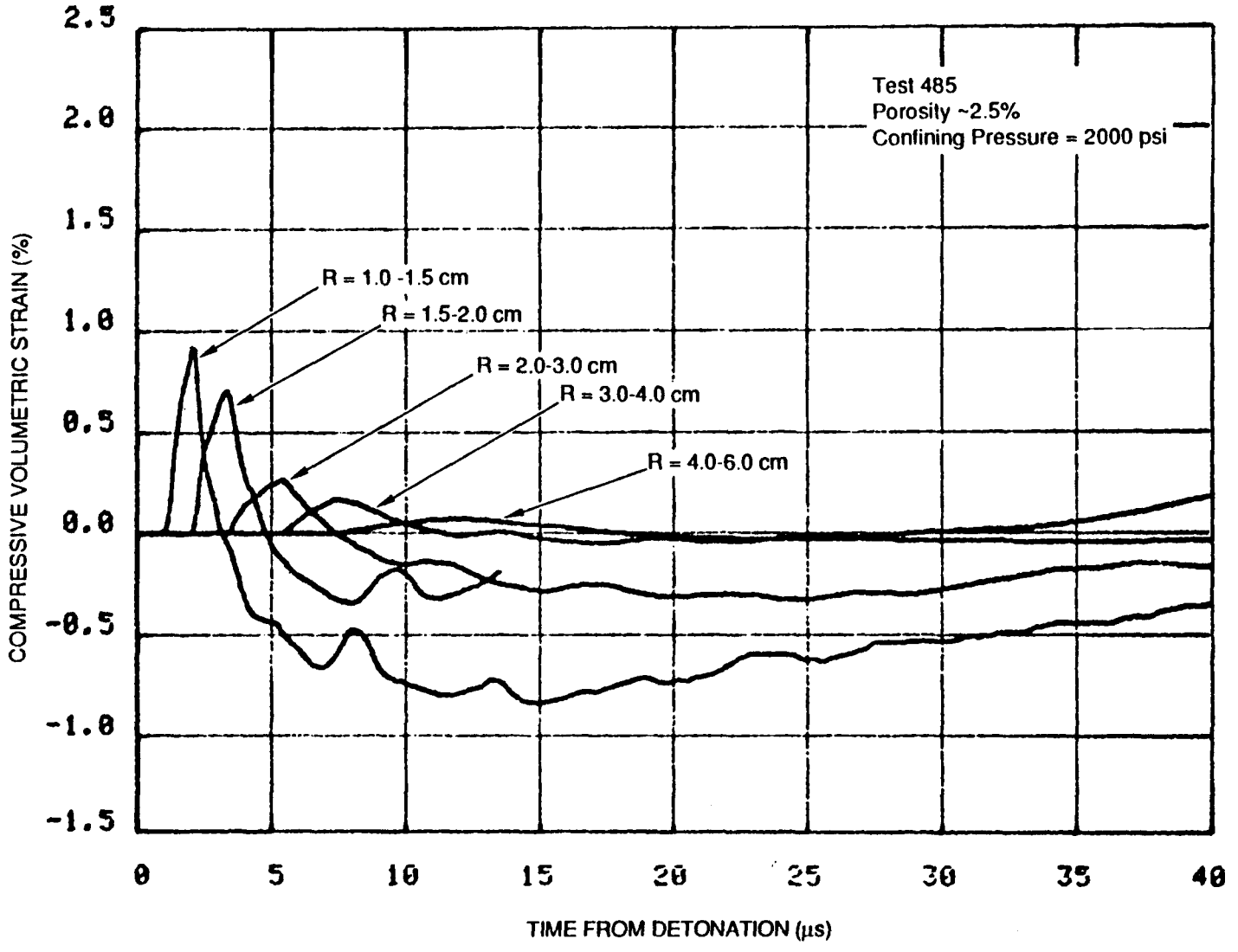

FIGURE A-1 VOLUMETRIC STRAIN OBTAINED FROM PARTICLE VELOCITIES IN FRACTURED/DRY SIERRA WHITE GRANITE, TEST 485

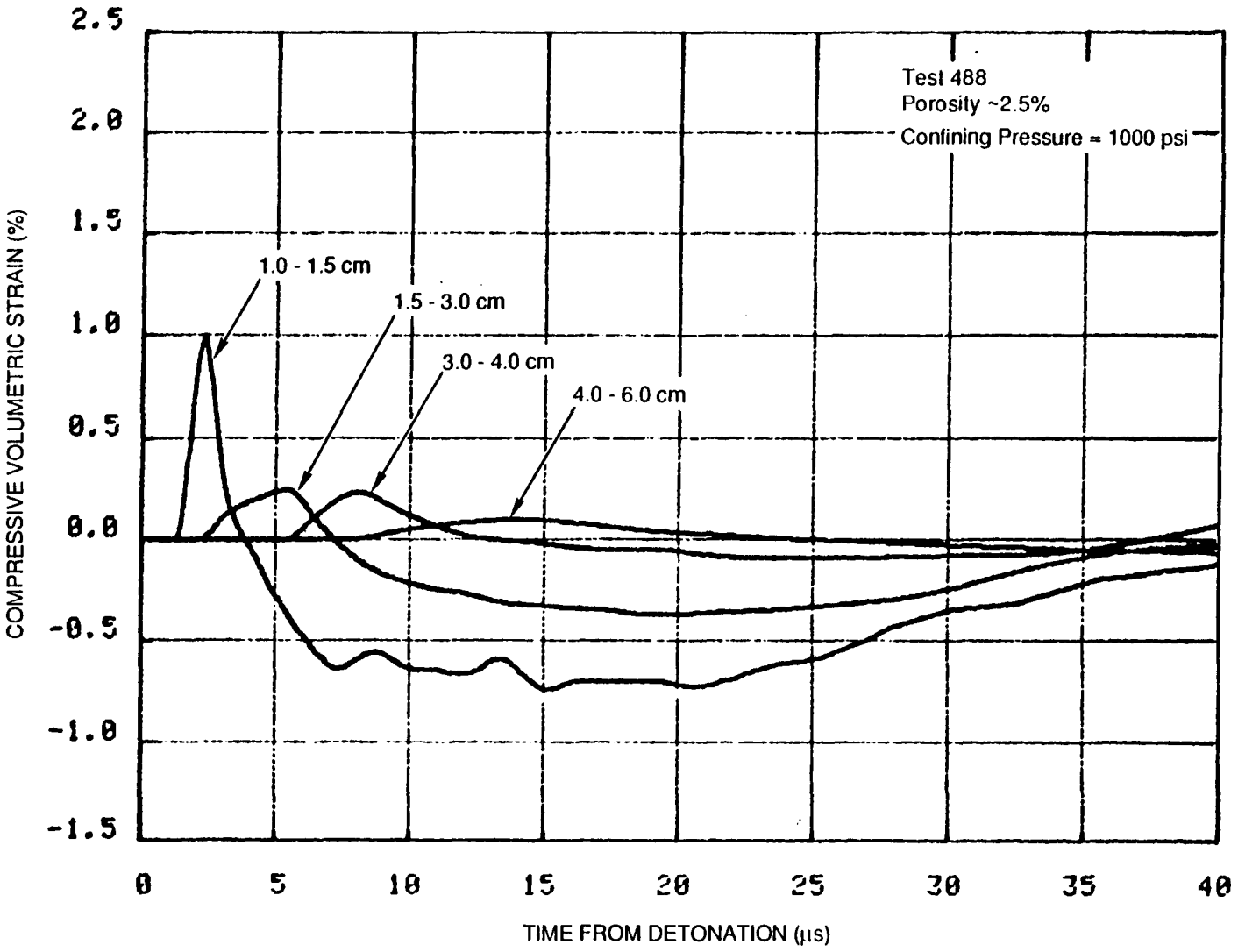

FIGURE A-2 VOLUMETRIC STRAIN OBTAINED FROM PARTICLE VELOCITIES IN FRACTURED/DRY SIERRA WHITE GRANITE, TEST 488

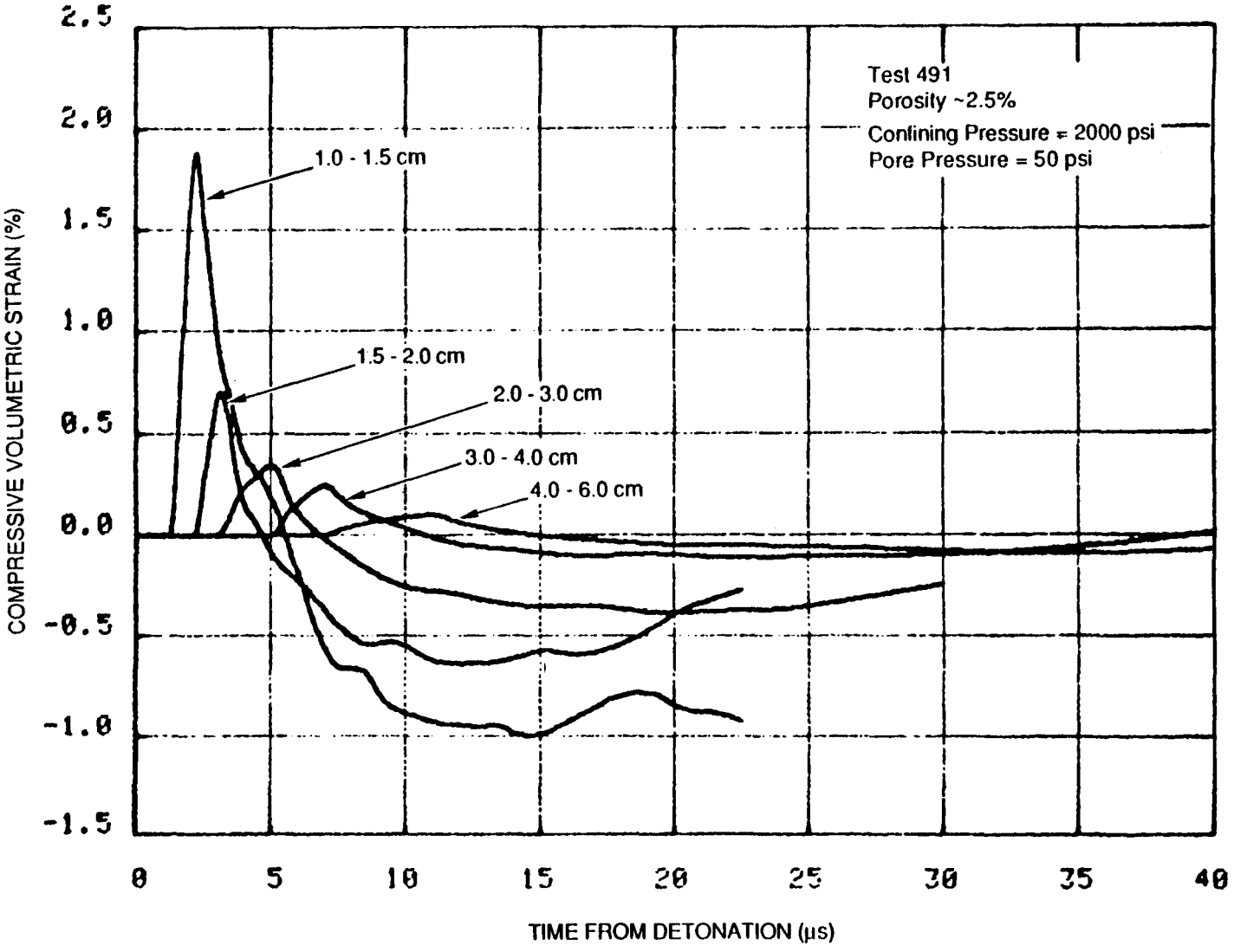

FIGURE A-3 VOLUMETRIC STRAIN OBTAINED FROM PARTICLE VELOCITIES IN FRACTURED/SATURATED SIERRA WHITE GRANITE, TEST 491

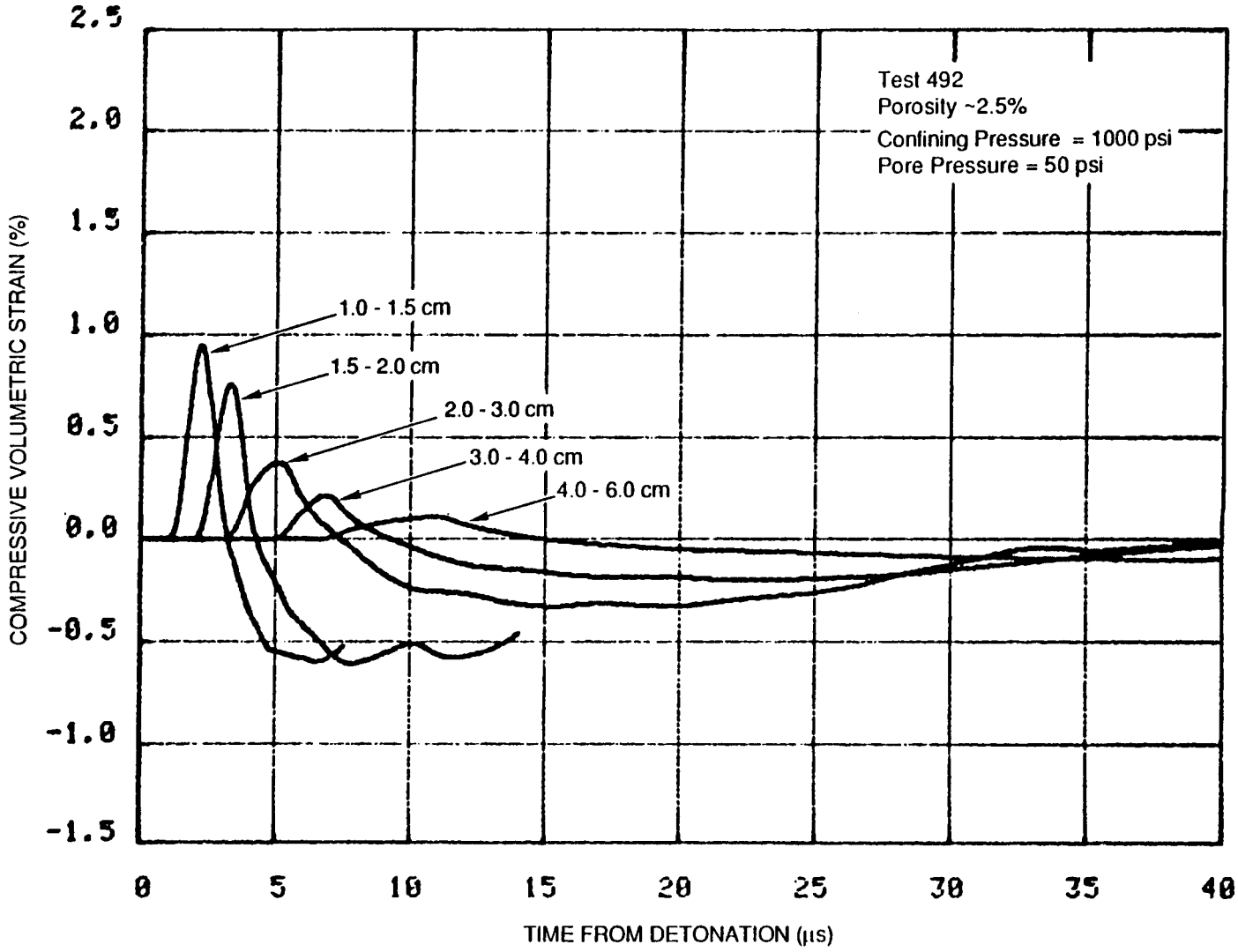

FIGURE A-4 VOLUMETRIC STRAIN OBTAINED FROM PARTICLE VELOCITIES IN FRACTURED/SATURATED SIERRA WHITE GRANITE, TEST 492

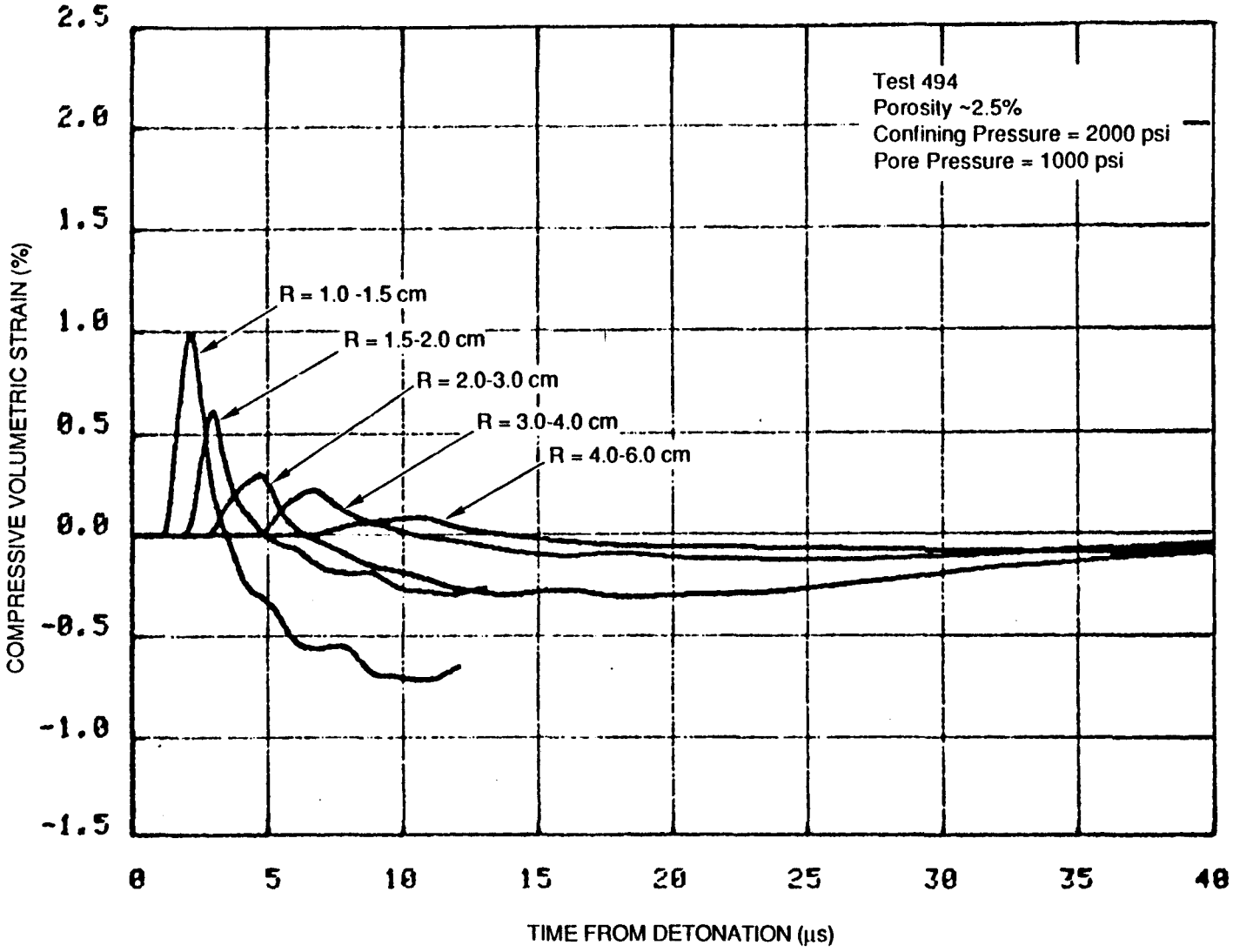

FIGURE A-5 VOLUMETRIC STRAIN OBTAINED FROM PARTICLE VELOCITIES IN FRACTURED/SATURATED SIERRA WHITE GRANITE, TEST 494

Appendix B

PEAK PARTICLE VELOCITIES AND DISPLACEMENTS FOR EXPERIMENTS IN HIGH POROSITY SIERRA WHITE GRANITE

Tables B-1 and B-2 summarize the peak velocities and displacements for all gas-fractured experiments with 2.4-2.9% porosity.

Table B-1

PEAK PARTICLE VELOCITIES IN GAS-FRACTURED SIERRA WHITE GRANITE[a] (m/s)

Test	Radial Gage Location (cm) 1.0	1.5	2.0	3.0	4.0	6.0
473	(125)	(80)	51	34	19	8.9
474	(140)	(75)	(60)	39	14.5	7.3
476	(180)	115	59	38	--	--
485	174,131	85	42	17	7.3	2.8
488	120	62	21	18.6	9.4	2.8
491	218	69	50	30	17	9.3
492	113	65	56	25	17	8
494	120	67	43	27.5	--	8

[a]Numbers in parentheses are approximate values.

Table B-2

PEAK PARTICLE DISPLACEMENTS IN GAS-FRACTURED SIERRA WHITE GRANITE[a] (μm)

Test	Radial Gage Location (cm) 1.0	1.5	2.0	3.0	4.0	6.0
473	225	175	108	83	78	56
474	265	143	113	91	61	51
476	145	95	65	44	--	--
485	137,155	85	60	43	27	15
488	184	107	--	59	39	18.7
491	(210)	113	85	62	42	30
492	(220)	110	81	57	45	28
494	220	123	79	54	37	25

[a]Numbers in parentheses are approximate values.

Appendix C

VELOCITY RECORDS FROM EARLIER INVESTIGATIONS TESTS 476, 308, 309, AND 310

Figures C-1 through C-5 show the particle velocity records obtained at radii 1.0, 1.5, 2.0, 3.0, 4.0, and 6.0 cm from the source center in gas-fractured dry Sierra White granite, Test 476. Figures C-6 through C-8 show the velocity records in gas-fractured saturated samples at 1.0, 3.0, and 6.0 cm, Tests 473 and 474. Figures C-9 through C-11 show the velocity records at the 2.0, 3.0, and 5.0 cm location in thermally fractured dry granite, Test 308, and intact and thermally fractured saturated granite, Tests 309 and 310.

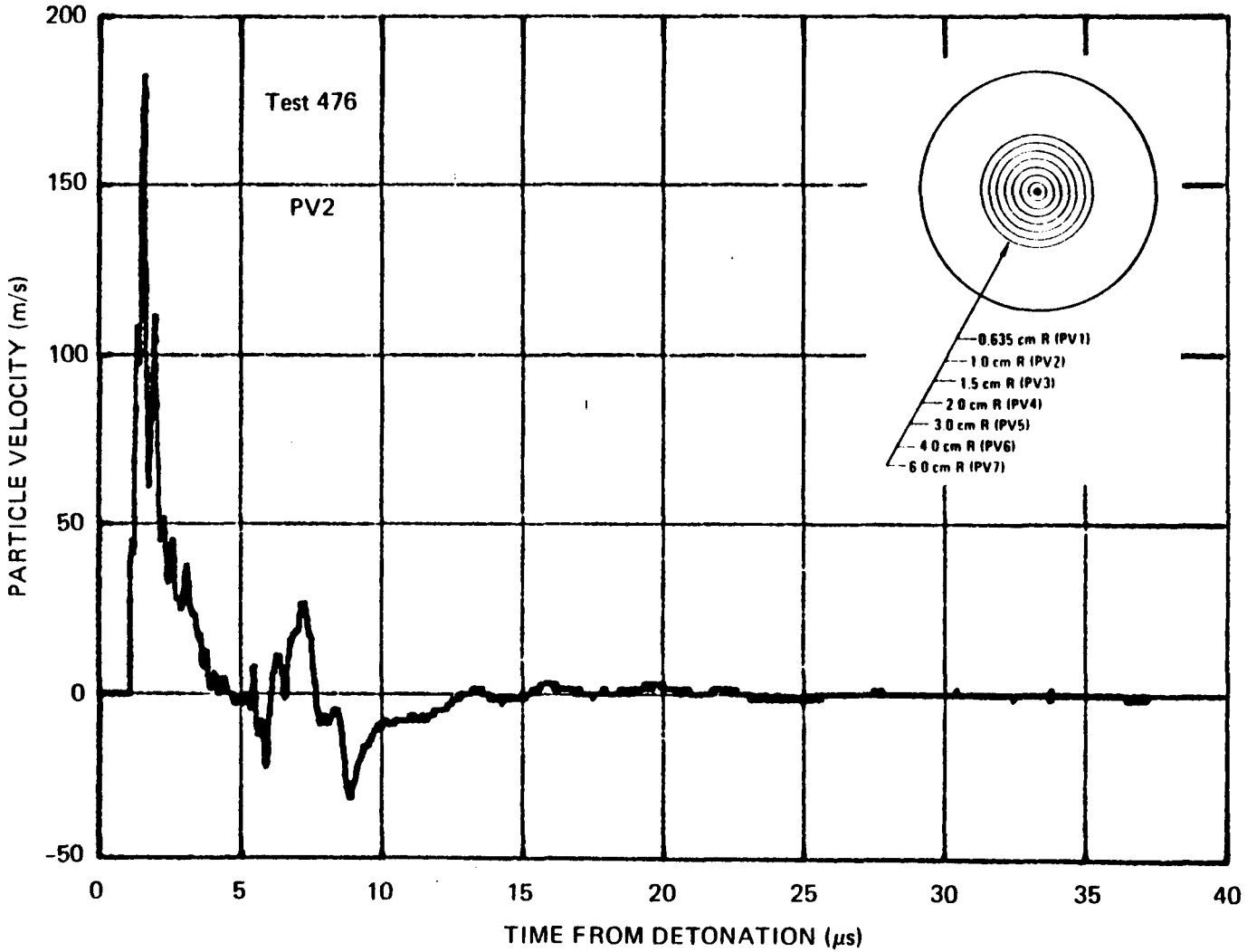

FIGURE C-1 PARTICLE VELOCITY 1.0 cm FROM CENTER OF COUPLED EXPLOSION IN FRACTURED/DRY SIERRA WHITE GRANITE, TEST 476

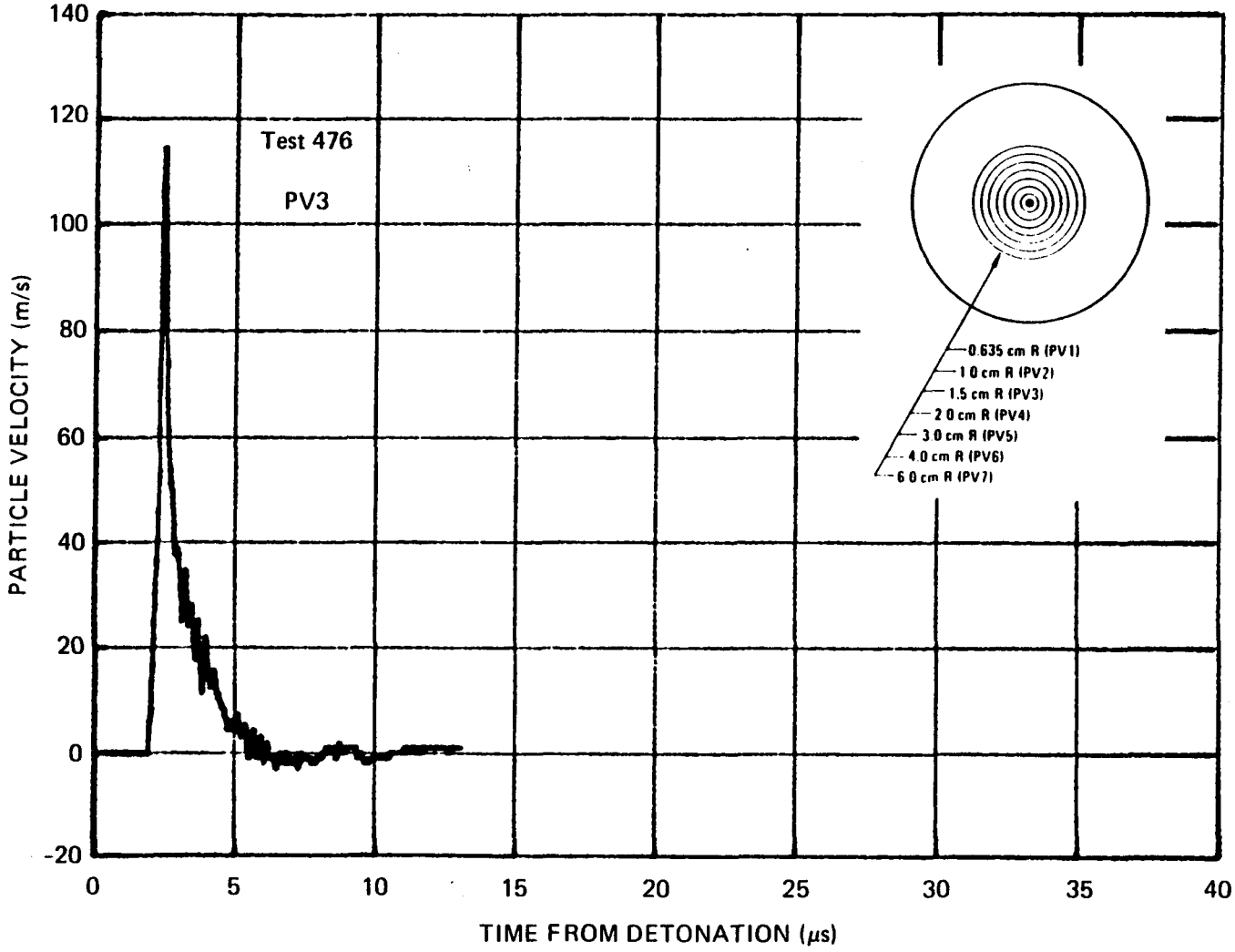

FIGURE C-2 PARTICLE VELOCITY 1.5 cm FROM CENTER OF COUPLED EXPLOSION IN FRACTURED/DRY SIERRA WHITE GRANITE, TEST 476

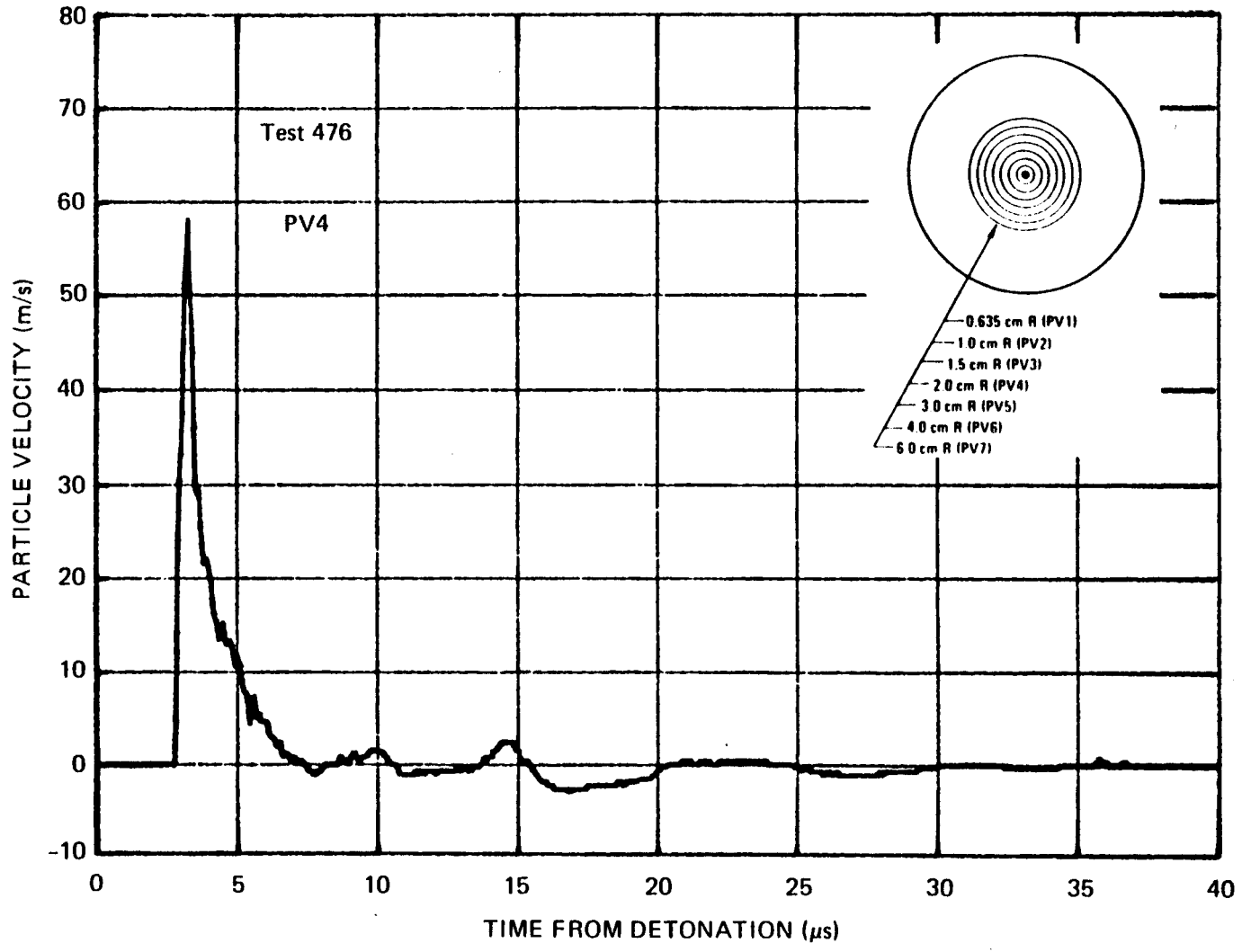

FIGURE C-3 PARTICLE VELOCITY 2.0 cm FROM CENTER OF COUPLED EXPLOSION IN FRACTURED/DRY SIERRA WHITE GRANITE, TEST 476

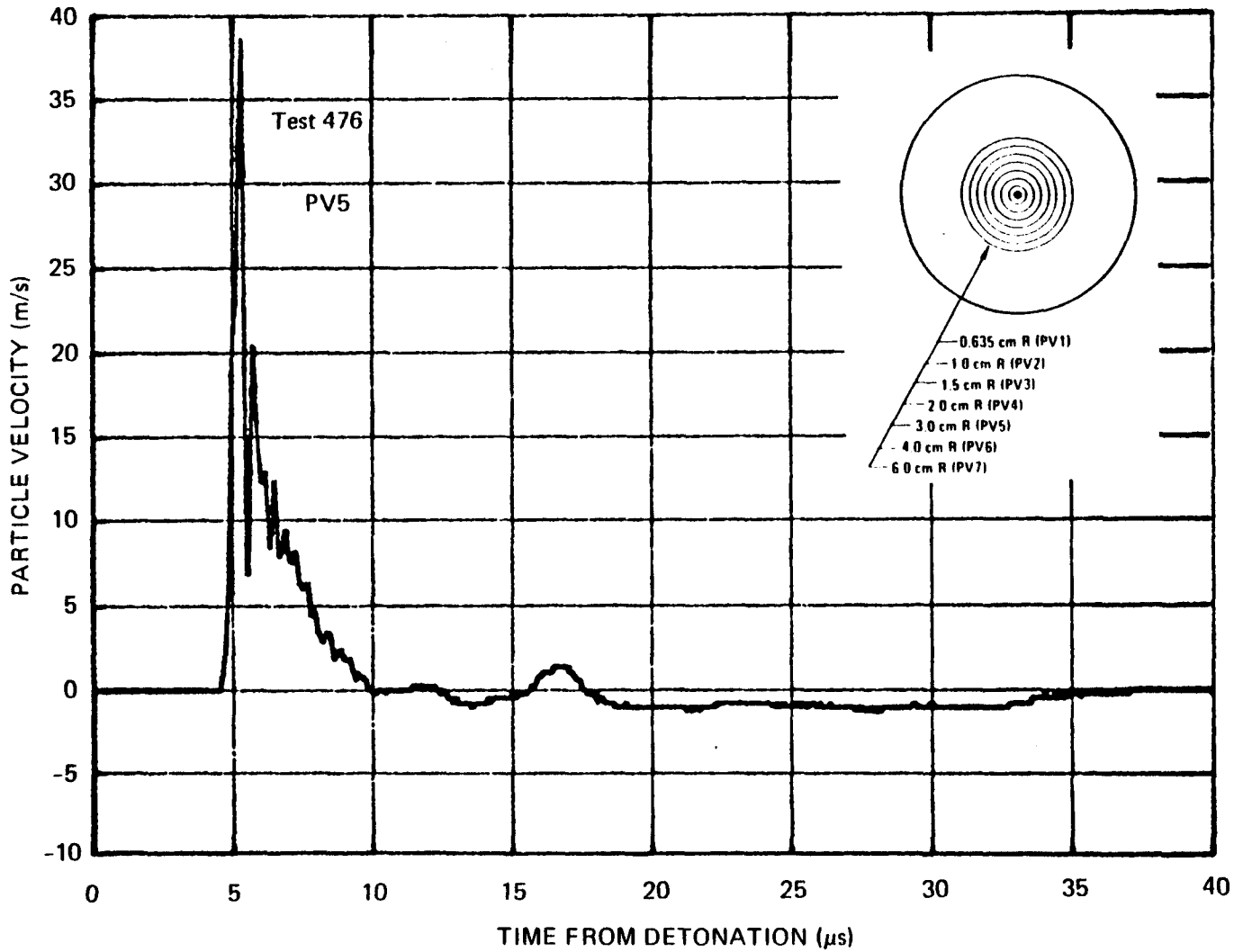

FIGURE C-4 PARTICLE VELOCITY 3.0 cm FROM CENTER OF COUPLED EXPLOSION IN FRACTURED/DRY SIERRA WHITE GRANITE, TEST 476

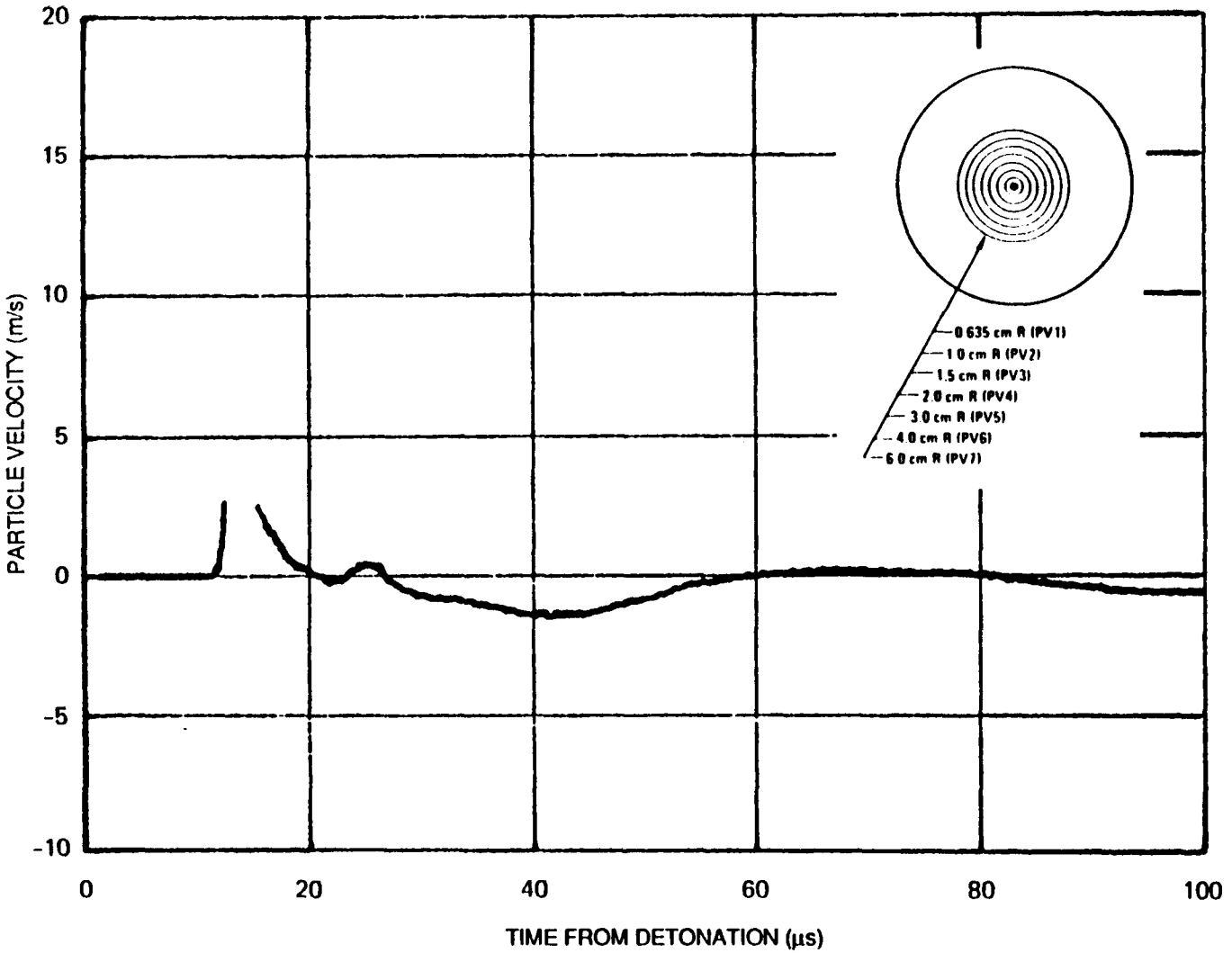

FIGURE C-5 PARTICLE VELOCITY 6.0 cm FROM CENTER OF COUPLED EXPLOSION IN FRACTURED/DRY SIERRA WHITE GRANITE, LONG TIME WINDOW, TEST 476

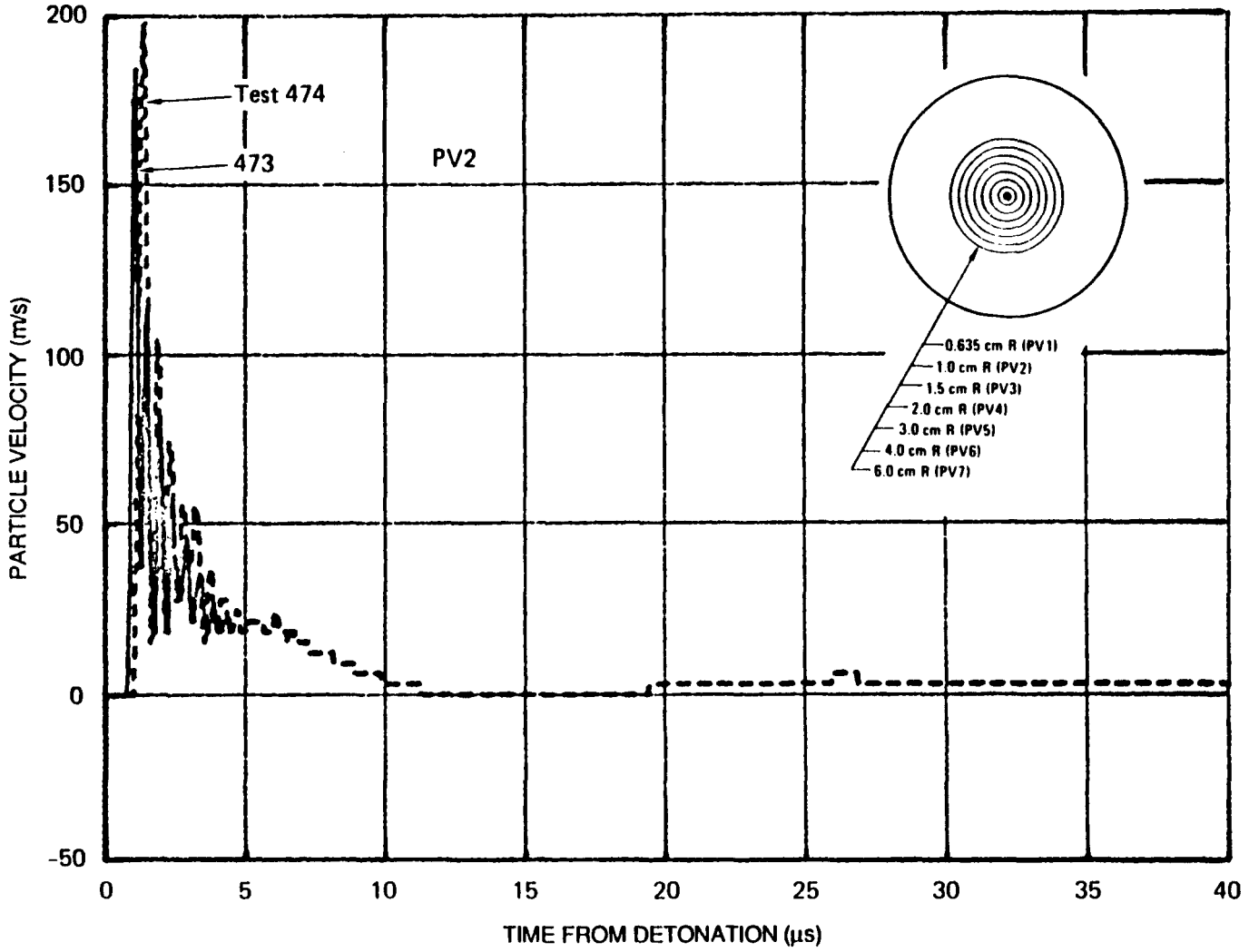

FIGURE C-6 PARTICLE VELOCITY 1.0 cm FROM CENTER OF COUPLED EXPLOSION IN FRACTURED/ SATURATED SIERRA WHITE GRANITE

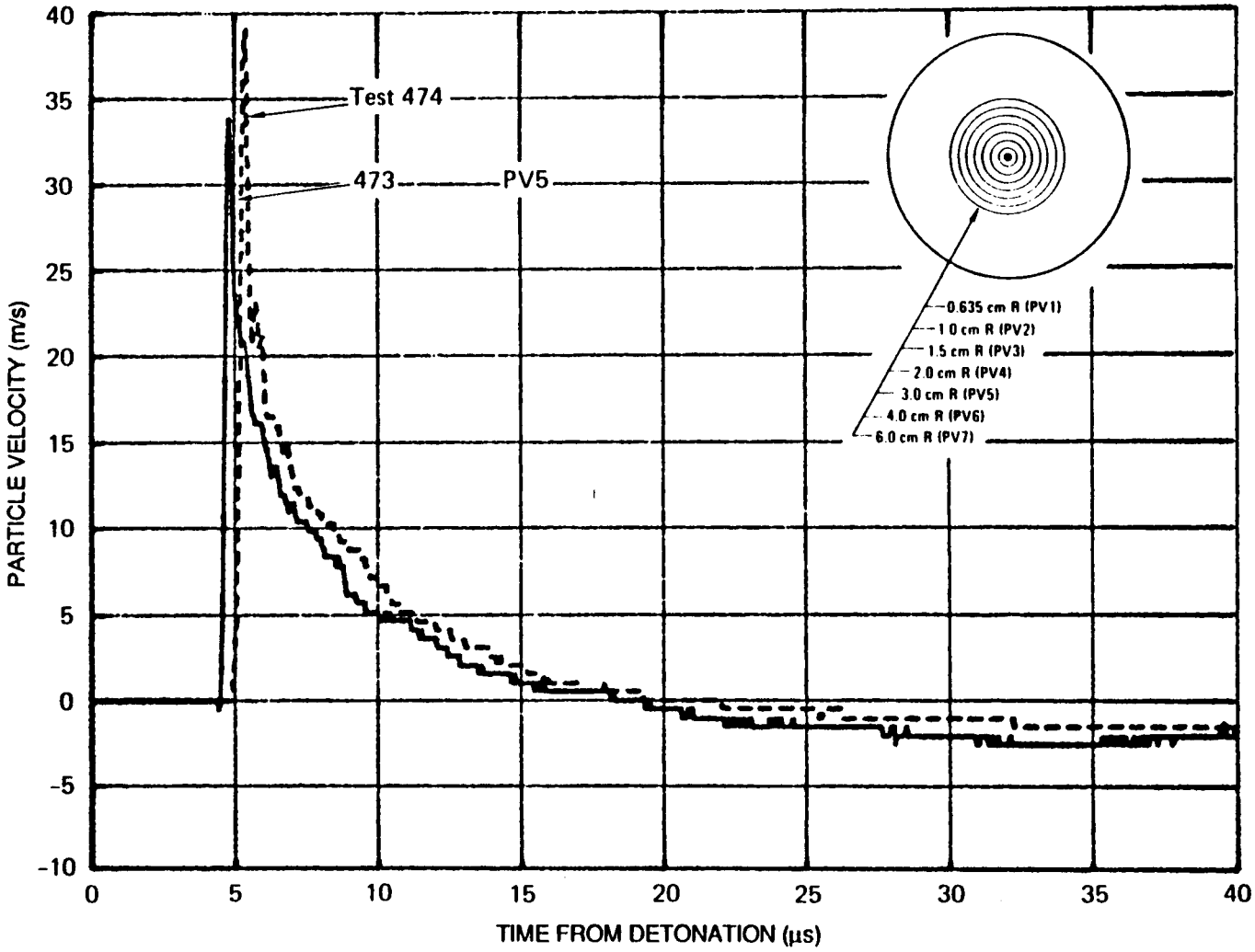

JA-8400-26

FIGURE C-7 PARTICLE VELOCITY 3.0 cm FROM CENTER OF COUPLED EXPLOSION IN FRACTURED/ SATURATED SIERRA WHITE GRANITE

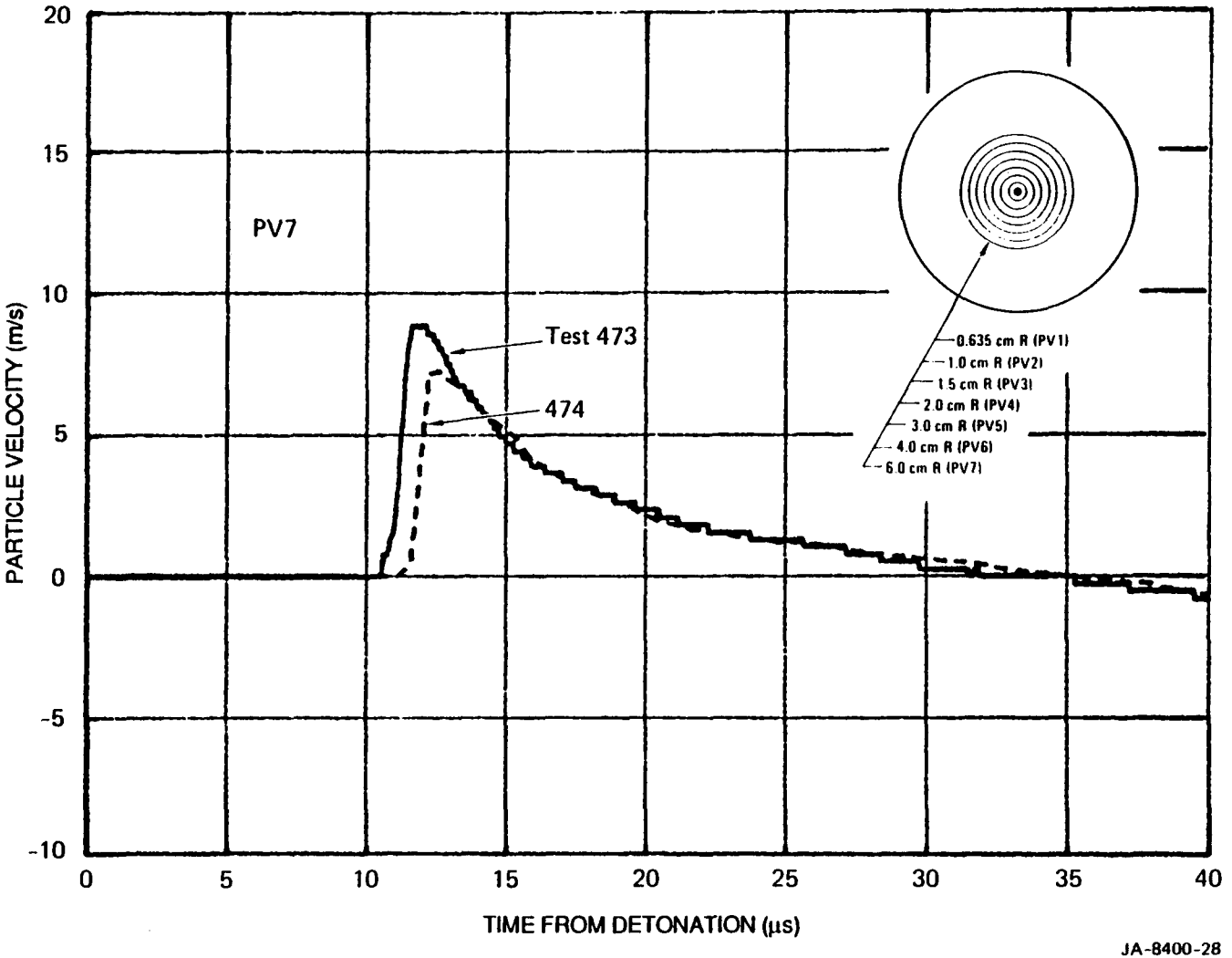

FIGURE C-8 PARTICLE VELOCITY 6.0 cm FROM CENTER OF COUPLED EXPLOSION IN FRACTURED/ SATURATED SIERRA WHITE GRANITE

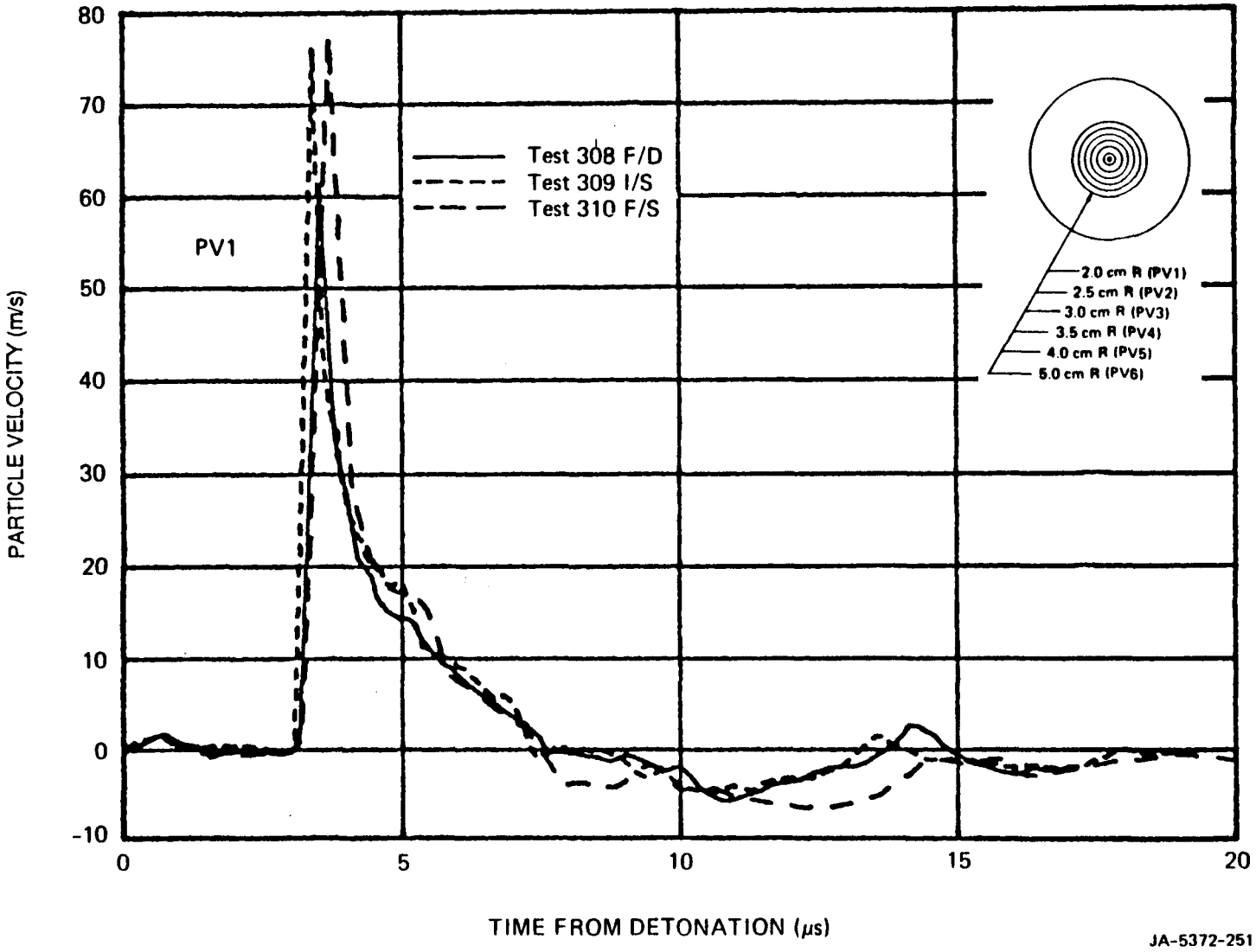

FIGURE C-9 PARTICLE VELOCITY 2.0 cm FROM CENTER OF COUPLED EXPLOSION IN FRACTURED/DRY, INTACT/SATURATED, AND FRACTURED/SATURATED SIERRA WHITE GRANITE, WITH FRACTURED POROSITY OF 1.2%

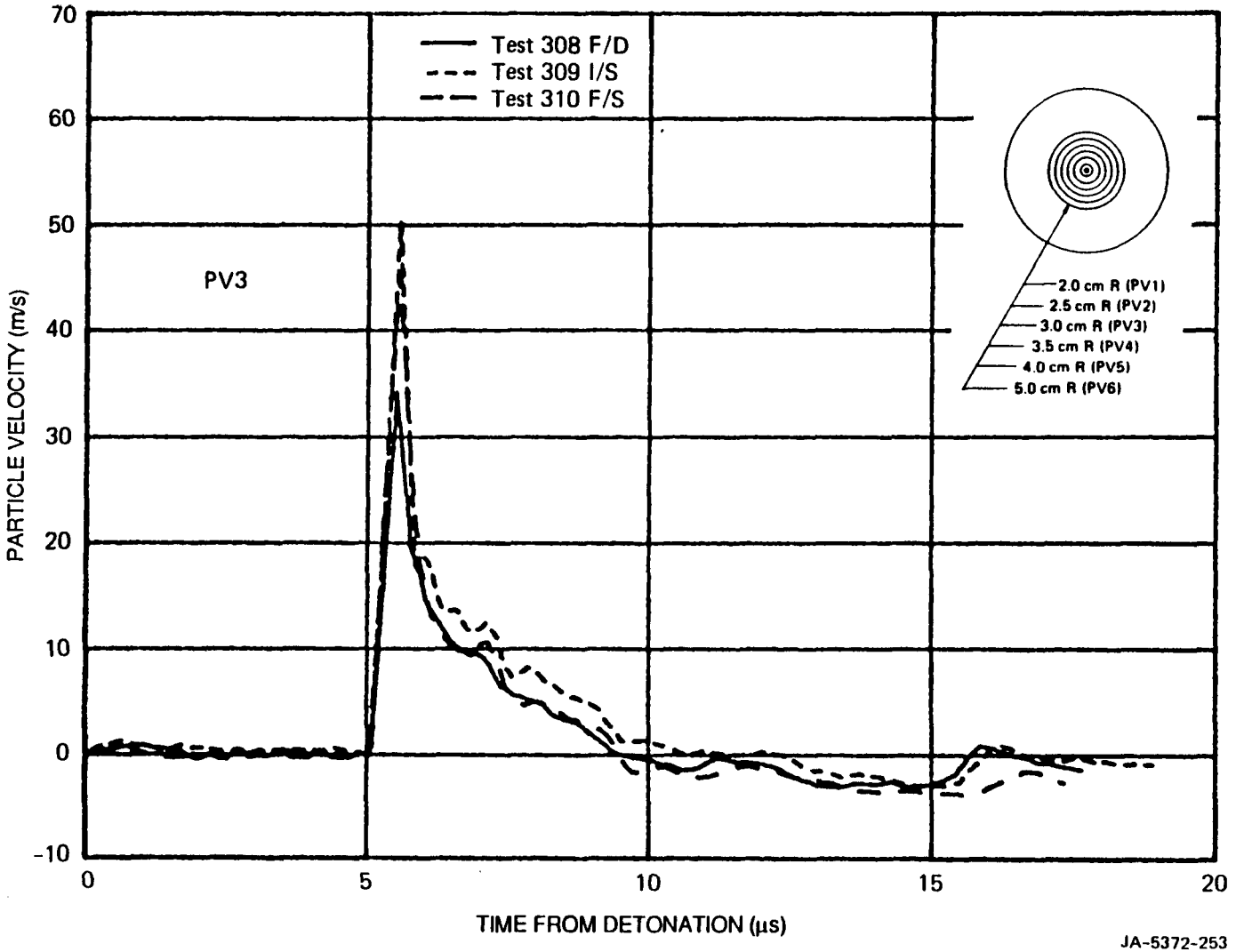

FIGURE C-10 PARTICLE VELOCITY 3.0 cm FROM CENTER OF COUPLED EXPLOSION IN FRACTURED/DRY, INTACT/SATURATED, AND FRACTURED/SATURATED SIERRA WHITE GRANITE, WITH FRACTURED POROSITY OF 1.2%

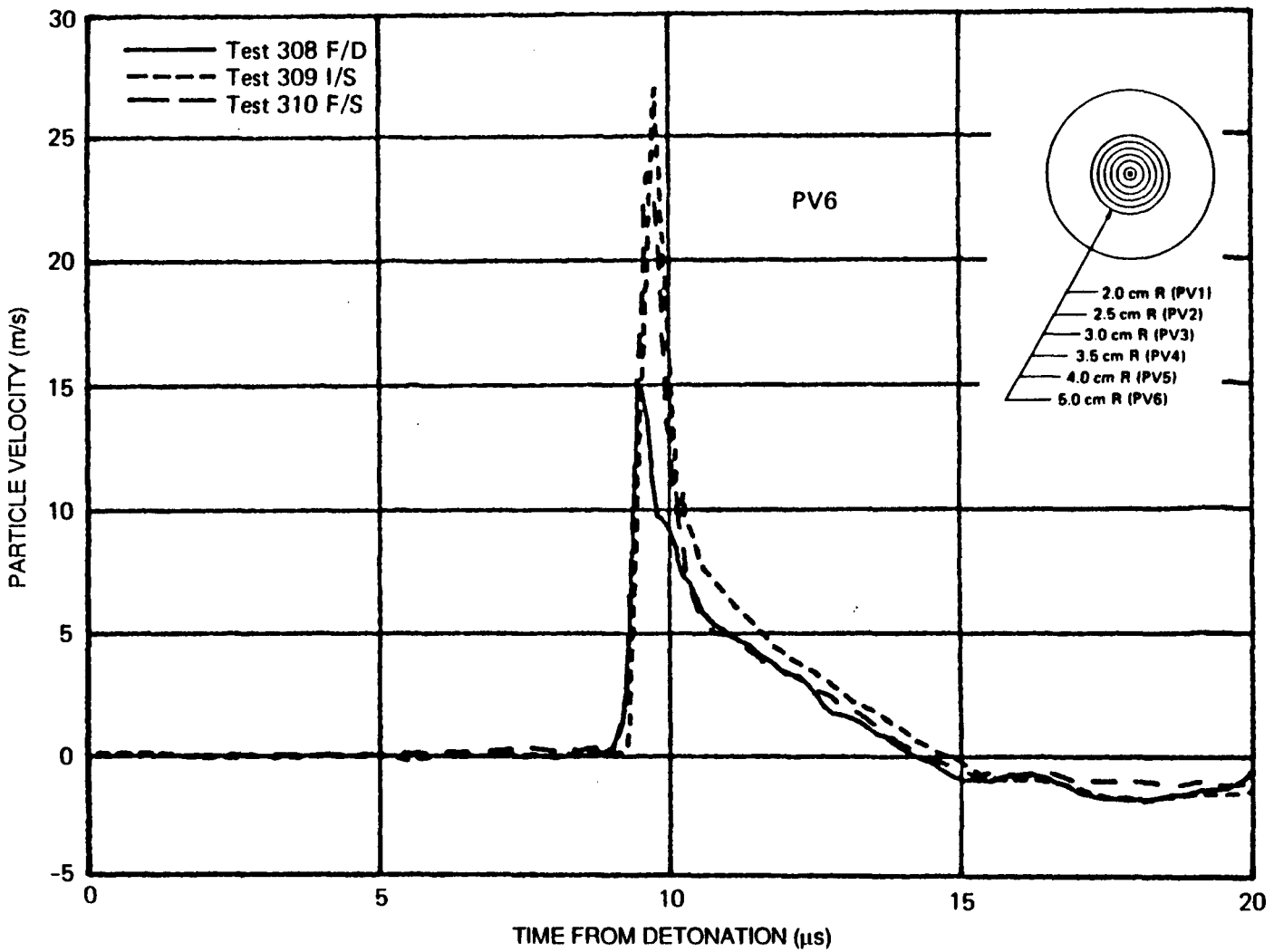

FIGURE C-11 PARTICLE VELOCITY 5.0 cm FROM CENTER OF COUPLED EXPLOSION IN FRACTURED/DRY, INTACT/SATURATED, AND FRACTURED/SATURATED SIERRA WHITE GRANITE, WITH FRACTURED POROSITY OF 1.2%

Appendix D

MATERIAL PROPERTIES FOR SIERRA WHITE GRANITE

In this section we present some basic physical properties for Sierra White granite.

Composition: 74% silica, 15% alumina, 2% iron oxides, 3% limes, 5% soda and potash, 0.3% combined water.

Connected porosity:

Intact:	0.8-1.0%
Thermally fractured:	1.2%
Gas fractured:	2.4-2.9% (SRI measurements on large samples)
	2.1-2.3% (NER measurements on small samples)

Dry bulk density: 2.64 g/cc

EFFECTIVE STRESS IN SOLIDS OF LOW POROSITY: CRACKED GRANITE

John G. Trulio

12 January 1988

APPLIED THEORY, INC.

930 South La Brea Avenue
Los Angeles, California 90036

EFFECTIVE STRESS IN SOLIDS OF LOW POROSITY: CRACKED GRANITE

Motions driven by charges of chemical explosive in granite cylinders have been measured in a recent series of laboratory experiments.[1] Intact (.8% porosity) and artificially cracked samples (up to 2.6% porosity) were so loaded, both dry and fully saturated. In the resulting nearly-spherical fields, peak radial displacement varied little (order of 10%) from case to case, except at the highest water contents. Relative to values for dry spheres, peak displacement then increased by a factor ϕ that grew with range, reaching $\sim 3\frac{1}{2}$ at the farthest ranges monitored ($\sim$11 charge radii), provided that pore pressure P_f was set equal initially to confining pressure. With P_f at half the confining pressure, ϕ dropped to 2.0 (and to 1.7 at $P_f \approx 0$).

These results mesh well with effective-stress theory, in a form that applies to solids of low porosity. The equations to which the theory then leads, taken with independent measurements of the strength and compressibility of dry cracked granite,[2] and of the compressibilities of water and intact granite, predict large decreases in strength in the cases where ϕ is large. Otherwise, they do not; indeed, they have the physically sensible - and observed - consequence that, as the porosity of saturated solid tends to zero, so in general do its effects on strength. They also suggest that the peak-displacement-increase factor ϕ should grow as mean stress drops, in keeping with experiment. It remains (a) to add the equations in question to material models, for numerical simulation of, and comparison with, measured motion in cracked granite, and (b) to compare the equations' predictions with quasistatic measurements of strength (as yet not made) in saturated rocks of low porosity.

1. Elements of the Model The solid portion of a cracked rock we term its "skeleton." The cracks are assumed simply connected, with the mean distance between crack surfaces in any direction small relative to sample dimensions. Intact rock between successive cracks forms the skeleton's "bones."[3] Subscripts k, s and f, respectively, refer uniformly herein to the three elements noted: skeleton, solid bones, and crack-filling fluid.

Emphasis here falls on changes in shear strength due to quasistatic hydrostatic compression. At a microscopic level - bone by bone - such compression is plainly non-hydrostatic and hugely complex. Hence, in that detail, the static equilibrium equations can't be solved for the stress and deformation produced by a given pressure on the sample's surface. Instead, the effective-stress concept is applied at macro-level, through simplifying assumptions (as usual):

(a) Loaded hydrostatically, the skeleton - dry or saturated - develops a mean stress P_k and volume strain Δ_k that are related by the formula

$$P_k = K(\Delta_k) \tag{1}$$

(b) In bulk or in the skeleton's cracks, the fluid has a pressure P_f and volume strain Δ_f that satisfy the relation

$$P_f = F(\Delta_f) \tag{2}$$

(c) Dry or wet, bone-solid responds hydrostatically to hydrostatic loads on the sample, and its mean stress P_s and volume strain Δ_s obey the rule that

$$P_s = S(\Delta_s) \tag{3}$$

(d) The skeleton's shear strength is determined by its mean stress P_k, and does not change with saturation.

(e) The sample's shear strength is just the strength of its skeleton.

Assumption (d) accords roughly with observation, though wetness alters strength somewhat and the third stress-invariant can affect it a good deal. Also, assumption (e) is quite realistic, and departures from (b) are ignorable except (perhaps) in thin sheets of fluid. Further, (a) and (c) make physical sense only for isotropic skeletons; moreover, since much the largest effects of saturation (when they <u>are</u> large) stem from (a) and (c), they will now be scrutinized.

2. <u>Skeleton, Bones, Fluid: Interacting Compressions, and Strength</u>

Assumptions (a) and (c) lend real bite to effective stress theory because the mechanical properties of the three model-elements (skeleton, bones, fluid)

all differ. As the prime example, the compressibility of bone-solid (often negligible, but not here), is smaller than that of the skeleton, which in turn runs from values far below water's, to well above. Further, over applied pressures of interest here, the skeleton's compressibility varies greatly and water's somewhat; that of the bones is almost constant. In all cases, however, the total pressure fixed quasistatically on the sample is balanced by a combination of fluid pressure and the skeleton's mean stress. Taking the bones as incompressible for the moment, most of the applied load and its changes will be borne by the fluid if the skeleton is the easier of the two to compress. For, with the fluid harder to compress, changes in the saturated skeleton's volume for a given change in load will be smaller than if the skeleton were dry. So, therefore, will changes in the skeleton's mean stress P_k, and hence in the sample's strength [assumptions (d) and (e)]. Likewise, if the fluid is more compressible than the skeleton, then increases in applied pressure will be borne mainly by the skeleton, whose volume changes - and hence changes in mean stress and strength - will approach those of its dry state. In sum, i) the skeleton's mean stress P_k (more generally its stress tensor) controls the sample's strength, ii) changes in frictional stress made by wetting bone-interfaces are a secondary matter, and iii) the relation between P_k and total applied pressure P can change drastically with saturation. Those are the key insights supplied by effective stress theory, whose effective (strength-setting) stress is P_k.

To the extent that bones compress, fluid has more space to fill, bears less (or no more) of the applied load, and hence has reduced effect on sample-strength. Bone compression is simplest in liquefied states; surrounded by fluid, each bone acquires both a uniform mean stress equal to the fluid's pressure ($P_s=P_f$) and the volume strain that mean stress implies [Eq. (3)]. Next, in sand skeletons, fluid all but surrounds each bone (sand grain), and should force its pressure almost evenly through each. A given bone, however, touches others over a small fraction of its surface; indeed, stress concentrations at contact-spots distribute the skeleton's pressure P_k among the bones. That distribution will be far from hydrostatic for any one bone, unless it contacts others at many well-scattered spots. Thus, in compressing the whole skeleton, some work serves not to compress its bones,[4] but to deform them. Hence, to assume that the skeleton's pressure P_k enters the bones as a hydrostatic load is to overestimate their compressions and the fluid's volume (for some details, see section 6) - and therefore to understate the fluid's effect on the strength of the sample. Likewise, that effect is overstated on assuming that skeletal pressure P_k causes no compression of the

bones (just distortion). Both limiting assumptions are explored in about equal detail below because, at low porosities, small fractional changes in bone-volume translate to much larger fractions of fluid volume (the amplification factor is the ratio, for the sample, of the solid's volume to the fluid's). Specifically:

$$P_s = \begin{cases} P_f + P_k \\ \quad \text{or} \\ P_f \end{cases} \qquad (4)$$

Contact spots simply-connect the skeleton, and hence preclude enclosing solid with a surface that lies entirely in fluid. Skeletal pressure derives therefrom: When a load is applied to the sample over a closed surface, part of it must be delivered directly to solid. Realistically (section 3), the lower the porosity, the larger that solid part tends to be. For a given porosity, however, its precise measure varies widely with crack geometry. So, therefore, do departures from hydrostatic loading of bones by pore-fluid - and again the physical trend is toward larger departures at lower porosities (the limit at issue). Thus, with only part of any closed surface passing through fluid, the mean stress P_f' that fluid causes at a point inside a bone is generally smaller than the fluid pressure P_f. So, therefore, is the complement that fluid adds onto the skeletal pressure P_k over solid portions of the sample's surface. That is, if P is the pressure applied to the sample, then $P = P_f' + P_k$, where $P_f' \leq P_f$. It follows that $P - P_f \leq P_k$: The effective (skeletal) pressure P_k is at least as large as $P - P_f$, and is generally larger in the low-porosity limit. Moreover, P_f should be replaced in Eq. (4) by P_f'. Yet, as discussed more fully below (section 5), the dependence of $P_f + P_k - P$ on crack geometry is such that, for the specific cases treated, the model holds to the usual assumption[5] about effective pressure (equivalent to $P_f' = P_f$):

$$P = P_f + P_k \qquad (5)$$

Relations among the volume strains complete the model (next section).

3. Hydrostats for Undrained Saturated Solids of Low Porosity

In the laboratory explosions cited above, granite's pre-shot confining pressure P^i was set either to 1 ksi or $\sim$2 ksi;[1] fluid pressures ran from about

zero (drained), to $\frac{1}{2}P^i$, to P^i itself. Once disturbed by a detonation, however, elements of granite change state so rapidly that undrained conditions can reasonably be assumed to hold (at least until peak displacements are reached). A hydrostat is therefore derived here for saturated porous solid, undrained, starting from a given fluid pressure P_f^i and total pressure P^i. By Eq. (5), skeletal pressure P_k^i is then equal to $P^i - P_f^i$. Eqs. (1), (2), and (3) thereupon fix the initial volume strains Δ_k^i, Δ_f^i, and Δ_s^i of the skeleton, fluid and bones.

It is convenient now to define all strains as zero in the state of zero stress, and to denote properties in that reference state by a superscript "o". Further, volume strain is related to specific volume v as follows:

$$\Delta_k = (v_k - v_k^o)/v_k^o \quad ; \quad \Delta_f = (v_f - v_f^o)/v_f^o \quad ; \quad \Delta_s = (v_s - v_s^o)/v_s^o \tag{6}$$

or

$$v_k = v_k^o(1+\Delta_k) \quad ; \quad v_f = v_f^o(1+\Delta_f) \quad ; \quad v_s = v_s^o(1+\Delta_s) \tag{7}$$

The specific volumes v_k^o (skeleton) and v_s^o (bone-solid) are related through the pore-volume-fraction α in the reference state. In particular, if V denotes volume, then

$$v_k^o = v_s^o + v_{pores}^o = v_s^o + \alpha v_k^o$$

whence (since the masses of skeleton and bones are identical):

$$v_k^o = v_s^o/(1-\alpha) \tag{8}$$

Undrained or not, the skeleton's volume is equal to that of bones-plus-fluid, and is also (by definition) that of the sample. Thus, making use again of the definition of specific volume ($v=V/m$; $m \equiv$ mass), we have

$$m_k v_k = m_s v_s + m_f v_f \quad ; \quad mv = m_k v_k \quad ; \quad m_k = m_s \tag{9}$$

It follows that

$$v_k = v_s + \mu v_f \quad ; \quad \mu = m_f/m_s \tag{10}$$

whereupon, using Eqs. (7) to replace v_k, v_s, and v_f, we find that

$$v_k^o(1+\Delta_k) = v_s^o(1+\Delta_s) + \mu v_f^o(1+\Delta_f) \tag{11}$$

Since Eq. (11) must hold in the initial state as well as all later ones, it implies that

$$\mu = [v_k^o(1+\Delta_k^i) - v_s^o(1+\Delta_s^i)] \,/\, [v_f^o(1+\Delta_f^i)] \tag{12}$$

If Eq. (12) is used now to eliminate μv_f^o from Eq. (11), the result is

$$v_k^o(1+\Delta_k) = v_s^o(1+\Delta_s) + [v_k^o(1+\Delta_k^i) - v_s^o(1+\Delta_s^i)]\,(1+\Delta_f)/(1+\Delta_f^i)$$

Division of this last equation by v_k^o yields [Eq. (7)]

$$1+\Delta_k = (1-\alpha)(1+\Delta_s) + [(1+\Delta_k^i) - (1-\alpha)(1+\Delta_s^i)](1+\Delta_f)/(1+\Delta_f^i)$$

so that

$$(\Delta_k-\Delta_k^i)(1+\Delta_f^i)-(\Delta_f-\Delta_f^i)(1+\Delta_k^i) = (1-\alpha)[(\Delta_s-\Delta_s^i)(1+\Delta_f^i)-(\Delta_f-\Delta_f^i)(1+\Delta_s^i)]$$

Modest reshuffling brings the latter equation to the form

$$\Delta_k-\Delta_k^i = (1-\alpha)(\Delta_s-\Delta_s^i) + [\alpha(1+\Delta_s^i) + \Delta_k^i-\Delta_s^i]\,(\Delta_f-\Delta_f^i)/(1+\Delta_f^i) \tag{13}$$

With Δ_k^i, Δ_f^i and Δ_s^i set by initial conditions (above), Eqs. (1)-(4) and (13) relate the six variables $P_k, P_f, P_s, \Delta_k, \Delta_f, \Delta_s$. By means of Eqs. (1)-(3), however, the three pressures can be removed from Eq. (4), leaving two relations among Δ_k, Δ_f, and Δ_s [namely, Eq. (4), so transformed, and Eq. (13)]. For a given value of one volume strain (Δ_k, say), the other two can be found from those two relations; Eqs. (1)-(3) then give P_k, P_f and P_s, and the total pressure P issues from Eq. (5). Further, note that the sample's volume strain Δ is identical to that of the skeleton (Δ_k); for the present undrained case, equality of Δ and Δ_k is obvious geometrically, and also follows formally from i) Eq. (7), ii) the identity $v \equiv V/m$, and iii) mass conservation.[6] Thus, for each value assigned to Δ_k (say), a point (P,Δ) of the sample's hydrostat emerges from the model. Moreover, since P_k is also obtained,

so is the sample's shear strength $Y(P_k)$ [assumption (4) of section (1)]. In particular, if σ_1 and σ_3 are the two principal-stress values that can differ at a spherical-field-point, then finite shear strength is expressed by

$$|\sigma_1-\sigma_3| \leqq Y(P_k) \qquad (14)$$

where $Y(P_k)$ comes from tests that cause the dry skeleton to fail in shear.

4. Pressure-Volume-Strength Relations

In applying the model to Sierra white granite, the functions $K(\Delta_k)$, $F(\Delta_f)$ and $S(\Delta_s)$ had first to be defined; so did $Y(P_k)$. Pressure-volume data for water[7] were gathered therefor, and fit with a cubic spline. That spline, taken as $F(\Delta_f)$, is plotted in Fig. 1 with the data-points fit. For $K(\Delta_k)$, a cubic spline was fit to data from a compressibility test;[8] a plot of the spline appears with the data in Fig. 2. Fig. 2, and hence the function $K(\Delta_k)$ used herein, shows somewhat less compressibility for $P_k \gtrsim 0$ (by $\sim$20%) than in other tests (all the data are at hand now, but not when the fits were made). The K-function of Fig. 2 therefore tends to understate the effects of saturation on strength. As for bone-solid, all the measurements set its compressibility so low that one can simply write

$$S(\Delta_s) = k\ \Delta_s\ ; \quad k = \text{bulk modulus, a constant} \qquad (15)$$

An estimate of 430 kilobars (kb) was obtained for k as the slope of the skeleton's mean-stress/volume-strain curve $[P_k=K(\Delta_k)]$ at $P_k \lesssim 1$ kb - a procedure recommended by the experimenters. The same procedure, applied to (P_k,Δ_k)-data from the other tests on cracked granite, puts k closer to 500 kb; from tests on intact granite come k-values of 600 kb or more. The higher k's seem more germane than the lower, because "bone-solid" refers to cemented grains plus the material's unconnected pore-space. In the end, however, values of 430 and 600 kb were both used for k; when a calculation was made using one value, it was redone with the other. As noted (section 1), the stiffer the bones (k=600 kb), the more saturation should affect strength; that proved true (below). As for $Y(P_k)$, the measurements that define it, and the cubic spline fit to them, appear in Fig. 3. One more point: Pore-fractions of 2.1 to 2.3% were measured for the lab samples used in compressibility tests, whereas the figure for explosive tests was $\sim$2.6%. With the source

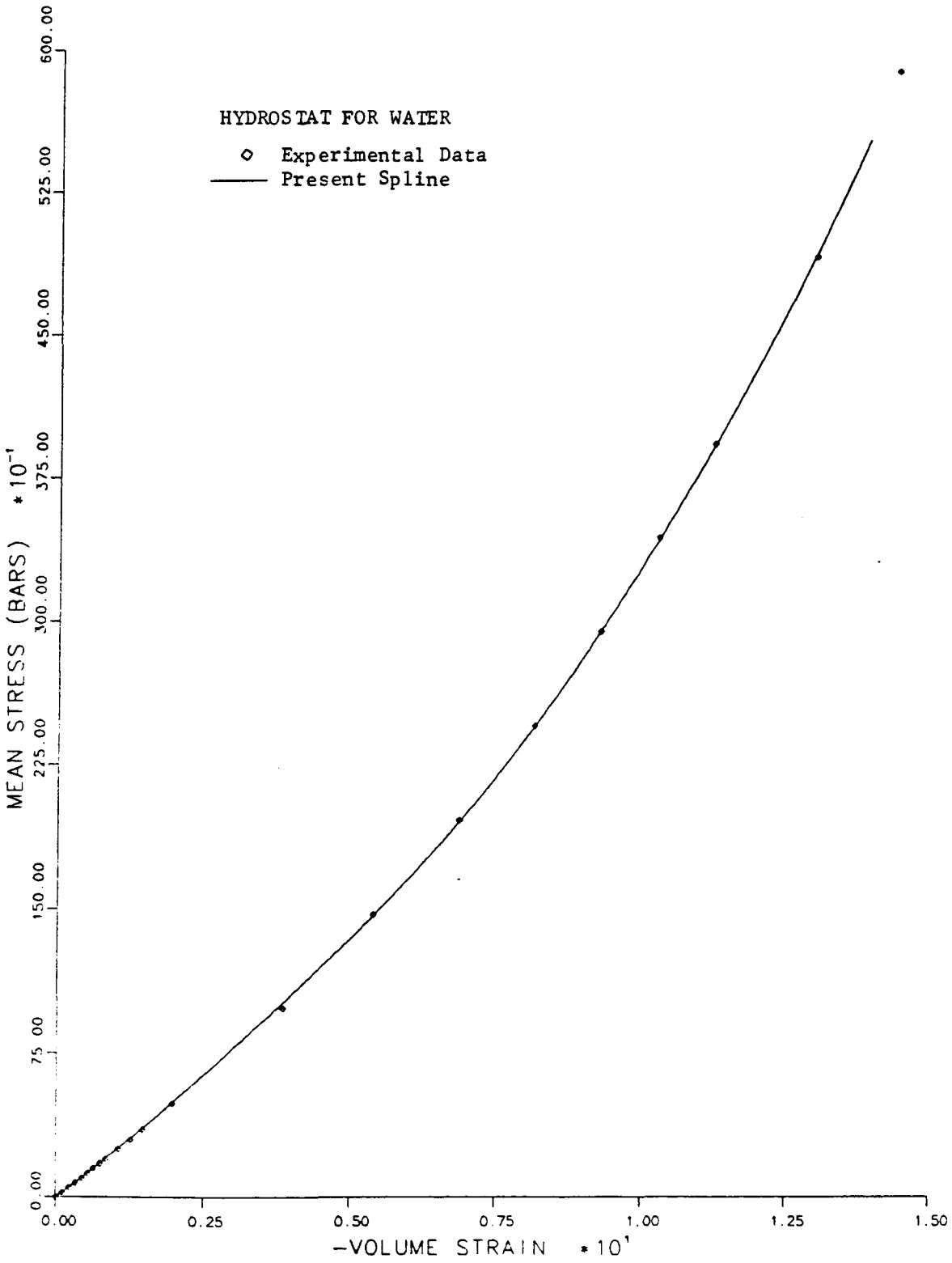

Figure 1. Mean Stress vs. Compressive Volume Strain for Water

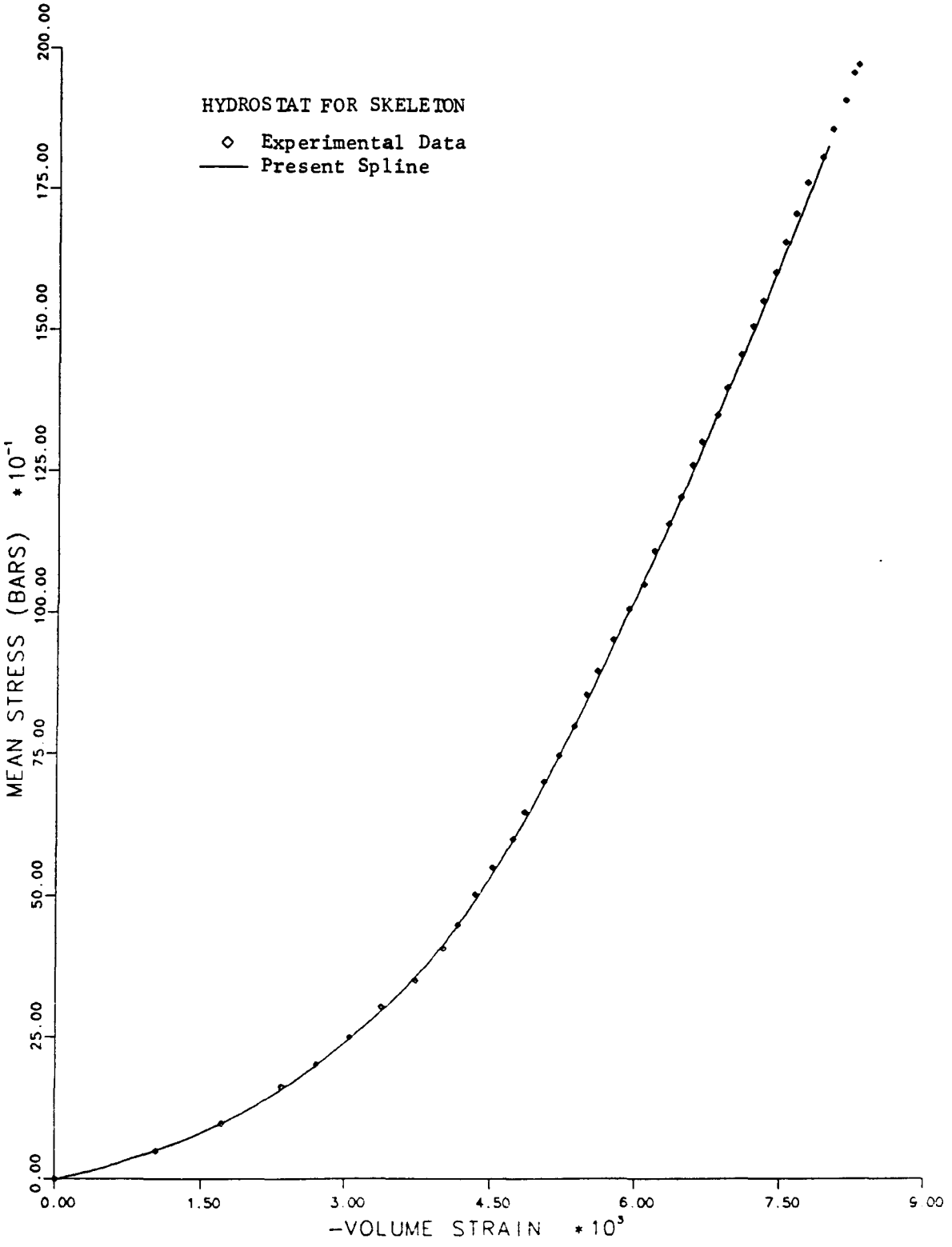

FIGURE 2. Mean Stress vs. Compressive Volume Strain for Dry Cracked Sierra White Granite.[2] Connected pore space accounts for ~1/40 of the total volume.

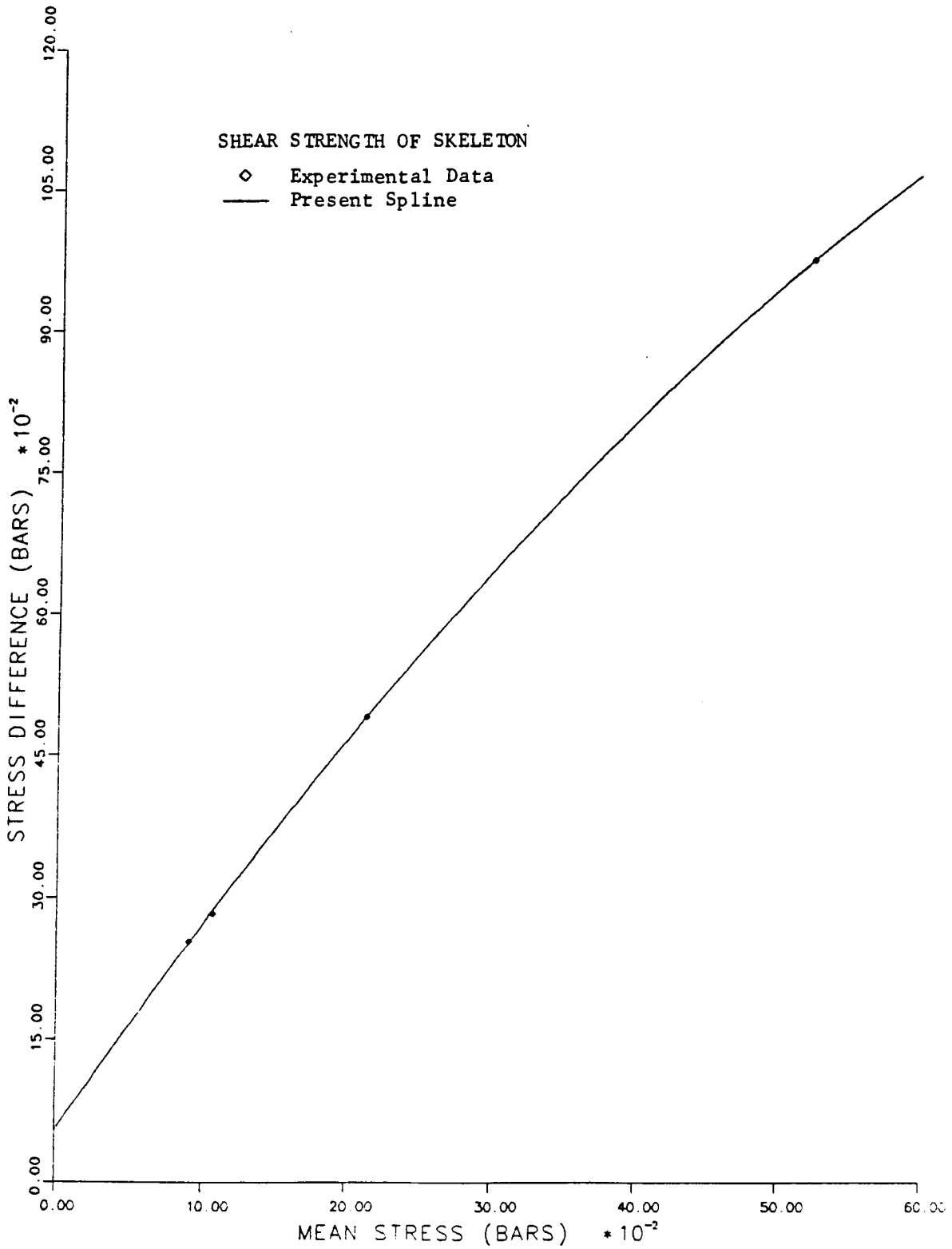

FIGURE 3. Shear Failure Locus. With two principal stresses equal, the curve tracks the difference of principal stresses in states of shear failure, as a function of mean stress.

of that difference unclear, the pore-fraction was set at 2½% in the calculations reported below. If α is indeed 2.2% for Fig. 2 and 2.6% for the explosive tests, then the spline of Fig. 2 doubtless makes the skeleton too stiff, and (hence) the effects of saturation too small - but probably not by much.

With α=2½%, hydrostats and associated strengths were calculated[9] for three initial states of total applied pressure P^i and pore-fluid pressure P_f^i, namely, (P^i,P_f^i)=(0,0), (0,.138) and (.138,0) kb. In each case, the resulting hydrostats are compared in Table 1; so are the hydrostats for water and the skeleton. The sample's strength Y, the quantity of chief interest, is plotted vs. total applied pressure P in Figs. 4 (k=430 kb) and 5 (600 kb). So is the dry skeleton's strength, to make plain the effects of saturation in each case. Evidently, the model gives concave yield surfaces; hence, it probably does not offer stability in Drucker's sense[10] - but neither do some strength measurements on saturated cracked granite of 2.5% porosity.[11]

Other properties of the model evidenced by Figs. 4 and 5, support the discussion above (sections 2, 3): a) In each of cases 1 through 6 (Table 1), strength is greater at all pressures for k=430 kb than for k=600 kb because stiffer bone-solid means less space for fluid at the same total volume strain Δ ($=\Delta_k$); for the same Δ (whence the same Δ_k, P_k and Y), fluid and total pressure are therefore greater. b) Other things being equal (k, P^i and P_f^i), strength is greater when bones bear the total pressure P ($P_s=P_k+P_f=P$) than when they feel only the pressure of fluid ($P_s=P_f$); again, at a given total volume strain Δ (hence fixed Δ_k, P_k and Y), bone-solid compresses more at the higher pressure, reducing P_f and with it P (P_k being fixed). [case 1 vs. case 2; 3 vs. 4; 5 vs. 6] c) Other things being equal (k, P^i and the formula for P_s), strength is lower at any pressure P for higher values of P_f^i; greater initial fluid compression (greater P_f^i) and smaller initial skeletal compression (smaller $P_k^i=P-P_f^i$) mean that more of the change from P^i to P comes from fluid ($P_f-P_f^i$) and less from the skeleton ($P_k-P_k^i$), in view of the increasing stiffness of both with increasing pressure. [case 3 vs. case 5; 4 vs. 6] d) Other things being equal (k, P_f^i and the formula for P_s), strength is higher at any pressure P for higher values of P^i; greater initial skeletal compression (greater P^i with P_f fixed) and the same initial fluid compression mean that more of the change from P^i to P comes from the skeleton and less from the fluid. [case 5 vs. case 1; 6 vs. 2] e) Other things being equal (k, P_k^i and the formula for P_s), strength is lower at any pressure P for higher values of P_f^i; the same initial skeletal compression and greater initial fluid compression (greater P_f^i) mean that more of the change from P^i to P comes

TABLE 1

COMPRESSIVE VOLUME STRAIN $-\Delta$, in %,
CALCULATED FOR SATURATED SIERA WHITE GRANITE
WITH CONNECTED POROSITY OF 2½%

Mean stress is positive in compression; volume strain, negative.

Blank spaces appear where compressibility data are needed for the dry solid at mean stresses above 2 kilobars; those data are presently unavailable.[2]

Bulk Modulus ($-dP/d\Delta$) of Solid plus Unconnected Pore Space = 430 kilobars (kb)

Case	P_k^i(kb)	P_f^i(kb)	P_s=	TOTAL MEAN STRESS P (kb)				
				1	2	3	4	5
1	0	0	P_f+P_k	.301	.560	.792		
2	0	0	P_f	.262	.460	.611	.747	
3	0	.138	P_f+P_k	.259	.523	.758		
4	0	.138	P_f	.228	.434	.587	.724	.853
5	.138	0	P_f+P_k	.460	.701			
6	.138	0	P_f	.408	.572	.716	.850	
Dry	--	--	--	.594	.841			
H_2O	--	--	--	3.82	7.02	9.44	11.4	13.2

Bulk Modulus ($-dP/d\Delta$) of Solid plus Unconnected Pore Space = 600 kb

Case	P_k^i(kb)	P_f^i(kb)	P_s=	TOTAL MEAN STRESS P (kb)				
				1	2	3	4	5
1	0	0	P_f+P_k	.243	.459	.649	.829	
2	0	0	P_f	.222	.402	.543	.665	.780
3	.0	.138	P_f+P_k	.209	.427	.618	.798	
4	.0	.138	P_f	.191	.376	.520	.643	.759
5	.138	0	P_f+P_k	.416	.615	.801		
6	.138	0	P_f	.384	.536	.666	.787	
Dry	--	--	--	.595	.841			
H_2O	--	--	--	3.82	7.02	9.44	11.4	13.2

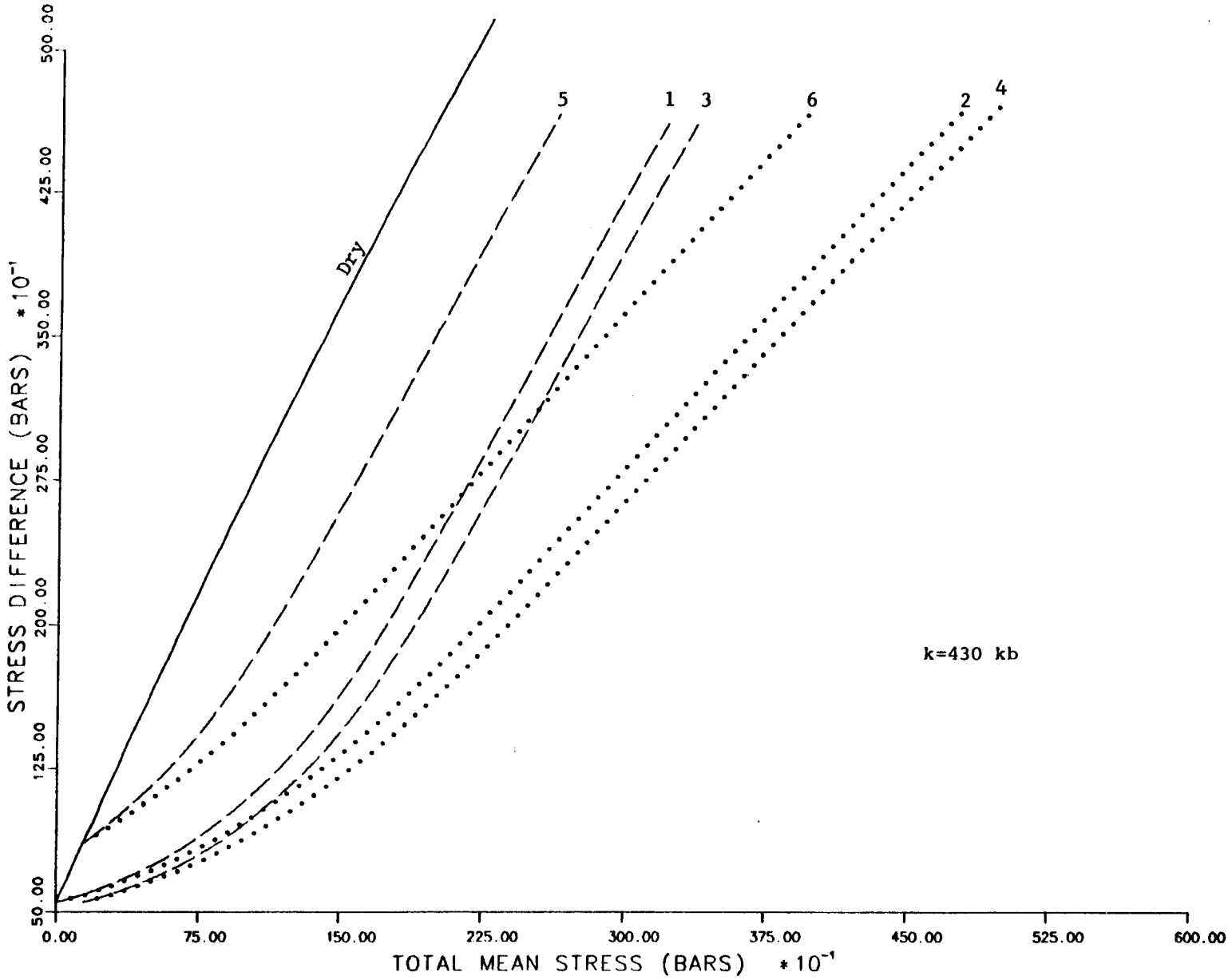

FIGURE 4. Calculated Strength of Saturated Sierra White Granite with 2.5% Connected Pore Volume, vs. Mean Stress. The bulk modulus of solid plus unconnected pore space is 430 kb. The curves are labeled 1 through 6 to denote the cases so numbered in Table 1. The solid line gives the strength of dry solid. For the dashed lines, $P_s=P_f+P_k$; for the dotted lines, $P_s=P_f$.

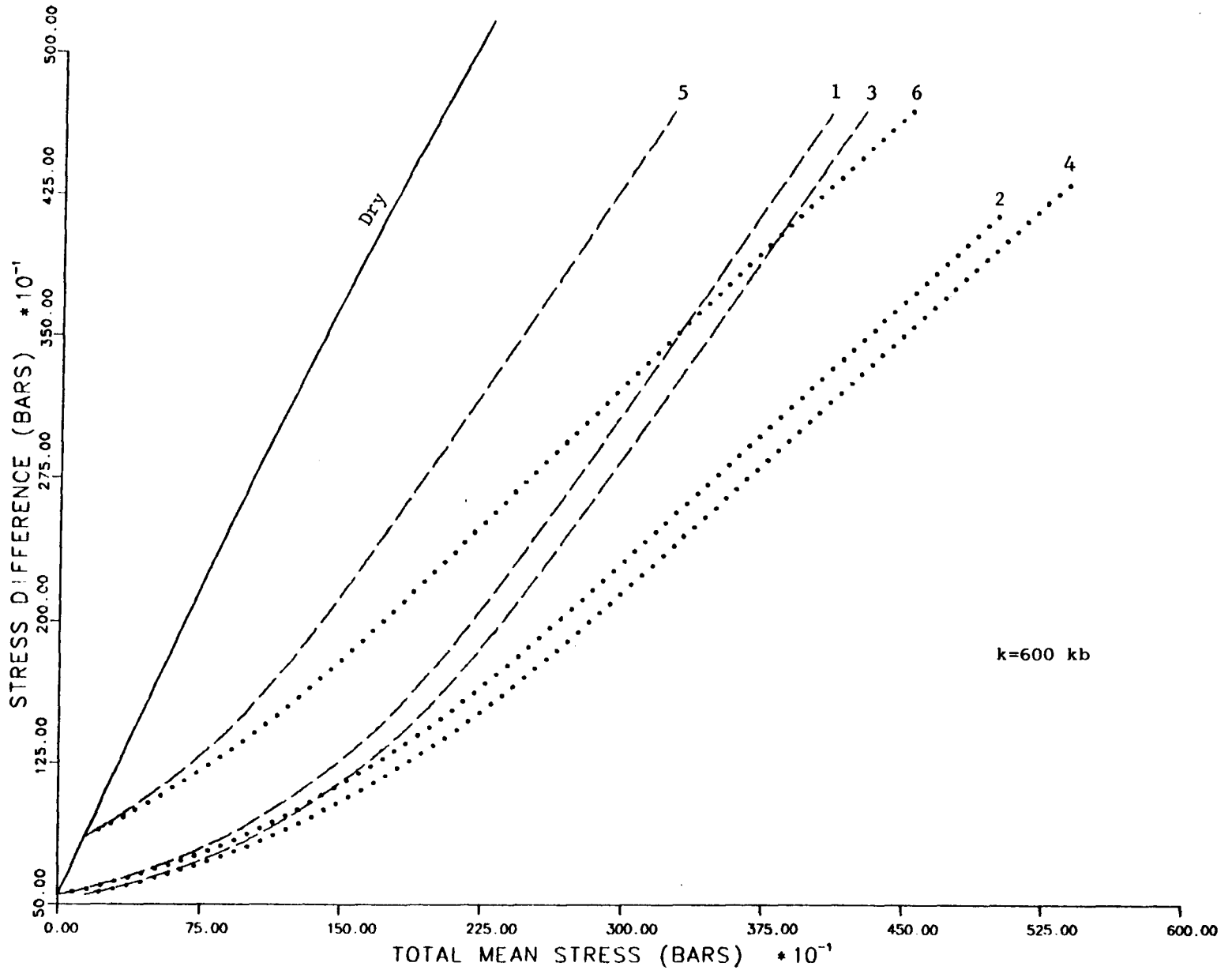

FIGURE 5. Calculated Strength of Saturated Sierra White Granite with 2.5% Connected Pore Volume, vs. Mean Stress. The bulk modulus of solid plus unconnected pore space is 600 kb. The curves are labeled 1 through 6 to denote the cases so numbered in Table 1. The solid line gives the strength of dry solid. For the dashed lines, $P_s=P_f+P_k$; for the dotted lines, $P_s=P_f$.

from the fluid and less from the skeleton. [case 3 vs. case 1; 4 vs. 2]

Strength grows with pressure P on every curve of Figs. 4 and 5. For P<1 kb, however, the rise is much slower for saturated skeletons than dry. Also, for all but the latter, each curve steepens markedly as P increases. This basic pattern reflects the skeleton's strongly nonlinear hydrostat (Fig. 2): With a bulk modulus only ∿1½ times that of water at zero pressure, but stiffening far more rapidly, the skeleton shoulders an ever-larger fraction of the applied load as P increases. Water stiffens too (Fig. 1), but much more slowly, offsetting a little the growth in skeletal stiffness. Instead, low pore-fraction dominates the buildup of fluid pressure; per kilobar, for example, fluid pressure reduces the volume of solid by ∿½% when k=430 kb and 1/6% when k=600 kb, which expands pore-volume by ∿5½% and 4%, respectively (cf. ∿4½% compression of fluid per kb of pore pressure). Thus, though skeleton and (especially) fluid are softer than either of the solids (k=430 or 600 kb), the sizable differences between Figs. 4 and 5 all flow strictly from the change in solid modulus. The same cause - weighty changes in pore pressure due to slight compressibility of solid - lies behind a striking separation of the six curves of each figure (4 and 5) into two groups of three [one with P_s=P (dashed lines, higher strength), and one with P_s=P_f (dotted lines, lower strength)]. For P<∿1 kb, corresponding curves in the two groups are separated by just a small fraction of either's strength, but with P=3 kb, strengths for P_s=P run ∿1½ times those for P_s=P_f; at still higher P's, the curves for P_s=P (cases 2,3,5) become almost parallel to the strength curve of the dry skeleton, while the curves for P_s=P_f (cases 2,4,6) approach a smaller fixed fraction of the dry-strength curve. Further, as P increases from P^i, the strengths of saturated skeletons quickly become small fractions of dry strength - < ½ even when the skeleton is initially compressed (P^i=P^i_k=.138 kb).

5. <u>Comments on the Model: Shapes of the Strength Curves</u> Identification of P-P_f as the pressure P_k borne by low-porosity skeletons (Eq. 5), and the simple lines to which the curves of Figs. 4 and 5 tend as P increases, both warrant further discussion. The latter topic is best pursued by writing Eqs. 1-5 and 13 in exact differential form (permissible since the seven variables P_k, P_s, P_f, Δ_k, Δ_s, Δ_f, and P are functionally related by those six equations). Thus, Eq. (13) implies

$$\lambda_k P_k = (1-\alpha)p_s + \beta\lambda_f P_f \quad ; \quad \beta \equiv [\alpha(1+\Delta_s^i) + \Delta_k^i - \Delta_s^i]/(1+\Delta_s^i) \qquad (16)$$

where

$$p_k \equiv dP_k/dP,\ p_s \equiv dP_s/dP,\ p_f \equiv dP_f/dP\ ;\ \lambda_k \equiv -k d\Delta_k/dP_k,\ \lambda_f \equiv -k d\Delta_f/dP_f \qquad (17)$$

and k remains equal to $-dP_s/d\Delta_s$, a bulk modulus of bone-solid (Eq. 14); λ_k is thus the solid's bulk modulus divided by that of the skeleton, and λ_f has similar meaning. Eq. 5 implies

$$p_k + p_f = 1 \qquad (18)$$

Eq. 4 provides two choices of a third relation among p_k, p_s, and p_f, namely;

$$p_s = \begin{cases} p_k + p_f = 1 \quad (P_s = P_k + P_f) & (19A) \\ p_f \quad (P_s = P_f) & (19B) \end{cases}$$

Taken with Eqs. 16 and 18, Eqs. 19A,B yield, respectively

$$p_k = \begin{cases} (1-\alpha+\beta\lambda_f)/(\lambda_k+\beta\lambda_f) & (20A) \\ (1-\alpha+\beta\lambda_f)/(\lambda_k+1-\alpha+\beta\lambda_f) & (20B) \end{cases}$$

The significance of p_k follows from Eq. (14): At the same P_k, and hence at the same strength, p_k is just slope of the model's strength curve for saturated solid, divided by that for dry solid.

For skeletal pressures P_k above $\sim$1 kb (strength >2 kb), the skeleton's bulk modulus has a nearly constant value (430 kb; k also has that value for one of our two bone-solids). Also, for fluid pressures of 1-3 kb, water's bulk modulus at room temperature varies $\sim$25% from 36 kb. On that basis (bulk moduli of 430 and 36 kb for skeleton and fluid), Eqs. 20A,B give the values of p_k listed in Table 2 for the cases considered herein. At strengths >2 kb, p_k is nearly constant in each case at the value shown in Table 2; the curves of Figs. 4 and 5 agree with the table.

6. Comments on the Model: Effective Stress and Pore Pressure Equating $P-P_f$ to P_k (Eq. 5) raises questions that are more basic. For, in the porous solids

TABLE 2

CRACKED SIERRA WHITE GRANITE AT PRESSURES OF 3 to 5 KILOBARS (kb): RATIO OF SLOPES OF STRENGTH LOCI

Strength is measured by the difference of principal stresses, $|\sigma_1-\sigma_3|$, in confined compression tests.[2]

The variable p_k is the ratio of the slope of the strength locus ($|\sigma_1-\sigma_3|$ vs. mean stress) for dry rock, divided by that of saturated rock, at the same strength-value.

Case	P_k^i(kb)	P_f^i(kb)	P_s^i=	k_s	$-\Delta_k^i \times 10^3$	$-\Delta_f^i \times 10^3$	$-\Delta_s^i \times 10^3$	β	λ_k	λ_f	p_k
1	0	0	P_k+P_f	430	0	0	0	.025	1.00	11.94	.98
2	0	0	P_f	430	0	0	0	.025	1.00	11.94	.56
1	0	0	P_k+P_f	600	0	0	0	.025	1.40	16.67	.77
2	0	0	P_f	600	0	0	0	.025	1.40	16.67	.50
3	0	.138	P_k+P_s	430	0	5.83	.32	.025	1.00	11.94	.98
4	0	.138	P_f	430	0	5.83	.32	.025	1.000	11.94	.56
3	0	.138	P_k+P_f	600	0	5.83	.23	.025	1.40	16.67	.77
4	0	.138	P_f	600	0	5.83	.23	.025	1.40	16.67	.50
5	.138	0	P_k+P_f	430	2.16	0	.32	.023	1.00	11.94	.98
6	.138	0	P_f	430	2.16	0	0	.023	1.00	11.94	.56
5	.138	0	P_k+P_s	600	2.16	0	.23	.023	1.40	16.67	.76
6	.138	0	P_f	600	2.16	0	0	.023	1.40	16.67	.49

of concern here, any surface E that encloses connected pores and solid must cut through both (section 2). A pressure P applied "uniformly" over E therefore pushes on patches of pore-fluid and on patches of solid. The quotation marks around "uniformly" flag the root issue: At the microscopic level of pores and bones, the pressure P is of course not delivered uniformly to patches of solid and fluid. Rather, physically, E is perhaps best conceived as the inner surface of a membrane whose strength permits redistribution over said surface of a load applied uniformly to its outer surface (as in lab tests). The normal stress on patches of E that lie in the stiffer material (skeleton vs. fluid) is, on average, >P (and < P, on average, over the patches in softer material). For dry skeletons, no confusion stems from all this. Averaged over the whole of E, the normal stress delivered to the dry skeleton <u>is</u> P. Hence, viewing the skeleton as a continuum, that average gives the normal traction at a point of E. Furthermore, on any plane, however oriented, the average of normal stress over the plane's section within E, is just P (force equilibrium);[12] the average tangential traction is zero (since traction is zero tangential to E). In treating the dry skeleton as a continuum, it therefore makes sense to define a) its state of stress, so produced, as hydrostatic with mean stress P, and b) its hydrostat as the set of (P,Δ)-pairs so produced, where Δ is the volume strain that accompanies the mean stress P. Nonetheless, large shear stresses can act inside E on closed surfaces that include macroscopic portions of E itself.[13] For present purposes, however, it suffices that the hydrostat (as just defined) tells what pressure must be applied over any surface enclosing dry skeletal material, in order to produce a given volume strain Δ. Moreover, in the absence of wetting effects [assumption (a) of section 1], the same hydrostat applies to the saturated skeleton; compressing it hydrostatically to volume strain Δ_k requires the same applied pressure (now denoted P_k to distinguish it from fluid pressure P_f and total applied pressure P) as for the dry skeleton.[14]

In contrast to the skeleton's hydrostat, the hydrostat for pore-fluid is an intrinsic property of the fluid substance, unrelated to the porosity of the skeleton it happens to fill. As a result, the amount by which a change in pore pressure will alter the pressure on a surface (like E, above) enclosing a fixed mass and volume of skeleton, is clear only in a few special cases. In one such case, of great moment, connected pore-space virtually surrounds each bone of the skeleton. Noting that a suspended bone (liquefaction) comes uniformly to the pressure of fluid around it, and appealing to continuity of effect,[15] we then have good

grounds for assuming that any change in pore pressure will cause an equal change in mean stress throughout each bone; little error should attend that assumption. Thus, all over the surface E (above), pore pressure P_f simply adds to the pressure P_k that brings the skeleton to a given volume strain (as Eq. 5 says). For saturated sands and soils, whose bones fluid almost surrounds, effective stress (the mean stress P_k that fixes shear strength) has indeed been taken with vast success as $P-P_f$.

Equating P_k to $P-P_f$ should also be valid for a solid of low connected porosity, if the "pores" form sheets that all but slice the solid into blocks. As porosity tends toward zero, however, so does the likelihood of finding it distributed that way (either in situ or in the laboratory). Instead, any such sheet is likely to be bridged by solid over a fraction of its area that tends to 1 as porosity goes to zero. Cracks then look more like tattered ribbons that cross here and there - or perhaps like puddles joined by tiny rills. So configured, pore fluid may not affect the bones' mean stress at all. Indeed, it doesn't for spherical pores set far apart in linear elastic solid, but linked by capillaries. Moreover, in that case, the normal force on any plane in the solid is independent of pore pressure (Appendix). Hence, taking E as the surface of a large cube of saturated solid, a given skeletal compression Δ_k is maintained by applying one and the same total pressure P, regardless of the pore pressure P_f. Thus, the effective pressure P_k is not $P-P_f$, but simply P; pore fluid fails to reduce effective stress, and the material's strength is the same saturated as dry. In addition, P_s is equal to P.

In broad terms, $P-P_f$ can be taken as the effective (strength-determining) pressure if the picture presented by saturated solid is roughly one of bones surrounded by pore fluid. If instead bone-solid surrounds pore fluid, connected or not, then the total pressure P appears strength-determining. If neither picture is an obvious choice, then we might write effective stress as $P-\varepsilon P_f$, where $\varepsilon < 1$. Given the complexity of real crack shapes, however, the proper form for effective stress must be decided mainly by experiment. In the absence of such experiments, Eq. 5 has been used here on the basis of i) visual observation of cracked Sierra white granite and ii) a strong (but subjective) sense that its pervasive cracks tend to surround solid, and not the reverse. As to the two forms of solid pressure P_s (Eq. 4), no strong case can be made for P_f+P_k over P_f. There too the decision rests with experiment.

7. Summary and Conclusions The model set forth herein permits effective stress, and hence shear strength, to be computed for saturated solids of low porosity under

hydrostatic loads. As at high porosity (sands and soils), shear-failure envelopes for such solids (cracked rocks) vary most with the ratio of pore-fluid stiffness to that of the solid skeleton. Of like impact on strength is the compressibility of the skeleton's bones (solid plus unconnected pores) - a minor factor at high porosity. The model takes account of all three materials and their hydrostats (dry skeleton, bone-solid, and fluid). From those hydrostats comes the hydrostat (mean stress P vs. volume strain Δ) for the saturated solid, given its porosity and initial state (pore pressure and total pressure).

The model assumes that in saturated solid i) all three materials retain their individual hydrostats and strengths, ii) the strength of the medium is the strength of its skeleton, iii) fluid pressure P_f, and the skeleton's mean stress P_k, sum to the medium's mean stress P; iv), when iii) holds, the mean stress P_s of bone-solid is $\geqq P_f$ and $\leqq$ P. The first of these is a working hypothesis, refinable at some cost in simplicity; strength and stiffness, for example, are not identical for dry and wet skeletons. The second (ii) seems accurate, but the third depends critically on pore geometry. It holds when the skeleton's bones are virtually surrounded by connected pore-fluid (as in sands and soils). Such patterns become ever less likely as porosity tends to zero, whence P then tends to P_k (so does P_s); for example, given spherical pores many radii apart in a linear elastic solid, but connected by capillaries, it follows that $P=P_k(=P_s)$. Since the stress that determines strength is P_k (i and ii, above), the "effective" stress in that physically meaningful sense then becomes P, rather than $P-P_f$ (effective when fluid surrounds bones). The subjective judgement here is that (iii) holds for the crack-enhanced granite that motivated this work. Even when (iii) holds, however, P_s can depend on P_k in many different ways. The reason: Under a hydrostatic load P_k on the skeleton, its bones change volume and shape. The formulas $P_s=P_f$ and $P_s=P_f+P_k$ (iv, above) express extremes of pure shear and pure compression of bones under the skeletal pressure P_k.

To describe saturated rock during explosions, the model was applied to undrained solid. Conservation of mass and space then relate linearly the volume strains of the skeleton (Δ_k), bone-solid (Δ_s) and fluid (Δ_f); the relation's linear coefficients are explicit functions of initial volume strains ($\Delta_k^i, \Delta_s^i, \Delta_f^i$) and the porosity α at zero stress. That relation, the three hydrostats (i), condition iii, and one of the two limiting conditions iv, comprise six equations among the seven model-variables Δ_k, Δ_s, Δ_f, P_k, P_s, P_f, and P (the medium's strain Δ is identical to Δ_k).

Those six reduce to a nonlinear algebraic equation relating any two of the strains; fixing Δ_f, a convenient choice, said equation is readily solved for the second strain's unique value. The five remaining variables then follow explicitly from the first two. The equations thus yield a point (P,Δ) of the medium's hydrostat, along with the skeleton's mean stress P_k in that state; from P_k flows the medium's strength at mean stress P. The full hydrostat and shear-strength envelope are obtained by repeating these steps for many values of Δ_f.

The calculations outlined were made for a crack-enhanced Sierra white granite (α=.025), the host medium in a series of explosive laboratory tests cited at the start of this paper. Two of the three sets of initial conditions employed were among those of the tests; the two have the same total pressure (P^i=.138 kb), but with zero pore pressure in one set and zero effective stress in the other. Initial stresses were all zero in the third set. In each case, hydrostats and strength envelopes were generated for two different bulk moduli of bone-solid (thought to be bounds); with each modulus, that was done for the two P_s-limits of condition iv, giving a total of 12 hydrostats and 12 strength envelopes. At total pressures up to $\sim$1 kb, all twelve envelopes lie below that of dry solid by factors $\geq$2 (often much larger). The factors run from 1.2 to 3 at P=3 kb, falling toward limiting values $\geq$1 at still higher P's. Their decrease with increasing P stems from a steady decrease in the ratio of water's bulk modulus to the skeleton's; both stiffen, but as water becomes relatively soft, it bears a smaller share of the total pressure load. That also explains why, for the same bone-solid-modulus and P_s-option, strength is least when P_f^i=.138 kb and greatest when P_k^i=.138 kb. In differential form, the model-equations show simply and precisely how the slope of a given envelope is set by the medium's porosity and modulus-ratios (fluid/solid; skeleton/solid), and why, with increasing shear strength, that slope increases toward a fixed (readily calculable) fraction of the slope for the dry skeleton. Further, for each pair of envelopes that differ only in bone-solid-modulus, the one with the lower modulus is weaker at all P's. For, stiffer solid means less compression of bones at any P, smaller pore volume, greater pore pressure, and hence smaller effective stress and strength. Likewise, other things being equal, an envelope with $P_s=P_f$ is uniformly weaker than that with $P_s=P_f+P_k$ because the former results in less bone-compression at any P.

Observed and calculated variations of displacement with strength[16,17] underlie correlations of a) strength predicted by the model with b) displacement measured during

the explosions cited. Dividing each peak displacement in saturated solid by the peak value measured in dry solid at the same range, gave displacement-increase-factors vs. range. Using data from other lab tests[2] to convert peak shock stress (from measured shock speeds and particle velocities) to mean stress, gave peak mean stress as a function of range in a given shot. For two shots, the present calculations permit corresponding ratios of shear strength (but now dry÷wet) to be found from the model. The results, shown in Fig. 6, bear out the assertion (above) that strength is much reduced (on the model) in cases of large displacement-increase, but not in the other cases. The prospects thus appear bright for explaining the explosive-test results simply, in terms of effective stress. Yet, the accuracy with which that can be done is not known now; indeed, it is not known how well the model predicts hydrostats and shear strengths for saturated solids in quasistatic lab tests.

Of the steps yet to be taken, the two critical ones look short enough to perform in parallel: i) Use the model-equations to represent saturated Sierra white granite in numerical simulations of the laboratory bursts; ii) measure the strength of that rock, quasistatically, vs. total pressure. If the calculated displacements, and especially the model's predictions of strength, meet with reasonable success, then further testing of the rock would be mainly hydrostatic, but with separate control of fluid pressure and total pressure. The issues: How does wetness affect the skeleton's compressibility? How does skeletal pressure affect pore volume? How do changes in fluid pressure affect total pressure? The first two questions can be answered by tests in which fluid pressure is held constant, and the third by tests in which, as fluid pressure is varied, total pressure is adjusted to keep the sample's volume fixed. For all three questions, the hardest task may lie in maintaining areas of contact between membrane (jacket) and fluid that represent cross-sections of the bulk material.

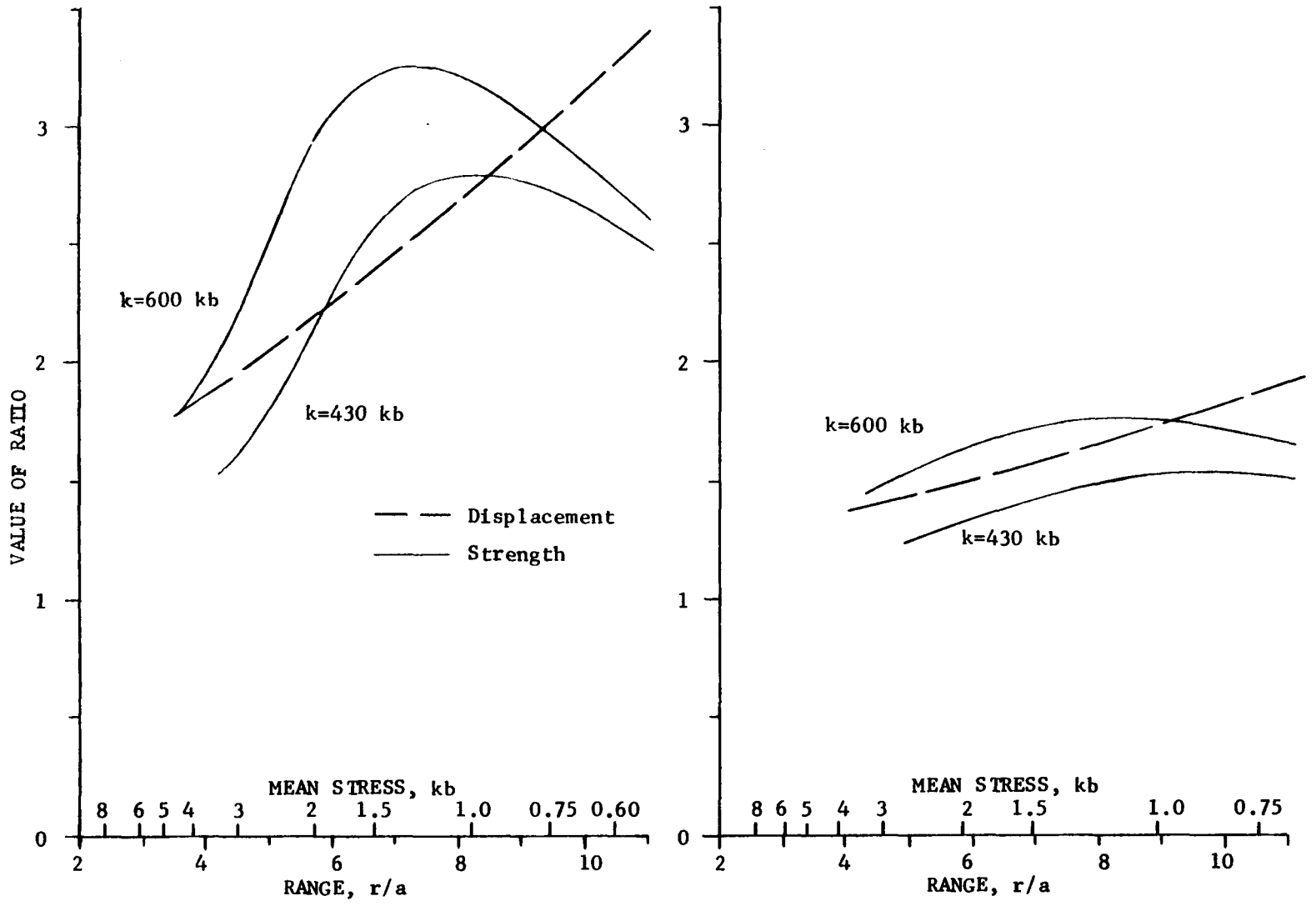

FIGURE 6. Ratios of Displacement (Saturated/Dry) and Strength (Dry/Saturated), vs. Scaled Slant Range and Mean Stress, for Sierra White Granite of 2.5% Pore Volume. Scaled slant range = r(radius)/a(charge radius).[1] Peak radial stress, found from peak particle velocity and shock speed measured in saturated solid, was converted to mean stress using measurements of Poisson's ratio.[2] Displacements were measured; strengths were calculated from the present model with $P_s=P_f+P_k$. Initial total pressure = .138 kilobars; effective stress initially zero in saturated solid for left-hand curves; initial pore pressure zero for those on right.

APPENDIX

At a point Q with Cartesian coordinates (x,y,z) and spherical coordinates (r,θ,ϕ),[18] let the principal axes of stress (and strain) lie along the radial (r), tangential (θ), and azimuthal (ϕ) directions, with σ_r, σ_θ, and σ_ϕ, respectively, as principal stresses. The Cartesian components of stress at Q are then given by

$$\sigma_{xx} = \sigma_r \mathrm{Sin}^2\theta\mathrm{Cos}^2\phi + \sigma_\theta \mathrm{Cos}^2\theta\mathrm{Cos}^2\phi + \sigma_\phi \mathrm{Sin}^2\phi \quad ; \quad \sigma_{xy} = (\sigma_r \mathrm{Sin}^2\theta + \sigma_\theta \mathrm{Cos}^2\theta - \sigma_\phi)\mathrm{Sin}\phi\mathrm{Cos}\phi$$

$$\sigma_{yy} = \sigma_r \mathrm{Sin}^2\theta\mathrm{Sin}^2\phi + \sigma_\theta \mathrm{Cos}^2\theta\mathrm{Sin}^2\phi + \sigma_\phi \mathrm{Cos}^2\phi \quad ; \quad \sigma_{yz} = (\sigma_r + \sigma_\theta)\mathrm{Sin}\theta\mathrm{Cos}\theta\mathrm{Sin}\phi \qquad (21)$$

$$\sigma_{zz} = \sigma_r \mathrm{Cos}^2\theta + \sigma_\theta \mathrm{Sin}^2\theta \quad ; \quad \sigma_{zx} = (\sigma_r - \sigma_\theta)\mathrm{Sin}\theta\mathrm{Cos}\theta\mathrm{Cos}\phi$$

In a static spherical field, the r-, θ-, and ϕ-directions define principal stress axes, no matter where Q is located. Further, $\sigma_\phi = \sigma_\theta$, and σ_r and σ_θ satisfy the stress-equilibrium equation

$$d\sigma_r/dr + 2(\sigma_r - \sigma_\theta)/r = 0 \qquad (22)$$

For a linear elastic medium, σ_r and σ_θ can both be expressed in terms of radial displacement, whence Eq. (22) allows both to be determined. If $\sigma_r = S_c$ at $r = r_c$ ("cavity radius"), and σ_r tends to S_∞ as r/r_c becomes infinite, then the results are these:

$$\sigma_r = S_\infty + (S_c - S_\infty)(r_c/r)^3$$

$$\sigma_\theta = S_\infty - \tfrac{1}{2}(S_c - S_\infty)(r_c/r)^3 \qquad (23)$$

It follows at once from Eqs. (23) that the mean stress P $[=(\sigma_r + 2\sigma_\theta)/3]$ is equal everywhere to S_∞; cavity pressure S_c has no effect on mean stress.

To compute the force on an arbitrary plane N in the elastic medium, choose the Cartesian z-axis as the normal to N from the center of symmetry a distance λ away; Figure 7 below shows the arrangement in a cross-section through the z-axis.

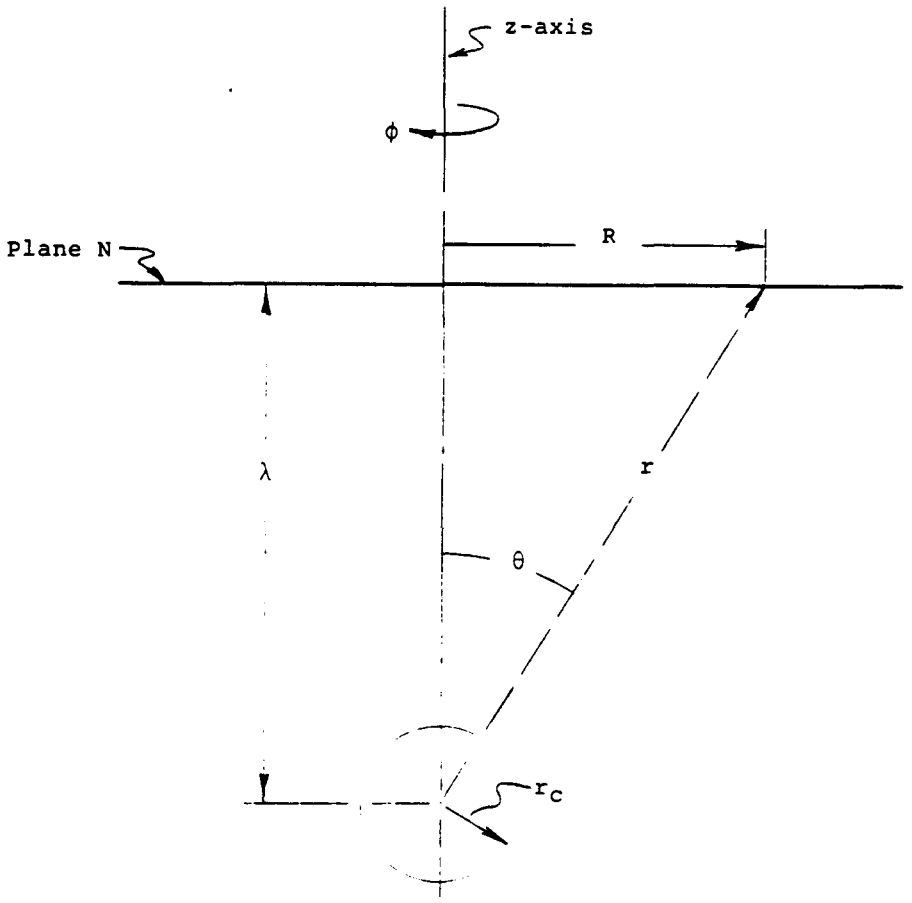

FIGURE 7. Schematic Showing Spherical Cavity in Linear Elastic Material. The normal force on arbitrary plane N is unaffected by cavity pressure.

The traction (force per unit area) at a point of N has σ_{zx}, σ_{zy} and σ_{zz}, respectively, as its x-, y-, and z-components. Moreover, at any such point, the spherical radius r and the distance R from the z-axis are evidently given by

$$r = \lambda \, \mathrm{Sec}\theta \quad ; \quad R = \lambda \, \mathrm{Tan}\theta \tag{24}$$

The traction σ_{zz} normal to N varies only with r and θ (Eqs. 21 and 23), and hence (Eq. 24) with θ alone over N. Between θ and $\theta+d\theta$, the area dA of the annulus ($0 \leq \phi \leq 2\pi$) subtended on N is just $2\pi RdR$ (with Eq. 24 relating R and θ), whence the normal force dF_n on the annulus is given by

$$dF_n = \sigma_{zz}dA = 2\pi\sigma_{zz}RdR = 2\pi\sigma_{zz}\lambda^2 \, \mathrm{Tan}\theta \, \mathrm{Sec}^2\theta \, d\theta \tag{25}$$

Using Eqs. 21 and 23 to eliminate σ_{zz} from Eq. 25, we obtain

$$dF_n = S_\infty dA + dF_n^C \tag{26}$$

where

$$dF_n^C = (S_C - S_\infty)(r_C/r)^3(\mathrm{Cos}^2\theta - \tfrac{1}{2}\mathrm{Sin}^2\theta)2\pi\lambda^2\mathrm{Tan}\theta \, \mathrm{Sec}^2\theta \, d\theta \tag{27}$$

Replacing r by λ Secθ (Eq. 24) in Eq. 27, we find that

$$dF_n^C = \pi(S_C - S_\infty)(r_C^3/\lambda)(3\mathrm{Sin}\theta \, \mathrm{Cos}^2\theta - \mathrm{Sin}\theta)d\theta \tag{28}$$

Integrating dF_n^C over $0 \leq \theta \leq \pi/2$ gives zero: The cavity pressure contributes nothing to the total normal force on N. Only the stress S_∞ that would appear uniformly through the medium if the cavity were absent, produces a normal force on N, and S_∞ acts there as a uniform traction.

If many cavities are present, all separated by many radii (in cubic-lattice-array, say), then Eq. 23 is only approximate. Slight changes in the stress at $r=r_C$ would be needed to keep it exact. Ignoring those, the force on N due to all cavities is exactly zero, even if they all communicate via capillaries to maintain the same pressure on every cavity wall. In addition, even a single cavity in a cube of finite size will produce some net force on N. Per unit area of N, however, that force tends to zero so rapidly with increasing sample-edge-length L [faster than $(r_C/L)^3$], that it appears a negligible edge-effect.

NOTES AND REFERENCES

1. G. Nagy and A. Florence, Spherical Wave Propagation in Low-Porosity, Brittle Rocks, Draft of SRII Technical Report for Final Report for Defense Advanced Research Projects Agency Contract No. 9168505 (April 1967).

2. R. Martin and K. Coyner, Physical Properties of Sierra White Granite for Intact and Crack Enhanced Specimens, Draft of New England Research, Inc. Final Report for Lawrence Livermore National Laboratory Contract No. 992405.

3. If a skeleton is simply connected, which tends to be the case in low-porosity rock, it won't be clear where one bone ends and another starts. In general, then, "bone" simply denotes intact rock between cracks.

4. The tensor equation for stress equilibrium is linear. Hence, taking the total stress at any point inside a bone as the sum of a part that fluid alone would cause, and a part due to skeletal pressure at contact spots, is rigorous.

5. Simply defining $P-P_f$ as "effective stress" is useful only if $P-P_f$ is equal to P_k. For, P_k sets the sample's strength.

6. Setting $\Delta=\Delta_k$ becomes a matter of definition if draining occurs; the "sample" then consists of an unchanging skeletal mass and a changing mass of fluid that fills its cracks.

7. American Institute of Physics Handbook, Dwight Gray (ed.), p. 2-152 and 2-153 (McGraw-Hill, 1957).

8. As plotted in Fig. 2, the measured points duplicate those presented by New England Research, Inc. in Fig. 7 of their Progress Report dated February 3, 1987: Physical Properties of Sierra White Granite. That plot was presented by NER at a review meeting in January 1987.

9. Small overall volume strains are attended by much larger volume strains in the fluid (section 2). Hence, Δ_f was treated as an independent variable in Eqs. (4) and (13) [with Eq. (4) written as $S(\Delta_s) = K(\Delta_k) + F(\Delta_s)$]. Specifically, Δ_f was increased from Δ_f^i in steps of .05%. At any one step, Eq. (4) was solved iteratively for Δ_s, using Eq. (13) to evaluate Δ_k for each guess at Δ_s. With Δ_f and Δ_s known, explicit formulas give $\Delta_k, P_f, P_s, P_k, P$, and $Y(\Delta_k)$ [Eqs. (13), (1),(2),(3),(5), and (14)].

10. Drucker's postulates don't necessarily imply yield-surface convexity; see for example, A. Palmer, G. Mayer and D. Drucker, Normality Conditions and Convexity of Yield Surfaces for Unstable Materials or Structural Elements, ASME Transactions, p. 464-470 (June 1967).

11. A. Duba, H. Heard and M. Santor, Effect of Fluid Content on the Mechanical Properties of Westerly Granite, Lawrence Livermore Laboratory Report No. UCRL-51626 (July 30, 1974).

12. Tractions differ from zero only on the part of the plane that intersects solid. If, within the sample, that part accounts for a fraction ψ of the plane's area, then the mean traction felt by solid has a normal component P/ψ (>P) - or P_k/ψ in the presence of fluid. The upper bound for P_s is therefore better written as P_f+P_k/ψ than P_f+P_k (Eq. 4), where ψ is a mean fraction of the surface area intercepted by solid on all planes through the sample. The correction is negligible when $\psi \gtrsim 1$ (low porosity), and also when $P_k << P_f$ (high porosity).

13. From the surface of an open crack inside a cube of compressed dry solid, project a right cylinder (not necessarily circular) normally outward to one face. Let one end-cap of the cylinder be the planar face-area it intercepts; let the other end-cap be the irregular crack-surface it intercepts. The force on the cylinder"s inner end-cap is zero. The force on its outer end-cap (total pressure x face-area intercepted), is directed normally to the face, and must therefore be balanced by shear tractions over the remainder of the cylinder's surface (i.e., the part other than its end-caps).

14. To test this requires independent control of the pressure on the skeleton; then the stress on the skeleton can be measured as a function of its volume strain at various levels of pore pressure.

15. The effect of fluid on the mean stress in a bone varies continuously with the fraction of a bone's surface in contact with the fluid. To see why, subdivide the area of contact into many tiny pieces. The total effect is the sum of the effects from every piece, and the effect of any one piece on the whole bone is tiny. Implicit here is the assumption that changes in the positions of particles of bone due to its loading can be neglected.

16. R. Terhune and H. Glenn, Estimate of Earth Media Shear Strength at the Nevada Test Site, UCRL 52358 (Nov. 3, 1977).

17. J. Trulio, Cowboy Trails, Phase I: Small-Scale Explosive Tests in Salt Domes, Part I, Section 2; Applied Theory, Inc. Report No. ATR-83-53-1 (15 June 1983).

18. See, for example, J. A. Stratton, Electromagnetic Theory, p. 52 (McGraw-Hill, 1941).

STUDIES OF EXPLOSION SOURCE FUNCTIONS AND AMPLITUDES USING AVAILABLE FAR-FIELD SEISMIC DATA (FINAL REPORT)

K. L. McLaughlin, I. N. Gupta, M. E. Marshall,

R. A. Wagner, and T. W. McElfresh

TELEDYNE GEOTECH ALEXANDRIA LABORATORIES

314 MONTGOMERY STREET

ALEXANDRIA, VA. 22314

PRESENTED TO:

LAWRENCE LIVERMORE NATIONAL LABORATORY

CONTRACT # 9422605

SPONSORED BY:

DEFENSE ADVANCED RESEARCH PROJECTS AGENCY

REPORT TGAL-87-6

JANUARY 1988

TABLE OF CONTENTS

SUMMARY

SECTION 1: Available seismic data for three US underground nuclear explosions in granite (HARDHAT, SHOAL, and PILEDRIVER) are reviewed to examine if differences in scaling or coupling can be observed in far-field seismic data. Furthermore, far-field P-wave data are examined in order to compare these three US granite shots with underground nuclear tests conducted in the southern Sahara. No evidence could be found to contradict simple yield scaling in the far-field seismic data. Data analyzed included Long Range Seismic Measurements (LRSM) digitized analog tape recordings at regional and teleseismic distances, as well as LRSM film data and readings from WWSSN short-period film chips at teleseismic distances.

SECTION 2: Analysis of seismic data is performed at a number of arrays and single stations to estimate the low-frequency level of the far-field P-wave from broadband seismograms derived from "short-period" recordings. The area under the initial P-wave pulse, Ω_0, and the spectral low-frequency asymptote, A_0, are compared as measures of the explosion size when corrected to equivalent explosion RDP and far-field P-wave moment. Broadband P-wave displacement seismograms are estimated by the use of both single station deconvolutions and the Shumway-Der deconvolution algorithm. When both instrument response and causal intrinsic attenuation operators are removed, it is found that the measured area under the initial broadband P-wave is an excellent measure of the far-field P-wave moment.

SECTION 3: The empirically derived explosion source functions of McEvilly and Johnson (1987) are used to predict teleseismic P-wave magnitudes based on the frequency-dependent t*(f) models of Der and Lees (1985). The predicted magnitudes are several tenths larger than are observed across the WWSSN network. We examine several assumptions inherent in the calculation including focusing-defocusing bias, the |pP/P| amplitude ratio, intrinsic attenuation, and scattering attenuation. If predicted teleseismic amplitudes are corrected for statistical biasing effects due to focusing-defocusing then the discrepancy between observed and predicted magnitudes is between 0.2 and 0.4 magnitude units. Scattering of P-waves by velocity heterogeneity in the lithosphere is just as reasonable an explanation for the additional needed attenuation as is the introduction of additional intrinsic attenuation. A few percent velocity variation (7% to 10% rms) of the lithosphere with scale lengths between 1 and 2 km in the crust and 2 and 4 km in the upper mantle is required to produce attenuation on the order of 0.2 to 0.4 magnitude units.

SECTION 1:

COMPARISON OF HARDHAT, PILEDRIVER, AND SHOAL USING AVAILABLE FAR-FIELD SEISMIC DATA

K. L. McLaughlin, I. N. Gupta, M. E. Marshall,

R. A. Wagner, and T. W. McElfresh

SUMMARY

Available seismic data for three US underground nuclear explosions in granite (HARDHAT, SHOAL, and PILEDRIVER) are reviewed to examine if differences in scaling or coupling can be observed in far-field seismic data. Furthermore, far-field P-wave data are examined in order to compare these three US granite shots with underground nuclear tests conducted in the southern Sahara. No evidence could be found to contradict simple yield scaling in the far-field seismic data. Data analyzed included Long Range Seismic Measurements (LRSM) digitized analog tape recordings at regional and teleseismic distances, as well as LRSM film data and readings from WWSSN short-period film chips at teleseismic distances.

INTRODUCTION

The U.S. testing experience in granite is limited to the three shots listed in Table 1-1. Two events, HARDHAT and PILEDRIVER, were located quite close to each other (horizontal separation about 346 m) within the Climax Stock granodiorite at NTS. The third event, SHOAL, was located 298 km to the northwest near Fallon, Nevada, in granodiorite of the Sand Springs Range. HARDHAT and SHOAL were both detonated at about 160 meters scaled depth whereas PILEDRIVER was placed 25% shallower at a scaled depth of 115 meters.

Table 1-1. EVENT INFORMATION

DATE	EVENT	O.T.	LAT. (°N)	LON. (°E)	h* (m)	Y* (Kt)	$h\ Y^{-1/3}$ $(m-Kt^{-1/3})$
HARDHAT	620215	18:00:00.	37.23	-116.06	290	5.9	160
SHOAL	631026	17:00:00.	39.20	-118.38	367	13	156
PILEDRIVER	660602	15:30:00.	37.23	-116.06	457	62	115

*Data from Murphy (1978)

HARDHAT was detonated before the WWSSN network was established, and little teleseismic data is available for that event. SHOAL and PILEDRIVER have maximum likelihood WWSSN m_b magnitudes of 4.86(0.05) and 5.48(0.04), respectively (McLaughlin et al., 1986a). Given the small size of HARDHAT with respect to SHOAL and PILEDRIVER, it is doubtful that teleseismic data would have been of adequate quality for HARDHAT even if the data had been available. However, the

Long Range Seismic Monitoring (LRSM) network was operational for all three events and recorded HARDHAT out to a distance of 12°. The paths to available LRSM stations for each event are shown in Figures 1-1a, 1-1b, and 1-1c. Unfortunately, due to changes in the configuration of the LRSM network between 1962 and 1966, only three stations were common for HARDHAT and PILEDRIVER, and the available data from these three stations are limited due to clipping at regional distances and non-detection at near teleseismic distance. Nevertheless, some comparisons can be made to explore the relative coupling and source scaling of these three events.

We present in this report several comparisons (either direct or indirect) between these events and the French underground nuclear tests that were conducted in granite in the southern Sahara. Material properties of Climax Stock granite and the granite from Taourirt Tan Afella Massif in southern Sahara are reviewed by Schock et al. (1972) and Heuze (1983). They conclude that material properties of the French and U.S. granites are not significantly different. Stevens et al. (1986) (their Figures 7 and 8) show that the near-field peak-velocity and peak-displacement data for the French and U.S. shots in granite are consistent with simple yield scaling. From our analysis of far-field seismic data, we conclude that although the free-surface interaction (pP) may vary between the events, the coupling of these granite shots was all much the same. This analysis includes:

(1) coda at two common LRSM stations, KN-UT and MN-NV, for HARDHAT and PILEDRIVER

(2) the deconvolved Pn displacement waveforms at station KN-UT for HARDHAT and PILEDRIVER,

(3) maximum likelihood Ms magnitudes from the LRSM network for HARDHAT, SHOAL, and PILEDRIVER,

(4) maximum likelihood WWSSN m_b magnitudes for PILEDRIVER, SHOAL, and the French Sahara shots,

(5) far-field P-wave moment estimates for the U.S. and French shots from deconvolved P waveforms at LRSM stations, and

(6) a comparison of attenuation corrected Lg spectra for SHOAL and HARDHAT from three-component LRSM stations at regional distances (Δ < 1000 km).

CODA ANALYSIS AT LRSM STATIONS KN-UT AND MN-NV

Since HARDHAT and PILEDRIVER were separated by only a few hundred meters, have a yield ratio of about 1-to-10, and were buried at different scale depths, they make a particularly interesting pair of explosions to test for variations in coupling and source scaling. However, the three available stations for HARDHAT and PILEDRIVER are somewhat disappointing; the HARDHAT P wave at WN-SD is barely detectable, HARDHAT clipped the analog FM tape and film recordings at MN-NV on the first swing of the P wave, while only the FM tape recordings at KN-UT stayed on scale for 5 seconds of the Pn wave for both events. In order to avoid the problems of working with clipped data, McLaughlin et al. (1986a) compared the coda of HARDHAT and PILEDRIVER at MN-NV and KN-UT to test for variation between the two events. They digitized film records for the two stations for the same time period of the seismogram (relative to the P onset) when both events were on scale and

above the background noise (Figure 1-2). The rms signal level was then computed from 8 successive 10-second windows and the relative size of the two events was examined. They concluded that the log-average ratio of the rms coda levels (see Table 1-2) of the two events was consistent with the log of the yield ratio of the two events. The coda energy was dominated by frequencies at 1 Hz or lower, and therefore differences in corner frequency between the two events should not be a factor.

Table 1-2. RMS CODA LEVEL RATIOS (TGAL-86-01)
AVERAGE OF 8 SUCCESSIVE 10 SECOND WINDOWS

STATION	$\log_{10}(\frac{\text{HARDHAT}}{\text{PILEDRIVER}})$
KN-UT	-0.85(0.02)
MN-NV	-1.05(0.02)
AVE	0.95(0.05)

ANALYSIS OF DECONVOLVED Pn AT KN-UT

The only well calibrated seismograms that recorded (on scale) both HARDHAT and PILEDRIVER are from the first 5 seconds of Pn recorded at KN-UT. The propagation paths from the source locations of PILEDRIVER and HARDHAT should be virtually identical and therefore any differences between the two records should be entirely attributable to variations in the seismic sources and not due to propagation effects. Using the two records at KN-UT, we deconvolved the Pn window to displacement, and the results are shown in Figure 1-3. The two traces are remarkably alike except for a negative pulse following the HARDHAT P pulse. The similarity of the two traces is particularly evident for up to 5 seconds after the initial P arrival.

Using the two deconvolved records, the spectra of 3.2 sec long Pn windows (with Parzen taper) are shown in Figures 1-4a and 1-4b. The spectral ratio HARDHAT/PILEDRIVER, corrected for noise, is shown in Figure 1-4c and, at low frequencies, agrees well with the ratio of yields. In fact, spectral ratio based on the von Seggern and Blandford (1972) scaling for granite (B = 2.04, k_0 = 16.8), with no pP, shown by the dashed curve, indicates excellent agreement up to at least 5 Hz. A comparison with Mueller and Murphy (1971) scaling, with the empirical constants for granite as given in Stevens and Day (1985), is also shown (dotted curve). Agreement with the observed data is again good.

A comparison of data on peak displacements, spectral amplitudes, and areas under the initial displacement pulse, Ω_0, obtained from the deconvolved waveforms (Figure 1-3), is given in Table 1-3.

Table 1-3. COMPARISON OF DECONVOLVED Pn AT KN-UT

	Peak Displ. (nm)	Ω_0 (nm-sec)	Spectra (nm-sec)
KN-UT PILEDRIVER	5458	1249	~900
KN-UT HARDHAT	684	121	~90
KN-UT $\log_{10}(\frac{\text{HARDHAT}}{\text{PILEDRIVER}})$	-0.90	-1.01	-1.0

Clearly, the area under the initial P-wave pulse and the spectral ratio (Figure 1-5) of the two Pn waves indicate that the moment of the two sources are in agreement with the ratio of the yields of the two events. This is in spite of the fact that it appears that HARDHAT exhibits a pP at KN-UT and PILEDRIVER does not.

MAX-LIKE Ms MAGNITUDES FROM THE LRSM NETWORK

McLaughlin et al. (1986a) determined maximum likelihood Ms magnitudes from LRSM data for HARDHAT, PILEDRIVER, and SHOAL. The Ms magnitudes are listed in Table 1-4. The Ms estimates are consistent with a single Ms:Log(yield) relationship with unit slope; Ms = Log(Y) + 2.7(0.02).

Table 1-4. MAXIMUM LIKELIHOOD LRSM Ms (TGAL-86-1)

EVENT	Ms	σ_{Ms}	σ	# signals	# noise
PILEDRIVER	4.48	0.06	0.20	13	0
SHOAL	3.80	0.06	0.26	27	8
HARDHAT	3.50	0.08	0.36	31	4

MAXIMUM LIKELIHOOD SHORT-PERIOD WWSSN MAGNITUDES

Blandford and Shumway (1982) demonstrated that the U.S. and French granite shots were consistent with a single m_b:Log(yield) relationship. Since then McLaughlin et al. (1986c) have estimated the differential intrinsic attenuation between the two test sites parameterized by $\delta\bar{t}^*$ to be 0.04(.07) sec. This supports the original supposition that there is no significant difference in the intrinsic attenuation beneath the two test sites. McLaughlin et al. (1986a) estimated maximum likelihood magnitudes from WWSSN film chip readings for 53 events from over 8 different test sites in a general linear model for simultaneous estimation of station effects and event magnitudes (referred to as GLM86). The estimates for the 7 granite events included in GLM86 are listed in Table 1-5. Marshall et al. (1979) give the yields for SAPHIR and RUBIS as 120 and 52 kt.

Table 1-5. MAXIMUM LIKELIHOOD WWSSN m_b (GLM86)				
EVENT	YIELD (kt)	m_b(A)	m_b(A/T)	σ_{mb}
PILEDRIVER	62	5.488	5.484	0.046
SHOAL	13	4.835	4.855	0.047
BERYL	-	4.978	5.019	0.079
RUBIS	52	5.516	5.469	0.051
SAPHIR	120	5.686	5.612	0.035
TOURMALINE	-	4.669	4.698	0.032
GRENAT	-	4.826	4.868	0.039

The data are consistent with an m_b:Log(yield) relationship (derived from the four shots with known yields, Table 1-5),

$$m_{b(A/T)} = 0.93(0.07)\ \mathrm{Log}(Y) + 3.74(0.11),\ \sigma_{m_b(A/T)} = 0.07$$

with unconstrained slope or with

$$m_{b(A/T)} = 0.90\ \mathrm{Log}(Y) + 3.79(0.03),\ \sigma_{m_b(A/T)} = 0.07$$

for a constrained slope of 0.90. These results indicate that there is no significant difference between the two test sites from the point of view of m_b:Log(yield), or $\overline{t^*}$.

COMPARISON OF FAR-FIELD P-WAVE MOMENTS

Once the P-wave attenuation along a source-to-receiver path is parameterized, the P wave may serve as an estimate of the seismic moment of the explosion. Assuming the von Seggern and Blandford (1972) granite source spectral shape for HARDHAT, PILEDRIVER and SHOAL, we have estimated the $\overline{t^*}$ for each path. Following the $\overline{t^*}$ estimate, we have deconvolved the P-wave to displacement and corrected for a causal attenuation operator with constant t* (Azimi et al., 1968). This same procedure has been performed by McLaughlin et al. (1986c) for the French Sahara explosions,

SAPHIR and RUBIS, by Douglas (1987) for PILEDRIVER, and by Douglas et al. (1987) for CANNIKIN, MILROW, and LONGSHOT. In order to be consistent with McLaughlin et al. (1986c), we have assumed that the source and receiver parameters are (ρ, α, β) = (2.7gm/cc, 5.8km/s, 3.3km/s). Estimated moments are listed in Tables 1-6a and 1-6b for PILEDRIVER and SHOAL respectively. The PIELDRIVER rms moment estimate of $7.8(0.1)x10^{22}$ dyne-cm is in excellent agreement with Stevens' (1986) estimate of $6.9(0.1)x10^{22}$ dyne-cm from surface waves. Free-field RDP measurements for PILEDRIVER, such as by Murphy(1978) who estimated the RDP to be at least $2x10^4$ m^3, are however a factor of about 3 larger than those estimated from the teleseismic data (Table 1-6a). Proposed explanations for the discrepancy between "free-field" RDP measurement and teleseismic far-field P-wave moment are (1) frequency dependent t*(f), (2) additional strain-dependent non-linear attenuation of the wave field in the near-field, (3) scattering attenuation in the lithosphere, and (4) loss of amplitude at interfaces in the crust and mantle. It is unlikely that interfaces such as the Moho can account for transmission losses of more than 10 or 20%, and McLaughlin and Anderson (1987) concluded that there is little direct evidence that scattering attenuation below 2 Hz is a significant source of attenuation of teleseismic P-waves. However, attenuation at 1 Hz due to velocity perturbations in the lithosphere of only a few percent with the appropriate wavelengths could account for the discrepancy (see Section 3 of this report). If a frequency-dependent t*(f) operator were assumed, the discrepancy would be somewhat reduced, but not entirely. Additional strain-dependent attenuation in granite is under consideration and being studied experimentally in the laboratory (Rimer et al., 1987). If the "free-field" sensors located within 1000

$m-kt^{-1/3}$ scaled range are biased estimates of the far-field P-wave radiation then there may be no discrepancy. These RDP measurements would be biased high if non-linear attenuation persists to greater scaled ranges.

Table 1-6a. PILEDRIVER P-WAVE MOMENT ESTIMATES

STA	Δ (deg)	t* (sec)	MOMENT (10^{23} dyne-cm)	RDP (10^4 m^3)
SV3QB	37.58	0.40	0.88	0.80
BE-FL	29.55	0.70	0.9	0.83
HN-ME	36.50	0.55	1.0	0.95
AX2AL	24.86	0.66	0.6	0.55
RK-ON	20.96	0.40	1.1	0.98
SI-BC	19.11	0.50	0.32	0.30
PG-BC	17.35	0.65	0.43	0.35
KC-MO	16.92	0.65	0.9	0.83
JP-AT	15.73	0.45	0.25	0.23
RMS			0.78	0.70
MEAN			0.70(0.1)	0.65(0.1)
G.M.			0.63	0.58
σ_{log10}			0.23	0.23

Table 1-6b. SHOAL P-WAVE MOMENT ESTIMATES

STA	Δ (deg)	t* (sec)	MOMENT (10^{21} dyne-cm)	RDP (10^2 m^3)
SK-TX	14.94	0.15	2.0	1.8
RY-ND	15.09	0.15	4.2	3.8
AP-OK	16.51	0.45	2.3	2.1
HH-ND	17.13	0.45	15.	13
DU-OK	18.51	0.45	11.	10.
EB-MT	19.34	0.45	7.2	6.5
RK-ON	20.88	0.40	6.7	6.1
EU-AL	25.43	0.45	67.	61.
BR-PA	30.32	0.45	2.8	2.6
DH-NY	32.84	0.45	6.6	6.0
LS-NH	34.68	0.45	8.3	7.6
HN-ME	37.17	0.45	9.4	8.5
RMS			21.	19.
MEAN			12.(0.4)	11.(5.)
G.M.			0.71	6.4
σ_{log10}			0.39	0.39

The RMS M_0 estimates listed in Table 1-6c are consistent with a linear relationship,

$$\text{Log(RMS } M_0) = \text{Log(Yield)} + 21.25(0.07)$$

based on the unclassified known yields of PILEDRIVER, SHOAL, RUBIS, and SAPHIR. The data are consistent with a uniform coupling for all three locations (Climax Stock, Sands Springs, and Taourirt Tan Afella Massif).

Table 1-6c. RMS EXPLOSION MOMENTS

Event	RMS M_0 (10^{23} dyne-cm)	# Observations
PILEDRIVER	0.78(0.1)	9
HARDHAT	0.08(0.02)	1
SHOAL	0.21(0.05)	12
SAPHIR	3.4(0.7)	10
RUBIS	0.9(0.1)	11
EMERAUDE	0.5(0.2)	2
GRENAT	0.3(0.2)	2

ATTENUATION CORRECTED SPECTRAL Lg COMPARISON

Nuttli (1986) has published m_b(Lg) estimates for SHOAL (5.19) and PILEDRIVER (5.84) based on regional WWSSN stations with the conclusion that the two events fit within a broader population of western Unite States (WUS) explosions. Because HARDHAT predated the installation of the WWSSN stations in the WUS, no such comparison can be made with the HARDHAT. Using the regional attenuation relationship for Lg, $Q = 210\, f^{0.6}$, from Chavez and Priestley (1986), we have corrected Lg spectra from SHOAL and HARDHAT for the LRSM network of regional stations in the WUS ($\Delta < 1000$ km). The spectra have been corrected to a

reference distance of 100 km; $e^{\pi f \frac{\Delta}{QU}} [\frac{\Delta}{\Delta_0}]^{1/2}$. The corrected Lg spectra are shown in Figures 1-5a and b. The spectral ratio SHOAL/HARDHAT in Figure 1-5c is virtually flat. Unfortunately, this comparison cannot be made for PILEDRIVER, since the regional recordings of Lg at MN-NV and KN-UT are clipped and the next closest LRSM station was WN-SD, over 12° away. The Lg attenuation clearly changes at this distance range as the Lg waves leave the WUS and propagate across the central and eastern U.S.

CONCLUSIONS

Analysis of available far-field seismic data for U.S. and French granite underground nuclear explosions has been performed using several methodologies including:

(1) coda at two common stations, KN-UT and MN-UT, for HARDHAT and PILEDRIVER

(2) the deconvolved Pn at KN-UT for HARDHAT and PILEDRIVER,

(3) maximum likelihood Ms magnitudes from the LRSM network for HARDHAT, SHOAL, and PILEDRIVER,

(4) maximum likelihood WWSSN m_b magnitudes for PILEDRIVER, SHOAL, and the French Sahara shots,

(5) far-field P-wave moment estimates for the U.S. and French shots,

(6) and a comparison of attenuation-corrected Lg spectra for SHOAL and HARDHAT from LRSM stations at regional distances.

All of the results indicate that coupling was the same in the three different granite environments.

SECTION 2:

P WAVES FROM NTS EVENTS RECORDED AT NORSAR, AWRE ARRAYS, AND LLNL STATIONS

K. L. McLaughlin, I. N. Gupta, and R. A. Wagner

SUMMARY

Analysis of seismic data is performed at a number of arrays and single stations to estimate the low-frequency level of the far-field P-wave from broadband seismograms derived from "short-period" recordings. The area under the initial P-wave pulse, Ω_0, and the spectral low-frequency asymptote, A_0, are compared as measures of the explosion size when corrected to equivalent explosion RDP and far-field P-wave moment. Broadband P-wave displacement seismograms are estimated by the use of both single station deconvolutions and the Shumway-Der deconvolution algorithm. When both instrument response and causal intrinsic attenuation operators are removed, it is found that the measured area under the initial broadband P-wave is an excellent measure of the far-field P-wave moment.

INTRODUCTION

Marshall (1972) and Douglas et al. (1987) have shown that the initial broadband P-wave displacement pulse can provide a direct measurement of the explosion source uncontaminated by pP and by early coda from scattered waves near source and receiver. The intrinsic attenuation is parametrized for the path by the familiar t*

parameter, and a causal attenuation operator is removed from the original seismogram as well as the instrument response, and a filter is applied to yield a broadband displacement seismogram. These deconvolutions can be performed using multichannel array data (Marshall et al., 1972; and Der et al., 1987) or with care using individual seismic station recordings (McLaughlin et al., 1986c). The resulting waveforms are equivalent explosion source functions (reduced velocity potentials, RVP, or isotropic moment rate functions, $\dot{M}(t)$).

The Shumway and Der (1985) procedure is preferred for the estimation of these source functions because it can use multichannel data to estimate simultaneously the source functions and individual site functions that can distort a single station signal. The Shumway-Der procedure is a maximum likelihood estimator that requires a combination of sources and receivers in an over-determined sense to estimate simultaneously the source and receiver functions. This is not often possible if only a single station is available for a suite of events or if events do not have a full complement of stations in the array. However, it is still useful to deconvolve seismic data from a single station to derive a broadband estimate of the P-pulse with the effects of instrument and attenuation operator removed. These convolutional operators (instrument and attenuation operator) serve to lengthen the initial pulse and complicate the interference of the direct phase with early arriving phases such as pP and scattered coda originating from near the source or near the receiver (McLaughlin et al., 1987b).

In this report we present analysis of deconvolved P-waves from NTS explosions detonated in tuff at teleseismic arrays (NORSAR, EKA, GBA, and WRA), at Lawrence Livermore National Laboratory, Livermore, California (LLNL) stations

(KNB, and ELK), and at two LRSM stations (KN-UT and MN-NV). We concentrate on the estimation of far-field P-wave moment estimation and the relationship of these estimates to yield and scaled depth. We compare results with moment estimates from surface waves (Stevens, 1986) and body wave magnitude m_b (Marshall et al., 1986).

Table 2-1 lists pertinent information for a number of events analyzed in this report (FAULTLESS is included in the list since it too was detonated in volcanic tuff although at a location some distance from NTS). Of particular interest are the average overburden densities and P-wave velocities for each event. These geophysical quantities are measured from VIBROSEIS up-hole times and a downhole gravimeter. These geophysical measurements represent the effective average velocity and density above the shot point. For comparison with the moment measures, we list the m_b magnitude of Marshall et al. (1986) when available (two decimal places with standard error), otherwise the USGS m_b magnitude is listed (one decimal place). The unclassified yields of a number of events are also listed.

Table 2-1. EVENT INFORMATION

DATE	EVENT	LAT	LONG	O.T.	m_b	h(m)	$\bar{\alpha}$	$\bar{\rho}$	Y(Kt)
1962046	HARDHAT	37.23N	116.06W	18:00:00.1	.	287.1	.	2.67	5.9
1965132	BUTEO	37.24N	116.43W	18:15:00.1	.	695.6	.	.	0.7
1966055	REX	37.27N	116.43W	15:55:07.0	4.8	671.2	.	.	16.
1966104	DURYEA	37.24N	116.43W	14:13:43.1	5.4	543.8	.	.	65.
1966153	PILEDRIVER	37.23N	116.06W	15:30:00.1	5.6	462.7	.	2.66	62.
1967143	SCOTCH	37.28N	116.37W	14:00:00.0	5.7	977.4	2.400	2.06	150.
1968019	FAULTLESS	38.63N	116.22W	18:15:00.1	6.3	975.4	.	.	.
1968026	CABRIOLET	37.28N	116.51W	16:00:00.1	.	51.8	.	1.77	2.3
1968117	BOXCAR	37.30N	116.46W	15:00:00.0	6.4	1165.9	2.680	1.93	1200.
1968343	SCHOONER	37.34N	116.57W	16:00:00.1	4.8	111.3	.	.	35.
1968354	BENHAM	37.23N	116.47W	16:30:00.0	6.3	1402.1	.	2.01	1100.
1969127	PURSE	37.28N	116.50W	13:45:00.0	5.8	598.8	.	.	.
1970085	HANDLEY	37.30N	116.53W	19:00:00.2	6.5	1206.1	.	2.13	.
1973157	ALMENDRO	37.25N	116.35W	13:00:00.1	6.16(0.02)	1063.8	3.083	2.10	.
1974058	LATIR	37.10N	116.05W	17:00:00.1	5.62(0.02)	641.0	1.707	1.74	.
1975059	TOPGALLANT	37.11N	116.06W	15:15:00.1	5.69(0.02)	713.2	1.653	1.90	.
1975134	TYBO	37.22N	116.47W	14:00:00.2	6.05(0.02)	765.0	2.275	1.96	.
1975154	STILTON	37.34N	116.52W	14:20:00.2	5.82(0.02)	731.5	2.150	1.89	.
1975170	MAST	37.35N	116.32W	13:00:00.1	6.05(0.02)	911.3	3.877	2.24	.
1975177	CAMEMBERT	37.28N	116.37W	12:30:00.2	6.20(0.02)	1310.6	2.900	2.13	.
1975301	KASSERI	37.29N	116.41W	14:30:00.2	6.30(0.02)	1265.0	3.040	1.98	.
1975324	INLET	37.22N	116.37W	15:00:00.1	5.96(0.02)	819.0	3.042	2.11	.
1976003	MUENSTER	37.30N	116.33W	19:15:00.2	6.28(0.02)	1452.4	2.900	1.98	.
1976043	FONTINA	37.27N	116.49W	14:45:00.2	6.24(0.02)	1219.0	2.860	2.03	.
1976045	CHESHIRE	37.24N	116.42W	11:30:00.2	5.92(0.02)	1167.0	3.210	2.11	.
1976069	ESTUARY	37.31N	116.36W	14:00:00.1	5.97(0.02)	868.1	2.660	1.98	.
1976074	COLBY	37.31N	116.47W	12:30:00.2	6.34(0.02)	1273.4	2.790	1.89	.
1976077	POOL	37.26N	116.33W	14:15:00.1	6.05(0.03)	879.3	2.865	1.96	.
1976077	STRAIT	37.11N	116.05W	14:45:00.1	5.87(0.02)	780.3	1.691	1.78	.
1978082	ICEBERG	37.10N	116.05W	16:30:00.2	5.70(0.02)	640.0	1.643	1.79	.
1978101	FONDUTTA	37.30N	116.33W	15:30:00.2	5.49(0.02)	633.0	2.299	2.12	.
1978101	BACKBEACH	37.23N	116.37W	17:45:00.1	5.54(0.02)	672.1	2.043	2.04	.
1978243	PANIR	37.28N	116.36W	14:00:00.2	5.66(0.02)	681.0	2.096	2.05	.
1978270	RUMMY	37.08N	116.05W	17:20:00.1	5.85(0.02)	640.0	1.748	1.88	.
1978350	FARM	37.27N	116.41W	15:30:00.2	5.63(0.02)	689.0	2.125	2.01	.
1979039	QUINELLA	37.10N	116.05W	20:00:00.1	5.60(0.02)	579.1	1.614	1.80	.
1979162	PEPATO	37.29N	116.46W	14:00:00.2	5.56(0.03)	681.0	1.887	1.93	.
1980117	COLWICK	37.25N	116.42W	17:00:00.1	5.54(0.02)	633.0	2.070	1.91	.
1981157	HARZER	37.30N	116.33W	18:00:00.1	5.5	637.0	2.056	1.98	.
1983244	CHANCELLOR	37.27N	116.36W	14:00:00.1	5.4	625.0	1.970	2.01	.

DATA ANALYSIS

A suite of NTS events recorded at NA0 was deconvolved of instrument and a causal attenuation operator with frequency independent t* = 0.4 sec. See McLaughlin et al. (1986) for details as to the filter that was applied to maximize the signal-to-noise ratio for each broadband displacement waveform. The P-wave moment for each event was subsequently estimated from the area under the initial displacement pulse, Ω_0. See Figure 2-1 for display of the broadband NA0 (approximately flat from 0.3 to 4.0 Hz) displacement traces. Table 2-2 lists the Log-moments (moment in dyne-cm) derived from these measurements of Ω_0 assuming the overburden velocity, $\overline{\alpha}$, and density, $\overline{\rho}$, for each event (listed in Table 2-1), and ρ = 2.5 gm/cc, α = 5.6 km/sec, and β = 3.2 km/sec at NA0. For those events for which no overburden density and velocity were available, we assumed $\overline{\alpha}$ = 3.16 and $\overline{\rho}$ = 2.13. These single station moment estimates are plotted against the moment estimates of Stevens (1986) in Figure 2-2 and against Marshall et al.'s m_b's in Figure 2-3. It was found that use of the overburden velocity and density (average between shot point and surface) for the geometrical spreading correction (see Aki and Richards, 1980) gives the best correlation of estimated P-wave moment with yield. Steven's moment estimates are on average 1.37(0.06) log units larger, with a standard deviation of 0.22. If we assume a slope of 0.9 for the m_b:Log(moment) relationship then

$$m_b(\text{Marshall}) = 0.9\ \text{Log(Stevens)} - 15.11(0.04),\quad \sigma = 0.14$$

and

$$m_b(\text{Marshall}) = 0.9\ \text{Log(NA0)} - 13.86(0.05),\quad \sigma = 0.21.$$

Neither the offset between the surface wave moment and the single station P-wave moment, nor the larger scatter for a single station moment versus the network m_b, is surprising given that the P-wave moment estimate is based on a single station. NTS explosion amplitudes at NA0 are generally low with respect to ISC. This estimate of course should improve by examining other stations and forming a network of stations.

Table 2-2. NA0 EXPLOSION MOMENT ESTIMATES

EVENT	$\bar{\rho}$ gm/cc	$\bar{\alpha}$ km/s	Ω_0 nm-sec	Log(M_0) dyne-cm	RDP m^3	Log(M_0) dyne-cm (STEVENS)
ALMENDRO	2.10	3.083	157	22.55	14040.	23.78
COLBY	1.89	2.790	254	22.67	25194.	.
COLWICK	1.91	2.070	31	21.56	3558.	22.91
ESTUARY	1.98	2.660	81	22.15	8042.	23.79
FONTINA	2.03	2.860	198	22.59	18712.	.
ICEBERG	1.79	1.643	114	21.96	15185.	23.15
INLET	2.11	3.042	23	21.70	2066.	.
KASSERI	1.98	3.040	178	22.58	16511.	.
LATIR	1.74	1.707	33	21.45	4373.	.
MAST	2.24	3.877	64	22.32	4925.	23.58
MUENSTER	1.98	2.900	141	22.45	13397.	.
PANIR	2.05	2.096	51	21.80	5615.	22.97
PEPATO	1.93	1.887	15	21.19	1794.	23.07
POOL	1.96	2.865	58	22.05	5573.	23.52
QUINELLA	1.80	1.614	58	21.66	7773.	.
RUMMY	1.88	1.748	60	21.74	7559.	23.12
STILTON	1.89	2.150	37	21.66	4188.	23.17
STRAIT	1.78	1.691	102	21.93	13429.	23.28
TOPGALLANT	1.90	1.653	81	21.83	10441.	22.83
TYBO	1.96	2.275	84	22.06	9074.	23.50

In conjunction with the single station deconvolutions, the Shumway-Der multi-channel maximum likelihood deconvolution method was utilized for estimation of Pahute Mesa explosion source functions from available data from NORSAR (73°), EKA (72°), GBA (128°), and WRA (117°). The source functions derived from EKA

data are shown in Figure 2-4a, b, and c. In each case we have deconvolved the Der and Lees (1985) tectonic-to-shield frequency dependent t*(f) causal attenuation operator and instrument response from the original data. It should be mentioned that in the case of the NORSAR data, the array consisted of the center element stations of the each of the NORSAR subarrays including NA0.

These source functions were used in two ways. First they were used to estimate equivalent far-field P-wave moments and RDP's. Second, they were convolved with attenuation operators to predict teleseismic magnitudes. In this way, the attenuation-dependent magnitude bias can be examined for NTS-type waveforms. We first describe the P-wave moment estimates.

Table 2-3a lists Ω_0 measured from the integrated area under the initial displacement P-pulse at each array for each event. In order to recover these estimates from the Shumway-Der deconvolution procedure which performs several normalizations of the raw data before deconvolution, we compute the rms amplitude across the array for each event and then reverse the normalization procedure in order to properly estimate the rms level across the array. From this analysis it is clear that the rms amplitude across the NORSAR array for Pahute Mesa events is substantially greater on average than the amplitude from the single array element NA0. The phenomenon of strong focusing-defocusing at large arrays is well known (Aki, 1973; Chang and von Seggern, 1980; Cormier 1986, 1987; McLaughlin, 1986; McLaughlin and Anderson, 1987) and demonstrates the need for a number of stations to provide coverage that will lead to an unbiased estimate of source size. Also, we used a causal frequency-dependent t*(f) attenuation operator for the entire NORSAR array and a frequency independent t*

attenuation operator for the single station NA0. Because t*(f) increases with decreasing frequency and because the frequency-dependent t*(f) is greater than the frequency-independent t*, the attenuation correction for the NORSAR array is about twice as large at 1 Hz as the correction for NA0.

Table 2-3a.

EVENT	ARRAY	Ω_0 (nm-sec)
BOXCAR	EKA	1249
CAMEMBERT	EKA	1253
CAMEMBERT	GBA	245
CHESHIRE	EKA	513
ESTUARY	EKA	542
ESTUARY	NORSAR	100
FAULTLESS	EKA	1277
FONTINA	EKA	963
HANDLEY	EKA	2370
INLET	EKA	792
INLET	NORSAR	540
KASSERI	EKA	1283
KASSERI	NORSAR	1544
KASSERI	GBA	233
KASSERI	WRA	32
MAST	EKA	700
MAST	NORSAR	510
MUENSTER	EKA	1233
MUENSTER	GBA	184
MUENSTER	WRA	29
PURSE	EKA	260
STILTON	NORSAR	350
TYBO	EKA	675
TYBO	GBA	134
TYBO	NORSAR	589

Table 2-3b. Moment Estimates From EKA array

EVENT	M_0 10^{24} dyne-cm	RDP m^3	Log(M_0)	Log(RDP)	Log(M_0) (Stevens)
boxcar	0.313	117034.	23.50	5.07	24.39
camembert	0.276	122677.	23.44	5.09	.
cheshire	0.131	47909.	23.12	4.68	23.79
estuary	0.101	57514.	23.01	4.76	23.79
faultless	0.320	119657.	23.50	5.08	.
fontina	0.203	97164.	23.31	4.99	.
handley	0.593	221980.	23.77	5.35	24.28
inlet	0.186	76054.	23.27	4.88	.
kasseri	0.293	127284.	23.47	5.10	.
mast	0.244	57542.	23.39	4.76	23.58
muenster	0.262	125208.	23.42	5.10	.
purse	0.065	24362.	22.81	4.39	23.42
tybo	0.100	77849.	23.00	4.89	23.50

The P-wave moment estimates derived from the EKA array relative to Stevens's surface wave moment estimate are on average 0.6 units low, with a standard deviation of 0.21 log units. The scatter with respect to Marshall et al.'s (1986) m_b is smaller (0.11 versus 0.21):

$$\text{Log}(M_0(\text{EKA})) - \text{Log}(M_0(\text{Stevens})) = -0.59(0.09), \quad \sigma = 0.21,$$

and

$$m_b(\text{Marshall}) = 0.90\ \text{Log}(M_0(\text{EKA})) - 14.8(0.03), \quad \sigma = 0.11.$$

The scatter of the Log(M_0(EKA)) P-wave measure is substantially smaller with respect to a network m_b than would be expected based on a single station m_b or even a small array such as EKA.

There was somewhat less data available from the NORSAR, GBA, and WRA arrays. These moment estimates are tabulated below. We can see that the single station NA0 P-wave moment estimates are 1.04(0.09) log units low with respect to the

entire NORSAR array.

Table 2-3c. Moment Estimates From NORSAR array					
EVENT	M_0 10^{24} dyne-cm	RDP m^3	Log(M_0)	Log(RDP)	Log(M_0) (Stevens)
inlet	0.127	51855.	23.10	4.71	.
kasseri	0.352	153059.	23.55	5.18	.
mast	0.177	41841.	23.25	4.62	.
stilton	0.046	42346.	22.67	4.63	23.17
tybo	0.087	67930.	22.94	4.83	23.50

Table 2-3d. Moment Estimates From GBA array					
EVENT	M_0 10^{24} dyne-cm	RDP m^3	Log(M_0)	Log(RDP)	Log(M_0) (Stevens)
camembert	0.165	73212.	23.22	4.86	.
estuary	0.057	32365.	22.76	4.51	.
kasseri	0.162	70528.	23.21	4.85	.
muenster	0.119	57028.	23.08	4.76	.
tybo	0.060	47089.	22.78	4.67	23.50

Table 2-3e. Moment Estimates From WRA array					
EVENT	M_0 10^{24} dyne-cm	RDP m^3	Log(M_0)	Log(RDP)	Log(M_0) (Stevens)
kasseri	0.035	15437.	22.55	4.19	.
muenster	0.030	14325.	22.48	4.16	.

A COMPARISON OF

TIME- AND FREQUENCY-DOMAIN MEASURES OF

TELESEISMIC P AND REGIONAL Pn MOMENT

In order to bridge the gap between regional and teleseismic P-wave measures and to increase our data base, we have combined data from several stations for comparison. Also we wish to compare spectral measures of the low-frequency asymptote of the P-

wave with the area under the P-wave pulse. To do this we have utilized a large set of explosions whose records are available at the broadband LLNL stations KNB and ELK as well as the events previously listed for NA0. To the KNB data we add data recorded at the LRSM station KN-UT, which was located a very short distance (0.8 km) from the current installation of the broadband station KNB. By including KN-UT (1961-1969), we can extend our studies to events with non-standard scaled depths of burial including two cratering shots, CABRIOLET and SCHOONER.

For each event-station pair, the instrument response was removed and in the case of NA0, a causal attenuation operator was also removed. The area under the deconvolved displacement broadband P-wave was measured, Ω_0. For comparison, a spectral measure of the low-frequency asymptote was made by a least squares fit to the the log-amplitude spectra assuming either an f^{-2} or f^{-3} high-frequency fall-off. The amplitude spectrum was assumed to have the form of either

$$\frac{A_{02}}{\sqrt{1+(f/f_c)^4}}$$

or

$$\frac{A_{03}}{\sqrt{1+(f/f_c)^6}}.$$

The least squares fit to the log-amplitude spectra was determined for the combination A_{02} (or A_{03}) and corner frequency, f_c. Examples of such fits are shown in Figures 2-5a through 2-5f for MAST at KNB and ELK. For completeness, the three P-wave measures, Ω_0, A_{02}, and A_{03}, are listed in Table 2-4 for NAO, KNB & KN-UT, and ELK. Although Ω_0 should be an equivalent measure of either A_{02} or A_{03}, we choose

to distinguish by notation between the three measures of P-wave moment in order to avoid confusion.

Table 2-4a. P-WAVE AREA, LOW-FREQUENCY ASYMPTOTE, AND CORNER FREQUENCY ESTIMATES

No.	DATE	EVENT	NA0				
			Ω_0	f^{-2}		f^{-3}	
			(nm-sec)	A_0 (nm-sec)	f_c (Hz)	A_0 (nm-sec)	f_c (Hz)
1	1962046	HARDHAT	.	.	.	.	.
2	1965132	BUTEO	.	.	.	.	.
3	1966055	REX	.	.	.	.	.
4	1966104	DURYEA	.	.	.	.	.
5	1966153	PILEDRIVER	.	.	.	.	.
6	1967143	SCOTCH	.	.	.	.	.
7	1968026	CABRIOLET	.	.	.	.	.
8	1968343	SCHOONER	.	.	.	.	.
9	1968354	BENHAM	.	.	.	.	.
10	1973157	ALMENDRO	157	735	0.3	343	0.7
11	1974058	LATIR	33	172	0.3	117	0.6
12	1975059	TOPGALLANT	81	262	0.3	148	0.7
13	1975134	TYBO	84	338	0.3	240	0.6
14	1975154	STILTON	37	281	0.3	134	0.7
15	1975170	MAST	64	205	0.5	112	1.0
16	1975177	CAMEMBERT	.	.	.	.	.
17	1975301	KASSERI	178	505	0.3	437	0.6
18	1975324	INLET	23	125	0.7	58	1.4
19	1976003	MUENSTER	141	625	0.3	742	0.5
20	1976043	FONTINA	198	572	0.3	475	0.6
21	1976045	CHESHIRE	.	.	.	.	.
22	1976069	ESTUARY	81	383	0.3	221	0.7
23	1976074	COLBY	254	622	0.3	574	0.6
24	1976077	POOL	58	220	0.5	130	1.0
25	1976077	STRAIT	102	315	0.3	262	0.6
26	1978082	ICEBERG	114	257	0.3	324	0.5
27	1978101	FONDUTTA	.	.	.	.	.
28	1978101	BACKBEACH	.	.	.	.	.
29	1978243	PANIR	51	145	0.4	107	0.7
30	1978270	RUMMY	60	321	0.3	229	0.6
31	1978350	FARM	.	.	.	.	.
32	1979039	QUINELLA	58	250	0.3	90	0.8
33	1979162	PEPATO	15	47	0.6	8	2.9
34	1980117	COLWICK	31	39	0.7	14	1.8

Table 2-4b. P-WAVE AREA, LOW-FREQUENCY ASYMPTOTE, AND CORNER FREQUENCY ESTIMATES

No.	EVENT	KN-UT & KNB					ELK				
		Ω_0	f^{-2}		f^{-3}		Ω_0	f^{-2}		f^{-3}	
		(nm-sec)	A_0 (nm-sec)	f_c (Hz)	A_0 (nm-sec)	f_c (Hz)	(nm-sec)	A_0 (nm-sec)	f_c (Hz)	A_0 (nm-sec)	f_c (Hz)
1	HARDHAT	121	246	2.3	191	3.5	.	.	.	.	.
2	BUTEO	13	17	>6.6	17	>6.6	.	.	.	.	.
3	REX	160	229	2.2	189	3.2	.	.	.	.	.
4	DURYEA	414	450	1.6	310	2.7	.	.	.	.	.
5	PILEDRIVER	1249	3656	1.1	1699	2.5	.	.	.	.	.
6	SCOTCH	1257	1585	1.4	937	2.6	.	.	.	.	.
7	CABRIOLET	12	20	2.3	13	3.8	.	.	.	.	.
8	SCHOONER	142	118	1.0	103	1.7	.	.	.	.	.
9	BENHAM	8627	36964	0.6	10760	<1.9	.	.	.	.	.
10	ALMENDRO	5626	13853	0.7	7205	1.7	2389	3336	1.2	1819	2.5
11	LATIR	.	.	.	.	.	.	.	.	.	.
12	TOPGALLANT	.	.	.	.	.	.	.	.	.	.
13	TYBO	2668	4831	1.2	3677	2.2	1391	2184	1.1	1230	2.3
14	STILTON	1325	2289	0.9	1289	2.0	1029	2434	0.7	1275	1.7
15	MAST	2890	4599	1.0	3133	2.0	1452	1849	1.4	1257	2.6
16	CAMEMBERT	5871	12533	0.8	7526	1.8	2834	5291	0.8	2155	2.1
17	KASSERI	.	.	.	.	.	.	.	.	.	.
18	INLET	2023	8382	0.6	4467	1.5	1039	1393	1.2	866	2.4
19	MUENSTER	7450	12906	0.7	7814	1.6	3269	5463	0.8	2785	1.9
20	FONTINA	8773	11692	0.7	9837	1.4	4202	11614	0.5	6429	1.3
21	CHESHIRE	2560	7819	0.9	4898	1.9	1219	1184	1.8	788	3.2
22	ESTUARY	2839	6330	0.6	3924	1.4	1448	1810	1.0	1100	2.1
23	COLBY	9167	23074	0.5	12556	1.3	5944	15389	0.4	11084	1.0
24	POOL	2725	5941	0.8	3529	1.8	1328	1968	1.1	1238	2.2
25	STRAIT	.	.	.	.	.	.	.	.	.	.
26	ICEBERG	.	.	.	.	.	.	.	.	.	.
27	FONDUTTA	595	589	1.3	377	2.5	389	440	1.3	281	2.5
28	BACKBEACH	806	1687	1.0	1302	1.9	374	556	1.4	385	2.5
29	PANIR	1223	2948	1.0	1447	2.3	.	.	.	.	.
30	RUMMY	.	.	.	.	.	.	.	.	.	.
31	FARM	900	2011	1.3	1210	2.6	.	.	.	.	.
32	QUINELLA	.	.	.	.	.	.	.	.	.	.
33	PEPATO	.	.	.	.	.	.	.	.	.	.
34	COLWICK	.	.	.	.	.	.	.	.	.	.

Figure 2-6a plots the Ω_0 measurements for 14 NTS events at KNB versus ELK. The regression, Log(KNB) = Log(ELK) + 0.28(0.07), can be used to adjust the ELK estimates to equivalent KNB values. Similarly we find that Log(NA0) = Log(ELK) - 1.34(0.13), Figure 2-6b, and Log(NA0) = Log(KNB) - 1.62(0.14), Figure 2-6c.

Even with this set of limited data we can see evidence for cube-root scaling. We have plotted the estimated corner frequency, f_c, versus the low-frequency asymptote, A_0, for both the f^{-2} and f^{-3} case from the NA0 P waves in Figures 2-6d and 2-6e for NA0 and Figures 2-6f and 2-6g for KNB and ELK respectively. Evidence for f_c proportional to $A_0^{-1/3}$ is clearly visible in both plots, although the trend is best seen in the f^{-3} case for NA0. This may not necessarily be an argument for f^{-3} source spectra so much as it is a demonstration of the trade-off in fitting bandlimited data to a parameterized model. In cases where the corner frequency is in the middle of the bandwidth, both f^{-2} and f^{-3} fit the data equally well. The corner frequencies fit by an f^{-2} model are always lower than corner frequencies fit by an f^{-3} model. For those cases where the f^{-3} corner frequency is located in the lower quartile of the bandwidth, the f^{-2} model corner frequency estimate saturates at the lower end of the bandwidth.

Plots of Ω_0 and A_{03} versus yield, based on 20 NTS shots recorded at NA0, are shown on log-log scale in Figures 2-6h and 2-6i, respectively. The actual scales are not shown because the yield values are classified. Results of linear regression with slope of unity are indicated on each plot. Note the somewhat better fit for Ω_0 as compared to A_{03}. The combined regional data from KNB (including KN-UT) and ELK provide the Ω_0 plot of Figure 2-6j. This fit is significantly better than the two fits for teleseismic data in Figures 2-6h and 2-6i. Applying the medium velocity-dependent

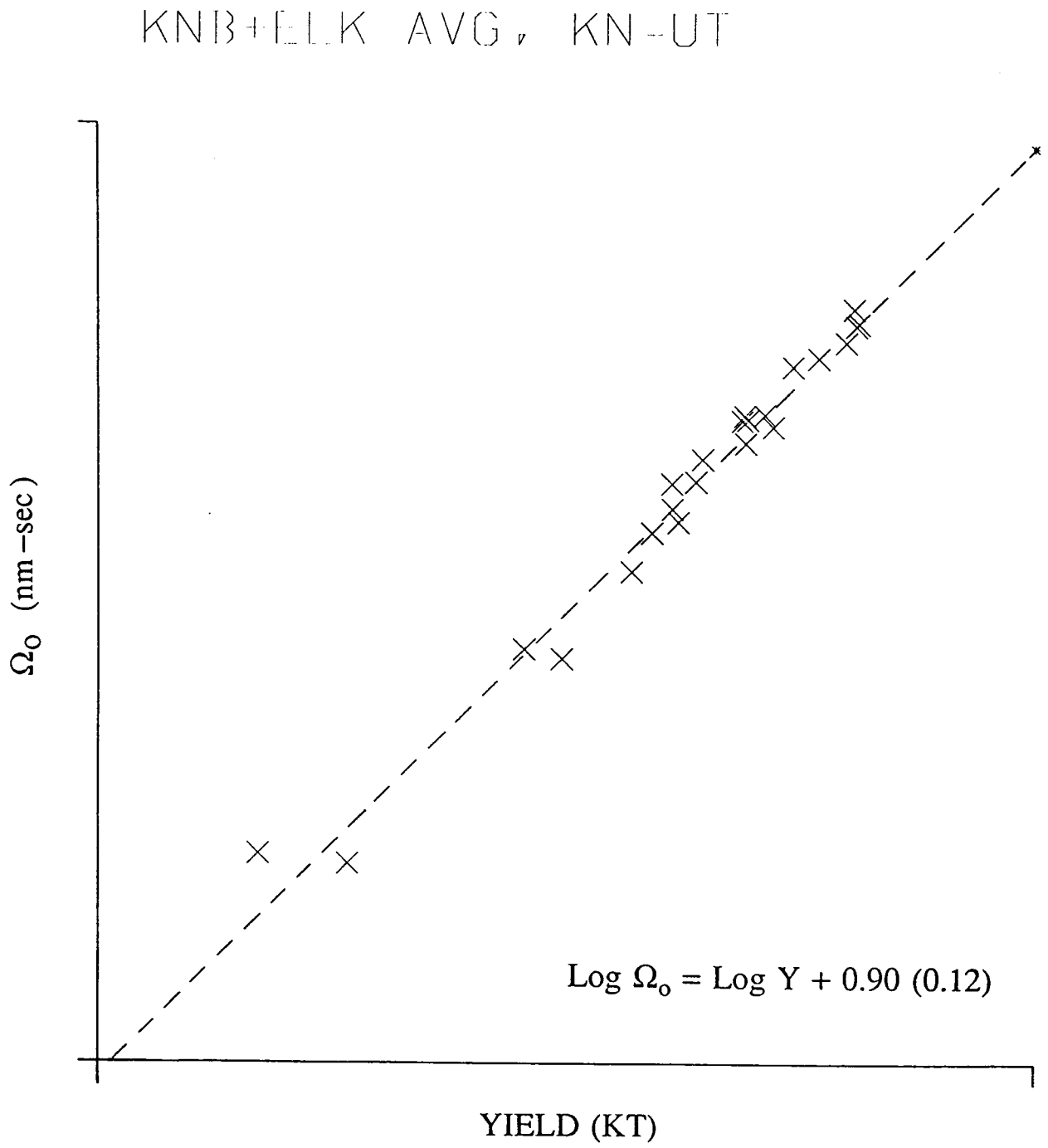
KNB+ELK AVG, KN-UT
Ω_o (nm-sec)
Log Ω_o = Log Y + 0.90 (0.12)
YIELD (KT)

Figure 2-6j

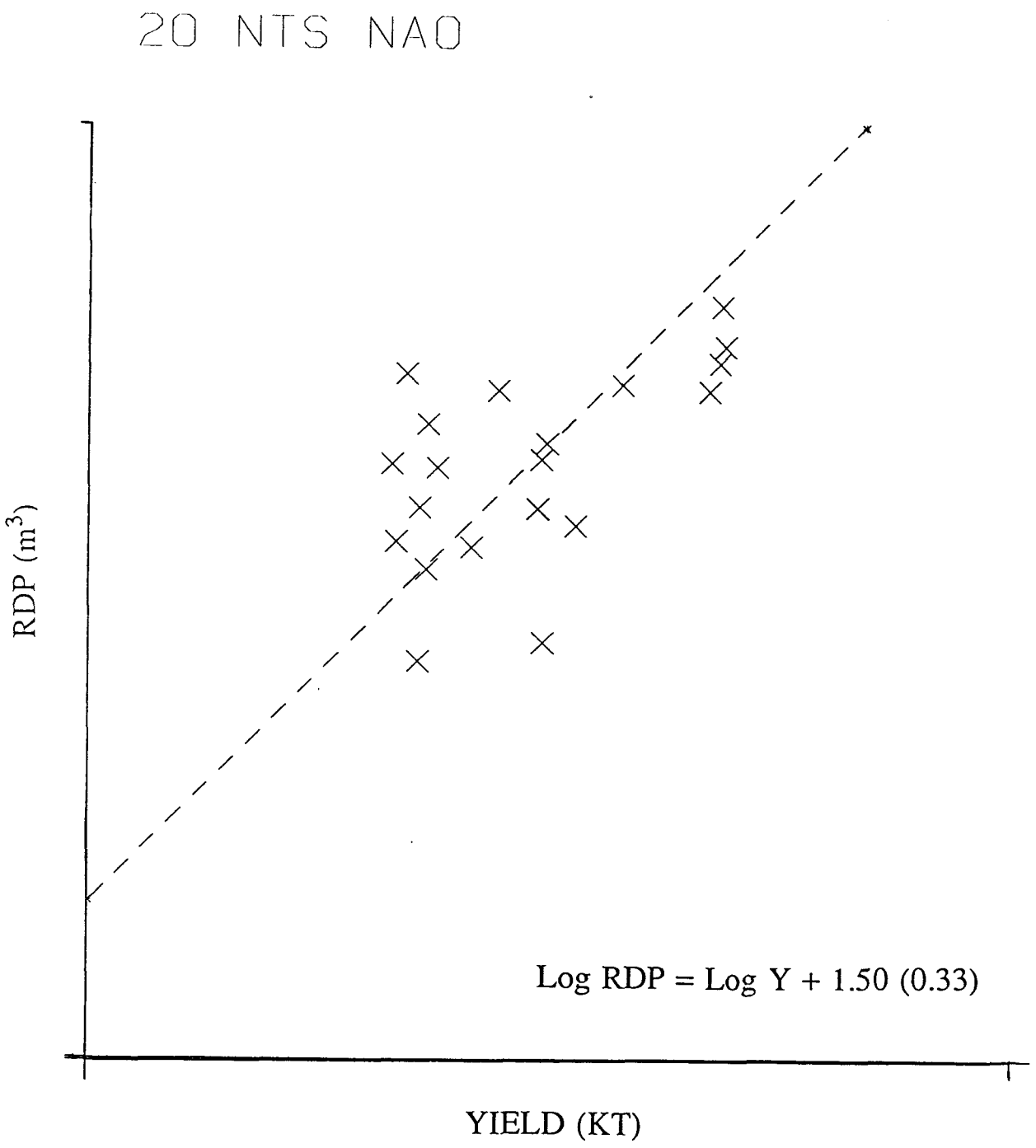

Figure 2-6k

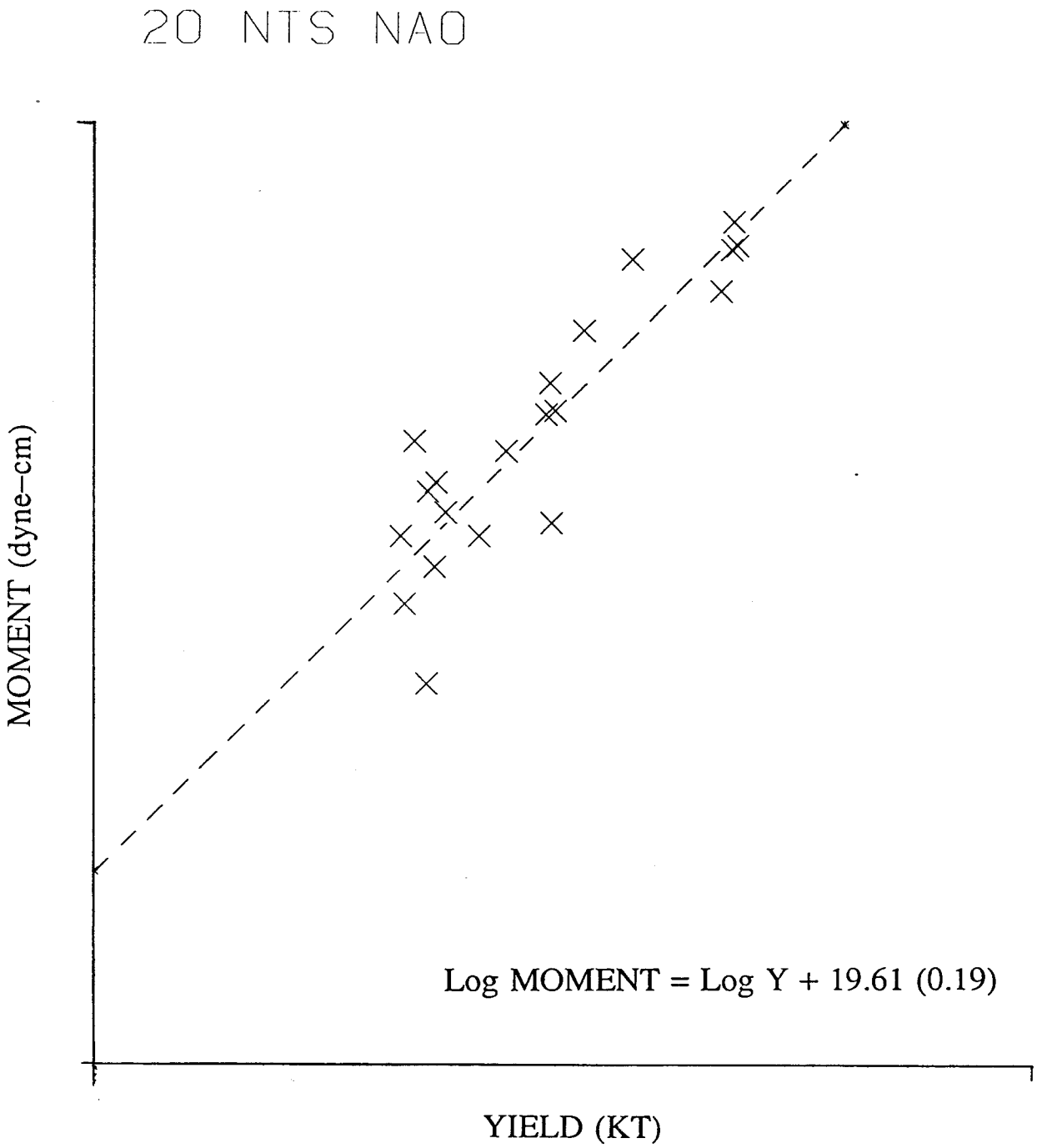

Figure 2-61

geometrical spreading terms (Aki and Richards, 1980) to the teleseismic measurements of Ω_0 at NA0, we obtained the RDP and seismic moment versus yield plots shown in Figures 2-6k and 2-6l, respectively. Results of linear regression, shown on each plot, indicate the moment to show a much improved correlation with yield (Figure 2-6l) than with RDP (Figure 2-6k) or Ω_0 (Figure 2-6h).

Plots of the various P-wave measures versus yield, with proper scales and identification of individual shots, are contained in a classified appendix to the report.

Although the time-domain measure of P-wave area, Ω_0, at a single station is better correlated to yield than the frequency domain measure, A_0, the length of the pulse measured in the time-domain does not correlate well with the inverse of the corner frequency derived from the spectra or the area of the pulse. It would appear that the spectral-domain measure is a better estimate of the corner frequency, whereas the time-domain measure is a better estimate of the P-wave moment of the explosion. The time-domain measure of P-wave moment makes no assumption about the explosion source spectral shape, and therefore it does not represent model-dependent trade-offs that increase uncertainty. The P-wave area measurement appears to be a robust measure of P-wave moment for both teleseismic and regional distances. However, at teleseismic distances an attenuation operator must be removed from the seismogram, and this necessitates an assumption about the spectral shape in order to estimate t*. Consequently, we are not without some form of model dependence.

CONCLUSIONS

We have used data from a single station NA0, the NORSAR array, and three AWRE arrays, as well as two stations of the LLNL network to examine the use of deconvolution procedures to estimate P-wave moment. The area under the displacement P-pulse at either teleseismic or regional distances gives a good direct measure of the moment of the explosion. The measurements are tabulated in this report to enable other researchers to compare the measurements with other seismic source parameters as well as available geophysical measurements that may shed light on coupling and source scaling. Plots of the P-wave integrated displacement measurements versus yield and scaled depth are presented in a classified appendix. The deconvolved P-waves are shown in Figures 2-8a through 2-8h for completeness.

The measurement of the deconvolved P-wave offers several advantages over the traditional Peak-to-Peak or zero-to-peak response of a standard instrument. Corrections for differential attenuation and instrument response can be made at each station or array to pre-whiten the response of the earth and instrument to a common bandwidth. The initial deconvolved P-wave is not affected by the interference of secondary phases such as pP. The P-wave integrated displacement estimation does not require a model for the seismic source spectrum or source time function in order to interpret the amplitude in terms of a P-wave moment or yield. However, in order to estimate the intrinsic attenuation, some form of source spectral model is usually assumed. Also, measurements made on signals with low signal to noise can be complicated by low-frequency noise contamination of the deconvolved waveforms.

Even when the RMS amplitude across an array such as NORSAR and a frequency dependent t*(f) causal attenuation operator are used, we find that the teleseismic P-wave moment estimate is low with respect to the surface wave moment estimate. Assuming that the other independent measures of moment are correct, this bias may be due to one or a combination of several factors. (1) The assumed attenuation parameter, t*, may be too small. (2) The finite bandwidth of the deconvolution limits the total integrated displacement that can be recovered. (3) Scattering attenuation is present in the propagation and not modeled by the minimum-phase attenuation operators parameterized by a t*(f). (4) Focusing-defocusing of the P-waves at the source may bias the few arrays for which we have data.

These possible systematic biasing effects on the far-field P-wave amplitude are examined in detail in Section 3 in an attempt to predict the teleseismic P-wave magnitude based on two recent explosion source estimates based on near-field data.

SECTION 3:

TELESEISMIC P WAVEFORMS AND mb's PREDICTED FROM NEAR-FIELD EXPLOSION SOURCE FUNCTION ESTIMATES: EVIDENCE FOR P-WAVE SCATTERING ATTENUATION?

K. L. McLaughlin

SUMMARY

The empirically derived explosion source functions of McEvilly and Johnson (1987) are used to predict teleseismic P-wave magnitudes based on the frequency-dependent t*(f) models of Der and Lees (1985). The predicted magnitudes are several tenths larger than are observed across the WWSSN network. We examine several assumptions inherent in the calculation including focusing-defocusing bias, the |pP/P| amplitude ratio, intrinsic attenuation, and scattering attenuation. If predicted teleseismic amplitudes are corrected for statistical biasing effects due to focusing-defocusing then the discrepancy between observed and predicted magnitudes is between 0.2 and 0.4 magnitude units. Scattering of P-waves by velocity heterogeneity in the lithosphere is just as reasonable an explanation for the additional needed attenuation as is the introduction of additional intrinsic attenuation. A few percent velocity variation (7% to 10% rms) of the lithosphere with scale lengths between 1 and 2 km in the crust and 2 and 4 km in the upper mantle is required to produce attenuation on the order of 0.2 to 0.4 magnitude units.

INTRODUCTION

It is important to account properly for the seismic energy loss of P waves radiated by contained nuclear explosions. Because trade-offs exist between the teleseismic intrinsic attenuation, the far-field seismic source time function, the source strength, and the parameterization of the non-linear free-surface interaction, there has been controversy over the dispensation of the seismic energy observed at teleseismic distances. Since the short-period seismic magnitude m_b remains the primary estimate of seismic yield, most work has centered around calibration of the m_b:Log(yield) relationship (Bache, 1982). Carpenter (1966) showed that an equivalent far-field explosion source time function, derived from measurements in the near-field of a contained explosion, predicted the teleseismic magnitude if the total intrinsic attenuation for the path was characterized by a frequency-independent Futterman (1962) attenuation operator with a t* of about 1 sec. Helmberger and Hadley (1981) came to a similar conclusion based on near-field seismic modeling and teleseismic magnitudes.

Both Carpenter (1966) and Helmberger and Hadley (1981) propagated the equivalent seismic source to teleseismic distances assuming that the far-field P-waveform was composed of a linear combination of P+pP. Douglas and Hudson (1983) commented on the trade-offs between the P+pP interference, the attenuation operator, and the source time function inherent in the Helmberger and Hadley study. In contrast, Frazier and Filson (1972) concluded that t* was less than 0.5 sec between NTS and NORSAR based on a comparison of near-field and teleseismic spectra of BOXCAR. Furthermore, Der and McElfresh (1977) concluded that the t* for NTS

was significantly less than 1.0 sec at 1 Hz, based on observations of teleseismic P-wave spectra.

These t* differences between researchers are in part due to the frequency dependence of attenuation in the Earth and the need to reconcile the attenuation of body waves with the damping of free oscillations as well as the laterally heterogeneous structure of the Earth's intrinsic attenuation (see Cormier, 1982). Several frequency-dependent Q models have been proposed for both tectonic and shield areas of the world (Minster, 1978; Anderson and Given, 1982; Der and Lees, 1985; Bache et al., 1985; Choy and Cormier, 1986; Taylor, 1986; and Der et al., 1987).

Recently, Burger et al. (1987) examined the t*(f) model of Minster (1978) versus constant t*, two source characterizations, and linear P+pP interference to explore model-dependent tradeoffs and to predict teleseismic amplitudes from Pahute Mesa NTS. They conclude that in order to match synthetic and observed teleseismic magnitudes predicted by near-field RDP's, the average teleseismic t* for Pahute Mesa events is between 0.8 and 1.0 sec, depending upon the parameterization of the source.

This apparent contradiction of high t* (0.8 to 1.0 sec) versus low t* (0.4 to 0.6 sec) between researchers has commonly been characterized by differences between those workers that fit spectra and those workers that fit amplitudes and/or synthetic seismograms. It has been characterized by differences in assumed source spectral shape, frequency-dependent versus frequency-independent t*, and time-domain versus frequency-domain modeling. What is clear at this juncture is that predicted NTS explosion short-period teleseismic P-waves are too large if near-field estimates of the explosion moment are used with attenuation models derived from studies based on

spectral shape. Intrinsic attenuation models with t* on the order of 1 sec are required in order to match teleseismic amplitudes. If we reject the models with t* greater than 0.55 sec, then we must question the assumptions upon which the far-field amplitudes are based. Either (1) near-field explosion moment estimates are biased high, (2) near-field source functions are incorrectly parameterized, (3) teleseismic P-wave amplitudes are biased measures of the explosion moment, or (4) intrinsic attenuation inadequately describes the attenuation of teleseismic P-waves.

If scattering attenuates P-waves in the lithosphere, then intrinsic attenuation models with minimum-phase responses and simple t*(f) parameterizations are inadequate to describe the P-wave attenuation mechanism. Recently, both Bache et al. (1985) and Taylor et al. (1986) have suggested that scattering may contribute to P-wave attenuation. Bache et al. found that their absorption-band intrinsic attenuation model (with minimum-phase response) did not properly disperse the initial high-frequency P-wave pulse, while Taylor et al. found that the ratio of P to S attenuation suggested scattering.

In this report, we utilize equivalent explosion source functions empirically derived from moment tensor inversions to predict teleseismic P-wave magnitudes. The work differs from previous work in that the explosion sources are not parameterized but rather are directly specified for the two explosions, CHANCELLOR and HARZER, as explicit functions of time. The isotropic source time functions were derived from an inversion procedure assuming only that the source can be described as an equivalent first-order moment-tensor point source. The inversion procedure uses the entire near-field seismogram in the frequency domain, given a Green's function for the medium.

The procedure follows Stump and Johnson (1977), and detailed analysis for the explosions HARZER and CHANCELLOR is reported by McEvilly and Johnson (1986). These source function estimates are broadband and based on the entire waveform of 18 or more near-field seismograms between 1.8 and 11 km from the epicenter.

In addition to the use of an empirical explosion source time function, we employ causal frequency-dependent attenuation operators based on the t*(f) models of Der and Lees (1985). These models are intended to represent average teleseismic paths from source to receiver. There are three models representing the sources and receivers either in a tectonic (low Q) region or a shield (high Q) region: shield to shield (S-S), tectonic to shield (T-S), and tectonic to tectonic (T-T). Since NTS is located in a tectonic region of the southern basin and range, it is expected that teleseismic paths to a network such as the WWSSN will span the range between the T-S and T-T attenuation operators.

TELESEISMIC P-WAVES FROM NEAR-FIELD RDP ESTIMATES

We have used the isotropic part (trace) of the moment tensor for HARZER and CHANCELLOR (Table 3-1a) inverted for the full moment tensor from near-field data by McEvilly and Johnson (1986) to predict teleseismic P wave waveforms and magnitudes. The working point density and velocity of McEvilly and Johnson's model are ρ_0 = 2.1 gm/cc and α_0 = 3.2 km/sec for both events, which were buried (depth: H in Table 3-1a) with about 3.5% and 6.1% of their containment depths above the water table (W.T. in Table 3-1a). Since peak RDP, Ψ (measured in m^3) and seismic moment, M (measured in dyne-cm) are related by $M = 4\pi\rho\alpha^2 \Psi$, the values of M =

1040×10^{20} and 560×10^{20} dyne-cm for HARZER and CHANCELLOR, respectively (McEvilly and Johnson, 1986) yield $\Psi = 3.9 \times 10^4$ and 2.1×10^4 m^3 for the two shots. The time domain isotropic moment, M, and the moment rate, $\dot{M}$, estimates of McEvilly and Johnson (1986) are shown in Figure 3-1a and b. The relationship between RVP (measured in m^3/sec) and moment rate (measured in dyne-cm/sec) is given by $\dot{M} = 4\pi\rho\alpha^2 \dot{\Psi}$. Therefore, it follows from Figures 3-1a and 3-1b that the rise times of the two RDP's are significantly different and contribute to the different ratios of RVP versus RDP for the two events. HARZER appears to be more emergent, and although the peak RDP of HARZER is larger than that of CHANCELLOR, the peak RVP of CHANCELLOR is larger than that of HARZER.

Table 3-1a. EVENT PARAMETERS (USGS)

EVENT	DATE	O.T.	LAT. (°N)	LONG. (°E)	H (m)	H(W.T.) (m)	ML(BKS)	m_b(USGS)
HARZER	19810606	18:00:00.1	37.303	-116.326	637	668	5.4	5.5
CHANCELLOR	19830901	14:00:00.1	37.273	-116.355	625	647	5.3	5.4

Available WWSSN data for HARZER and CHANCELLOR were analyzed to obtain the maximum-likelihood magnitudes for the two events. Constraining the standard deviation, σ, to 0.25, the following results were obtained from measurements of A/T:

Table 3-1b. MAXIMUM-LIKELIHOOD ESTIMATES FROM WWSSN DATA

EVENT	m_b(a)	m_b(b)	m_b(max)
HARZER	4.975(0.070)	5.265(0.048)	5.527(0.036)
CHANCELLOR	4.853(0.093)	5.198(0.093)	5.401(0.086)

We have convolved these isotropic seismic source function estimates with three separate t*(f) operators from Der and Lees (1985), corresponding to shield-to-shield,

tectonic-to-shield, and tectonic-to-tectonic paths (Figure 3-2a, and b). These three causal frequency-dependent t*(f) attenuation operators have $\overline{t^*}$ = 0.20, 0.45, and 0.70 seconds at 1 Hz, and t* = 0.30, 0.55 and 0.80 sec at 1 Hz, respectively.

Table 3-2a.
PEAK OF ATTENUATED RVP (dyne-cm/sec)

EVENT	S-S	T-S	T-T
HARZER	721	565	465
CHANCELLOR	553	345	267

Table 3-2b.
PEAK OF ATTENUATED RDP (dyne-cm)

EVENT	S-S	T-S	T-T
HARZER	610	520	450
CHANCELLOR	390	280	230

In order to predict displacement amplitudes at teleseismic distances we apply a geometrical spreading factor to convert the attenuated RVP's to far-field displacement P-waveforms. Carpenter (1966) gives a geometrical spreading factor that predicts for a distance of 50° an integrated P-wave displacement of 1 nm-sec from a source with RDP, $\Psi = (110\ m^3)x(\frac{\alpha_1\rho_1}{\alpha_0\rho_0})^{1/2} = 168\ m^3$ for $\rho_0 = 2.1$, $\alpha_0 = 3.2$, $\rho_1 = 2.72$, $\alpha_1 = 5.8$. Using equations for geometrical spreading from Aki and Richards (1980) with the J-B travel-time tables gives a 1 nm-sec P-wave integrated displacement from an isotropic source with moment, $M = 4.63x\ 10^{20}$ dyne-cm, or RDP, $\Psi = 170\ m^3$. The free surface effect and crustal layering have been ignored. Given these relations, the predicted P-waveforms are predicted for a teleseismic distance of 50°, and their peak displacement amplitudes are tabulated in Table 3-3a. After convolution with the response of a short-period WWSSN instrument, the waveforms can be seen in Figure 3-3a and b

with amplitudes listed in Table 3-3b. Amplitudes are zero-to-peak for the "Pa" phase and 1/2 peak-to-peak for the "Pab" phase.

Table 3-3a. PEAK P-WAVE DISPLACEMENT AT 50 DEGREES (nm) (NO FREE SURFACE EFFECT) (HARD ROCK SITE) (NO pP)

EVENT	S-S	T-S	T-T
HARZER	160	120	100
CHANCELLOR	120	75	58

Table 3-3b WWSSN AMPLITUDES AT 50 DEGREES (nm) (NO FREE SURFACE EFFECT) (HARD ROCK SITE) (NO pP)

	Pa			Pab		
EVENT	S-S	T-S	T-T	S-S	T-S	T-T
HARZER	94	48	30	204	126	78
CHANCELLOR	178	80	36	434	194	94

The predicted m_b values for these RVP's are tabulated below (Table 3-4a) assuming the free surface effect at the receiver is a factor of 2, and using the Veith and Clawson (1972) "P" factors. Since the presense or absence of pP does not effect the m_b(Pa) and m_b(Pab) readings for events of this depth (pP-P > 0.5 sec), we can safely ignore the P+pP interference problem which becomes an issue for measurements of the m_b(Pbc) or m_b(Pmax) phases. Since NTS is a tectonic site and the WWSSN network is distributed between tectonic and shield type site locations, we should expect that the WWSSN network average m_b should be a weighted average of the T-S and T-T m_b predictions. The predicted m_b(Pab) values for the WWSSN network are expected to lie between 5.43 and 5.77 for HARZER and 5.65 and 5.96 for CHANCELLOR. Likewise the m_b(Pa) values for the WWSSN network are expected to lie between 5.45 and 5.65 for HARZER and between 5.53 and 5.87 for CHANCELLOR.

Table 3-4a. WWSSN INSTRUMENT m_b AT 50 DEGREES (FREE SURFACE EFFECT) (HARD ROCK SITE) (NO pP)						
	m_b(Pa)			m_b(Pab)		
EVENT	S-S	T-S	T-T	S-S	T-S	T-T
HARZER	5.94	5.65	5.45	5.98	5.77	5.43
CHANCELLOR	6.22	5.87	5.53	6.31	5.96	5.65

The predicted pP-P times for both HARZER and CHANCELLOR are about 0.55 seconds, based on McEvilly and Johnson's (1986) velocity model of Pahute Mesa. The overburden velocities in Table 2-1 of Section 2 for these two events would predict pP-P times in excess of 0.6 sec. This wouldl constitute a constructive interference of P+pP for these RVP's convolved attenuation operators and WWSSN instrument response. Whether the pP actually exists in real data or not, the upper bound on the predicted m_b(Pmax) can be derived by assuming a P+pP doublet with a 0.55 second delay time. The predicted m_b without a pP constitutes a lower bound on the m_b(Pmax). The predicted m_b(Pmax) without pP is the m_b(ab) magnitude tabulated above. Consequently we can bound the m_b(Pmax) that would be predicted from these estimated RDP's. See Figure 3-4a and b for the synthetic WWSSN waveforms for a 0.6 second pP-P delay and S-S, T-S, and T-T attenuation operators.

Table 3-4b. m_b WWSSN INSTRUMENT AT 50 DEGREES (FREE SURFACE EFFECT) (HARD ROCK SITE) (P+pP)						
	m_b(Pmax)			m_b(Pab)		
EVENT	S-S	T-S	T-T	S-S	T-S	T-T
HARZER	6.25	6.11	5.88	5.98	5.77	5.43
CHANCELLOR	6.44	6.11	5.88	6.31	5.96	5.65

If we take the mean of the T-S and T-T operators and if the m_b(Pmax) estimates serve as upper bounds on the network m_b, then we have m_b = 6.0 for both HARZER

and CHANCELLOR. This value is between 0.5 and 0.6 magnitude units higher than the observed teleseismic magnitudes for these two events.

DISCUSSION

There is no reason to believe that these two events have unusually low magnitudes compared to other events at Pahute Mesa. Therefore we are faced with choosing from several hypotheses to reduce the predicted teleseismic magnitudes to match observed magnitudes. (1) We can increase the intrinsic attenuation. (2) There is a correctable bias due to the log-normal distribution of seismic amplitudes. (3) Defocusing of seismic waves beneath the test site can introduce a net bias into the teleseismic network amplitude. (4) We can modify pP and hence reduce the constructive interference contributing to the m_b(max) phase. (5) Finally we can hypothesize attenuation due to scattering along the teleseismic path. Traditionally, researchers have accounted for the missing energy by intrinsic attenuation. First, however, we would like to examine two systematic biases that may be present in the teleseismic estimates of the source size.

McLaughlin (1986) and McLaughlin and Anderson (1987) point out that synthetic magnitudes predicted from simple geometric spreading will always be systematically high compared to network average magnitudes because of the log-normal distribution of seismic amplitudes. This theory assumes that the network magnitude scatter is largely due to random focusing-defocusing of P waves along the teleseismic path. The synthetic teleseismic amplitude properly predicts the RMS amplitude of the network and not the median or geometric mean of the network amplitude which is computed

when magnitudes are averaged over the network. The magnitude bias, B_s, due to this focusing effect can be estimated from the network variance, σ^2, of the network magnitudes for the event, $B_s = \sigma^2 \ln(10)$. Typical values of network magnitude σ are between 0.30 and 0.35, and they would predict a focusing bias, B_s, between 0.21 and 0.28 magnitude units. We adopt a median value of $B_s = 0.25$. This leaves the m_b(Pmax) values for HARZER and CHANCELLOR (5.75) between 0.25 and 0.35 magnitude units higher than the observed (USGS) magnitudes of 5.5 and 5.4.

Another related source of systematic error is the possibility that the test site suffers from a net amplitude deficiency due to the focusing-defocusing produced by velocity anomalies beneath the test site. Cormier (1986 and 1987) has successfully predicted a large part of the teleseismic amplitude anomaly pattern observed across the WWSSN stations from a velocity model for NTS derived from travel-time anomalies by Taylor (1983). If we use Cormier's predicted magnitude anomalies to predict the average bias for the WWSSN network of stations at distances between 25° and 95°, then we conclude that the 64 stations are low with respect to a laterally homogeneous model by 0.03 magnitude units (see Figure 3-5a, b, c). McLaughlin et al. (1986) used a maximum likelihood estimator to smooth magnitudes over the focal sphere and found that the average Pahute Mesa event was 0.05 magnitude units lower due to focusing-defocusing. Since the Cormier magnitude anomaly prediction is based on a velocity model inversion that had limited resolution, it is probable that it underestimates the focusing-defocusing due to the velocity anomaly beneath NTS. Therefore, we consider the Cormier model confirmation of the biasing effects of uneven sampling on the focal sphere in the presence of focusing-defocusing, and estimate the focusing-defocusing

bias, B_f, to be 0.05 magnitude units to conform with the results of the maximum-likelihood analysis.

The teleseismic m_b(Pmax) depends strongly on the assumed P+pP constructive interference effect, and if we reduce the amplitude of pP or increase the pP-P delay time, there could be less need to increase attenuation. However, since the "a" and "ab" phases of the P wave are not sensitive to the P+pP interference effects, these amplitudes can serve as independent measures of the P wave amplitude. In Table 3-4b, the predicted T-T m_b(Pab) HARZER magnitude is 0.46 units less than the predicted T-T m_b(Pmax). The Log(Pmax/Pa) statistics for well coupled Pahute Mesa shots below the water table in the mid magnitude 5 range suggest that Log(Pmax/Pa) ~ 0.45 and Log(Pmax/Pab) ~ 0.24 on average over the WWSSN network (McLaughlin et al, 1986a). We conclude therefore that the predicted "Pa" and "Pab" amplitudes must also be reduced to agree with the observed teleseismic amplitudes, regardless of the P+pP interference. These "Pa" and "Pab" amplitudes however indicate that the "Pmax" amplitudes due to a strong P+pP constructive interference are not out of line for events of this size at Pahute Mesa. This does not prove that pP exists, since any secondary phase can contribute to the amplitudes measured as "Pmax".

The remaining alternatives are attenuation by linear dissipative intrinsic attenuation and attenuation by scattering. McLaughlin and Anderson (1987) and McLaughlin, Anderson, and Der (1985) argue that peak-amplitude attenuation may occur from scattering with little net change in the average spectra. In effect, scattering can attenuate the direct wave and supplement the coda with scattered waves to leave the net spectral shape invariant. Since scattering does not necessarily result in a minimum

phase attenuation operator, it is possible that the direct wave would experience non-minimum phase dispersion from such an interaction. McLaughlin and Anderson (1987) argue that this delay of high frequencies is indeed observed in teleseismic waveforms. They observed a net average group delay of 3 to 4 Hz P-wave energy relative to 1 Hz P-wave energy. This stochastic dispersion could only be observed for waveforms with enough bandwidth (high Q paths) such that the 3 to 4 Hz energy had significant signal-to-noise. However, there is no reason to believe that this sort of dispersion does not occur with lower Q paths such as from NTS. Linear dissipative mechanisms have causal minimum phase responses and therefore can not emulate this delay of high frequencies. Additional evidence for scattering can be found in the study of Bache et al. (1985). They found it necessary to introduce a mixed-phase operator that delayed high frequency energy in the P-wave in order to model both the initial rise-time of an explosion in the time domain and be consistent with the amplitude spectra.

Based on the numerical experiments of McLaughlin, Anderson, and Der (1985), and Frankel and Clayton (1986), a peak-amplitude attenuation of 0.2 to 0.4 magnitude units may be accomplished with a few percent of random velocity variation in the lithosphere with the proper scale lengths. Given that small scale lateral heterogeneities are required to account for stochastic dispersion and large scale heterogeneities are required to account for focusing-defocusing observations, it is reasonable to assume that the "heterospectra" of the Earth varies in some continuous fashion.

For example, in the range of $ka \approx 1$ to 2, peak-amplitude attenuation is proportional to the variance of the velocity variation, v^2 (McLaughlin, Anderson, and Der,

1985). Q is about 100 for a medium with an rms velocity variation of 10% ($\nu = 0.1$) whether the medium has a Gaussian, exponential, or self-similar autocorrelation (Frankel and Clayton, 1986). Therefore, if we simplistically consider the heterogeneity to be confined to the upper lithosphere in a layer of thickness, h, then the log-amplitude attenuation from two passes through the lithosphere is $\mathrm{Log}(A) = -\frac{\pi f}{\ln(10)} \frac{2h}{\bar{\alpha}} Q^{-1}{}_0 (\frac{\nu}{\nu_0})^2$, where $Q_0 = 100$, and $\nu_0 = 0.1$. $\bar{\alpha}$ is the average velocity over depth range, h. If Log(A) is between 0.2 and 0.4 then and we let $\nu = 0.1$ then we can confine the heterogeneity to between 30 and 60 km. Scale lengths of such heterogeneity for ka in the range of 1 to 2 would be between 1 and 2 km in the crust and 2 and 4 km in the upper mantle. However, if we allow heterogeneity to decrease with depth as suggested by Flatte' et al, (1987), then the heterogeneity must extend to greater depths. This is not altogether an unlikely situation. Since peak-amplitude attenuation is sensitive to the square of the rms velocity variation, then if the heterogeneity is significantly less than 10% the heterogeneity must extend to considerable depth. Obviously, without further constraints such models are non-unique as to depth extent and degree of heterogeneity.

CONCLUSIONS

The t*(f) models of Der and Lees (1985) will over-predict teleseismic peak amplitudes when used with realistic explosion source functions for NTS. However, if predicted teleseismic amplitudes are corrected for statistical biasing effects due to focusing-defocusing, then the discrepancy between observed and predicted magnitudes

is between 0.2 and 0.4 magnitude units. Scattering of P-waves by velocity heterogeneity in the Earth is just as reasonable an explanation for the additional needed attenuation as is the introduction of additional intrinsic attenuation. A few percent velocity variation (7% to 10% rms) of the lithosphere with scale lengths between 1 and 2 km in the crust and 2 and 4 km in the upper mantle are required to produce attenuation on the order of 0.2 to 0.4 magnitude units.

This work does not prove that scattering attenuates P-waves. However, we know that the Earth is laterally heterogeneous and there is ample evidence for scattering in the lithosphere, so that the required heterogeneity is within reasonable bounds. Certainly, we can not attenuate P-wave peak-amplitudes more than 0.4 magnitude units by scattering. One way to view these results is as upper bounds or integral constraints on the lateral heterogeneity of the Earth.

ACKNOWLEDGEMENTS

We would like to thank L. R. Johnson of U. C. Berkeley for use of his isotropic moment tensor function estimates derived from the inversion of HARZER and CHANCELLOR near-field data and V. F. Cormier of University of Connecticut for his NTS defocusing results.

REFERENCES

Aki, K. (1983). Scattering of P waves under the Montana LASA, J. Geophys. Res. 78, 1334-1346.

Aki, K. and P. G. Richards (1980). Quantitative Seismology, Theory and Methods, Vol. I., W. H. Freeman and Co., San Francisco.

Azimi, S. A., A. V. Kalinin, V. V. Kalinin, and B. L. Pivovarov (1968). Impulse and transient characteristics of media with linear and geometric absorption laws, Izvestiya, Physics of the Earth, 88-93.

Bache, T. (1982). Estimating the yield of underground nuclear explosions, Bull. Seism. Soc. Am. 72, S131-168.

Bache, T. C., P. D. Marshall, and L. B. Bache (1985). Q for teleseismic P waves from central Asia, J. Geophys. Res. 90, 3575-3587.

Blandford, R. R. (1976). Experimental determination of scaling laws for contained and cratering explosions, SDAC-TR-76-3, Teledyne Geotech, Alexandria, Virginia.

Blandford, R. R. M. F. Tillman, and D. F. Racine (1977). Empirical m_b:Ms at the Nevada Test Site with Applications to mb-Yield Relations, SDAC-TR-76-14, Teledyne Geotech, Alexandria, Virginia.

Blandford, R. R. and R. H. Shumway (1982). Magnitude-yield for nuclear explosions in granite at the Nevada Test Site and Algeria: joint determination with station effects with data containing clipped and low-amplitude signals, VSC-TR-82-12, Teledyne Geotech, Alexandria, Virginia.

Blandford, R. R., R. H. Shumway, R. Wagner, and K. L. McLaughlin (1984). Magnitude yield for nuclear explosions at several test sites with allowance for station effects, truncated data, amplitude correlation between events within test sites, absorption, and pP, TGAL-TR-83-6, Teledyne Geotech, Alexandria, Virginia.

Burger, R. W., T. Lay, C. G. Arveson, and L. J. Burdick (1985). Estimating seismic yield, pP parameters and tectonic release characteristics at the Novaya Zemlya test site, WCCP-R-85-03, Woodward Clyde Consultants, Pasadena, Ca.

Burger, R. W., T. Lay, and L. J. Burdick (1987). Average Q and yield estimates from the Pahute Mesa test site, Bull. Seism. Soc. Am. 77, 1274-1294.

Carpenter, E. W. (1966). A quantitative evaluation of teleseismic explosion records, Proc. Roy. Soc. A, 290, 396-407.

Chang, A. and D.V. von Seggern (1980). A study of amplitude anomaly and m_b bias at LASA subarrays. J. Geophys. Res. 85, 4811-4828.

Chavez, D. E., and K. F. Priestley (1986). Measurement of frequency dependent Lg attenuation in the Great Basin, Geophys. Res. Lett. 13, 551-554.

Choy, G. L., V. F. Cormier (1986). Direct measurement of the mantle attenuation operator from broadband P and S waveforms, J. Geophys. Res. 91, 7326-7342.

Cormier, V. F. (1982). The effects of attenuation on seismic body waves, Bull. Seism. Soc. Am. 72, S169-S200.

Cormier, V. (1986). An application of the propagator matrix to dynamic ray tracing: The focusing and defocusing of body waves by three-dimensional velocity structure in the source region, Geophys. J. R. astr. Soc. 87, 1159-1180.

Cormier, V. F. (1987). Focusing and defocusing of teleseismic P waves by known three-dimensional structure beneath Pahute Mesa, Nevada test site, Bull. Seism. Soc. Am. 77, 1688-1703.

Der Z. A., T. W. McElfresh, and C. P. Mrazek (1977). The effect of crustal structure on station magnitude anomalies (magnitude Bias), SDAC-TR-77-1 Teledyne Geotech, Alexandria, Virginia.

Der, Z. A. and A. C. Lees (1985). Methodologies for estimating t*(f) from short-period body waves and regional variations of t*(f) in the United States, Geophys. J. R. astr. Soc. 82, 125-140.

Der, Z. A., A. C. Lees, R. H. Shumway, T. W. McElfresh, and M. E. Marshall (1986). Multichannel deconvolution of P waves at seismic arrays and three component stations, TGAL-86-06, Teledyne Geotech, Alexandria, Virginia.

Der, Z. A., A. C. Lees, and V. F. Cormier (1986). Frequency dependence of Q in the mantle underlying the shield areas of Eurasia, Part information, The Q model, Geophys. J. R. astr. Soc. 87, 1103-1112.

Der, Z. A., E. Smart, and A. H. Chaplin (1978). Short period S wave attenuation under the United States, SDAC-TR-78-6, Teledyne Geotech, Alexandria, Virginia.

Der, Z. A., R. H. Shumway, and A. C. Lees (1987). Multi-channel deconvolution of P waves at seismic arrays, Bull. Seism. Soc. Am. 77, 195-211.

Der, Z. A., T. W. McElfresh, R. Wagner and J. Burnetti; also, Errata, Bull. Seism. Soc. Am., 75, 1222 (1985). Spectral characteristics of P waves from nuclear explosions and yield estimation, Bull. Seism. Soc. Am. 75, 379-390.

Der, Z. A., T. W. McElfresh, and A. O'Donnell (1982). An investigation of the regional variations and frequency dependence of anelastic attenuation in the mantle under the United Sates in the 0.5-4 Hz band, Geophys, J. R. astr. Soc. 69, 67-100.

Der, Z. A., T. W. McElfresh, and C. P. Mrazek (1979). Interpretation of short-period P-wave magnitude anomalies at selected LRSM stations, Bull. Seism. Soc. Am. 69, 1149-1160.

Der, Z.A. T. W. McElfresh, R. Wagner, and J. Burnetti (1985a). Spectral Characteristics of P Waves from Nuclear Explosions and Yield Estimation, Bull. Seism. Soc. Am. 75, 379-390.

Der, Z.A. T. W. McElfresh, R. Wagner, and J. Burnetti (1985b). ERRATA: Spectral Characteristics of P Waves from Nuclear Explosions and Yield Estimation, Bull. Seism. Soc. Am. 75, 1222.

Douglas, A. (1966). A Special Purpose Least Squares Programme, AWRE Report No. O-54/66, HMSO, London.

Douglas, A. (1987). Differences in upper mantle attenuation between the Nevada and Shagan River test sites: Can the effects be seen in P-wave seismograms?, Bull. Seism. Soc. Am. 77, 270-276.

Douglas, A. and J. A. Hudson (1983). Comments on: "Time functions appropriate for nuclear explosions", by L. J. Burdick, and D. V. Helmberger and "Seismic source functions and attenuation from local and teleseismic observations of the NTS events JORUM and HANDLEY", by D. V. Helmberger and D. M. Hadley (1981). Bull. Seism. Soc. Am. 73, 1255-1264.

Douglas, A., P. D. Marshall, and J. B. Young (1987). The P waves from the Amchitka Island explosions, Geophys. J. R. astr. Soc. 90, 101-117.

Frankel, A., and R. W. Clayton (1986). Finite difference simulations of seismic scattering: implications for the propagation of short-period seismic waves in the crust and models for crustal heterogeneity, J. Geophys. Res. 91, 6465-6489.

Filson, J. and C. W. Frazier (1972). Multisite estimation of explosive source parameters, J. Geophys. Res. 77, 2045-2061.

Flatte', S. M., R.-S. Wu, and Z.-K. Shen (1987). Inversion of the medium spectrum under NORSAR from phase and amplitude fluctuations of seismic P-waves (ABSTRACT), EOS 68, 353.

Frazier, C. W. and J. Filson (1972). A direct measurement of the Earth's short-period attenuation along a teleseismic ray path, J. Geophys. Res. 77, 3782-3787.

Futterman, D. W., (1962). Dispersive body waves, J. Geophys. Res. 67, 13 5279-5291.

Gupta, I. N., K. L. McLaughlin, and R. Wagner (1985). Analysis of regional data from cratering and non-cratering nuclear explosions, TGAL-85-05, Teledyne Geotech, Alexandria, Virginia.

Gupta, I. N. and R. R. Blandford (1987). A study of P waves from NTS explosions: near-source information from teleseismic observations?, Bull. Seism. Soc. Am. 77, 1041-1056.

Gupta, I. N., R. R. Blandford, R. A. Wagner, J. A. Burnetti, and T. W. McElfresh (1985). Use of P coda for determination of yield of nuclear explosions, Geophys. J. R. astr. Soc. 83, 541-554.

Hanks, T. C. and M. Wyss (1972). The use of body-wave spectra in the determination of seismic-source parameters, Bull. Seism. Soc. Am. 62, 561-589.

Helmberger, D. V. and D. M. Hadley (1981). Seismic source functions and attenuation from local and teleseismic observations of the NTS events JORUM and HANDLEY, Bull. Seism. Soc. Am. 71, 51-67.

Heuze, F. E. (1983). A review of geomechanics data from French nuclear explosions in the Hoggar granite, with some comparisons to tests in U. S. granite, UCID-19812, Lawrence Livermore Laboratory, Livermore, California.

Marshall, P. D. (1972). Some seismic results from a worldwide sample of large underground explosions, AWRE Report O 49/72, AWRE, MOD(PE), Aldermasten, Berks., U.K.

Marshall, P. D., D. L. Springer, and H. C. Rodean (1979). Magnitude corrections for attenuation in the upper mantle, Geophys. J. R. astr. Soc. 57, 609-638.

Marshall, P. D., R. C. Lilwall, and J. Farthing (1986). Body wave magnitudes and locations of underground explosions at the Nevada Test Site 1971-1980, AWRE Report O 21/86, AWRE, MOD(PE)., Aldermaston, Berks., U.K.

McEvilly, T. V. and L. R. Johnson (1986). Regional studies with broadband data, DARPA/AFGL Seismic Research Symposium, 6-8 May 1986, 44-51.

McLaughlin, K. L. (1986). Network magnitude variation and magnitude bias, Bull. Seism. Soc. Am. 76, 1813-1816.

McLaughlin, K. L. and L. M. Anderson (1987). Stochastic dispersion of P waves due to scattering and multipathing, Geophys. J. R. astr. Soc. 89, 933-963.

McLaughlin, K. L., L. M. Anderson, and Z. A. Der (1985). Investigation of scattering and attenuation of seismic waves using 2-dimensional finite difference calculations, in Multiple Scattering of Waves in Random Media and Rough Surfaces, the Pennsylvania State University, Editors V. J. Varadan and V. K. Varadan.

McLaughlin, K. L., I. N. Gupta, and R. Wagner (1985). Finite Difference Cratering Support, Task 1 Final Report, Magnitude Determination of Cratering and Non-Cratering Nuclear Explosions, TGAL-85-03, Teledyne Geotech, Alexandria, Virginia.

McLaughlin, K. L., L. M. Anderson, and A. C. Lees (1987b). Effects of local geologic structure on Yucca Flats, Nevada test site, explosion waveforms: Two-dimensional linear finite-difference simulations, Bull. Seism. Soc. Am. 77, 1211-1222.

McLaughlin, K. L., R. H. Shumway, R. O. Ahner, M. E. Marshall, T. W. McElfresh, and R. A. Wagner (1986a). Determination of event magnitudes with correlated data and censoring: a maximum likelihood approach, TGAL-86-01, Teledyne Geotech, Alexandria, Virginia.

McLaughlin, K. L., R. O. Ahner, R. Wagner, and M. Marshall (1986b). Maximum Likelihood Magnitudes, and log(Pmax/Pa) at Novaya Zemlya and Eastern Kazakh test sites, TGAL-86-02, Teledyne Geotech, Alexandria, Virginia.

McLaughlin, K. L., R.-S. Jih, Z. A. Der, and A. C. Lees (1986c). The effects of near-source topography on explosion waveforms: teleseismic observations and linear finite difference calculations, AFGL-TR-86-0159, TGAL-86-03, Teledyne Geotech, Alexandria, Virginia.

McLaughlin, K. L., M. E. Marshall, R. Wagner, W. Chan, A. C. Lees, and R.-S. Jih, (1987a). A maximum likelihood general linear model (GLM87) for inter-test site magnitude:yield estimation and P-wave measures of yield at Novaya Zemlya and Sinkiang test sites, TGAL-87-05, Teledyne Geotech, Alexandria, Virginia.

Minster, J. B. (1978). Transient and impulse responses of a one dimensional attenuating medium, Part II. A parametric study, Geophys. J. R. astr. Soc. 52, 503-524.

Mueller, R. A. and J. R. Murphy (1971). Seismic characteristics of underground nuclear detonations, Bull. Seism. Soc. Am. 61, 1675-1692.

Murphy, J. R. (1978). A review of available free-field seismic data from underground nuclear explosions in salt and granite, CSC-TR-78-0003, Computer Sciences Corporation, Falls Church, Virginia.

Nuttli, O. (1986). Yield estimates of Nevada test site explosions obtained from seismic Lg waves, J. Geophys. Res. 91, 2137-2151.

Rimer, N, J. L. Stevens, and S. M. Day (1987). Effects of pore pressure, fractures, and dilatancy on ground motion in granite, AFGL-TR-87-0136, SSS-R-87-8670, S-Cubed, La Jolla, California.

Schock, R. N., A. E. Abey, H. C. Heard, and H. Louis (1972). Mechanical properties of granite from the Taourirt Tan Afella Massif, Algeria, UCRL-51296, Lawrence Livermore Laboratory, Livermore, California.

Shumway, R. H. and Z. A. Der (1985). Deconvolution of multiple time series, Technometrics 27, 385-393.

Stevens, J. L. (1986). Estimation of scalar moments from explosion-generated surface waves, Bull. Seism. Soc. Am. 76, 123-151.

Stevens, J. L. and S. M. Day (1985). The physical basis of m_b : M_s and variable frequency magnitude methods for earthquake/explosion discrimination, J. Geophys. Res. 90, 3009-3020.

Stevens, J. L., N. Rimer, and S. M. Day (1986). Constraints on modeling of underground explosions in granite, AFGL-TR-86-0264, SSS-R-87-8312, S-cubed, La Jolla, California.

Stump, B. W. and L. R. Johnson (1977). The determination of source properties by the linear inversion of seismograms, Bull. Seism. Soc. Am. 67, 1489-1502.

Taylor, S. R. (1983). Three-dimensional crust and upper-mantle structure at the Nevada test site, J. Geophys. Res. 88, 2220-2232.

Taylor, S. R., B. R. Bonner, and G. Zandt (1986). Attenuation and scattering of broadband P and S waves across North America, J. Geophys. Res. 91, 7309-7325.

Veith, K.F. and G.E. Clawson (1972). Magnitude from short period P-wave data, Bull. Seism. Soc. Am. 62, 435-452.

Werth, G. C. and R. F. Herbst (1963). Comparison of amplitudes of seismic waves from four explosions in four mediums, J. Geophys. Res. 68, 1463-1475.

von Seggern, D. H. and R. R. Blandford (1972). Source time functions and spectra for underground explosions, Geophys. J. R. astr. Soc. 31, 83-87.

LIST OF TABLES

FIGURE CAPTIONS

Figure 1-1a. LRSM stations which recorded HARDHAT.

Figure 1-1b. LRSM stations which recorded SHOAL.

Figure 1-1c. LRSM stations which recorded PILEDRIVER.

Figure 1-2. Digitized (20 points/sec) film records of late coda from MN-NV and KN-UT for HARDHAT and PIELDRIVER. After correction for DC offest and long-term drift, the rms signal level was computed for 8 successive 10-second windows of each record.

Figure 1-3. Deconvolved Pn displacement waveforms for HARDHAT and PILEDRIVER at KN-UT. The ratio of the areas under the initial P pulses for the two events is consistent with the yield ratio of the two events. HARDHAT appears to show a negative pulse that can be interpreted as pP, while PILEDRIVER does not.

Figure 1-4a. HARDHAT vertical Pn recording at KN-UT and spectra (not corrected for instrument response) of signal (denoted by +) and of noise.

Figure 1-4b. Similar to Figure 1-3a for PILEDRIVER.

Figure 1-4c. Spectral ratio (HARDHAT/PILEDRIVER) of Pn, corrected for noise, from recordings at KN-UT. Theoretical ratios based on von Seggern and Blandford (dashed curve) and Mueller and Murphy (dotted curve) scaling for granite show excellent agreement up to about 5 Hz.

Figure 1-5a. Maximum likelihood estimate of the HARDHAT Lg displacement spectrum from 32 channels (horizontal and vertical) corrected for attenuation using Chavez and Priestley Q(f) and to a reference distance of 100 km. All stations less than 1000 km. Network mean and one network standard deviation is shown for each frequency. Above 5 Hz, estimate is contaminated by noise. The amplitude is in arbitrary units.

Figure 1-5b. Maximum likelihood estimate of the SHOAL Lg displacement spectrum from 24 channels (horizontal and vertical) corrected for attenuation using Chavez and Priestley Q(f) and to a reference distance of 100 km. All stations less than 1000 km. Network mean and one network standard deviation is shown for each frequency. Above 5 Hz, estimate is contaminated by noise. The amplitude is in arbitrary units.

Figure 1-5c. Spectral ratio (SHOAL/HARDHAT) of maximum likelihood network attenuation corrected spectra shown in Figures 1-5a and 1-5b. Above 5 Hz, estimate is contaminated by noise. The amplitude ratio is in arbitrary units.

Figure 2-1a. Broadband displacement seismograms derived from single channel deconvolution of NA0 records. The maximum zero-to-peak values (in nm) are indicated for each shot.

Figure 2-1b. Broadband displacement seismograms derived from single channel deconvolution of NA0 records. The maximum zero-to-peak values (in nm) are indicated for each shot.

Figure 2-1c. Broadband displacement seismograms derived from single channel deconvolution of NA0 records. The maximum zero-to-peak values (in nm) are indicated for each shot.

Figure 2-1d. Broadband displacement seismograms derived from single channel deconvolution of NA0 records. The maximum zero-to-peak values (in nm) are indicated for each shot.

Figure 2-2. P-wave moment estimates versus surface wave moment estimates of Stevens (1986). The dashed line is the least squares fit with slope of unity and Log(NA0) = Log(STEVENS) - 1.37.

Figure 2-3. P-wave moment estimates plotted against Marshall et al's (1986) m_b values. The dashed line is the least squares fit with slope of 0.9 and m_b = 0.9 Log(NA0) + 13.86 (0.05).

Figure 2-4a. Equivalent far-field sources (RVP) for TYBO, STILTON, PURSE, and MUENSTER derived by deconvolution of array data at EKA.

Figure 2-4b. Equivalent far-field sources (RVP) for MAST, KASSERI, INLET, HANDLEY, and FONTINA derived by deconvolution of array data at EKA.

Figure 2-4c. Equivalent far-field sources (RVP) for FAULTLESS, ESTUARY, CHESHIRE, CAMEMBERT, and BOXCAR derived by deconvolution of array data at EKA.

Figure 2-5a. Displacement spectral fit of MAST at station KNB for corner frequency, f_c, and low-frequency asymptote, A_0, assuming f^{-2} high-frequency fall-off. Model spectrum (denoted by -) is a least squares fit to the log-amplitude spectrum (denoted by *).

Figure 2-5b. Displacement spectral fit of MAST at station KNB for corner frequency, f_c, and low-frequency asymptote, A_0, assuming f^{-3} high-frequency fall-off. Model spectrum (denoted by -) is a least squares fit to the log-amplitude spectrum (denoted by *).

Figure 2-5c. Displacement spectral fit of MAST at station ELK for corner frequency, f_c, and low-frequency asymptote, A_0, assuming f^{-2} high-frequency fall-off. Model spectrum (denoted by -) is a least squares fit to the log-amplitude spectrum (denoted by *).

Figure 2-5d. Displacement spectral fit of MAST at station ELK for corner frequency, f_c, and low-frequency asymptote, A_0, assuming f^{-3} high-frequency fall-off. Model spectrum (denoted by -) is a least squares fit to the log-amplitude spectrum (denoted by *).

Figure 2-6a. Ω_0(ELK) versus Ω_0(KNB) for 14 NTS events. The dashed line is the least squares fit with slope of unity and Log(ELK) = Log(KNB) - 0.28(0.07).

Figure 2-6b. Ω_0(KNB) versus Ω_0(NA0) for 11 NTS events. The dashed line is the least squares fit with slope of unity and Log(NA0) = Log(KNB) - 1.61(0.14).

Figure 2-6c. Ω_0(ELK) versus Ω_0(NA0) for 10 NTS events. The dashed line is the least squares fit with slope of unity and Log(NA0) = Log(ELK) - 1.35(0.13).

Figure 2-6d. Log corner-frequency, f_c, versus log A_0 assuming fall-off rate of f^{-2} for 20 NTS events recorded at NA0. The dashed line shows the f_c proportional to $A_0^{-1/3}$ trend.

Figure 2-6e. Log corner-frequency, f_c, versus log A_0 assuming fall-off rate of f^{-3} for 20 NTS events recorded at NA0. The dashed line shows the f_c proportional to $A_0^{-1/3}$ trend.

Figure 2-6f. Log corner-frequency, f_c, versus log A_0 assuming fall-off rate of f^{-2} for 16 NTS events, all 16 recorded at KNB (denoted by O) and only 14 at ELK (symbol X). The dashed line shows the f_c proportional to $A_0^{-1/3}$ trend.

Figure 2-6g. Log corner-frequency, f_c, versus log A_0 assuming fall-off rate of f^{-3} for 16 NTS events, all 16 recorded at KNB (denoted by O) and only 14 at ELK (symbol X). The dashed line shows the f_c proportional to $A_0^{-1/3}$ trend.

Figure 2-6h. Ω_0 versus yield, on log-log scale, for 20 NTS events recorded at NA0. The dashed line is the least squares fit with slope of unity.

Figure 2-6i. A_0 (assuming fall-off rate of f^{-3}) versus yield, on log-log scale, for 20 NTS events recorded at NA0. The dashed line is the least squares fit with slope of unity.

Figure 2-6j. Ω_0 versus yield, on log-log scale, for 23 Pahute Mesa and Yucca Flats shots, recorded at KN-UT, KNB, and ELK. The ELK values are adjusted to KNB values and the average of the two station values are plotted. The dashed line is the least squares fit with slope of unity.

Figure 2-6k. RDP (derived from Ω_0) versus yield, on log-log scale, for 20 NTS events recorded at NA0. The dashed line is the least squares fit with slope of unity.

Figure 2-6l. Moment (derived from Ω_0) versus yield, on log-log scale, for 20 NTS events recorded at NA0. The dashed line is the least squares fit with slope of unity.

Figure 2-7a. Deconvolved displacement seismograms for KN-UT.

Figure 2-7b. Deconvolved displacement seismograms for KN-UT.

Figure 2-7c. Deconvolved displacement seismograms for KNB.

Figure 2-7d. Deconvolved displacement seismograms for KNB.

Figure 2-7e. Deconvolved displacement seismograms for KNB.

Figure 2-7f. Deconvolved displacement seismograms for ELK.

Figure 2-7g. Deconvolved displacement seismograms for ELK.

Figure 2-7h. Deconvolved displacement seismograms for ELK.

Figure 3-1a. Isotropic source moment (below)(in 10^{20} dyne-cm) and isotropic source moment-rate (above)(in 10^{20} dyne-cm/sec) for HARZER from McEvilly and Johnson (1986).

Figure 3-1b. Isotropic source moment (below)(in 10^{20} dyne-cm) and isotropic source moment-rate (above)(in 10^{20} dyne-cm/sec) for CHANCELLOR from McEvilly and Johnson (1986).

Figure 3-2a. Attenuation t*(f) models from Der and Lees (1985), T-T is tectonic to tectonic path, T-S is tectonic to shield path, and S-S is shield to shield path.

Figure 3-2b. Time domain attenuation operators for the t*(f) models from Der and Lees (1985) in Figure 3-2a, T-T is tectonic to tectonic path, T-S is tectonic to shield path, and S-S is shield to shield path.

Figure 3-3a. CHANCELLOR RVP convolved with a WWSSN response and with either a T-T (bottom), T-S (middle), or S-S (top) attenuation operator.

Figure 3-3b. HARZER RVP convolved with a WWSSN response and with either a T-T (bottom), T-S (middle), or S-S (top) attenuation operator.

Figure 3-4a. CHANCELLOR RVP convolved with a WWSSN response, a P+pP operator, and with either a T-T (bottom), T-S (middle), or S-S (top) attenuation operator. pP/P = -1, pP-P = 0.6 sec.

Figure 3-4b. HARZER RVP convolved with a WWSSN response, a P+pP operator, and with either a T-T (bottom), T-S (middle), or S-S (top) attenuation operator. pP/P = -1, pP-P = 0.6 sec.

Figure 3-5a. Focusing-defocusing pattern on a 45° lune of the lower hemisphere equal-area focal sphere with reduction velocity of 8 km/s predicted by Cormier (1987) for Pahute Mesa. Symbols represent magnitude anomaly relative to laterally homogeneous earth. Plus signs are high magnitudes and diamonds are low magnitudes.

Figure 3-5b. Focusing-defocusing pattern of Figure 3-5a as a function of azimuth.

Figure 3-5c. Predicted magnitude anomalies for WWSSN stations. The net value is 0.03 magnitudes units. Note the cluster of stations in the 0 to 50° azimuth range with low amplitudes.

Figure 1-1a.

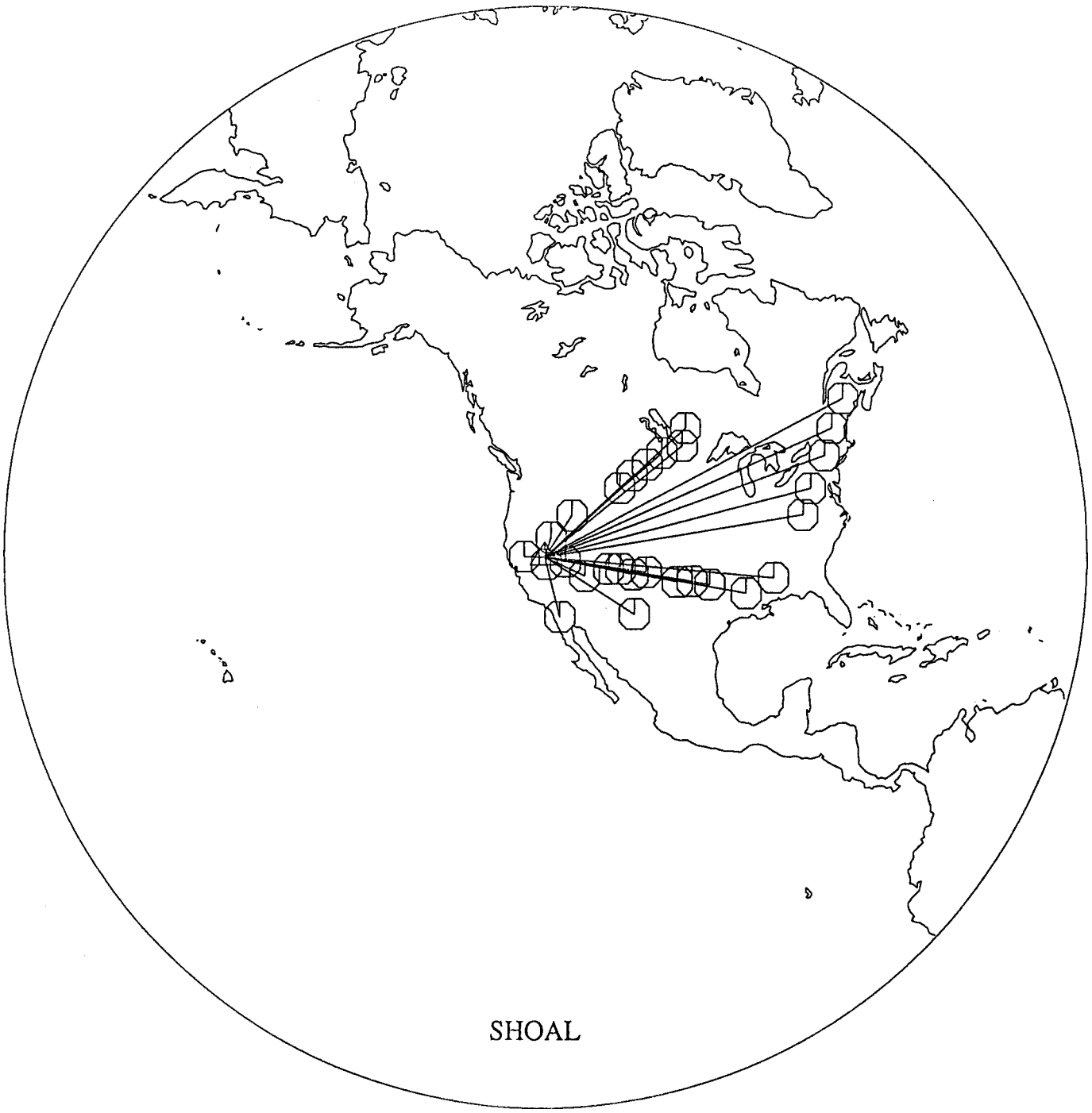

Figure 1-1b

PILEDRIVER

Figure 1-1c

HARDHAT 15 FEBRUARY 1962

1600 POINTS.

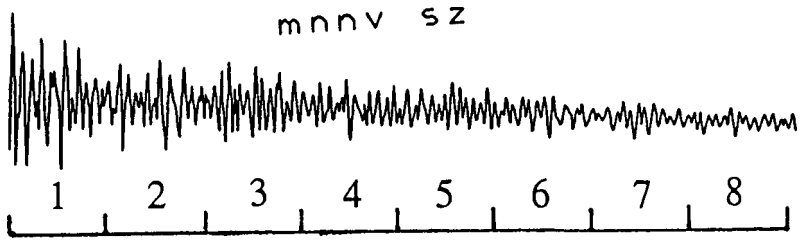

HARDHAT 15 FEBRUARY 1962

1600 POINTS.

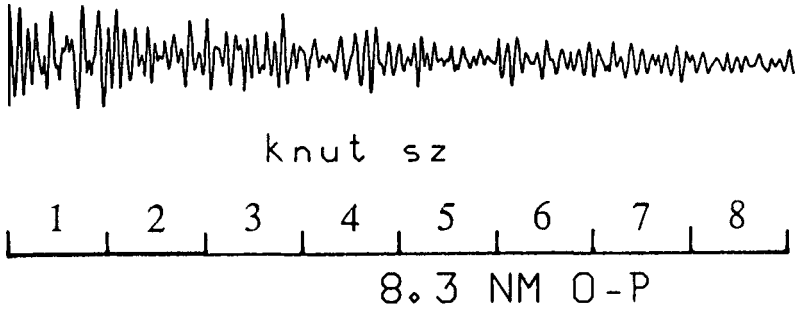

PILEDRIVER 2 JUNE 1966

1600 POINTS.

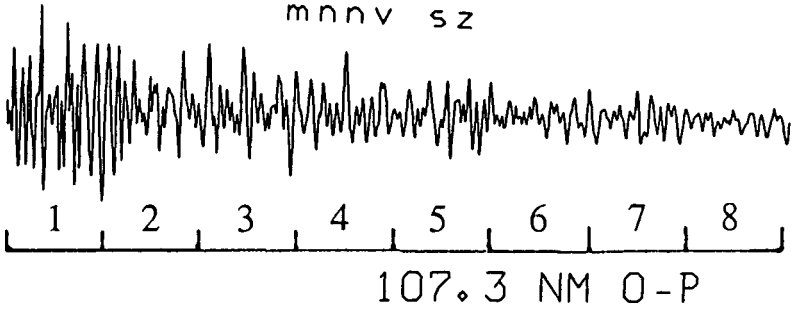

PILEDRIVER 2 JUNE 1966

1600 POINTS.

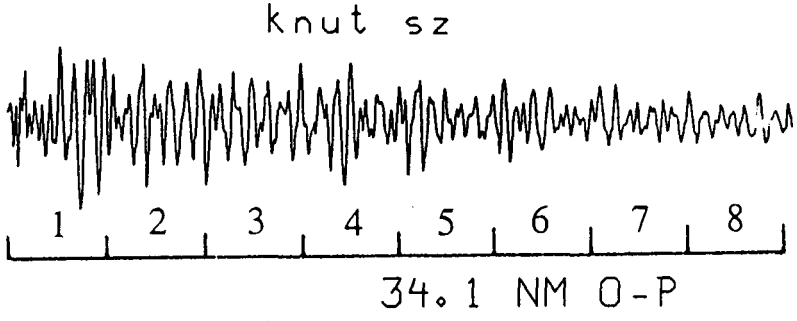

Figure 1-2

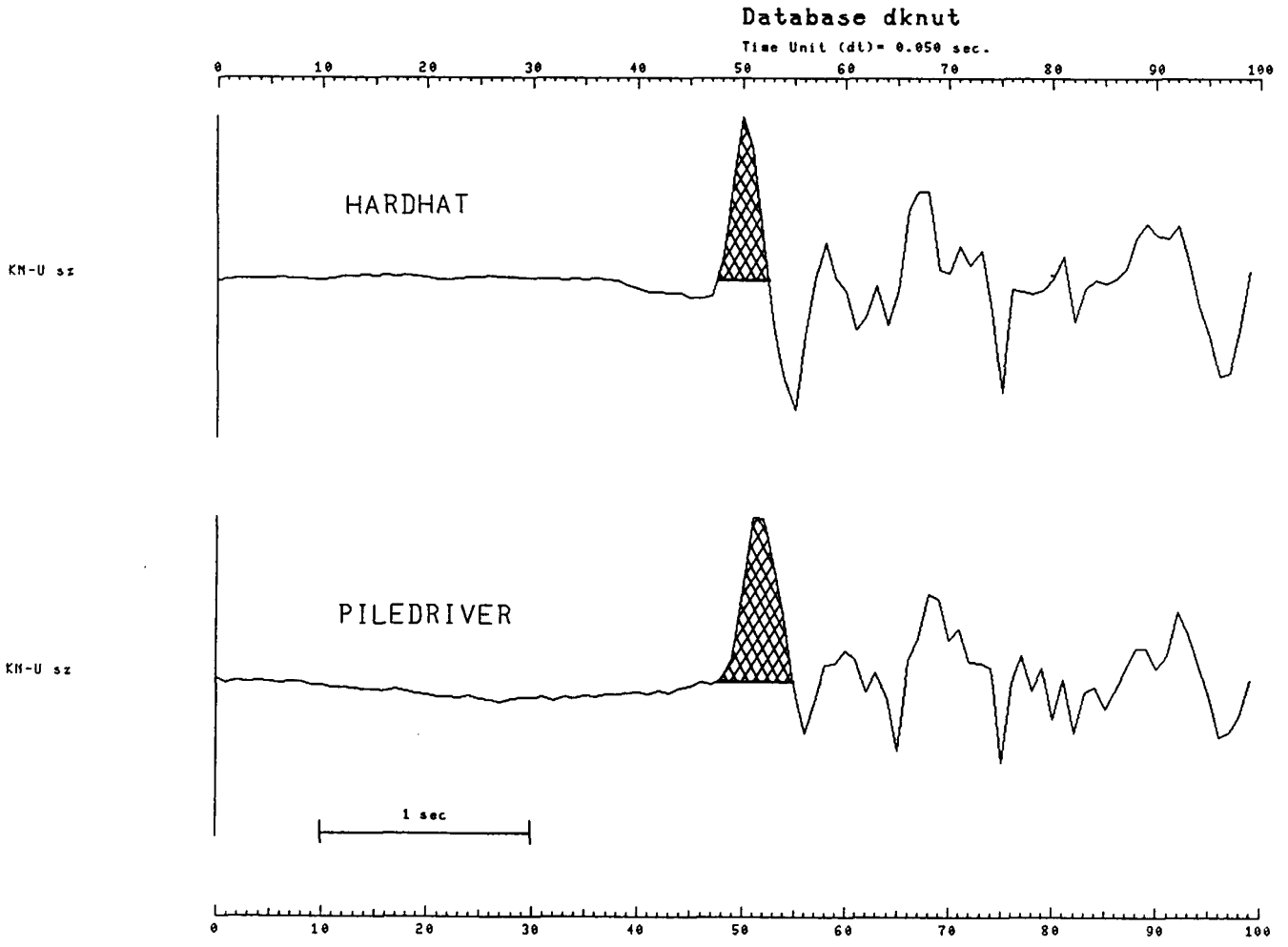
Database dknut
Time Unit (dt)= 0.050 sec.
0
10
20
30
40
50
60
70
80
90
100
HARDHAT
KN-U sz
PILEDRIVER
KN-U sz
1 sec

Figure 1-3

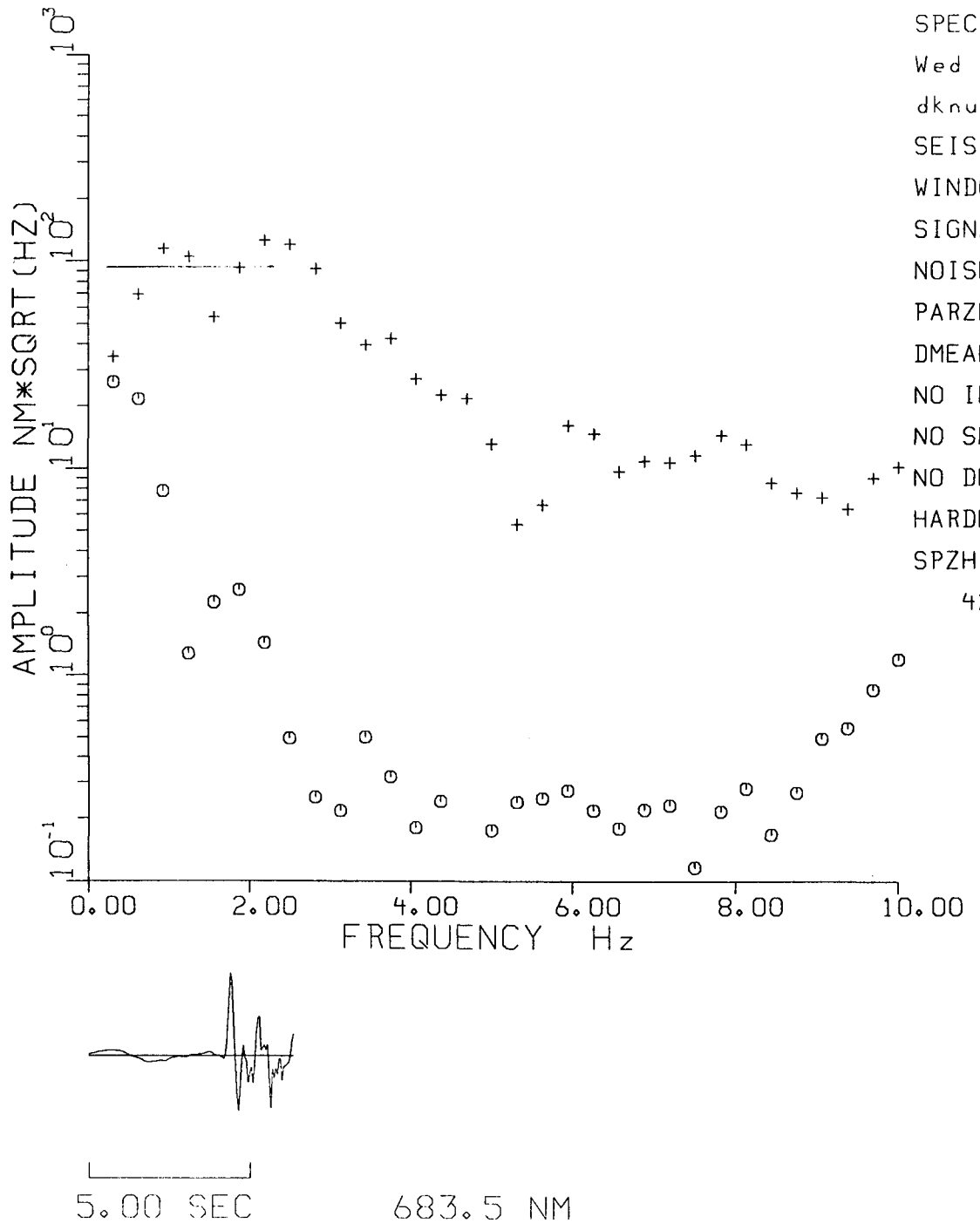
SPECALC vers 1.3
Wed Jul 1 12:19:11 1987
dknut
SEIS # 1
WINDOW = 64
SIGNAL 377 64
NOISE 313 64
PARZEN TAPER
DMEAN2 64 POINTS
NO INST CORRECTION
NO SMOOTHING
NO DECIMATION
HARDHAT dknut
SPZH P64 (NO SMOO)
42421 HARDHAT DECONVOL
AMPLITUDE NM*SQRT(HZ)
10^{3}
10^{2}
10^{1}
10^{0}
10^{-1}
0.00
2.00
4.00
6.00
8.00
10.00
FREQUENCY Hz
5.00 SEC
683.5 NM

Figure 1-4a

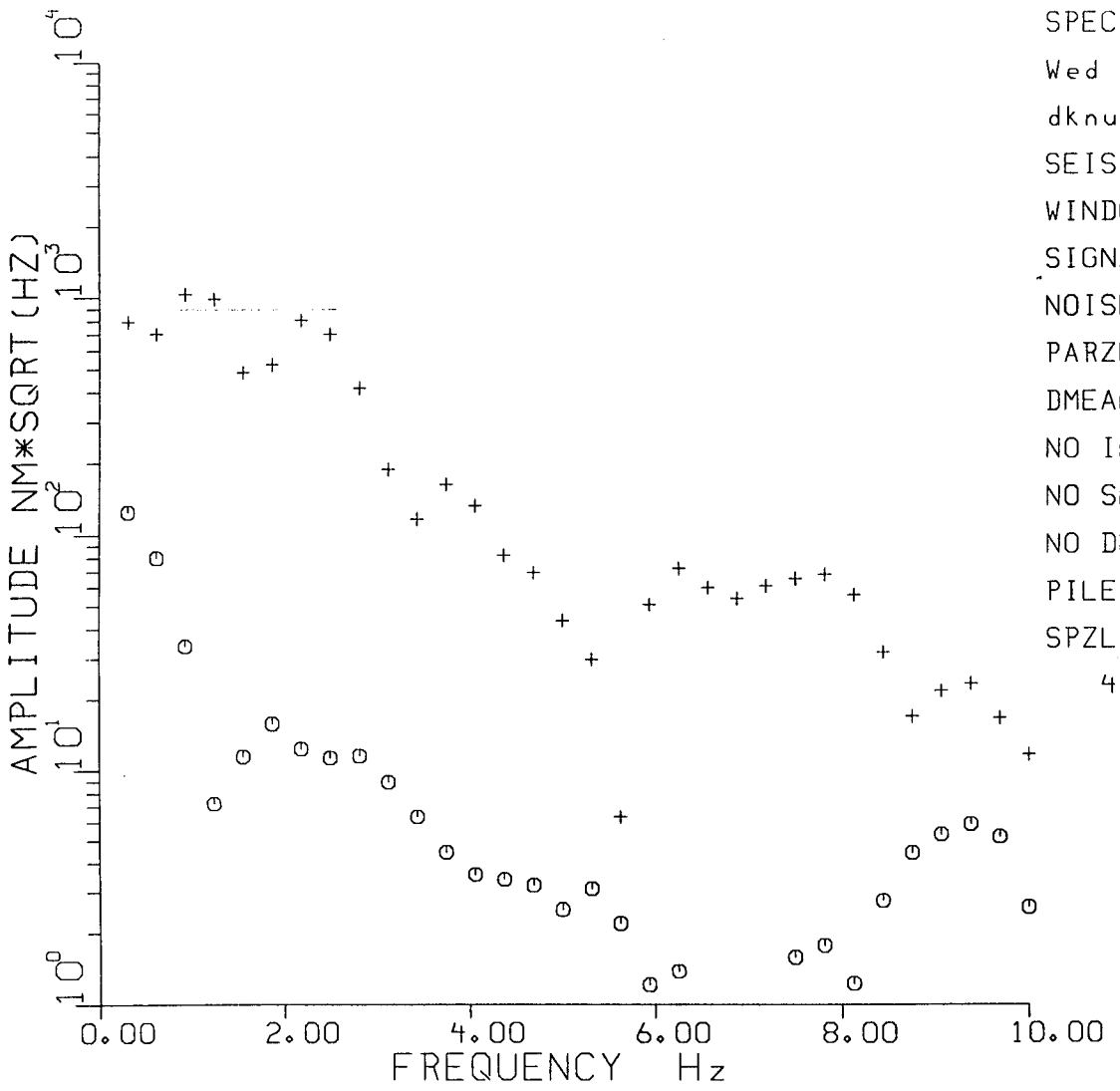

SPECALC vers 1.3
Wed Jul 1 12:18:58 1987
dknut
SEIS # 1
WINDOW = 64
SIGNAL 269 64
NOISE 205 64
PARZEN TAPER
DMEAN2 64 POINTS
NO INST CORRECTION
NO SMOOTHING
NO DECIMATION
PILEDRIVER dknut
SPZL P64 (NO SMOO)
45415 PILEDRIVER DECONVOL

5.00 SEC 5457.8 NM

Figure 1-4b

RATIO vers 1.2

Wed Jul 1 12:26:38 1987

HARDHAT/PILEDRIVER KN-UT SPZH/SPZL DECON P64

NOISE POWER SUBTRACTED FROM SIGNAL POWER

S/N POWER THRESHOLD = 2.0 N

NO SMOOTHING

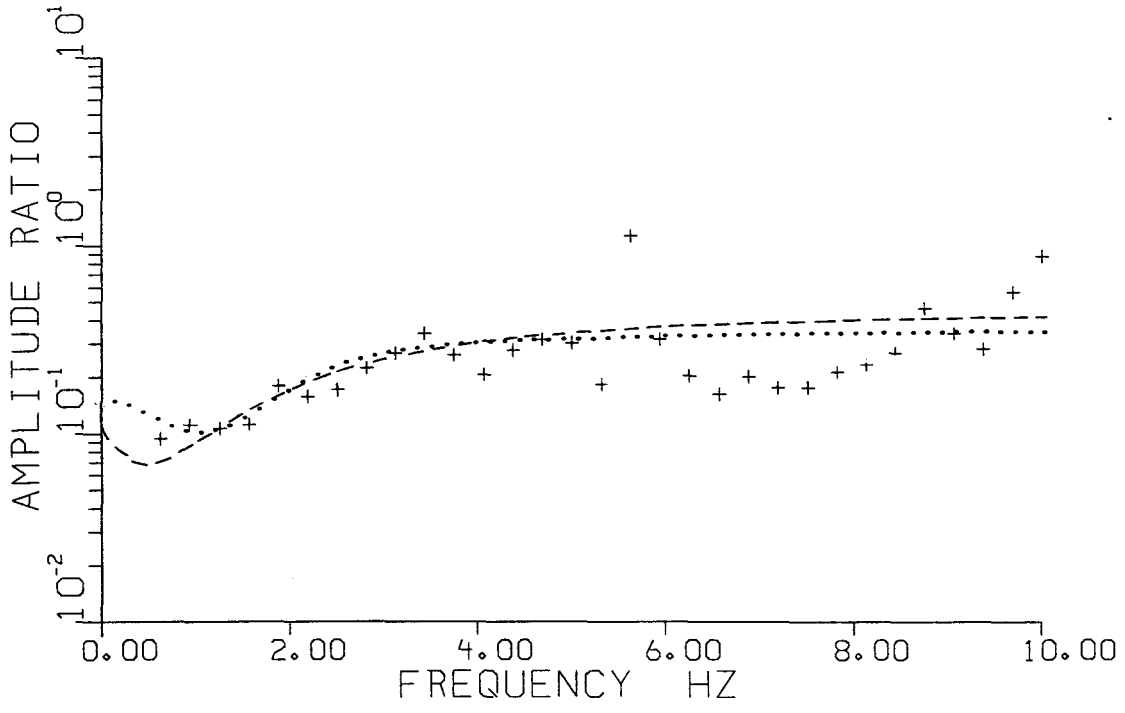

Figure 1-4c

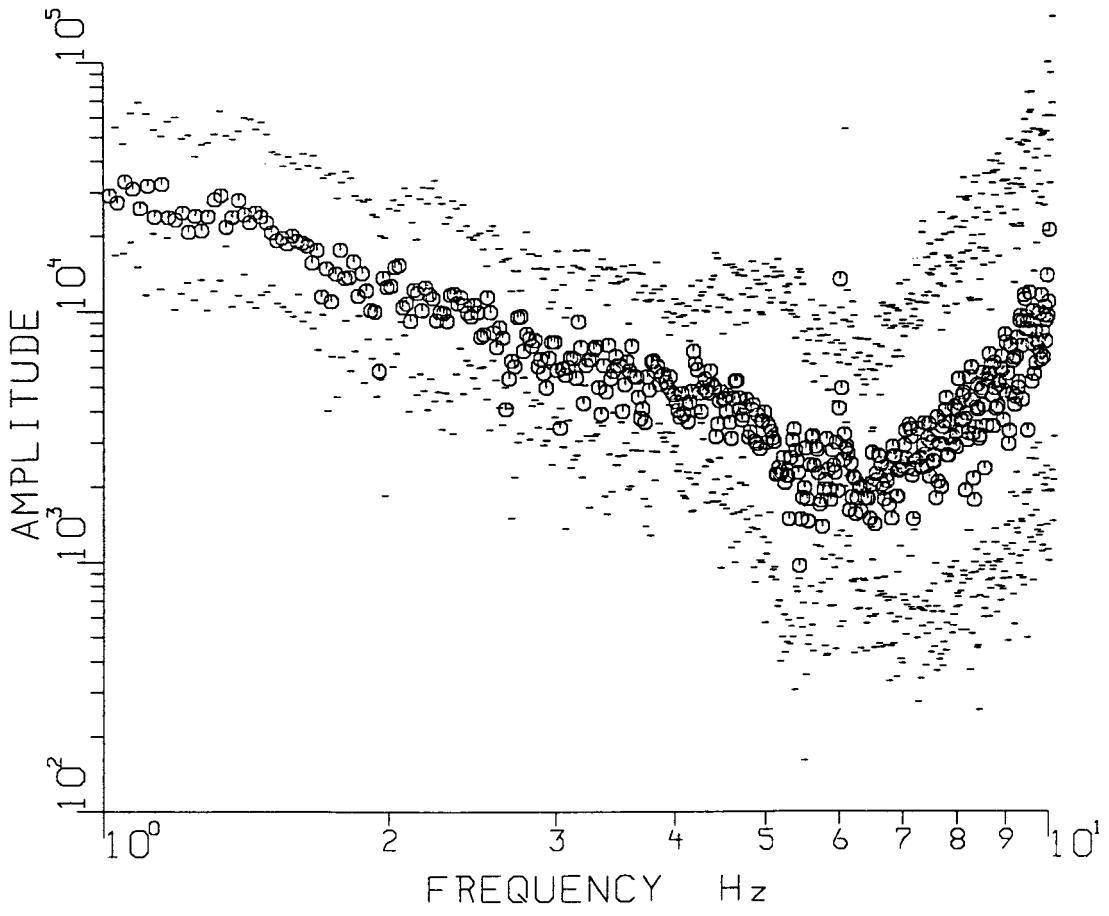
32 SPECTRUM AVERAGE
0.50 - 1.50 Hz SCAL
AMPLITUDE
10^2
10^3
10^4
10^5
10^0
2
3
4
5
6
7
8
9
10^1
FREQUENCY Hz
HARDHAT Lg Z & H Inst & Q correction
Program avspc vers 1.0

Figure 1-5a

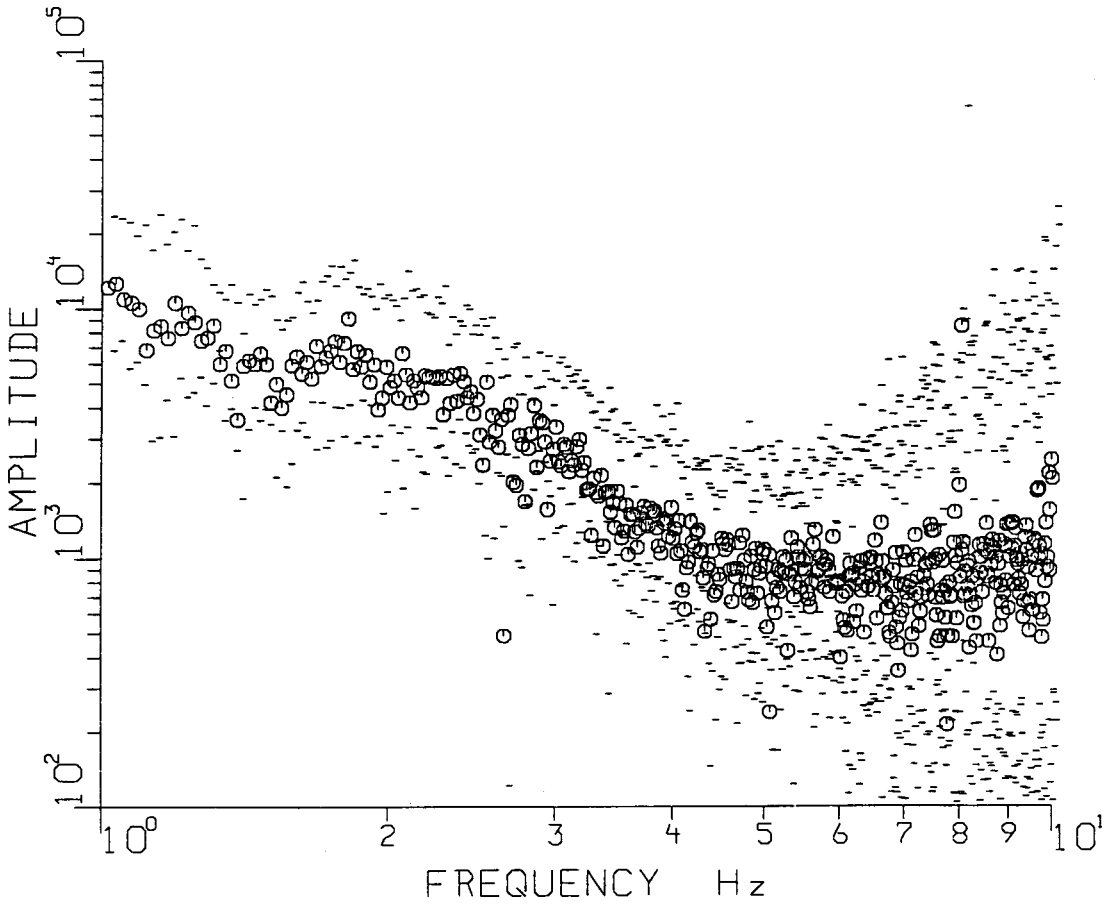
24 SPECTRUM AVERAGE
0.50 - 1.50 Hz SCAL
AMPLITUDE
10^5
10^4
10^3
10^2
10^0
2
3
4
5
6
7
8
9
10^1
FREQUENCY Hz
SHOAL Lg Z & H Inst & Q correction
Program avspc vers 1.0

Figure 1-5b

RATIO vers 1.2

Tue Jun 9 14:43:52 1987

SHOAL/HARDHAT FROM AVSPC, dist<1000km

NOISE POWER NOT SUBTRACTED FROM SIGNAL POWER

S/N POWER THRESHOLD = 0.0 N

NO SMOOTHING

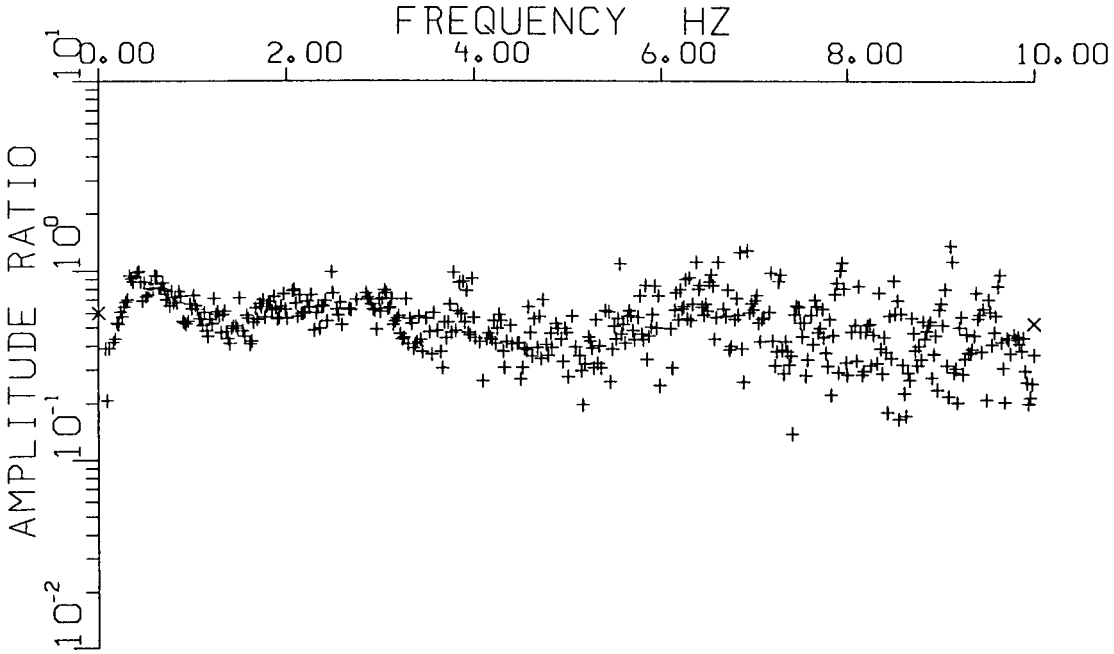

FREQ BAND	SLOPE	+/-	Y INTERC	AV INTEG	AV RATIO	SD
1.0-4.0	-5.633E-03	8.835E-03	0.599E+00	-0.236E+00	-0.236E+00	9.200E-02
3.0-6.0	-2.490E-02	1.231E-02	0.620E+00	-0.320E+00	-0.320E+00	0.130E+00
1.0-3.0	5.038E-02	1.268E-02	0.481E+00	-0.217E+00	-0.221E+00	7.267E-02
3.0-5.0	-6.994E-02	1.961E-02	0.928E+00	-0.312E+00	-0.310E+00	0.117E+00

Figure 1-5c

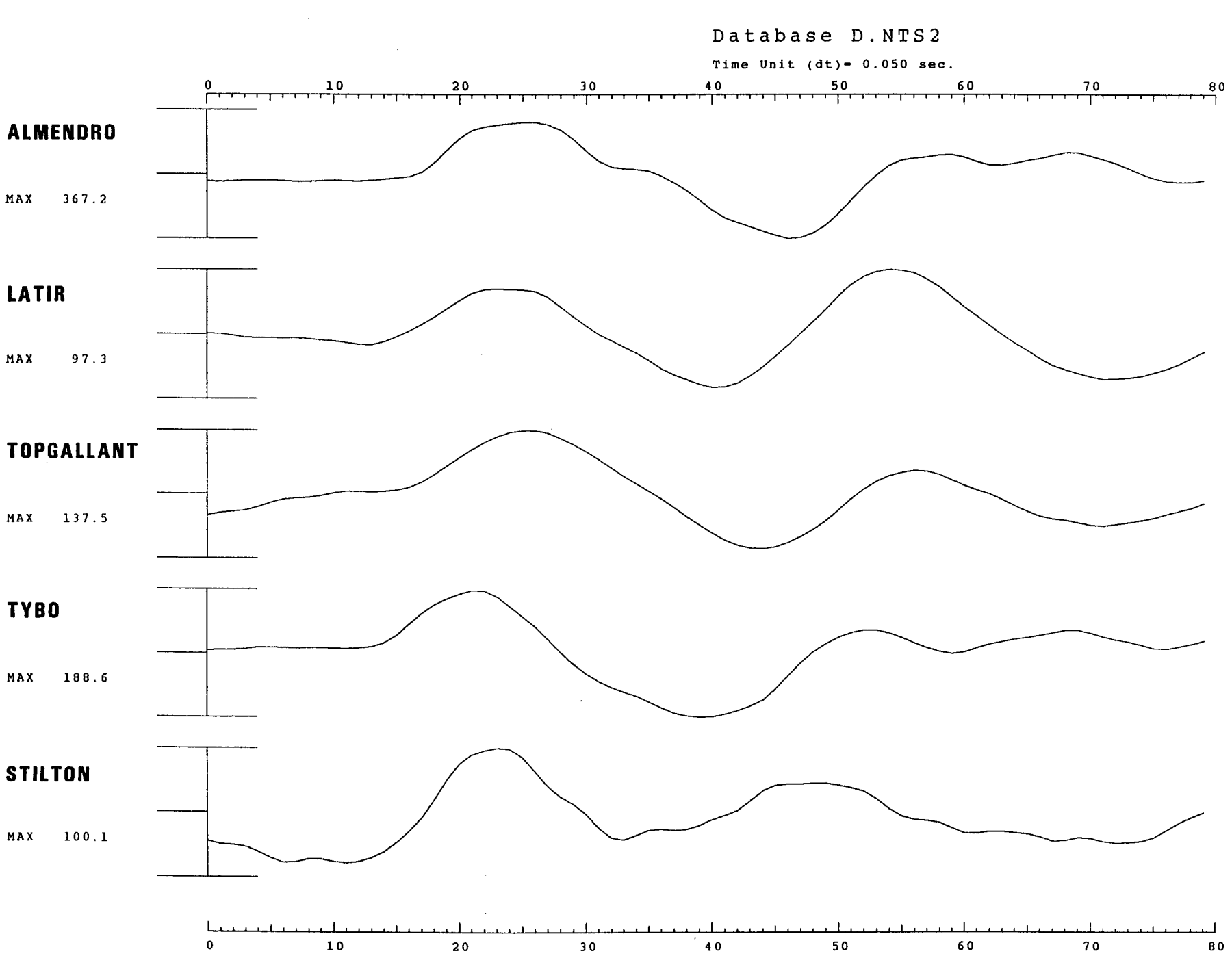
Database D.NTS2
Time Unit (dt)= 0.050 sec.
0
10
20
30
40
50
60
70
80
ALMENDRO
MAX 367.2
LATIR
MAX 97.3
TOPGALLANT
MAX 137.5
TYBO
MAX 188.6
STILTON
MAX 100.1

Figure 2-1a

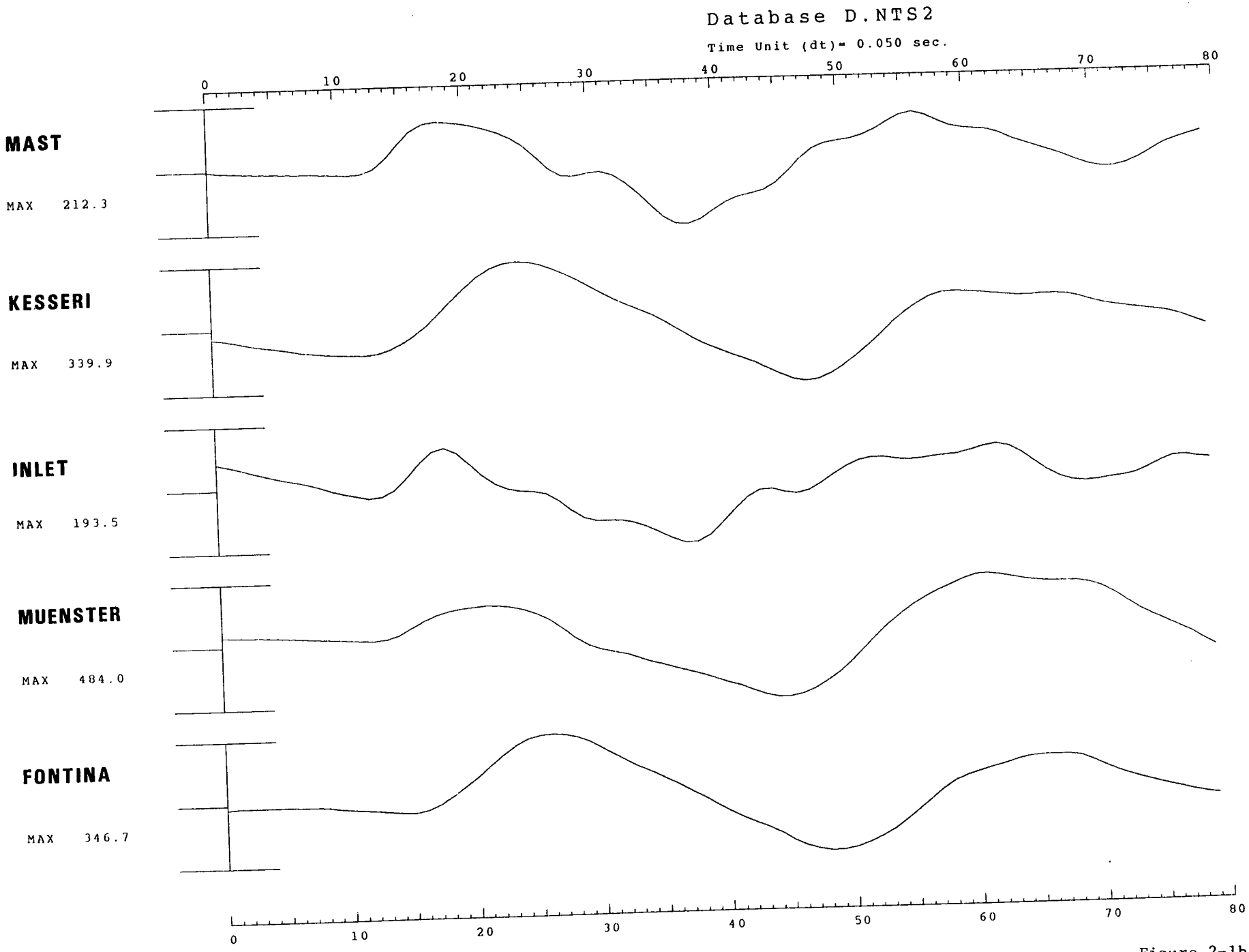
Database D.NTS2
Time Unit (dt)= 0.050 sec.
0
10
20
30
40
50
60
70
80
MAST
MAX 212.3
KESSERI
MAX 339.9
INLET
MAX 193.5
MUENSTER
MAX 484.0
FONTINA
MAX 346.7

Figure 2-1b

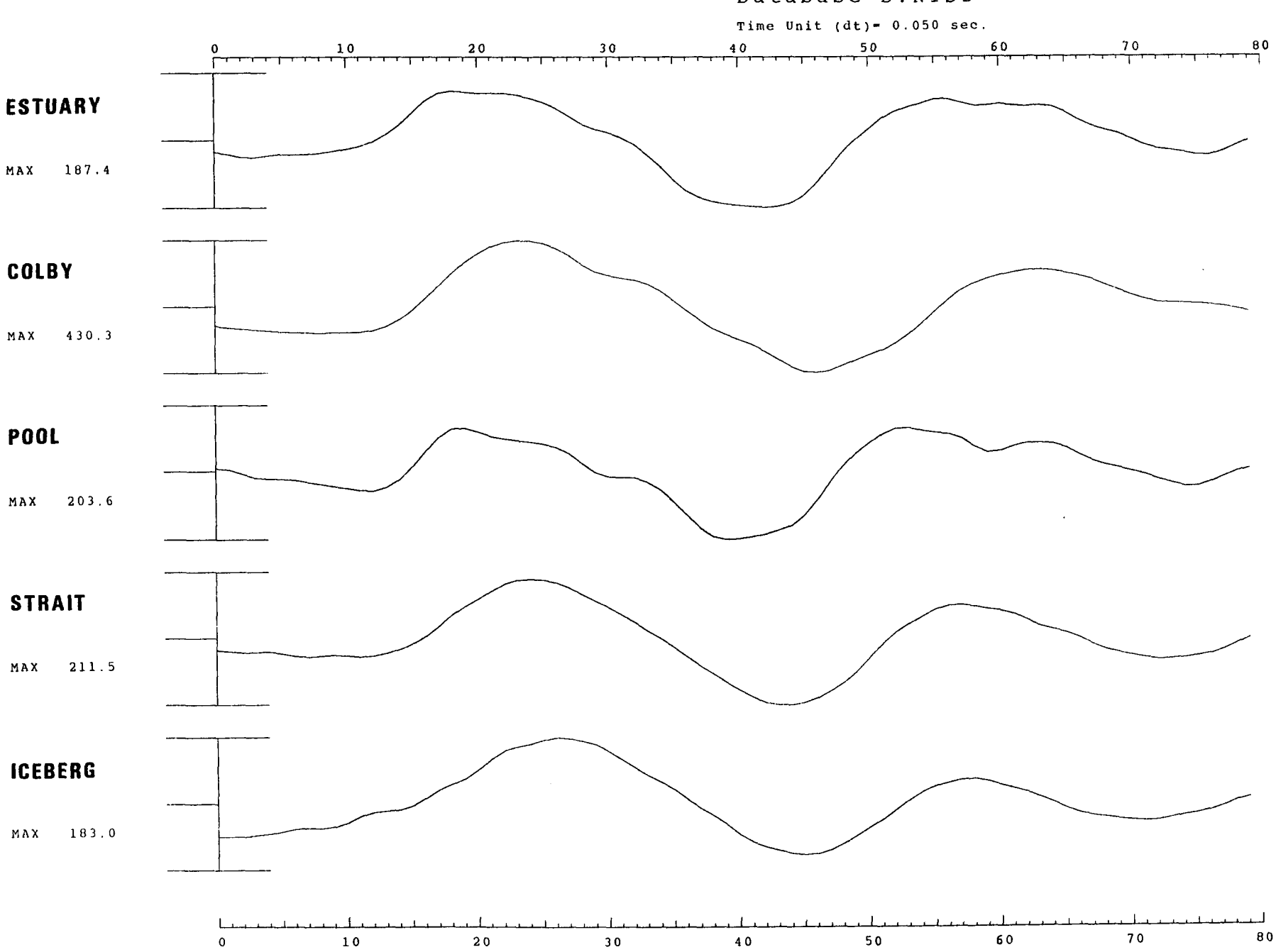
Database D.NTS2
Time Unit (dt)= 0.050 sec.
0
10
20
30
40
50
60
70
80
ESTUARY
MAX 187.4
COLBY
MAX 430.3
POOL
MAX 203.6
STRAIT
MAX 211.5
ICEBERG
MAX 183.0

Figure 2-1c

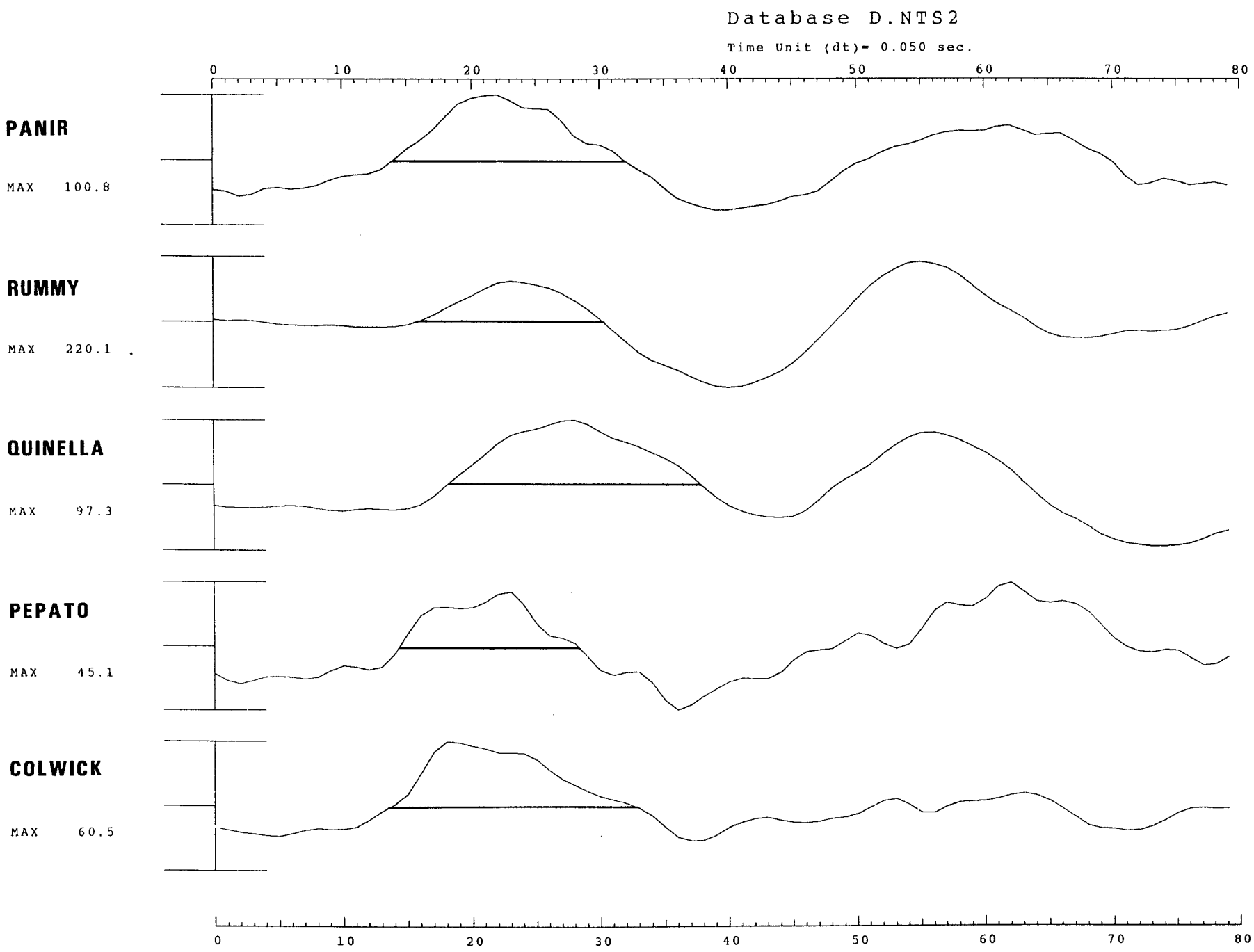
Database D.NTS2
Time Unit (dt)= 0.050 sec.
0
10
20
30
40
50
60
70
80
PANIR
MAX 100.8
RUMMY
MAX 220.1
QUINELLA
MAX 97.3
PEPATO
MAX 45.1
COLWICK
MAX 60.5

Figure 2-1d

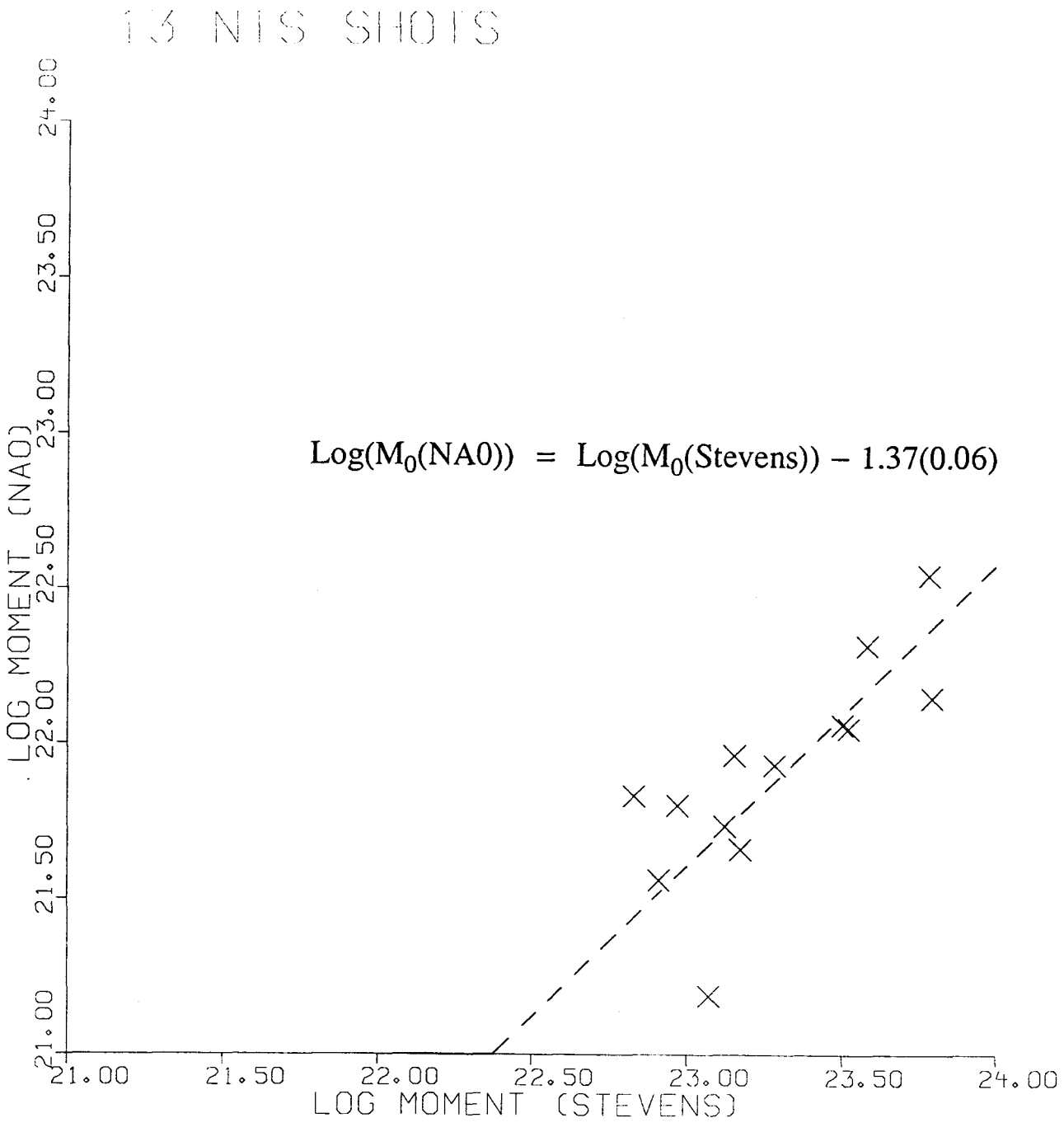
13 NIS SHOTS
Log(M0(NA0)) = Log(M0(Stevens)) – 1.37(0.06)
LOG MOMENT (NAO)
21.00
21.50
22.00
22.50
23.00
23.50
24.00
LOG MOMENT (STEVENS)

Figure 2-2

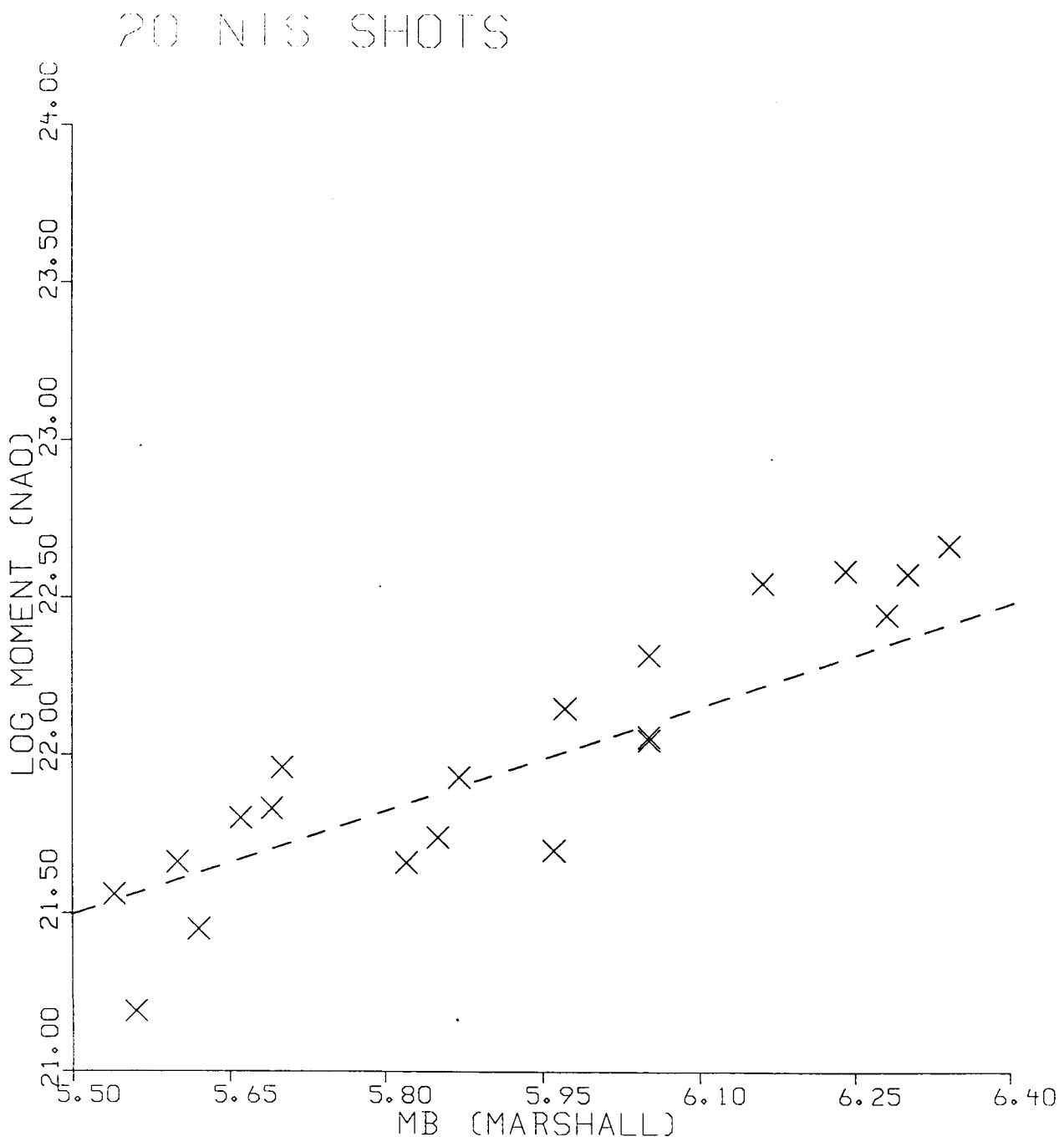
20 NTS SHOTS
LOG MOMENT (NAO)
21.00
21.50
22.00
22.50
23.00
23.50
24.00
5.50
5.65
5.80
5.95
6.10
6.25
6.40
MB (MARSHALL)

Figure 2-3

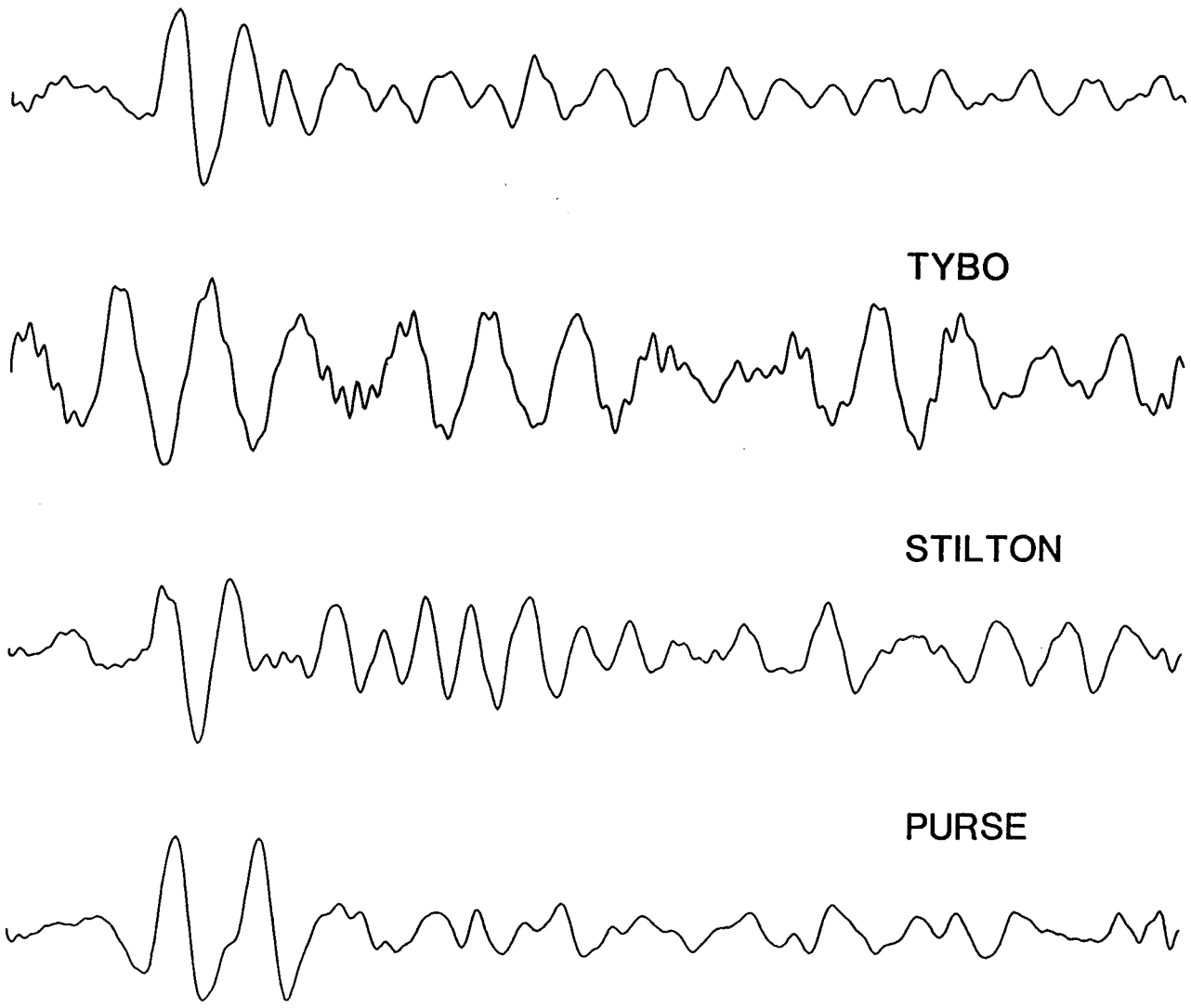

Figure 2-4a

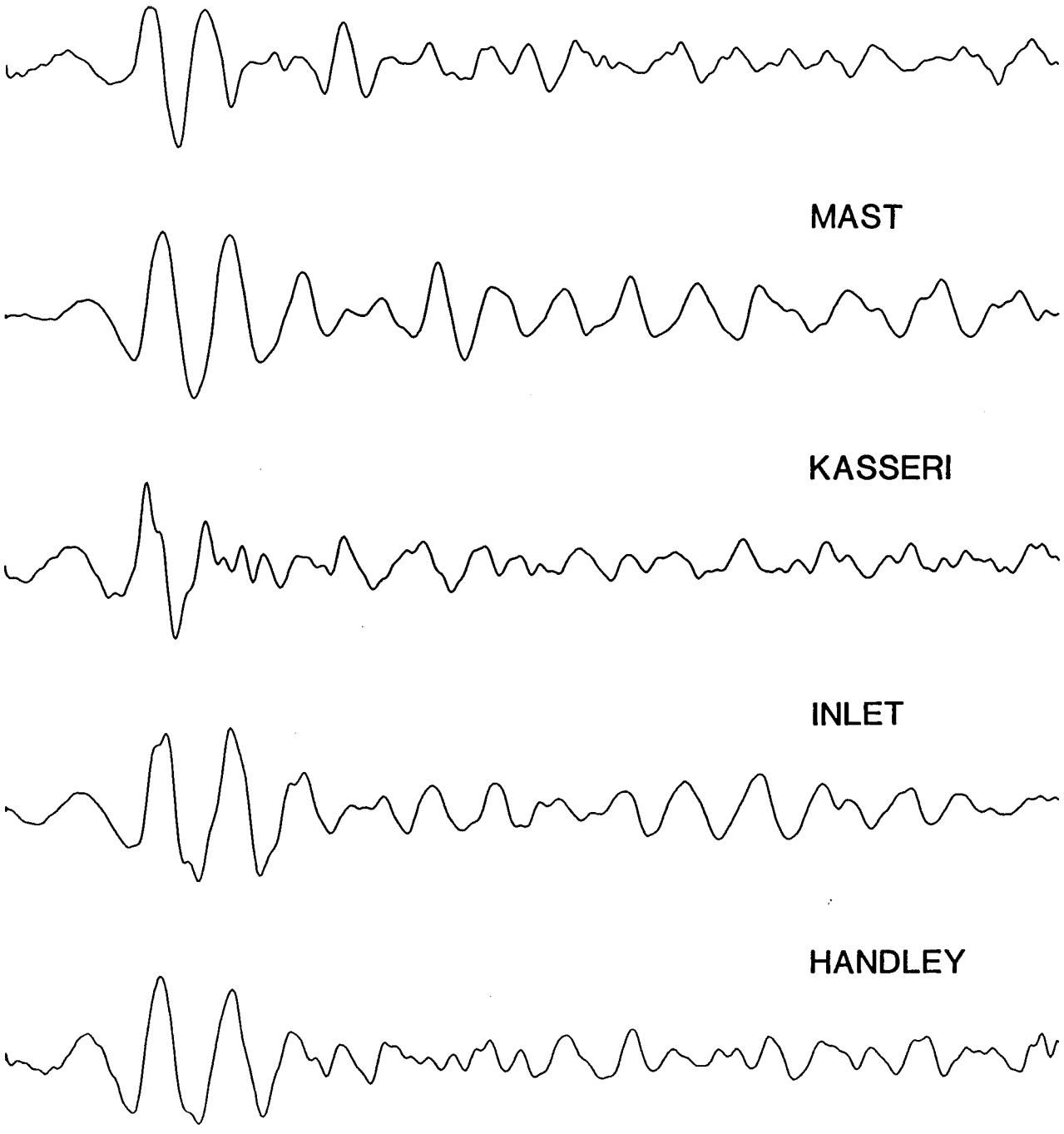

Figure 2-4b

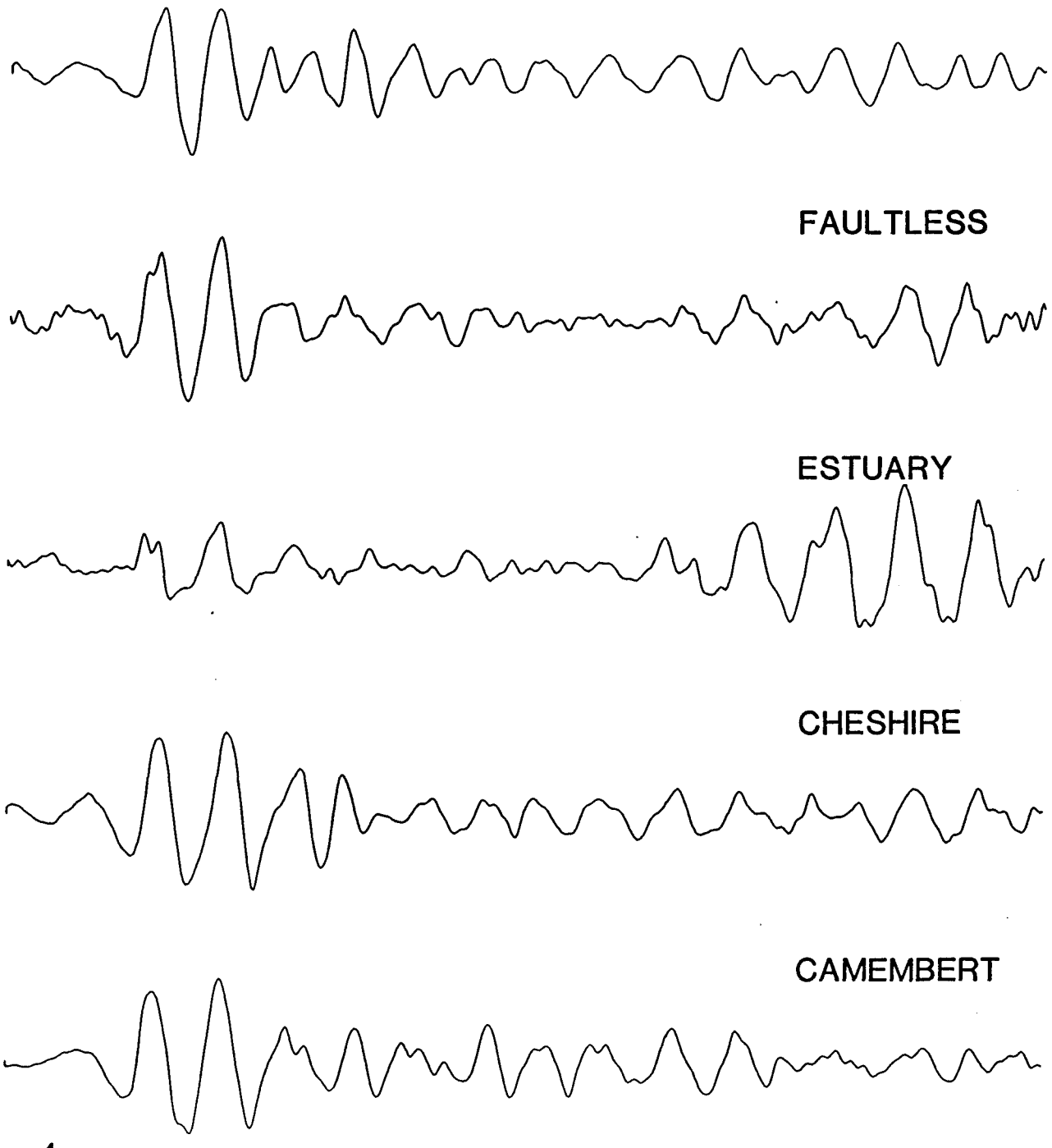

Figure 2-4c

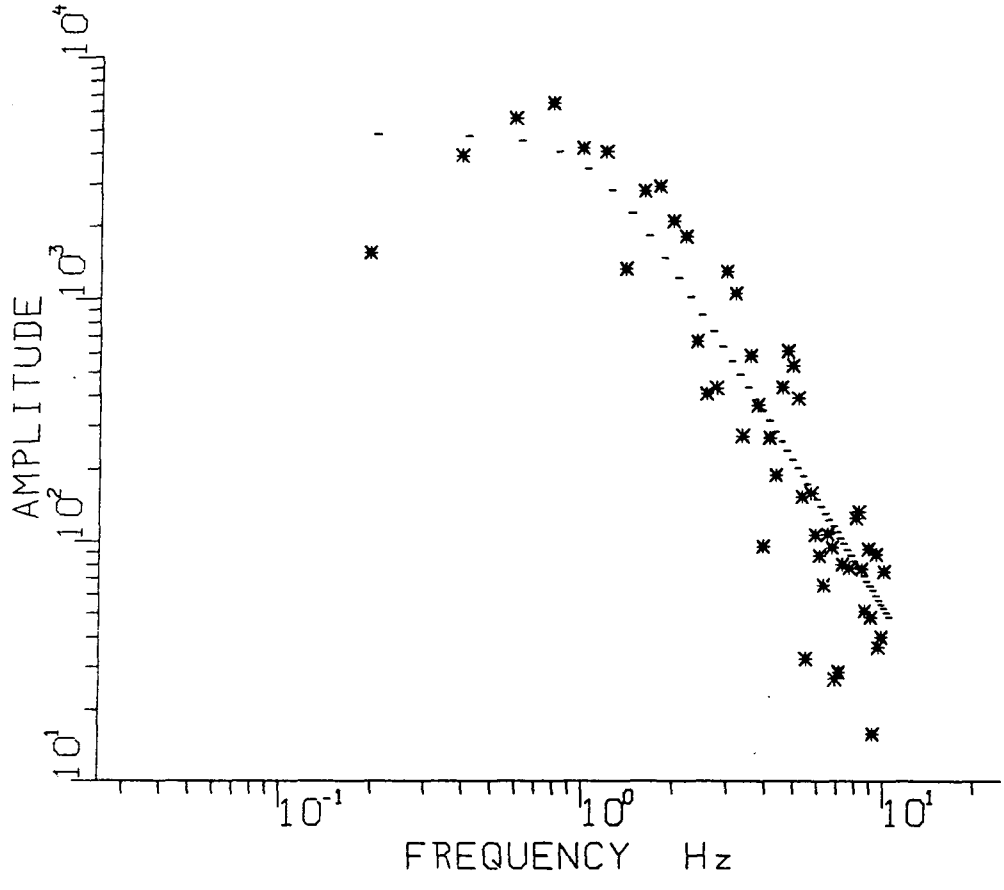

fcfit vers 1.4
Input: mast.KNB.Pn25(
f: 0.10 - 10.00 Hz
fc: 0.10 - 10.00 Hz
dfc = 0.10 Hz
S/N = 2.0
exp = 2.0
N = 49
SD = 0.2777

fc = 1.00 Hz Ao = 4599.4169

mast KNB sz Pn256

Figure 2-5a

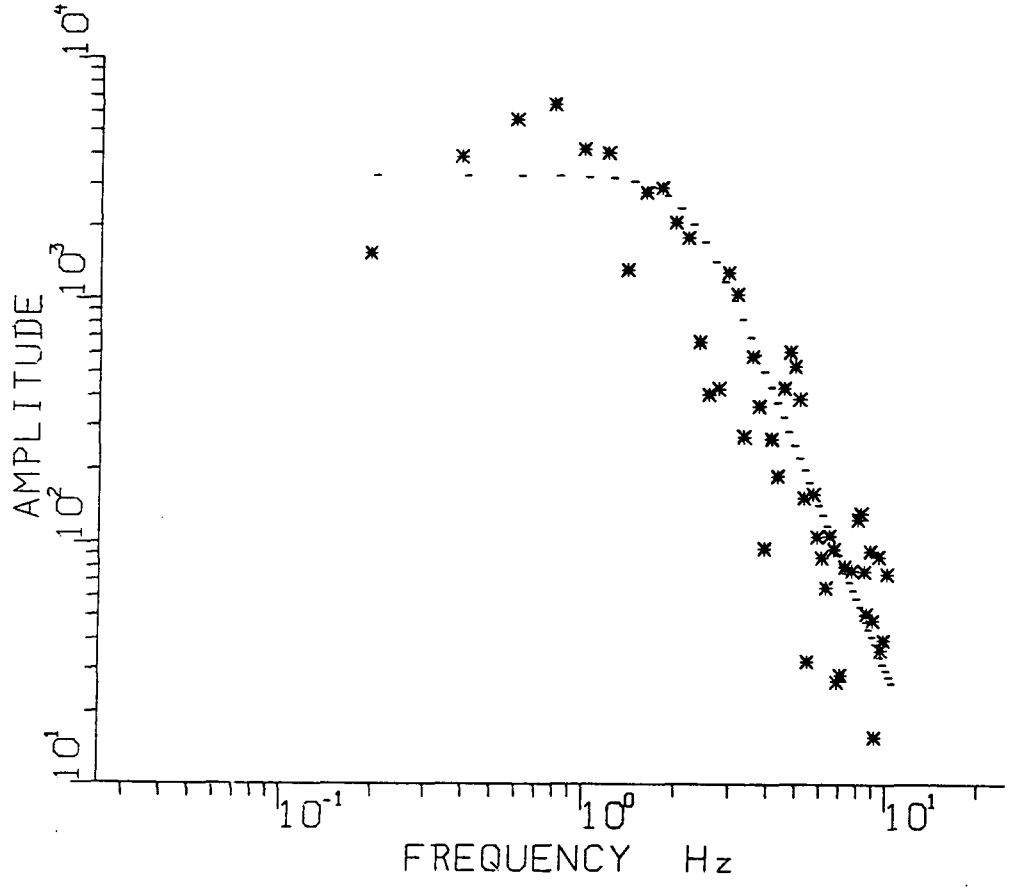

fcfit vers 1.4
Input: mast.KNB.Pn25(
f: 0.10 - 10.00 Hz
fc: 0.10 - 10.00 Hz
dfc = 0.10 Hz
S/N = 2.0
exp = 3.0
N = 49
SD = 0.2994

fc = 2.00 Hz Ao = 3133.0178

mast KNB sz Pn256

Figure 2-5b

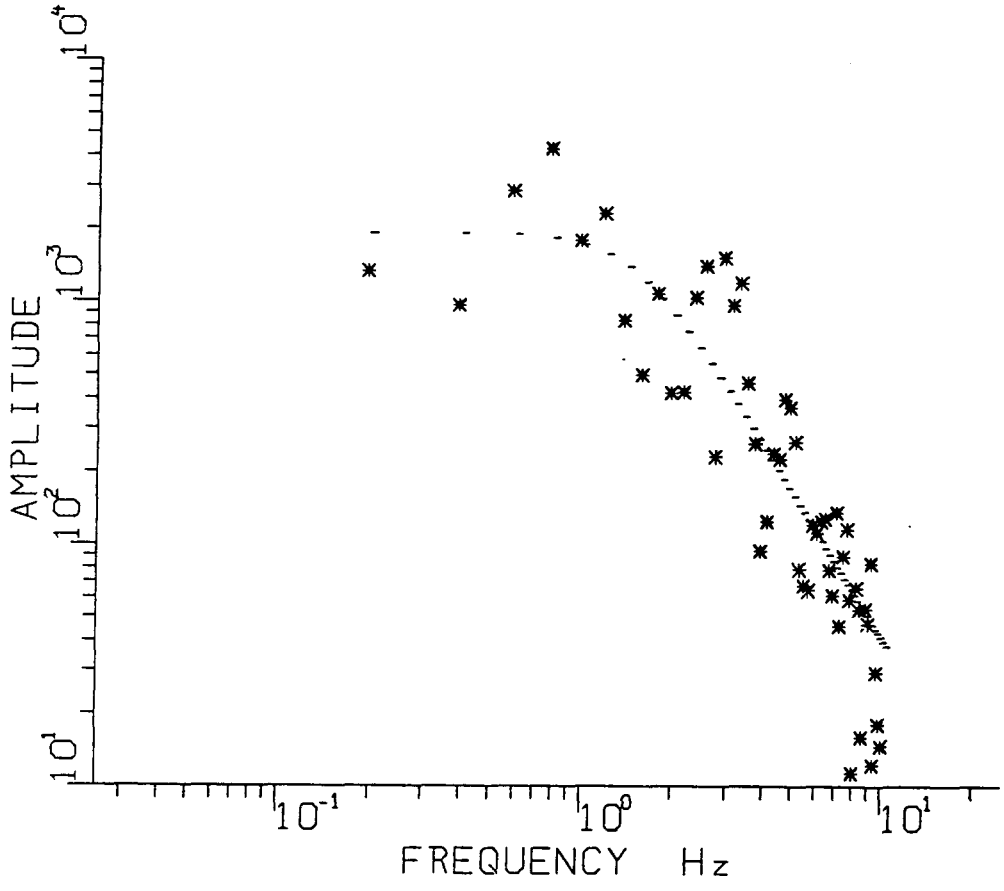

fcfit vers 1.4
Input: mast.ELK.Pn25(
f: 0.10 - 10.00 Hz
fc: 0.10 - 10.00 Hz
dfc = 0.10 Hz
S/N = 2.0
exp = 2.0
N = 51
SD = 0.2904

fc = 1.40 Hz Ao = 1848.8126

mast ELK sz Pn256

Figure 2-5c

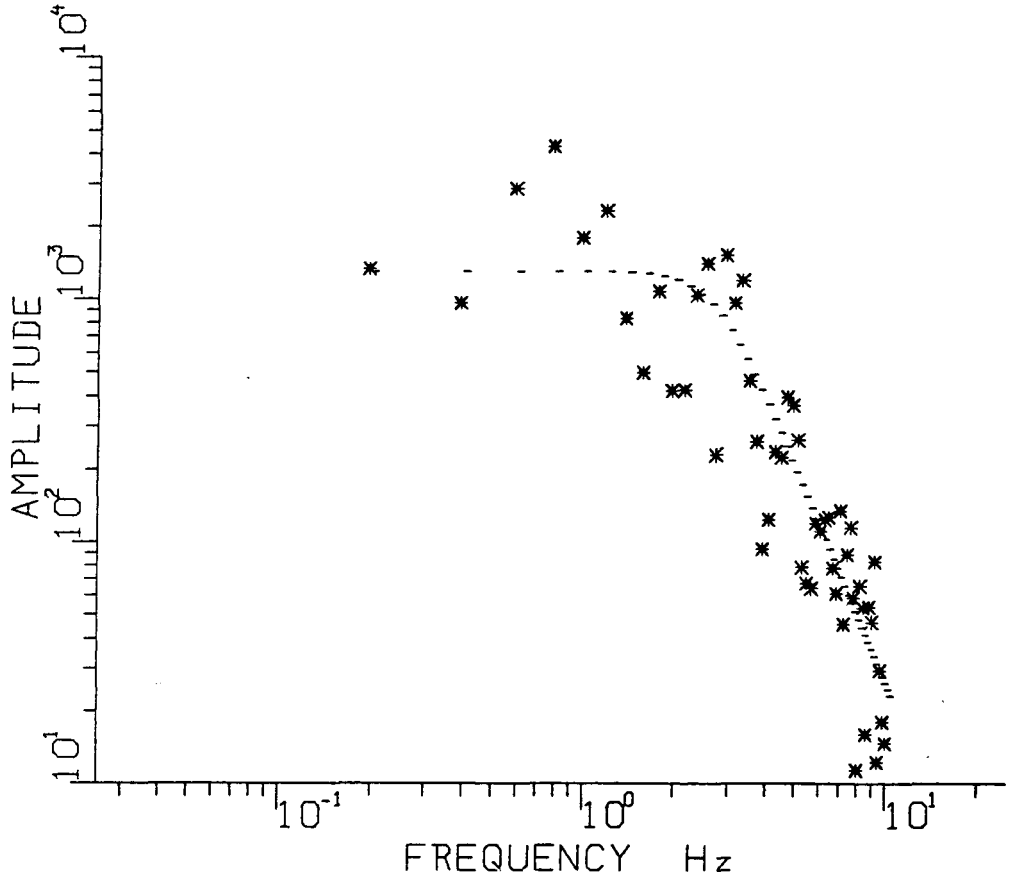

fcfit vers 1.4

Input: mast.ELK.Pn25(

f: 0.10 - 10.00 Hz

fc: 0.10 - 10.00 Hz

dfc = 0.10 Hz

S/N = 2.0

exp = 3.0

N = 51

SD = 0.2828

fc = 2.60 Hz Ao = 1256.7327

mast ELK sz Pn256

Figure 2-5d

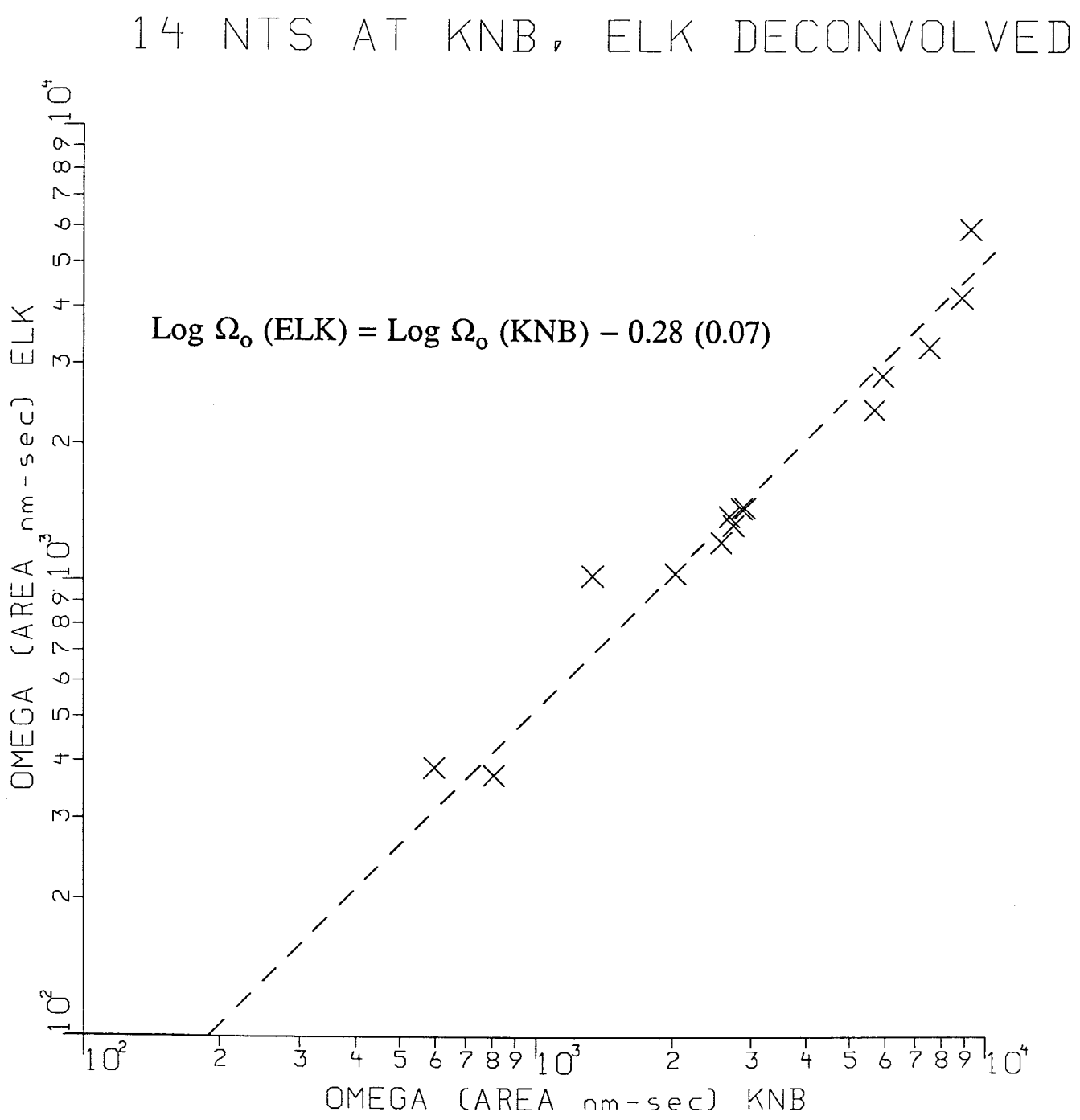
14 NTS AT KNB, ELK DECONVOLVED
Log Ω_o (ELK) = Log Ω_o (KNB) – 0.28 (0.07)
OMEGA (AREA nm-sec) ELK
OMEGA (AREA nm-sec) KNB
10^2
10^3
10^4

Figure 2-6a

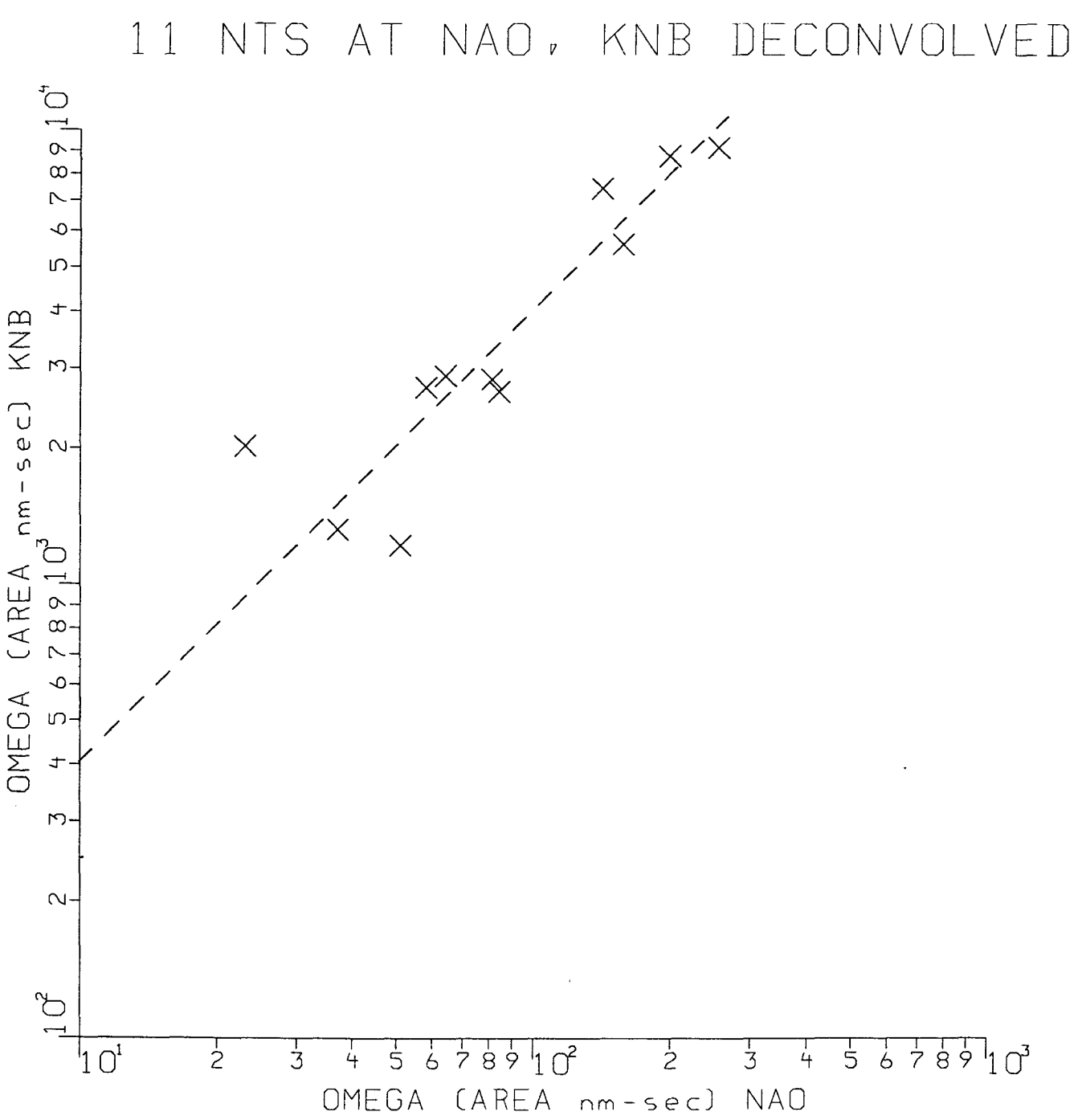
11 NTS AT NAO, KNB DECONVOLVED
OMEGA (AREA nm-sec) KNB
OMEGA (AREA nm-sec) NAO
10^2
10^3
10^4
10^1
10^2
10^3

Figure 2-6b

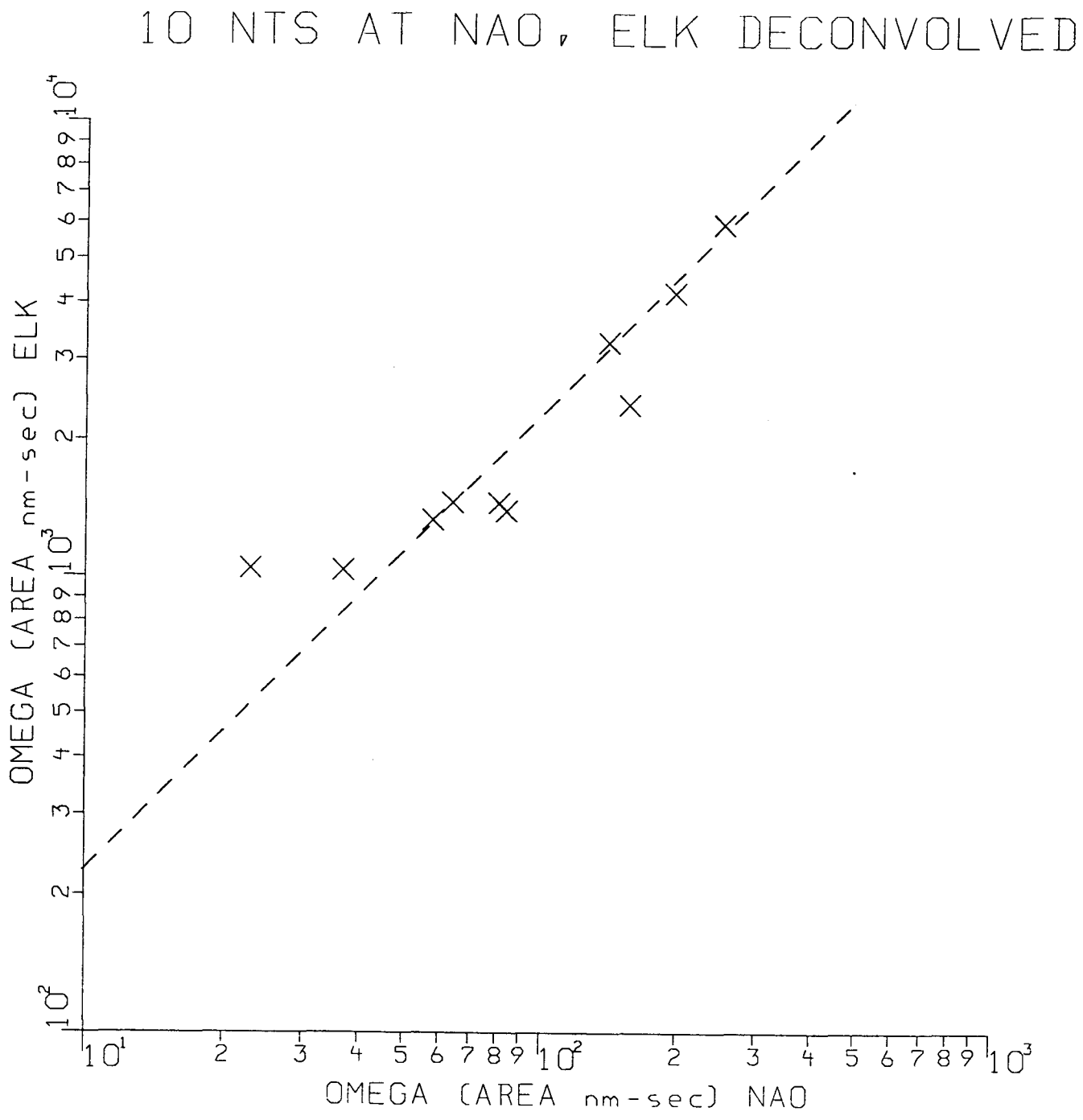
10 NTS AT NAO, ELK DECONVOLVED
OMEGA (AREA nm-sec) ELK
OMEGA (AREA nm-sec) NAO
10^2
10^3
10^4
10^1
10^2
10^3

Figure 2-6c

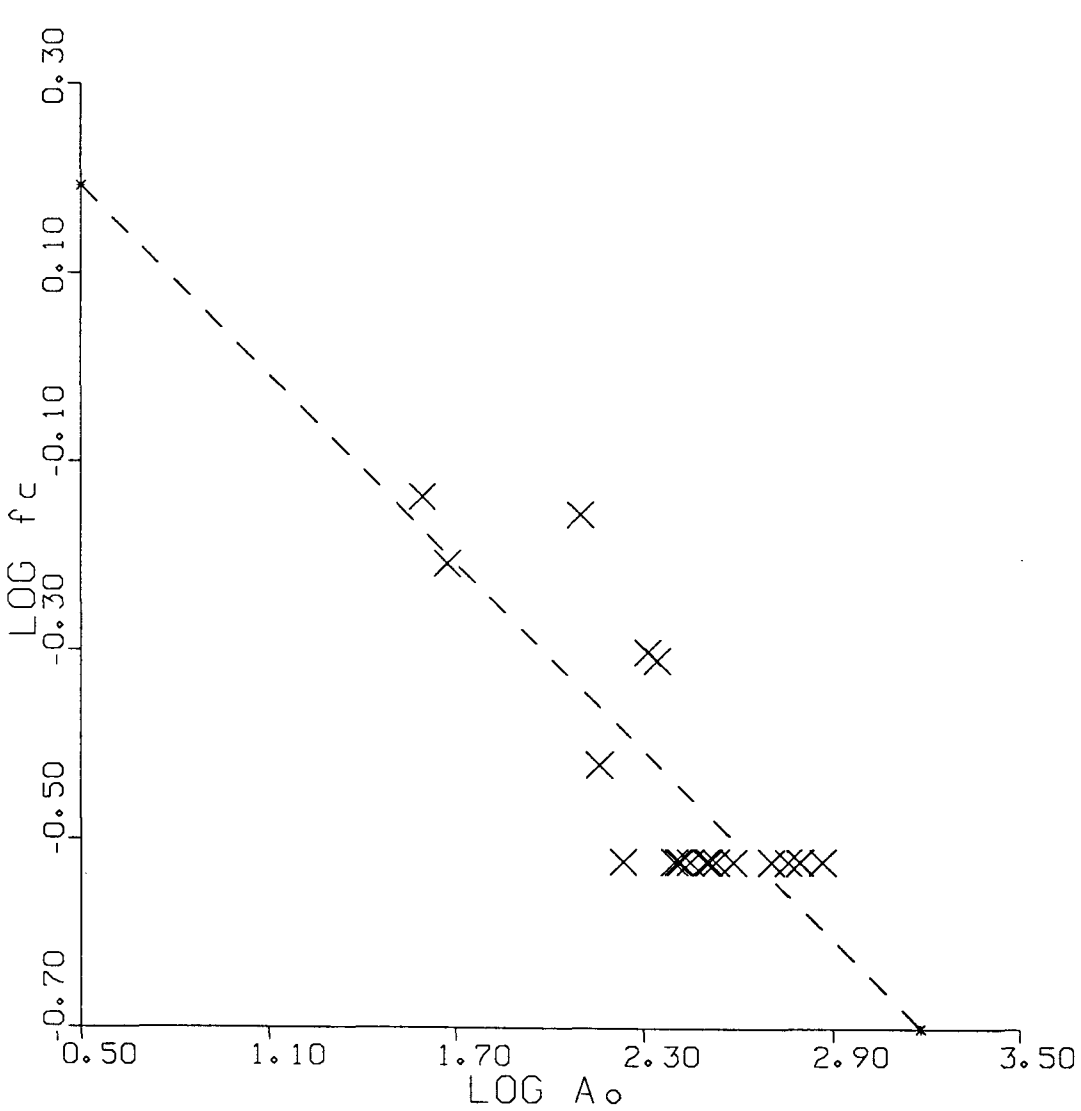
20 NTS NAO,P6.4,COS,T*=.4,EX=2
0.30
0.10
-0.10
-0.30
-0.50
-0.70
LOG fc
0.50
1.10
1.70
2.30
2.90
3.50
LOG A.

Figure 2-6d

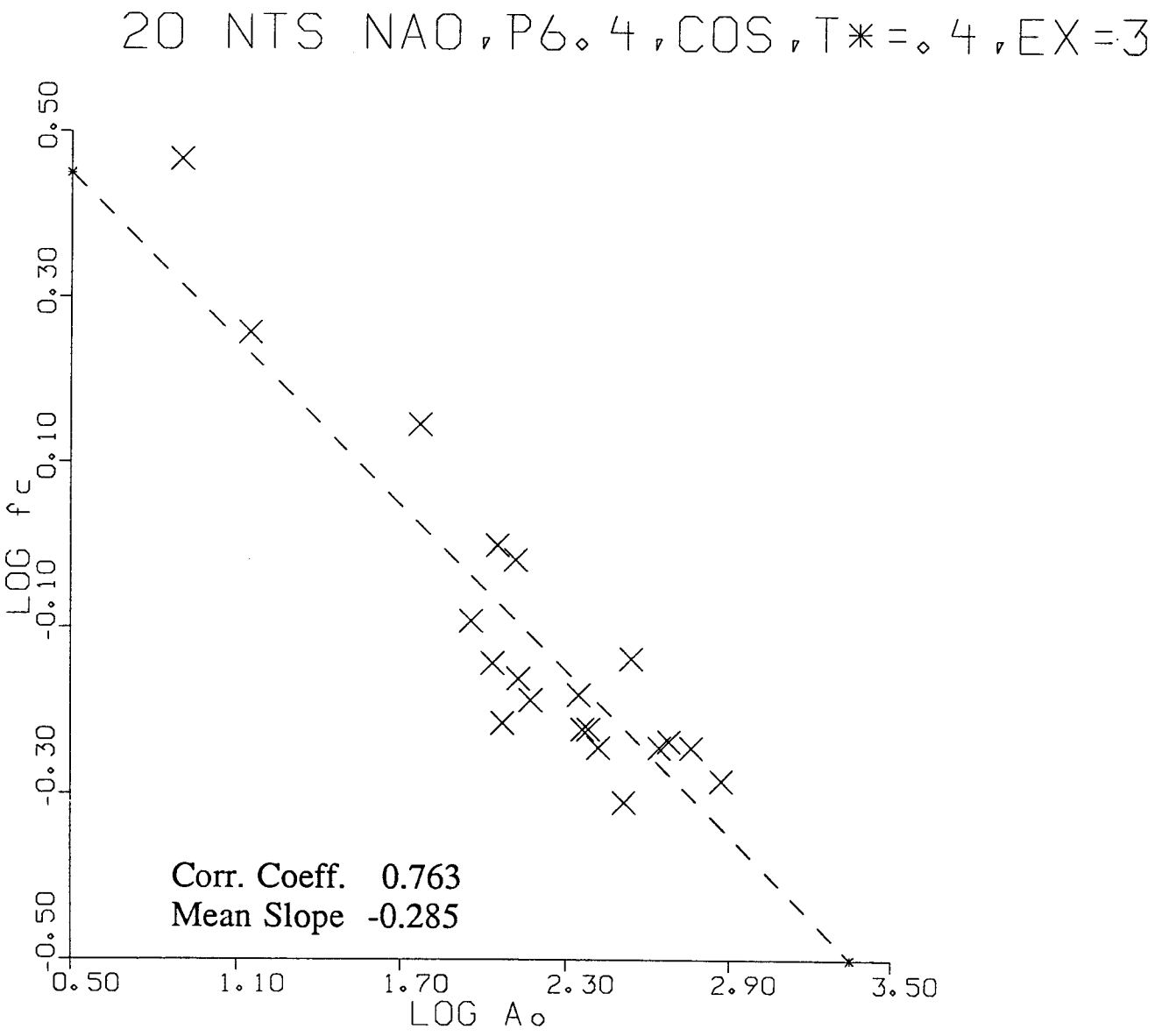
20 NTS NAO, P6.4, COS, T*=.4, EX=3
0.50
0.30
0.10
-0.10
-0.30
-0.50
LOG fc
0.50
1.10
1.70
2.30
2.90
3.50
LOG Ao
Corr. Coeff. 0.763
Mean Slope -0.285

Figure 2-6e

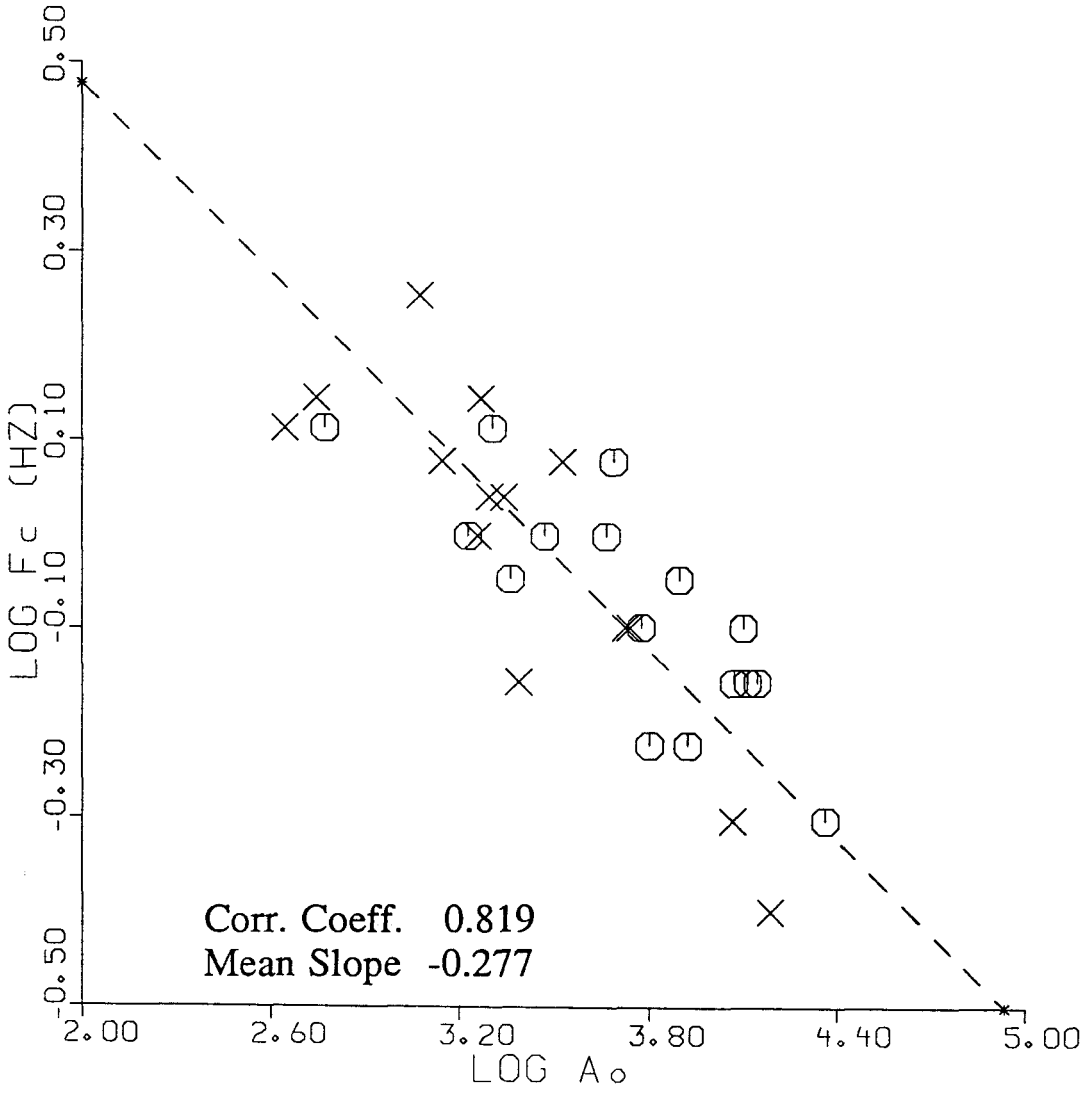
16NTS ELK(X),KNB(O),P5.12,EX=2
LOG Fc (HZ)
0.50
0.30
0.10
-0.10
-0.30
-0.50
2.00
2.60
3.20
3.80
4.40
5.00
LOG Ao
Corr. Coeff. 0.819
Mean Slope -0.277

Figure 2-6f

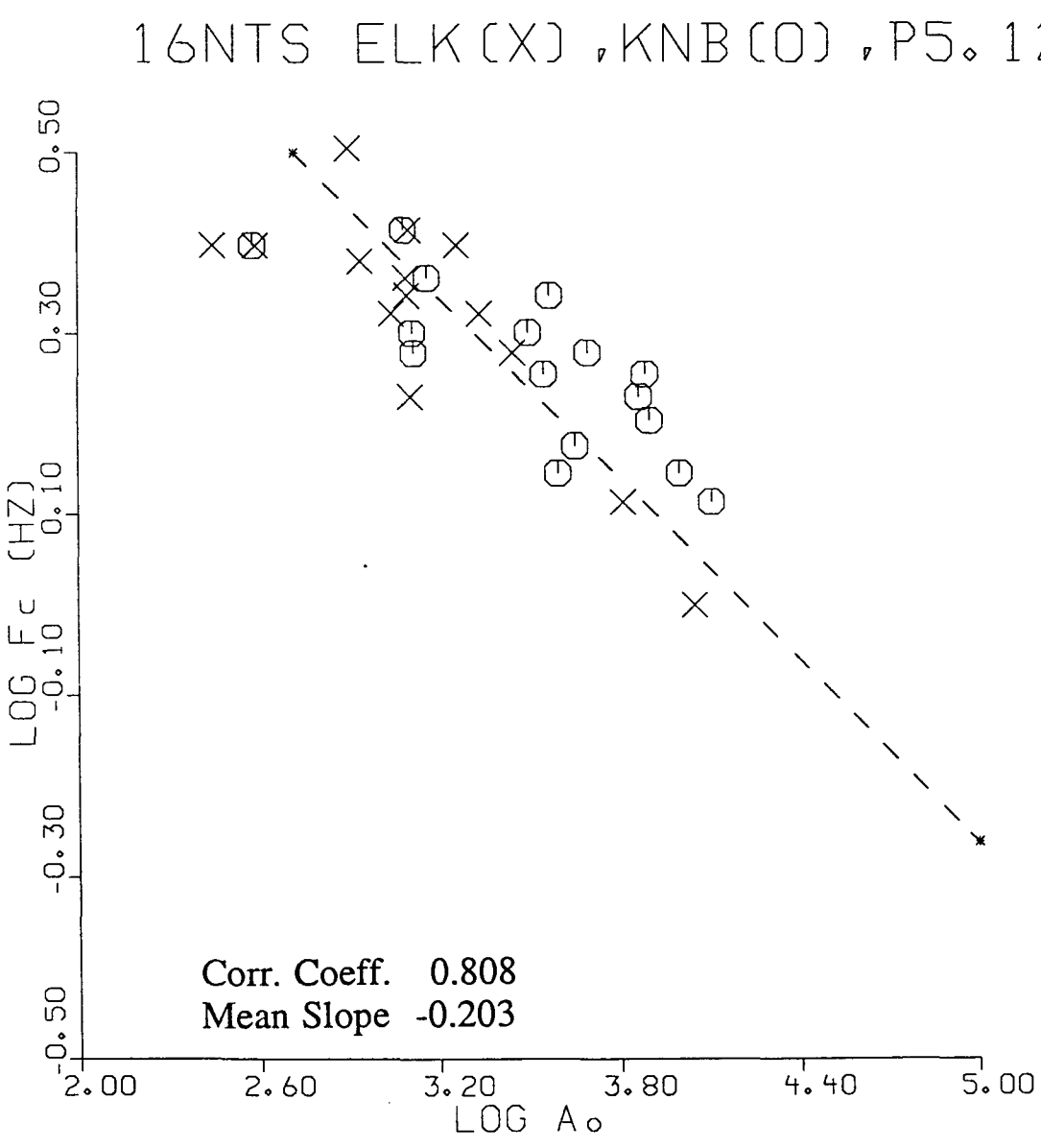
16NTS ELK(X),KNB(O),P5.12,EX=3
LOG Fc (HZ)
0.50
0.30
0.10
-0.10
-0.30
-0.50
2.00
2.60
3.20
3.80
4.40
5.00
LOG Ao
Corr. Coeff. 0.808
Mean Slope -0.203

Figure 2-6g

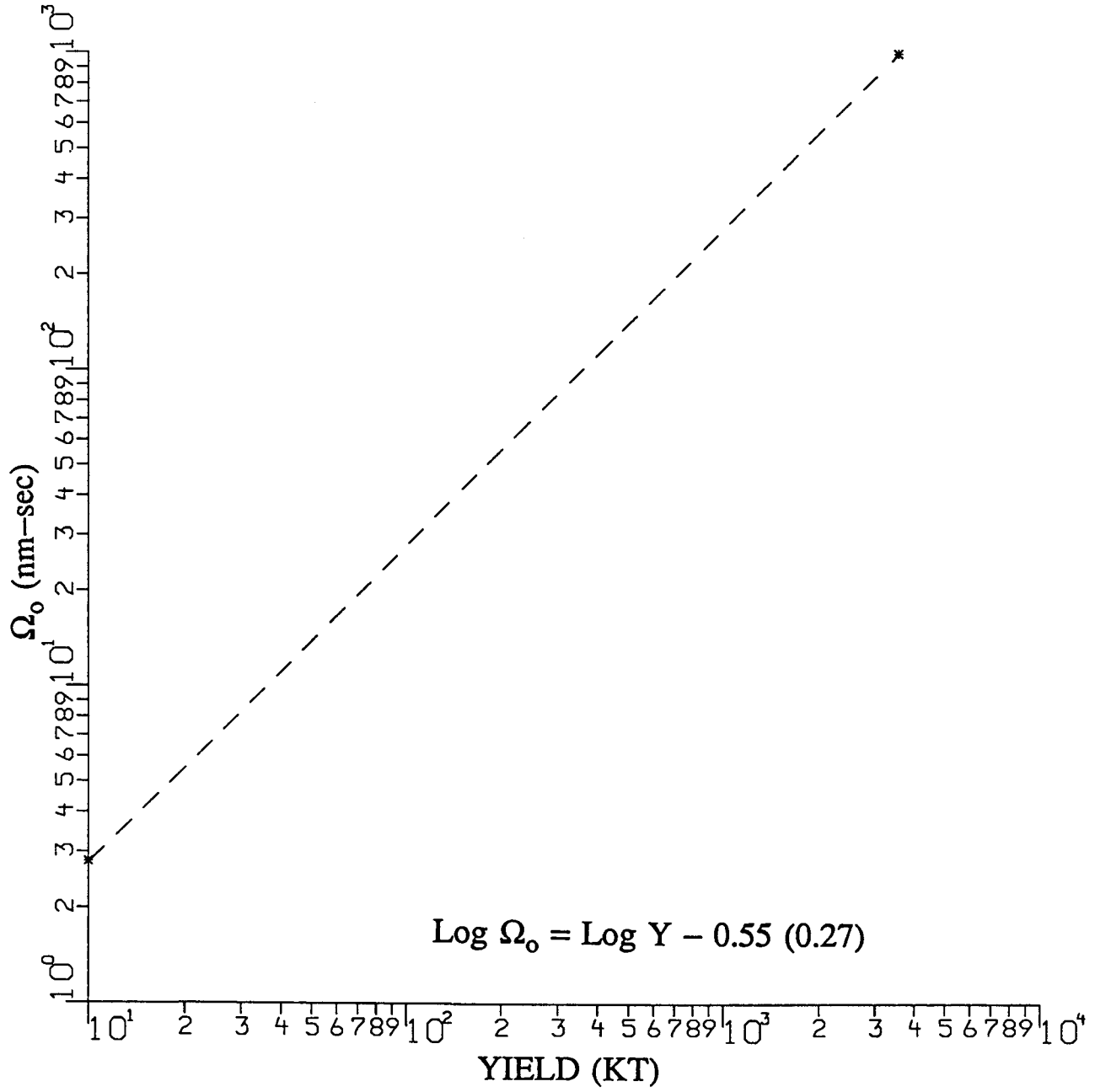

Figure 2-6h

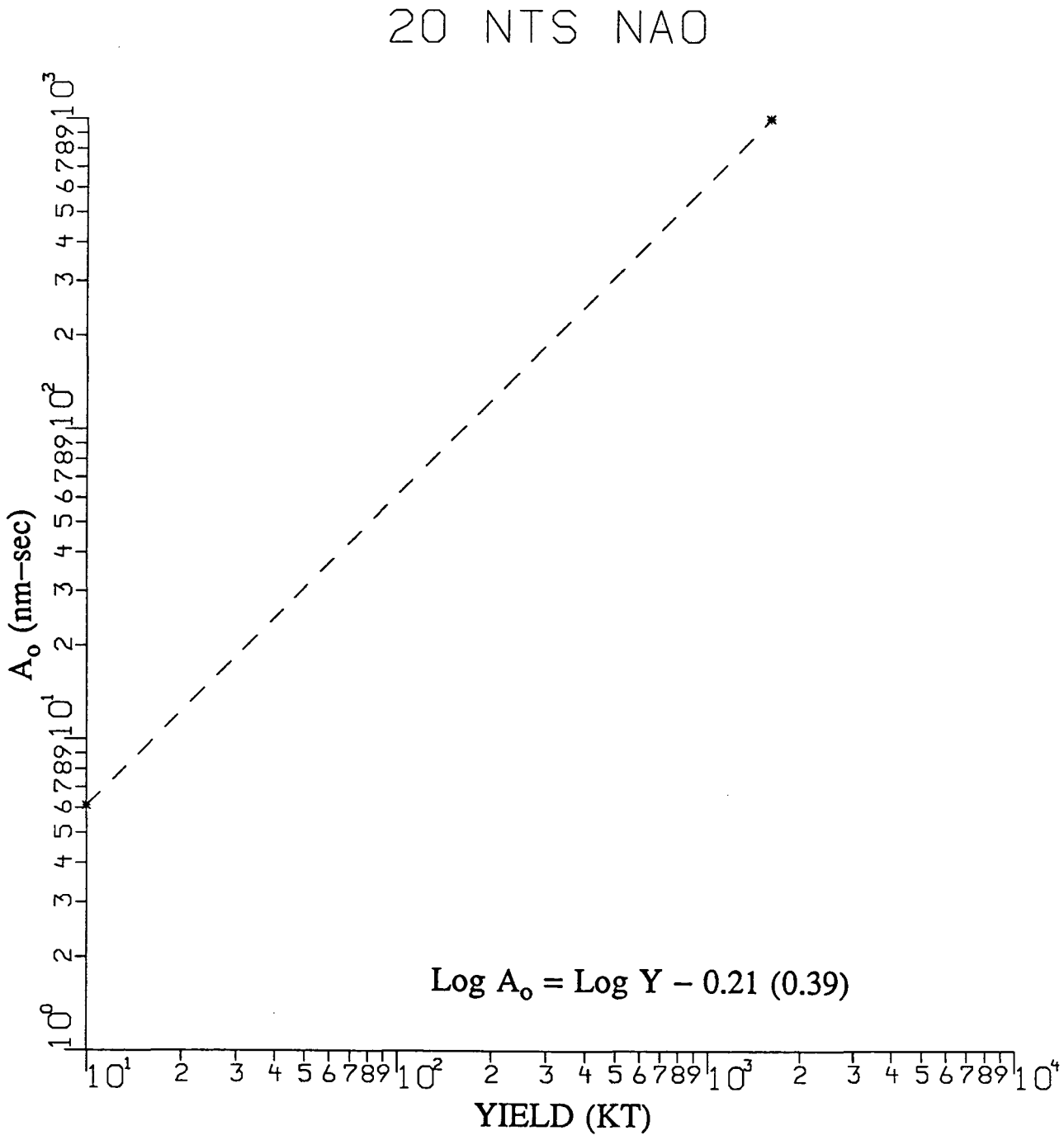
20 NTS NAO
A_o (nm–sec)
10^0 2 3 4 5 6 7 8 9 10^1 2 3 4 5 6 7 8 9 10^2 2 3 4 5 6 7 8 9 10^3
10^1 2 3 4 5 6 7 8 9 10^2 2 3 4 5 6 7 8 9 10^3 2 3 4 5 6 7 8 9 10^4
YIELD (KT)
Log A_o = Log Y – 0.21 (0.39)

Figure 2-6i

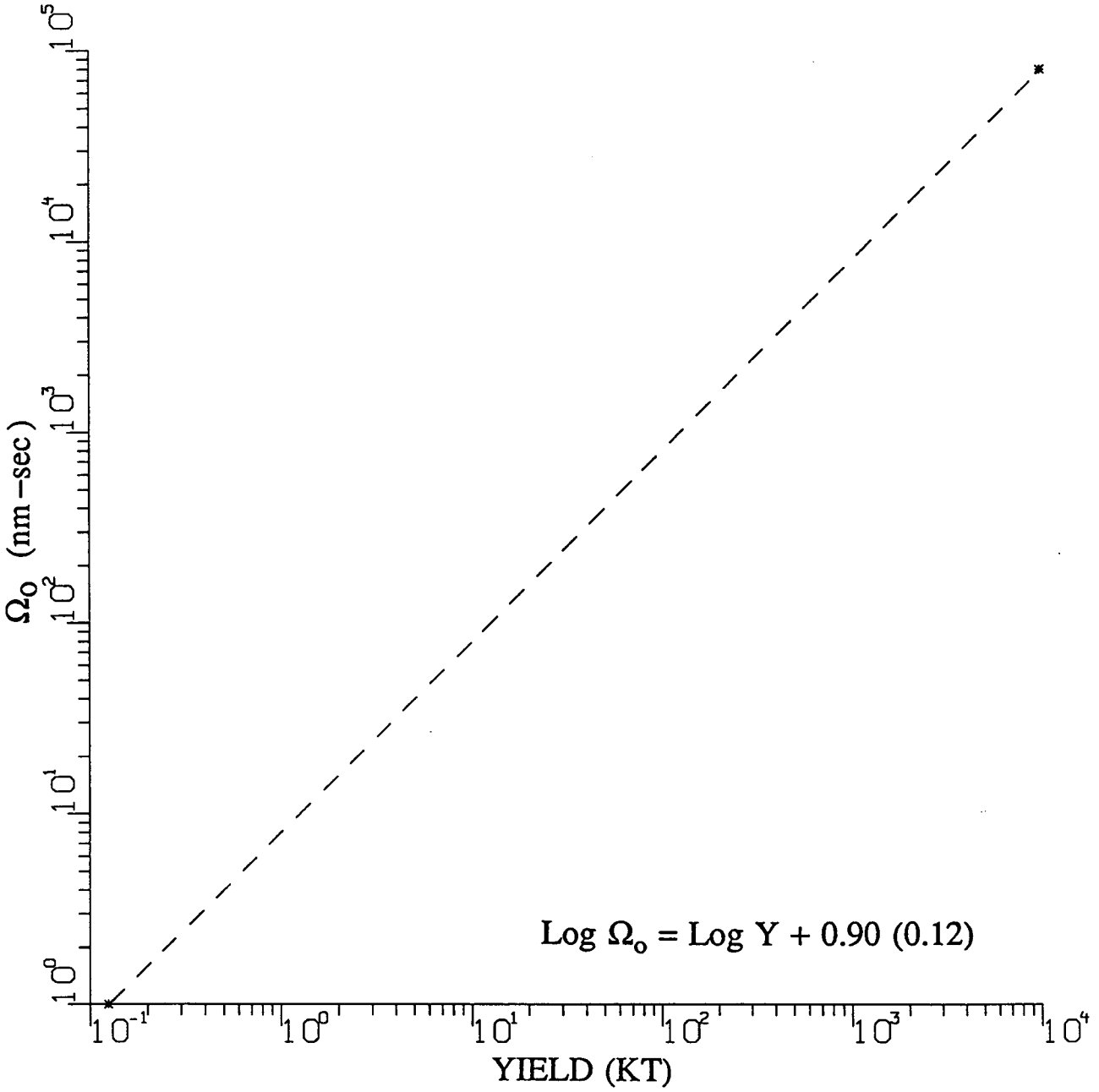
KNB+ELK AVG, KN-UT
Ω_o (nm-sec)
10^0
10^1
10^2
10^3
10^4
10^5
10^{-1}
10^0
10^1
10^2
10^3
10^4
YIELD (KT)
Log Ω_o = Log Y + 0.90 (0.12)

Figure 2-6j

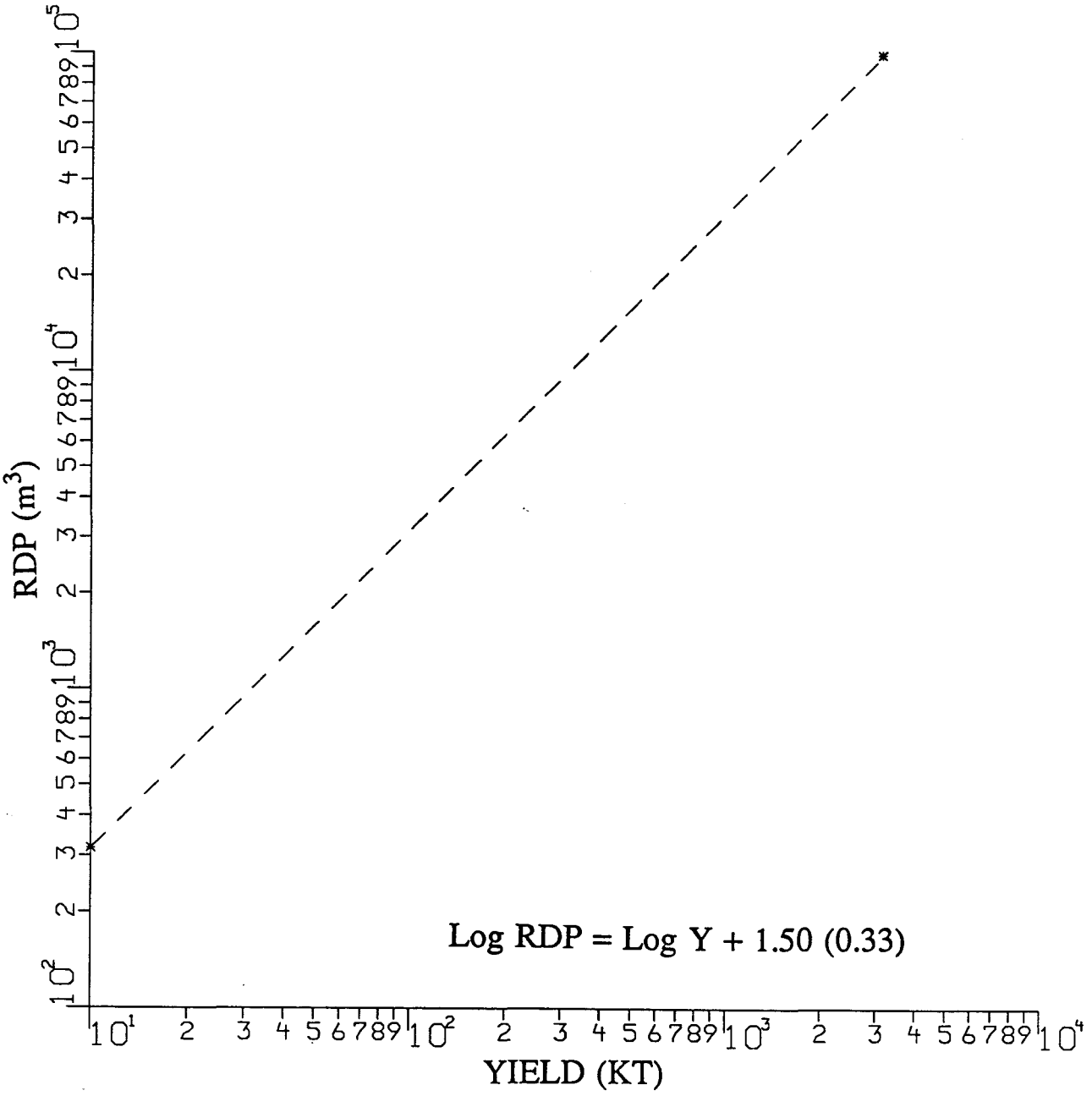

Figure 2-6k

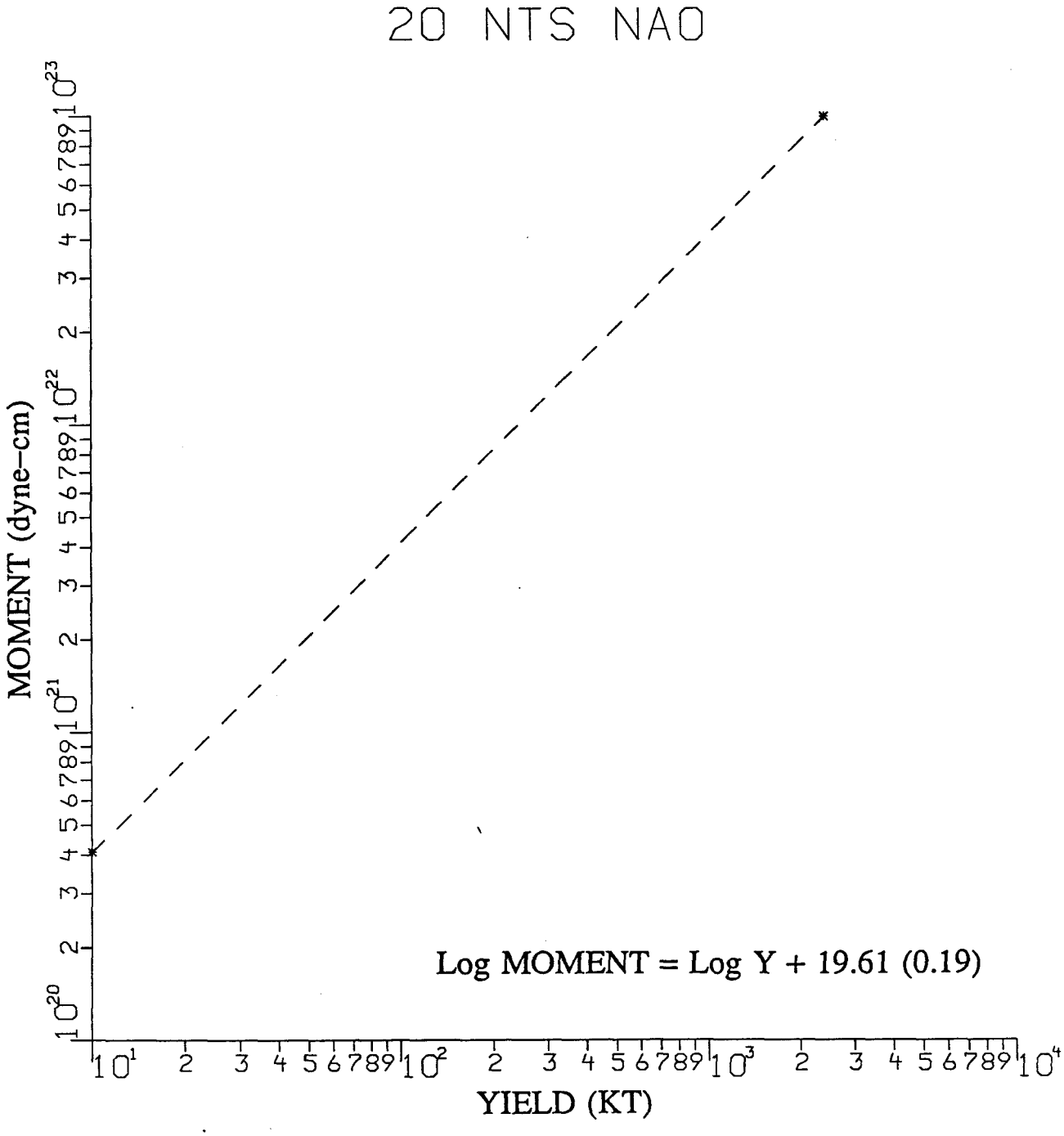

Figure 2-61

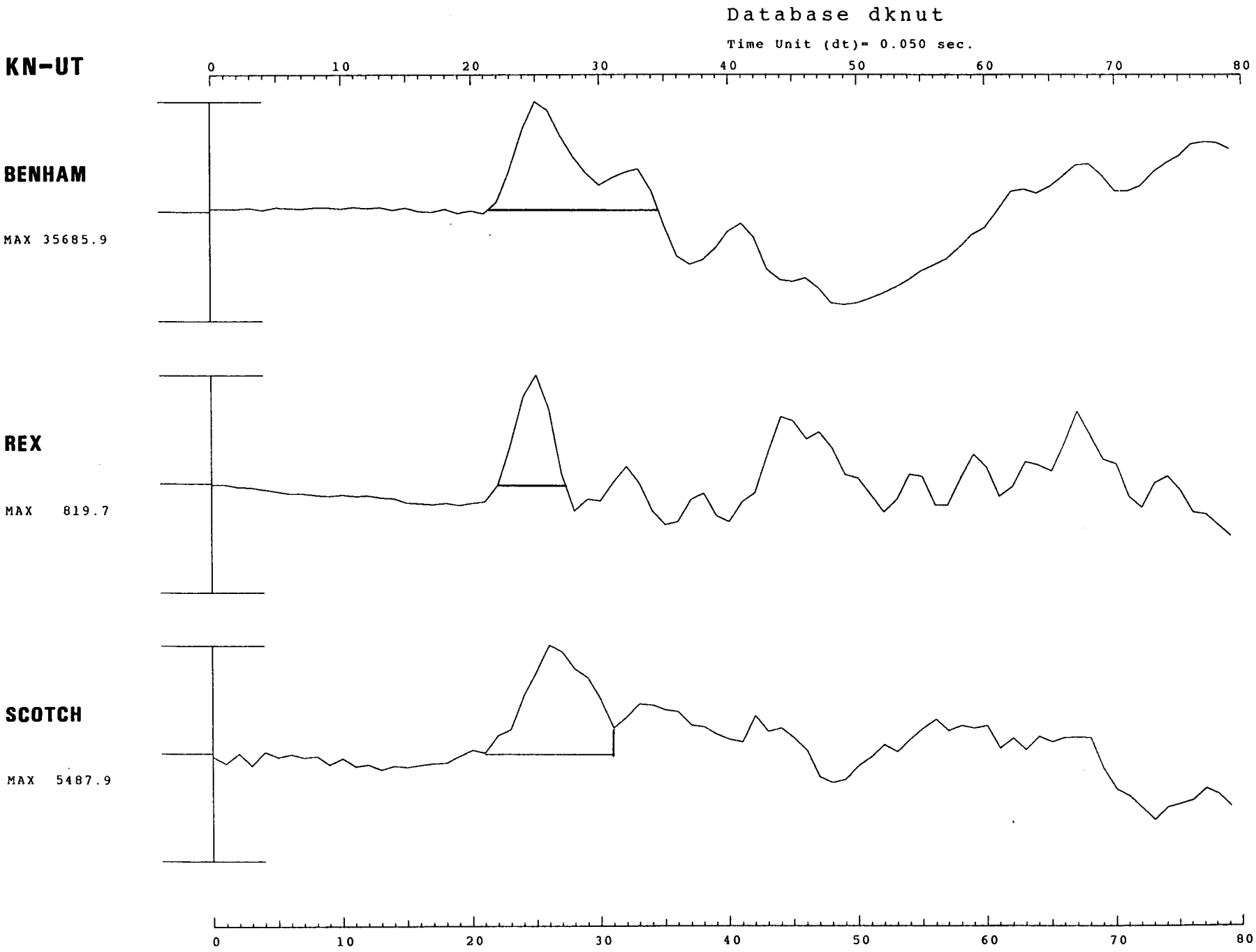
Database dknut
Time Unit (dt)= 0.050 sec.
KN-UT
0
10
20
30
40
50
60
70
80
BENHAM
MAX 35685.9
REX
MAX 819.7
SCOTCH
MAX 5487.9
0
10
20
30
40
50
60
70
80

Figure 2-7a

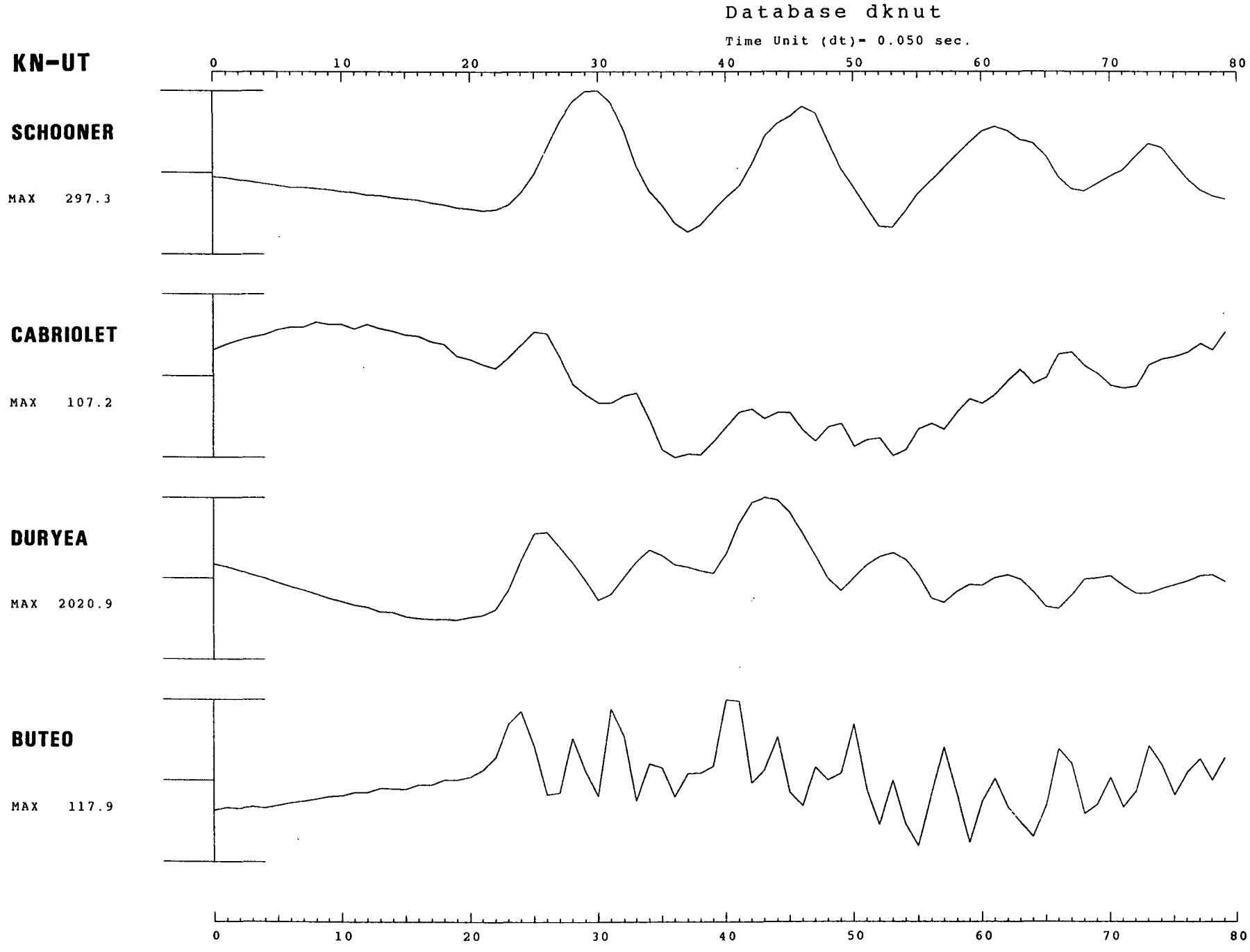
Database dknut
Time Unit (dt)= 0.050 sec.
KN-UT
0
10
20
30
40
50
60
70
80
SCHOONER
MAX 297.3
CABRIOLET
MAX 107.2
DURYEA
MAX 2020.9
BUTEO
MAX 117.9

Figure 2-7b

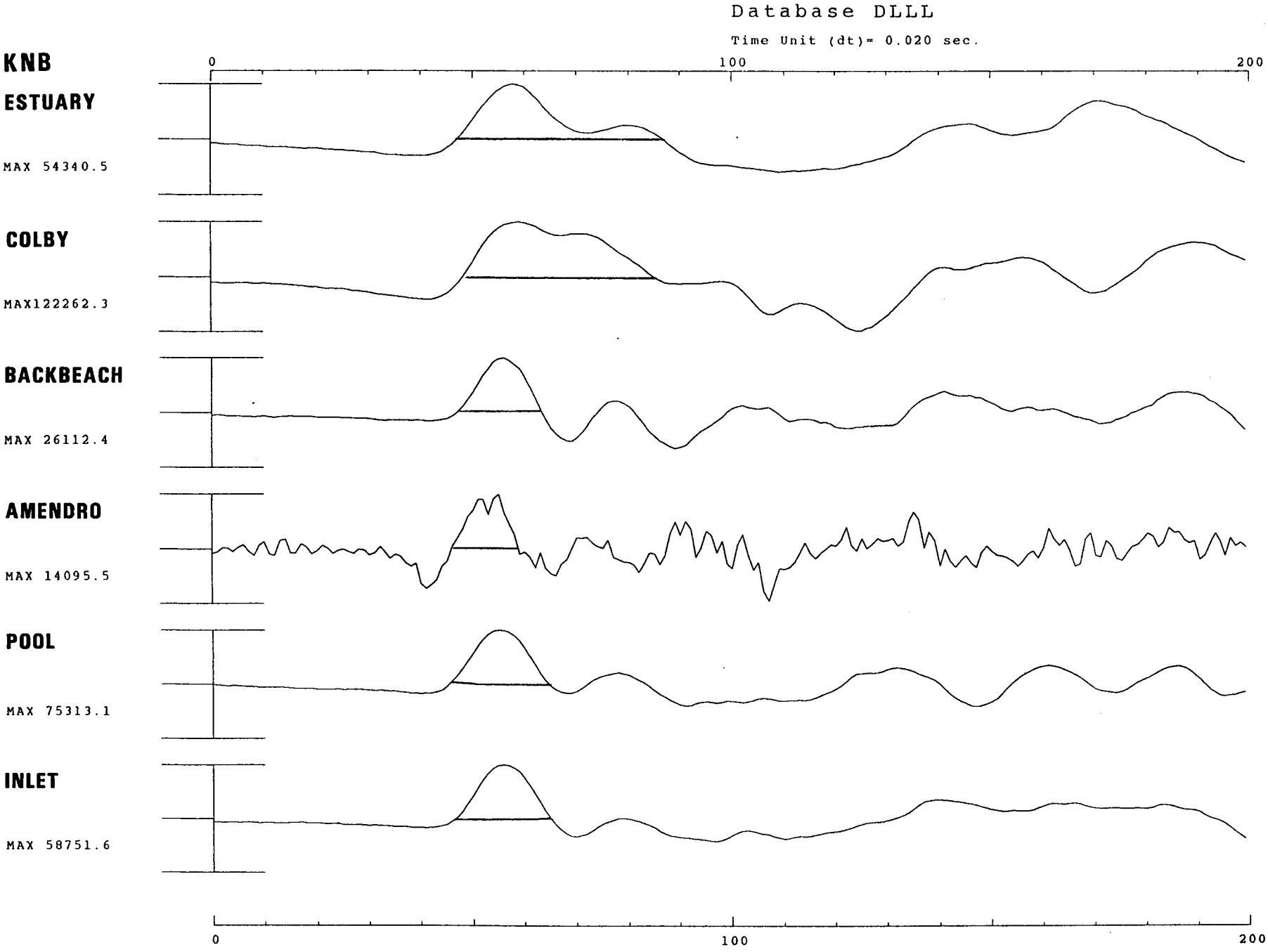
Database DLLL
Time Unit (dt)= 0.020 sec.
KNB
0
100
200
ESTUARY
MAX 54340.5
COLBY
MAX122262.3
BACKBEACH
MAX 26112.4
AMENDRO
MAX 14095.5
POOL
MAX 75313.1
INLET
MAX 58751.6
0
100
200

Figure 2-7c

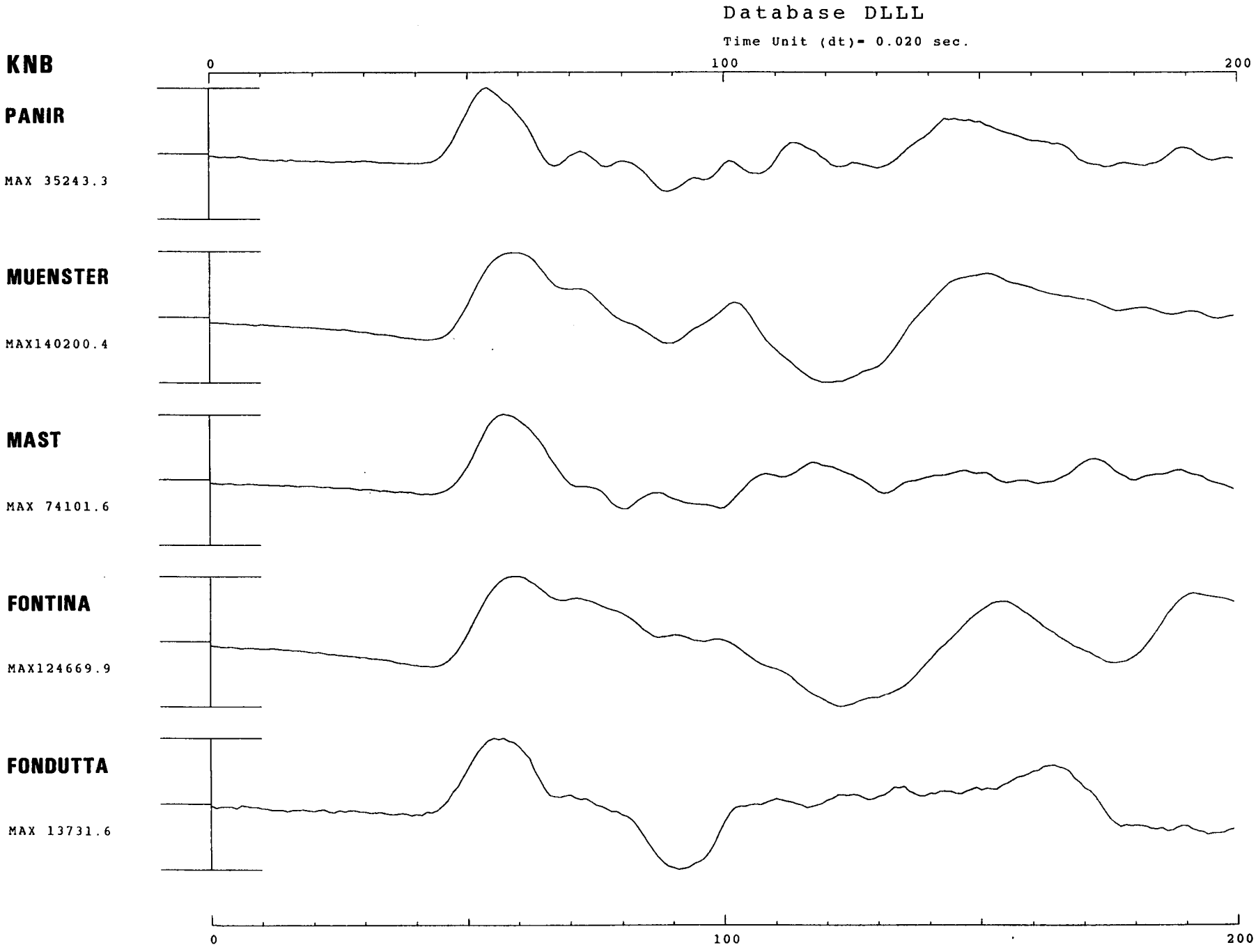
Database DLLL
Time Unit (dt)= 0.020 sec.
KNB
0
100
200
PANIR
MAX 35243.3
MUENSTER
MAX140200.4
MAST
MAX 74101.6
FONTINA
MAX124669.9
FONDUTTA
MAX 13731.6
0
100
200

Figure 2-7d

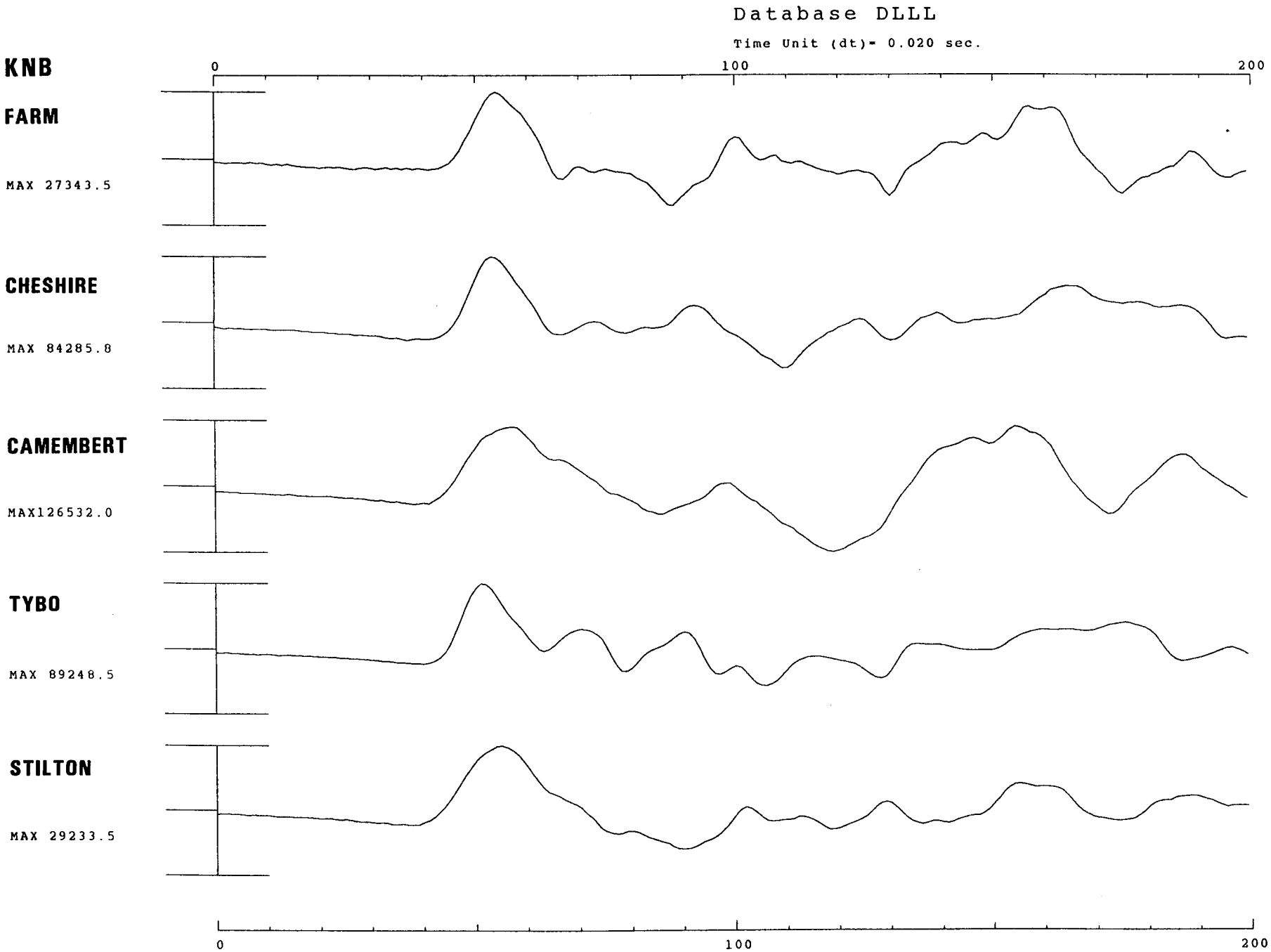
Database DLLL
Time Unit (dt)= 0.020 sec.
KNB
0
100
200
FARM
MAX 27343.5
CHESHIRE
MAX 84285.8
CAMEMBERT
MAX126532.0
TYBO
MAX 89248.5
STILTON
MAX 29233.5
0
100
200

Figure 2-7e

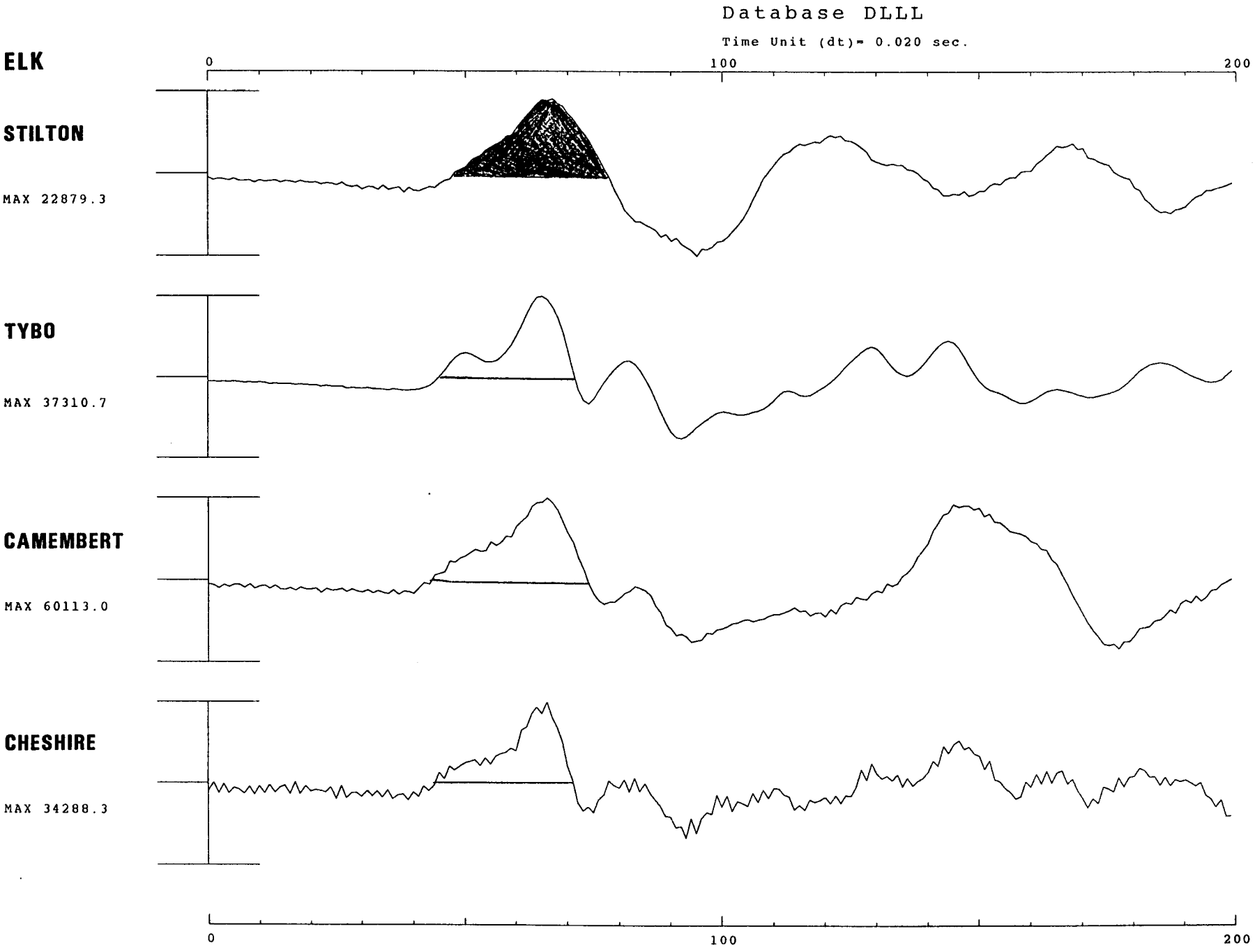
Database DLLL
Time Unit (dt)= 0.020 sec.
ELK
0
100
200
STILTON
MAX 22879.3
TYBO
MAX 37310.7
CAMEMBERT
MAX 60113.0
CHESHIRE
MAX 34288.3
0
100
200

Figure 2-7f

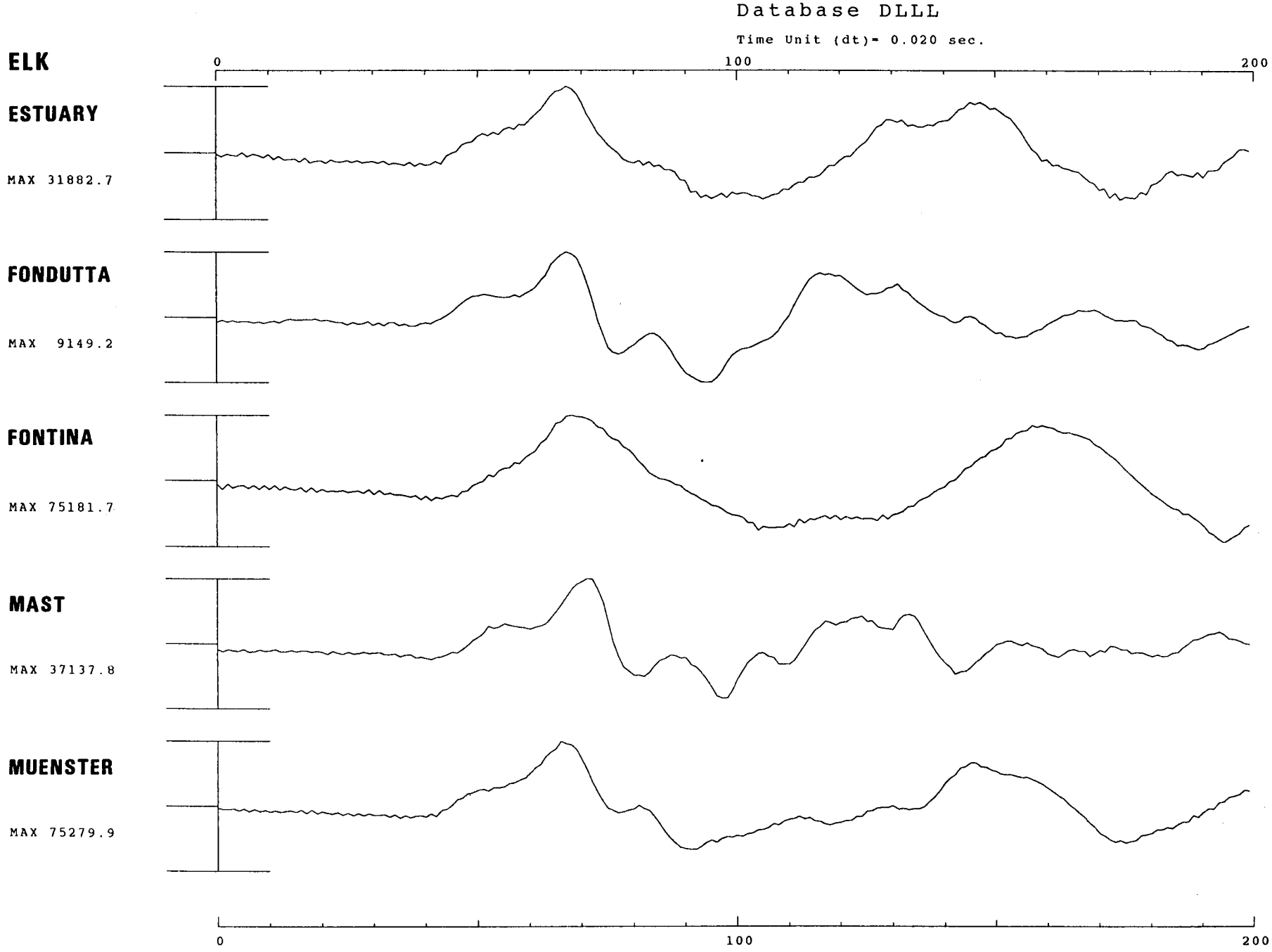
Database DLLL
Time Unit (dt)= 0.020 sec.
ELK
0
100
200
ESTUARY
MAX 31882.7
FONDUTTA
MAX 9149.2
FONTINA
MAX 75181.7
MAST
MAX 37137.8
MUENSTER
MAX 75279.9
0
100
200

Figure 2-7g

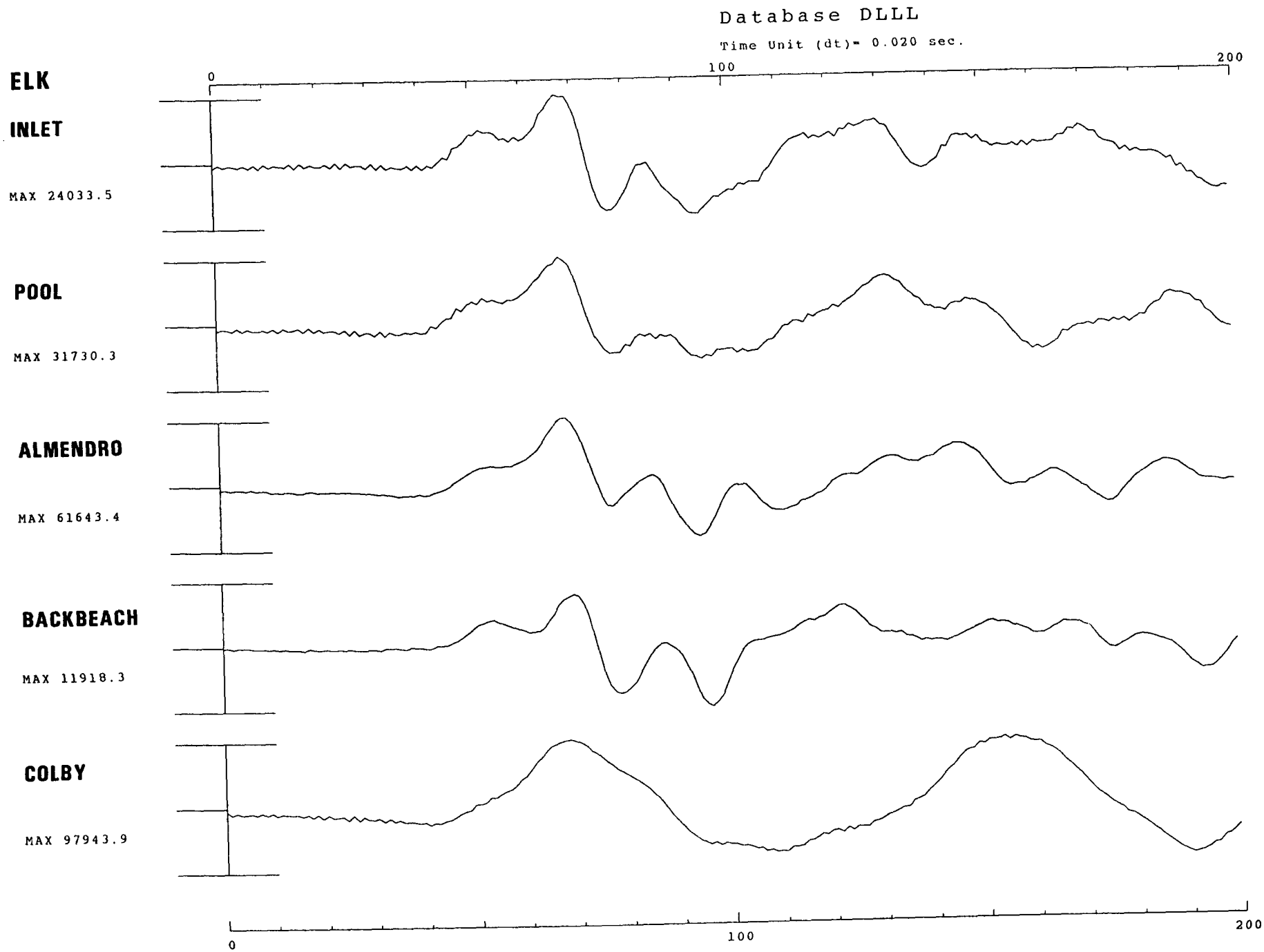
Database DLLL
Time Unit (dt)= 0.020 sec.
ELK
INLET
MAX 24033.5
POOL
MAX 31730.3
ALMENDRO
MAX 61643.4
BACKBEACH
MAX 11918.3
COLBY
MAX 97943.9
0
100
200

Figure 2-7h

HARZER

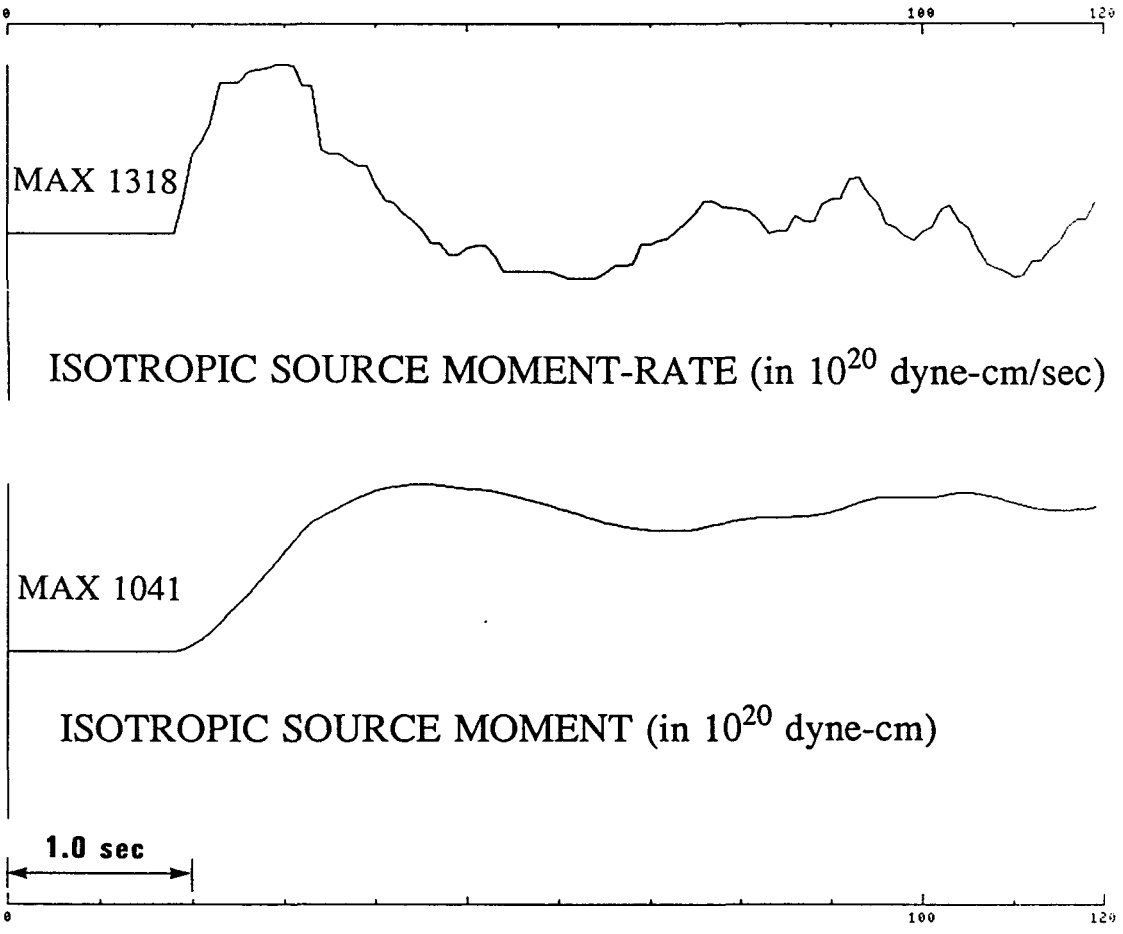

Figure 3-1a

CHANCELLOR

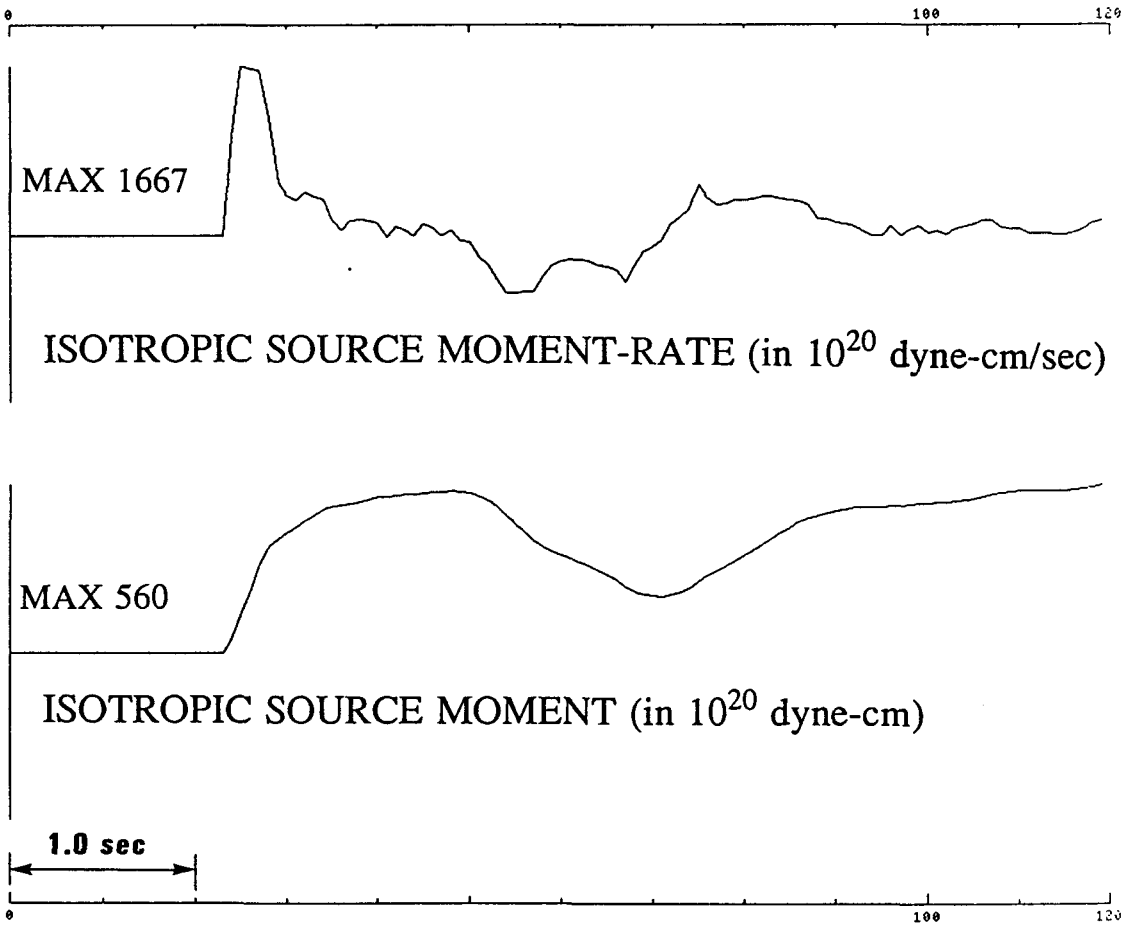

Figure 3-1b

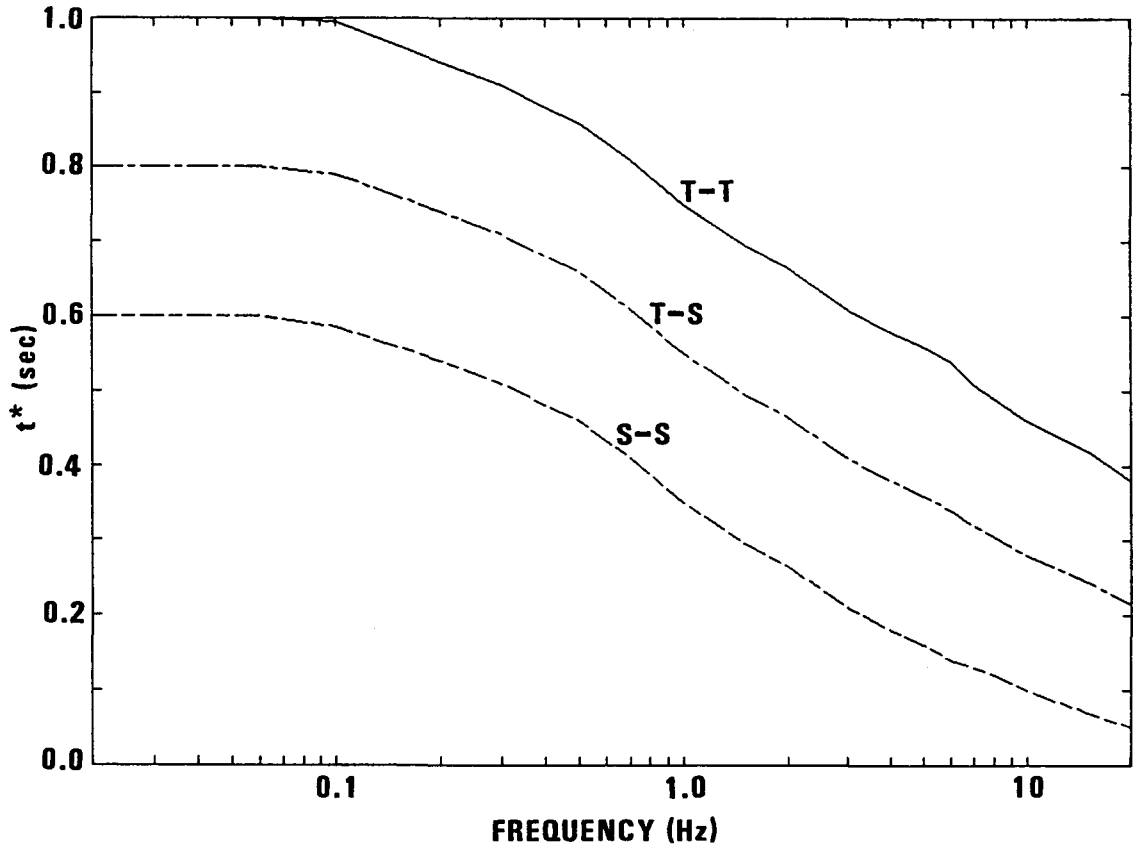

Figure 3-2a

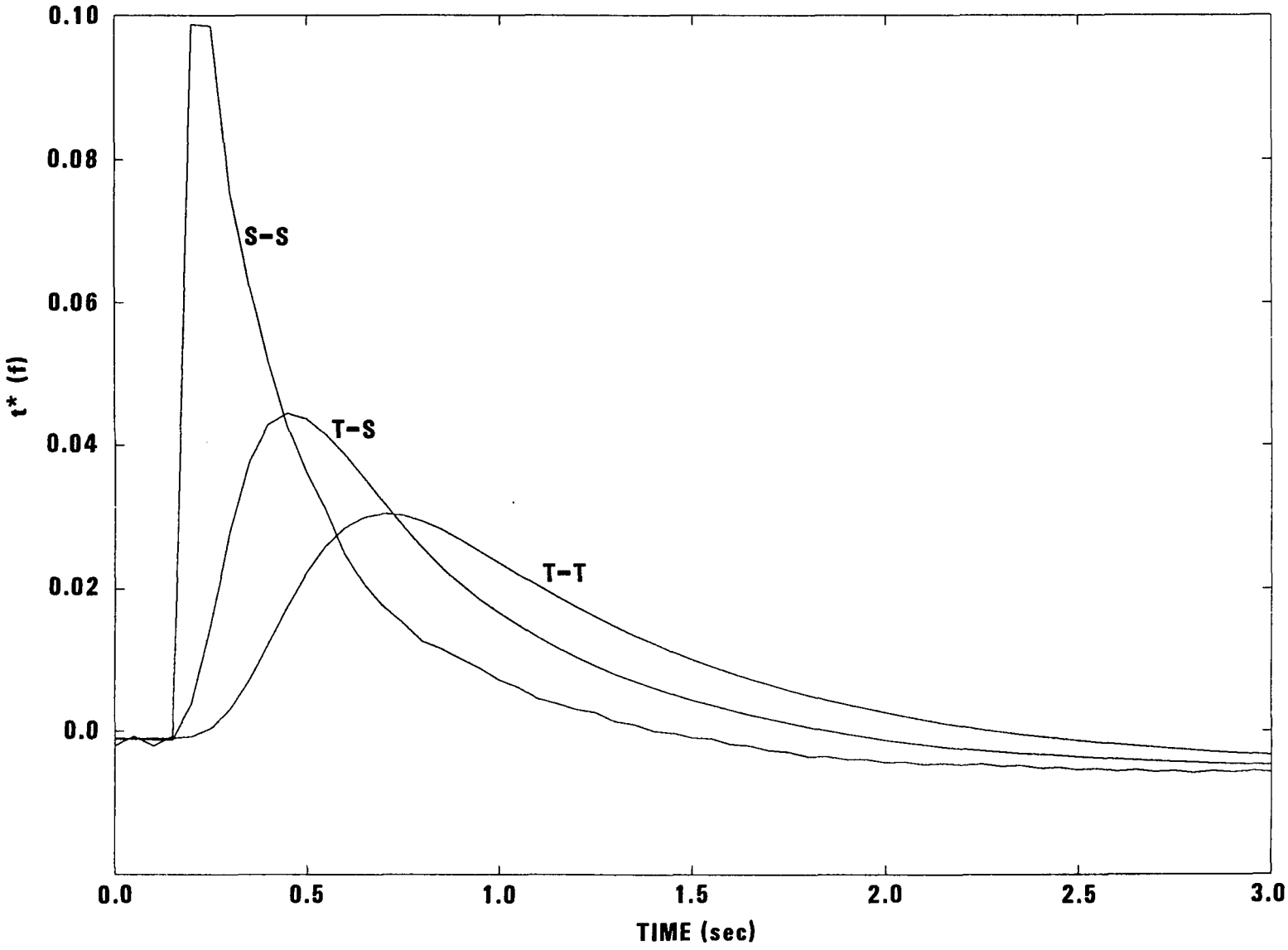

Figure 3-2b

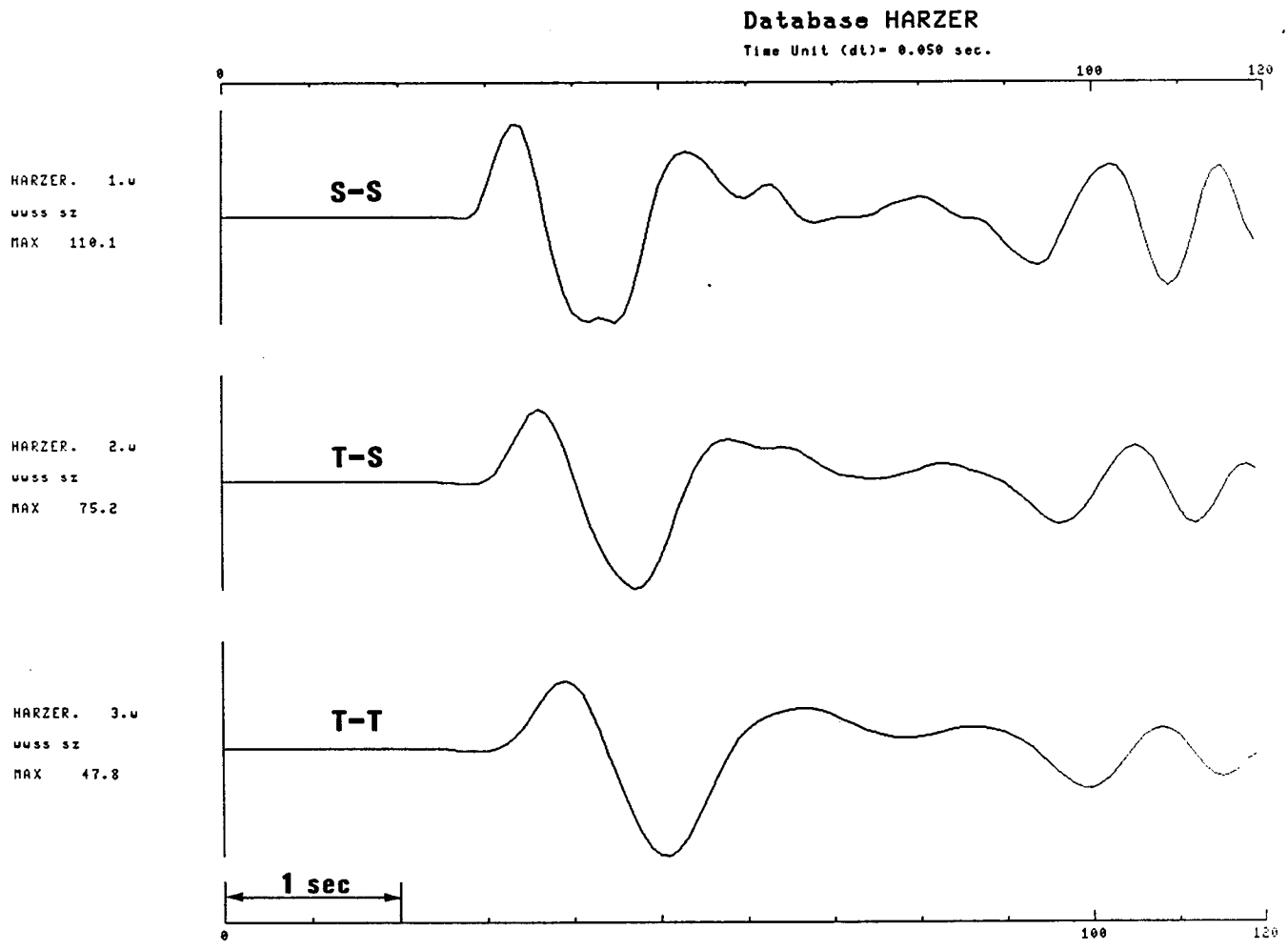
Database HARZER
Time Unit (dt)= 0.050 sec.
0
100
120
HARZER. 1.u
uuss sz
MAX 110.1
S-S
HARZER. 2.u
uuss sz
MAX 75.2
T-S
HARZER. 3.u
uuss sz
MAX 47.8
T-T
1 sec
0
100
120

Figure 3-3a

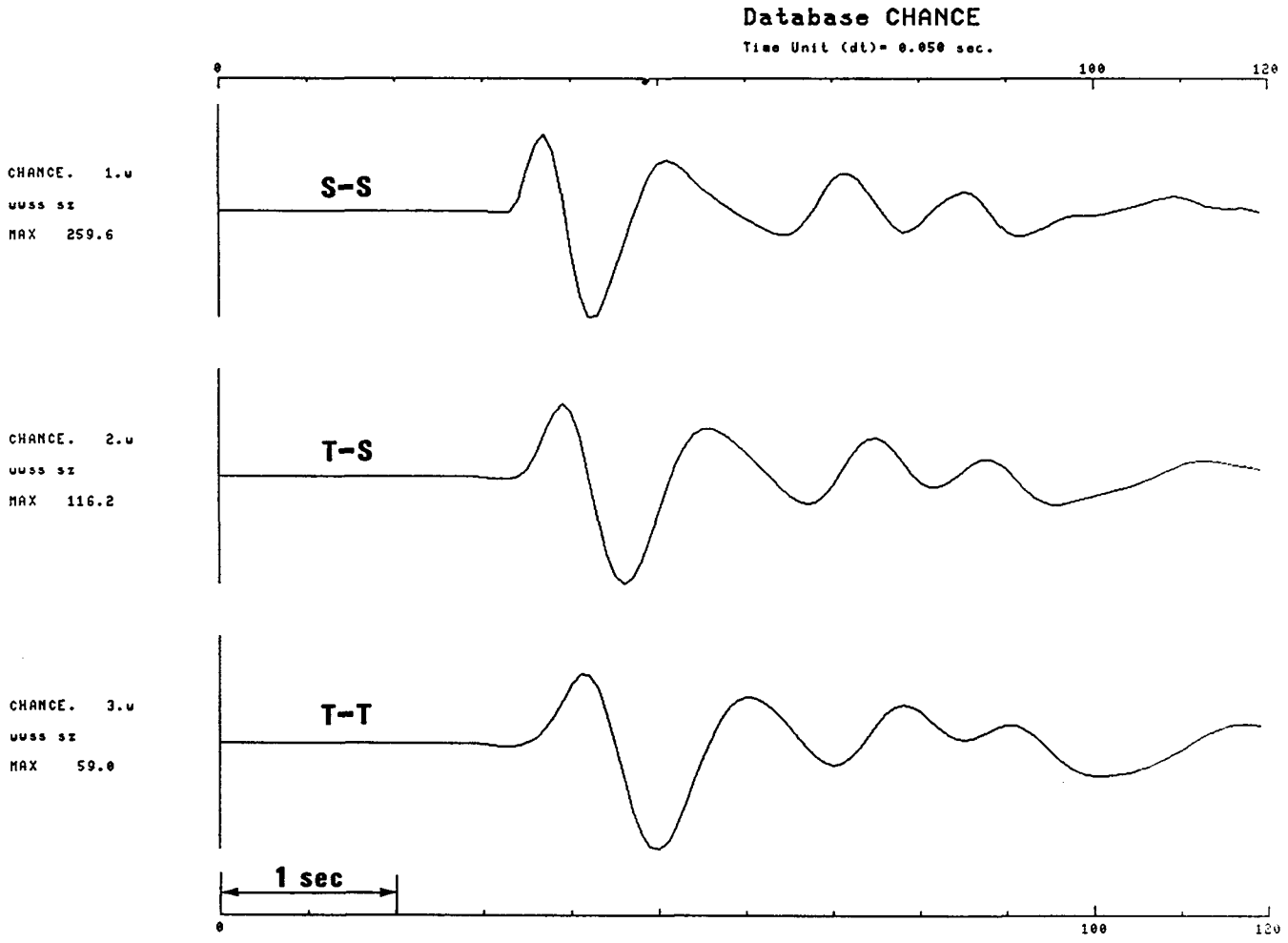
Database CHANCE
Time Unit (dt)= 0.050 sec.
0
100
120
CHANCE. 1.u
uuss sz
MAX 259.6
S-S
CHANCE. 2.u
uuss sz
MAX 116.2
T-S
CHANCE. 3.u
uuss sz
MAX 59.0
T-T
1 sec
0
100
120

Figure 3-3b

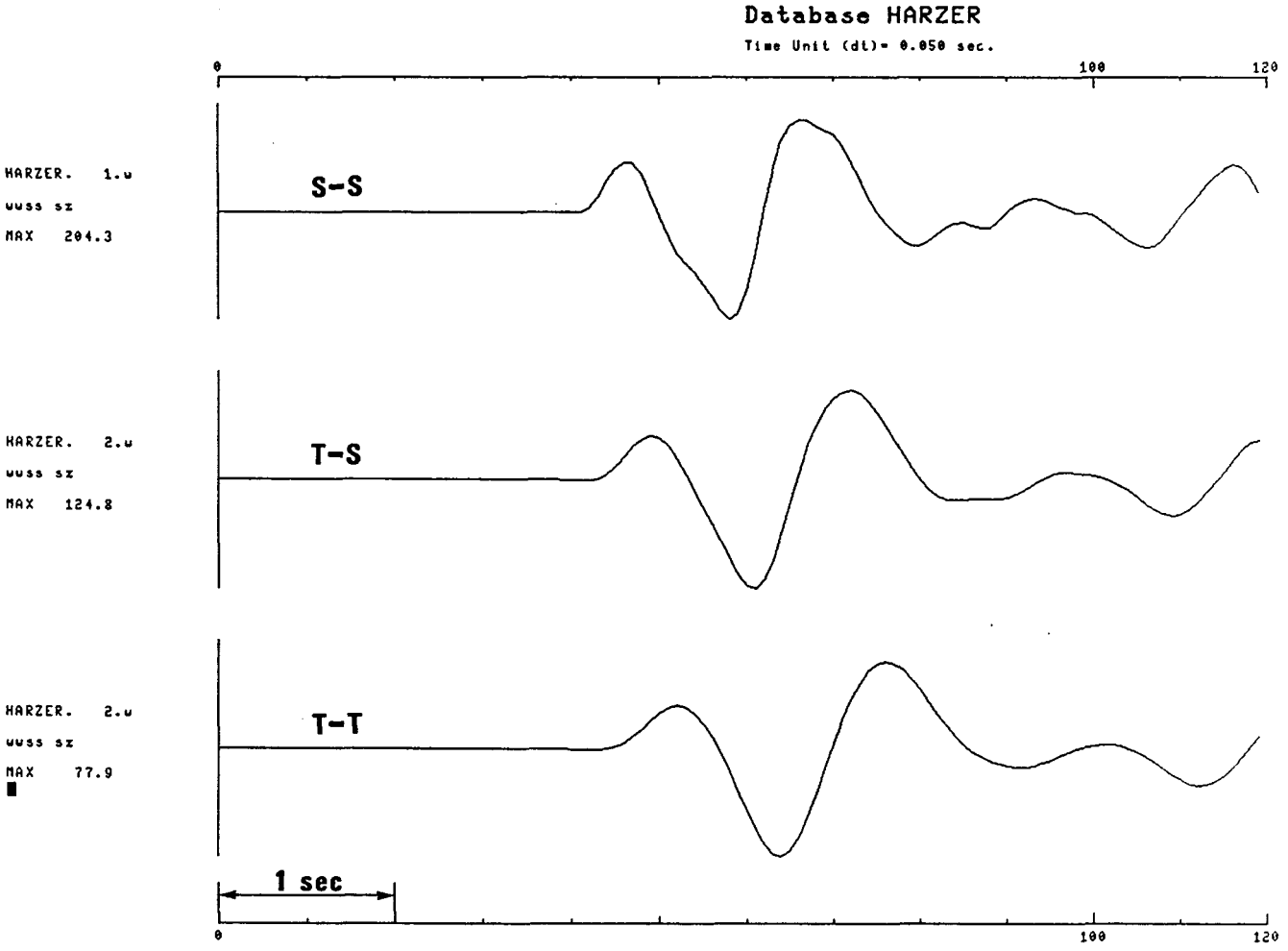
Database HARZER
Time Unit (dt)= 0.050 sec.
0
100
120
HARZER. 1.u
uuss sz
MAX 204.3
S-S
HARZER. 2.u
uuss sz
MAX 124.8
T-S
HARZER. 2.u
uuss sz
MAX 77.9
T-T
1 sec
0
100
120

Figure 3-4a

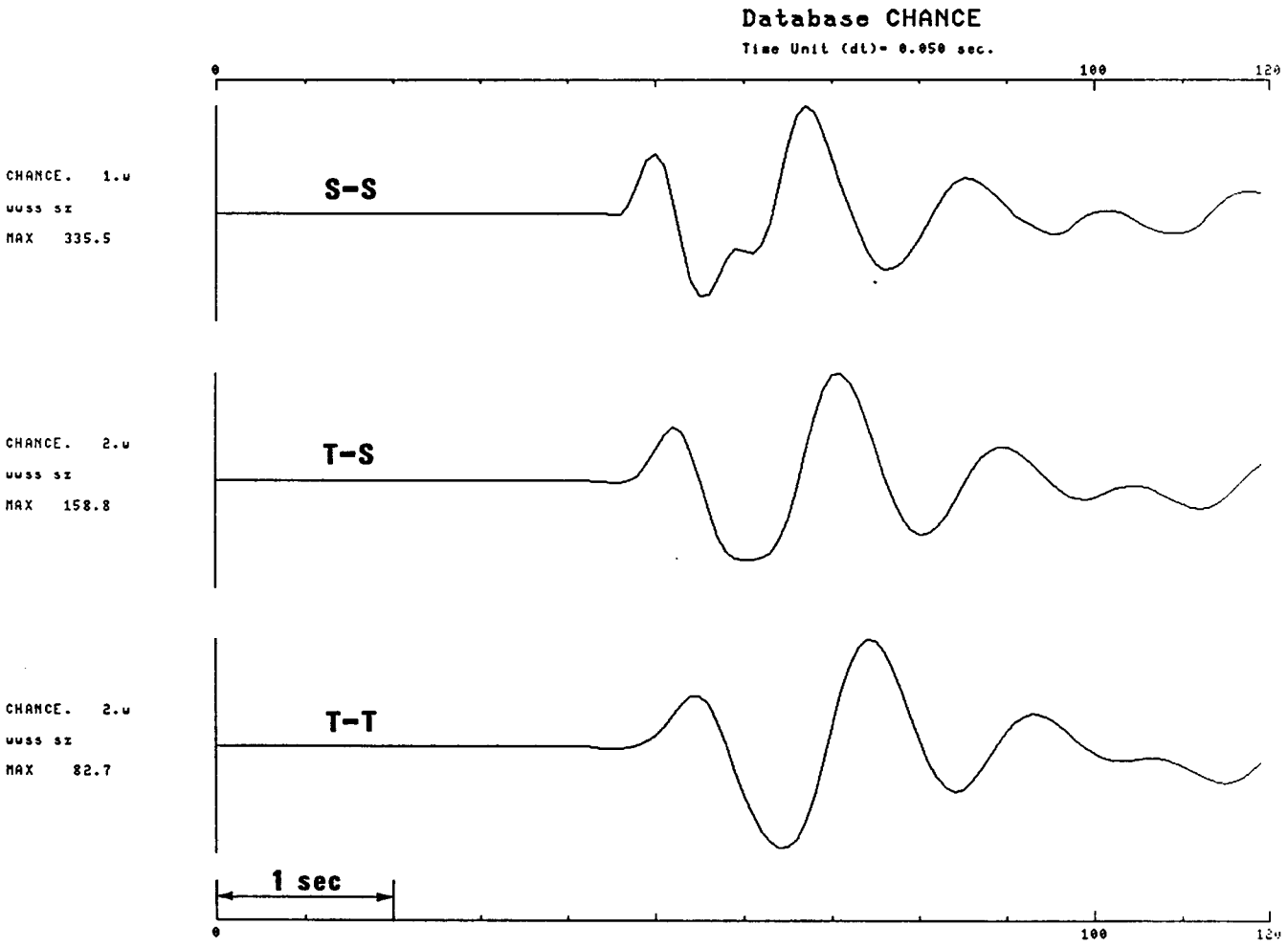
Database CHANCE
Time Unit (dt)= 0.050 sec.
0
100
120
CHANCE. 1.u
uuss sz
MAX 335.5
S-S
CHANCE. 2.u
uuss sz
MAX 158.8
T-S
CHANCE. 2.u
uuss sz
MAX 82.7
T-T
1 sec
0
100
120

Figure 3-4b

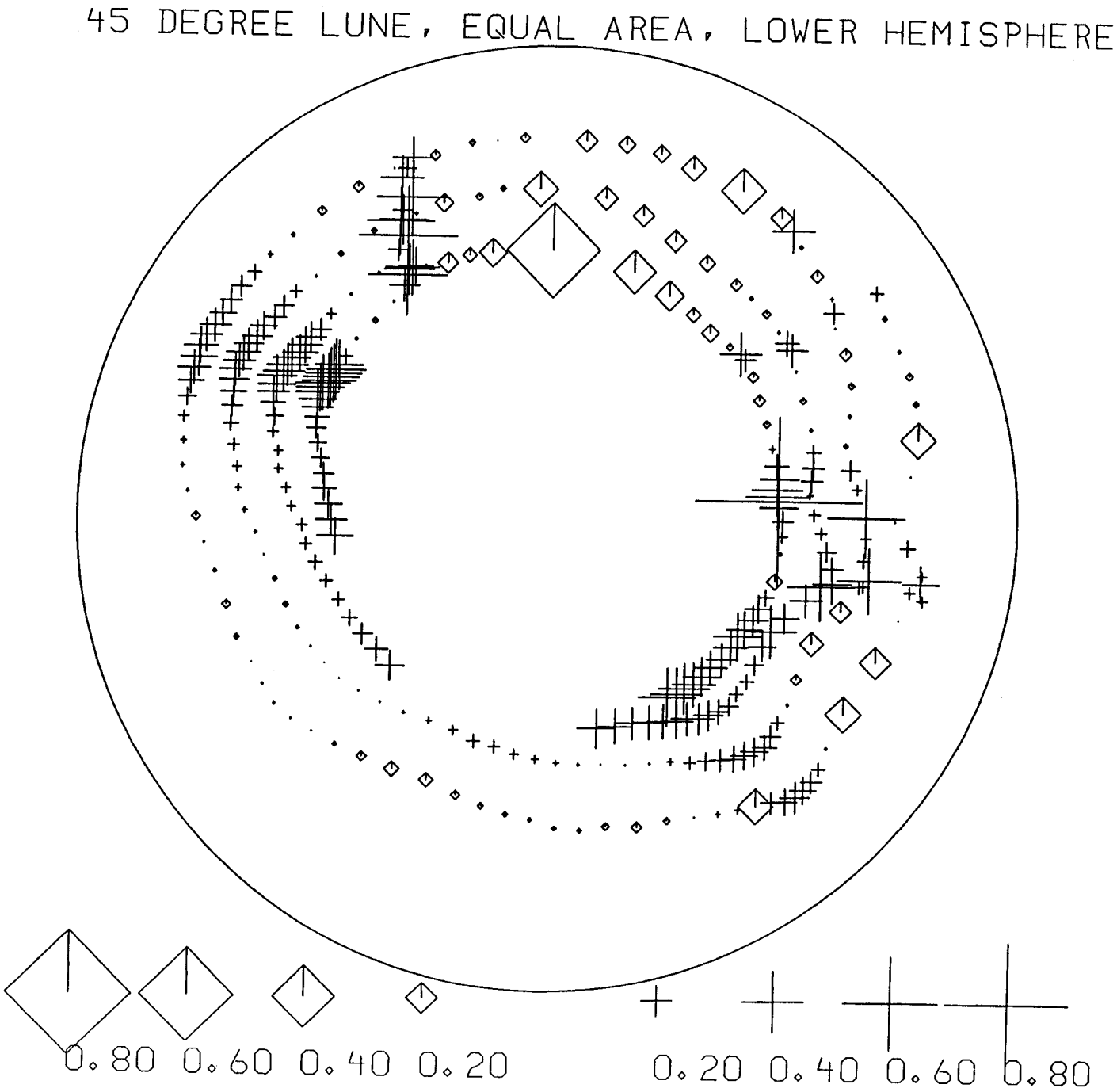
45 DEGREE LUNE, EQUAL AREA, LOWER HEMISPHERE
0.80 0.60 0.40 0.20
0.20 0.40 0.60 0.80

Figure 3-5a

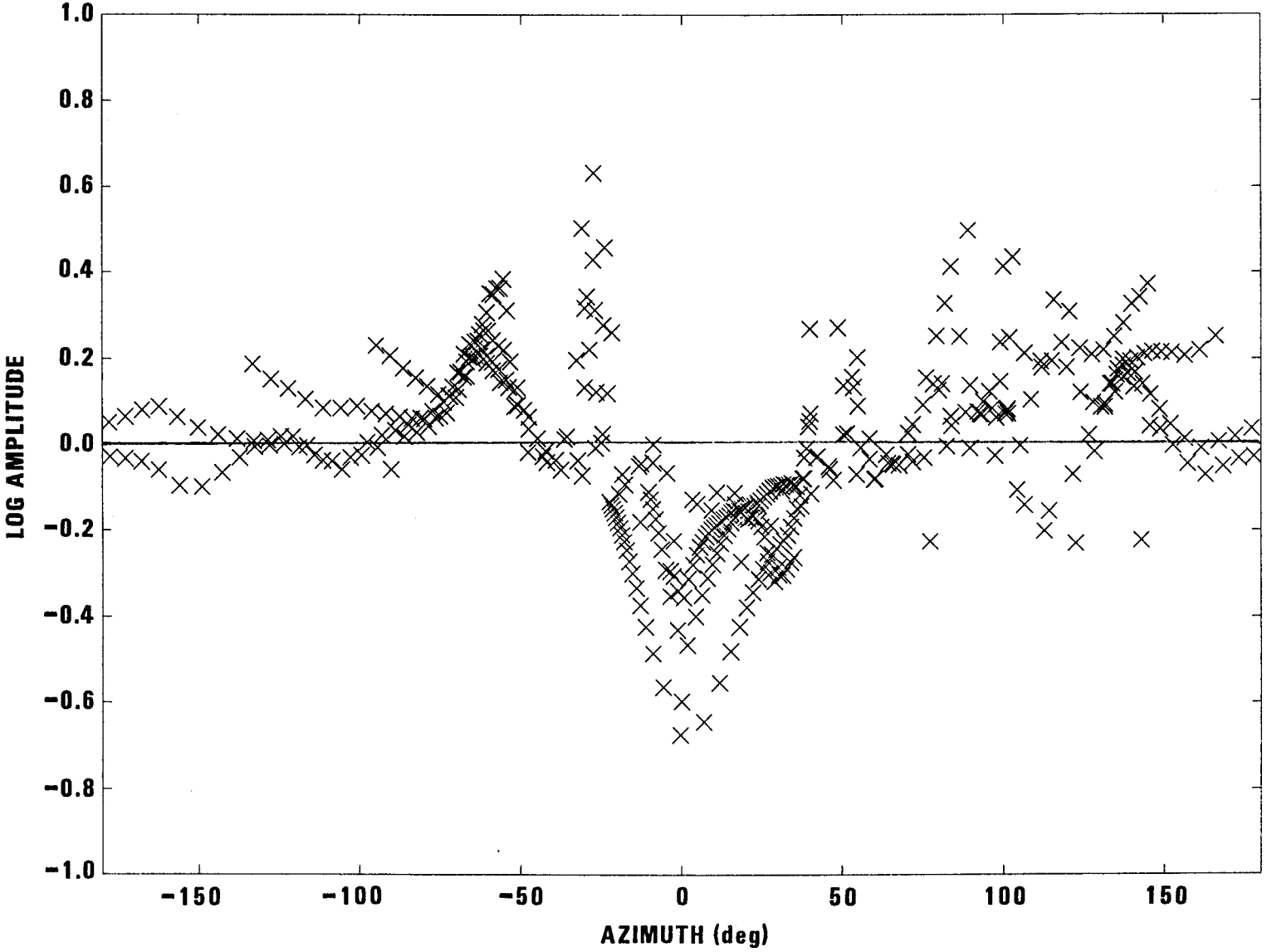
1.0
0.8
0.6
0.4
0.2
0.0
-0.2
-0.4
-0.6
-0.8
-1.0
LOG AMPLITUDE
-150
-100
-50
0
50
100
150
AZIMUTH (deg)

Figure 3-5b

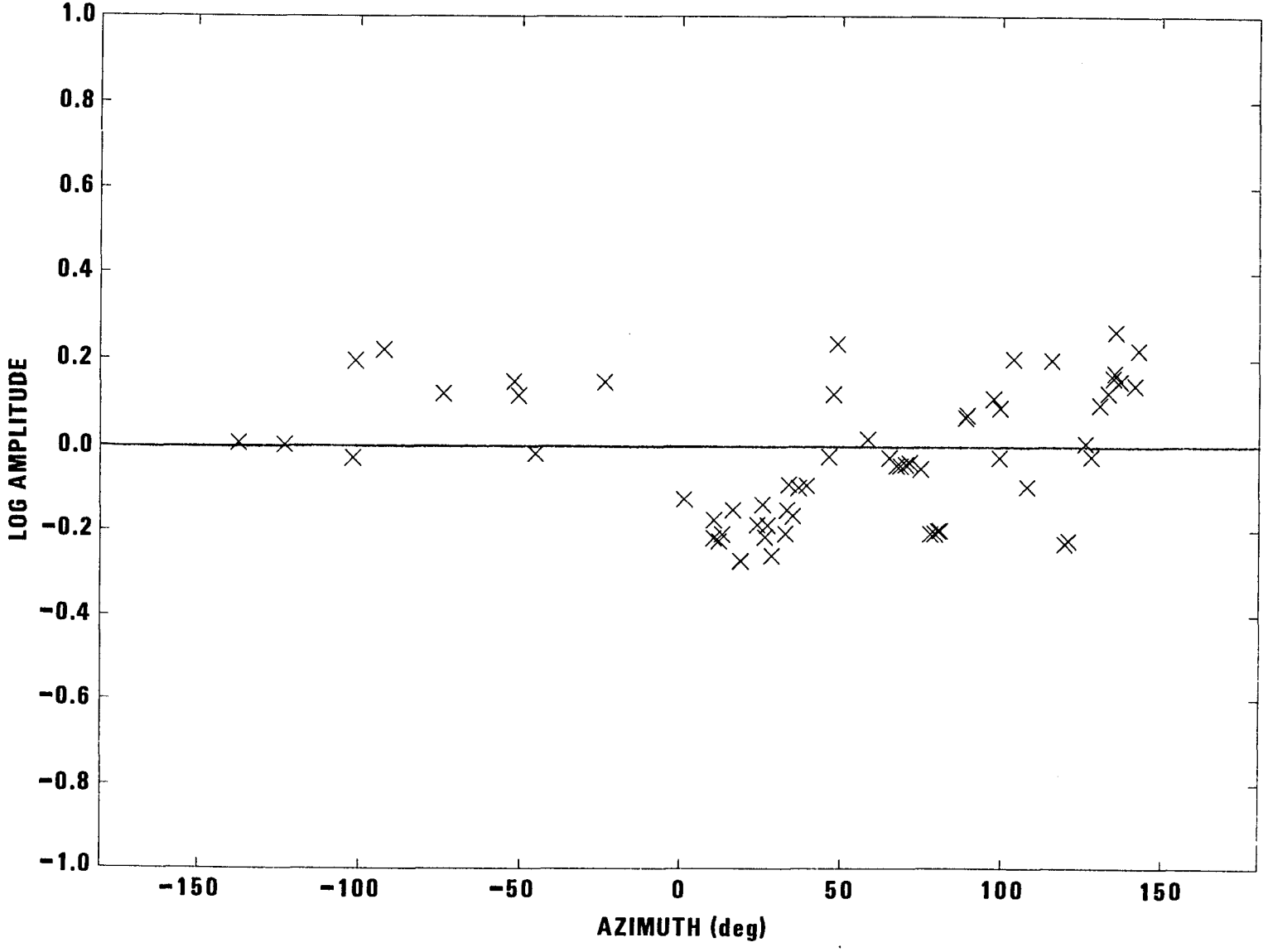
1.0
0.8
0.6
0.4
0.2
0.0
-0.2
-0.4
-0.6
-0.8
-1.0
LOG AMPLITUDE
-150
-100
-50
0
50
100
150
AZIMUTH (deg)

Figure 3-5c

Copy No. 17

MRC-R-1107

DRAFT

NONLINEAR SEISMIC ATTENUATION FROM COWBOY AND OTHER EXPLOSIVE SOURCES

W. R. Wortman
G. D. McCartor

Contract No. LLNL 9092505

30 September 1987

Prepared For: Lawrence Livermore National Laboratory
P.O. Box 808
Livermore, CA 94550

Mission Research Corporation
735 State Street, P.O. Drawer 719
Santa Barbara, CA 93102-0719

TABLE OF CONTENTS

LIST OF ILLUSTRATIONS

LIST OF TABLES

ACKNOWLEDGMENTS

Access to the Cowboy data were optained through the efforts of Neil Perl of Applied Theory. The Sierra granite and dome salt model data were supplied by Donald Larson and Marvin Denny of LLNL. In the course of this work, helpful discussions were held with the above individuals as well as Robert Blandford of DARPA, John Trulio of Applied Theory and Steven Day of S-CUBED.

SECTION 1

INTRODUCTION

In order to characterize a distant seismic pulse according to the energy which generated it, a source function is needed which can be used to initiate the signal at sufficient range from the event that the subsequent propagation can be described in *linear* terms according to the properties of the earth. Thus an observed seismic signal implies a source function which may be compared with known functions for discrimination and yield estimation[1]. The properties of such source functions must be known to use this technique. Near-field data from various events have been taken. The smallest strains observed, due to practical free field instrument placement selection, are typically no less than 10^{-5} and are often much greater. If the pulse at the extreme range undergoes no further significant nonlinear modification, its characterization can supply the needed source function. However, if any additional nonlinear changes are important, a useful source function cannot be determined. Consequently, it is important to characterize any possible nonlinear attenuation of moderate strain pulses, preferably through methods which allow generalization to all placement media of interest.

SECTION 2

REVIEW OF ATTENUATION DATA FOR SALT

The most comprehensive attenuation data, over the range of moderate strains, exists in the medium of salt. For explosive sources the laboratory results of Larson[2] covers strains from 10^{-1} to 10^{-3}, the Salmon field test[3] covers strains for 10^{-3} to 10^{-4} while the Cowboy field test series[4] covers strains from 10^{-4} to 10^{-5}. The Rockwell laboratory[5] decaying oscillations complete the salt data by ranging from 10^{-5} to 10^{-8}. The essential results of these experiments will now be reviewed.

Larson's laboratory data were taken from the effects of a series of small chemical explosives in blocks of pressed salt. Velocity data were taken at several gauges such that the totality of the examples from all shots covered peak velocity to compressional velocities, which is approximately the peak strain, of 10^{-1} to 10^{-3}. Using a triplet of records from a single shot, it was estimated that over peak strains of 1.4×10^{-3}, 7.0×10^{-4} and 4.6×10^{-4}, the Q changes from 12.5 to 24.9. The corner frequency for this small scale experiment was about 5×10^{4} Hertz.

The Salmon data were generated by a 5.3 kT nuclear explosion in salt. The work by McCartor and Wortman[6] as well as McLaughlin and Gupta[7] shows that the high quality data clearly indicate a high level of attenuation. It is estimated that for peak strains from 4×10^{-3} to 3×10^{-4}, the effective Q is to order of 10 at a corner frequency of about 6 Hertz. This Q appears nearly constant over the order of magnitude strain range available. However, in view of the fact that small strain data from other experiments indicate a much larger Q, it seems certain that there are residual nonlinearities at the extreme range of the Salmon data so that Q must increase at larger ranges (and so smaller strains).

Tittmann[5] has studied the attenuation of flexural and torsional harmonic oscillations of salt samples. It has been found that the attenuation, expressed in terms of Q^{-1} as a function of strain amplitude, tends to be nearly constant for strains from 10^{-8} to 10^{-6}, then increase for greater strains. The attenuation is a decreasing function of confining pressure with an average Q of approximately 200 at 10^{-6} strain at a frequency of 400 Hertz for confinement consistent with the explosions.

The regime covered by the Cowboy experiments overlaps that for Salmon, by beginning at strains of about 5×10^{-3} and extending out to 10^{-5}. The Cowboy experiments consisted of a series of shots over a range of yields, both coupled and uncoupled, such that the individual events generally had only a few instruments in operation. Several authors have combined these data by invoking the experimentally compelling evidence for simple scaling[2,8], which suggests that the velocity pulse data from various yields can be equated by scaling all times and distances by the cube root of the yield. This is particularly dramatic when peak velocity is plotted against scaled range giving a consistent curve over about ten orders of magnitude in yield. Larson has pointed out that the full velocity pulses, as well as their peak values, tend to be preserved through scaling.

Trulio[9] has analyzed the scaling-combined Cowboy data to estimate Q as dictated by decrease in peak displacement with range by using one decade at a time in the frequency domain. He has found that attenuation decreases as range increases in a fashion inconsistent with linearity expressed as dispersive harmonic potential waves. If the coupled Cowboy data are fit assuming a Q independent of range (possibly due only to scatter in the data), Q must be a function of frequency ranging from about 5 at low frequencies (1 Hz at Salmon scale) to nearly 100 at high frequencies (32 Hz at Salmon scale). However, simple scaling is inconsistent with this fit since scaling requires linearity coupled with a Q independent of frequency. If the decay of the reduced displacement potential is fit by the form $\exp(-\omega r/2cQ)$, it is seen that simple scaling can result so long as, for constant c, Q is a function of a variable which is unchanged by scaling — such as ωr. Trulio has shown that the a range of data from Salmon, through Cowboy and Cowboy Trails, do have the property that an effective Q can be expressed as a function of ωr for all the experiments. Obviously this indicates that at fixed frequency, the attenuation expressed in terms of Q, is dependent upon range. Since it is assumed that the medium is approximately homogeneous, the implication is clear that the attenuation must be amplitude dependent and so nonlinear.

Minster and Day[10] have used the scaled peak velocity and displacement data for Cowboy to determine if these data require an amplitude (nonlinear) or frequency dependent Q for consistency. It is determined that a Q^{-1} which consists of a small constant (consistent with small strain data from Tittmann) plus a term proportional to the peak strain provides a good fit to the data. The observed attenuation effects do not firmly indicate the need for a frequency dependent Q but indicate that an amplitude dependent Q provides a more convincing fit than a constant Q. Based on the small strain Q, which is several hundred, seen in the Rockwell experiments, it is concluded that there must be nonlinear attenuation in the Cowboy strain regime.

SECTION 3

COWBOY DATA

The Cowboy experiment[4] consisted of a series of 17 chemical explosions in a salt dome. Nine of these were tamped, or coupled, events with yields ranging from 20 to 1000 pounds. The remainder of the shots were decoupled, or cavity, events which consisted of: four shots in 30 foot diameter spherical cavities, with the charge located in the center with yields of 200 to 1000 pounds; and four shots in 12 foot diameter cavities with yields of 20 to 1903 pounds. For the following discussions, we shall be concerned chiefly with the tamped cases; Table 1 gives a summary of the data available from tamped shots. The table indicates range (R), yield (Y), peak velocity from this analysis (UPDAT), peak velocity quoted by Murphey[4] (VPMUR) and scaled range (RCS). Copies of all records are reproduced in Appendix A.

Table 1. Cowboy Data from Tamped Shots.

Shot & Sensor	R (FT)	Y (LB)	UPDAT (I/S)	VPMUR (I/S)	RCS ($FT/LB^{.33}$)
01C.1.2.03.V	19.4	100.	7.2	12.	7.15
01C.1.2.04.V	36.	100.	9.6	9.4	13.3
04C.1.3.07.V	19.3	100.	93.6	90.	4.16
04C.1.3.08.V	35.9	100.	30.1	28.4	7.73
07C.2.2.03.V	49.0	200.	38.3	40.	8.4
07C.2.2.02.V	50.3	200.	38.7	42.	8.6
07C.2.2.01.V	79.4	200.	14.7	15.5	13.6
07C.2.1.17.VB	452.5	200.	0.51	1.0	77.5
16C.1.2.04.V	157.0	200.	3.9	3.9	26.9
16C.1.2.03.V	173.0	200.	3.1	3.0	29.7
16C.1.3.07.V	223.	200.	3.3	3.4	38.2
16C.1.3.08.V	207.	200.	3.7	3.7	35.5
16C.2.1.17.VB	431.	200.	1.13	1.1	73.8
16C.2.1.17.VC	431.	200.	1.07	1.0	73.8
17C.1.3.07.V	99.	200.	11.9	11.2	17.
17C.1.3.08.V	116.	200.	9.4	9.1	19.9
17C.1.2.03.V	150.	200.	4.5	4.4	25.7
17C.1.2.04.V	167.	200.	4.1	4.1	28.6
17C.2.1.17.VC	274.	200.	1.8	1.8	47.
09C.2.3.02.V	50.5	500.	49.5	48.	6.38
09C.2.3.01.V	79.6	500.	20.5	20.	10.
09C.2.3.04.V	79.7	500.	24.6	23.	10.
09C.2.1.17.VB	368.8	500.	2.1	2.0	46.6
11C.2.4.01.V	77.5	1000.	47.5	46.	7.75
11C.2.4.15.V	208.2	1000.	6.7	6.5	20.8
11C.2.1.17.VB	477.7	1000.	2.2	2.1	47.8
13C.2.5.04.V	80.9	1000.	40.	40.	8.1
13C.2.4.15.V	351.7	1000.	2.1	4.3	35.2
13C.2.1.17.VB	585.5	1000.	.63	1.3	58.6

SECTION 4

DATA SELECTION AND MANIPULATION

The technique to be employed is the use of pairs of records from the same shot to establish the character of attenuation between the two. Use of a single shot eliminates all uncertainty about scaling or shot-to-shot variation. Ideally, pairs should have the properties that they are: representative of general trends; spaced sufficiently far in range to show attenuation above experimental uncertainty; and yet not so distant in range as to encompass changing attenuation character. The first consideration can be taken into account by direct examination of the records. For example, Figure 1 indicates the peak velocity as a function of scaled range for the tamped cases with a labeling according to the shot number.

An example of a desirable record pair comes from shot 7. These are shown in Figure 2. For this case the pulses are quite similar and the peak velocity values follow the general trends. This is probably the cleanest record pair available.

Based exclusively on the peak amplitude, it may appear that a shot 4 pair is ideal for the smaller range (or larger strain) since the record pair follows the trend of all the data and appear to have suitable spacing. The two velocity records from shot 4 are given in Figure 3. Note that while the peak velocities are reasonable, the character of one of the records is not. In particular, that from gauge 7 shows significantly more noise and the main peak split into two narrow peaks. This is a good example of a record which is not suitable for analysis even though the peak velocity appears satisfactory; it is not representative and we do not want to bias the results using data which have obvious problems. Consequently, we have chosen pairs which look most promising in that their peak amplitudes follow the trends of all the data and that their waveforms are relatively simple and consistent with each other.

The totality of the Cowboy data shows a variety of features including irregular effects almost certainly due to inhomogeneities in the salt medium. It is important to avoid treating these anomalies as equivalent to regular features. Thus we have selected the data pairs carefully and smoothed the tails of the waveforms in such a way as to make the final result similar to those seen in the (remarkable pure) Salmon tests.

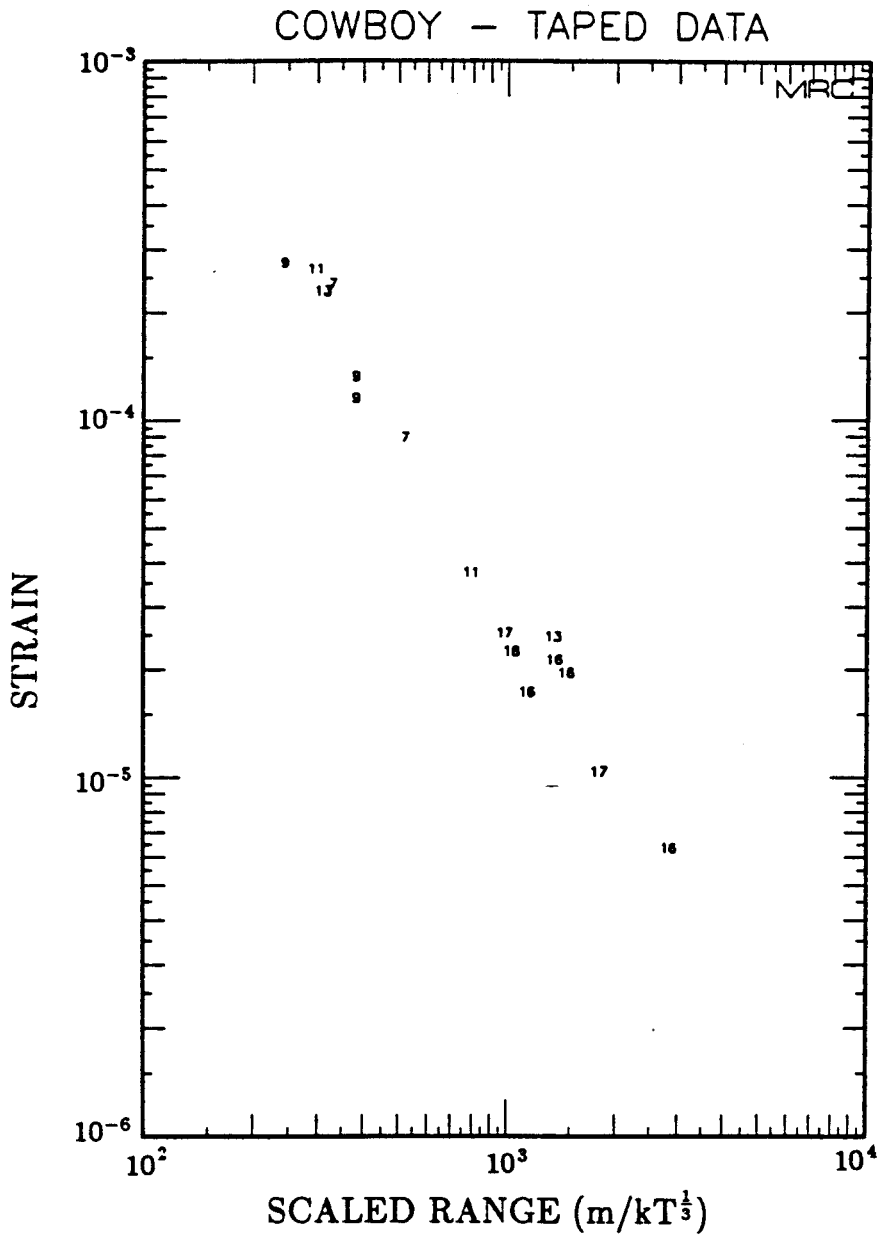

Figure 1. Peak velocities versus scaled range for Cowboy data used in this analysis. Numbers correspond to the shot designation.

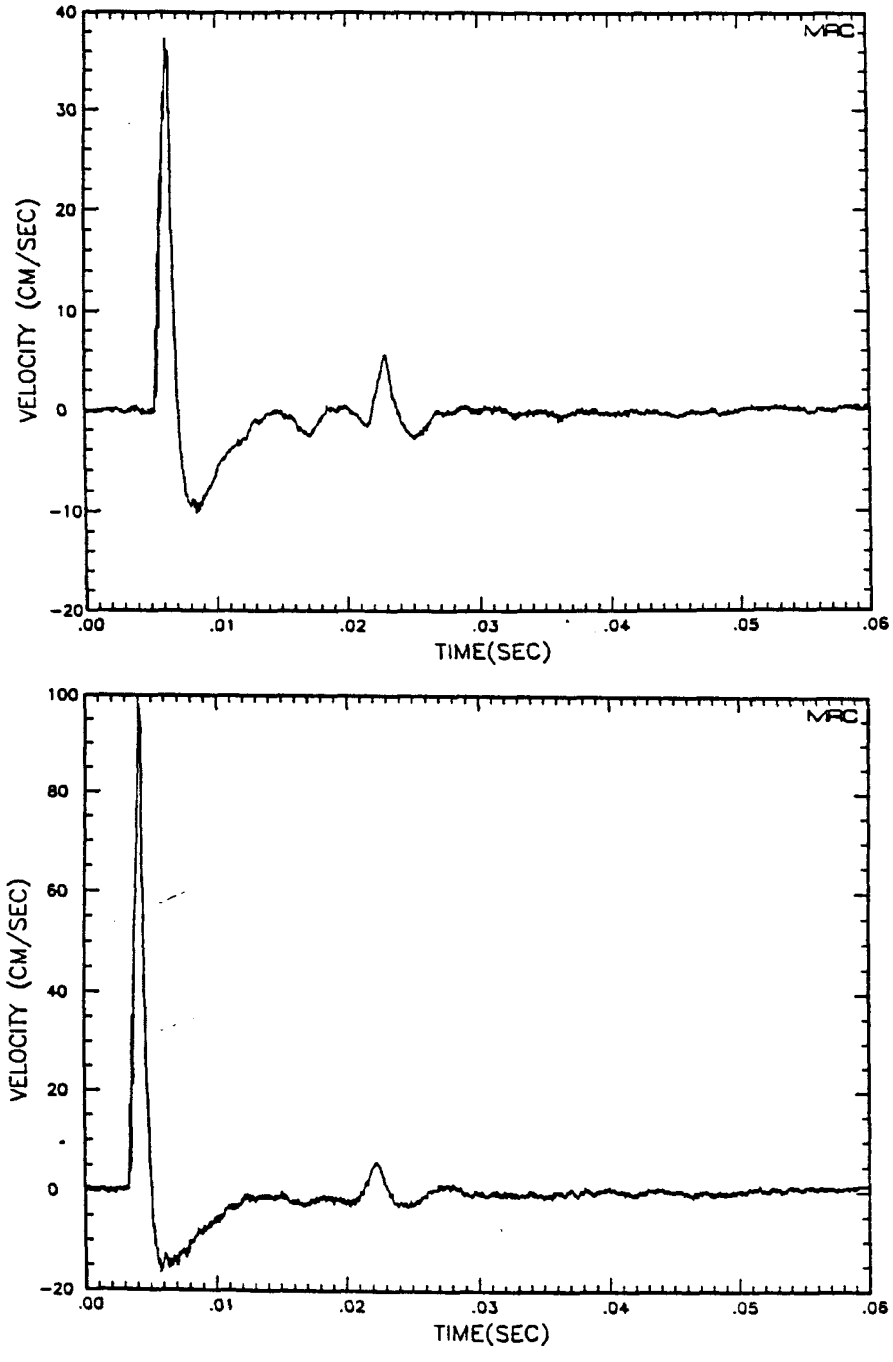

Figure 2. A best case velocity record pair from Cowboy shot 7.

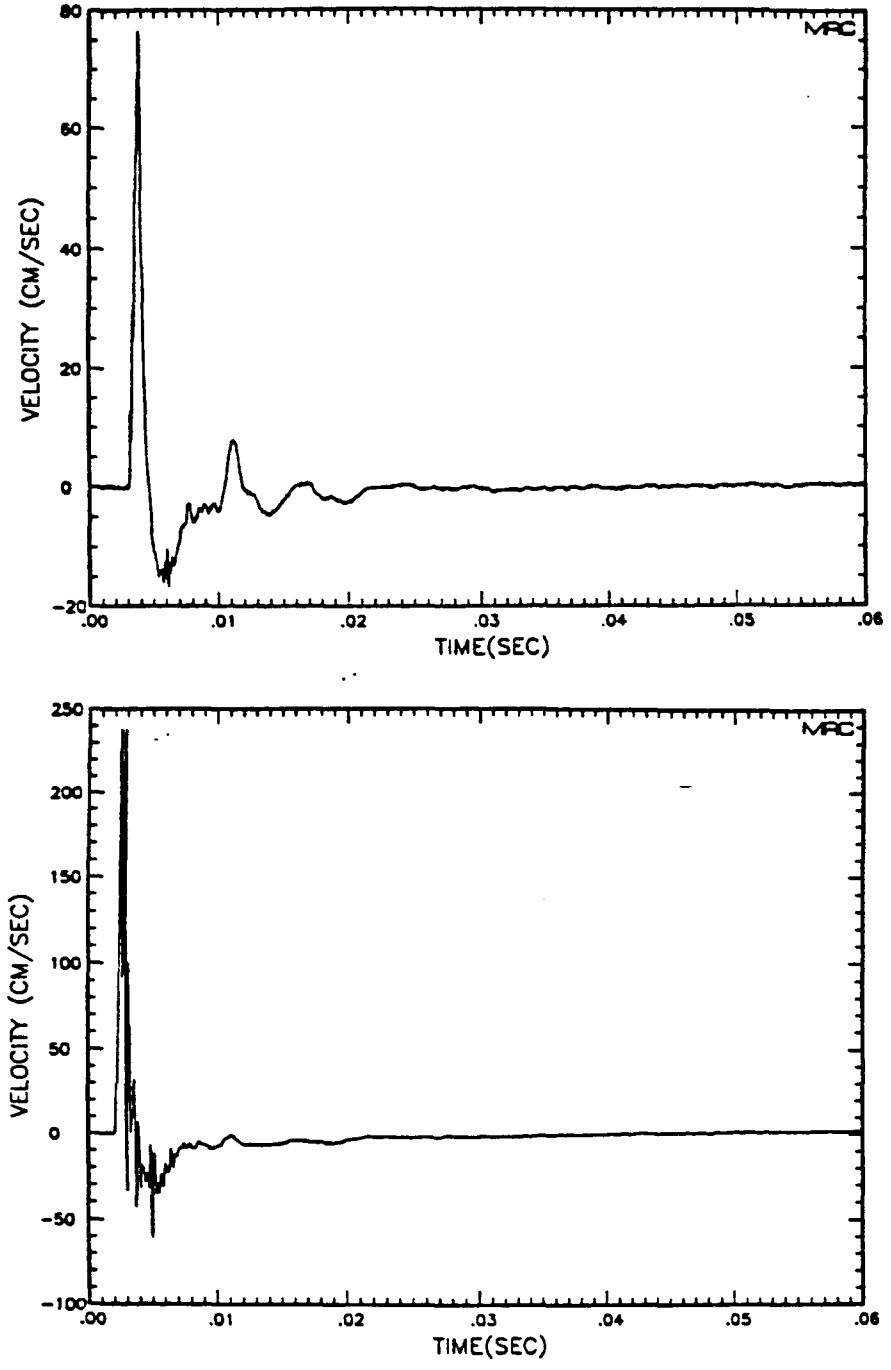

Figure 3. An example of a velocity record pair from Cowboy shot 4 which has a flawed character and is unsuitable for analysis. From sensors 8 and 7.

4.1 Truncation

We have instituted a procedure for smoothing the raw data by ignoring contributions before the pulse arrival as well as by eliminating contributions from the pulse past the first full cycle. Such windowing of the data is clearly justified in ignoring fluctuations before the pulse arrives. However, without knowledge of the pure waveform, unique truncation of the pulse is not possible. Given the Salmon data showing one or one and one half significant cycles, it seems reasonable to use only the first cycle of the data records for analysis. Furthermore, if all the records are truncated in a similar fashion, we can be more confident that the details of the method will not affect comparisons of pairs of such records.

As seen in Figure 4, a raw record consists of low level noisy fluctuation before pulse arrival, a fairly pure cycle of explosively driven pulse and a tail which is some mixture of additional oscillations. The Salmon data generally show only a single significant cycle while the Cowboy records usually have several cycles of decreasing amplitudes. This suggests that the tail is not a fundamental feature. We have chosen to cleanse the records by a sort of windowing which retains only the initial cycle of the velocity record. The tail has been forced to go smoothly to zero by one of two procedures. The first, appropriate when the second maximum is nearly at zero velocity, consists of forming a linear baseline running from the beginning at the initial pulse rise and going the zero slope position of the second maximum. Over this interval the corrected record consists of the difference between the original and the baseline. The remainder of the corrected record is set to zero velocity. This results in a single cycle which goes smoothly to zero at both ends. A second approach as been used for those records (generally at larger ranges) which have pronounced second and higher maxima. For this case the tail is terminated by constructing a smooth arc from a joining point half way between the first minimum and the next zero to the axis. This arc is taken as a segment of an ellipse which is constructed to insure continuity of the function and its first derivative at the joining point. The arc is forced to have zero derivative at the axis. This arc is then substituted for the original data past the joining point. All data prior to pulse arrival are set to zero so the result is again a single cycle which goes smoothly to zero at both ends.

The effects of carrying out this smoothing are illustrated in Figure 5. In this sequence a pair of records has been examined with and without smoothing, the reduced velocity potentials (RVP) determined and Q estimated by the spectral ratio of

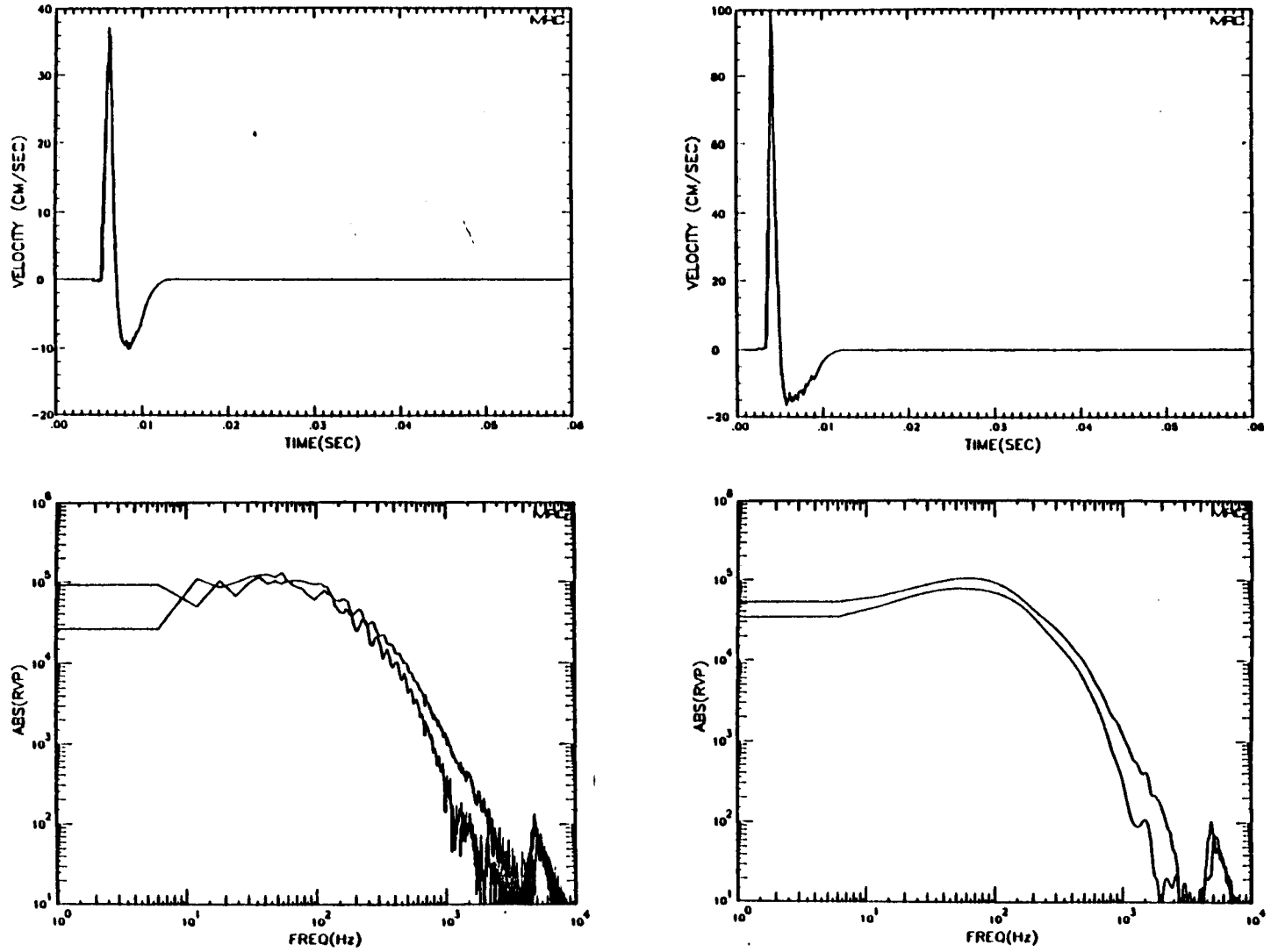

Figure 4. Cowboy shot 7 velocity record pair after smoothing (a and b, compare with Figure 2), their associated RVPs (c and d) and the Q estimates (e and f). From sensors 1 and 2.

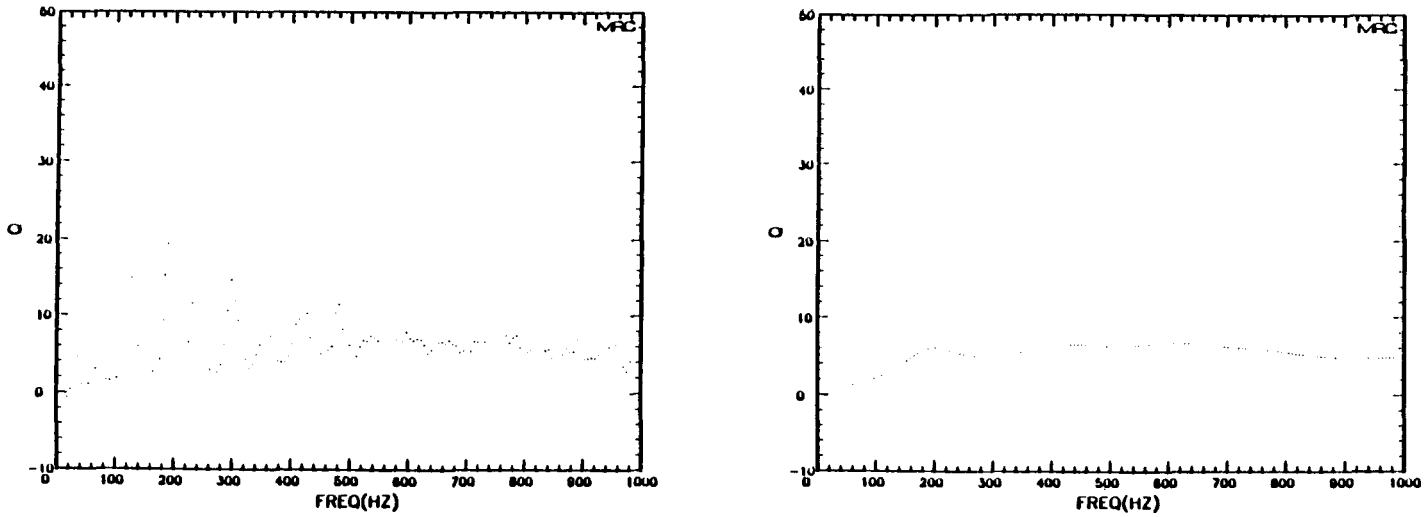

Figure 4. Cowboy shot 7 velocity record pair after smoothing (a and b, compare with Figure 2), their associated RVPs (c and d) and the Q estimates (e and f). From sensors 1 and 2 (continued).

the RVPs. It is reassuring that the general character of the result does not change but the much smoother spectra produce smoother Q. Generally the unsmoothed records tend to produce scalloped RVPs due to the presence of an oscillating tail which produces an interference structure in the frequency domain.

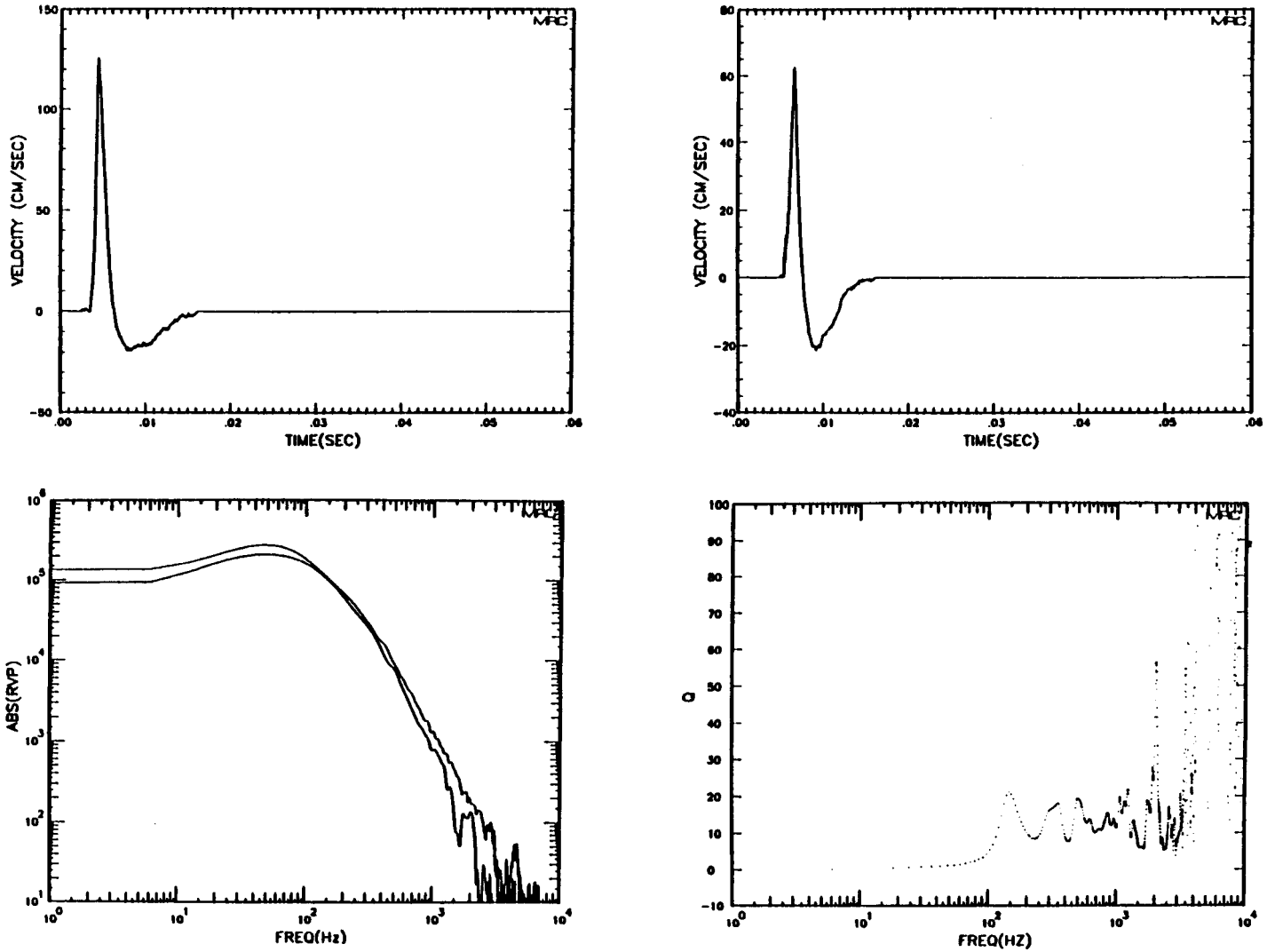

Figure 5. Velocity record pair (a and b), RVPs (c) and effective Q estimate (d). From Cowboy shot 9, sensors 2 and 4.

SECTION 5

ANALYSIS OF COWBOY DATA

The review in Section 2 seems to suggest that the Cowboy data indicate nonlinear attenuation. However, the analyses are based on the explicit assumption of scaling in order to build a sufficiently large database to allow useful fits to be carried out. While scaling for peak velocity amplitudes seems an experimental fact (albeit without any theoretical foundation) , the use of the assumption for scaling pulse *shapes* seems less clear. In view of the lack of any obvious physical basis for scaling, and the potential for altering the results of any analysis, we feel compelled to attempt to better define possible nonlinear behavior without use of the scaling assumption. This means that the Cowboy data cannot be used as a unit, but only within a given shot in the series. Since the individual shots had only of few instruments in operation, we are generally limited to finding records in pairs which allow attenuation estimates to be made.

Our approach to the possibility of direct demonstration of nonlinearities of the Cowboy attenuation data will be by attempting to cast the observed attenuation in linear terms and seeking contradictions. That is, we wish do determine if it is possible to find a linear $Q(\omega)$ which is consistent with the data but which is independent of amplitude. If this is not possible, the implication is that there must be an amplitude dependent attenuation. If there is a $Q(\omega)$ which is consistent with the data, we must conclude that the data are internally consistent with linearity. In the case of Salmon data, a similar exercise revealed that a Q independent of amplitude can represent the data but the value of Q required was so much smaller than that expected at small strains that some nonlinear transition must be required between the strain ranges represented.

As demonstrated by Kjartannson[11] and detailed in Appendix B, it is possible to reduce to quadrature the problem of linear propagation and attenuation in a medium which has a Q which is independent of frequency. For this case the RVP can be explicitly determined from a velocity record and the result is proportional to the familiar factor

$$exp(-\omega r/2cQ)$$

where the phase speed c is a known mild function of ω for constant Q. The rates of two

RVP in the frequency domain is given by

$$\exp\left(\frac{\omega(r-a)}{2cQ}\right) = \left|\frac{\tilde{v}(r,\omega)}{\tilde{v}(a,\omega)}\right| \frac{\left|\frac{i\omega}{ca} - \frac{\omega}{2cQa} - \frac{1}{a^2}\right|}{\left|\frac{i\omega}{cr} - \frac{2}{2cQr} - \frac{1}{r^2}\right|}$$

where r and a are two radii and $\tilde{v}$ is the Fourier transform of the velocity record. We wish to exploit this result to look for nonlinear effects as follows:

1. Assume that the data are consistent with the above expression for linear attenuation due to a Q;
2. Use the data records in pairs to estimate that $Q(\omega)$ using a constant c chosen to be consistent with the general pulse motion;
3. Use as many data record pairs as possible to determine the Q as a function of peak velocity (or peak strain or scaled range);
4. The resulting Q estimates are then to be examined to determine if they could be consistent with a constant Q. If not the implication is that there must be nonlinear effects which dictate the decay of the waveform.

In Figures 5 through 14 pairs of data records are given along with their RVP estimates and the $Q(\omega)$ which results from the ratio of the RVP pair. These results were produced using a sampling interval of 20 microseconds and 8192 data points. Generally the nonzero portion of the data record covers less than 0.01 seconds and the corner frequency is about 100 Hertz. At this sampling interval, the frequency resolution is about 6 Hertz. The data generally fall into the noise shortly after 1000 Hertz. Thus the useful frequency range is from about one decade around the corner frequency although the lower end of the spectrum is sometimes significantly influenced by the smoothing technique as evidenced by some pairs for which the smoothed pairs give a negative Q at low frequencies (at frequencies for which the unsmoothed records give positive Q).

There are some qualitative features of the results for effective Q which are sufficiently consistent to allow comment. First it is evident that the totality of the results *do not* strongly suggest that a constant Q can provide a fit to the data. Generally the estimates for Q tend to increase with frequency. Generally the Q estimates decrease with decreasing peak amplitude.

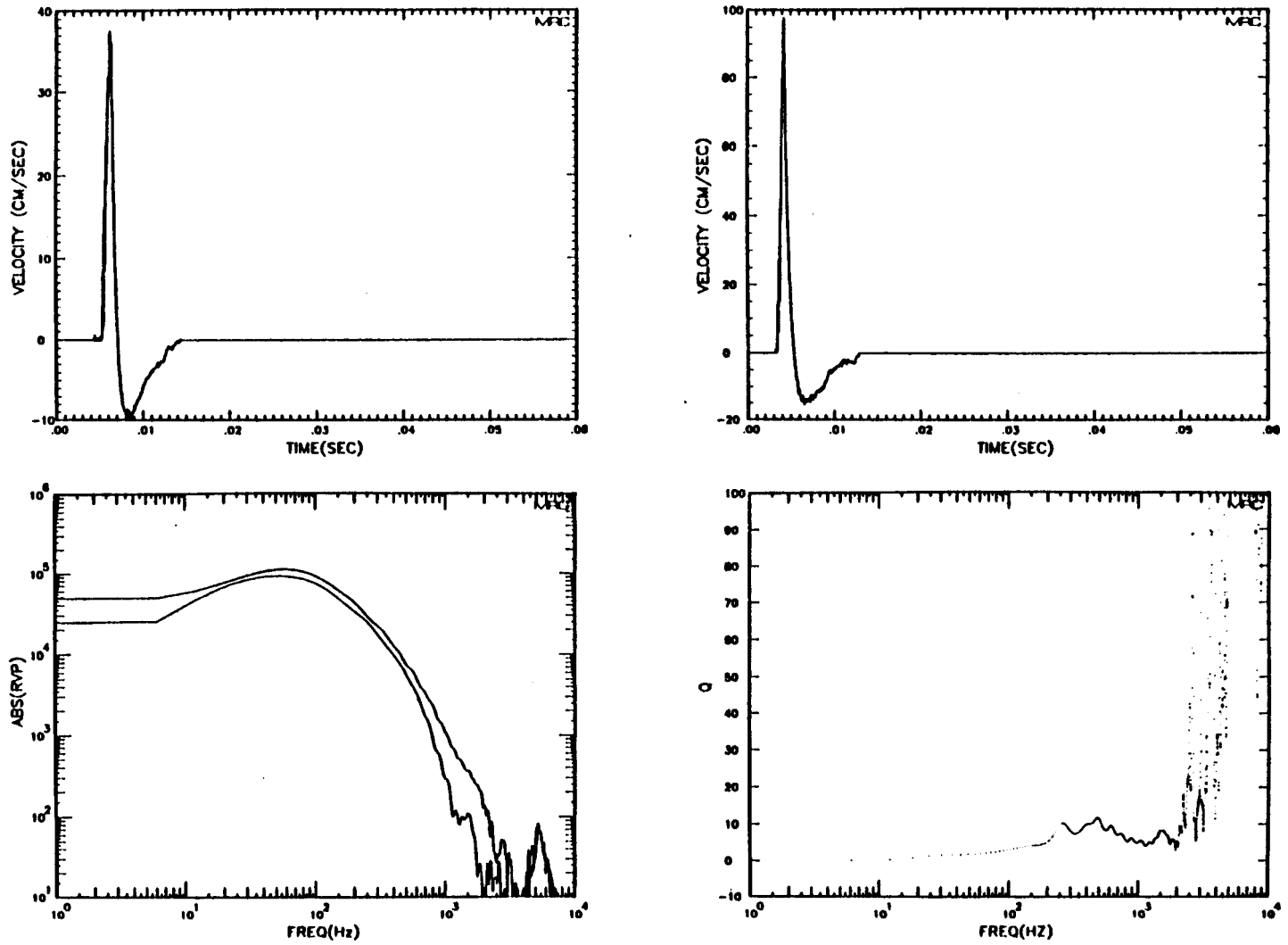

Figure 6. Velocity record pair (a and b), RVPs (c) and effective Q estimate (d). From Cowboy shot 7, sensors 1 and 3.

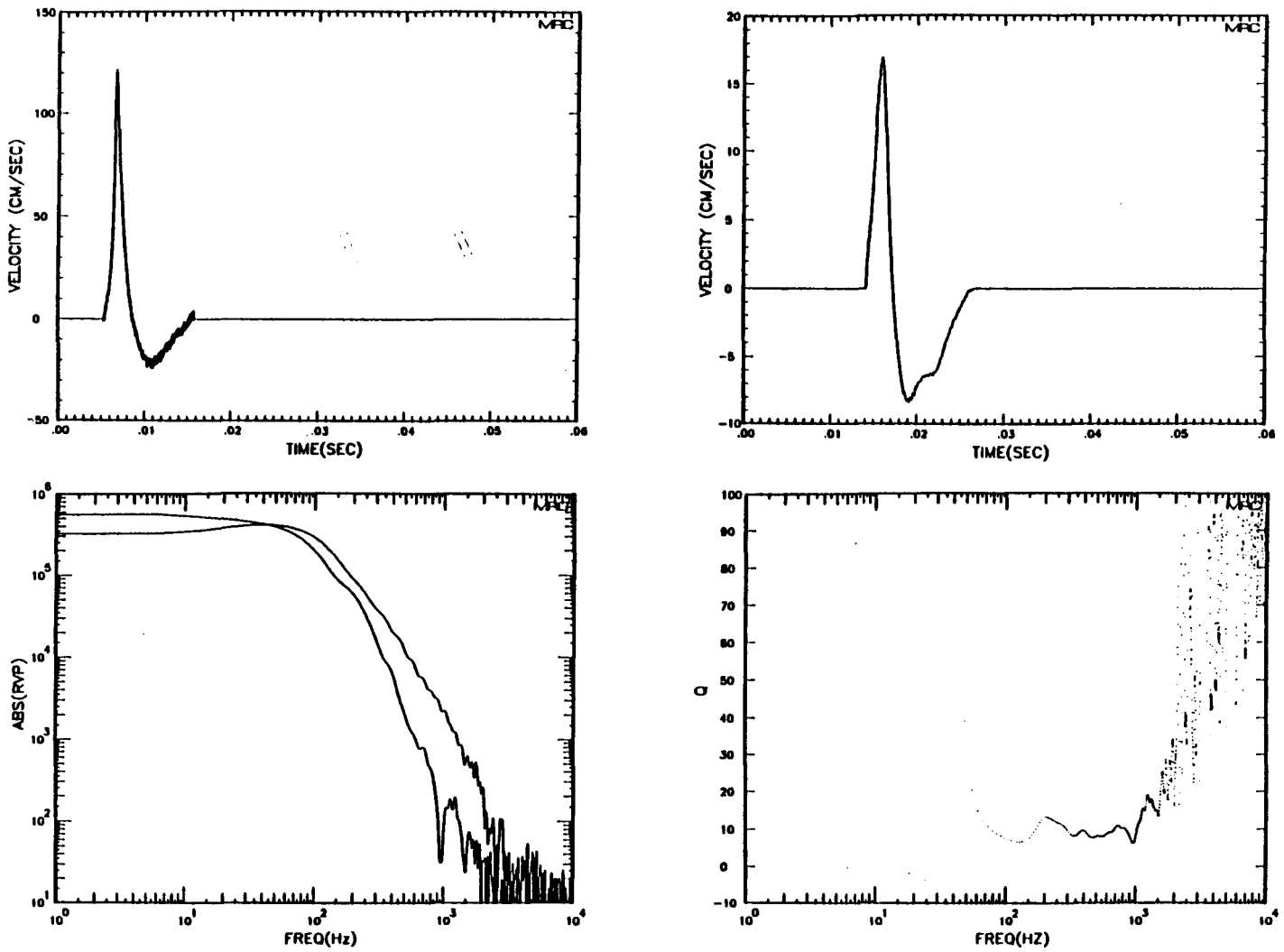

Figure 7. Velocity record pair (a and b), RVPs (c) and effective Q estimate (d). From Cowboy shot 11, sensors 1 and 15.

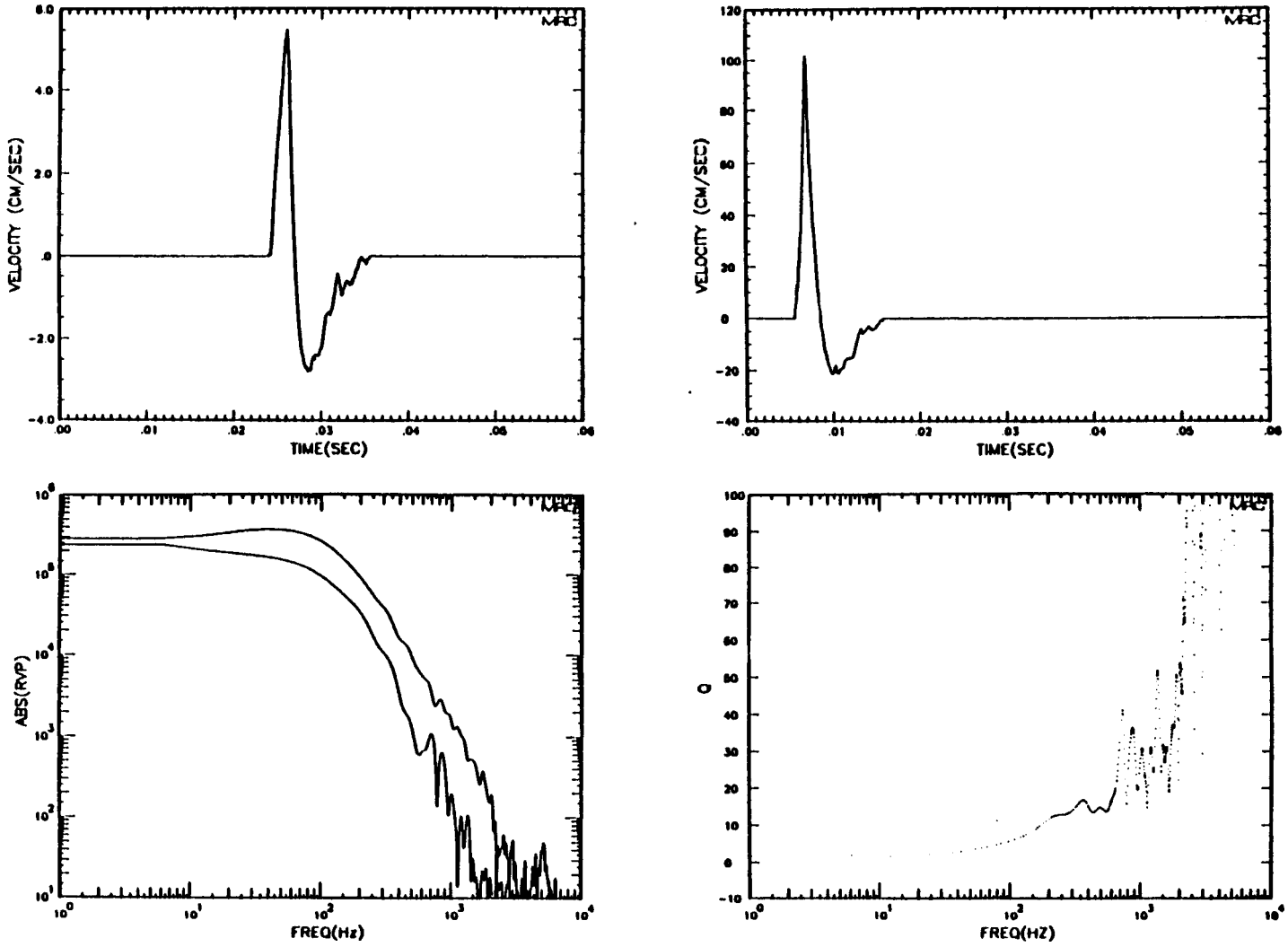

Figure 8. Velocity record pair (a and b), RVPs (c) and effective Q estimate (d). From Cowboy shot 13, sensors 15 and 4.

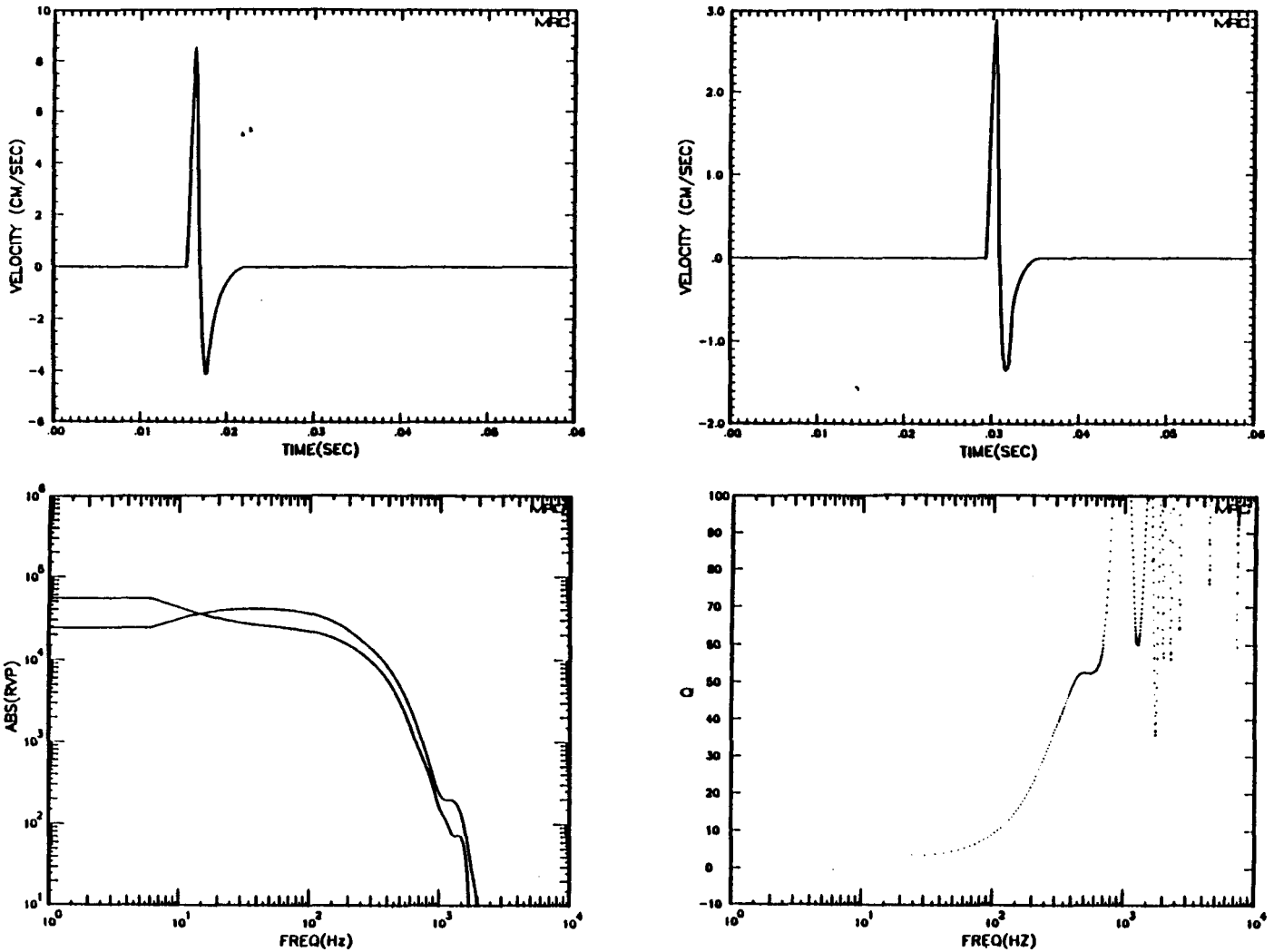

Figure 9. Velocity record pair (a and b), RVPs (c) and effective Q estimate (d). From Cowboy shot 16, sensors 7 and 17.

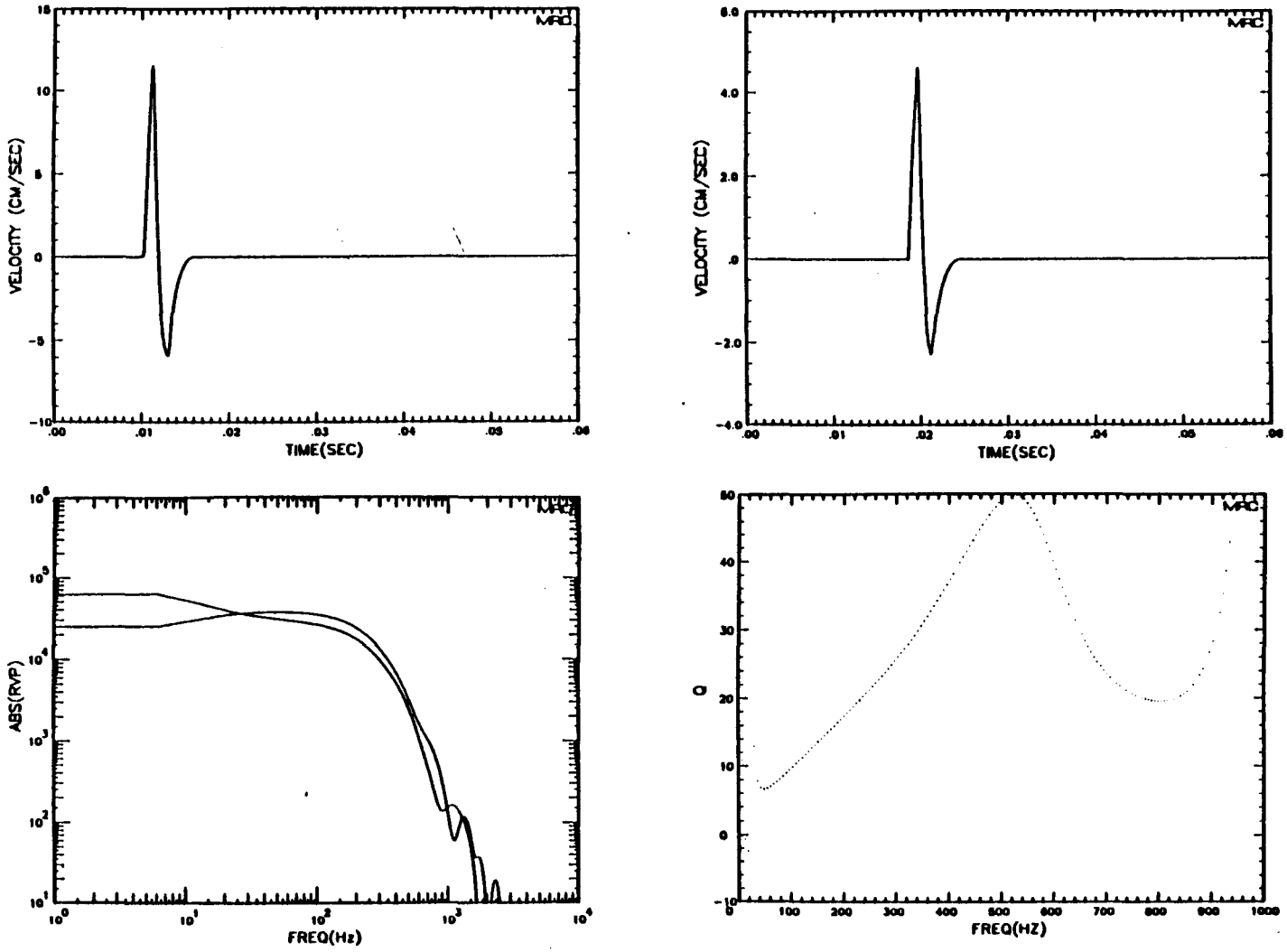

Figure 10. Velocity record pair (a and b), RVPs (c) and effective Q estimate (d). From Cowboy shot 17, sensors 3 and 17.

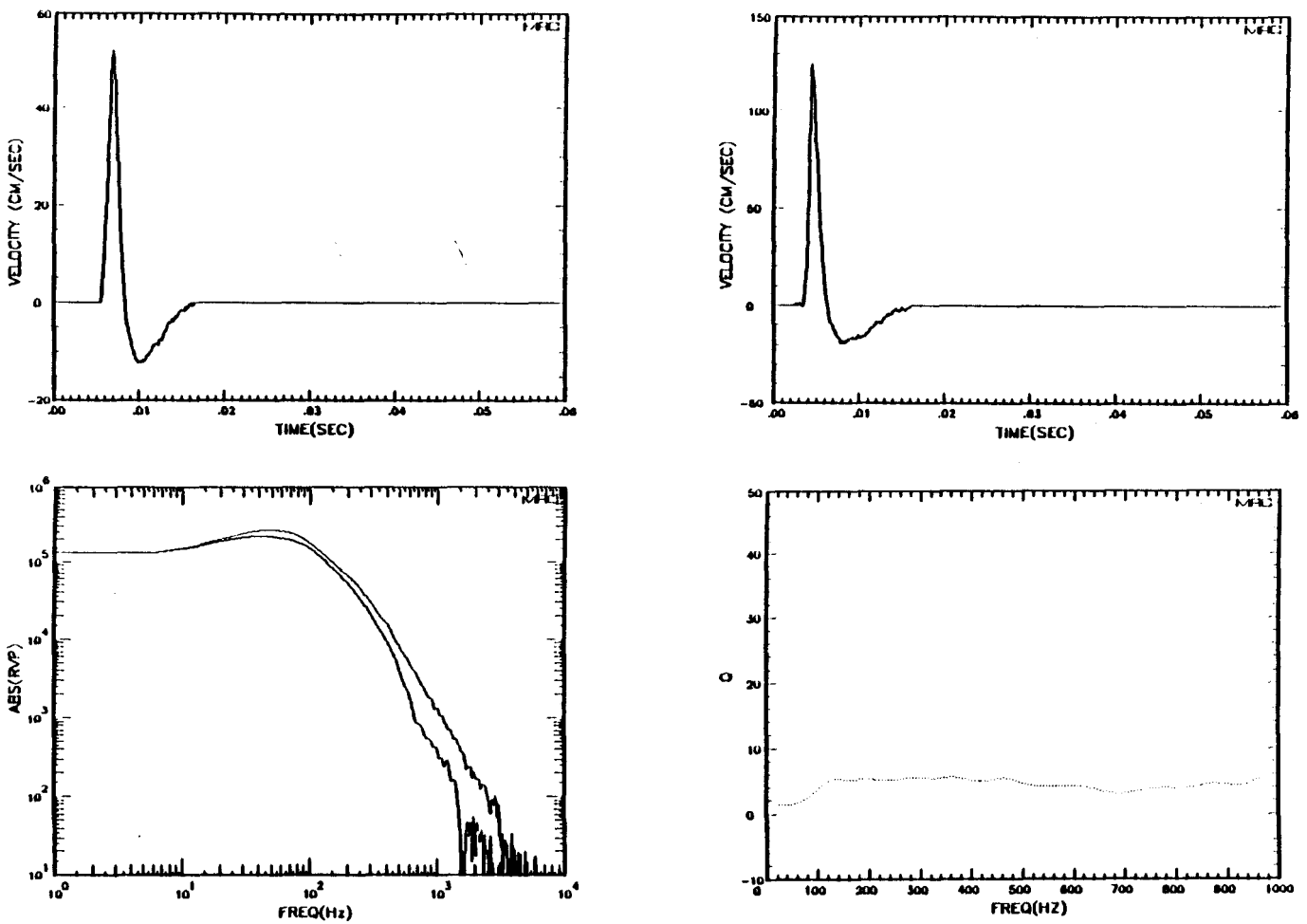

Figure 11. Velocity record pair (a and b), RVPs (c) and effective Q estimate (d). From Cowboy shot 9, sensors 2 and 1.

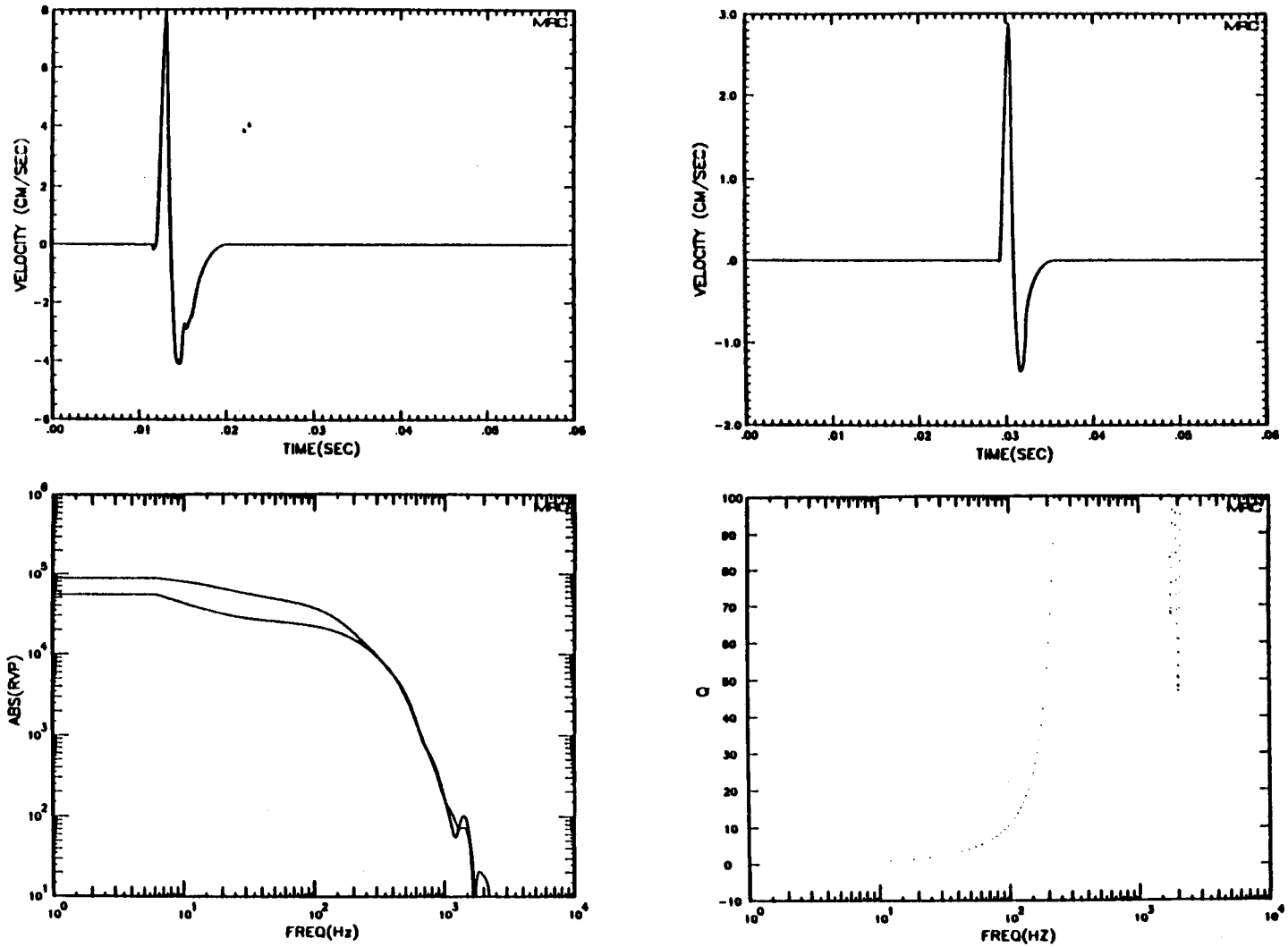

Figure 12. Velocity record pair (a and b), RVPs (c) and effective Q estimate (d). From Cowboy shot 16, sensors 3 and 17.

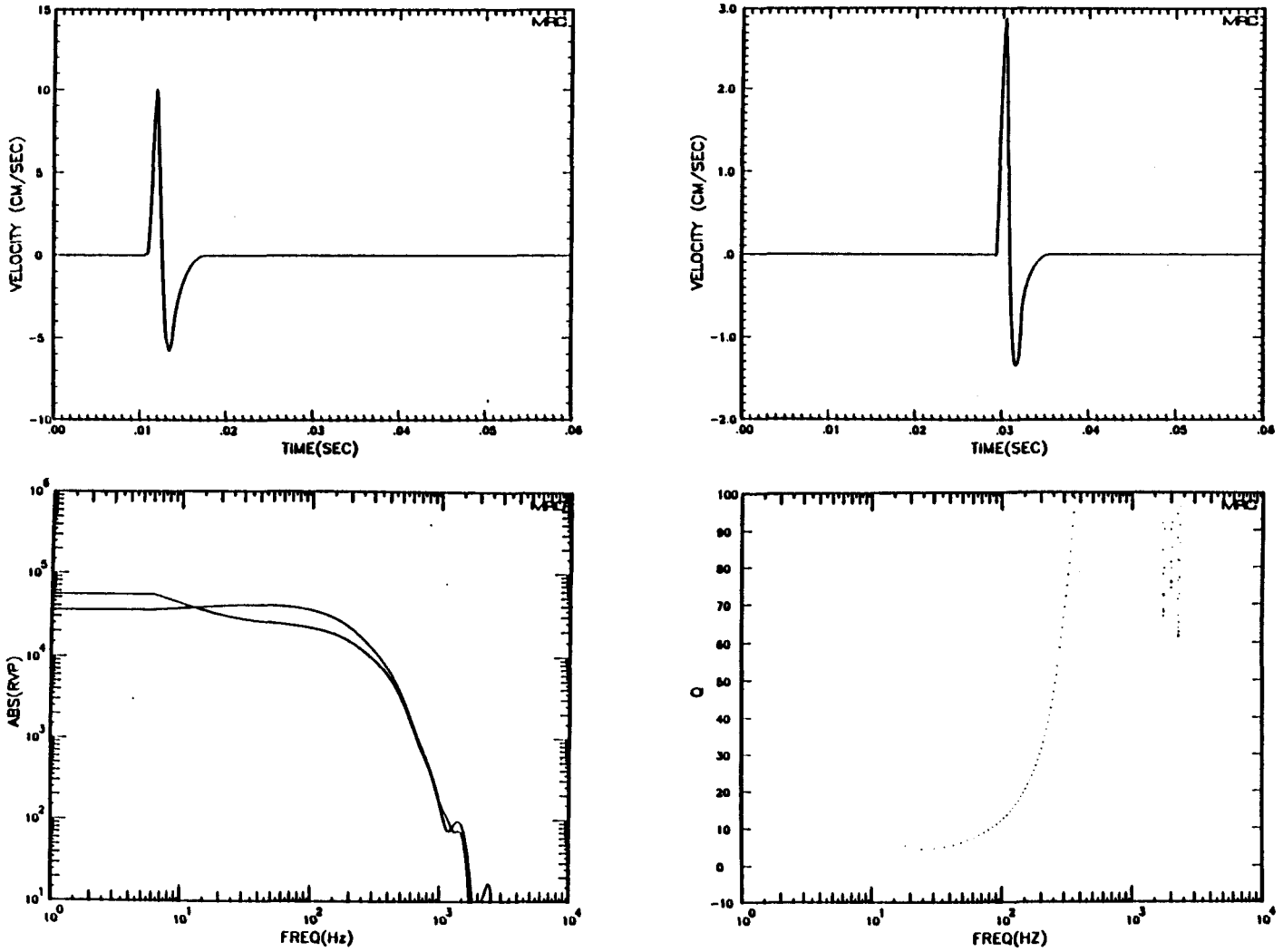

Figure 13. Velocity record pair (a and b), RVPs (c) and effective Q estimate (d). From Cowboy shot 16, sensors 4 and 17.

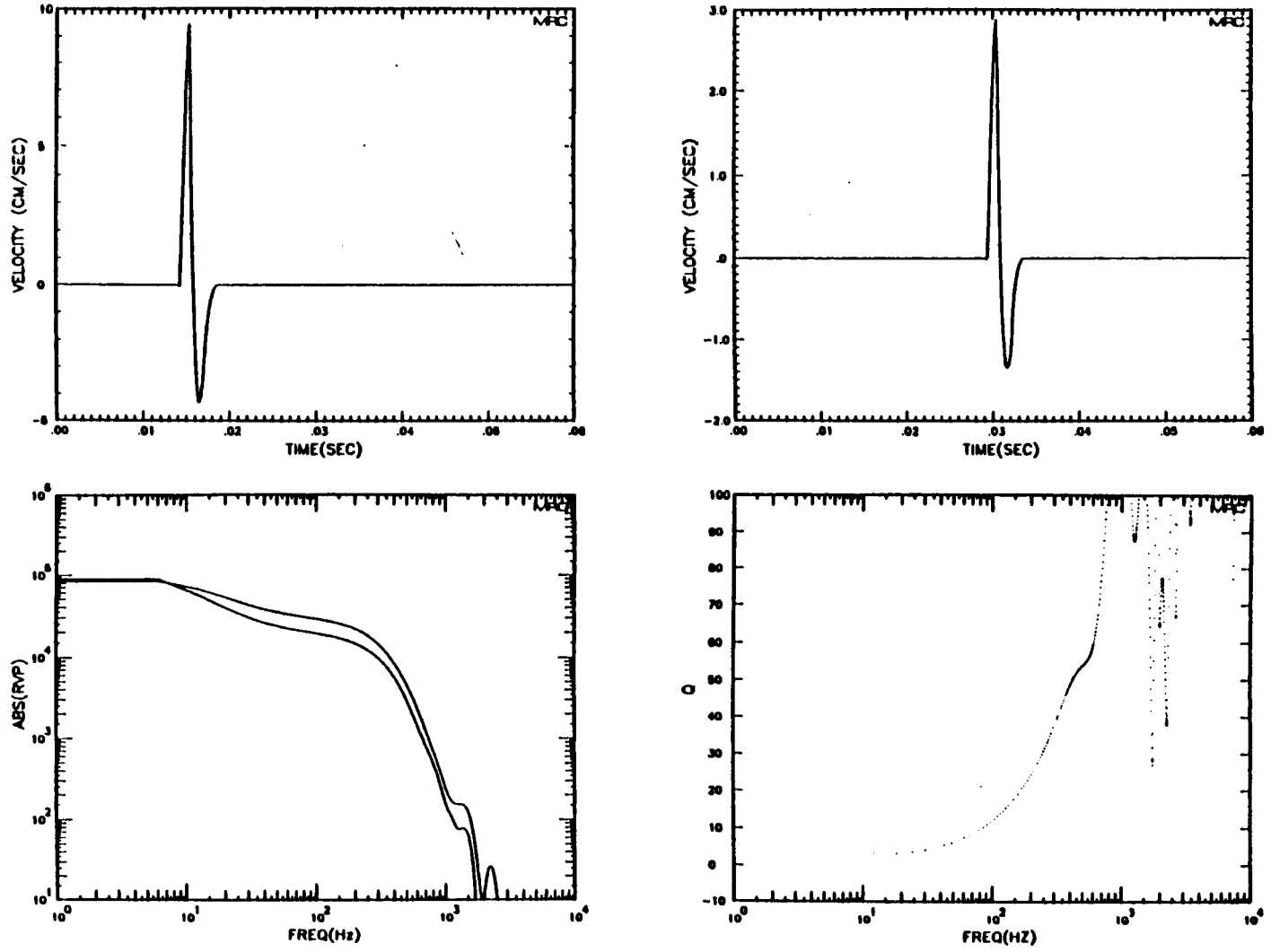

Figure 14. Velocity record pair (a and b), RVPs (c) and effective Q estimate (d). From Cowboy shot 16, sensors 8 and 17.

5.1 Amplitude Dependence

A determination of Q as a function of peak strain, ϵ, (using peak velocity over the phase speed as an approximation to the peak strain) has been found by plotting Q^{-1} versus ϵ in Figure 15. The horizontal bars on the points give the range of the pair of peak strains while the vertical bars indicate the range of Q^{-1} which comes from a decade of frequencies centered around the corner frequencies (in all cases the greatest attenuation is from lower frequencies). On this same curve we have plotted the Q^{-1} which Minster and Day[10] found using scaled Cowboy data in conjunction with a concurrent fit to the decline of peak velocity and peak displacement enforced by a Q^{-1} which is taken as the sum of a constant and a term proportional to ϵ.

5.2 Frequency Dependence

Note that over the examples Q is somewhat irregular as a function of frequency but it has a general trend of starting near zero and going toward a value of the order of 10 (or a bit more at the larger ranges).

A Q^{-1} estimate has been found by least square fitting the experimentally determined effective $Q(\omega)$ using the form

$$Q^{-1}(\omega) = Q_0^{-1} + B/\omega$$

so Q_0^{-1} is the limiting value at large ω. This form including the B term was chosen due to the tendency of the data to suggest that Q becomes small at small ω. Such a behavior could result from anomalies of the experimental techniques if, for example, the instruments were not sufficiently accurately calibrated leading to a scale expansion or compression which was not predictable from case to case. This would shift the RVP spectrum without changing its shape. The inclusion of such an effect, in the presence of a constant Q_0, would give a nonzero value for B. Note that when the term with B is included in the decay factor

$$exp(-\omega r/2cQ)$$

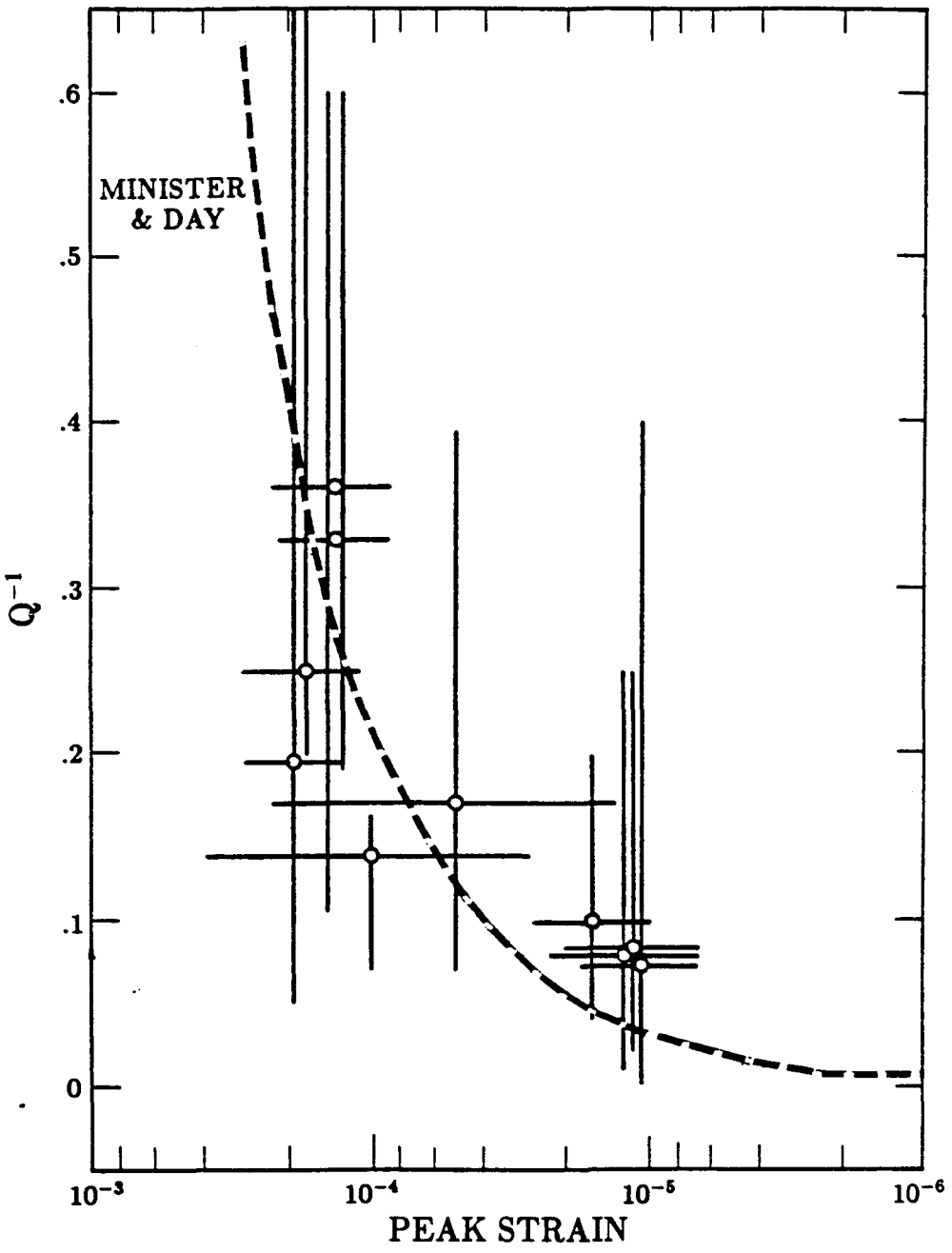

Figure 15. Cowboy Q estimates as a function of peak strain. The horizontal bars represent the two record strain values while the vertical bars indicate the spread of Q over a decade of frequency. The fit of Minister and Day is provided.

there results a uniform decrease in the spectral context. Of course we cannot rule out the possibility that there may exist an attenuation mechanism which does in fact attenuate the spectrum uniformly.

The results of the least squares fits to the set of $Q^{-1}(\omega)$, using frequencies below 1000 Hertz, are given in Figure 16; the value of the fit to B is also shown in order to see if there is a consistency to its behavior with range or with data record pair. No such consistency is seen in the B behavior although it does seem to be positive (random calibration errors would give a mean B of zero) at least at larger ranges. However the amount of data is limited and the least squares fits are not always terribly good (that is, the experimental Q is not very close to the form being fit).

The results for amplitude and frequency dependence are in general accord with those of Trulio [9] although a one-for-one comparison is difficult due both to use of scaling and different analysis methods. Trulio's trends are that attenuation (effective Q^{-1}) decreases with frequency, roughly like (scaled frequency)$^{-1}$ at fixed scaled range, and attenuation decreases with range roughly like (scaled range)$^{-1}$ at fixed scaled frequency.

5.3 Decoupled examples

In order to get more and better estimates of Q at small strains, we have examined some pairs of records from *decoupled* events in the Cowboy series. If Q is a linear material property, the differences in waveform between coupled and decoupled will not matter.

It is consistently the case that the decoupled data are more variable, noisy and oscillatory that those from coupled events. An example of the rather inconclusive $Q(\omega)$ estimates from a decoupled event is given in Figure 17. Note that the Qs tend to be rather large and variable while the minimum values are typically greater than 100 at moderate frequencies which contain most of the pulse energy. Negative Q values reflect the small differences in the compared RVPs in conjunction with noise levels comparable with these differences. Still it appears that the attenuation from decoupled events, which have lower peak strains, is smaller than those for the coupled case. This is consistent with the hypothesis that the effective Q^{-1} decreases with strain but the data are not of adequate quality to make any more positive statement.

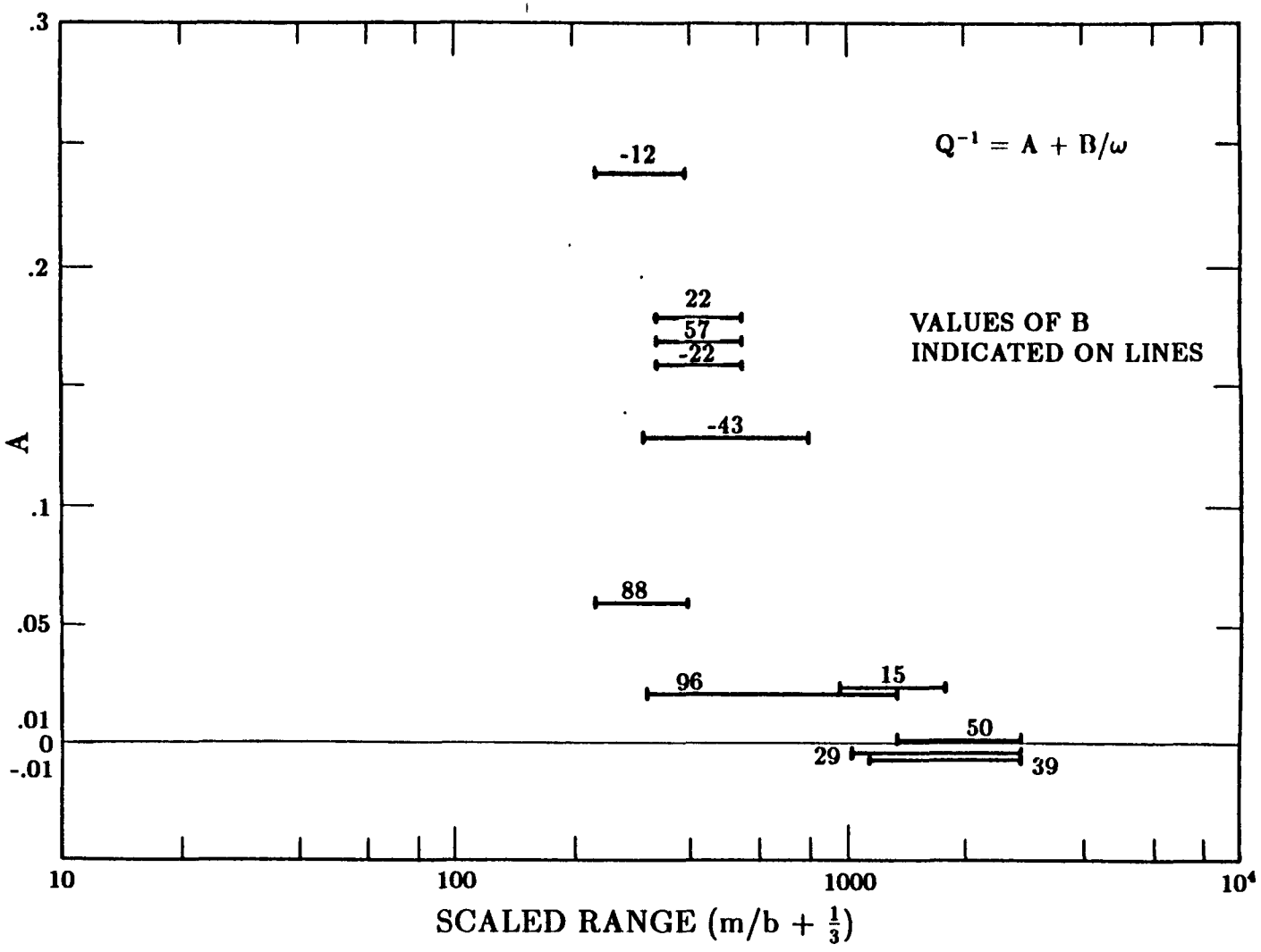

Figure 16. Values of Q_0^{-1} found from fits of the form $Q^{-1} = Q_0^{-1} + B/\omega$ to Cowboy Q estimates. Values of B are shown are indicated across the horizontal bars indicating the range of strains in the pairs.

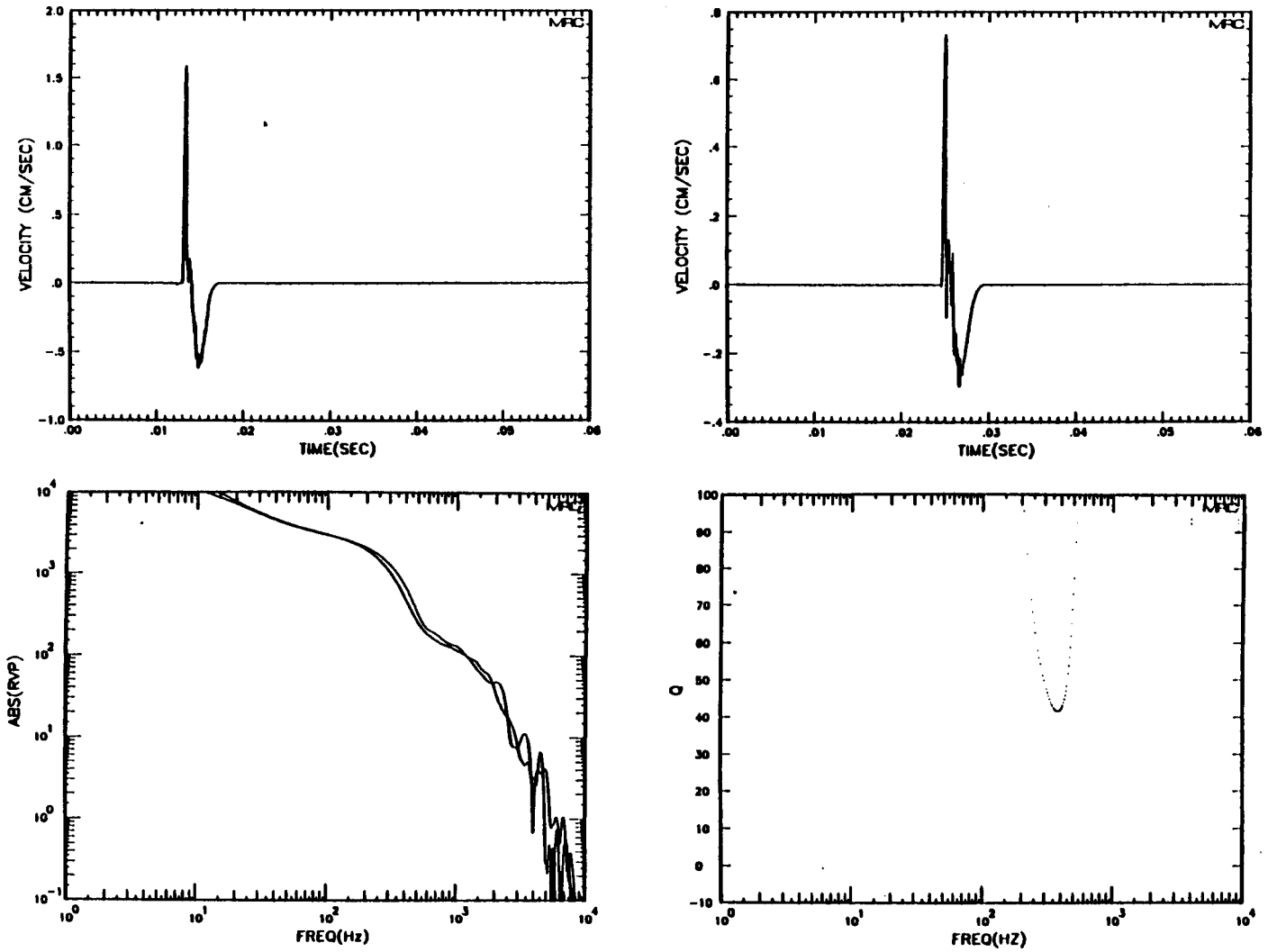

Figure 17. Decoupled Q estimate using a velocity record pair from Cowboy shot 8, sensors 11 and 17.

SECTION 6

DISCUSSION OF SALT DATA IMPLICATIONS

There are several sources of data for attenuation of signals in the salt medium. These cover, often nonoverlapping, regions of strain and frequency and these results suggest a dependence on both strain and frequency. In order to attempt to isolate any strain dependence which is shared by the various experiments we have taken the results for Q at the dominant (corner frequency for pulses) frequency of each experiment. This could be interpreted as some mean Q from the experiments. These Q^{-1} estimates as a function of strain at the dominant frequency for the experiments in salt are shown in Figure 18. The values for Cowboy are just those from Figure 17. The two from the Salmon data are from McCartor and Wortman and McLaughlin and Gupta and give a corresponding estimate but at greater strains and a lower frequency. The older Livermore results from Larson are at a much higher frequency but at strains comparable with Salmon. Finally the Rockwell results for smaller strains are from a different sort of experiment so it is less clear that the results should be compared directly. Still the Rockwell values are suggestive of the expected trend toward small attenuation at small strains.

Apart from the Livermore data, the results are consistent with a tendency for increasing attenuation with increasing strain. However, there is certainly no evident trend for frequency dependence across the experiments since Salmon lies between the Livermore and extrapolated Cowboy results for the largest strains.

Estimates of effective Q as a function of frequency from Fourier analysis of the individual Cowboy and Salmon experiments generally indicate a rather consistent frequency dependence — namely, Q decreases with decreasing frequency below the corner frequency. Figure 19 illustrates this point by showing the effective Q^{-1} at approximately the same strain as determined from a pair of Cowboy records and a pair of Salmon records. The corresponding corner frequencies are indicated. Note that while the trends are the same, there is clearly not a single Q (ω) which could describe the outcome. However, if the results are cube root scaled in frequency, giving them a common corner frequency, the resulting Q's nearly coincide. This should not be surprising since the empirically observed scaling behavior requires this in order to succeed.

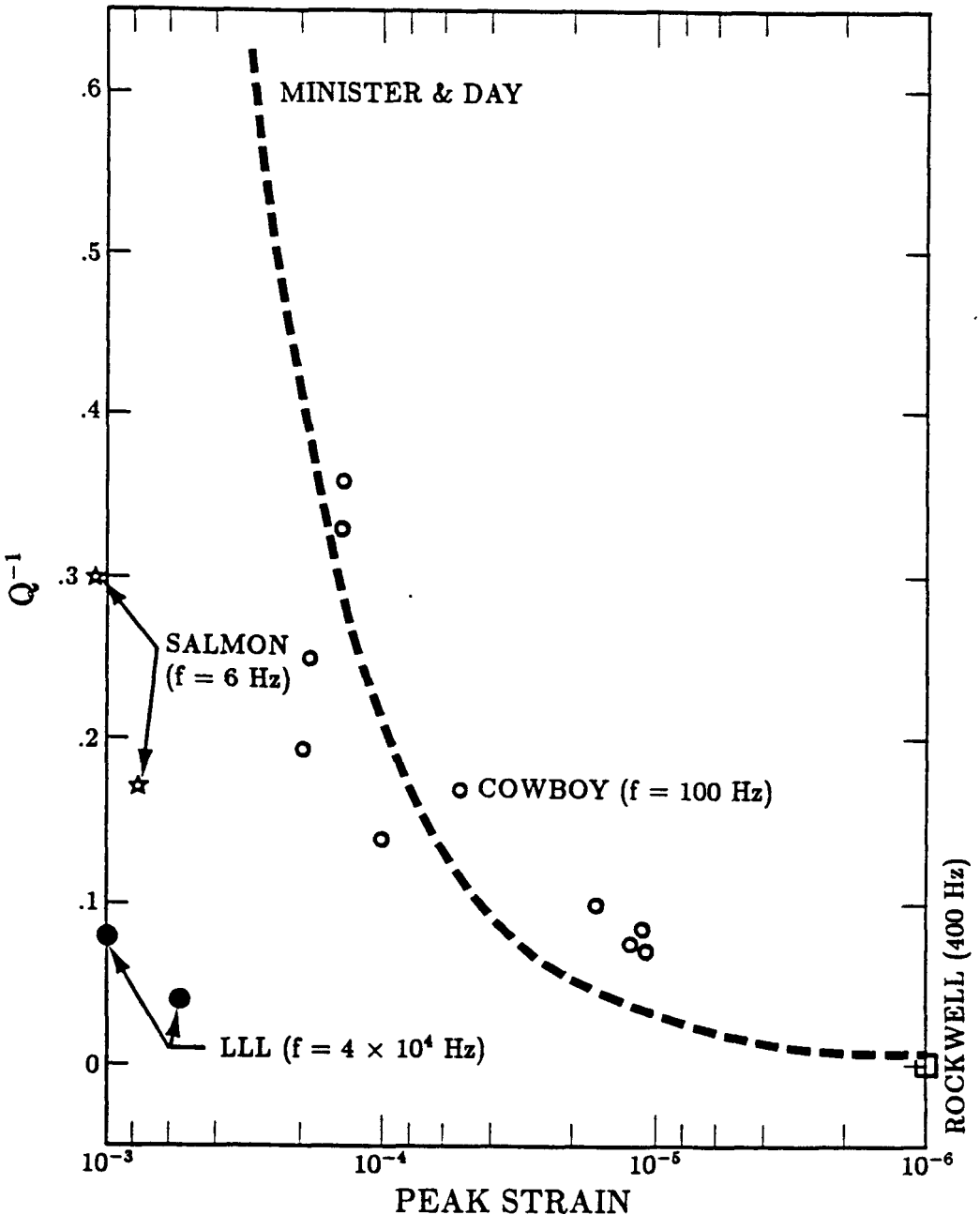

Figure 18. Q^{-1} estimates as a function of strain at the corner frequency for the experiments in salt which are available.

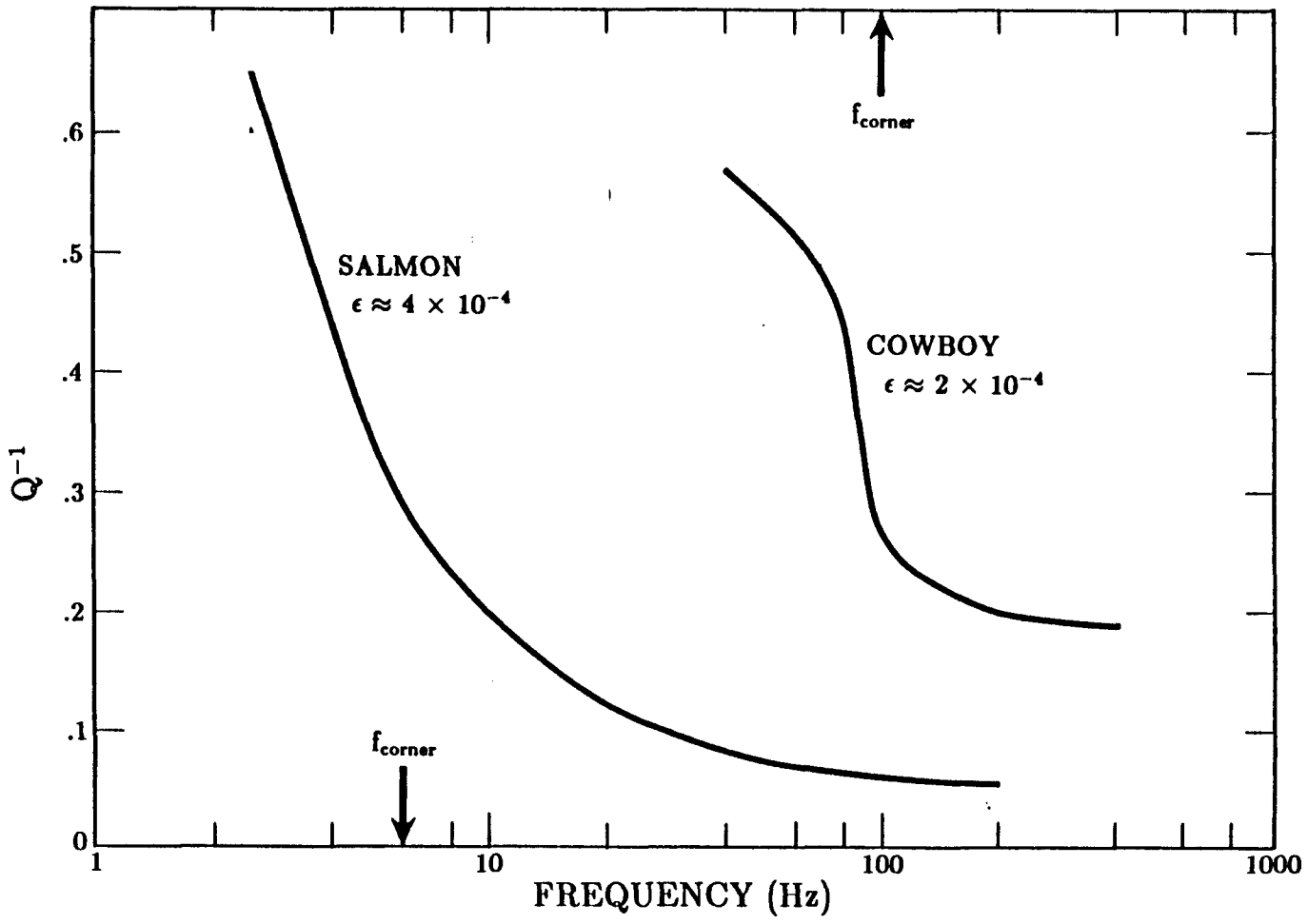

Figure 19. Q^{-1} estimates as a function of frequency for Salmon and Cowboy.

Note that this means if data from different experiments which obey scaling, such as Cowboy and Salmon which have different frequency scales, are combined through scaling before Q is determined, the result will be an apparent consistency of Q. However this is a deceptive effect since the effective Q derived is a function of frequency which is a scaled frequency. *This Q is clearly not a simply a material property describing the inherent attenuation of the medium, but some function of the pulse itself.*

The clear implication of the Cowboy data, especially when combined with other explosively generated pulse attenuation, is that in the moderate to high strain regime the mechanisms must be nonlinear. The strongest evidence is in the amplitude dependence of the attenuation in that the effective Q must increase with decreasing amplitude to be consistent with the data. Furthermore, observed cube root scaling of pulse attenuation in the presence of a linear mechanism requires that the associated Q be nearly independent of frequency for a constant phase speed. The data from both Cowboy and Salmon both indicate that the effective Q is distinctly smaller at low frequencies which also contradicts the linearity hypothesis. In short, the data from explosively generated pulses indicates that in the strain regime of 10^{-3} to 10^{-6} the attenuation is nonlinear.

Attempts to describe a rheology in terms of the familiar but inappropriate Q function could lead to contradictions since Q is inherently a linear concept. Ideally one would like to determine a constitutive relation between stress and strain which stems from the physical character of the medium and which, given nonlinearity, is generally a function of the character of the propagating pulse, at least for strong pulses.

A major source of guidance in determination of such a relation is the experimentally observed scaling with the cube root of the yield of explosively generated pulse attenuation. In comparing the pulse results for evidence of the character of attenuation, it must be kept in mind that the pulse lengths and shapes immediately after their generation must scale to some degree. This is a consequence of the yield and material strength determining a length scale (which is proportional to the cube root of the yield) while the compressional signal speed then determines an associated time scale. The result is that a point explosion in a particular medium will generate a pulse, immediately outside the strongly inelastic region, which must approximately scale before any attenuation.

The limitations implicit in scaling have been discussed in substantial detail by Trulio [8]. Given an initial pulse which scales, the requirement of having the further

attenuation scaling is very restrictive indicating that the constitutive relation must be a rate independent. Put another way, the requirement is that the medium must not have any inherent length or time scales built in (or at least none which is in the range of the scales of the experiments which have been done). Thus the stress must be expressible in terms of quantities which scale including the strain, the pulse period and the pulse length (note that the energy of the pulse scales). There is no need for the dependence to be linear or local in time or space. An elementary example of a nonlinear constitutive relation which provides scaling (and an effective Q proportional to ω) has been given by McCartor and Wortman[6].

In summary, an examination of the Cowboy data reveals that the attenuation is not of a linear character in as much as the effective Q is a function of both strain and frequency. However, the data from Cowboy along with Salmon and small scale salt tests do fit the rules of simple scaling, i.e., when distances and times are scaled by the cube root of the yield. This provides a powerful constraint on any nonlinear constitutive relation which is to describe the near-field attenuation of seismic pulses as well as indicating that the initial conditions for such propagation must also scale.

SECTION 7

LIST OF REFERENCES

1. Examples of such considerations are: Mueller, R. A. and J. R. Murphy, Seismic Characteristics of Underground Nuclear Detonations, Bull. Seis. Soc. Am., 61, 1975, 1971; and Murphy, J. R., Seismic Coupling and Magnitude/Yield Relations for Underground Nuclear Detonations in Salt, Granite, Tuff/Rhyolite and Shale Emplacement Media, CSC-TR-77-0004, Computer Sciences Corporation, 1977.
2. Larson, D. B., "Inelastic Wave Propagation in Sodium Chloride," Bull. Seis. Soc. Am. 72, 2107 (1982).
3. Perret, W. R., Free-Field Particle Motion from a Nuclear Explosion in Salt, Part I, Project Dribble, Salmon Event, VUF-3012, Sandia Laboratory, 1967.
4. Murphey, B. F., "Particle Motions Near Explosions in Halite," J. Geophys. Res. 66, 947 (1961).
5. Tittmann, B. R., Non-Linear Wave Propagation Study, SC5361.3SAR, Rockwell International Science Center, 1983.
6. McCartor, G. D., and W. R. Wortman, Experimental and Analytic Characterization of Nonlinear Seismic Attenuation, MRC-R-900, Mission Research Corp., 1985.
7. McLaughlin, K. L. and I. N. Gupta, "Strain and Frequency Dependent Attenuation Estimates in Salt from Salmon and Sterling Near-Field Data," Teledyne Geotech, to be submitted to Geophysical Research Letters, 1986.
8. Trulio, J., Simple Scaling and Nuclear Monitoring, ATR-78- 45-1, Applied Theory, Inc., 1978.
9. Trulio, J., Applied Theory, Inc., private communications, 1986.
10. Minister, J. B. and S. M. Day, "Decay of Wave Fields Near an Explosive Source Due to High-Strain Nonlinear Attenuation," J. Geophys. Res. 91, 2113 (1986).
11. Kjartansson, E., "Constant Q-wave Propagation and Attenuation," J. Geophys. Res. 84, 4737 (1980).

Appendix A

COWBOY RAW DATA RECORDS

Project Cowboy, which has been reported in detail by Murphey[1], consisted of the detonation of a series of high-explosive charges buried in a Louisiana salt dome. The charges ranged from 20 to about 2000 pounds. Some charges were placed in 6 or 15 foot radius cavities for demonstration of the decoupling effects of such placement. The other explosions were tamped in their holes to give fully coupled examples. While the purpose of the experiments pertained to decoupling of seismic signals, a variety of moderate strain region measurements were taken using subsurface velocity and displacement gauges. These measurements allow the determination of the decay of explosively generated near-field pulses with range in a relatively uniform medium.

The properties of the shots and the location of instrumentation for the shots are given in Table A-1. Generally there were up to eight measurements for each shot but in most cases there were fewer.

Table A-1. Cowboy measurement properties.

Tamped				15 Foot Cavity				6 Foot Cavity			
Gage	Distance (ft)	Shot No.	W (lbs)	Gage	Distance (ft)	Shot No.	W (lbs)	Gage	Distance (ft)	Shot No.	W (lbs)
1.2.03.V	19.4	1	20	2.1-2-V	50.5	5	200	1.1-2-V	20.7	3	20
1.2-04-V	36			2.1-1-V	79.7			1.1-1-V	35.1		
1.3-7-V	19.3	4	100	2.1-4-V	23.9	6	200	1.1-6-V	36.2		
1.3-8-V	35.9			2.1-2-V	50.5			1.1-5-V	10.6	3	100
2.2-3-V	49	7	200	2.1-1-V	79.5			1.1-2-V	20.7		
2.2-2-V	50.3			2.1-6-V	80			1.1-1-V	35.1		
2.2-1-V	79.4			2.1-11-V	200.1			1.1-6-V	36.2		
2.2-4-V	80.6			2.1-1-V	23.9	8	500	1.1-5-V	19.6	12	929
2.1-17-VB	452.5			2.1-2-V	50.5			1.1-2-V	20.7		
1.2-4-V	157	16	200	2.1-5-V	49.9			1.1-1-V	35.1		
1.2-3-V	173			2.1-5-DR	49.4			1.1-6-V	36.2		
1.3-7-V	223			2.1-1-V	79.7			1.1-9-V2	100.7		
1.3-8-V	207										
2.1-17-VB	431			2.-1-6-V	80			2.1-17-VF	461.2		
2.1-17-VC	431			2.1-11-V	200.1			1.1-5-V	19.6	14	1903.4
1.3-7-V	99	17	200	2.1-17-VA	366.6			1.1-2-V	20.7		
1.3-8-V	116			2.1-4-V	23.9	10	1000	1.1-1-V	35.1		
1.2-3-V	150			2.1-5-V	49.4			1.1-6-V	36.2		
1.2-4-V	167			2.5-5-DR				1.1-9-V2	100.7		
2.1-17-VC	274			2.1-2-V	50.5			2.1-17-VB	461.2		
2.3-2-V	50.5	9	500	2.1-1-V	79.7						
2.3-1-V	79.6			2.1-6-V		80					
2.3-4-V	79.7			2.1-11-V	200.1						
2.1-17-VB	368.8			2.1-17-VA	366.6						
2.4-1-V	77.5	11	1000								
2.4-15-V	208.2										
2.4-15-DR											
2.1-17-VB	477.7										
2.5-4-V	80.9	13	1000								
2.4-15-V	351.7										
2.4-15-DR											
2.1.17.VB	585.5										

Figure A-1 gives reproductions of most of the raw data records from digitized versions of the original analog recordings provided to us by Neil Perl of Applied Theory. As pointed out by Murphey, the coupled shots have reasonable representation of the rapid initial rise of the signal while the decoupled cases (which have higher frequency components) often have a distorted rise due to ringing of the instrument packages. Consequently, the decoupled data must be regarded with some suspicion. The instrument response for the gauges used for Cowboy have not been adequately defined to allow reliable corrections to be applied to the data. Trulio[3] and Thornbrough[2] have recorded those data which do exist. It must be noted that generally more than one type of instrument was used for a given shot so that some care must be taken in making comparisons. Even in those cases for this the same type instrument was used, the responses may differ for different range settings.

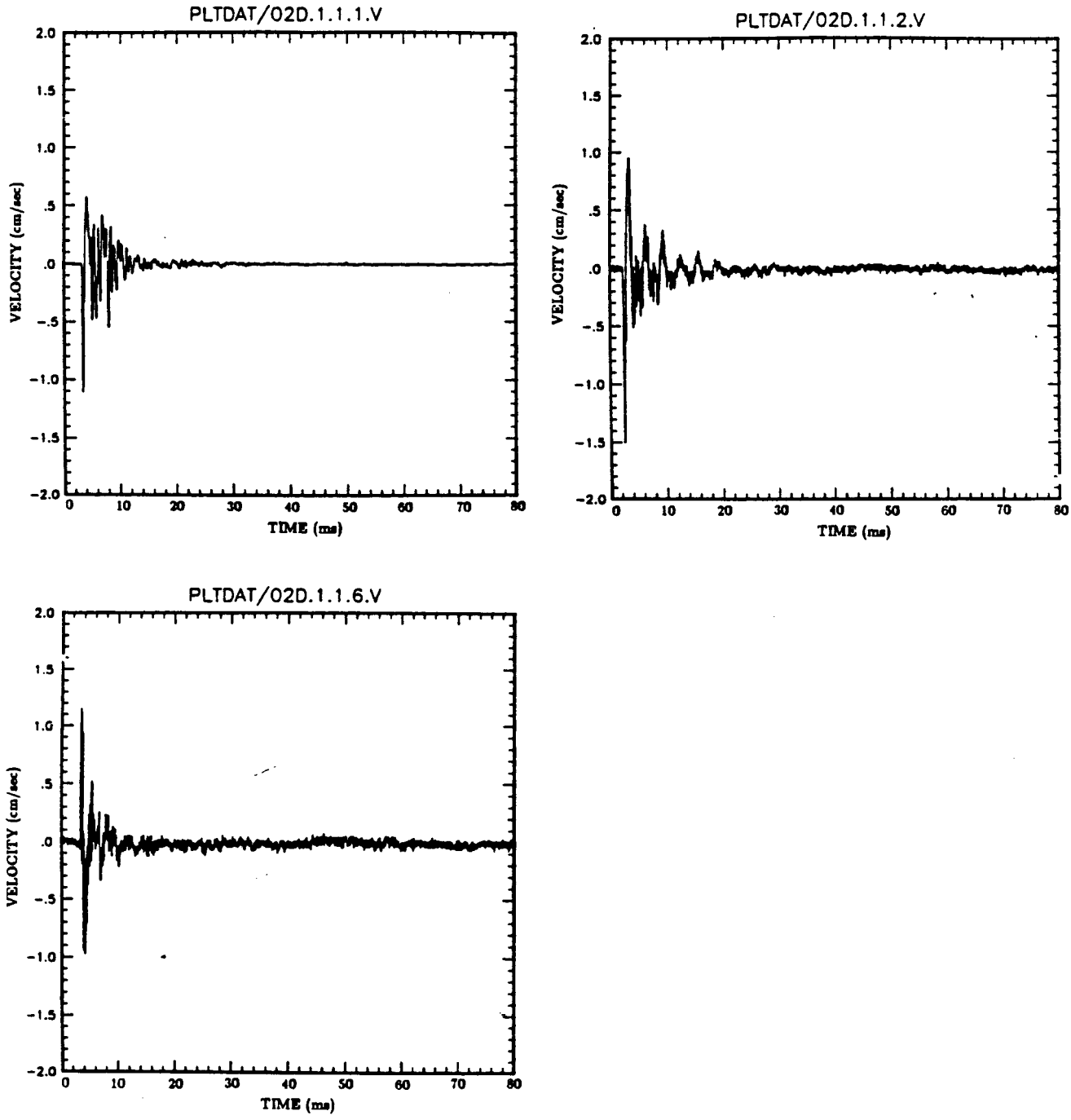

Figure A-1. Cowboy raw data records.

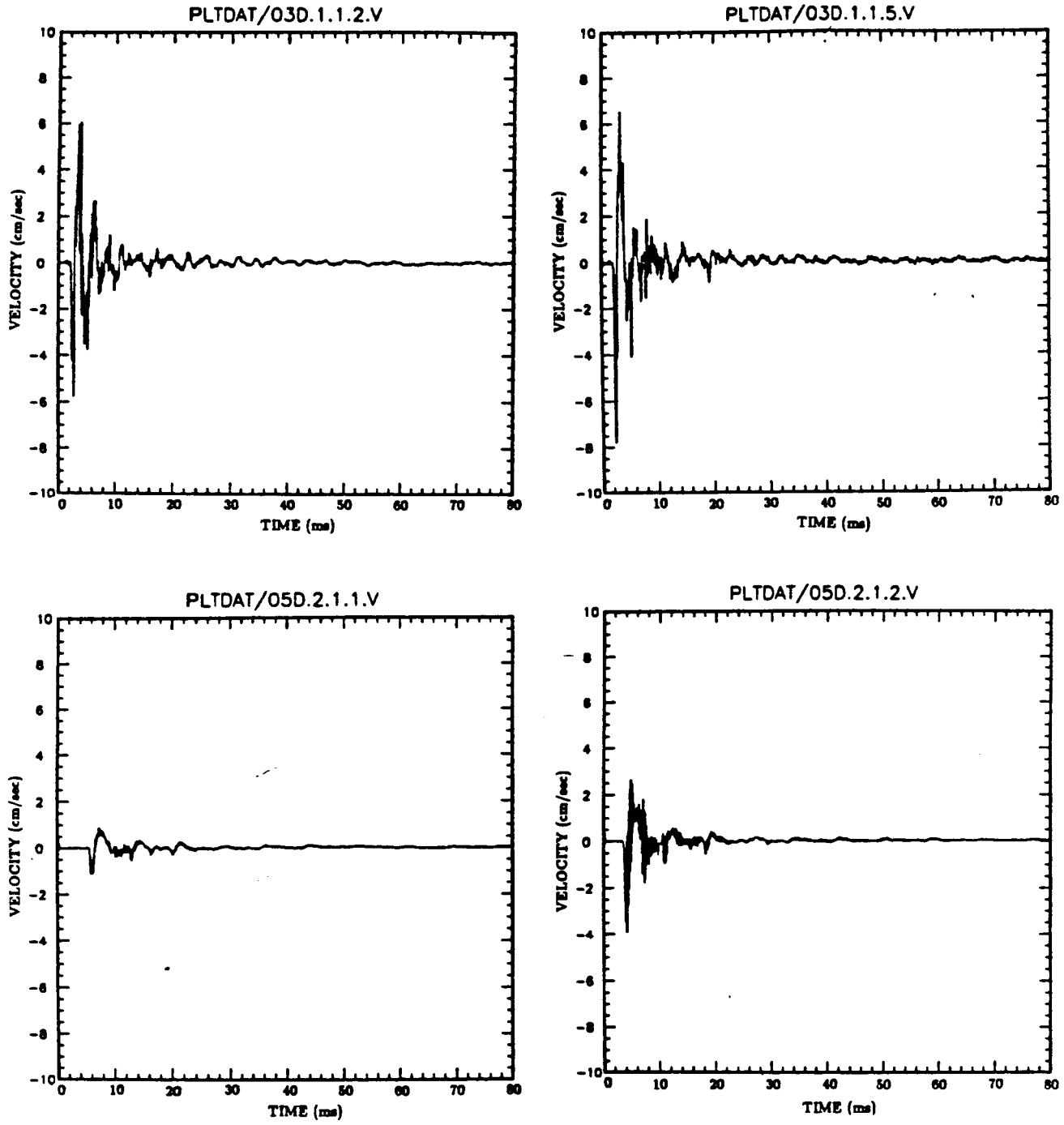

Figure A-1. Cowboy raw data records (continued).

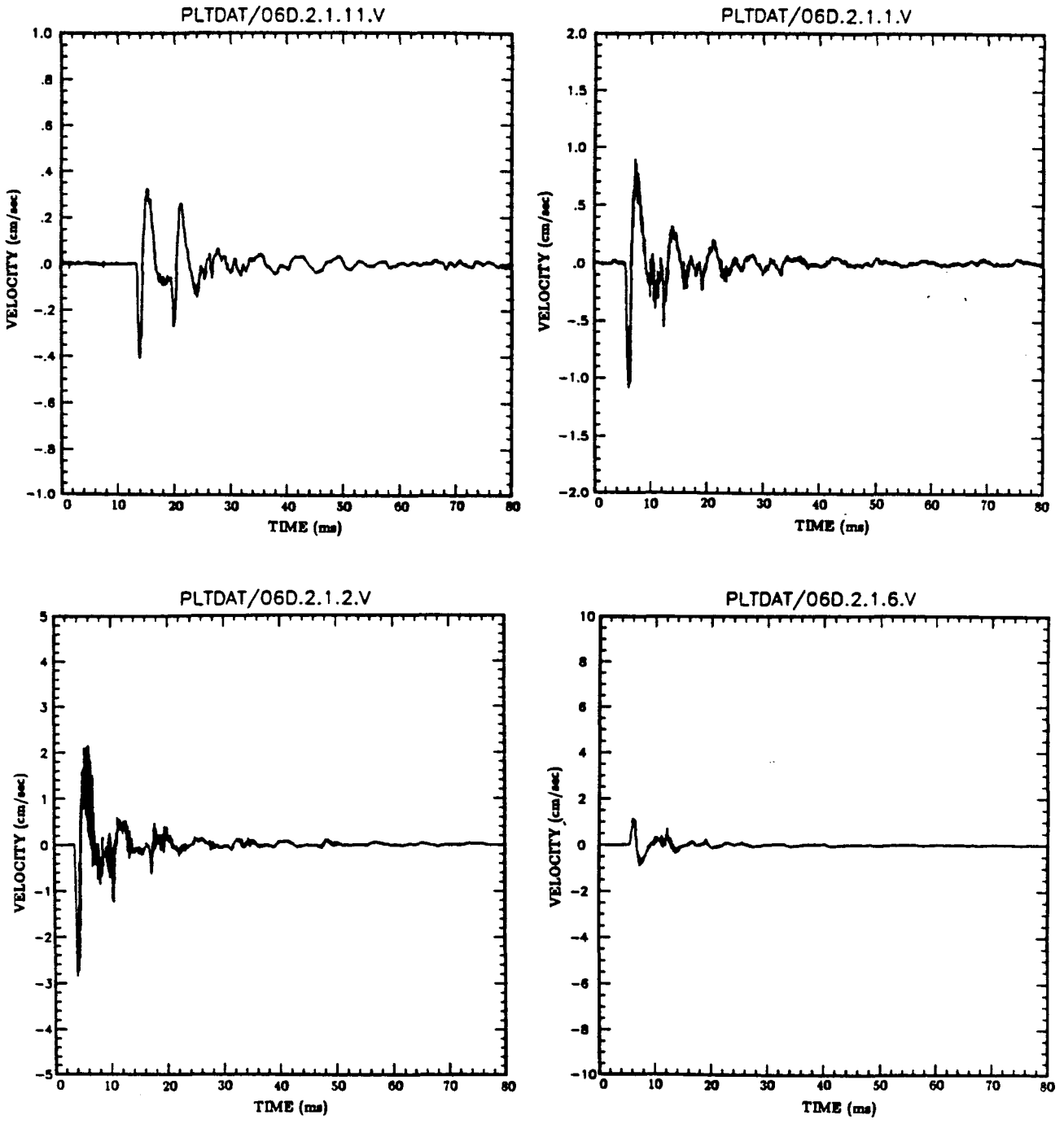

Figure A-1. Cowboy raw data records (continued).

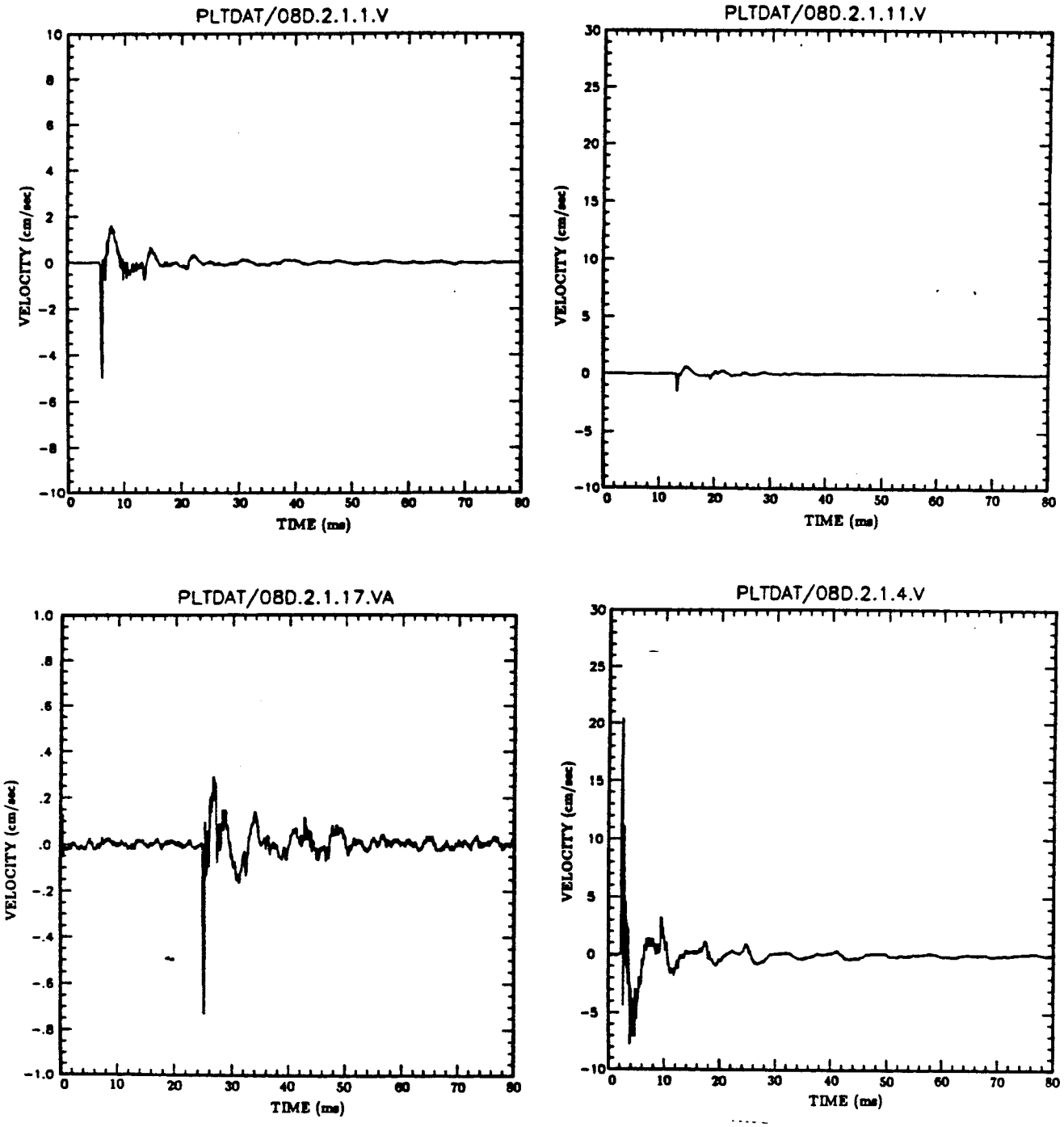

Figure A-1. Cowboy raw data records (continued).

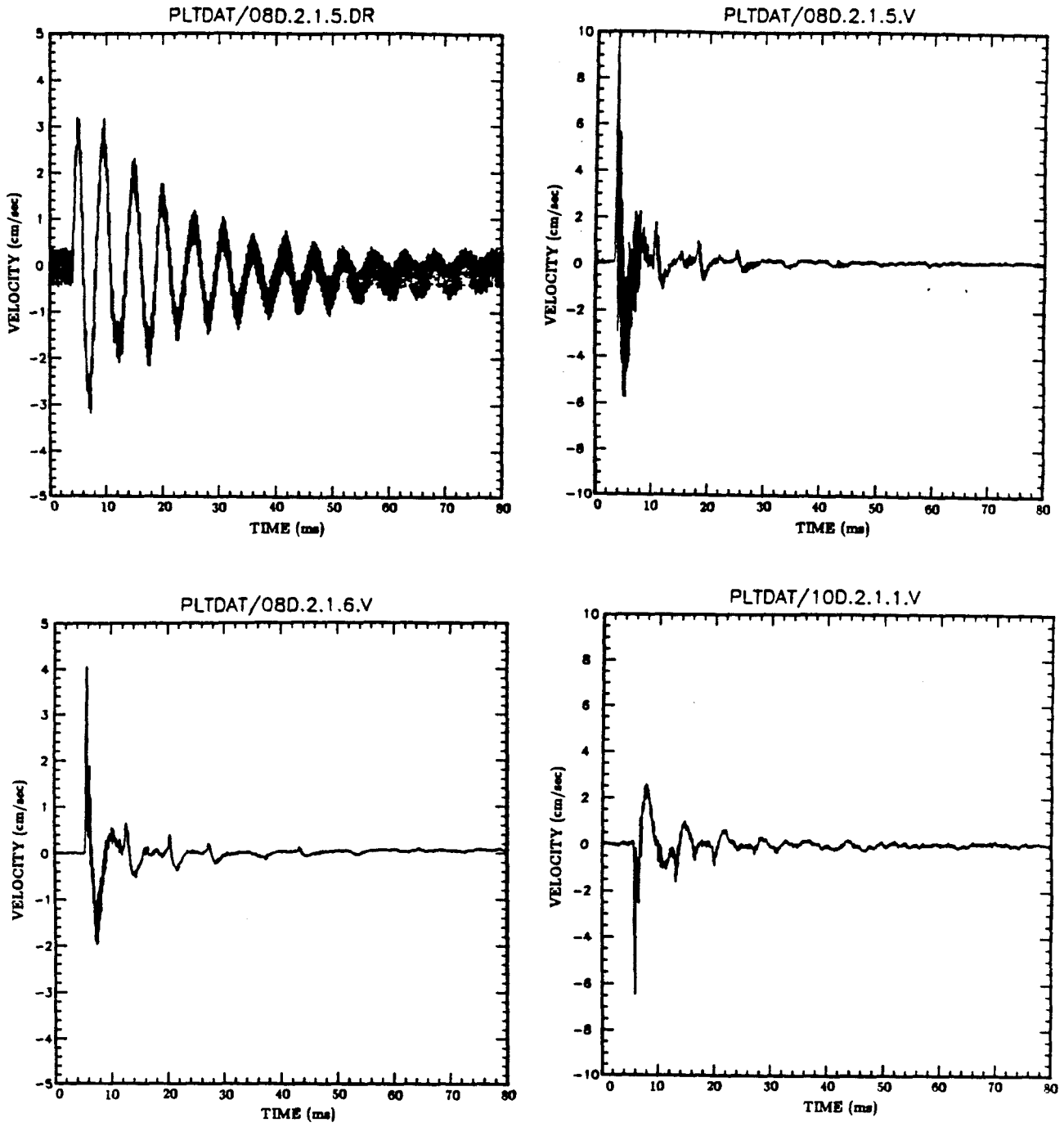

Figure A-1. Cowboy raw data records (continued).

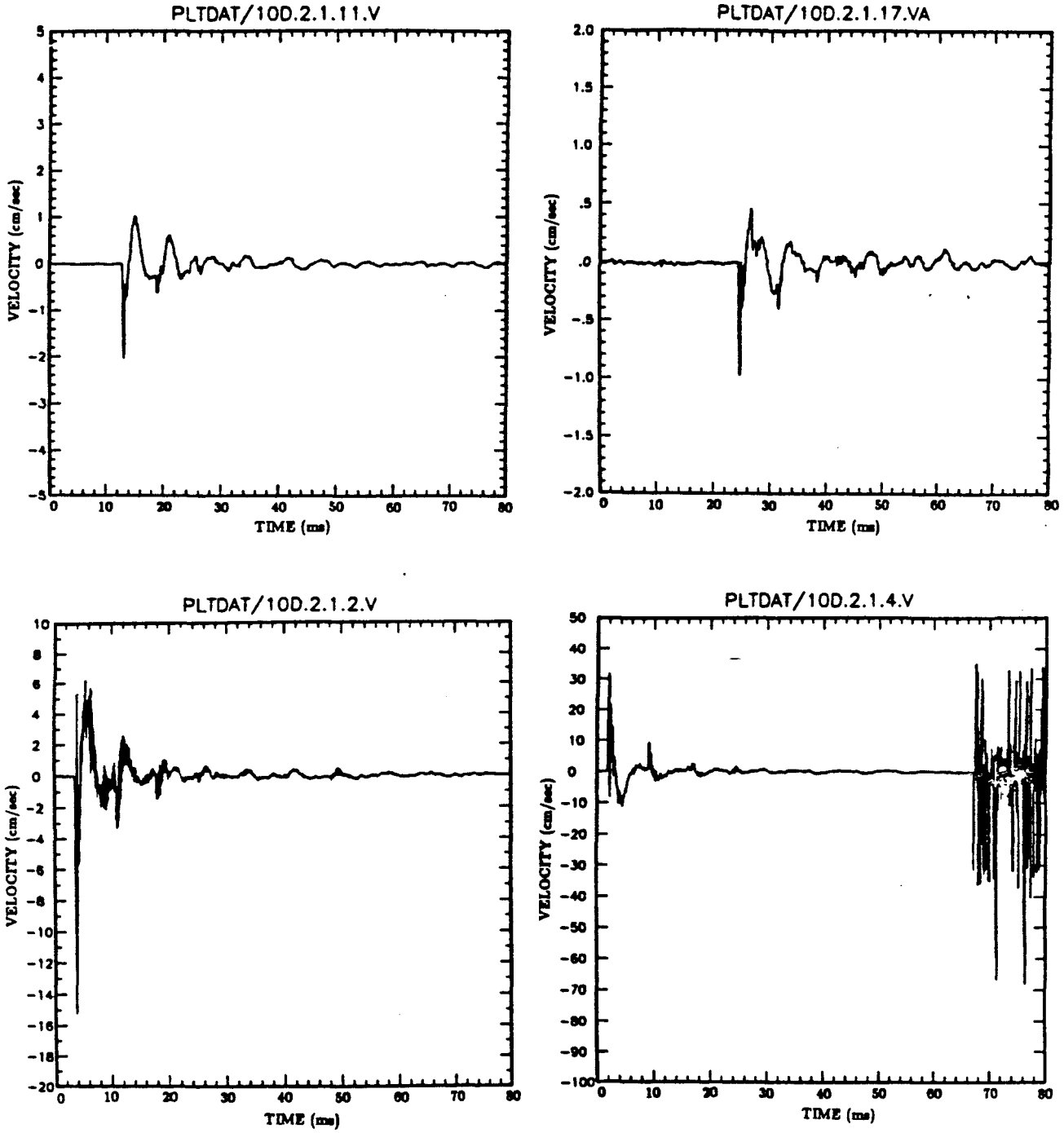

Figure A-1. Cowboy raw data records (continued).

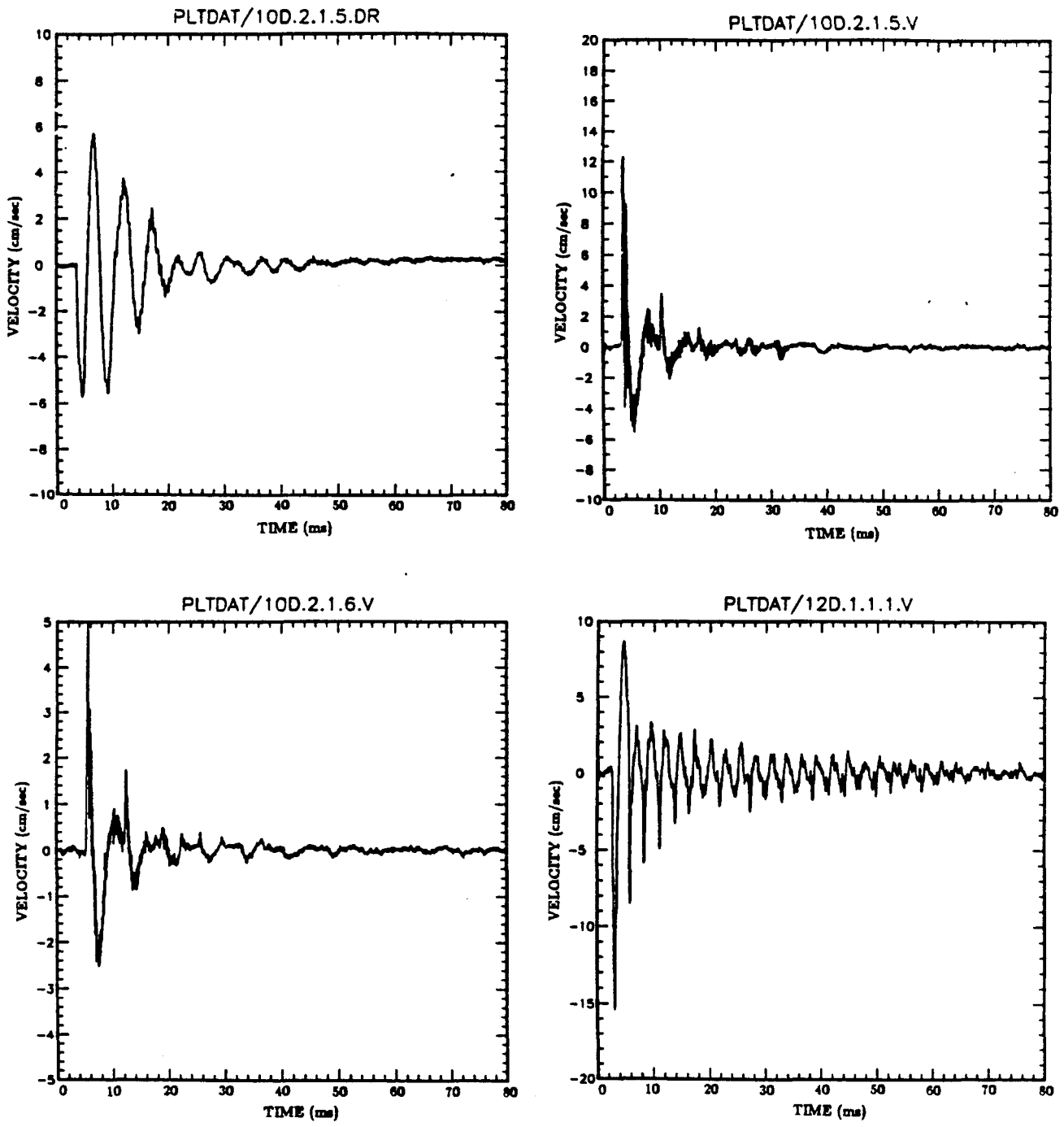

Figure A-1. Cowboy raw data records (continued).

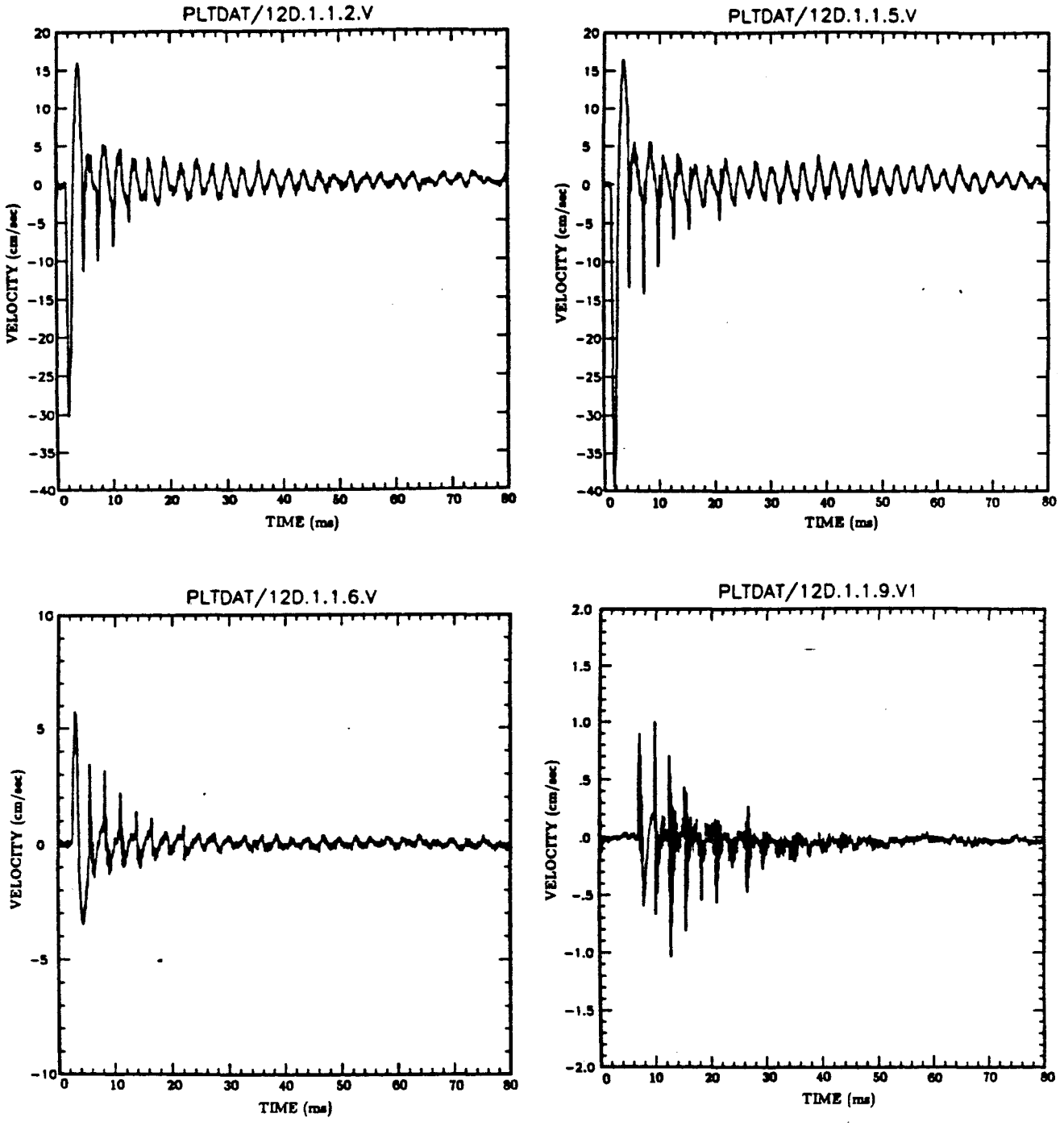

Figure A-1. Cowboy raw data records (continued).

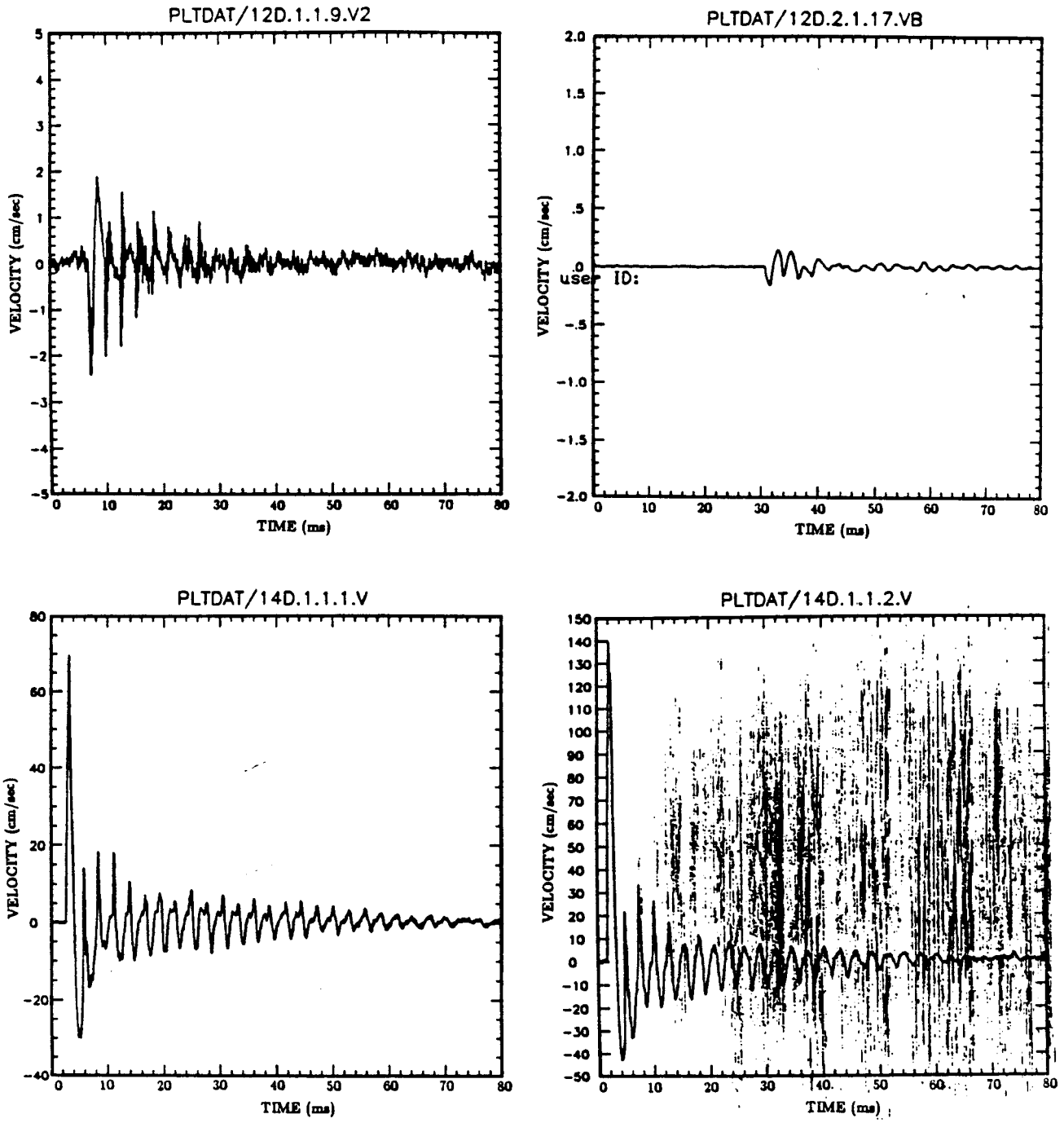

Figure A-1. Cowboy raw data records (continued).

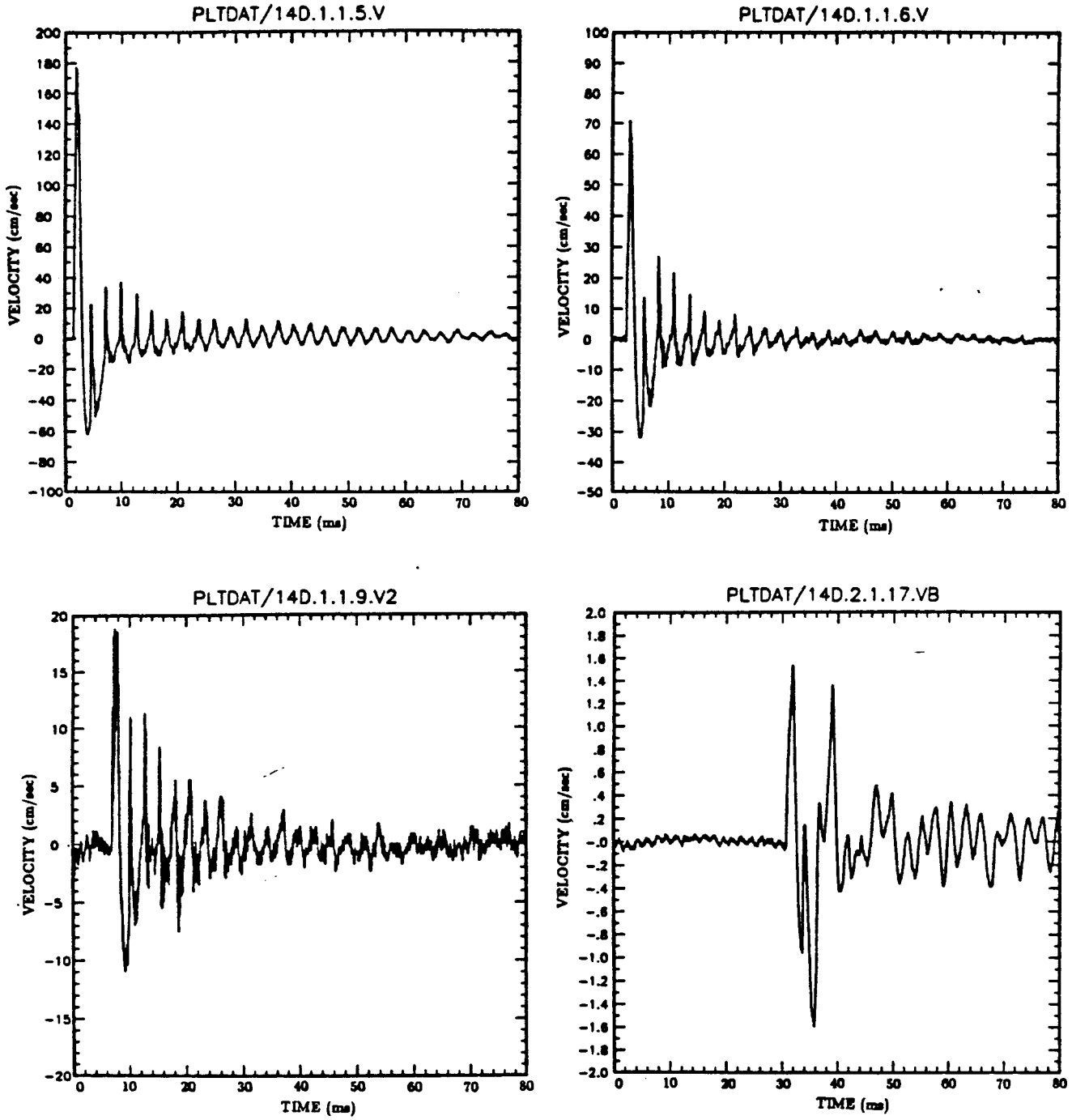

Figure A-1. Cowboy raw data records (continued).

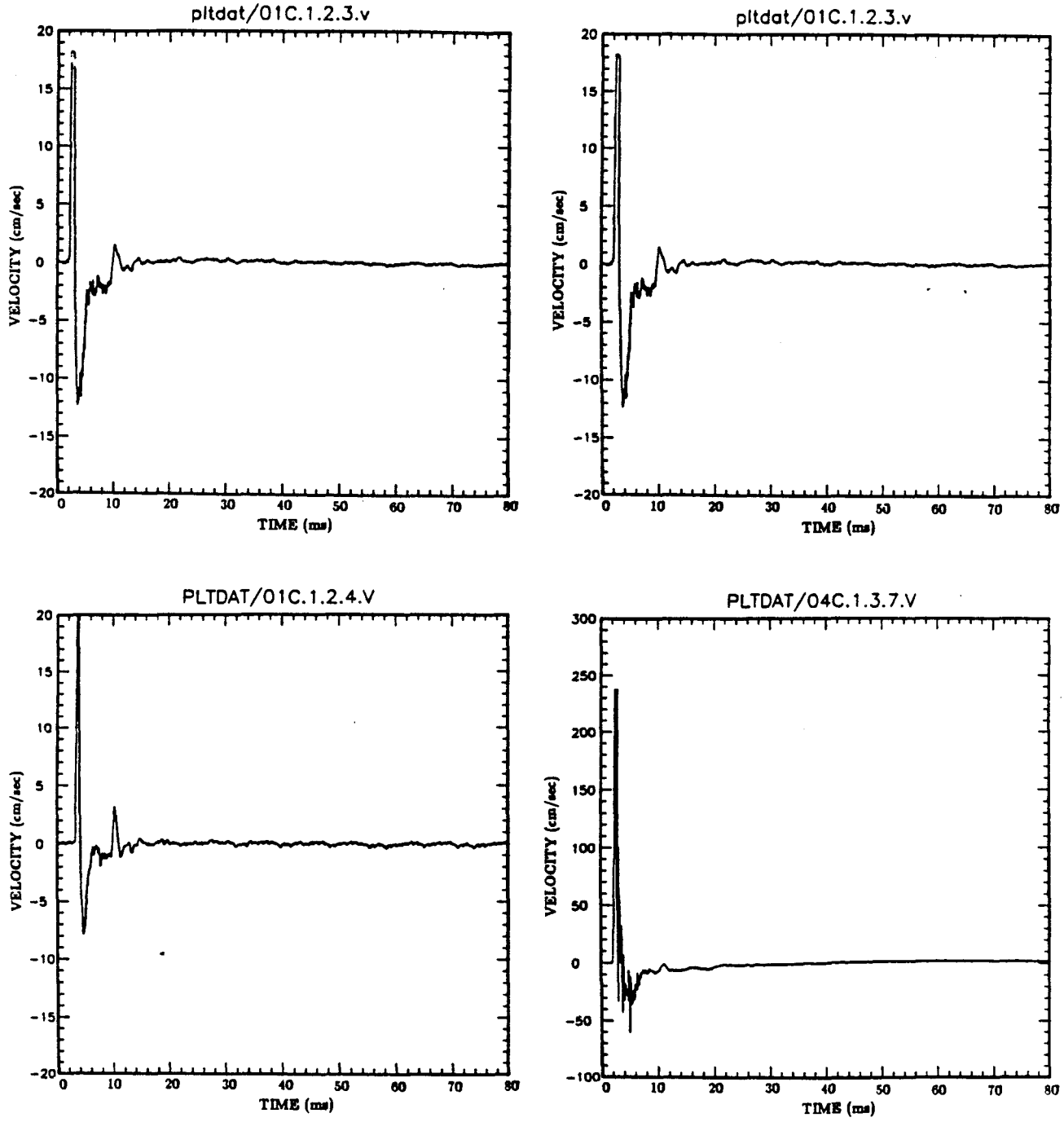

Figure A-1. Cowboy raw data records (continued).

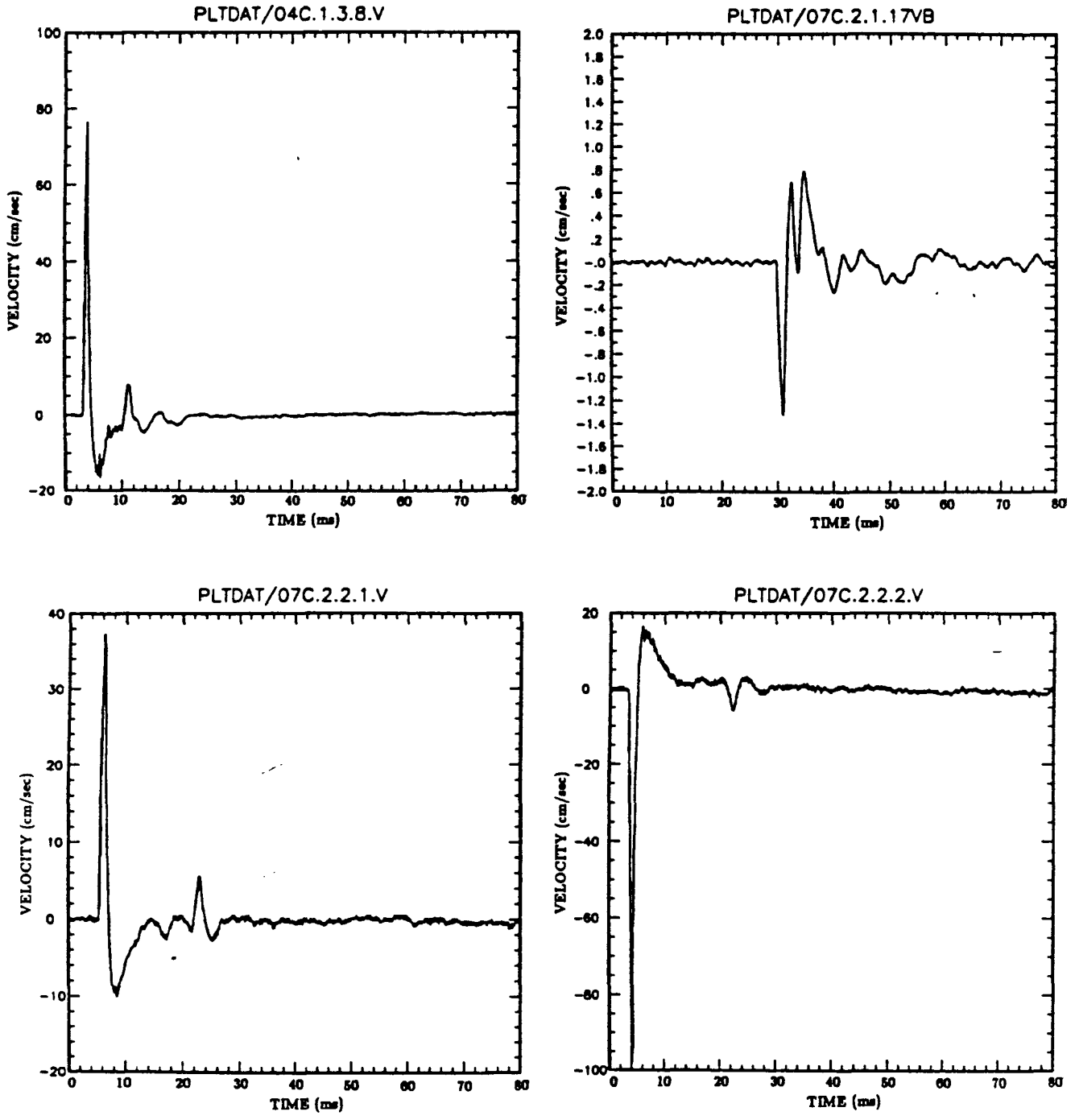

Figure A-1. Cowboy raw data records (continued).

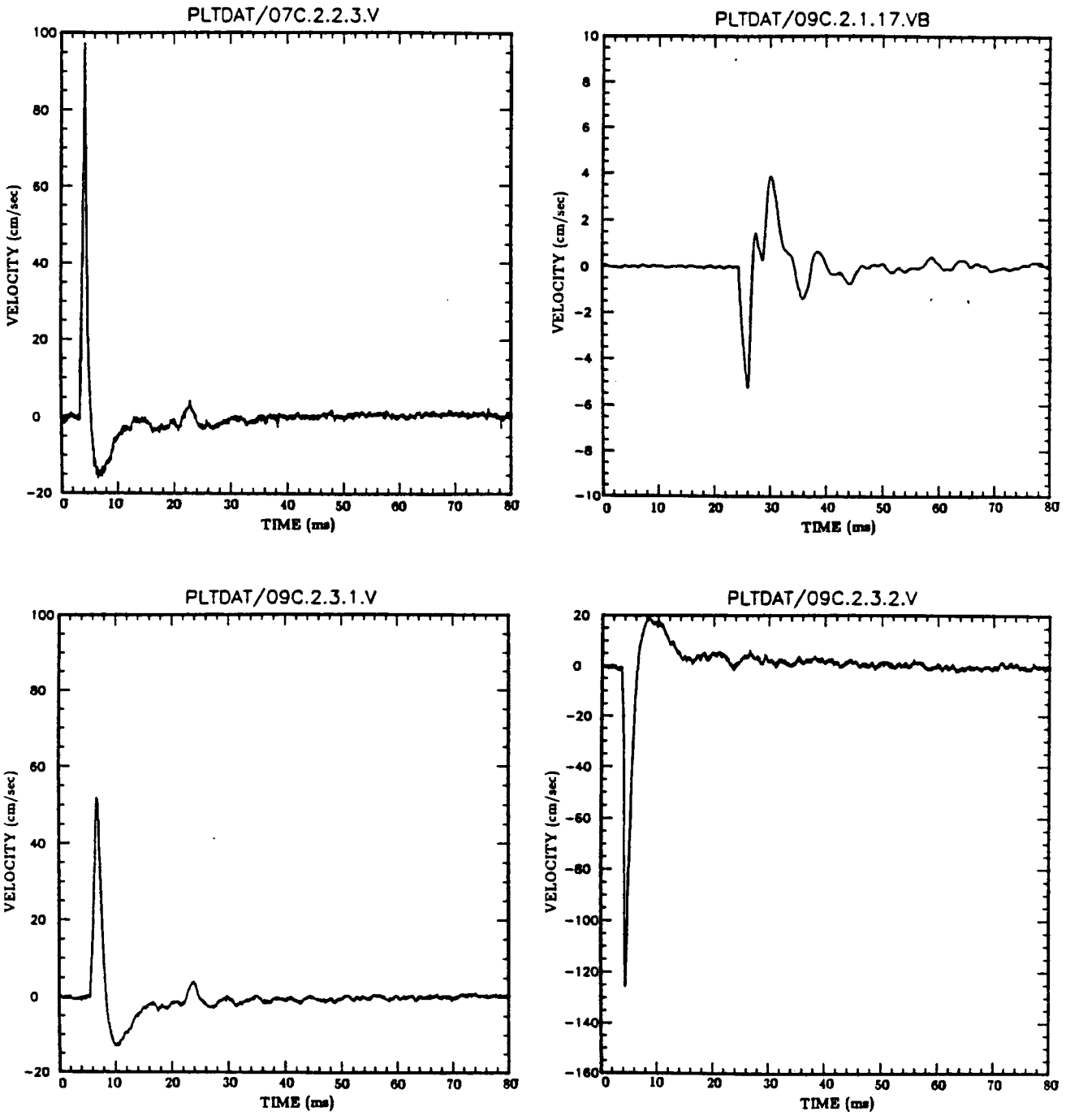

Figure A-1. Cowboy raw data records (continued).

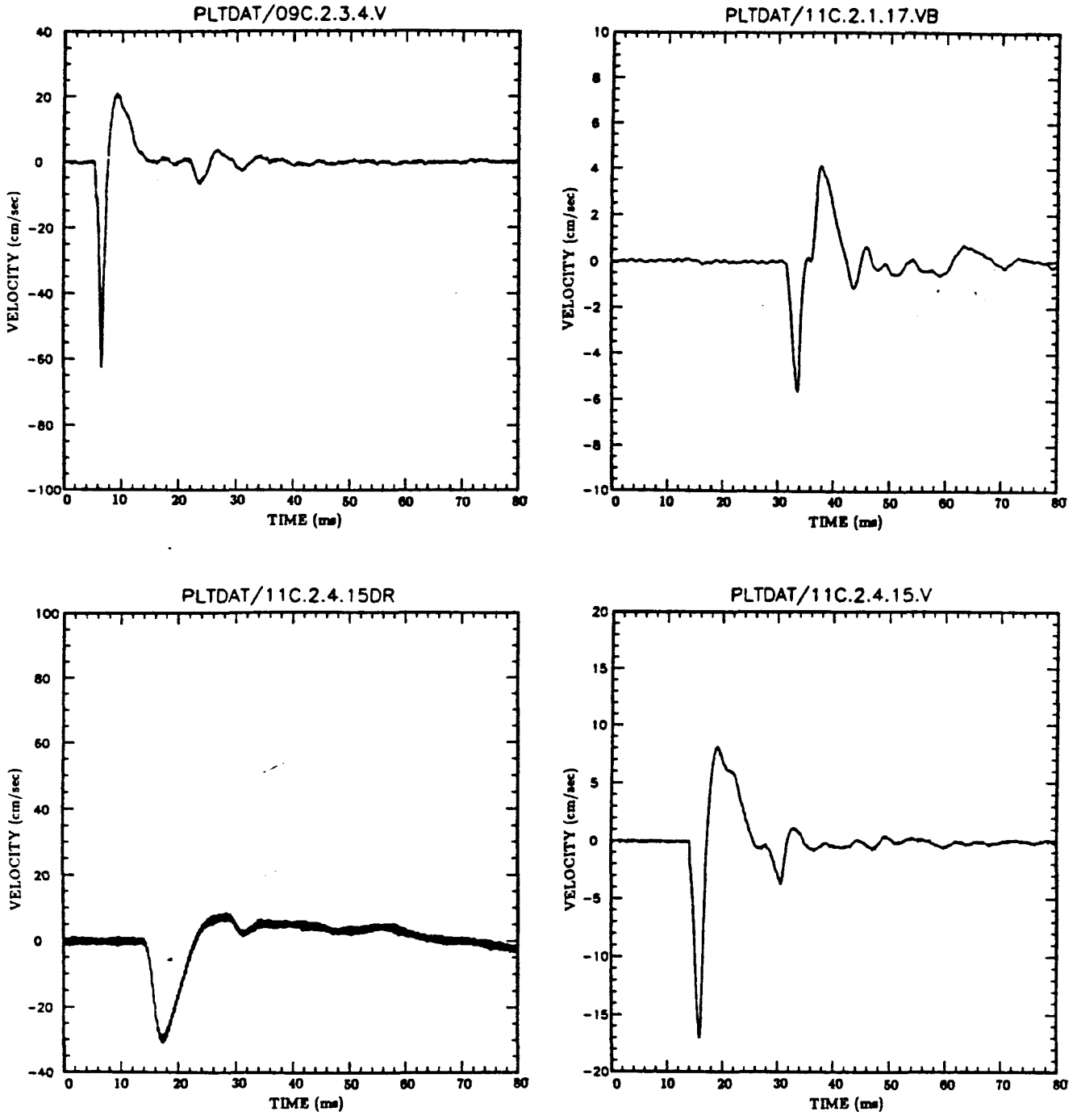

Figure A-1. Cowboy raw data records (continued).

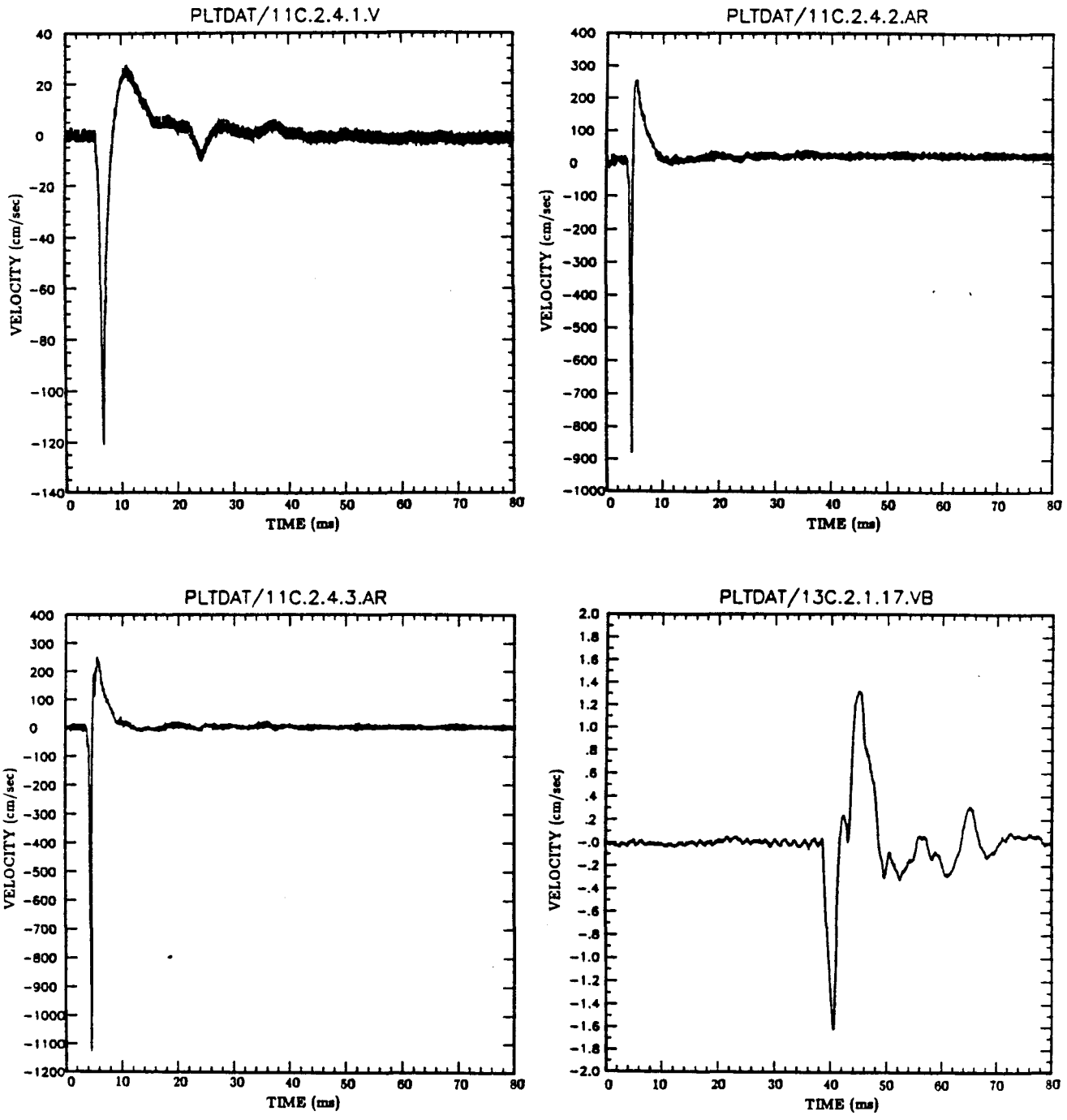

Figure A-1. Cowboy raw data records (continued).

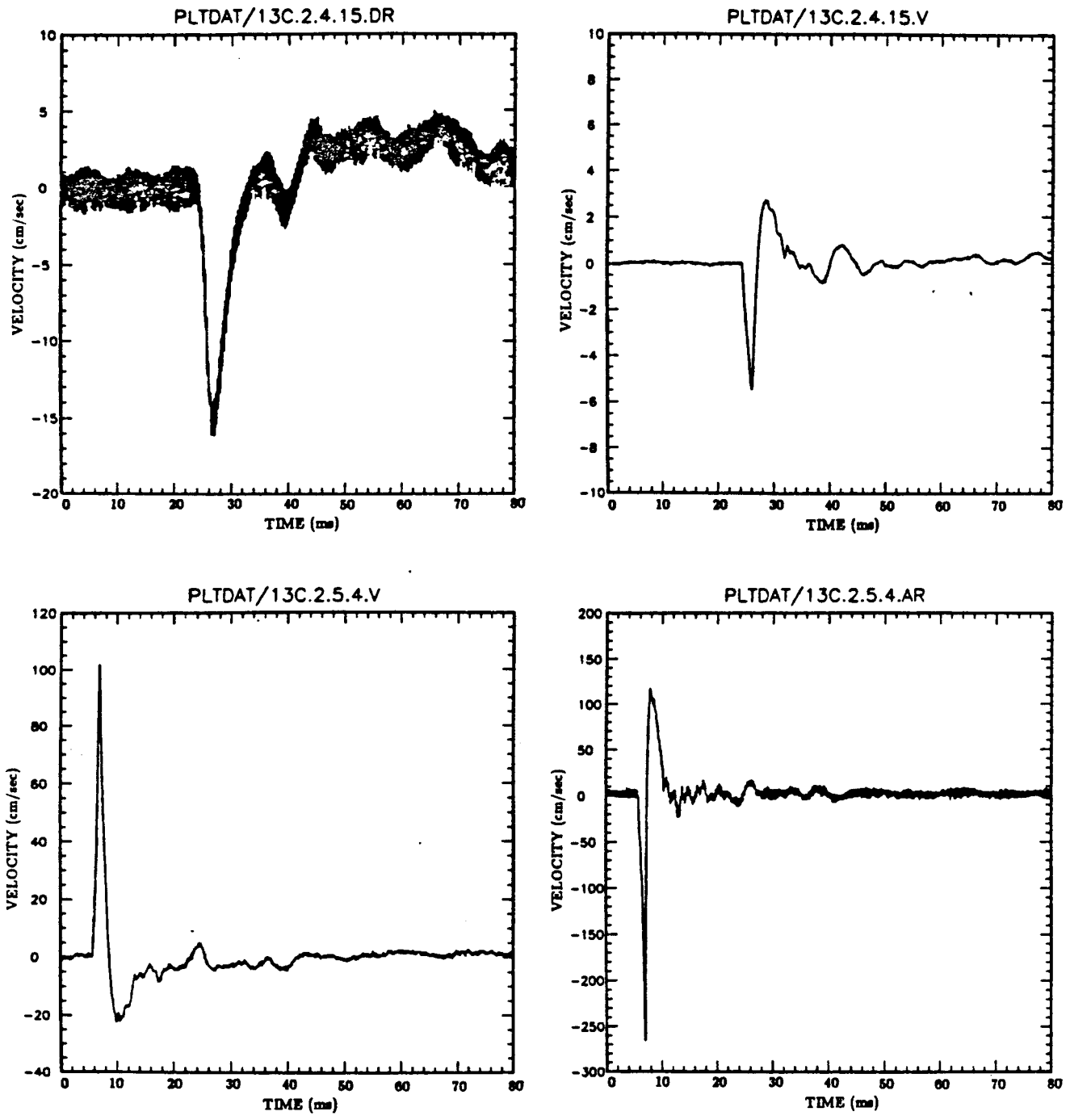

Figure A-1. Cowboy raw data records (continued).

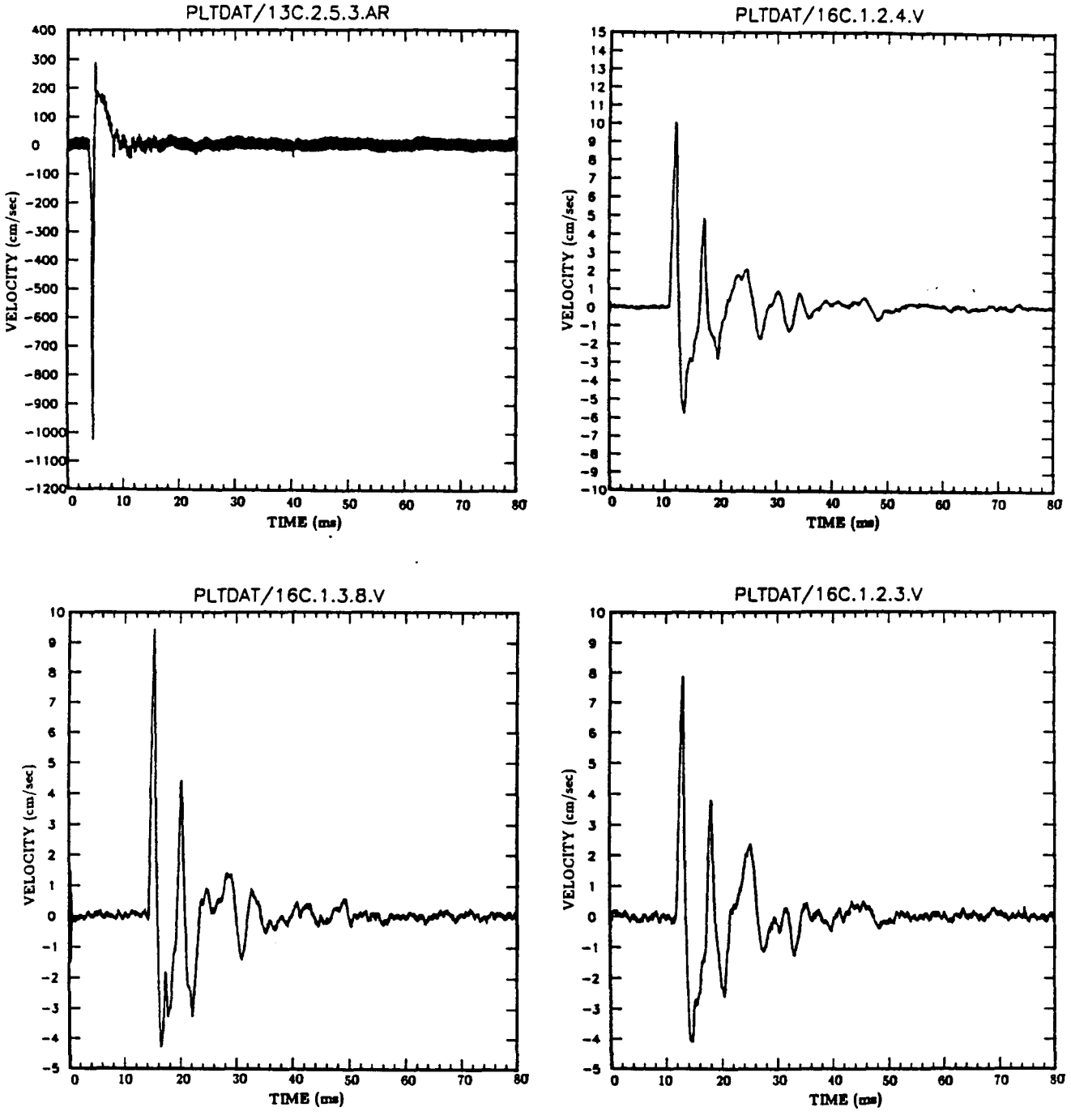

Figure A-1. Cowboy raw data records (continued).

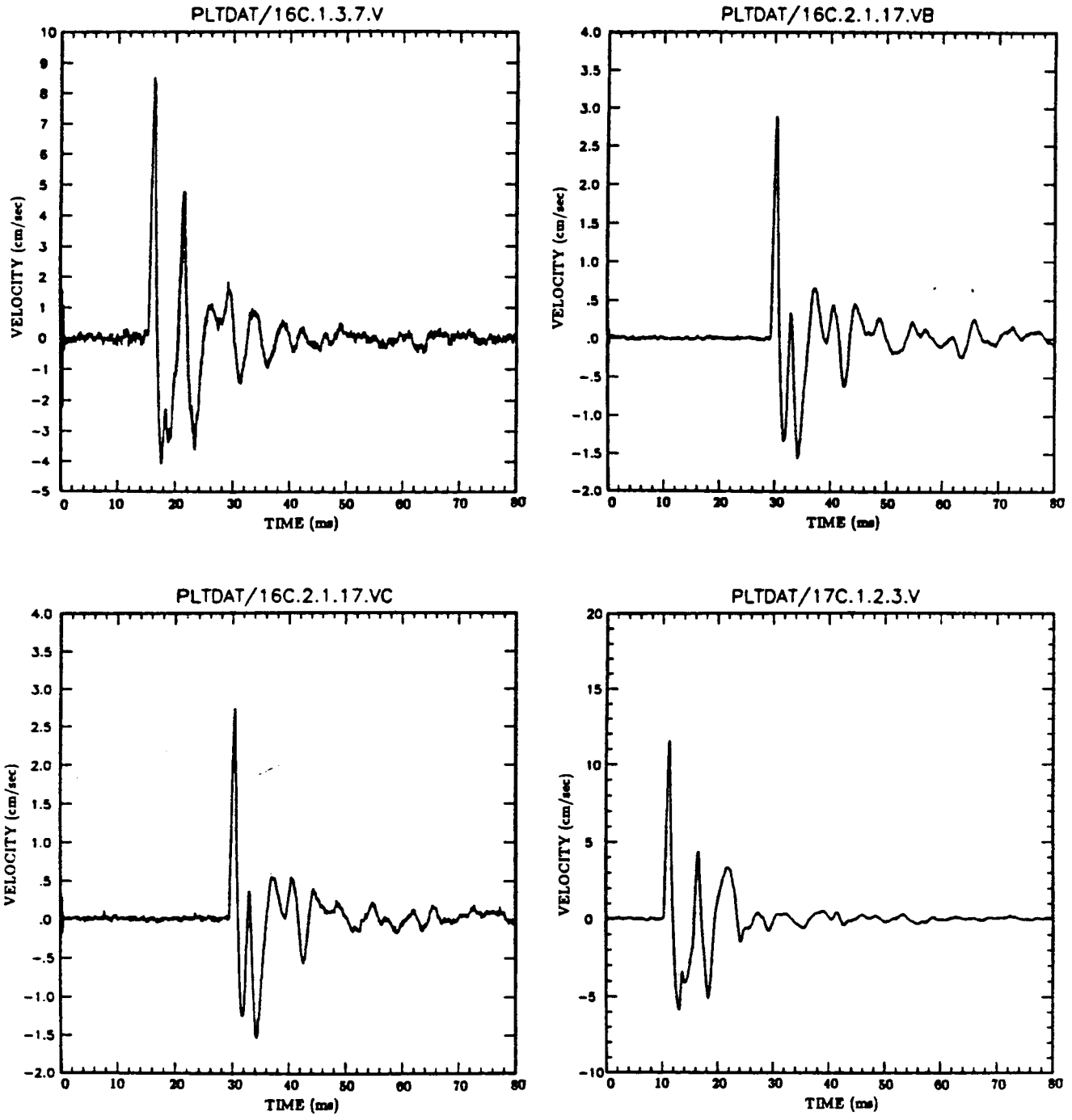

Figure A-1. Cowboy raw data records (continued).

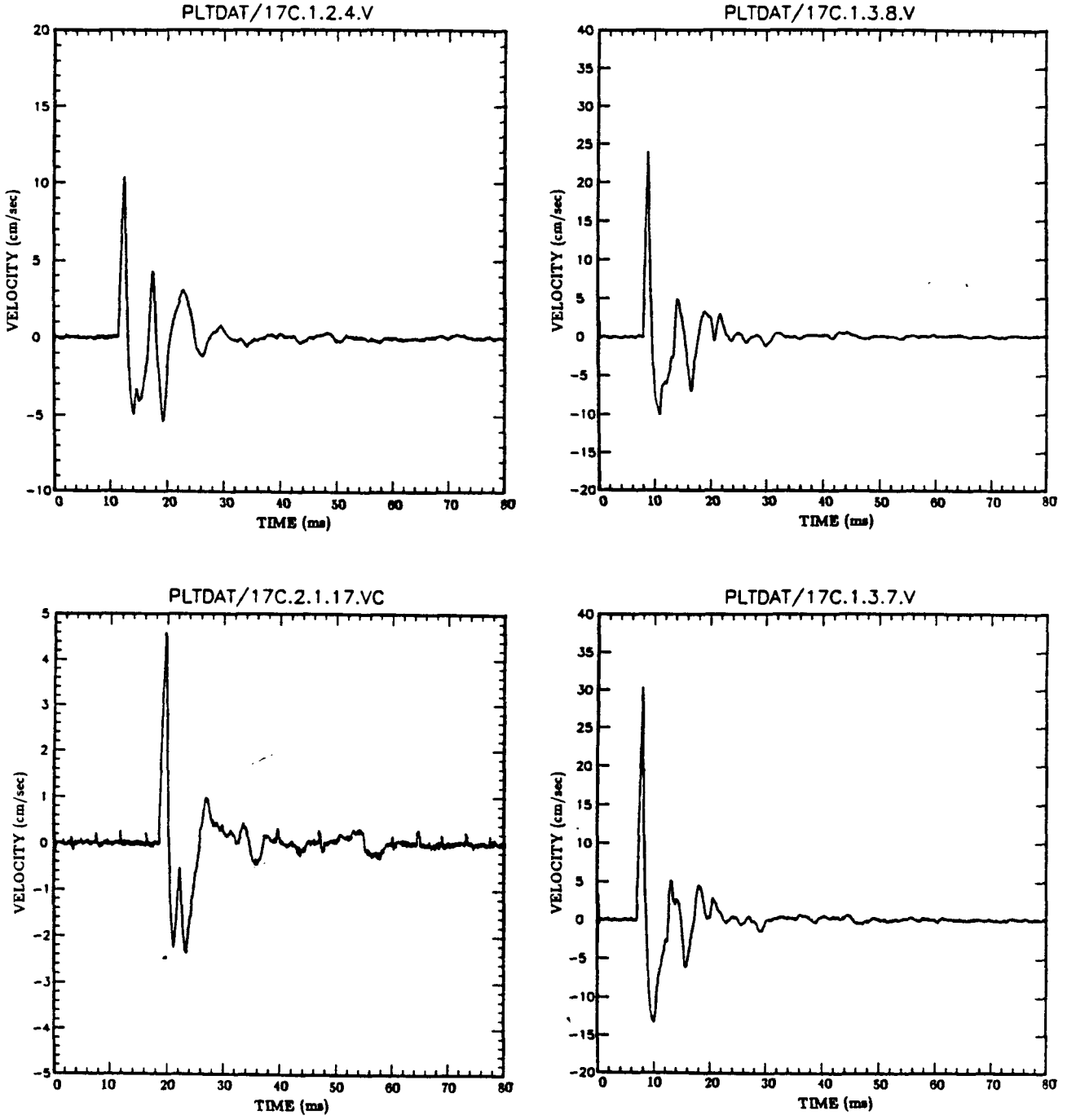

Figure A-1. Cowboy raw data records (continued).

APPENDIX A REFERENCES

A–1 Murphey, B. F., "Particle Motions Near Explosions in Halite," J. Geophys. Res. 66, 947 (1961).

A–2 Thornbrough, A. D., E. S. Ames and H. L. Hawk, INSTRUMENTATION SYSTEMS—Project Cowboy, SC-4470(RR), Sandia Corp., 1960.

A–3 Trulio, J., Simple Scaling and Nuclear Monitoring, ATR-78- 45-1, Applied Theory, Inc., 1978.

Appendix B

CONSTANT Q FORMULATION

B.1 Techniques for Pulse Propagation

The basic structure of the equations of motion for a spherical pulse propagating in an isotropic medium can be expressed as

$$\rho \frac{\partial^2 u}{\partial t^2} = \frac{1}{r^2}\left(\frac{\partial}{\partial r}\left(r^2 \sigma_{rr}\right)\right) - \frac{2}{r}\sigma_{\theta\theta} \qquad (B-1)$$

where the stress components, σ, are related to the strain components, ϵ, which are provided by the radial displacement u through

$$\epsilon_{rr} = \frac{\partial u}{\partial r}$$

and

$$\epsilon_{\theta\theta} = \frac{u}{r}$$

It is necessary to have or find some constitutive relation between ϵ and σ in order to fix the propagation of a pulse. If a linear relation between ϵ and σ is taken, a general form which is convenient to work with is as follows:

$$\sigma_{rr} = (\lambda + 2u)\int m(t-\tau)\,\epsilon_{rr}(\tau)d\tau + 2\lambda \int m(t-\tau)\,\epsilon_{\theta\theta}(\tau)d\tau$$

and

$$(B-2)$$

$$\sigma_{\theta\theta} = (\lambda + 2u)\int m(t-\tau)\,\epsilon_{\theta\theta}(\tau)d\tau + \lambda \int m(t-\tau)\,\epsilon_{rr}(\tau)d\tau$$

where m(t) is the derivative of the relaxation function. If m(t) is a delta function, the relations reduce to the standard elastic result with the Lame constants λ and μ. If we introduce the definition of the reduced displacement potential, ϕ, as

$$u(r,t) = \frac{\partial}{\partial r}\left(\phi(r,t)/r\right) \qquad (B-3)$$

the equation of motion can be written in compact form in the frequency domain as

$$\frac{\partial}{\partial r}\left(\frac{1}{r}\left(\rho\omega^2\tilde{\phi} + \tilde{m}(\omega)(\lambda+2\mu)\frac{\partial^2}{\partial r^2}\tilde{\phi}\right)\right) = 0 \qquad (B-4)$$

where $\tilde{\phi}$ will generally be a function of both r and ω. From this form we see that the advancement of ϕ can be expressed as

$$\phi(r,t) = \frac{1}{2\pi}\int \tilde{\phi}(0,\omega)\, e^{-i\omega t}\, e^{i\omega r/\alpha\sqrt{\tilde{m}}}\, d\omega \qquad (B-5)$$

where the apparent p-wave velocity is given by

$$\alpha^2 = (\lambda+2\mu)/\rho \qquad (B-6)$$

and $\tilde{\phi}(0,\omega)$ is the Fourier transform of the ϕ at r=0.

Kjartannson [1] has shown that there is a choice for m(t) which will give a Q which is exactly constant and which provides a phase velocity which is nearly constant over a wide range of frequency provided Q is not too small. This choice for m is

$$\tilde{m}(\omega) = \left|\frac{\omega}{\omega_0}\right|^{2\gamma}\exp\left(i\pi\gamma\,\mathrm{sgn}(\omega)\right) \qquad (B-7)$$

where γ and ω_0 are arbitrary real parameters. Thus $\alpha\sqrt{m}$ is the complex p-wave velocity. The observed pulse propagation velocity can be used to fix the value of ω_0 and the parameter γ can be expressed in terms of a constant Q by noting that the phase relation between ϵ and σ gives Q which can then be written as

$$Q^{-1} = \tan(\pi\gamma) \quad . \qquad (B-8)$$

We can write

$$\phi(r,t) = \frac{1}{2\pi}\int d\omega\, \tilde{\phi}(0,\omega)\exp\left(-i\omega\left(t-\frac{r}{c}\right)\right)\cdot\exp\left(-\omega r\ \mathrm{sgn}(\omega)/(2cQ)\right) \qquad (B-9)$$

where

$$c = c_0|\frac{\omega}{\omega_0}|^{\gamma} / \cos(\pi\gamma/2) \qquad (B-10)$$

So that the displacement will be advanced by

$$u(r,t) = \frac{1}{2\pi}\int d\omega\, u(a,\omega)\ \exp\left(-i\omega\left(t-\frac{r-a}{c}\right) - \omega(r-a)\,\mathrm{sgn}(\omega)/(2cQ)\right)$$

$$\times \frac{\frac{i\omega}{cr} - \frac{\omega\,\mathrm{sgn}(\omega)}{2cQr} - \frac{1}{r^2}}{\frac{i\omega}{ca} - \frac{\omega\,\mathrm{sgn}(\omega)}{2cQa} - \frac{1}{a^2}} \qquad (B-11)$$

While equation B-9 is specific to the Kjartannson assumptions, it provides a generic form which is often taken to be an indication of the attenuation which is associated with Q. That is, we see that Q forces an exponential decay with range of the RDP by a factor

$$\exp\left(-\frac{\omega r}{2cQ}\right) \quad ,$$

and this provides a common definition of Q which is applied to experimental data by taking the phase velocity c to be constant, normally at the nominal speed of the pulse. Again, this is possible only because c is at most a slowly changing function of frequency so that the pulse retains a form which does not change greatly with range.

Manipulating the relations among the RDP, Q and the velocity in the frequency domain provides an operational definition of the experimental value of Q through the equation

$$\exp\left(\frac{\omega(r-a)}{2cQ}\right) = \left|\frac{\tilde{v}(r,\omega)}{\tilde{v}(a,\omega)}\right| \frac{\left|\frac{i\omega}{ca} - \frac{\omega}{2cQa} - \frac{1}{a^2}\right|}{\left|\frac{i\omega}{cr} - \frac{\omega}{2cQr} - \frac{1}{r^2}\right|} \qquad (B-12)$$

which provides an implicit expression for Q from the data. In practice it is found that the second term on the right hand side of equation B-12 is nearly independent of Q for Q not too small that one can write

$$\exp\left(-\frac{\omega(r-a)}{2cQ}\right) = \left|\frac{\tilde{v}(r,\omega)}{\tilde{v}(a,\omega)}\right| \frac{\left|\frac{i\omega}{a} - \frac{c}{a^2}\right|}{\left|\frac{i\omega}{r} - \frac{c}{r^2}\right|} \quad . \qquad (B-13)$$

APPENDIX B REFERENCE

B–1 Kjartansson, E., "Constant Q-wave Propagation and Attenuation," J. Geophys. Res. 84, 4737 (1980).

Appendix C

LLNL DOME SALT SMALL SCALE EXPERIMENT

In May of 1987, a small scale simulation of explosively generated pulse propagation in a dome salt model was carried out at Lawrence Livermore National Laboratory. For this a 0.622 kJ sample of high explosive was detonated in a mined salt block approximately one cubic meter in volume. Velocity sensors were placed at several ranges from the source so that the attenuation could be determined. The ranges to the sensors along with other properties are indicated in Table C-1. The raw data records from the sensors are reproduced in Figure C-1.

The times for onset of signal at the sensors and the times for the first peak signal are given in Figure C-2. Note that there is some irregularity in the propagation speeds between various pairs of sensors (with a mean speed of 3.2 km/sec). This is thought to result from inhomogeneities in the block associated with the cutting and reassembly required to insert sensors in the material. Peak velocities and displacements (as determined by a direct integration of the velocity records) are given in Figure C-3. There is a substantial level of fluctuation in the peak values which again is taken to indicate that the model is not ideal. Consequently, there must be considerable uncertainty in interpretation of the results.

We have attempted to estimate the effective Q associated with the attenuation by forming the ratio of the RVPs taken from "corrected" records, that is, those with the obviously inappropriate tails smoothly removed after the first cycle. Figure C-4 shows the corrected records 4 and 7 (mean strain $\approx 2 \times 10^{-5}$), the RVPs and a scatter plot of the Q as a function of frequency. There is substantial scatter in the results. This is associated with noisy character of the data. The only trends which seem clear are the tendency for Q to be small at frequencies below the corner frequency ($\approx 6 \times 10^3$ Hz), and for Q to increase fairly quickly above. Above about 10^5 Hz the noise swamps the signal. The Q value in the neighborhood of the corner is less than 5. In spite of the small Q and substantial amplitude difference between the pair, the noise is sufficiently large to cast doubt on the result. A pair with a wider range of amplitudes, records 4 and 13, is shown in Figure C-5. For this case (with peak strains of 4×10^{-5} and 2×10^{-6}) the Q shows the same trends but it may be somewhat larger which is consistent with

Table C-1. DOME06 Sensor Properties.

Sensor #	Range (meters)
1	0.076
2	0.076
3	0.129
4	0.129
5	0.227
6	0.227
7	0.370
8	0.370
9	0.556
10	0.556
11	0.755
12	0.755
13	0.957
14	0.957
15	1.170
16	1.170

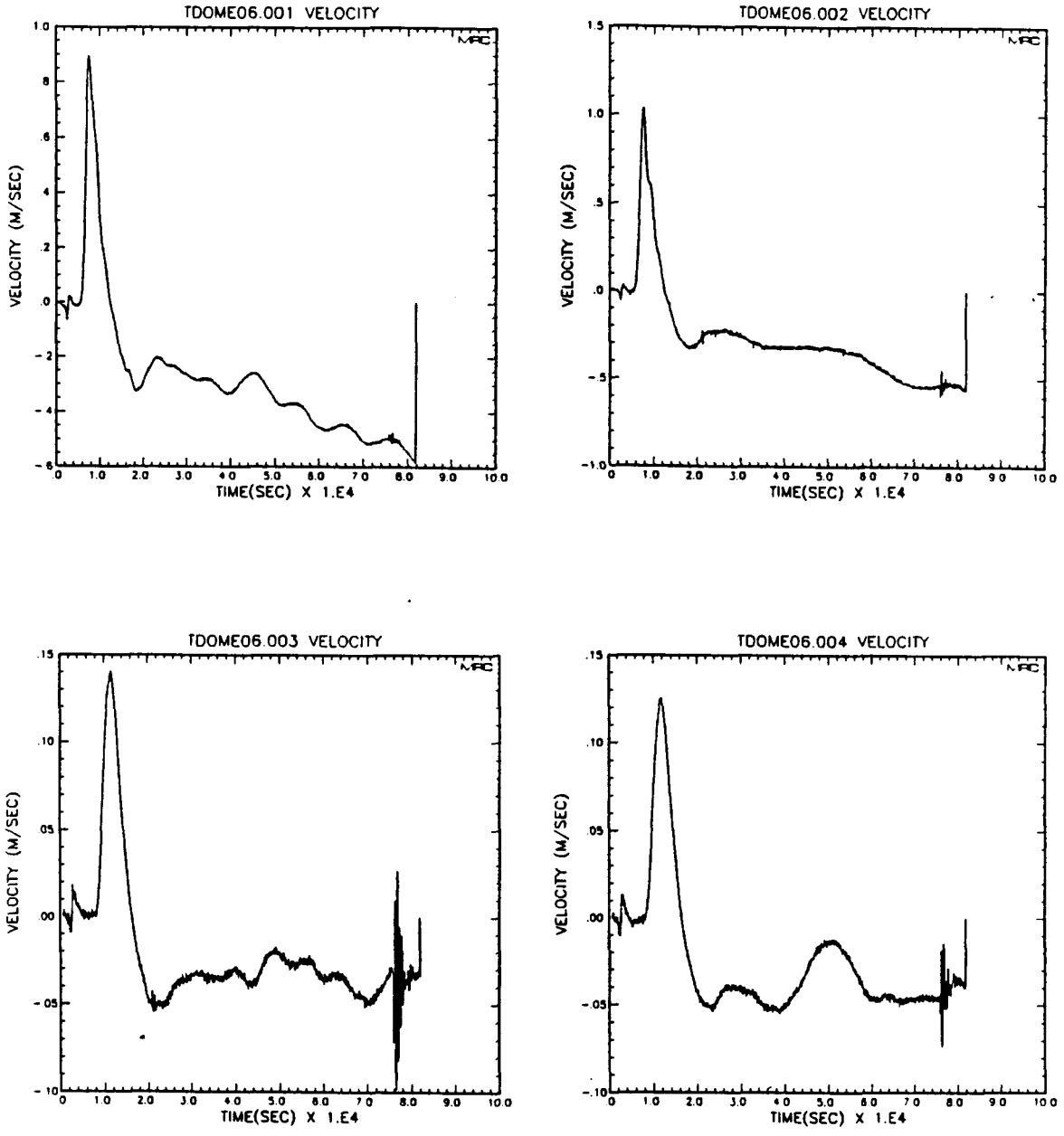

Figure C-1. Velocity records from the DOMEO6 experiment.

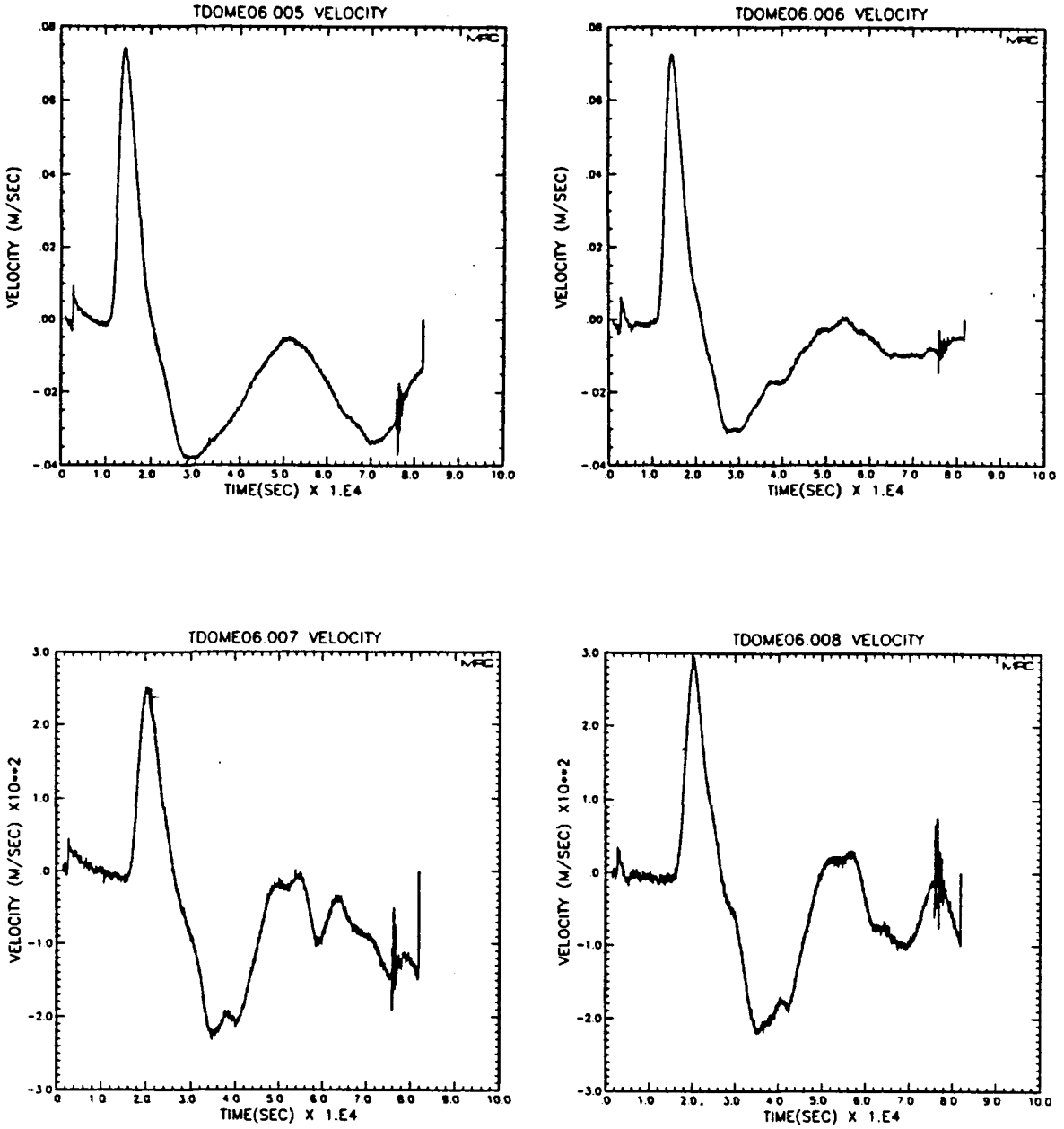

Figure C-1. Velocity records from the DOMEO6 experiment (continued).

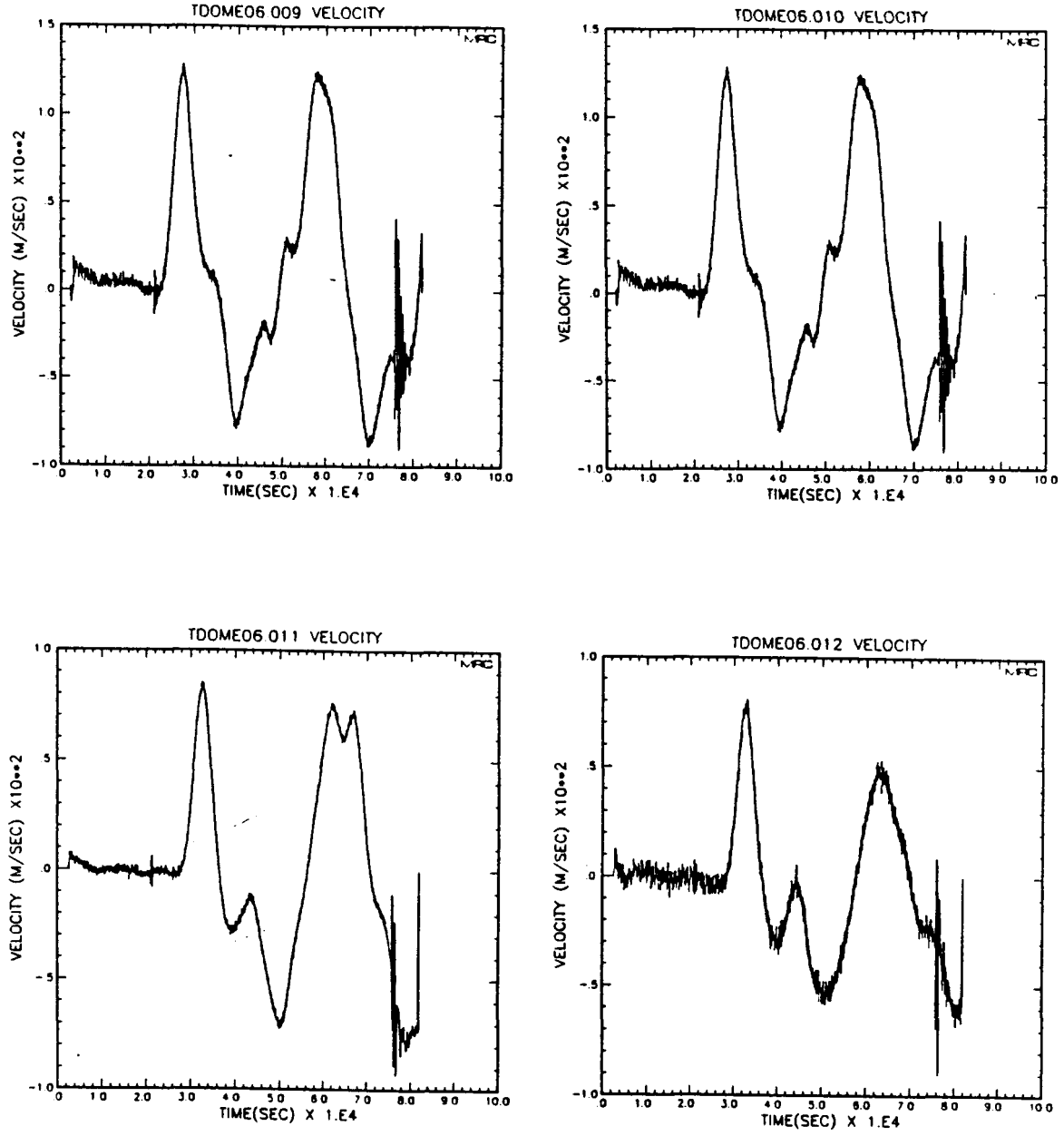

Figure C-1. Velocity records from the DOMEO6 experiment (continued).

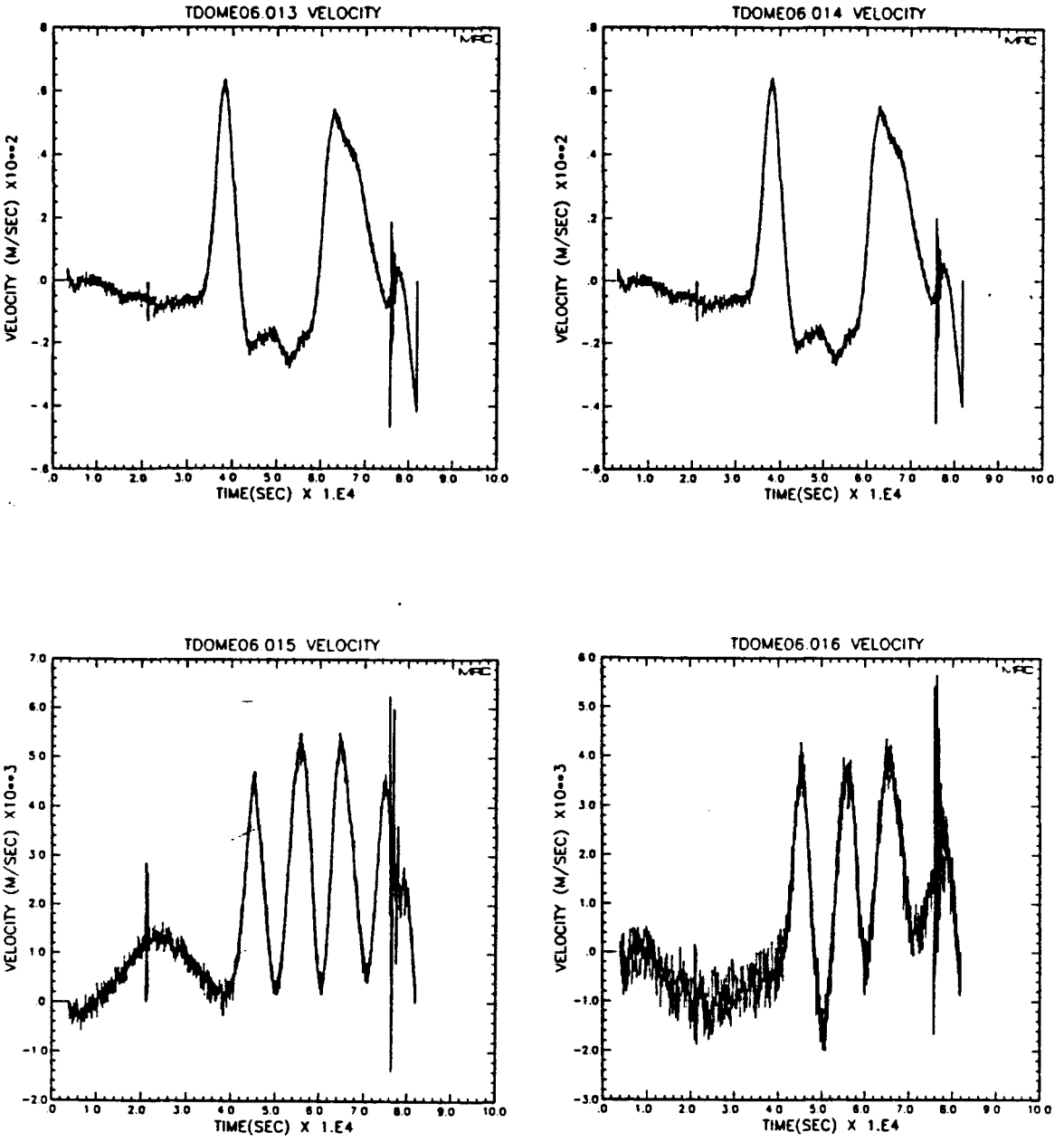

Figure C-1. Velocity records from the DOMEO6 experiment (continued).

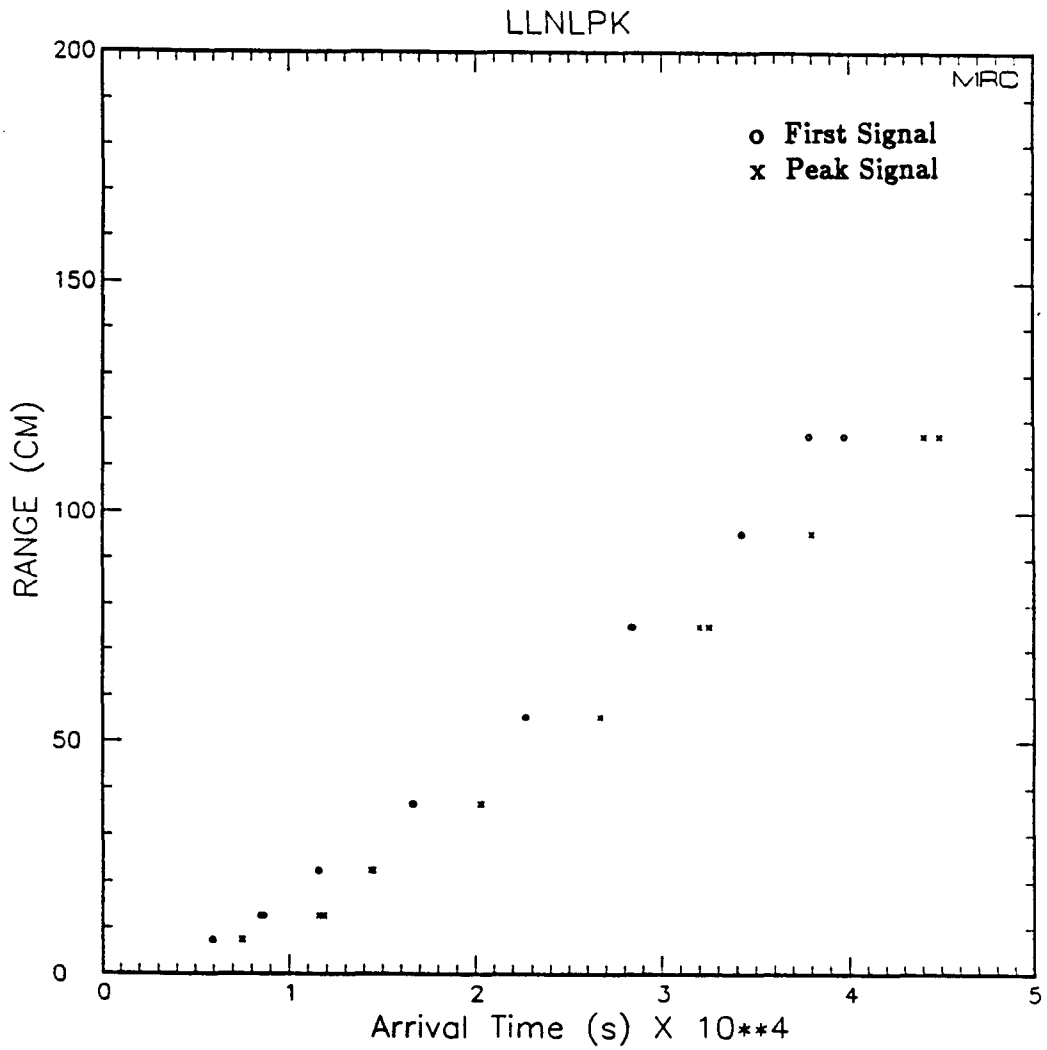

Figure C-2. Arrival times of pulse and first peak in the pulse plotted against the range to the sensor.

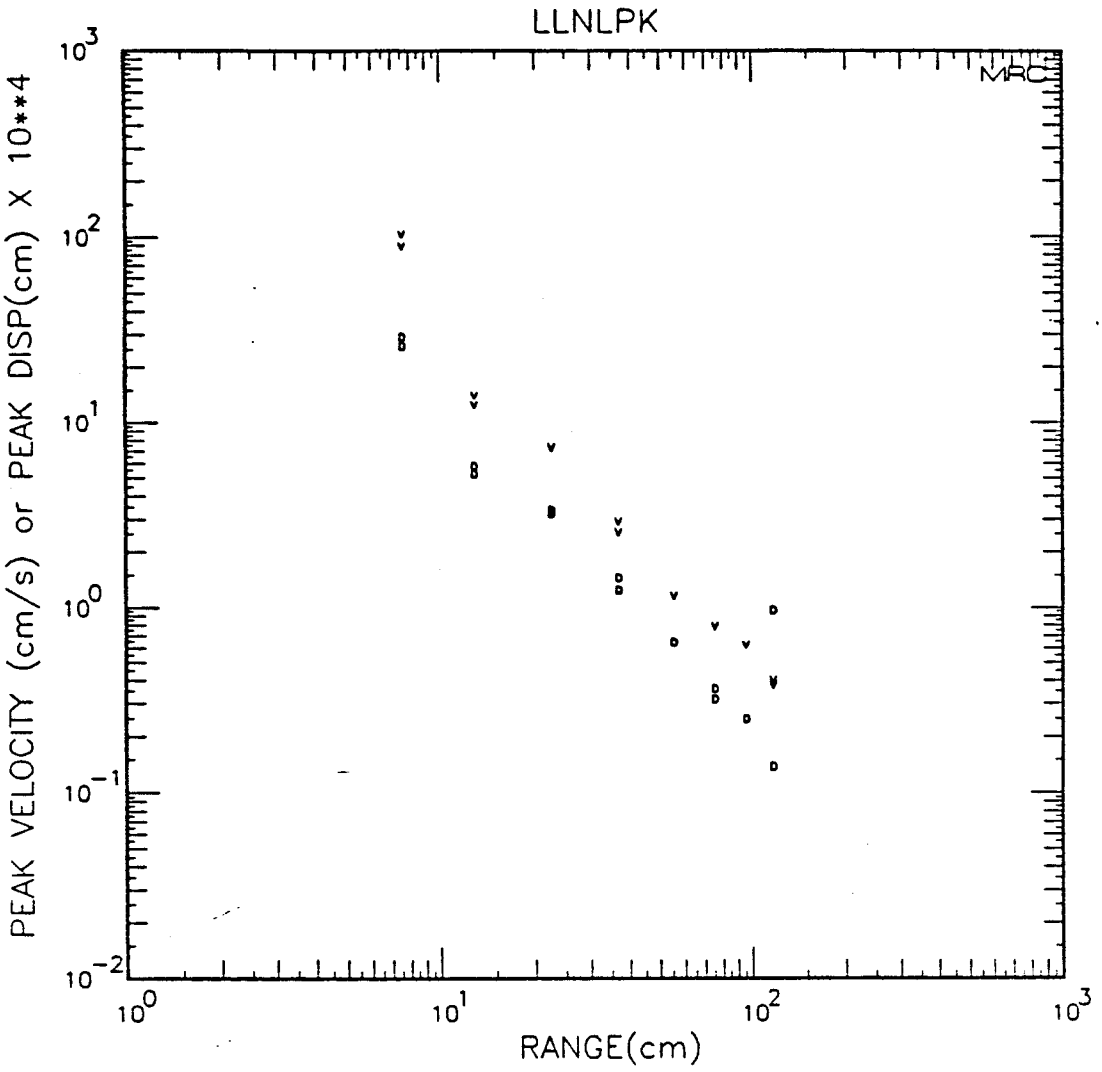

Figure C-3. Peak velocities and displacements as a function of the range to the sensor.

a decrease of attenuation with decreasing amplitude. However, these data are not of sufficient quality to draw any firm conclusions.

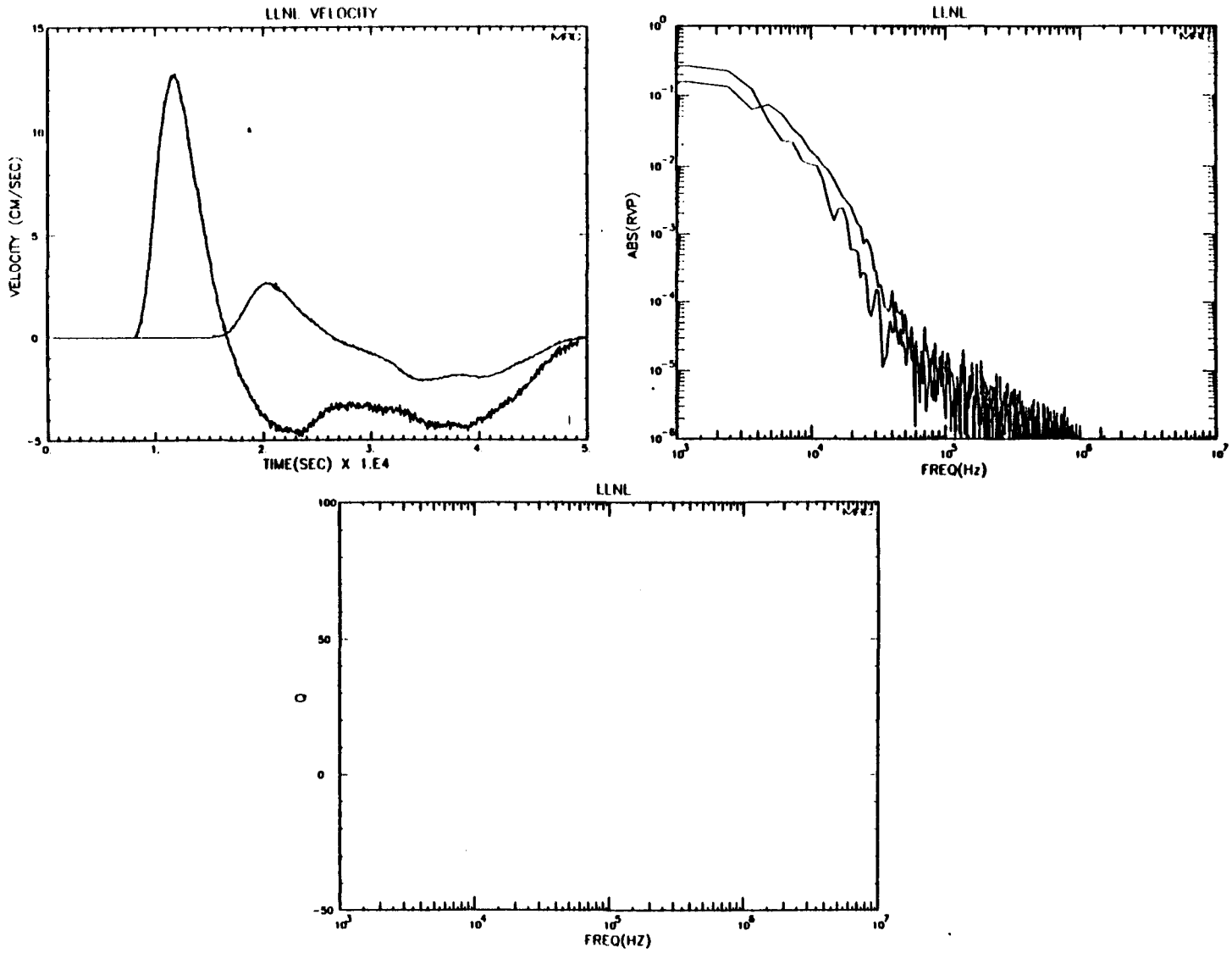

Figure C-4. Records 4 and 7, RVPs and Q estimate.

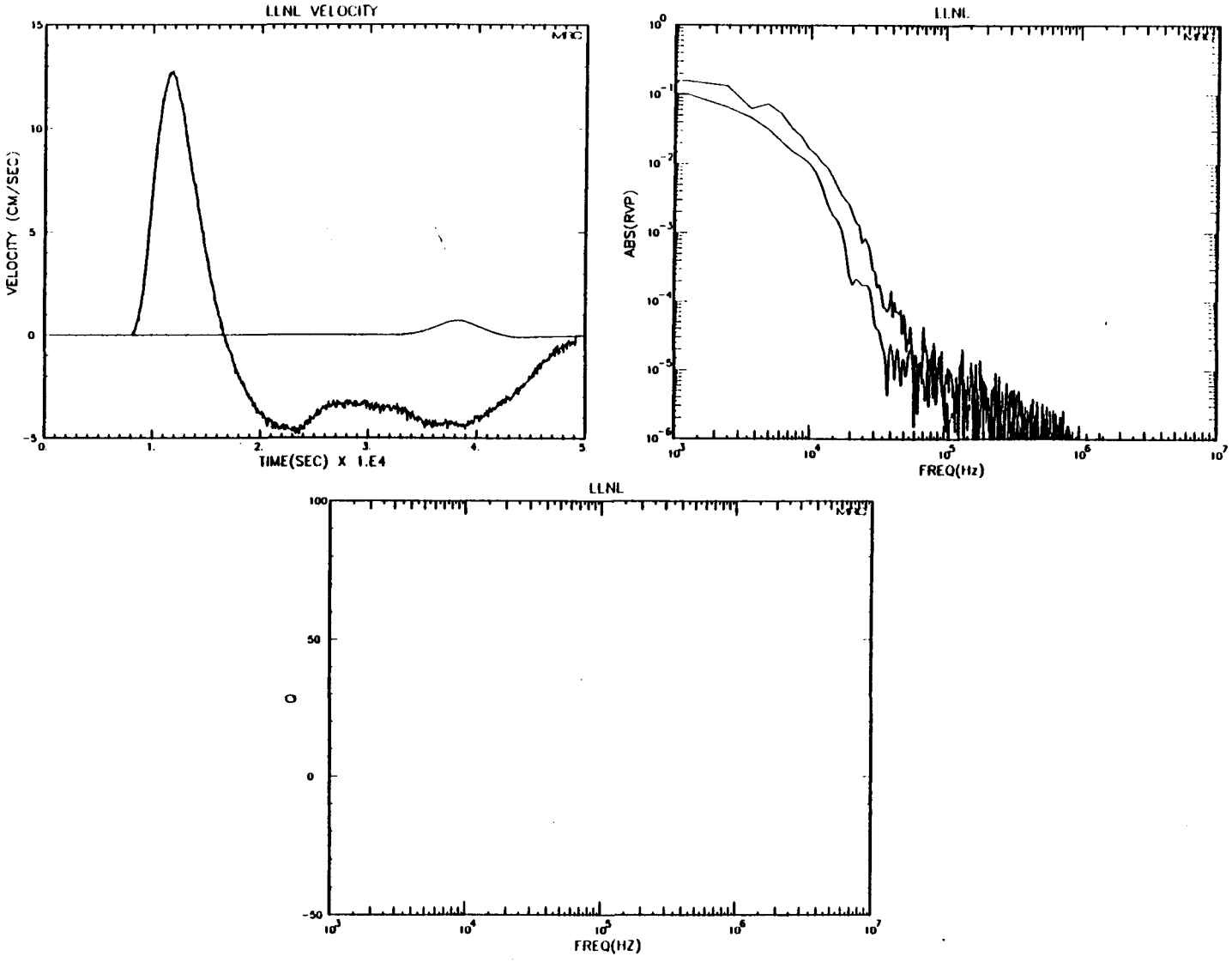

Figure C-4. Records 4 and 7, RVPs and Q estimate (continued).

Appendix D

LLNL SIERRA GRANITE SMALL SCALE EXPERIMENT

In 1987, a small scale simulation of explosively generated pulse propagation in a Sierra granite model was carried out at Lawrence Livermore National Laboratory. For this a 0.622 kJ sample of high explosive was detonated in a Sierra granite block approximately one cubic meter in volume. Velocity sensors were placed at several ranges from the source so that the attenuation could be determined. The ranges to the sensors along with other properties are indicated in Table D-1. The raw data records from the sensors are reproduced in Figure D-1.

The times for onset of signal at the sensors and the times for the first peak signal are given in Figure D-3. The propagation speeds associated with the differences in arrival times are quite stable, especially after the first few, and the compressional speed is approximately 3.8 km/sec. Peak velocities and displacements (as determined by a direct integration of the velocity records) are given in Figure D-4. These are remarkably smooth for both quantities indicating that the results may be taken to be give a meaningful measure of the attenuation.

We have attempted to estimate the effective Q associated with the attenuation by forming the ratio of the RVPs taken from "corrected" records, that is, those with the obviously inappropriate tails smoothly removed after the first cycle. Figure D-5 shows as a best case the corrected records 6 and 9 (mean strain $\approx 1.9 \times 10^{-5}$), the RVPs and a scatter plot of the Q as a function of frequency. The trends which seem clear are for Q to be small at frequencies below the corner frequency ($\approx 3 \times 10^4$ Hz), and for Q to increase mildly above. Above about 10^5 Hz the noise swamps the signal. The Q value in the neighborhood of the corner is about 15. The Q from four pairs of records is shown in Figure D-6. For these cases (with mean strains from 3.3×10^{-4} to 4.2×10^{-6}) the Qs are rather irregular but some trends are evident. First, all the examples show that the effective Q becomes small at frequencies below the corner frequency. Second, the Qs tend to increase with increasing strain, at least at lower frequencies. Finally, the Qs at larger frequencies do not show any particular trend but they are rather irregular. For the most part, these data are not of sufficient quality to draw any firm conclusions but the suggested trends do follow those from other such experiments.

Table D-1. SIERRAL42 Sensor Properties.

Sensor #	Range (meters)
1	0.078
2	0.108
3	0.144
4	0.144
5	0.205
6	0.304
7	0.304
8	0.457
9	0.669
10	0.669
11	0.925
12	1.209
13	1.209
14	1.505
15	1.505
16	1.807

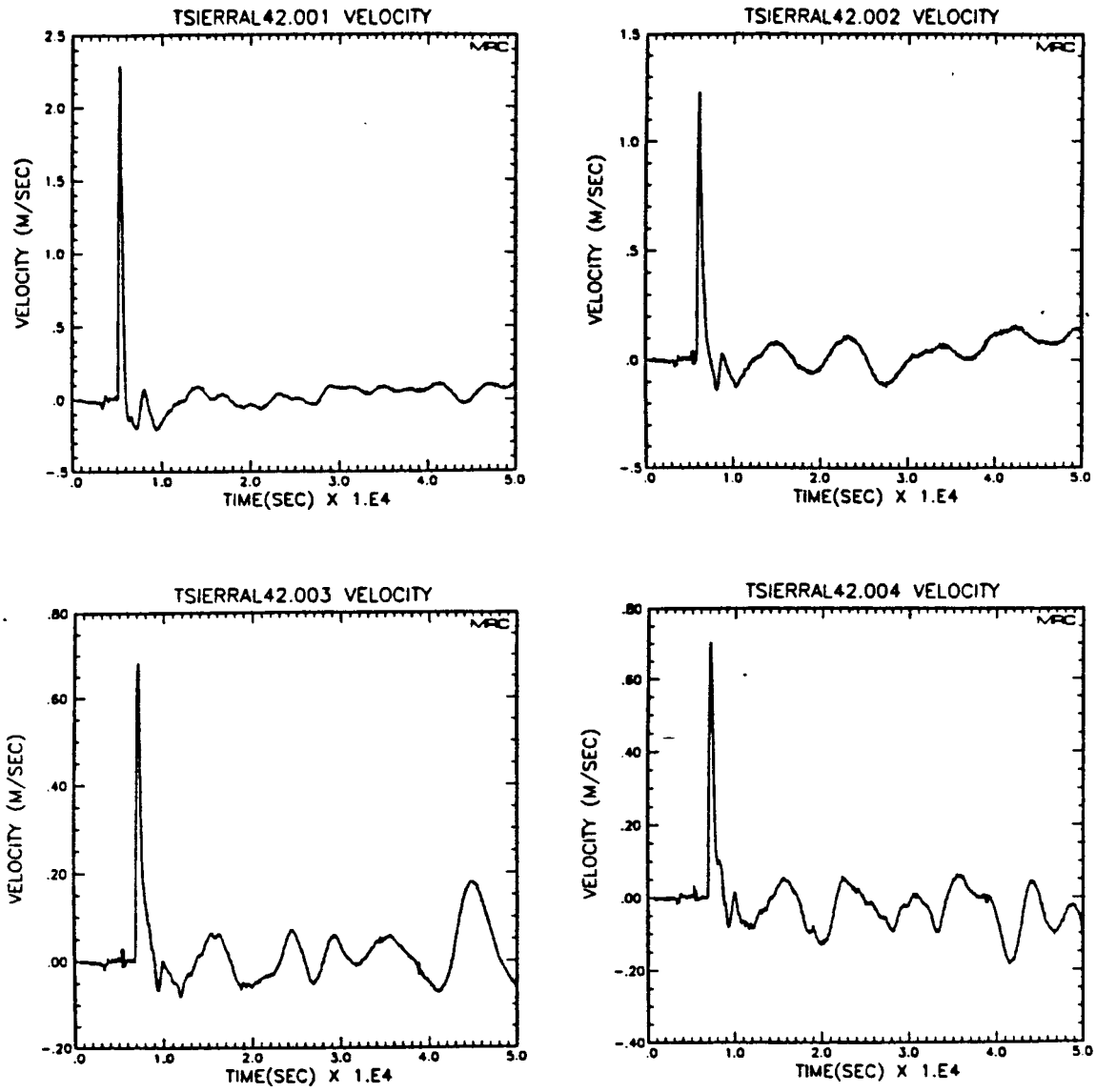

Figure D-1. Velocity records from the SIERRA42 experiment.

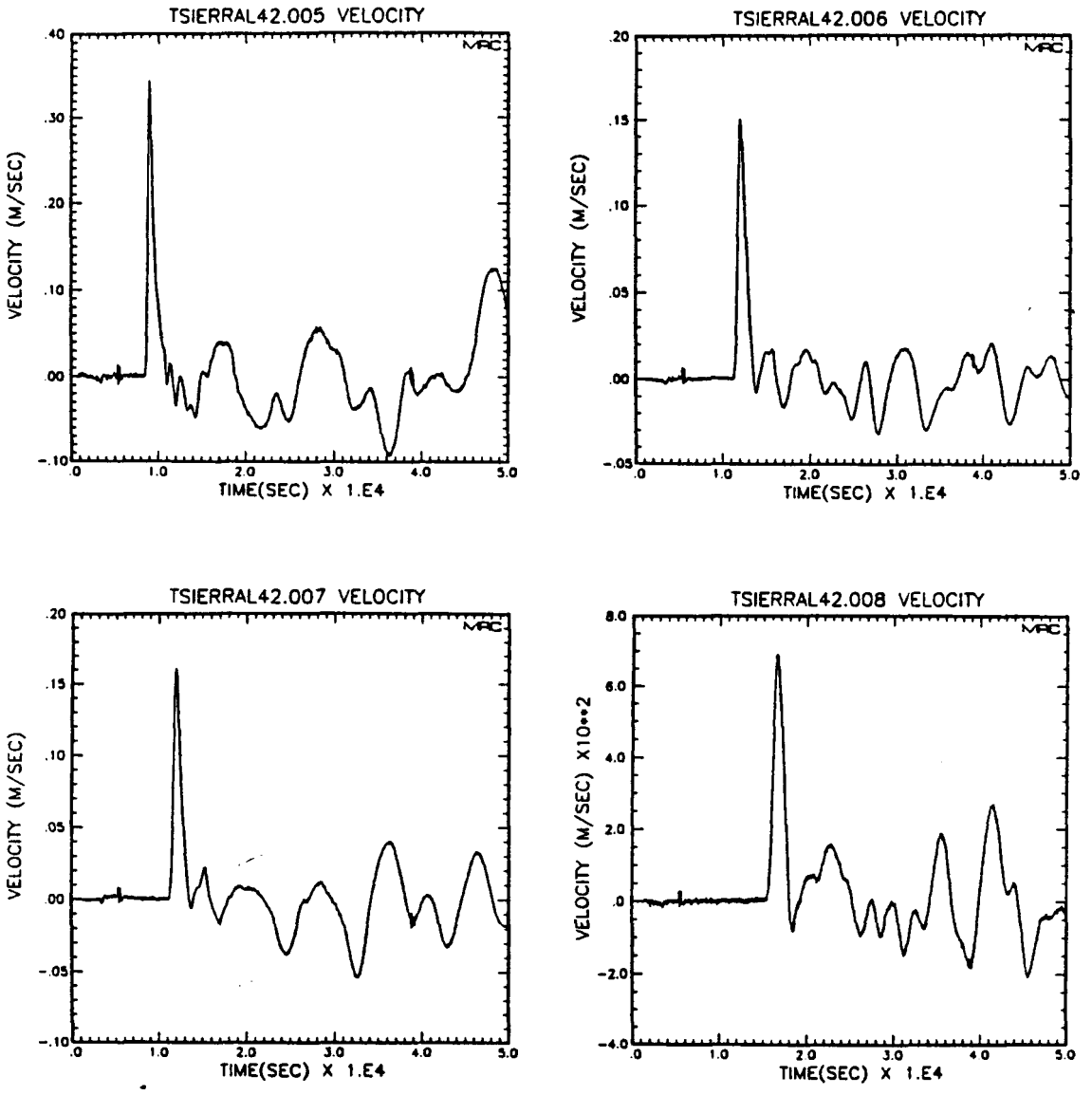

Figure D-1. Velocity records from the SIERRA42 experiment (continued).

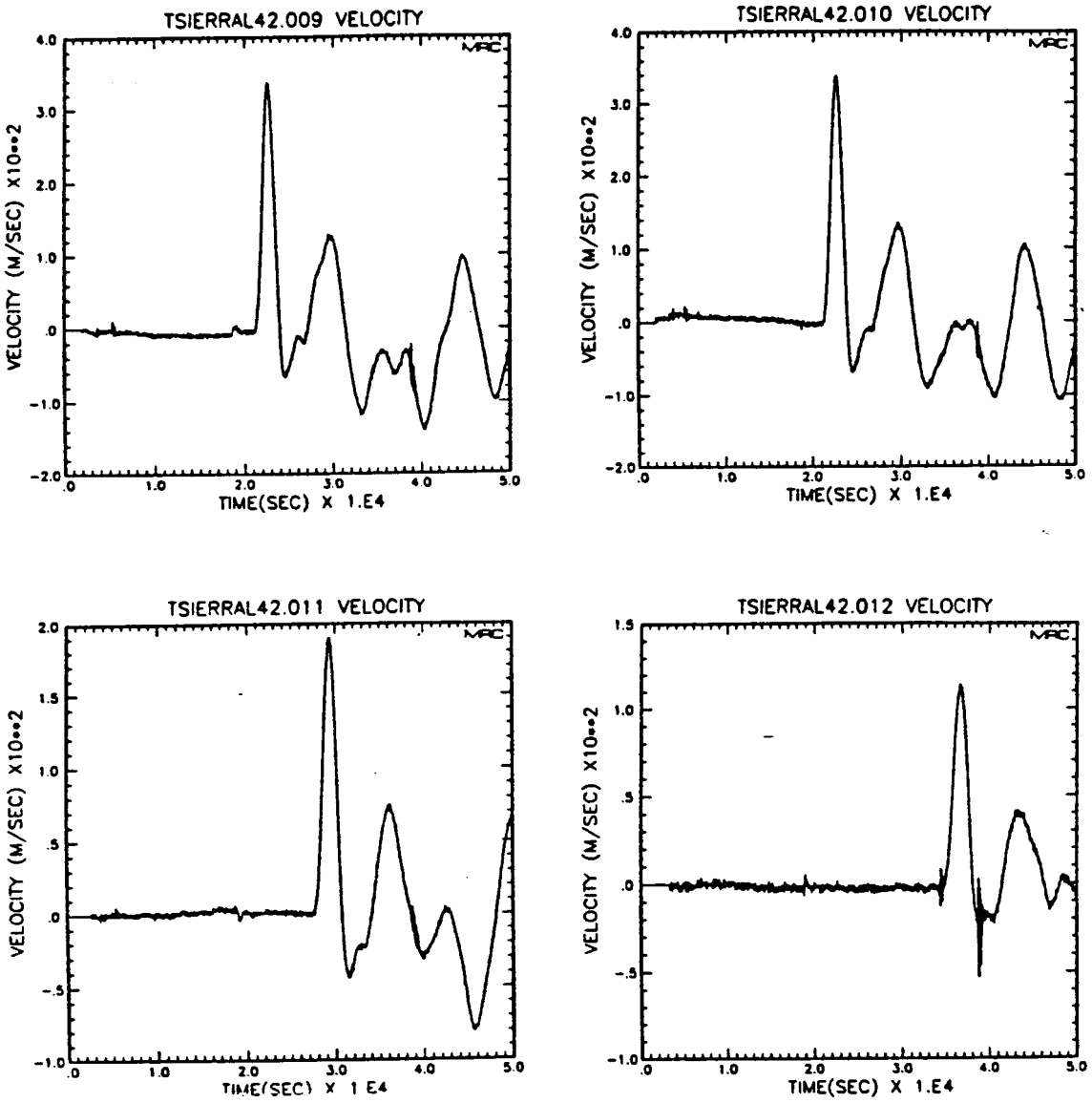

Figure D-1. Velocity records from the SIERRA42 experiment (continued).

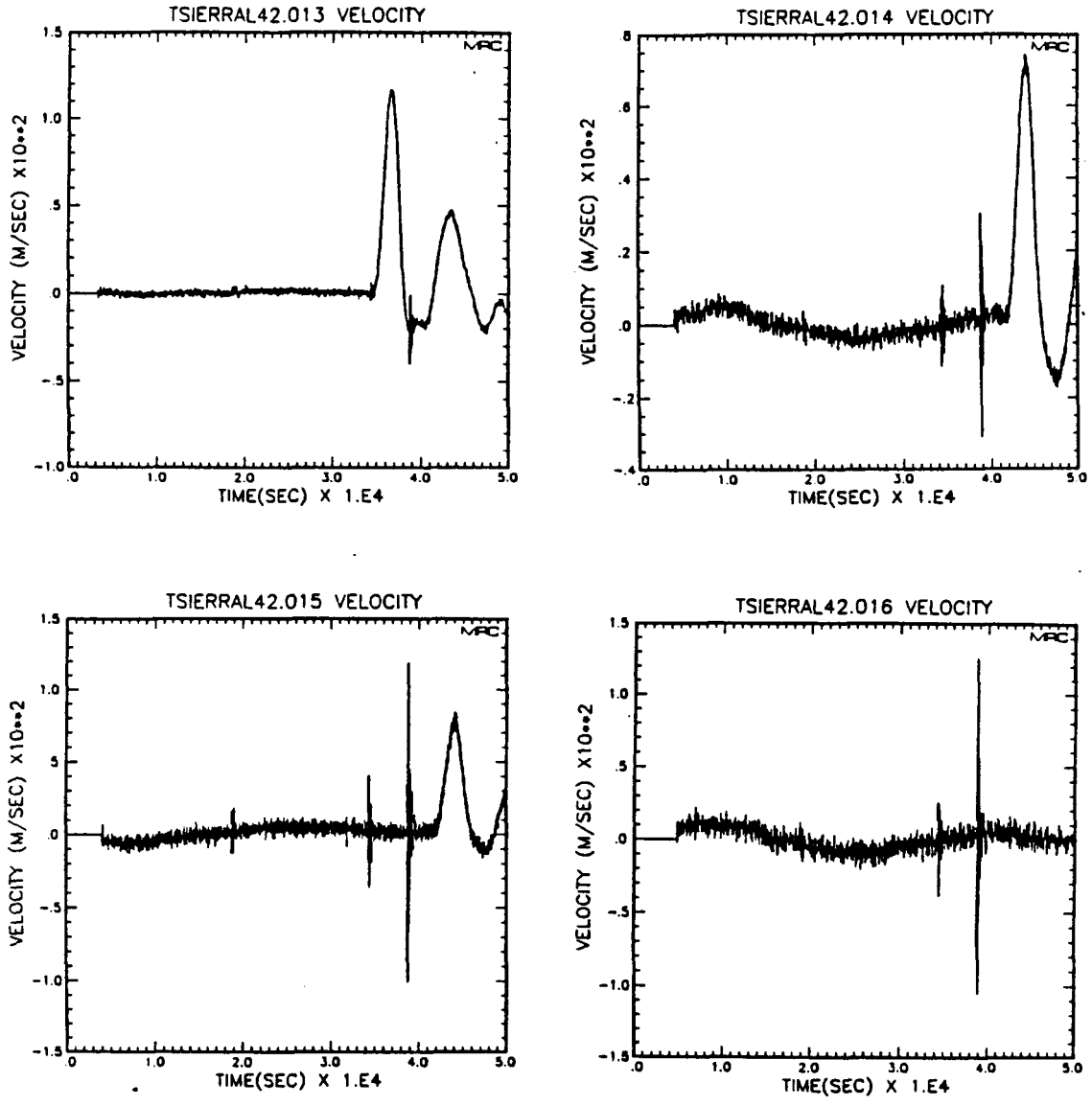

Figure D-1. Velocity records from the SIERRA42 experiment (continued).

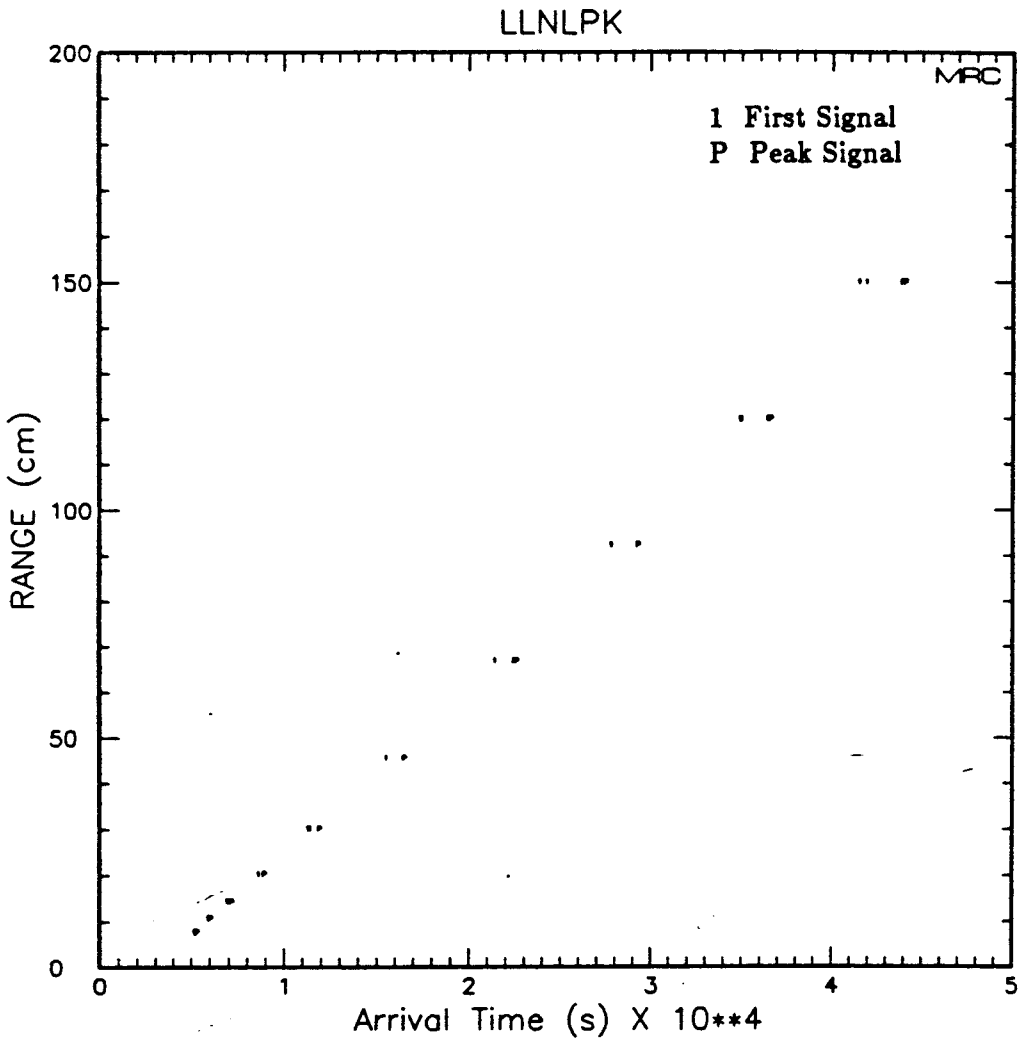

Figure D-2. Arrival times of pulse and first peak in the pulse plotted against the range to the sensor.

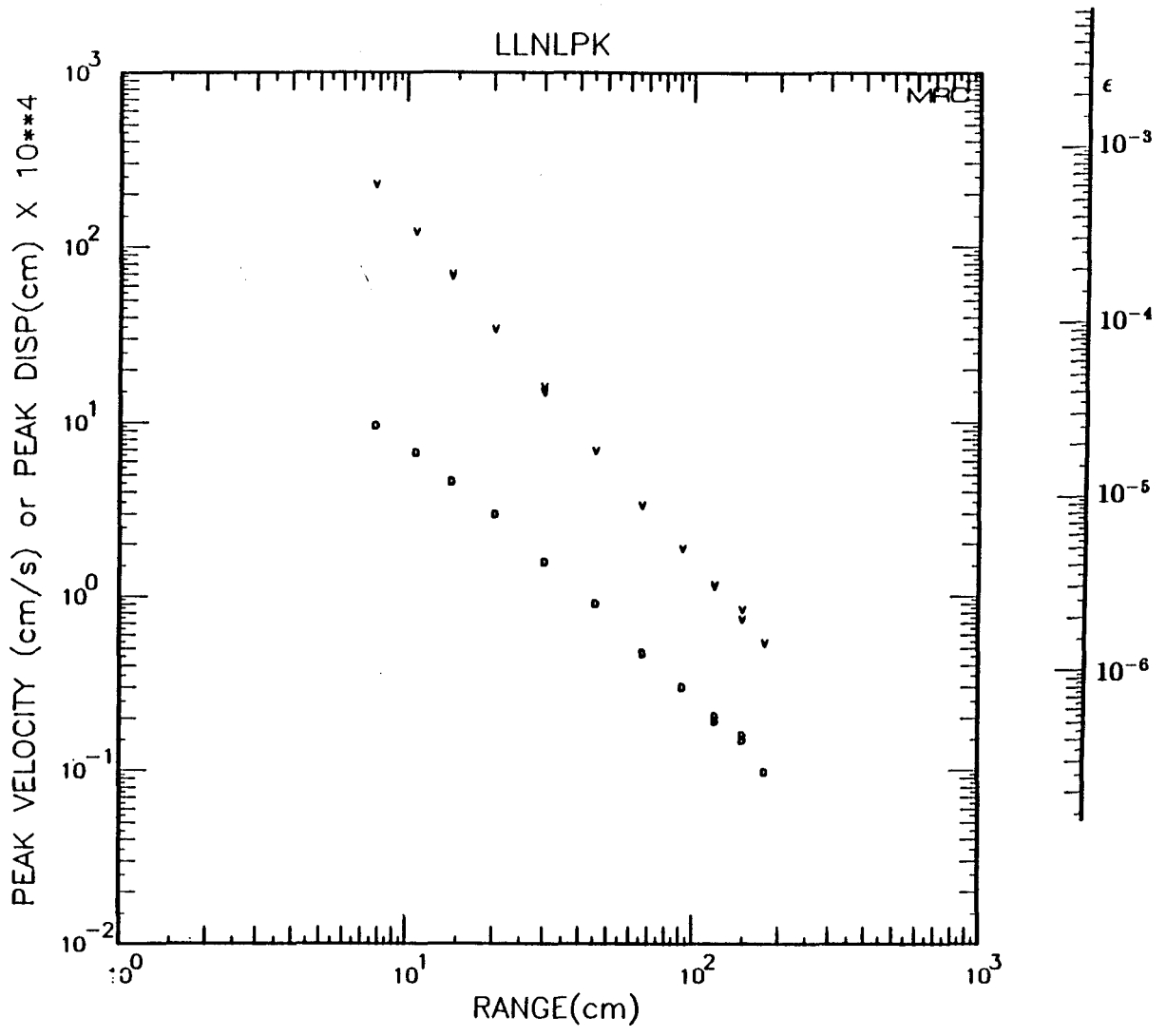

Figure D-3. Peak velocities and displacements as a function of the range to the sensor.

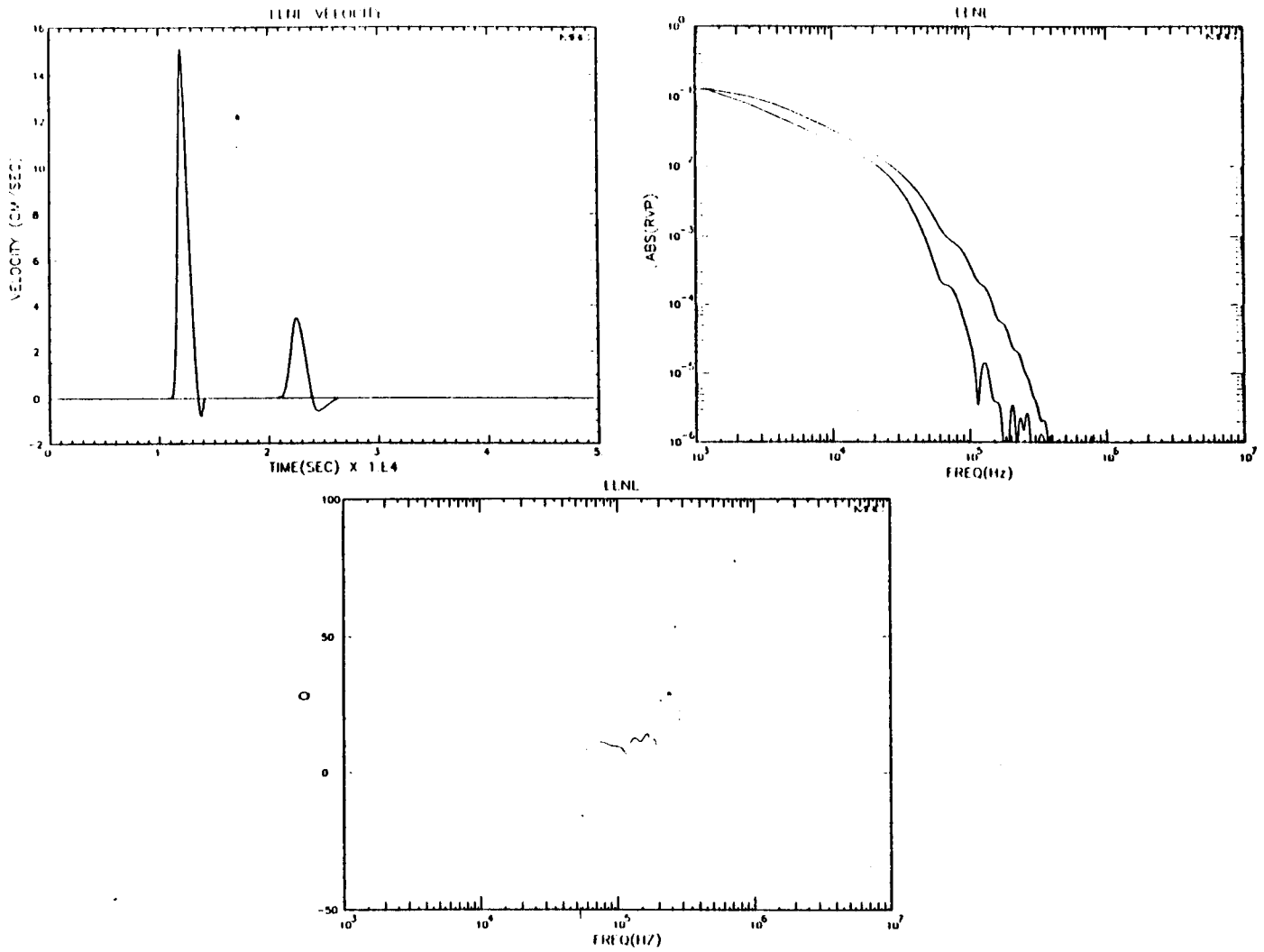

Figure D-4. Records 6 and 9, RVPs and Q estimate.

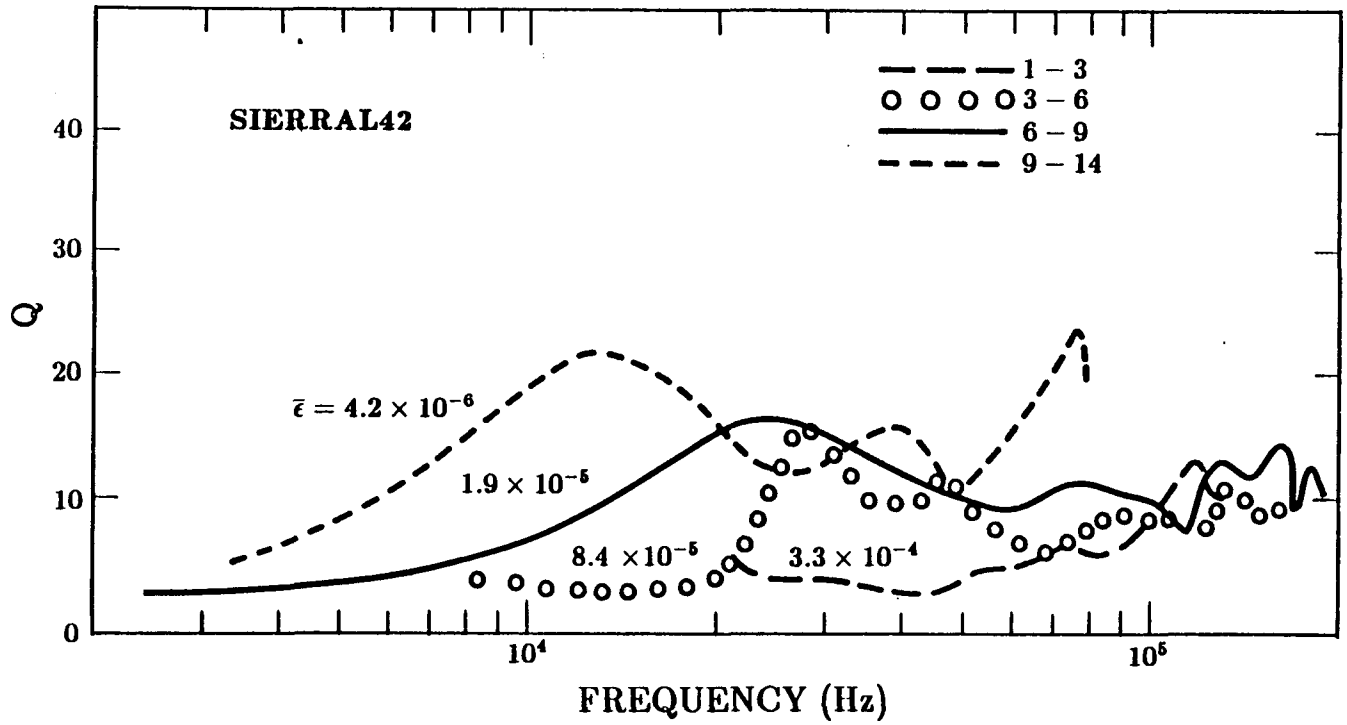

Figure D-5. Q estimates for four record pairs $\bar{\epsilon}$ is mean strain value.

The velocity and displacement peak values can be used to get an estimate to Q through a procedure similar to that employed by Minster and Day [1]. This consists of taking the velocity record at the closest range and determining how the peak values would have changed for a specified Q using Fourier synthesis. Following Minster and Day, we take a quasi-linear approximation to allow an estimate of the effects of a nonlinear Q. This is done by taking Q to be instantaneously constant over a short step and then changing the constant as the pulse progresses. Using this method, an effective Q which is a function of the local peak strain may be determined to fit the observed decay of peak amplitudes. The result of such an effort is given in Figure D-7. While the search for Q functions was not exhaustive, it was determined that the form

$$Q^{-1} = \frac{1}{20} + \frac{1}{20} * (V_{peak}/V_{smallest\ range})$$

gives as good a fit as can be managed with this linear form. Generally the velocity and displacement peaks fall off differently so as to restrict the mix of constant and linear forms needed. This indicates that the mean Q ranges only from about 10 to 20 over the range of the data so that strong nonlinearities in the sense of amplitude dependent effective Q are really forced by these data. However, this is not necessarily to say that the data are indicative of linear behavior. Since attenuation data in granite at strains below 10^{-6} typically give Qs of over one hundred, the totality of the data do suggest nonlinearity. However, these experiments are not adequate to define it character.

Records from SIERRAL42 have a noise component which is readily visible. The RVP and Q estimates from the records thus have a level of frequency domain noise which limits the utility of the estimates under some conditions. In order to determine significance of the noise, we have taken a single record and attempted to extract the noise contribution to the RVP. This has been done by selection of two portions of the record from sensor 9. The first being that from the single cycle of the pulse with smooth truncation of the record before and after and the other being a interval of equal length (about 0.6×10^{-4} sec) before the pulse arrives. This early segment consists of noise alone with the linear trends removed. The resulting data segments are pictured in Figure D-8. The resulting pair of RVP estimates from the two segments is shown in Figure D-9. The noise becomes comparable with the signal for frequencies greater than 10^5 Hertz. For lower frequencies, the signal rapidly becomes dominant. Since the portion of the spectrum for which granite Q estimates were found was below 10^5 Hertz, it is concluded that the noise does not play a significant role in these estimates.

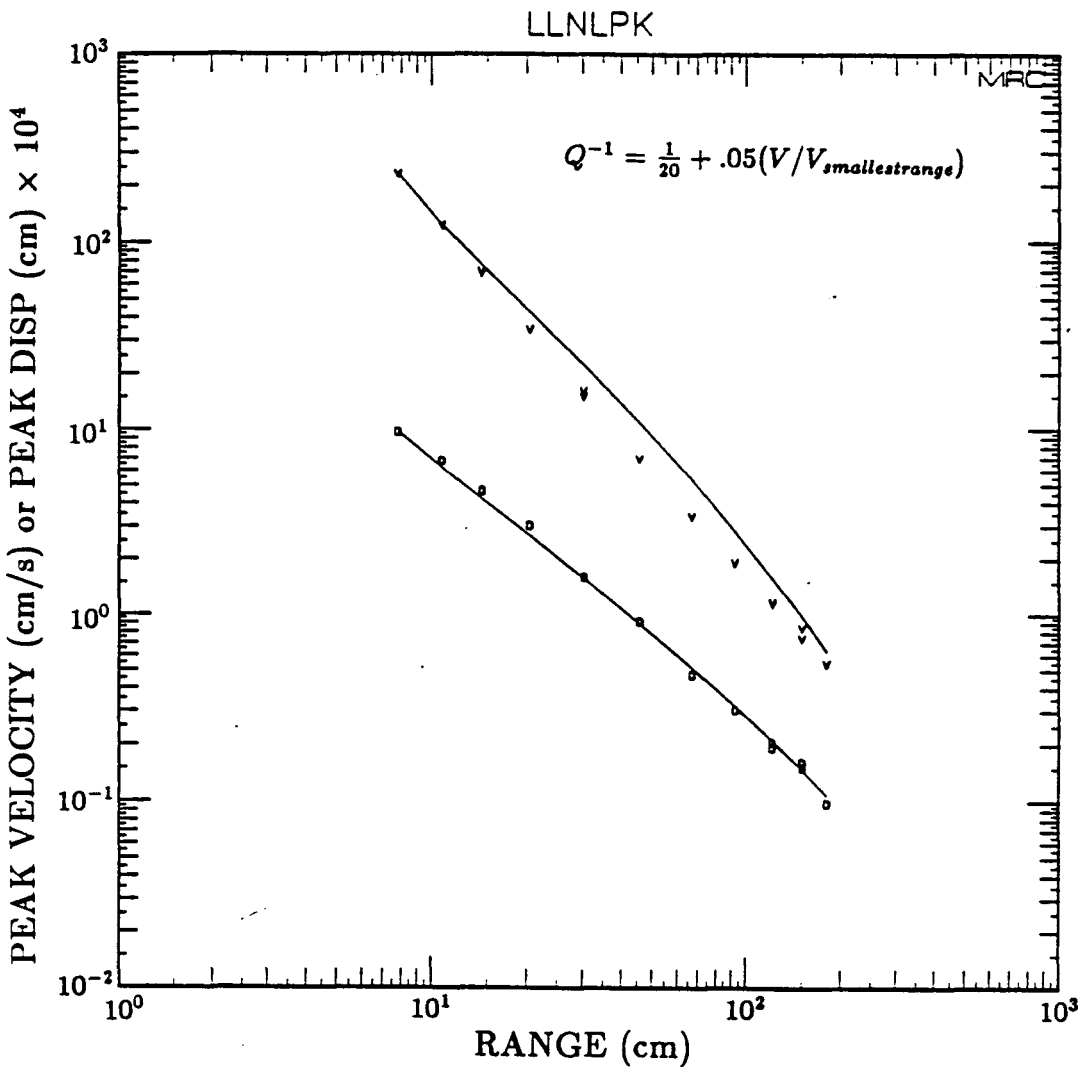

Figure D-6. Fit to peak velocity and displacements by an effective nonlinear Q function.

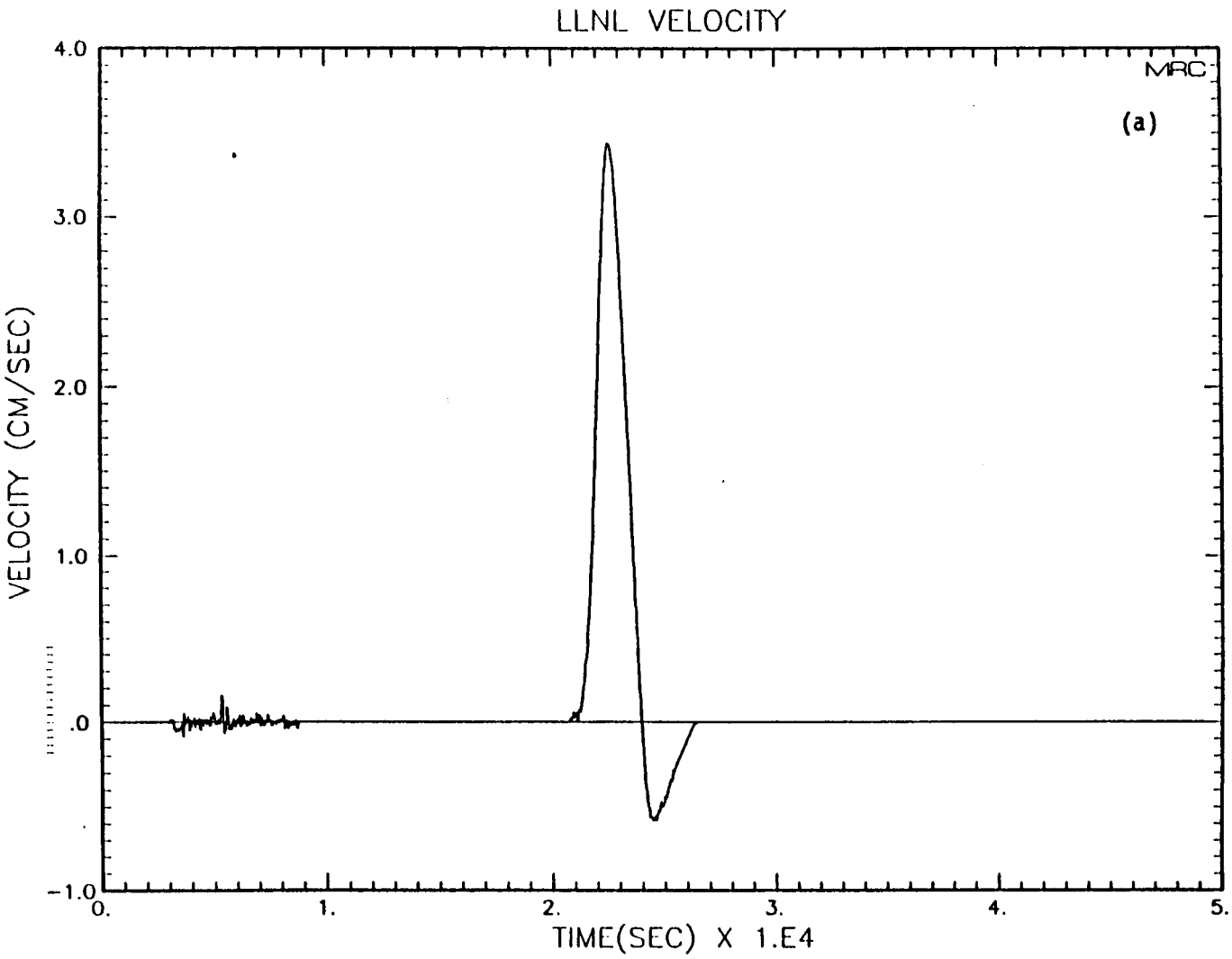

Figure D-7. Signal and noise segments from sensor 9 (a) and their RVPs (b).

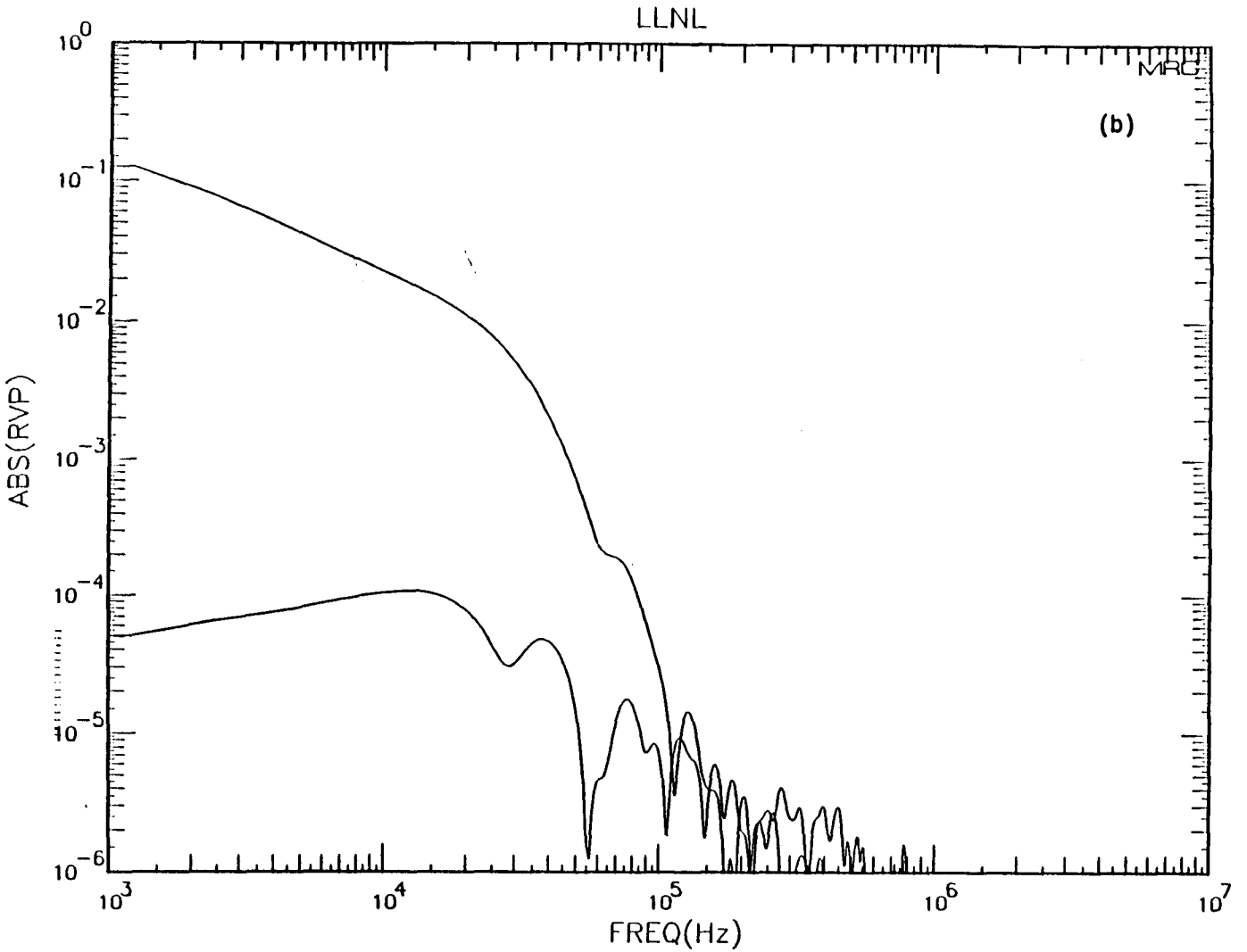

Figure D-7. Signal and noise segments from sensor 9 (a) and their RVPs (b) (continued).

APPENDIX D REFERENCE

D–1 Minister, J. B. and S. M. Day, "Decay of Wave Fields Near an Explosive Source Due to High-Strain Nonlinear Attenuation," J. Geophys. Res. 91, 2113 (1986).

Work performed under the auspices of the U.S. Department of Energy by Lawrence Livermore National Laboratory under Contract W-7405-Eng-48.